Springer Geology

Yu Huang · Faquan Wu
Zhenming Shi · Bin Ye
Editors

New Frontiers in Engineering Geology and the Environment

Proceedings of the International Symposium on Coastal Engineering Geology, ISCEG-Shanghai 2012

Springer

Yu Huang • Faquan Wu
Zhenming Shi • Bin Ye
Editors

New Frontiers in Engineering Geology and the Environment

Proceedings of the International Symposium on Coastal Engineering Geology, ISCEG-Shanghai 2012

Springer

Editors
Yu Huang
Department of Geotechnical Engineering
Tongji University
Shanghai
People's Republic of China

Faquan Wu
Institute of Geology and Geophysics
Chinese Academy of Sciences
Beijing
People's Republic of China

Zhenming Shi
Department of Geotechnical Engineering
Tongji University
Shanghai
People's Republic of China

Bin Ye
Department of Geotechnical Engineering
Tongji University
Shanghai
People's Republic of China

ISBN 978-3-642-31670-8 ISBN 978-3-642-31671-5 (eBook)
DOI 10.1007/978-3-642-31671-5
Springer Heidelberg New York Dordrecht London

Library of Congress Control Number: 2012942020

Printed on acid-free paper

Springer is part of Springer Science+Business Media (www.springer.com)

Preface

A better living in the future environment is the common wish of the whole of humankind. Since most metropolitan cities are located in coastal regions, coastal engineering geology has become a major concern in human activities. Many engineering geological problems have been encountered in the process of planning, construction, and service in coastal regions.

Bin Ye	Bjorn Schouenborg
Bruce Riddolls	Cheng Zhao
Chenrong Zhang	Dmitry Malinin
Dmitry Sergeev	Eric Yee
Fang Liu	Faquan Wu
Feifan Ren	Fernando Barrio
Guanlin Ye	Henry Hongwen Zhang
Inmaculada Rodriguez	James S. Griffiths
Jie Zhang	Keith Turner
Mark van der Meijde	Mashaallah Khamehchiyan
Michael Cocjin	Morteza Hashemi
Ozgur ACIR	Paul Nathanail
Ping Yang	Resat Ulusay
Robert Hack	Ruilin Hu
Runqiu Huang	Sharon Leigh Cundill
Shengwen Qi	Simin Jiang
Steve Parry	Umberto Gori
Xiaoying Zhuang	Xilin Lu
Xiaoying Zhuang	Yong Tan
Yonggui Chen	Yujun Cui

This proceedings contains 53 peer reviewed technical papers presented during the International Symposium on Coastal Engineering Geology held in Shanghai, China, September 20–21, 2012. The papers discuss a variety of topics including land resources development and utilization, geo-environmental problems, geodisaster prevention, and mitigation in coastal regions. This collection of papers covers recent case histories, theoretical advances, laboratory and field testing, and design methods beneficial to practitioners, researchers, and other professionals.

Each paper published in this proceedings was evaluated by two or more reviewers. The editors would like to thank the authors for their contributions and to the following 38 individuals who reviewed one or more papers for this geotechnical special publication:

Under the auspices of the International Association for Engineering Geology and the Environment (IAEG), the International Symposium on Coastal Engineering Geology was hosted by Tongji University and the China National Group, IAEG. The editors would like to express their gratitude to all participants who came a long way from different parts of

the world. Special thanks must be given to Prefessors Carlos Delgado, Runqiu Huang and Yongsheng Li who were instrumental in organizing the international symposium. We also wish to thank the National Natural Science Foundation of China and Tongji University for their invaluable support and sponsorship which made this symposium possible.

China, May 30, 2012

Yu Huang
Faquan Wu
Zhenming Shi
Bin Ye

Contents

Co-Seismic Fault Effects of Landslides Triggered by Wenchuan Ms 8.0 Earthquake, China

R. Q. Huang and W. L. Li

Abstract

"5.12" Wenchuan Earthquake (Ms = 8.0) triggered tens of thousands of landslides throughout an area of about 100,000 km^2. The distribution of landslides is definitely affected by the such factors as geomorphology, topography, lithology and human engineering activities, but the distribution of earthquake-triggered landslides are mainly controlled by the co-seismic fault, for they present zontal distribution along the co-seismic fault. Through the studies of three geo-hazard concentration areas including Dujiangyan to Wenchuan Road, Beichuan to Anxian County area, and Magong to Hongguang area, it is found that Wenchuan Earthquake-triggered landslides has the following co-seismic effects: (1) Wenchuan Earthquake is a thrust fault earthquake, the distribution of landslides show marked "hanging wall and footwall effects", manifested by that the distribution concentration in the hanging wall of seismic fault is higher than that in the footwall and the former coverage is wider than the latter as well as that the scale of landslides is larger than that in the footwall; (2) the strong development zones of landslides are within the range of 7 km in the hanging wall of co-seismic fault. The ranges of 7–11 km in the hanging wall and 0–5 km in the footwall can be delimited as the middle development zones. A vast majority of large-scale landslides are distributed within the range of 5 km from the fault, and large-scale landslides are unlikely to occur within the range of over 10 km; (3) the transitional and staggered positions of fault are the concentration areas of landslides and large-scale landslides are likely to occur in these positions; (4) the preferred direction of landslide is NW–SE, basically vertical to the spreading direction of Yingxiu-Beichuan Fault. This may be because that Longmenshan Fault Zone has always been affected by the tectonic stress field of NW–SE extrusion area since Cenozoic Time; (5) the earthquake-triggered landslides mainly occur in the zones of seismic intensity IX and higher. The concentration of landslides in the seismic intensity zones XI is the same with that in seismic intensity zones X; the concentration in the seismic intensity zones IX equals to 1/3 of the abovementioned one; the concentration in the seismic intensity zones VIII is only 1/10 of the abovementioned one.

Keywords

Wenchuan earthquake • Co-seismic landsliding • Earthquake fault effect • Hanging wall effect • Locked segment effect

1 Introduction

At 14:28 May 12, 2008 (Beijing time), a great earthquake measured at 8.0 Ms according to the China Seismological Bureau struck Yingxiu Town (31.0°N, 103.4°E) of WenchuAnxian County, 70 km northwest of Chengdu, the

R. Q. Huang (✉) · W. L. Li
State Key Laboratory of Geo-hazard Prevention and Geoenvironment Protection, Chengdu University of Technology, Chengdu, 610059, People's Republic of China

Y. Huang et al. (eds.), *New Frontiers in Engineering Geology and the Environment*,
DOI: 10.1007/978-3-642-31671-5_1,

capital of Sichuan, causing the frontal and central faults (Jingyou-Guanxian Fault and Yingxiu-Beichuan Fault) of the Longmenshan Fault Zone between the Western part of the Sichuan Basin and the eastern margin of the Qinghai-Tibet Plateau to rupture, resulting in the formation of an earthquake rupture zone of around 300 km long (Huang 2008; He et al. 2008). The Wenchuan earthquake had a high magnitude and large energy release causing a strong destructive force and large area of influence. The epicenter of the strong earthquake was located in the medium to high mountain areas just West of Sichuan Basin, where the geological environment is quite weak, therefore a large number of landslides such as slope collapses, debris flows and landslides were triggered. Their extremely large numbers, wide coverage, complex types and serious destruction shocked the people all over the world. It is estimated that the number of earthquake-triggered landslides by this event was over 50,000 throughout an area of about 440,000 km^2 (Huang 2008).

Early studies on historical earthquakes indicate that the landslides such as landslides and collapses will be triggered when the magnitude of earthquake is higher than 4.0 (Keefer 1984; Yao 1986; Li 2003). Earthquake-triggered landslides have aroused people's concern widely for the heavy destruction they have brought. Just in the Twentieth century, earthquake-triggered landslides have caused the death of tens of thousands of people and the material loss of billions of dollars in the world (Li 2003). A large earthquake in a mountainous region can trigger thousands of landslides throughout areas of more than 100,000 km^2 in a few minutes, and the loss caused by landslides account for about 40 % in the total loss resulting from earthquake (Solonenko 1976; Keefer 1984). Not only did Seismologists and geologists carry out the studies to clarify the internal dynamics of the earthquake event (Hu 1995; Mao et al. 1998), but they also applied statistical methods to analyze the relationship between the distribution of landslides and such factors as the earthquake magnitude, seismic intensity, the distance from the epicenter or the surface projection of the fault rupture, the slope steepness and the rock type after many earthquakes (Keefer 1984, 2000; Jibson et al. 2000; Wang et al. 2002; Bao et al. 2005; Mohammad et al. 2006). The Wenchuan earthquake triggered tens of thousands of landslides, which provided lots of scientific data for earthquake-triggered landslides study.

After the "5.12" Wenchuan earthquake, the Ministry of Land and Resources (MLR) immediately organized dozens of geologist terms from the whole country to make an inventory of the landslides that directly threaten people's lives and property in the 42 earthquake-hit counties of Sichuan province. The identified landslides, collapses and debris flows were around 15,000, in which there were 4,970 newly increased landslides including 1,701 landslides, 1,844 collapses, 304 debris flows and 1,093 unstable slopes (Yin 2008).

However, the abovementioned inventory is only directed at the hazards that directly threaten people's lives and property. There are numerous slope-collapses, debris flows and landslides in uninhabited regions or posing only indirect threat to the human habitat. Their estimated number of these additional landslides is 30,000–40,000. As these additional landslides are numerous and spread over a large area, it is difficult to map their locations in a short period; we have to resort to the various remote-sensing (RS) data collected after the earthquake. (1) The imagery of the Japanese satellite ALOS (with a spatial resolution of 10 m); (2) the aerial photography collected by the Air Command and the China Aero Geophysical Survey and Remote Sensing Center for Land and Resources; (3) other RS data sources (SPOT, ETM, etc.). The interpreted number of landslides in 10 extremely serious earthquake-hit counties and 6 serious earthquake-hit counties was 6,877, together with the investigated 4,311 geohazrds, constituting the total number of 11,308 (Fig. 1). Huang and Li (2009) analyzed the relationship between the distribution of these landslides and the distance from co-seismic fault, slope, elevation, and lithology, and found that Wenchuan Earthquake-triggered landslides presented the zontal distribution along the co-seismic fault and the linear distribution along the rivers; the areas within the range of 10 km from the co-seismic fault in the hanging wall, the gradient range of 20–50 ° and the canyon section with the elevation of below 1500–2000 m were strong development zones of landslides; different lithology had nothing to do with the development of landslides, but it determined the type of landslides. Generally speaking, landslides usually occur in the soft rocks, whereas rockfalls and avalanches are likely to occur in hard rocks.

The distribution of landslides is definitely affected by the such factors as geomorphology, topography, lithology and human engineering activities, but the distribution of earthquake-triggered landslides are mainly controlled by the co-seismic fault. Most scholars analyzed the relationship between the distribution of landslides and the distance form the co-seismic fault and discovered the rule that the distance from the co-seismic fault is in inverse ratio to the development of landslides (Keefer 1984; Rodriguez et al.1999; Jibson et al. 2004). However, Huang and Li (2009) have already pointed out that when the distance from the co-seismic fault was the same, the concentration of landslides in the hanging wall of fault was obviously higher than that in the footwall; the concentration of landslides in the staggered and transitional positions of fault was also comparatively high. This suggests that the co-seismic fault has some specific effects on the distribution of landslides, but there are few studies on this aspect. Thus, based on the studies of Huang and Li (2009), this paper chose the three geo-hazard concentration areas, Dujiangyan-Wenchuan highway, Beichuan-Anxian County area and Magong-Hongguang area (see Fig. 1), as typical

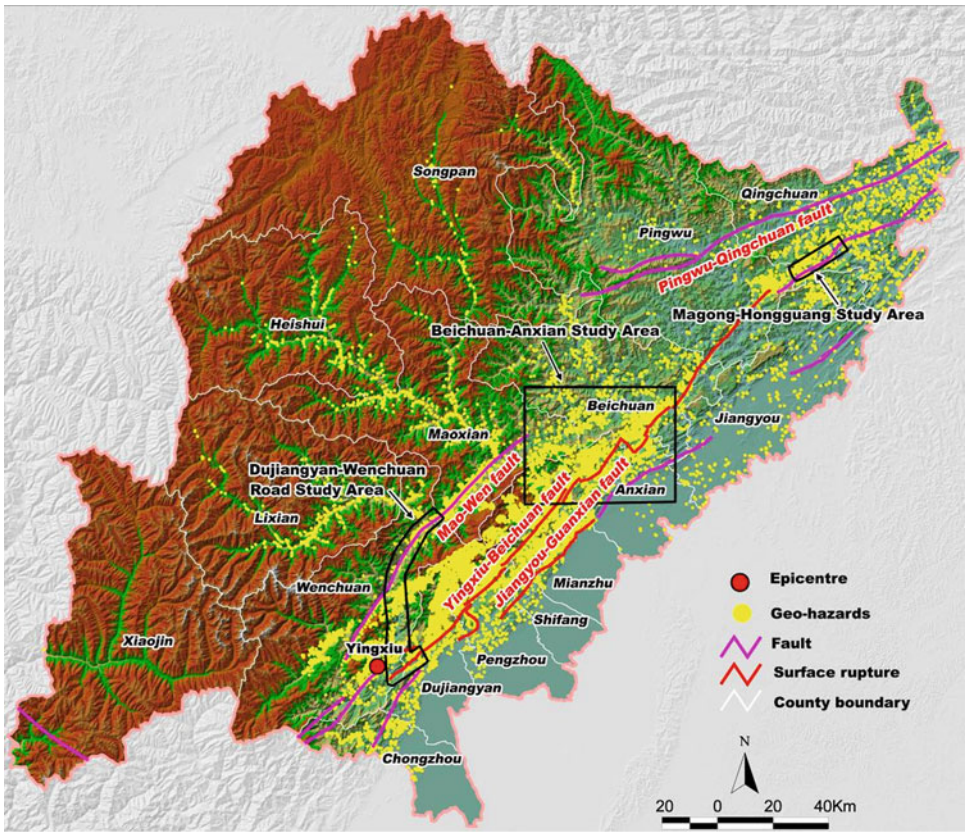

Fig. 1 Regional distribution of geo-hazards in the heavy disaster area

study areas and explored the specific co-seismic effects on the spatial distribution of earthquake-triggered landslides.

2 Typical Study Areas

As is shown in Fig. 1, the three typical study areas selected by us are respectively located in the two ends and central position of the co-seismic fault, Yingxiu-Beihcuan Fault. Moreover, both field investigation and remote-sensing interpretation have indicated that the three areas are the strong development zones of earthquake-triggered landslides, that's why we selected these areas as typical study ones. In the following parts, the specific situation of these areas will be introduced respectively.

2.1 Dujiangyan-Wenchuan Highway Study Area

Dujiangyan-Wenchuan Highway is a part of No. 213 National Highway, spreading along the Min River and covering the length of ~90 km. It is the lifeline connecting Wenchuan County and surrounding counties to Dujiangyan. Due to Wenchuan Earthquake, a large amount of collapses and landslides occurred along the two sides of the Min river, resulting in the serious damage of Dujiangyan-Wenchuan highway, which took workers three months to repair it. We adopted post-earthquake aerial photos (0.5 m resolution) to interpret the landslides and damage along the road and got the result as follows: there are 307 landslides and the average concentration is 3.5/km; about 22 km long road was damaged or buried by landslides and on average about 24 % road section was damaged. Figure 2 shows the statistic analysis of distribution concentration of landslides and damage extent of roads (the ratio between the length of road section occupied by accumulative and the total length of accounted road section) within the study area of Dujiangyan-Wenchuan section of No. 213 National Highway.

2.2 Beichuan-Anxian Study Area

Beichuan-Anxian study area, the most seriously damage area of this earthquake, is located in the junction area of Beichuan, Anxian, Mianzhu and Maoxian county (see Figs. 1 and 2) and is ~110 km away from Yingxiu town. The earthquake had not only completely destroyed the Beichuan County, but it also triggered many typical landslides in this area, including the largest landslide triggered

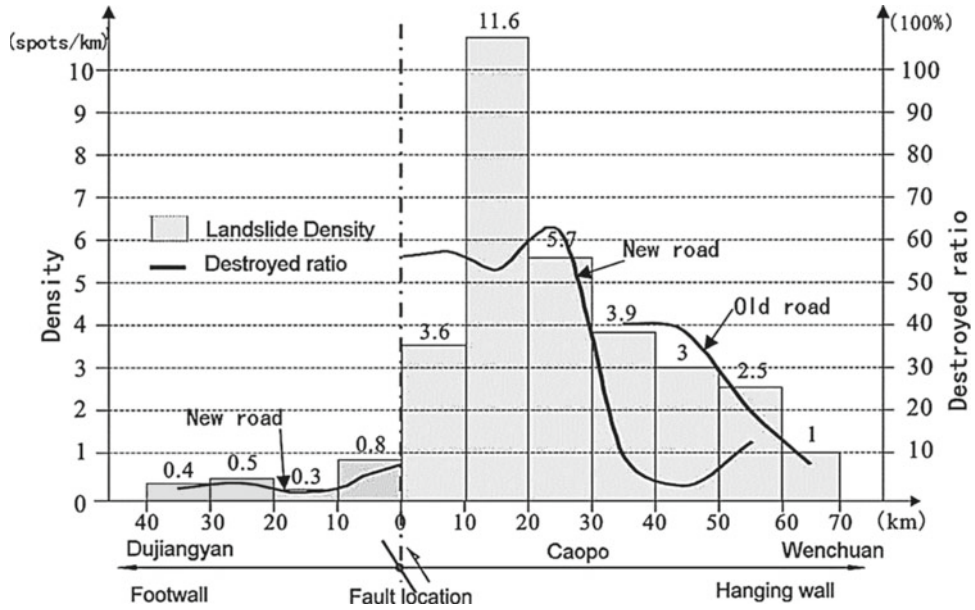

Fig. 2 Difference of the landslides development in the hanging wall and the foot wall along the Dujiangyan-Wenchuan section of national highway 213. Destroyed ratio means the percentage of the length of the road blocked by landslides to the total length of the road

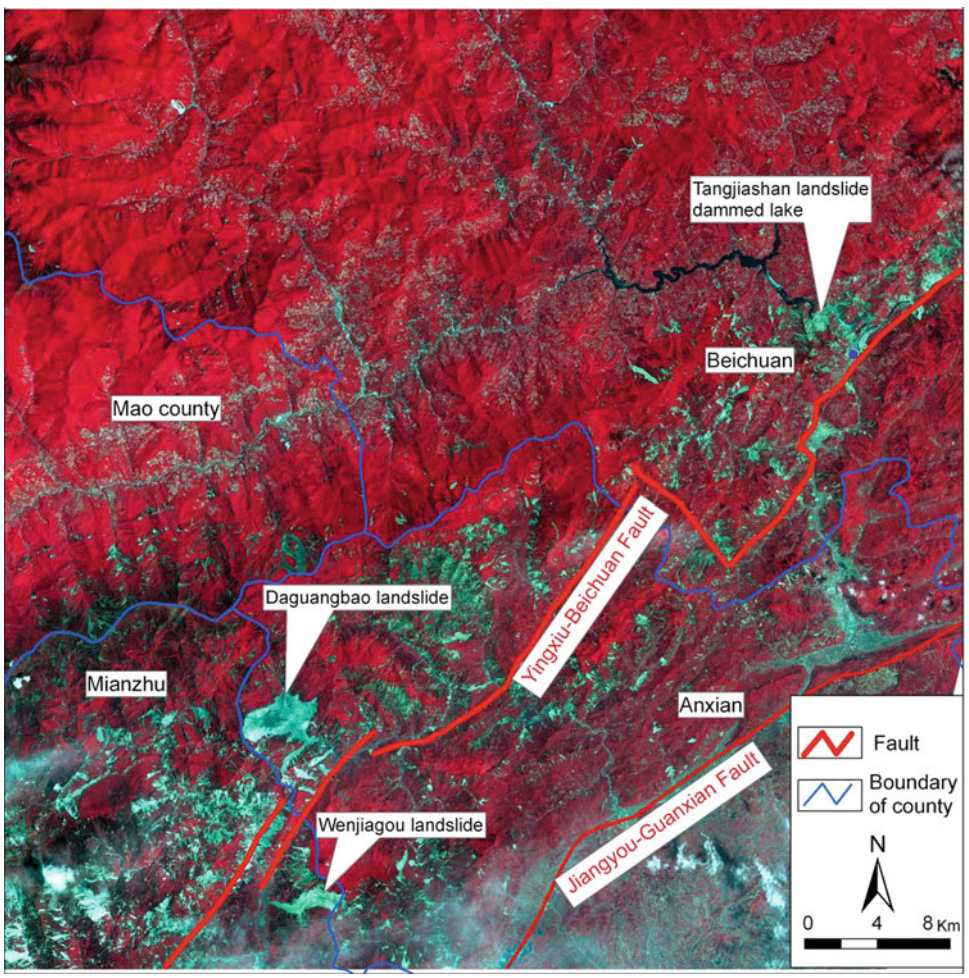

Fig. 3 Alos 432 false color image of the Beichuan-Anxian area after the Wenchuan earthquake (date 4th June 2008, copyright JAXA AVNIR-2, Japan)

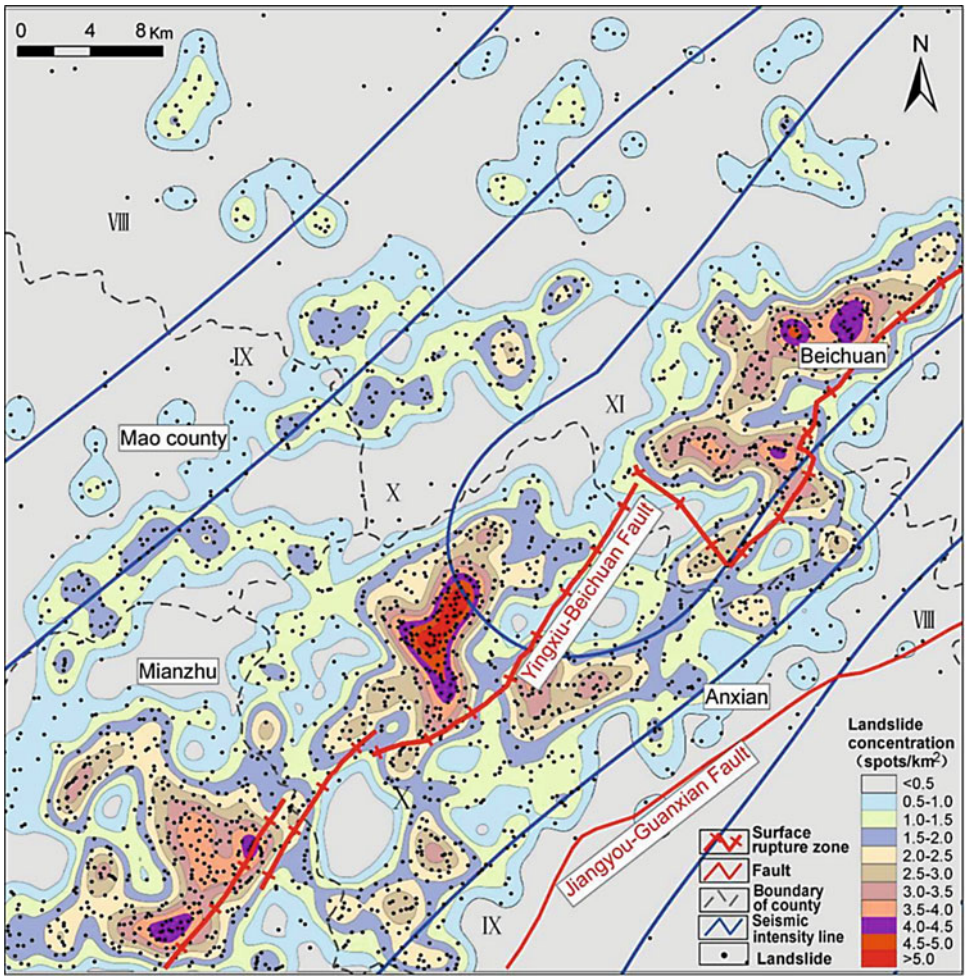

Fig. 4 The geo-hazard concentration map of the Beichuan-Anxian detailed study area

by this Earthquake-Daguangbao Landslide in Anxian County, the second largest landslide-Wenjiagou Landslide in Mianzhu County and Tangjiashan Barrier Lake in Beichuan County (Fig. 3). The total area of this region is ~2,809 km^2 and the main rocks within it include slates, sandstones, phyllites, carbonates, and magmatic rocks. We gave a detailed interpretation to the post-earthquake Alos remote-sensing images of this area (10 m resolution) and used computers to s automatically abstract the area of landslides, thus we obtained the following result: in this region there are 2,244 landslides covering an area of 134 km^2, which occupies 5 % of the total area; the average density of landslides is 0.8/km ^{2} and the average area is ~60,000 m^2. Without taking the scale of landslides into account, we compiled the landslides density map of this region by using ARCGIS (see Fig. 4); we also conducted buffer analysis to the co-seismic fault and calculated the distribution area of landslides within different distance range from the co-seismic fault. See Table 1 for more details.

2.3 Magong-Hongguang Study Area

Field investigation and remote-sensing interpretation showed that the landslides within the band area of Magong Town to Hongguang Town were of comparatively high concentration and large scale, for Yingxiu-Beichuan Fault exactly pass through this area. The famous Donghekou Landslide is distributed in this area. The area of the study region is ~97 km^2 and the main rocks within it are phyllites and carbonates. Through the interpretation to the post-earthquake aerial images of this region, we got the result as follows: in this region there are 795 landslides (Fig. 5) covering the area of 9.9 km^2, which occupied nearly 10 % of the total area; there are 327 landslides covering 8.6 km^2, there are 468 collapses covering 1.3 km^2. The average area of landslides is ~12,500 m^2 and the area of 35 landslides is larger that 50,000 m^2. We also made buffer analysis to the co-seismic fault and calculated the distribution area of landslides within different distance range. See Table 2 for more details.

Table 1 The relationship of landslides to fault within Beichuan-Anxian study area

0–1	81	12.9	15.9	69	5.8	8.4
1–2	72	13.4	18.5	65	6.1	9.3
2–3	73	11.4	15.6	62	4.7	7.5
3–4	74	11.4	15.5	59	3.6	6.1
4–5	73	10.6	14.4	56	3.2	5.8
5–6	74	8.8	11.9	52	2.0	3.8
6–7	75	8.2	11.0	50	2.1	4.2
7–8	75	5.2	7.0	47	0.9	2.0
8–9	74	3.6	4.8	45	0.9	2.0
9–10	73	3.3	4.5	41	0.5	1.3
10–11	73	3.2	4.4	38	0.5	1.4
11–12	72	1.8	2.5	36	0.1	0.2
12–13	70	1.2	1.7	33	0.0	0.0
13–14	68	1.6	2.4	–	–	–
14–15	65	1.9	2.9	–	–	–
15–16	63	1.2	1.9	–	–	–
16–17	60	1.3	2.1	–	–	–
17–18	57	1.0	1.7	–	–	–
18–19	54	0.4	0.7	–	–	–
19–20	52	0.2	0.3	–	–	–
>20	778	0.8	0.1	–	–	–
Total	2,156	103.4	4.8	653	30.4	4.7

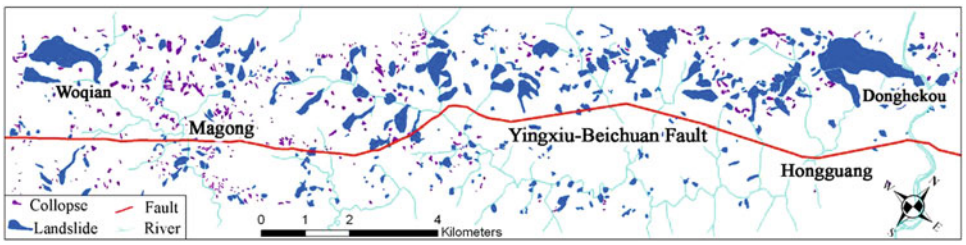

Fig. 5 The geo-hazard distribution of Magong-Hongguang study area

3 Analysis of Co-Seismic Effects of Landslides

3.1 Hanging Wall and Footwall Effects

Abrahamson and Somerville (1996) studied the strong earthquake records of Northridge Earthquake in the California State of America and such records of other thrust fault earthquakes and found acceleration peak value in the Hanging wall of co-seismic fault is higher than that in the footwall; through the studies of Taiwan Chi–Chi Earthquake, Yu and Gao (2001) further proved the "Hanging wall and footwall effects" of thrust fault earthquakes and found that decrease of acceleration peak value is rather slow in the Hanging wall whereas its decrease is quite fast in the footwall. Both the analysis of seismic source and the analysis of seismic wave spectrum suggest that the rupture way of this earthquake is thrust with dextral slip movement (He et al. 2008). As for Wenchuan Earthquake, some scholars (Chen 2008a, b) have also pointed out the existence of "Hanging wall and footwall effects" by giving the example that the houses in the hanging wall of fault completely collapsed in Beichu County Town while those in the footwall were less damaged. Through the statistics of landslides distribution within the abovementioned typical areas, we found that the "Hanging wall and footwall effects" is quite striking in the occurrence of landslides.

From Fig. 6, it can be clearly seen that the distribution of landslides in the hanging wall and footwall are obviously

Table 2 The relationship of landslides to fault within Magong-Hongguang study area

Distance from fault (m)	Hanging wall			Footwall		
	Area (km^2)	Landslide area (km^2)	Landslide area in buffees (%)	Area (km^2)	Landslide area (km^2)	Landslide area in buffees (%)
0–500	11	0.8	7.0	11	0.4	3.7
500–1,000	11	1.6	14.5	11	0.5	4.8
1,000–1,500	11	2.1	18.8	11	0.3	2.8
1,500–2,000	11	2.3	21.1	8	0.2	2.5
2,000–2,500	8	1.5	18.5	–	–	–
2,500–3,000	4	0.2	4.1	–	–	–
Total	56	8.5	15.2	41	1.4	3.4

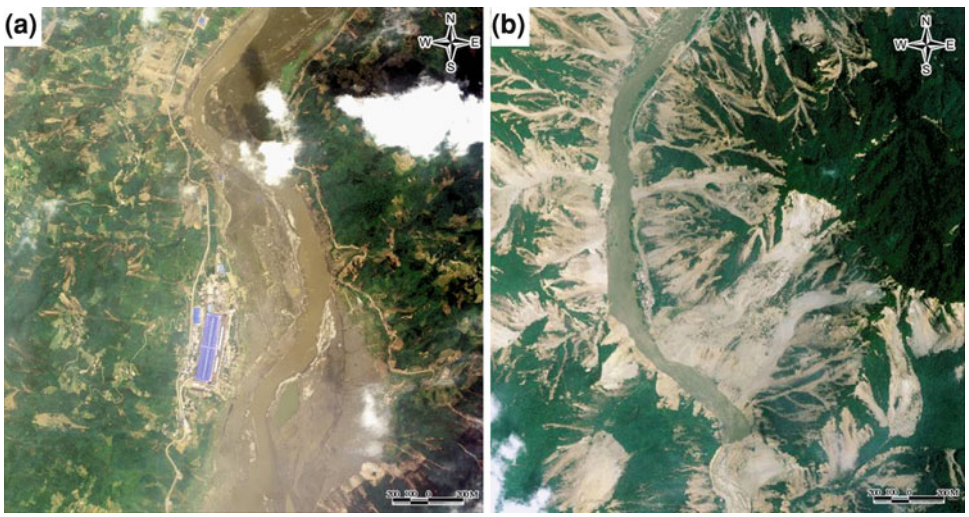

Fig. 6 Aerial photos of Dujiangyan-Wenchuan Road study area after the Earthquake, (**a**) footwall, (**b**) hanging wall

different. The landslides in the footwall are of low concentration and small scale, and the road damage is rather light; while the landslides in the hanging wall are of comparatively high concentration and large scale, and the road damage is quite serious. From the statistical data of Fig. 2, with Yingxiu Town through which the co-seismic fault, Yingxiu-Beichuan Fault passes as the line, the developing extent of landslides in the hanging wall of fault is quite different from that in the footwall. In the hanging wall area of fault, the linear density of landslides along the road reaches the largest number of 11.6/km when it is 10–12 km away and the road damage ration reaches 62 %; the density within the range of 0–10 km is a little small, but this doesn't deny the development of landslides. It is because that single volume of landslides in this section is much bigger. The average liner density of landslides within the range of 0–30 km in the hanging wall is about 6.8/km, while in the footwall, the density of landslides is 0.5–0.8/km, equivalent to only 1/10 of the former one.

From Fig. 4, it can be observed that landslides of Beichuan-Anxian study area are mainly concentrated in three zones, Beichuan, Anxian and Mianzhu and the maximum area density reaches 3.5–6.0/km^2. What's worth attention is that the three concentration zones are all located in the hanging wall of co-seismic fault, Yingxiu-Beichuan Fault. From the statistics data of Table 1, it can be seen that the area of landslides in the hanging wall of the fault is 103.4 km^2, occupying 77 % of the total area of landslides in this study region; the area of landslides in the footwall is 30.4 km^2, which is less than 1/3 of that in the Hanging wall. The percentage of landslides area in each buffer within the range of 0–7 km in the hanging wall is larger than 10 %, the largest one is in the buffer area of 1–2 km, reaching 18.5 %, in the footwall no percentage is higher than 10 %. The area of landslides within the range of 0–5 km in the hanging wall accounts for 16 %, while the percentage in the same area of footwall is only 8 %, equivalent to half of the former one. The area of landslides within the range of 5–10 km in the hanging wall is 7.8 %, while it is only 2.7 % in the footwall, equivalent to 1/3 of the former one. Within the range of beyond 20 km from the co-seismic fault, there are still a few landslides; whereas almost no landslide occurs within

the range of over 12 km in the footwall. Therefore, It can be concluded that "Hanging wall and footwall effects" are quite obvious in this study area.

From Fig. 5, the geo-hazard distribution figure of Magong-Hongguang study area, we can get a qualitative understanding that the landslides in the hanging wall of fault are of higher concentration density and larger scale than that in the footwall, which is a marked evidence of "Hanging wall and footwall effects". From the statistics data of Table 2, it can be seen that in this study area 546 landslides are distributed in the hanging wall, covering the area of 8.5 km^2, which accounts for 15.2 % of the total area, and the average area of landslides is 15,000 m^2; 249 landslides are found in the footwall, covering the area of 1.4 km^2, which accounts for 3.4 % of the total area, and the average area of landslides is 5,600 m^2. The number of landslides in the hanging wall of co-seismic fault is 2 times of that in the footwall; the total area of landslides is 6 time more than that in the footwall; the area percentage is 4.5 times of that in the footwall; and the area of single geo-hazard is 2.7 times of that in the footwall. These data provides further proof of "Hanging wall and footwall effects".

What's more, we made statistics for the correlation between the distribution of 85 large landslides with the area of over 50,000 km^2 in the three typical study areas and the co-seismic fault, and got the result as shown by Fig. 7. Seventy two large landslides are distributed in the hanging wall of co-seismic fault, Yingxiu-Beichuan Fault, occupying 85 % of the total number.

The other 13 large landslides are distributed in the footwall of Yingxiu-Beichuan Fault, but it is also distributed in the Hanging wall of another earthquake fault, Jiangyou-Guanxian Fault, which is not the main earthquake fault, but it was acted partially during the earthquake Their occurrence can be attributed to dual effects of Yingxiu-Beichuan Fault and Jiangyou –Guanxian Fault, thus all the 85 large landslides can be considered to be distributed in the hanging wall of co-seismic fault.

In brief, the "Hanging wall and footwall effects" are clearly shown in the distribution of Wenchuan earthquake triggered landslides. This is not only manifested by that the distribution concentration in the hanging wall of seismic fault is higher than that in the footwall and the former coverage is wider than the latter, but it is also manifested by that the scale of landslides is larger than that in the footwall.

3.2 Distance Effect

From the statistics data of Tables 1 and 2, it can be found that the distance from the co-seismic fault is inversely proportional to the concentration of landslides. This has already mentioned by some scholars (Keefer 1984, 2000; Jibson et al. 2004). After a detailed analysis, we discovered some specific rules.

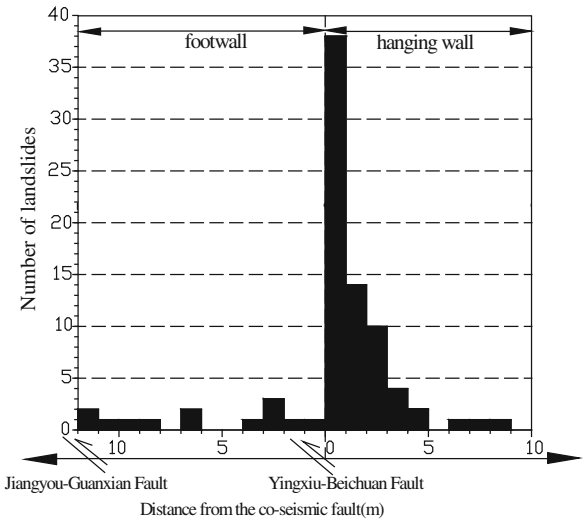

Fig. 7 The relationship of large landslides number to fault distance within the study areas

Firstly, due to abovementioned "Hanging wall and footwall effects", when the distance from the co-seismic fault is the same, the development concentration of landslides in the hanging wall is obviously higher than that in the footwall. Secondly, Huang and Li (2008) have already mentioned that the strong development zones of landslides are within the range of 10 km in the hanging wall of fault, but according to the data of Table 2, it is more accurate to limit the range of 10 km to the range of 7 km, which also matches the result of field investigation. The area percentage of landslides in each buffer area within this range is larger than 10 %. The most developing area of landslides is the range of 1–2 km from the co-seismic fault, and the area percentage of landslides reaching 18.5 %; the ranges of 7–11 km in the hanging wall of fault and 0–5 km in the footwall can be delimited as the middle development zones, and the area percentage of landslides is 4–10 %; other areas are the weak development zones of landslides triggered by this earthquake. Moreover, from the statistics of 85 large landslides (Fig. 7), it can be found that the distance of 39 (46 %) landslides from the co-seismic fault is less than 1 km, and 74 landslides (87 %) are distributed within the range of 5 km from the co-seismic fault, including the such huge landslides as Daguangbao Landslide, Wenjiagou Landslide, Donghekou Landslide, etc. Only 3 large landslides are over 10 km away. This indicates that the distribution of large landslides are still controlled by the co-seismic fault. The shock of seismic wave to the slope bodies is the deciding factor which can trigger large landslides. The nearer it is from the co-seismic fault, the stronger the

Table 3 Landslide concentration in the different seismic intensity zones

Seismic Intensity	Landslide number	Number percent (%)	Area (km^2)	Landslide concentration (landslides/km^2)
VIII	73	3.3	612	0.1
IX	267	11.9	622	0.4
X	1,330	59.3	1,101	1.2
XI	574	25.6	474	1.2

effect of seismic wave to the slope bodies is, the easier large landslides will be triggered; vice versa, the scale of landslides is comparatively small.

From Fig. 4, it can observed that the seismic intensity is proportional to the distribution concentration of landslides. The three high landslides concentration zones are located in the zones with seismic intensities of X and XI. Table 3 is the statistics of correlation between the development concentration of landslides and the seismic intensity. It can be seen that the concentration of landslides in the seismic intensity zones XI is nearly the same with that in seismic intensity zones X. This decreases dramatically to 1/3 in the seismic zone IX while in seismic zone VIII it drops to only 1/10. Thus it can be concluded that the earthquake-triggered landslides mainly occur in the zones of seismic intensity IX and higher.

The two largest landslides caused by the Wenchuan Earthquake, the Daguangbao and Wenjiagou Landslides are located in seismic intensity zone X. However, it will be noted that in some cases there is no clear relationship between the seismic intensity zone and the concentration of landslides. This is because the seismic intensity is determined by the observed damage to houses and buildings, thus the landslides concentration and scale zoning may not completely match with the seismic intensity zoning.

3.3 Snipping Effect

Both field investigation and remote-sensing interpretation indicate that the several staggered and transitional areas along Yingxiu-Beichuan Fault are the strong development zones of landslides. We call these phenomena as "Snipping effect". Figure 4, the figure of geo-hazard distribution concentration in Beichuan-Anxian study area, also shows that these concentration zones are just located in the local staggered and transitional positions of the Yingxiu-Beichuan fault. The concentration zone around Beichuan City in particular corresponds to the area with the largest co-seismic displacement. This apparently shows that the local staggered and transitional positions played a role of locked segments along Yingxiu-Beichuan fault and were snipped suddenly during the fault dislocation, thus more energy was released in these parts, resulting in much stronger shocks and forming the concentration of landslides.

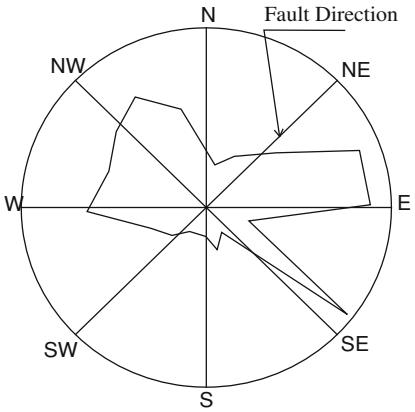

Fig. 8 Rose diagram of slip direction from landslides within study area

3.4 Direction Effect

The sliding direction of landslide is mainly controlled by topography. Commonly, the water system on both sides of Longmenshan Mountain is vertical to the strike of the mountain and Longmenshan fault belt, so the sliding direction of landslide will be naturally parallel to the strike of Longmenshan and fault, namely, NE ~ SW. The sliding directions statistics were completed about the large or giant landslides happening in 85 places which had limited distance away from fault, Fig. 8. Although the sliding directions of large scale landslides relatively scatter, the dominant direction is still NW ~ SE and close to EW. In other words, they are vertical to the strike of seismic fault or have a big angle with it. This demonstrates that the propagation of seismic wave of intense earthquake absolute controls the sliding direction of landslide instead of the topography condition under intense earthquake. Just because of the maximum intensity of seismic wave along the vertical direction to fault, slope body is fractured by shake and is thrown out. At last, a series of projectile type of large scale landslide collapses happen. Meanwhile, this also

demonstrates that earthquake wave and the intensity of ground movement have clear direction characteristics. In other words, it reaches the maximum value in the vertical direction to fault.

In fact, the phenomenon aforementioned is consistent with the observation in site. These buildings were destroyed heavily if their extension was parallel to fault, because they were influenced extremely by the ground motion vertical to fault. On the contrary, these buildings whose extension was vertical to fault were destroyed relatively lightly.

4 Conclusions

Through the studies of three typical areas, the following conclusions of co-seismic effect on the development and distribution of Wenchuan Earthquake-triggered landslides can be drawn:

1) The rupture way of this earthquake is thrust with dextral slip movement. The "Hanging wall and footwalls effects" of thrust fault earthquakes are quite striking in the distribution of Wenchuan Earthquake-triggered landslides. This is not only manifested by that the distribution concentration in the hanging wall of seismic fault is higher than that in the footwall and the former coverage is wider than the latter, but it is also manifested by that the scale of landslides is larger than that in the footwall.
2) Generally speaking, the distance from the co-seismic fault is inversely proportional to the concentration of landslides. The strong development zones of landslides are within the range of 7 km in the hanging wall of fault; the strongest development area of landslides is the range of 1–2 km from the co-seismic fault; the ranges of 7–11 km in the hanging wall of fault and 0–5 km in the footwall can be delimited as the middle development zones. The different distance from the co-seismic fault determines the intensity of seismic shocks, and thus control the scale of landslides. A vast majority of large-scale landslides are distributed within the range of 5 km from the fault, and large-scale landslides are unlikely to occur within the range of over 10 km;
3) During the earthquake, the local staggered and transitional positions were sheered and became cracked because of the fault dislocation, thus extra energy was released, resulting in stronger shocks. These areas are the concentration areas of landslides and large-scale landslides are likely to occur in these positions.
4) The landslides of Wenchuan Earthquake present NE-SW zontal distribution along the Yingxiu-Beichuan Fault in space. The preferred direction of landslide is NW–SE, basically vertical to the spreading direction of Yingxiu-Beichuan Fault. This may be because that Longmenshan Fault Zone has always been affected by the tectonic stress field of NW–SE extrusion area since Cenozoic Time.
5) The earthquake-triggered landslides mainly occur in the zones of seismic intensity IX and higher. The concentration of landslides in the seismic intensity zones XI is 1.21/km^2, which is nearly the same with that in seismic intensity zones X and the highest concentration reaches 5.59/km^2; the concentration in the seismic intensity zones IX is 0.43/km^2, which equals to 1/3 of the abovementioned one; the concentration in the seismic intensity zones VIII is 0.12/km^2, which equals to only 1/10 of the abovementioned one.

Acknowledgments The authors are grateful for the financial support from 973 National Basic Research Program (2008CB425801) and the State Key Laboratory of Geohazards Prevention and Geoenvironment Protection (SKLGP).

References

Abrahamson, N. A., & Somerville, P. G. (1996). Effects of the hanging wall and footwall on ground motions recorded during the Northridge earthquake. *Bulletin of the Seismological Society of America*, *86*(1B), S93–S99.

Bao, Y. J., Gao, M. T., & Jiang, H. (2005). Probabilistic analysis of earthquake-induced landslides. *Chinese Journal of Rock Mechanics and Engineering, 24*(1), 66–70 (In Chinese).

Chen, Y. T. (2008). Why was Wenchuan earthquake so serious? (2008-06-26). http://www.sciencenet.cn/htmlnews/2008/6/200862781145413208421.html (In Chinese).

Chen, Y. T. (2008b). On the magnitude and the fault length of the great Wenchuan earthquake. *Science & Technology Review, 26*(10), 26–27. (In Chinese).

He, H. L., Sun, S. M., Wang, & S. T. et al. (2008). Rupture of the MS 8.0 Wenchuan earthquake seismology and geology *30*(2), 359–361. (In Chinese).

Hu, G. T. (1995). Landslide Dynamics. Beijing: Geological Publishing House (In Chinese).

Huang, R. Q. (2008). Characteristics of geological disasters of 5.12 Wenchuan earthquake and recommendation on its impact on reconstruction. *Chinese Geological Education, 2*, 21–24. (In Chinese).

Huang, R. Q., & Li, W. L. (2008). Research on development and distribution rules of geohazards induced by Wenchuan earthquake on 12th May, 2008. *Chinese Journal of Rock Mechanics and Engineering*, *27*(12), 2585–2592. (In Chinese).

Huang, R. Q., & Li, W. L. (2009). Analysis of the landslidings triggered by the 12 May (2008) Wenchuan earthquake, China. *Bulletin of Engineering Geology and the Environment*, *68*(3), 363–371.

Jibson, R. W., Harp, E. L., & Michael, J. A. (2000). A method for producing digital probabilistic seismic landslide hazard maps. *Engineering Geology, Special Issue, 58*, 3–4.

Jibson, R. W., Harp, E. L., Schulz, W., & Keefer, D. K. (2004). Landslides triggered by the 2002 Denali Fault, Alaska, earthquake and the inferred nature of the strong shaking. *Earthquake Spectra, 20*, 669–691.

Keefer, D. K. (1984). Landslides caused by earthquakes. *Geological Society of America, 95*, 406–421.

Keefer, D. V. (2000). Statistical analysis of an earthquake-induced landslide distribution—the 1989 Loma Prieta, California event. *Engineering Geology, 58*, 231–249.

Li, Z. S. (2003). The state of the art of the research on seismic landslide hazard at home and abroad. *Journal of Catastrophology, 18*(4), 64–70 (In Chinese).

Mao, Y. L., Hu, G. T., & Zhao, F. S. et al. (1998). Mechanics of the landslide sliding caused by seismic. *Journal of Xi'an Engineering University, 20* (4), 45–48 (In Chinese).

Mohammad, R., Mahdavifar, Shahryar Solaymani, Mohammad, K., & Jafari, (2006). Landslides triggered by the Avaj, Iran earthquake of June 22, 2002. *Engineering Geology, 86*, 166–182.

Rodriguez, C. E., Bommer J. J., & Chandler, R. J. (1999). Earthquake induced landslides: 1980–1997. *Soil Dynamics Earthquake Engineering, 18*, 325–346.

Solonenko, V. P. (1976). Landslides of collapses in seismic zone and other prediction. *Bulletin of the International Association of. Engineering Geology, 15*, 4–8.

Wang, W. N., Nakamura, H., Tsuchiya, S., & Chen, C. C. (2002). Distributions of landslides triggered by the Chi–Chi earthquake in central Taiwan on September 21, 1999. *Journal of the Japan Landslide Society, 38*(4), 318–326.

Yao, Q. L. (1986). Study on earthquake-induced landslide hazards in loess region. M. S Paper at the Geological Institute SSB.

Yin, Y. P. (2008). Researches on the landslides triggered by Wenchuan earthquake Sichuan. *Journal of Engineering Geology, 16*(4), 433–444 (In Chinese).

Yu, Y. X., & Gao, M. T. (2001). Effects of the hanging wall and footwall on peak acceleration during the Chi–Chi earthquake. *Taiwan. Acta Seismologica Sinica, 23*(6), 615–621. (In Chinese).

Large Deformation Analysis for Costal Geo-Disasters Using Continuum and Discrete Modeling

A. Yashima, S. Moriguchi, R. Uzuoka, H. Nonoyama, and K. Sawada

Abstract

Various kinds of geo-disasters have occurred, such as soil avalanches, landslides, failure of river dike, liquefaction and scoring. These disasters have caused serious damage to infrastructures and human activities. Numerical simulations are one of the powerful tools for predicting (1) when the failure will take place, (2) where the failure take place, (3) how far the collapsed soil mass will flow, and (4) how large the impact force to structures will be. In this paper, FEM, CFD, DEM and SPH are introduced as numerical methods for costal geo-disasters. Brief explanation of theory of each numerical method will be described in this paper. Based on simulated results, advantages and disadvantages of different methods are discussed.

Keywords

Geo-disasters • FEM • CFD • DEM • SPH

1 Introduction

A lot of disasters have occurred in the world. Infrastructures and human lives have been damaged by costal geo-disasters. There are various kinds of costal geo-disasters reported as shown in Fig. 1. Researchers and government officers of each country are making effort to reduce the damage, It is however still difficult to prevent those disasters.

Numerical simulations are one of the powerful tools for predicting geo-disasters (1) when the failure will take place, (2) where the failure take place, (3) how far the collapsed soil mass will flow, and (4) how large the impact force to structures will be. Today, we have many kinds of numerical methods, such as Finite Element Method (FEM), Boundary Element Method (BEM), Computational Fluid Dynamics, Smoothed Particle Hydrodynamics (SPH) (Lucy 1977; Gingold and Monaghan 1977), Discrete Element Method (DEM) (Cudall and Strack 1979) and Discontinues Deformation Analysis (DDA). These methods are roughly categorized based on deformation level (Fig. 2). We can apply a method to simulate costal geo-disasters, but it is necessary to select suitable method based on the deformation level of each geo-disaster. In this paper, typical numerical results by FEM, CFD, DEM and SPH are introduced and advantages and disadvantages of different methods are discussed.

A. Yashima (✉)
Gifu University, 1-1 Yanagido, Gifu, Japan
e-mail: yashima@gifu-u.ac.jp

S. Moriguchi
Department of Civil Engineering, Gifu University, 1-1 Yanagido, Gifu, Japan

R. Uzuoka
Faculty of Engineering, The University of Tokushima, 2-1 Minamijyousanjima-cho, Tokushima, Japan

H. Nonoyama
Department of Civil Engineering, Nagoya University, Furo-cho, Chikusa-ku, Nagoya, Japan

K. Sawada
River Basin Research Center, Gifu University, c1-1 Yanagido, Gifu, Japan

Y. Huang et al. (eds.), *New Frontiers in Engineering Geology and the Environment*,
DOI: 10.1007/978-3-642-31671-5_2,

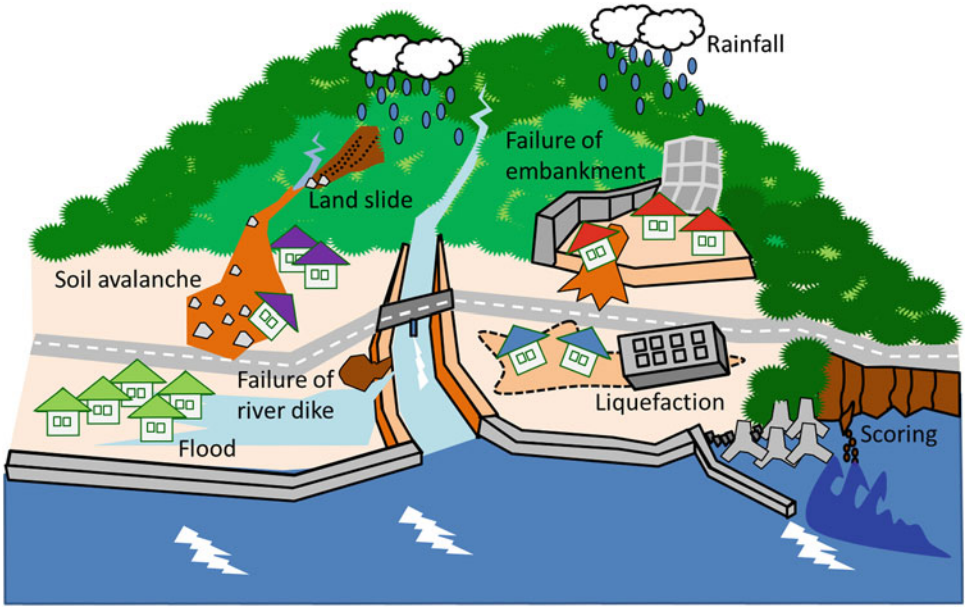

Fig. 1 Soil-water interaction related geo-disasters

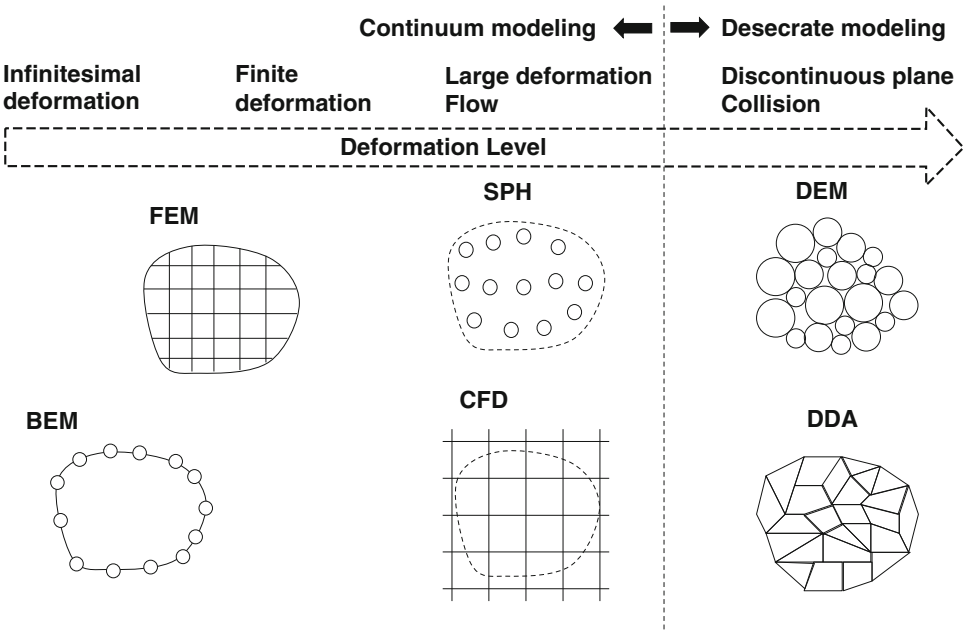

Fig. 2 Numerical methods used in simulations of geo-disasters

2 Stability Analysis Using FEM

A numerical simulation using FEM is introduced in this section. Soil–water coupled FEM analyses based on Biot's porous media theory (Biot 1962) have been studied since 1970s (e.g. Zienkiewicz and Shiomi 1984), and a lot of important research achievements that are about saturated soils have been reported. However, prediction of behaviours of unsaturated soils are still challenging research topic. In this paper, a dynamic stability analysis of unsaturated slope is shown. The seismic behavior of unsaturated and saturated fill and the failure process are discussed through the numerical simulations. In addition, the effect of the ground water level on the seismic behavior is discussed through parametric studies.

2.1 Governing Equations

Using porous media theory (de Boer 2000; Schrefler 2002), we derive the governing equations which include the momentum balance equations of the overall three-phase material (soil, water and air) and the mass and momentum balance equations of the pore water and air. The details of the numerical method are referred to Uzuoka and Borja (2011).

Mass balance equation for α phase ($\alpha = (s : soil,\ w : water,\ a : air)$) is

$$\frac{D^{\alpha}\rho^{\alpha}}{Dt} + \rho^{\alpha}\mathrm{div}\mathbf{v}^{\alpha} = 0 \tag{1}$$

where D^{α}/Dt is the material time derivative with respect to α phase, ρ^{α} is the partial density of α phase, $\mathbf{v}^{\alpha}$ is the velocity vector of α phase. The mass exchange among three phases is ignored here. The linear momentum balance equation of α phase is

$$\rho^{\alpha}\frac{D^{\alpha}\mathbf{v}^{\alpha}}{Dt} = \rho^{\alpha}\mathbf{a}^{\alpha} = \mathrm{div}\boldsymbol{\sigma}^{\alpha} + \rho^{\alpha}\mathbf{b} + \hat{\mathbf{p}}^{\alpha} \tag{2}$$

where $\mathbf{a}^{\alpha}$ is the acceleration vector of α phase, $\boldsymbol{\sigma}^{\alpha}$ is the Cauchy stress tensor of α phase, $\mathbf{b}$ is the body force vector, $\hat{\mathbf{p}}^{\alpha}$ is the interaction vector of α phase between other phases.

Constitutive equations are the followings. The partial Cauchy stress of each phase is derived (e.g. Borja 2006) as

$$\begin{aligned}\boldsymbol{\sigma}^{s} &= \sigma' - (1-n)(s^{w}p^{w} + s^{a}p^{a})\mathbf{I}, \quad \boldsymbol{\sigma}^{w} = -ns^{w}p^{w}\mathbf{I},\\ \boldsymbol{\sigma}^{a} &= -ns^{a}p^{a}\mathbf{I}\end{aligned} \tag{3}$$

where σ' is the effective stress tensor, so-called average skeleton stress (Gallipoli et al. 2003), p^{w} is the pore water pressure and p^{a} is the pore air pressure. The stress is defined as positive in tension and the pressures are defined as positive in compression. n is the porosity, s^{w} is the degree of water saturation, and s^{a} is the degree of air saturation. The interaction vector for each phase is assumed as

$$\hat{\mathbf{p}}^{s} = -\hat{\mathbf{p}}^{w} - \hat{\mathbf{p}}^{a}, \quad \hat{\mathbf{p}}^{\alpha} = p^{\alpha}\mathrm{grad}n^{\alpha} - \frac{n^{\alpha}\rho^{\alpha R}g}{k^{\alpha s}}n^{\alpha}\mathbf{v}^{\alpha s} \tag{4}$$

where g is the gravity acceleration, n^{α} is the volume fractions of α phase, $\rho^{\alpha R}$ is the intrinsic density of α phase, $k^{\alpha s}$ is the permeability coefficient of α phase (water or air). The compressibility of pore water under an isothermal condition is assumed as

$$\frac{D^{s}\rho^{wR}}{Dt} = \frac{\rho^{wR}}{K^{w}}\frac{D^{s}p^{w}}{Dt} \tag{5}$$

where K^{w} is the bulk modulus of pore water. The compressibility of pore air under an isothermal condition assumed as

$$\frac{D^{s}\rho^{aR}}{Dt} = \frac{1}{\Theta\bar{R}}\frac{D^{s}p^{a}}{Dt} \tag{6}$$

where Θ is the absolute temperature and $\bar{R}$ is the specific gas constant of air. The constitutive relation between water saturation and suction is assumed as

$$\frac{D^{s}s^{w}}{Dt} = c\frac{D^{s}p^{c}}{Dt} = c\frac{D^{s}(p^{a}-p^{w})}{Dt} \tag{7}$$

where c is the specific water capacity and p^{c} is the suction. The specific water capacity is calculated from the water retention curve (WRC) as shown in the next section.

Combining the balance and constitutive equations, we derive the governing equations which include the momentum balance equations of the over-all three-phase material and the mass and momentum balance equations of the pore water and air with the following assumptions. (1) the soil particle is incompressible, (2) the mass exchange among phases is neglected, (3) The material time derivative of relative velocities and advection terms of pore fluids to the soil skeleton are neglected, (4) an isothermal condition are assumed. The momentum balance equation of the overall three-phase material is derived as

$$\rho\mathbf{a}^{s} = \mathrm{div}\{\boldsymbol{\sigma}' - (s^{w}p^{w} + s^{a}p^{a})\mathbf{I}\} + \rho\mathbf{b} \tag{8}$$

where ρ is the overall density of three-phase material and $\mathbf{a}^{s}$ is the acceleration vector of soil skeleton. The mass and momentum balance equations of the pore water and air are derived as

$$\begin{aligned}&n\left(\frac{s^{w}p^{wR}}{K^{w}} - \rho^{wR}c\right)\frac{D^{s}p^{w}}{Dt} + n\rho^{wR}c\frac{D^{s}p^{a}}{Dt} + s^{w}\rho^{wR}\mathrm{div}\,\mathbf{v}^{s}\\ &\quad + \mathrm{div}\left\{\frac{k^{ws}}{g}(-\mathrm{grad}\,p^{w} + \rho^{wR}b - \rho^{wR}a^{s})\right\} = 0\end{aligned} \tag{9}$$

$$\begin{aligned}&n\left(\frac{s^{a}}{\Theta\bar{R}} - \rho^{aR}c\right)\frac{D^{s}p^{a}}{Dt} + n\rho^{aR}c\frac{D^{s}p^{a}}{Dt} + s^{a}\rho^{aR}\mathrm{div}\,\mathbf{v}^{s}\\ &\quad + \mathrm{div}\left\{\frac{k^{as}}{g}(-\mathrm{grad}\,p^{a} + \rho^{aR}b - \rho^{aR}a^{s})\right\} = 0\end{aligned} \tag{10}$$

where ρ^{wR} and ρ^{aR} are the intrinsic densities of pore water and air respectively, $\mathbf{v}^{s}$ is the velocity vector of soil skeleton, k^{ws} and k^{as} are the permeability coefficient of water and air respectively. This simplified formulation is called u-p^{w}-p^{a} formulation. Although the governing equations are derived in the regime of finite strain, we assume infinitesimal strain in the following study for simplicity.

2.2 Constitutive Equations

2.2.1 Constitutive Equation for Water Retention Curve

The specific water capacity c is calculated from the water retention curve (WRC). The WRC is assumed as

$$\begin{aligned}s^{w} &= (s_{s}^{w} - s_{r}^{w})s_{e}^{w} + s_{r}^{w}, \quad s_{e}^{w} = \left\{1 + \exp(a_{\mathrm{lg}}p^{c} + b_{\mathrm{lg}})\right\}^{-c_{\mathrm{lg}}},\\ p^{c} &= p^{a} - p^{w}\end{aligned} \tag{11}$$

where s_{s}^{w} is the saturated (maximum) degree of saturation, s_{r}^{w} is the residual (minimum) degree of saturation and s_{e}^{w} is the effective water saturation. The relationship between s_{e}^{w} and suction p^{c} is assumed as a logistic function with the material parameters a_{lg}, b_{lg} and c_{lg}. The logistic WRC is a

Fig. 3 Aerial photograph of the collapsed fill slope (Miyagi Engineering Co. Ltd.)

continuous function at $p^c = 0$; therefore the convergence in the iterative numerical scheme can be achieved (Uzuoka and Borja 2011). The above WRC is modified to fit "wetting" curve during undrained cyclic shear as shown in later. The permeability coefficient of water and air are assumed to be dependent on the effective water saturation as

$$k^{ws} = k_s^w (s_e^w)^{\xi_k}, \quad k^{as} = k_s^a (1 - s_e^w)^{\eta_k} \tag{12}$$

where k_s^w is the saturated (maximum) coefficient of water permeability, k_s^a is the dry (maximum) coefficient of air permeability, ξ_k and η_k are the material parameters.

2.2.2 Constitutive Equation for Effective Stress

A simplified elasto-plastic constitutive equation for effective stress is used here. Assuming that plastic deformation occurs only when the deviatoric stress ratio changes, the yield function is assumed as

$$f = \sqrt{\frac{3}{2}} \|\boldsymbol{\eta} - \boldsymbol{\alpha}\| - k = \sqrt{\frac{3}{2}} \|\mathbf{s}/p' - \boldsymbol{\alpha}\| - k = 0 \tag{13}$$

where p' is the mean effective stress, $\mathbf{s}$ is the deviatoric stress tensor, k is the material parameter which defines the elastic region. $\boldsymbol{\alpha}$ is the kinematic hardening parameter (back stress) and its nonlinear evolution rule (Armstrong and Frederick 1966) is assumed as

$$\dot{\boldsymbol{\alpha}} = a\left(\frac{2}{3} b \dot{\mathbf{e}}^p - \boldsymbol{\alpha} \dot{\varepsilon}_d^p\right), \quad \dot{\varepsilon}_d^p = \sqrt{\frac{2}{3}} \|\dot{\mathbf{e}}^p\| \tag{14}$$

where a, b are the material parameters, $\dot{\mathbf{e}}^p$ is the plastic deviatoric strain rate tensor. With non-associated flow rule, the plastic potential function is assumed as

$$g = \sqrt{\frac{3}{2}} \|\boldsymbol{\eta} - \boldsymbol{\alpha}\| + M_m \ln\left(p'/p'_a\right) = 0 \tag{15}$$

where M_m is the material parameter which defines the critical state ratio, p'_a is p' when $\|\boldsymbol{\eta} - \boldsymbol{\alpha}\| = 0$. Finally the elastic module are assumed as

$$K^e = -K^* p' \quad G^e = -G^* p' \tag{16}$$

where K^e is the elastic bulk modulus, G^e is the elastic shear modulus, K^* and G^* are the dimensionless elastic module respectively.

2.3 A Real Fill Slope Failure

Failure of an actual fill slope is reproduced using the dynamic three-phase coupled method explained in previous sub sections. The fill slope is located on old valley at Tsukidate town in Miyagi prefecture. Figure 3 shows an aerial photo of the site after the failure. The fill slope in Fig. 4 was partially collapsed and flowed during the 2003 Miyagi earthquake (Uzuoka et al. 2005). The fill material is a volcanic sandy soil.

2.4 Simulations of the Real Fill Slope Failure

The fill slope failure explained in previous subsection is reproduced using two dimensional seismic analysis.

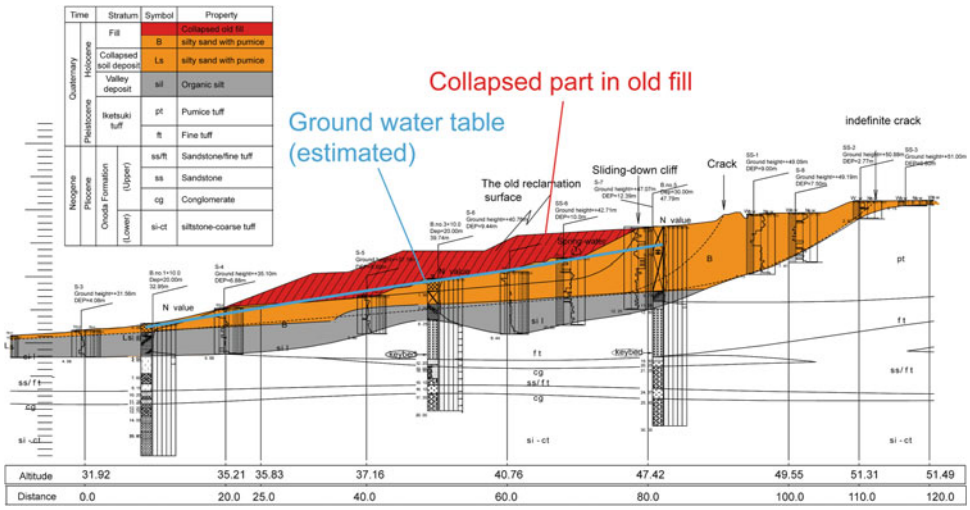

Fig. 4 Damaged fill slope during the 2003 Miyagi earthquake (Uzuoka et al. 2005)

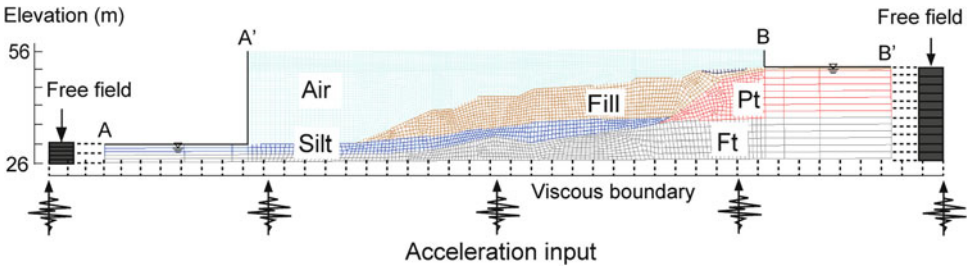

Fig. 5 Two dimensional models and boundary conditions of the fill

Assuming plane strain condition, the cross section is used for finite element modelling. Figure 5 shows a numerical model used in this simulation. The fill is elasto-plastic material, pumice tuff (Pt) and fine tuff (Ft) are linear elastic material with Lamé's constants λ and μ. Kelvin type viscosity is assumed in all materials and its viscous coefficient is proportional to the elastic modulus with a multiplier coefficient α. Table 1 shows the material parameters for each layer. Other parameters of fill material (elasto-plastic material) are summarized in Table 2. The material parameters of the constitutive models for effective stress and WRC are determined through the calibration of the undrained cyclic triaxial tests with unsaturated soil (Kazama et al. 2006).

In the seismic analysis, the input acceleration in Fig. 6 is applied through dampers at the bottom. The lateral boundaries are also supported with dampers which are connected to the free field motions. The free field motions are separately calculated by one dimensional seismic response analyses. The input acceleration history is a calculated wave by using empirical Green's function method using two aftershocks comparing several seismic intensities surrounding Tsukidate town (Fukumoto et al. 2007).

Before the seismic analysis, a static self-weight analysis is performed in order to determine the initial stress and moisture conditions. The soil displacement at the bottom boundary is fixed in all directions and the side boundaries are vertical rollers. The bottom and right boundaries are impermeable. A–A' and B–B' lines in Fig. 5 are permeable with constant total water heads. These water heads are assumed to reproduce the ground water levels as estimated in Fig. 4. The ground water level was estimated to be low because it had not rained for a week before the earthquake. However the actual ground water level was not measured before the earthquake. Mori et al. (2011) showed that the ground water level in a fill slope significantly affected the seismic behavior of fill slope; therefore we perform parametric studies in order to discuss the effect of the ground water level on the seismic behavior of fill slope. In additional case, continuous rain of 1 mm/day for 10 days is considered to simulate high ground water level in the fill slope. Thus two different situations of water level are considered, the case of low water level (Case 1) and the case of high water level (Case 2).

Figure 7 shows the initial distributions of suction and water saturation in the elasto-plastic fill obtained by the static self-weight analysis in Case 1. The air entry value of the fill is about 10 kPa, therefore the boundary between saturated and unsaturated portions is located slightly above the ground water table. The ground water table roughly agrees with the measured one after the earthquake (Uzuoka et al. 2005). Figure 8 shows results of Case 1, the distributions of absolute horizontal displacement, deviatoric strain and effective stress reduction ratio (ESRR) after the earthquake. The ESRR is defined as $1 - p'/p'_0$ where p'_0 is the initial value of mean effective stress. Large deviatoric strain is generated around the toe and top of

Table 1 Material parameters for all soil layers

	Fill	Silt	Pt	Ft
Porosity, n	0.48	0.43	0.43	0.43
Intrinsic density of soil skeleton, $\rho^{sR}(t/m^3)$	2.48	2.68	2.74	2.74
Intrinsic density of water, $\rho^{wR}(t/m^3)$	1.0	1.0	1.0	1.0
Permeability coefficient of water, $k_s^w(m/s)$	1.1×10^{-4}	1.0×10^{-9}	1.0×10^{-11}	1.0×10^{-11}
Permeability coefficient of air, $k_s^a(m/s)$	1.0×10^{-6}	1.0×10^{-10}	1.0×10^{-12}	1.0×10^{-12}
Permeability parameters of water and air, ξ_k/η_k	3.0/0.33			
Lame's constant, λ (kPa)		181812	437290	1125000
Lame's constant, μ (kPa)		45453	437290	1125000
Viscous coefficient parameter, α	0.001	0.0048	0.0019	0.00096

Table 2 Material parameters of the fill

Elasto-plastic model parameters		WRC parameters	
Dimensionless shear modulus, G^*	600	Maximum degree of saturation, s_s^w	0.99
Dimensionless bulk modulus, K^*	30	Minimum degree of saturation, s_r^w	0.255
Nonlinear hardening parameter, a	857	Main drying curve, a_{lg}, b_{lg}, c_{lg}	7, 7, 0.05
Nonlinear hardening parameter, b	–1.47	Main wetting curve, a_{lg}, b_{lg}, c_{lg}	0.037, 1, –2
Critical state stress ratio, M_m	1.47	Scaling parameter, p_2^c(kPa)	–5
Yield function parameter, k	0.09		
Physical parameters			
Prosity, n	0.48	Intrinsic density of air, ρ^R (t/m^3)	1.23×10^{-3}
Bulk modulus of water, K^w (kPa)	2.0×10^6	Gas parameter, $1/\bar{R}\Theta$ (s^2/m^2)	1.25×10^{-5}

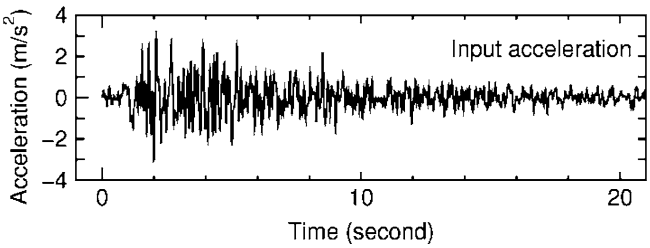

Fig. 6 Time history of input acceleration (Fukumoto et al. 2007)

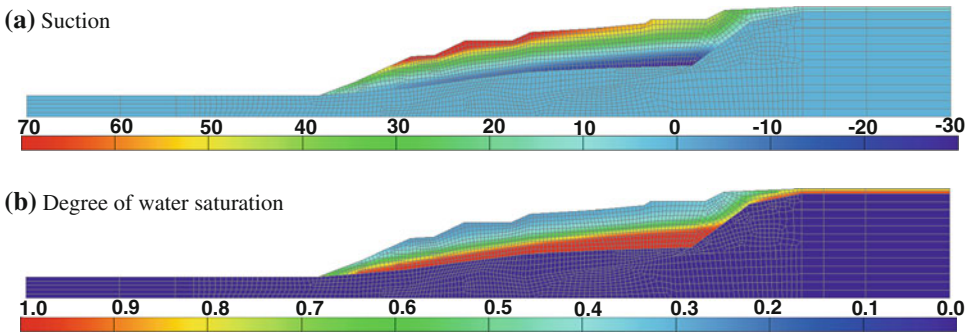

Fig. 7 Initial distributions of suction and water saturation before the earthquake (Case 1). **a** Suction, **b** Degree of water saturation

the fill near the base. Corresponding to the strain distribution, residual horizontal displacement around the toe and top of the fill is large leftward, which is comparable to the damaged configuration of the fill in Fig. 4. The ESRR in the fill does not reach 1.0. Therefore complete liquefaction does not occur even in the saturated part. However, the ESRR in the unsaturated fill above the ground water table reaches about 0.8, which reduces the stiffness and strength of unsaturated fill.

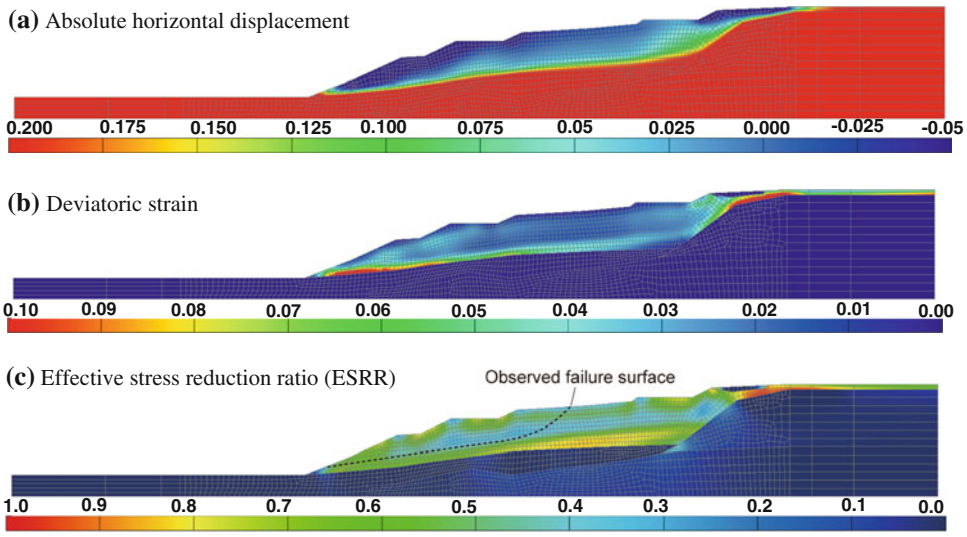

Fig. 8 Distributions of displacement, deviatoric strain and ESRR after the earthquake (Case 1). **a** Absolute horizontal displacement, **b** Deviatoric strain, **c** Effective stress reduction ratio (ESRR)

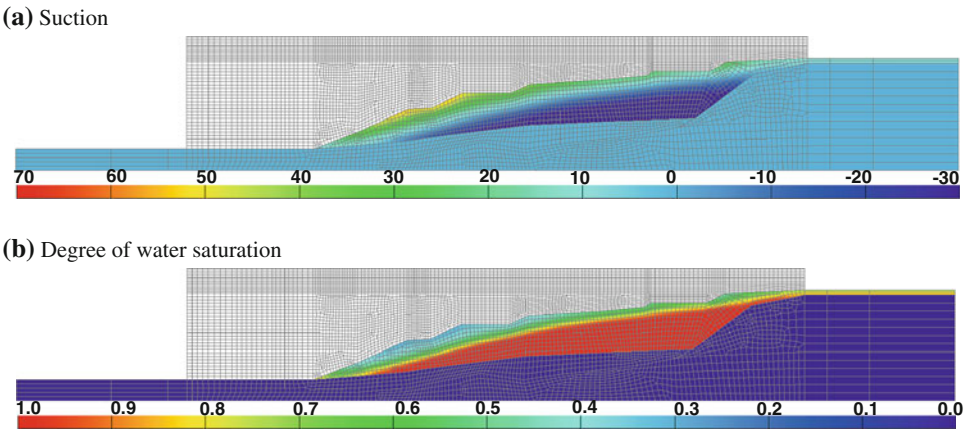

Fig. 9 Distributions of suction and water saturation before the earthquake (Case 2). **a** Suction, **b** Degree of water saturation

Figure 9 shows the initial distributions of suction and water saturation in Case 2 (high water level condition). Figure 10 shows the distributions of absolute horizontal displacement, deviatoric strain and effective stress reduction ratio (ESRR) obtained in Case 2. Large deviatoric strain is generated around the toe and top of the fill near the base similar to the previous case in Fig. 8. In addition, larger deviatoric strain is generated along the ground water level in the middle part. Corresponding to the strain distribution, residual horizontal displacement of the whole fill slope is large leftward, which is not comparable to the damaged configuration of the fill in Fig. 4. The ESRR in the fill reaches about 0.9 near the top of the slope in the saturated part. Therefore complete liquefaction does not occur even with high ground water level. The deformation mode in Case 2 does not correspond to the observed one. Thus real ground water level is estimated to be lower than that in Case 2. It can be therefore summarized water level assumed in Case 1 corresponds to real water level.

2.5 Sammy of FEM

As shown in this section, FEM can predict behaviors of saturated and unsaturated grounds under seismic condition. By using developed numerical framework and constitutive models, we can predict various kinds of behaviors of soils. In addition, FEM is well known in engineering field, and it has high reliability. These are advantages of FEM. There is however a disadvantage. When FEM is applied to large deformation problems, it is difficult to keep enough calculation accuracy due to mesh distortion.

3 Flow Simulation Using CFD and DEM

Some results of flow simulations of soils using CFD and DEM are introduced in this section. First, numerical framework of CFD based method is explained, and then a flow simulation of the real fill slope explained in previous section is shown. Second, numerical framework of DEM is

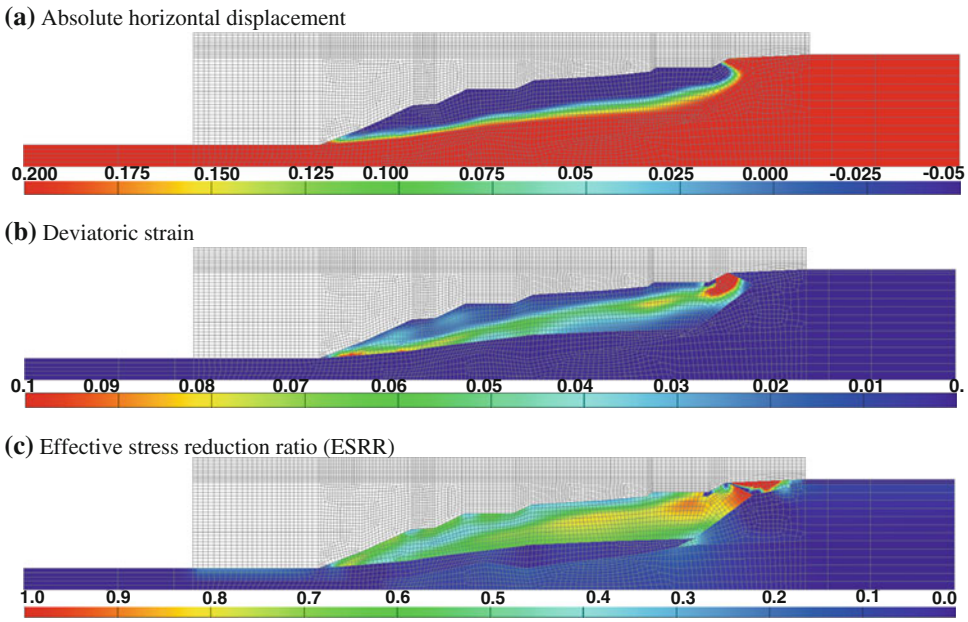

Fig. 10 Distributions of displacement, deviatoric strain and ESRR after the earthquake (Case 2). **a** Absolute horizontal displacement, **b** Deviatoric strain **c** Effective stress reduction ratio (ESRR)

shown briefly. Then simulations of sand flow simulation using both CFD and DEM are introduced.

3.1 Numerical Framework of CFD Based Method

An Eulerian type CFD based method is proposed for flow problems of soils, such as soil avalanche, high speed landslide, sediment flow after slope failure (e.g. Moriguchi et al. 2005, 2009; Sawada et al. 2004). In the method, soils are assumed to be Bingham fluid which is one of the non-Newtonian fluids. Bingham fluid model is described by following equation in one dimensional condition.

$$\tau = \eta_0 \dot{\gamma} + \tau_{\min} \tag{17}$$

where τ is the shear stress, $\boldsymbol{\eta}_0$ is the viscosity after yield, $\dot{\gamma}$ is the shear strain rate and $\tau_{\min}$ the yield strength. When shear stresses below the yield stress, a Bingham fluid behaves as a rigid body and does not deform, but when the shear stress surpasses the yield stress, flow failure occurs resulting in very large deformations. The following Coulomb equation is widely accepted to express the shear strength of a given soil.

$$s = c + \sigma \tan \varphi \tag{18}$$

where s is the shear strength, c is the cohesion, $\sigma$is the normal stress and φ is the internal friction angle. In this study, we use this basic failure criterion to formulate a constitutive model for geometrials subjected to flow. Substituting the shear strength s in Eq. (18) by the yield strength $\tau_{\min}$ in Eq. (17) and representing the normal stress σ by the hydraulic pressure p, following modified Bingham model is obtained.

$$\tau = \eta\dot{\gamma} + c + p \tan \varphi \tag{19}$$

By formulating above equation, we can obtain an equivalent Newtonian viscosity of Bingham fluid as follows,

$$\eta' = \frac{\tau}{\dot{\gamma}} = \eta_0 + \frac{c + p \tan \varphi}{\dot{\gamma}} \tag{20}$$

The equivalent Newtonian viscosity η' described in above equation is used in governing equation.

In some paper published by authors (Moriguchi et al. 2005; Sawada et al. 2004), soils are treated as compressible material, however, soils are treated as incompressible material in this paper. Detailed numerical formulations are summarized by Moriguchi et al. (2009).

A motion equation of flowing material is represented by the following equation,

$$\frac{\partial \mathbf{u}}{\partial t} + \mathbf{u} \cdot \nabla \mathbf{u} = -\frac{1}{\rho} \nabla p + \frac{2}{\rho} \nabla [\eta'(\mathbf{V})] + \mathbf{g} \tag{21}$$

where, $\mathbf{u}$ is the velocity vector, ρ is the density, $\mathbf{V}$ is the strain rate tensor, $\mathbf{g}$ is the gravity vector. The Confined Interpolation Profile (CIP, Yabe and Aoki 1995) method is used to solve the advection terms of the above equation and other terms are solved using the finite different method. In order to capture the surface of flowing material, an implicit function, called density function, which indicates the occupancy of the material at each calculation point, is used. The change of the density function is solved using Tangent of Hyperbola for Interface Capturing (THINC) method (Xiao et al. 2005). By using the THINC method, we can keep sharp interface even in Eulerian mesh system. In addition, total mass of flow material can be kept.

Table 3 Numerical parameters of flow simulation of the real fill slope failure

	Air	Granular material
ρ Density (kg/m^3)	1.25	1800.0
C_s Sound speed (m/s)	340.0	1500.0
η Viscosity coefficient (Pa · s)	0.00002	_
η_0 Viscosity after yield (Pa · s)		1.0
c Cohesion (Pa)		1000.0
ϕ Internal friction angle (degree)	_	5.7
Δx, Δy Mesh size (m)	$\Delta x = 2.0$ $\Delta y = 0.5$	
$N_x \times N_y$ Number of meshes	100×60	
^{g} Gravity acceleration (m/s^2)	9.81	

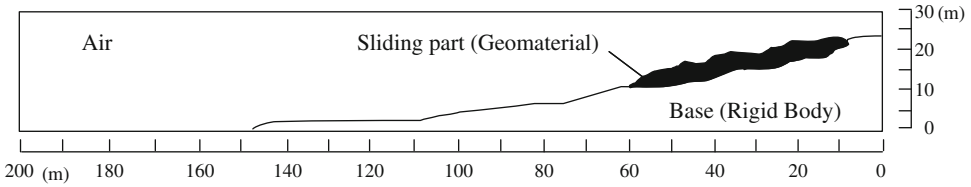

Fig. 11 Numerical model of flow simulation of the real fill slope failure

3.2 Flow Simulation of the Real Fill Slop Failure

A flow simulation using the CFD based method is introduced in this subsection. The fill slope failure explained in Sect. 2 is targeted also in this simulation. Although process before failure is reproduced in FEM analysis, flow behavior after failure is targeted in this simulation.

In order to determine numerical parameters, sample soil is obtained in the site of fill slope failure soon after the incident, and some in-site experiments were conducted. In the experiments, a soil-slump test was also carried out. The cohesion and the internal friction angle are determined by conducting a series simulation of soil-slump test (Moriguchi et al. 2005). Numerical parameters determined from the experimental results and the simulated results are shown in Table 3.

From topographic surveying data and related maps, a two-dimensional numerical model was prepared as shown in Fig. 11. The shadow part denotes the sliding part, and non-sliding part in the incident is considered as rigid body in the simulation. The non-slip boundary condition is used for the bottom boundary and surface of the rigid body.

Figure 12 shows simulated surface configurations at different times. As shown in the result, final run-out distance is about 190 m. According to literatures (e.g. Koyanagi 2003; The Japanese Geotechnical Society 2003), observed run-out distance was about 180 m, therefore simulated result corresponds to observed travel distance with high accuracy.

3.3 Brief Explanation of DEM

Because DEM is very famous numerical method, its theory is explained briefly. The method is based on discrete modeling, and its theory is totally different from the other methods introduced in this paper. The method can calculate the movement of assembly of particles and it has been widely used to simulate the behavior of granular material. Generally, an interparticle force model is shown in Fig. 13. Spring and dashpot are considered in both normal and tangential directions and the slider is used to describe the friction angle at the surface of particles. Based on the interparticle force model, collision force is calculated when collision of particles arise, then movement of each particle are calculated. Because of rapid development of performance of computers, large number of particle is getting to be used in recent studies. In addition, not only sphere element but also non-spherical elements is getting to be used for simulation of granular materials.

3.4 A Flow Simulation of a Flume Experiment

3D numerical simulations of sand flow in a small-scale flume experiment are carried out (Denlinger and Iverson 2001) using the DEM (discrete modeling) and the CFD (continuum modeling). The experiment employed a rectangular flume with a bed surface inclined at 31.4 degrees tapering to a horizontal run-out position (shown in Fig. 14). Figure 15 shows the

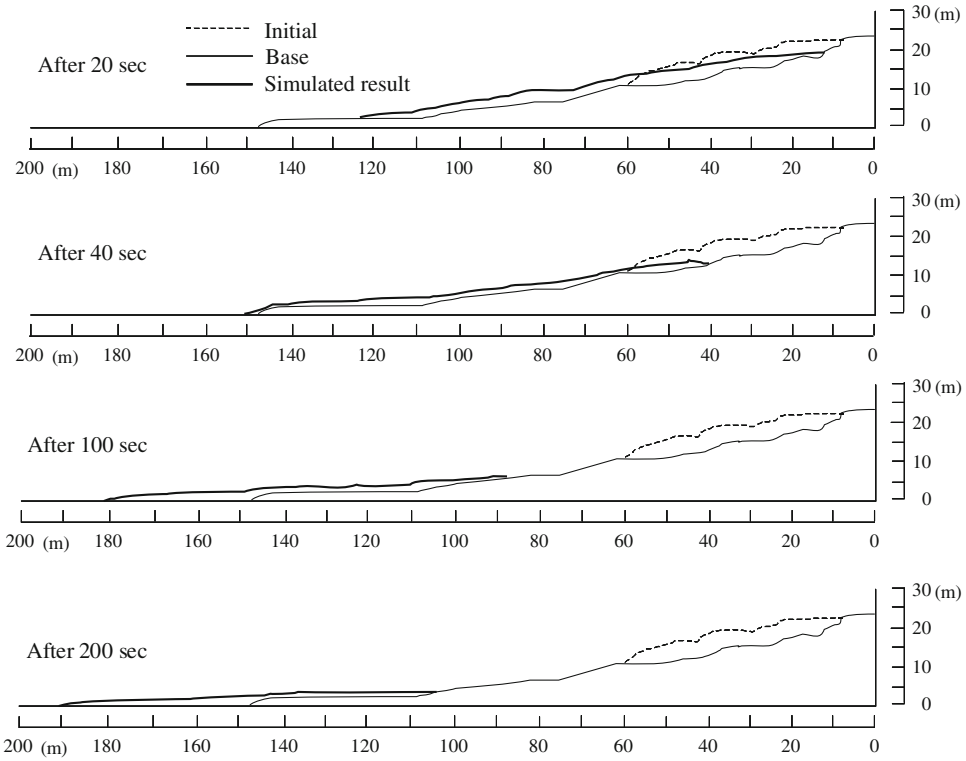

Fig. 12 Simulated surface configurations

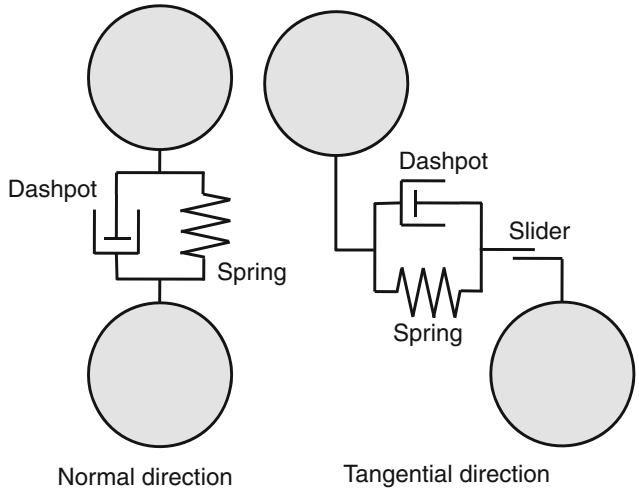

Fig. 13 Interparticle force model of DEM

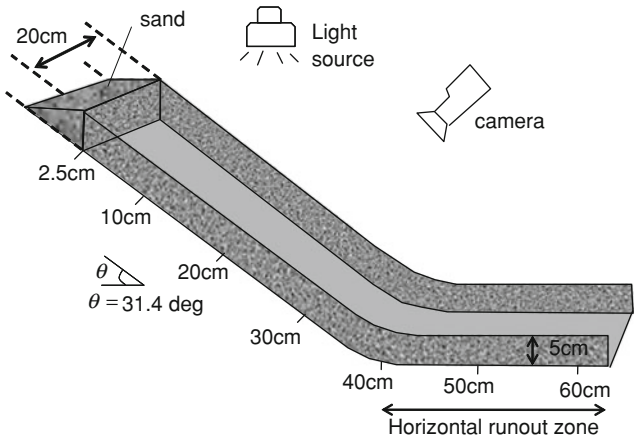

Fig. 14 Model slope used in the experiment

thickness distribution at different time obtained from the experiment. The internal friction angle and initial density of the sand were 40 degrees and 1600 kg/m^3. Density of sand grain is 2650 kg/m^3 and typical grain diameter was 0.5 mm.

Figures 16 and 17 show numerical models used in DEM and CFD simulation, respectively. In the DEM simulation, 35,410 spherical particles with diameter 2 mm are set on the top part of the flume considering the initial density of the sand. In the numerical model of CFD simulation, the inclination of the flume is described by changing direction of the gravity acceleration. Parameters used in this simulation are summarized in Table 4. Three cases are considered in both DEM and CFD simulations. In the DEM simulation, the spring coefficient and the dumping coefficient of interparticle model are changed. Same values of the coefficients are used in both normal and tangential direction. 29 degrees is used as the bottom friction angle in all cases. The value is reported in the literature as the static friction angle between sand grain and bottom surface of flume. On the other hand, in CFD simulation, only bottom friction is changed. 29, 20, 15 degrees were used for each cases. Numerical formulation about the bottom friction is

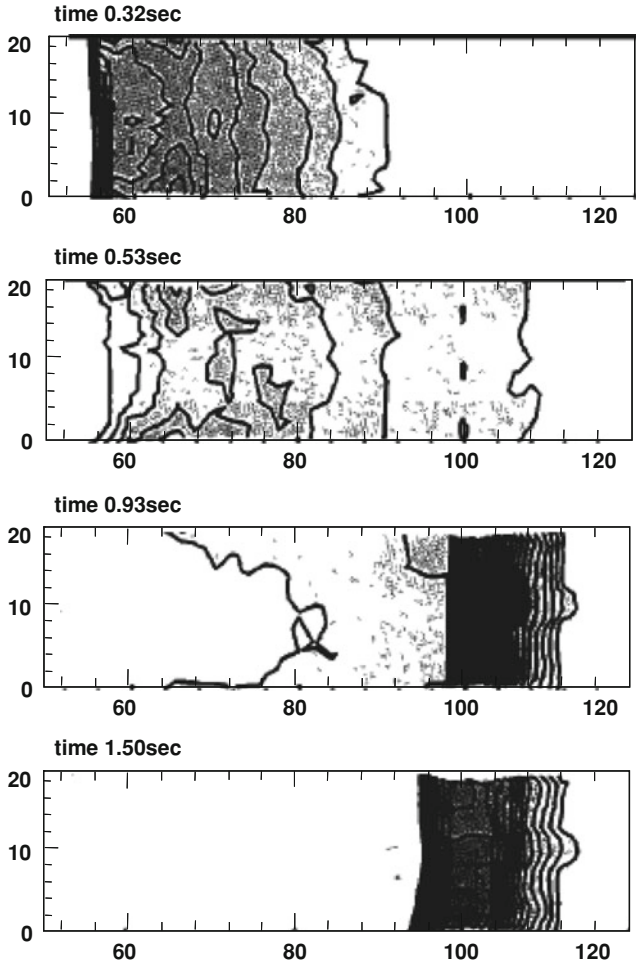

Fig. 15 Thickness distribution of sand (Denlinger and Iverson 2001)

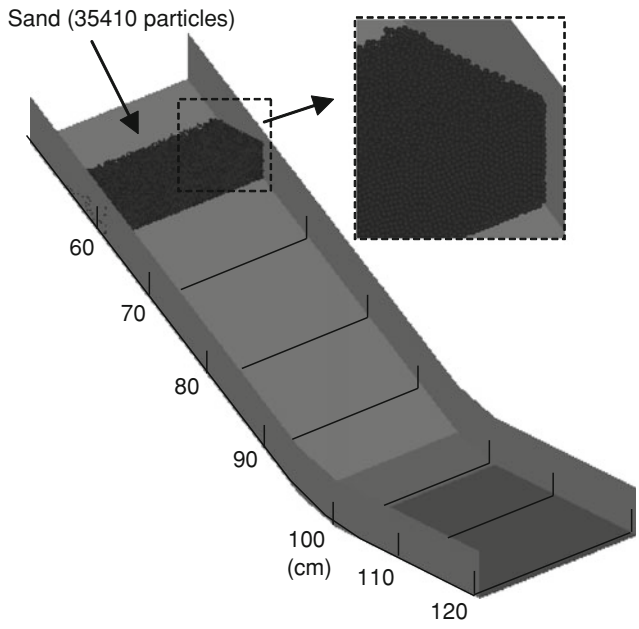

Fig. 16 Numerical model (DEM)

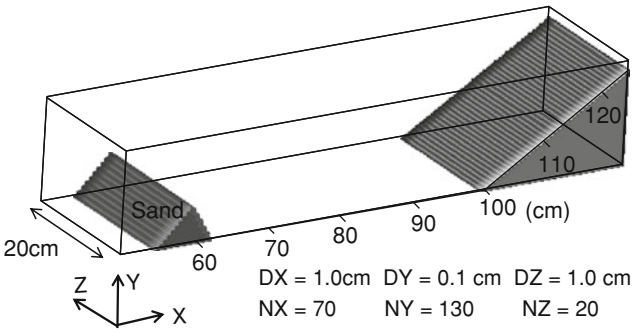

Fig. 17 Numerical model (CFD)

summarized by Moriguchi et al. (2010). Other parameters are determined based on condition of the experiment and are fixed in all cases.

Figures 18 and 19 shows the thickness distributions at different time simulated in DEM and CFD simulations, respectively. As shown in Fig. 18, values of the elastic and the dumping coefficients strongly affect the flow behavior. When the high value of elastic coefficient is used, high fluidity can be seen in the simulated result. In contrast, high value of dumping coefficient makes the flow slower. By adjusting these parameters, it is possible to reproduce the experimental result. The result of Case DEM-3 is in good agreement with the thickness distribution obtained from the experimental. According to the results of CFD simulations (shown in Fig. 19), the simulated flows are strongly depends on the value of the bottom friction, and it is confirmed that the result is in agreement with the experimental result when a small bottom friction angle is used. When 29 degrees are used as bottom friction, the sand dose not reach the end part of the flume and stops on the inclined part. This tendency is totally deferent from the results of the DEM simulation. It can be considered that the different between the DEM and the CFD simulations attribute to the rotation of sand grains. In DEM simulation, the effect of the rotation can be described directly and dynamic friction angle at the bottom surface become lower than 29 degrees. On the other hand, the rotation cannot be considered in the CFD simulation because the method is based on continuum modeling. Therefore we have to use the dynamic friction angle as an input parameter of the bottom friction angle.

3.5 Sammy of CFD and DEM

It is possible to predict flow behaviors of soils by using CFD and DEM. These methods are getting to become strong tool for large deformation problems. However, these methods also have disadvantages. In CFD simulation, it is difficult to keep historical information of soils, such as history of the strain and loading. Thus there is a difficulty when

Table 4 Parameters used in simulations of the flume experiment

Case	Initial density of sand mass (kg/m^3)	Density of sand grain (kg/m^3)	Friction angle of sand (degree)	Bottom friction (degree)	Spring constant (N/m)	Damping coefficient (N s)
DEM-1	$1.6X10^3$	$2.65\ X10^3$	40	29	$1.0X\ 10^6$	$1.0X\ 10^6$
DEM-2	$1.6X10^3$	$2.65\ X10^3$	40	29	$1.0X\ 10^6$	$5.0X\ 10^3$
DEM-3	$1.6X10^3$	$2.65\ X10^3$	40	29	$5.0X\ 10^6$	$3.0X\ 10^3$
CFD-1	$1.6X10^3$	–	40	29	–	–
CFD-2	$1.6X10^3$	–	40	20	–	–
CFD-3	$1.6X\ 10^3$	–	40	15	–	–

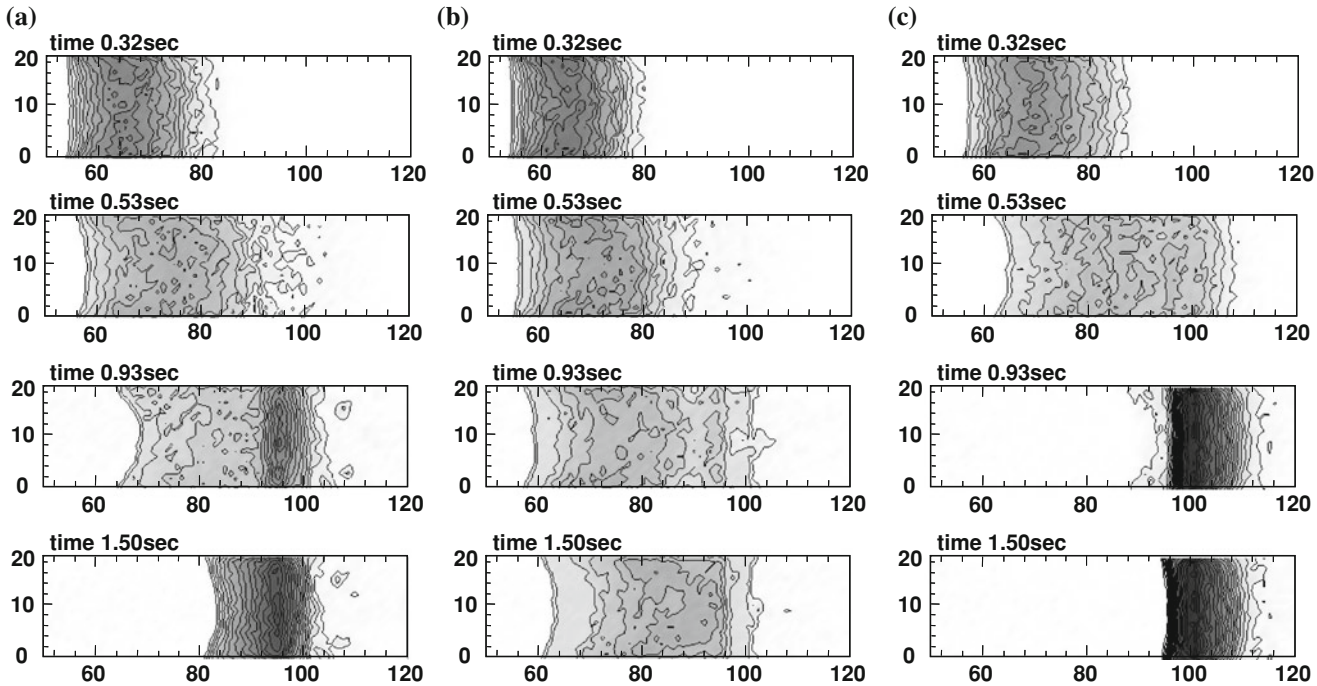

Fig. 18 Thickness distributions of sand (DEM). **a** DEM-1, **b** DEM-2, **c** DEM-3

constitutive models developed in the research field of geomechanics are used in the simulation. It is important to select problems with engineering judgment. Disadvantage of DEM is difficulty of parameter setting. Although some research achievements have been reported, problem of parameter setting is not solved completely.

4 Continuous Simulations of Deformation, Failure and Flow Using SPH

An example of SPH method is introduced in this section. As explained in previous sections, FEM, CFD and DEM have each applicable scope that depends on deformation level. In contrast, applicable scope of SPH is not restricted by deformation level. In other word, SPH can simulate all deformation level, such as small deformation, failure and flow. In this section, basic theory of SPH is explained, and then a simulation of real scale excavation experiment is shown. Numerical results of SPH are compared with experimental results, results of FEM, the safety factor obtained from conventional limit equilibrium method. Based on the comparison, advantages and disadvantages of SPH are discussed.

4.1 Basic Theory of SPH

SPH method is one of the particle methods. In the method, objects are expressed as an assembly of particles. If the motions of the particles are solved individually, the

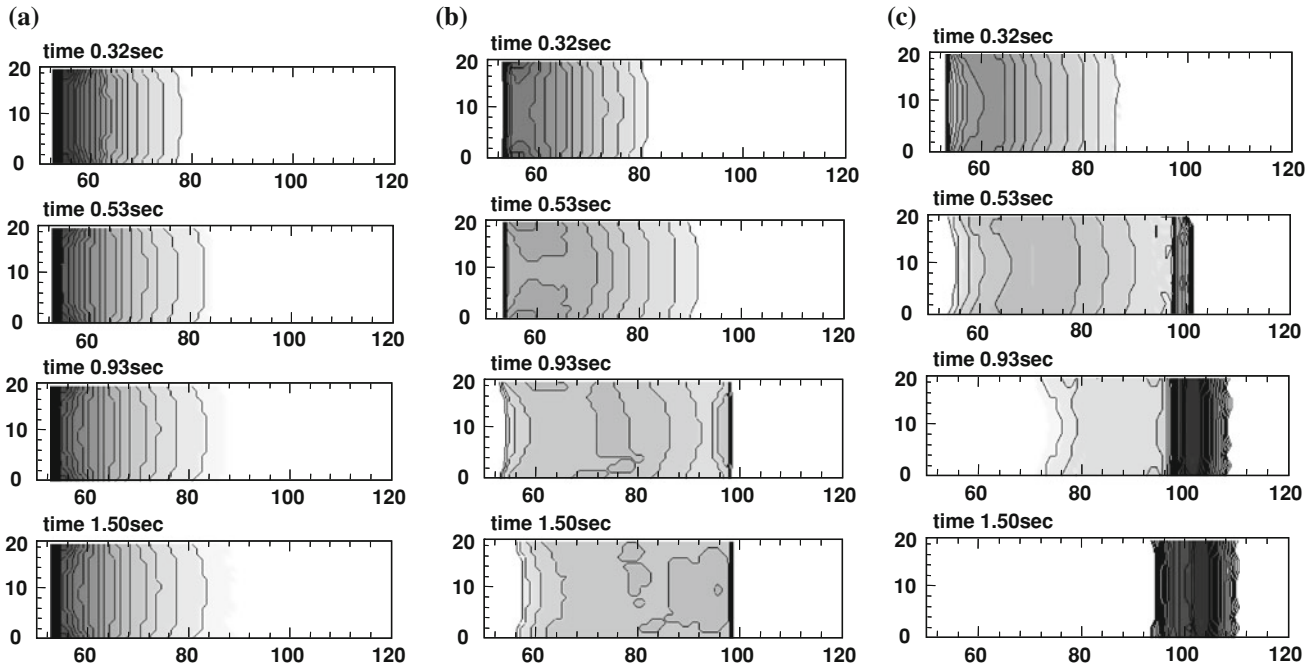

Fig. 19 Thickness distributions of sand (CFD). **a** CFD-1, **b** CFD-2, **c** CFD-3

deformation behavior of the continuum cannot be represented by this technique. In order to treat an object as a continuum, a unique interpolation theory is used. This interpolation theory includes two key approximations: a kernel approximation and a particle approximation. Using the kernel approximation, a bell–shaped distribution profile is estimated around a reference particle α.

The kernel approximations are based on neighboring particles β located at points x^{β} within the support domain $\kappa^d h$ of a smoothing function W for the reference particle α, which is located at point x^{α}, as shown in Fig. 20.

Here, κ^d is a parameter that determines the radius of the support domain and is determined by the smoothing functions. Also, h is the radius of the influence domain. The radius of the support domain is obtained by multiplying the radius of the influence domain by the parameter κ^d. The radius of the influence domain is obtained by multiplying the initial interparticle distance by the parameter β^h. In the first step of the interpolation, we define a smoothed physical quantity $< f(x^{\alpha}) >$ for the physical quantity $f(x^{\alpha})$ at the reference particle α as follows:

$$\langle f(x^{\alpha})\rangle = \int_{\Omega} f(x^{\beta}) W(x^{\alpha} - x^{\beta}, h) dx = \int_{\Omega} f(x^{\beta}) W(r, h) dx^{\beta} \tag{22}$$

where $r = \left|x^{\alpha} - x^{\beta}\right|$ and Ω is the volume of the integral that contains x^{α} and x^{β}. The smoothing function W satisfies the following three conditions.

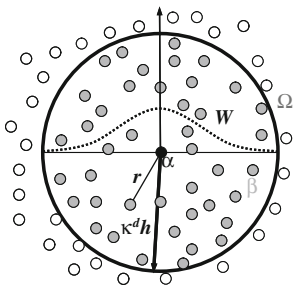

Fig. 20 Expression of a physical quantity using the SPH method

The first condition is the normalization condition:

$$\int_{\Omega} W(r, h) dx^{\beta} = 1 \tag{23}$$

The second condition is the delta function property, which holds when the smoothing length approaches zero:

$$\lim_{h \to 0} W(r, h) = \delta(r) \tag{24}$$

The third condition is the compactness condition:

$$\lim_{h \to 0} W(r, h) = 0 \quad \text{when } \left|x^{\alpha} - x^{\beta}\right| > \kappa^d h \tag{25}$$

where defines the nonzero area of the smoothing function.

In the second step of the interpolation, the physical quantity $< f(x^{\alpha}) >$ for the reference particle α is expressed as the summation of the distribution of the assumed physical quantities $f(x^{\beta})$ for each particle. Thus, the physical quantity can be expressed in terms of N discrete points:

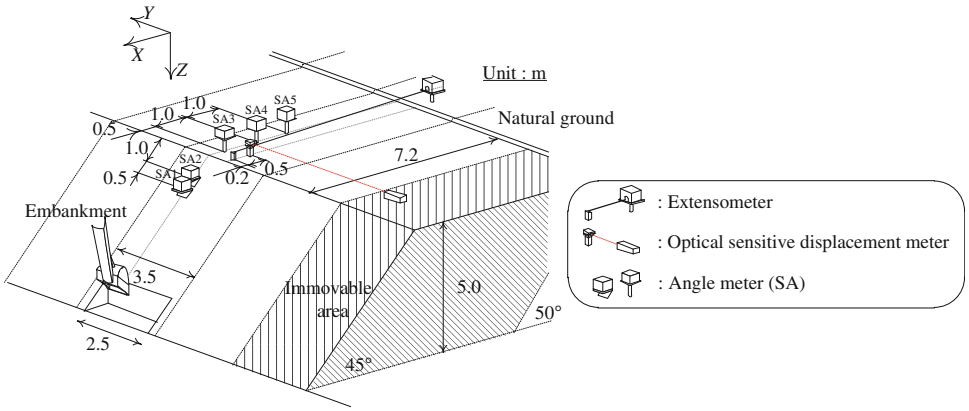

Fig. 21 Schematic view of the field test setup (Itoh and Toyosawa 2009)

$$dx^{\beta} = \frac{m^{\beta}}{\rho^{\beta}} \tag{26}$$

where dx^{β} is the volume, m^{β} is the mass, and ρ^{β} is the density of the neighboring particles β. Equation (22) is transformed via the above equation as follows:

$$\langle f(x^{\alpha})\rangle = \sum_{\beta}^{N} \frac{m^{\beta}}{\rho^{\beta}} f\left(x^{\beta}\right) W(r,h) = \sum_{\beta}^{N} \frac{m^{\beta}}{\rho^{\beta}} f\left(x^{\beta}\right) W^{\alpha\beta} \tag{27}$$

where $W^{\alpha\beta}$ is the smoothing function that expresses the contribution from the neighboring particles β to the reference particle α. Equation (27) is a formula for evaluating a physical quantity via the SPH method. It is also possible to approximate the spatial gradient of a physical quantity in a similar way, using the spatial derivative of the smoothing function. The spatial derivative of Eq. (22) can be written as

$$\begin{aligned} \nabla\langle f(x^{\alpha})\rangle &= \nabla \int_{\Omega} f\left(x^{\beta}\right) W(x^{\alpha} - x^{\beta}, h) dx^{\beta} \\ &= \int_{\Omega} f\left(x^{\beta}\right) \nabla W(r,h) dx^{\beta} \\ &= \int_{\Omega} f\left(x^{\beta}\right) \nabla W^{\alpha\beta} dx^{\beta} = \sum_{\beta}^{N} \frac{m^{\beta}}{\rho^{\beta}} f\left(x^{\beta}\right) \nabla W^{\alpha\beta} \end{aligned} \tag{28}$$

Furthermore, the above equation can be transformed as follows:

$$\nabla\langle f(x^{\alpha})\rangle = \frac{1}{\rho^{\alpha}} \sum_{\beta}^{N} m^{\beta} \left(f\left(x^{\beta}\right) - f(x^{\alpha})\right) \nabla W^{\alpha\beta} \tag{29}$$

$$\nabla\langle f(x^{\alpha})\rangle = \rho^{\alpha} \sum_{\beta}^{N} m^{\beta} \left(\frac{f(x^{\alpha})}{(\rho^{\alpha})^{2}} + \frac{f\left(x^{\beta}\right)}{(\rho^{\beta})^{2}}\right) \nabla W^{\alpha\beta} \tag{30}$$

where ρ^{α} is the density of the reference particle α. In the two–step interpolation theory, it is possible to calculate any physical quantity and its first derivative.

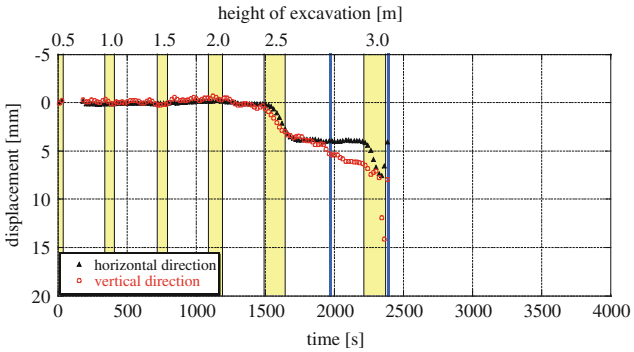

Fig. 22 Time history of the displacement obtained by the optical sensitive displacement meter (Itoh et al. 2007)

4.2 A Real Scale Excavation Experiment

Itoh et al. (2007) conducted a real scale excavation experiment of embankment. The test embankment used in the experiment was 5 m in height and 3.5 m in width, with a slope angle of 45 degrees, and was composed of Kanto Loam and Narita sand. In the experiment, embankments with and without surface compaction were constructed. The failure of the test embankment was triggered by destabilization of the slope due to excavation at the toe of the slope. The slope was excavated using a backhoe, and the excavation was carried out in several stages. The excavation depth for a single stage was about 0.5 m, and the width of the excavation was 2.5 m. After each excavation stage, the slope was left undisturbed for 5 min. Excavation continued until slope failure occurred. Figure 21 shows the positions of the measuring instruments. As shown in the figure, two angle meters were placed on the slope surface, and three angle meters were placed at the top of the slope. An extensometer and an optical sensitive displacement meter were also placed at the top of the slope.

Figure 22 shows the time history of the displacement, obtained in the experiment by the optical sensitive displacement meter placed 0.7 m from the top of slope. Figure 23 shows photos taken at excavation height of 2.5 and 3.0 m. When the excavation depth reached 2.5 m, a 3 mm

Fig. 23 Failure process (Itoh and Toyosawa 2009). **a** at excavation height of 2.5 m, **b** at excavation height of 3.0 m

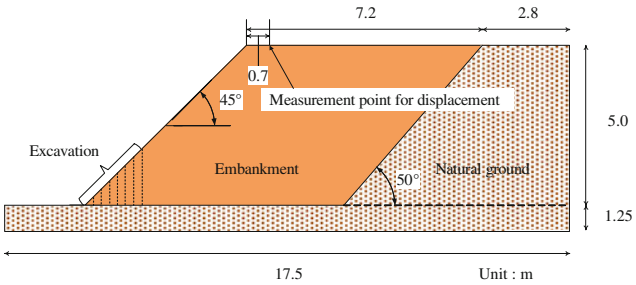

Fig. 24 Numerical model (Koitabashi et al. 2008)

displacement appeared in both the horizontal and vertical directions, and this displacement was maintained in both directions at the conclusion of the stage. A localized slope failure then appeared, as shown in Fig. 23a. Moreover, when the excavation depth reached 3.0 m, a massive failure (including the crown) occurred, as shown in Fig. 23b.

4.3 Simulations of the Real Failure Experiment

The real-scale experiment was reproduced in a previous study, using two- and three-dimensional FEM analyses. Figure 24 illustrates the numerical model used in the FEM analysis. In order to reproduce the conditions of the experiment, the excavation depth for a single stage was set at 0.5 m. In the three-dimensional analysis, the width of the excavation was 2.5 m, and the unexcavated part was simulated. The parameters used in this analysis were determined from in situ laboratory test. In this study, SPH method is applied to simulation of the real-scale experiment. The parameters used in this analysis are listed in Tables 5 and 6. The Drucker–Prager model with a non-associated flow rule is used as the constitutive model. The dilatancy angle was set to 0.0 degree. The isotropic stress corresponding to static earth pressure is used as the initial stress condition. As same as FEM analysis, the excavation is represented by particle (element) removal. For the boundary conditions, the horizontal direction on the side of the natural ground is fixed, and the

Table 5 Analytical parameters

Number of particles including the wall		10633
Initial interparticle distance	r_0 [m]	0.1
Radius of the support domain	$k^d h$ [m]	0.21
Time increment	Δt [s]	0.0001
Artificial viscosity parameter	α^{vis}, β^{vis}	1.0
Artificial stress parameter	ε^{AS}	0.30

Table 6 Material parameters

		Embankment	Natural ground
Density	γt [kN/m^3]	16.4	20.0
Young's modulus	E [kPa]	4850.0	8000.0
Poisson's ratio	ν	0.35	
Cohesion	c [kPa]	7.68	70.0
Internal friction angle	ϕ [deg]	36.34	5.0
Dilatancy angle	Ψ [deg]	0.0	

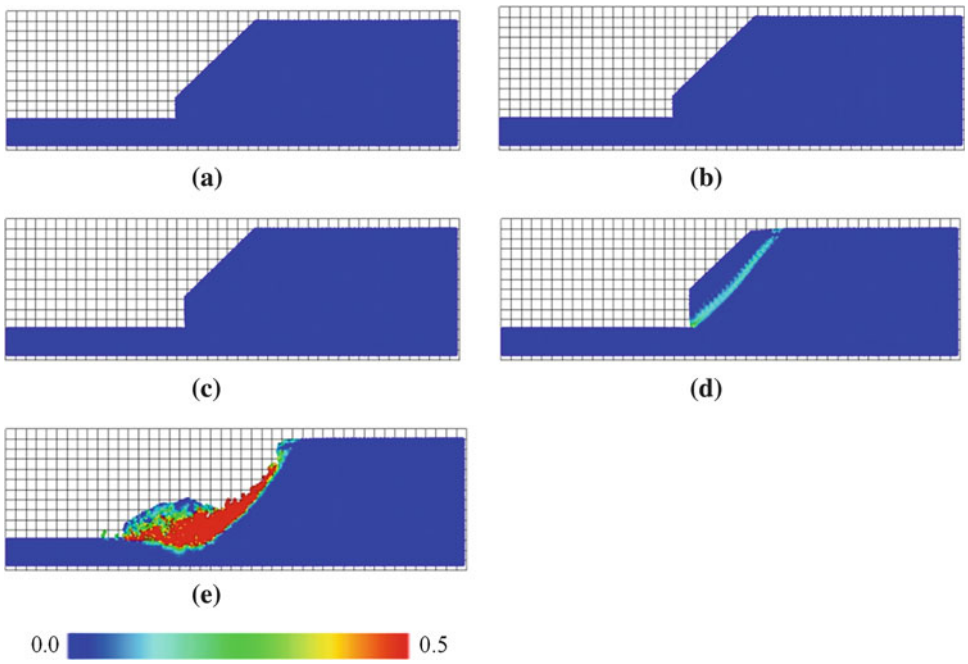

Fig. 25 Distribution of maximum shear strain at the different excavation heights. **a** Excavation height of 0.5 m, **b** Excavation height of 1.0 m, **c** Excavation height of 1.5 m, **d** Excavation height of 2.0 m, **e** Excavation depth of 2.5 m

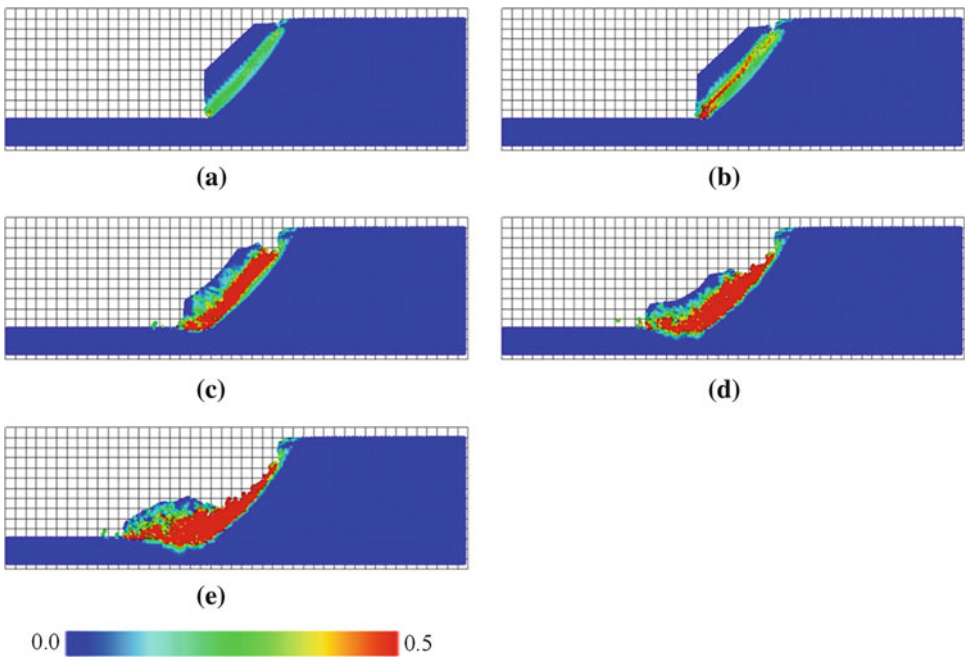

Fig. 26 Distribution of maximum shear strain at an excavation depth of 2.5 m. **a** After 1.0 s, **b** After 2.0 s, **c** After 3.0 s, **d** After 4.0 s, **e** After 5.0 s

vertical direction is free. The bottom boundary of the natural ground is fixed in both directions. The effect of pore water pressure is not taken into account.

Figures 25 show the distribution of the maximum shear strain at each excavation height obtained by SPH. Figure 25 indicates that the modeled embankment deforms when the excavation height reaches 2.0 m, and a massive failure occurred when the excavation depth reached 2.5 m. Deformations of the embankment at different times after the 2.5 m excavation are shown in Fig. 26. Vertical displacements obtained from the experiment, FEM analysis and SPH are shown in Fig. 27 all together. The values of the safety factor described in the figure are calculated using conventional limit equilibrium method (Fellenius method). Because there is a different between rage of displacements obtained by SPH and that obtained in the experiment and FEM analysis, two axes are used in the figure. As we can see from the figure, deformation obtained by FEM is in good agreement with the experimental results before failure, but FEM cannot reproduce large deformation after massive failure. On the other hand, in the result of SPH, although excavation stage of massive failure is little faster than that of the experiment,

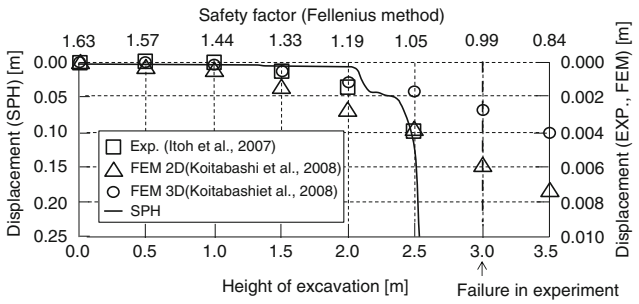

Fig. 27 Distribution of maximum shear strain at an excavation depth of 2.5 m

failure process is roughly reproduced. In addition, it can be seen large deformation after failure is described.

4.4 Sammy of SPH

Based on the comparison between the experimental result and SPH, it is found the SPH has the difficulty in analyzing the stress, strain and deformation in the slope with a high degree of accuracy. This point is a disadvantage of SPH. However, SPH can predict total process, such as small deformation, failure and final flow. Therefore the method is capable of wide application.

5 Concluding Remarks

FEM, CFD, DEM and SPH were introduced as numerical methods for large deformation problems induced by costal geodisasters. Each numerical method has an advantage for a specific problem. On the other hand, same method has disadvantage for other specific problems. It is still difficult to solve all deformation process, from initial small deformation to large deformation, with high calculation accuracy. It is therefore important for engineers to select an appropriate numerical method for each deformation level based on engineering judgment.

References

Armstrong, P. J., & Frederick C. O. (1966). *A mathematical representation of the multiaxial Bauschinger effect, C.E.G.B. Report RD/B/N731*. Berkeley Nuclear Laboratories, Berkeley, UK.

Biot, M. A. (1962). Mechanics of deformation and acoustic propagation in porous media. *Journal of Applied physics, 33*, 1482–1492.

Borja, R. I. (2006). On the mechanical energy and effective stress in saturated and unsaturated porous continua. *International Journal of Solids and Structures, 43*(6), 1764–1786.

Cudall, P. A., & Strack, O. D. L. (1979). A discrete numerical model for granular assemblies. *Geotechnique, 29*(1), 47–65.

de Boer, R. (2000). Contemporary progress in porous media theory. *Applied Mechanics Reviews, 53*(12), 323–369.

Denlinger, R. P., & Iverson, R. M. (2001). Flow of variably fluidized granular masses across three-dimensional terrain. *Journal of Geophysical Research, 106*(B1), 553–566.

Fukumoto, S., Unno, T., Sento, N., Uzuoka, R., & Kazama, M. (2007). Estimation of strong ground motions at tsukidate landslide site during the 2003 Sanriku-Minami earthquake. *Journal of Japan Association of Earthquake Engineering, 7*(2), 160–179.

Gingold, R. A., & Monaghan, J. J. (1977). Smoothed particle hydrodynamics: theory and application to non-spherical stars. *Monthly Notices of the Royal Astronomical Society, 181*, 375–389.

Gallipoli, D., Gens, A., Sharma, R., & Vaunat, J. (2003). An elasto-plastic model for unsaturated soil incorporating the effects of suction and degree of saturation on mechanical behaviour. *Geotechnique, 53*(1), 123–135.

Itoh, K., Takeyama, M., Toyosawa, Y., & Sano, T. (2007). The development of slope failure detection as a two-dimensional displacement sensor system using a large beam and optical sensor. *Journal of JSCE, Division C, 63*(2), 502–515.

Itoh, K., & Toyosawa, Y. (2009). Field test of slope failure during slope cutting work. *Journal of JSCE, Division C, 65*(1), 254–265.

Kazama, M., Takamura, H., Unno, T., Sento, N., & Uzuoka, R. (2006). Liquefaction mechanism of unsaturated volcanic sandy soils. *Journal of Geotechnical Engineering, Japan Society of Civil Engineers, 62*(2), 546–561.

Koitabashi, T., Suemasa, N., Itoh, K., & Toyosawa, Y. (2008). Mechanism of slope failure caused by toe excavating, *The 43th Japan National Conference on Geotechnical Engineering* pp. 869–870.

Koyanagi, K. (2003). Some challenges in earthquake damage surveys. *The Japanese Geotechnical Society, 52*(1), 16–18.

Lucy, L. B. (1977). A numerical approach to the testing of the fission hypothesis. *Astronomical Journal, 82*, 1023–1024.

Mori, T., Uzuoka, R., Chiba, T., Kamiya, K., & Kazama, M. (2011). Numerical prediction of seepage and seismic behavior of unsaturated fill slope, *Soils and Foundations* (in press).

Moriguchi, S., Borja, R. I., Yashima, A., Sawada, K ,& Oda K. (2010). Discrete and continuum modeling of sand flow experiment, *Geomechanics and Geotechnics*: *From Micro to Macro*, pp. 531–536.

Moriguchi, S., Yashima, A., Sawada, K., Uzuoka, R., & Ito, M. (2005). Numerical simulation of flow failure of Geomaterials based on fluid dynamics. *Soils and Foundations, 45*, 155–166.

Moriguchi, S., Borja, R. I., Yashima, A., & Sawada, K. (2009). Estimating the impact force generated by granular flow on a rigid obstruction. *Acta Geotechnica, 4*(1), 57–71.

Sawada, K., Moriguchi, S., Yashima, A., Zhang, F., & Uzuoka, R. (2004). Large deformation analysis in Geomechanics using CIP method. *JSME International Journal, Fluids and Thermal Engineering, Special Issue on CIP, Series B, 47*(4), 735–743.

Schrefler, B. A. (2002). Mechanics and thermodynamics of saturated/unsaturated porous materials and quantitative solutions. *Applied Mechanics Reviews, 55*(4), 351–388.

The Japanese Geotechnical Society (2003). Report of Seismic Hazard of Sanriku-Minami Earthquake and Miyagi Prefecture North Earthquake.

Uzuoka, R., & Borja, R. I. (2011). Dynamics of unsaturated poroelastic solids at finite strain. *International Journal for Numerical and Analytical Methods in Geomechanics*, DOI: 0.1002/nag.1061. (in press).

Uzuoka, R., Sento, N., Kazama, M., & Unno, T. (2005). Landslides during the earthquake on May 26 and July 26, 2003 in Miyagi. *Japan, Soils and Foundations, 45*(4), 149–163.

Xiao, F., Honma, Y., & Kono, T. (2005). A simple algebraic interface capturing scheme using hyperbolic tangent function. *International Journal for Numerical Methods in Fluids, 48*, 1023–1040.

Yabe, T., & Aoki, T. (1995). An universal solver for hyperbolic equations by cubic polynomial interpolation. *Computer Physics Communications, 66*, 219–232.

Zienkiewicz, O. C., & Shiomi, T. (1984). Dynamic behavior of saturated porous media: The generalized Biot formulation and its numerical solution. *International Journal for Numerical and Analytical Method in Geomechanics, 8*, 71–96.

Seismic Design of Piles in Liquefiable Soils

S. Bhattacharya, R. Sarkar, and Y. Huang

Abstract

Lands around the coasts are often reclaimed, contain fill materials/loose fills and therefore potentially liquefiable under moderate to strong shaking. Collapse and/or severe damage to pile-supported structures are still observed in liquefiable soils after most major earthquakes e.g. the 2011 Japan earthquake, 2010 Chile earthquake, the 2008 Wenchuan earthquake, the 2004 Sumatra earthquake, the 2001 Bhuj earthquake, the 1995 Kobe earthquake. Poor performance of pile foundations remains a great concern to the earthquake engineering community. A comprehensive overview of pile damages observed in the recent earthquakes is presented in this paper. This paper also critically reviews all the established pile failure theories. Deficiencies of the existing pile failure theories are highlighted. Various analyses procedures for piles in liquefiable soils are discussed.

Keywords

Pile failure • Liquefaction • Earthquake

1 Introduction

Construction of structures in coastal areas and pile foundations:

Due to increase in population and limiting land resources, infrastructures are often constructed on reclaimed lands, see for example the Port Island in Kobe (Japan), Saltlake and Rajarhat in Kolkata (India). Also coastal areas often have loose alluvial deposit that are liquefiable, see Gobindraju & Bhattacharya (2012). Figure 1 shows a photograph of a coastal town from the recent 2011 Tohoku earthquake where widespread destruction may be observed. One particular aspect of this earthquake, see Bhattacharya et al. (2011), is that tsunami caused extensive damage rather than the strong shaking or liquefaction.

Buildings and bridges on loose to medium dense sands are often built on piles to limit settlements because the surface ground layers are often not stiff enough to support the structures. In an earthquake if these loose sands are saturated, they lose strength as excess pore water pressure is generated and the soil tends to liquefy. This means that if the soil is on a slope it will flow down slope which is often termed as *"lateral spreading"*. Lateral spreading is a term used to represent the permanent lateral ground displacement after an earthquake. It is often found after an earthquake that the buildings supported on piles have collapsed or suffered excessive damage. The next section of the paper described observed damages from some of the recent earthquakes.

S. Bhattacharya (✉) · R. Sarkar
Department of Civil Engineering, University of Bristol, Queens Building, University Walk, Bristol, BS8 1TR, U.K
e-mail: S.Bhattacharya@bristol.ac.uk

Y. Huang
Tongji University, Shanghai, China

Y. Huang et al. (eds.), *New Frontiers in Engineering Geology and the Environment*,
DOI: 10.1007/978-3-642-31671-5_3,

Fig. 1 Devastation of a Coastal City during Japan Earthquake 2011 [Photo courtesy Dr K.Goda]

2 Observed Damage of Pile Supported Structures During Earthquakes in Liquefiable Soils

Examination and analysis of case histories of pile-supported structures revealed important aspects in the failure mechanisms. Since the 1964 Niigata Earthquake, liquefaction-induced damage has been an important design consideration. There have been several case studies of failures related to liquefaction phenomena reported since 1964. This section reviews cases of collapsed structures founded on piles.

2.1 Tohoku (Japan) Earthquake: March 2011

The 9.0 magnitude (Mw) earthquake occurred on 11th March 2011 in the north-western Pacific Ocean at a relatively shallow depth of 32 km with its epicenter approximately 72 km east of the Oshika Peninsula of Tohoku, Japan, lasting approximately 6 min. The earthquake caused 5–8 m up thrust on a 180-km wide seabed at 60 km offshore from the east coast of Tohoku. This resulted in a major tsunami that brought widespread destruction. Severe liquefaction were also observed. Many structures such buildings, manholes were tilted and sunk into the sediments, even when they remained structurally intact. Some degree of soil liquefaction is common in almost any major earthquake. The long duration of the earthquake might have played key role in the liquefaction induced damage. Many details of the earthquake can be found in Bhattacharya et al. (2011). Figure 2 show the collapse of a pile-supported building in Onagawa due to a combination of tsunami and liquefaction. The piles of the building were completely uprooted. Good performance of a modern pile-supported building in Minami Sunamachi (Tokyo) is reported in Bhattacharya et al. (2011).

2.2 Chile Earthquake (Maule) 2010

A large magnitude (8.8 Mw) earthquake strike Chile on 27th Feb 2010. The epicentre of the earthquake was located in the offshore Maule VII Region of Chile at a depth of 35 km as reported by the USGS. Three bridges over Bio–Bio river (in Concepcion city) were severely damaged. The city of Concepcion located at 105 km from the Earthquakes epicenter, suffered severe damage to infrastructure and buildings. Soil liquefaction evidence was observed in the North side of the river Bio–Bio and also noted by the GEER recognizance survey team.

The Bio–Bio Bridge indicated in Fig. 3a was the most damaged bridge with failure of multiple spans. This bridge was inaugurated to the public in the year 1943 and was closed to traffic in 2002 as it was deemed to be a safety risk due to its deteriorated condition. For the 1960 Valdivia Earthquake, the bridge suffered similar damage to spans and

Fig. 2 Pile building failure in Onagawa during 2011 Japan earthquake

was repaired with a steel beam covering a length of 45 m in the north side of the bridge and maintaining the same foundations made of wood piles. Lateral spreading could induce strength degradation and bending failure in the bridge. However, this explanation doesn't necessarily explain the failure of spans in the middle extension of the bridge. Figure 3b shows Llacolen bridge damage during the same Chile earthquake.

2.3 Wenchuan Earthquake (China) in 2008

Wenchuan earthquake was of the major earthquake that struck China. In this earthquake several hundred bridges collapsed. Figure 4 shows the collapse of one of the spans of the MPZ (Miaoziping bridge in Chengdu). The reasons for collapse of so many bridges can be summarized as follows: (a) Site effects: many of the bridges that collapsed were near the epicenter of the earthquake due to strong near field motion. The recorded horizontal PGA is near about 1 g and the recorded vertical near field PGA in Wolong Station is 948.1 gal i.e. 0.95 g; (b) Geological hazards due to earthquake i.e. mainly due to landslides, rockfall. These failures occurred immediately or during the earthquake. (c) Effects of liquefaction mainly in the river bridges; (d) Inadequate structural consideration: Poor beam column stiffness, irregular shape causing stiffness irregularity (bridges curved in plan); (e) Active Fault movement and surface fracture induced by active fault.

2.4 Bhuj (India) Earthquake

The Bhuj earthquake (magnitude, $M_w = 7.7$) that struck the Kutch area in Gujarat at 8.46 AM (IST) on January 26, 2001 was the most damaging earthquake in India in the last 50 years. The epicenter of the quake was located at 23.4°N, 70.28°E and at a depth of 25 km, which is to the north of Bacchau town (Fig. 5). This earthquake has caused extensive damage to the life and property. Figures 6 shows failure of a pile-supported Kandla Port tower. This tower was located in laterally spreading ground. This tower tilted possibly due to the interaction between axial load induced settlement owing to liquefaction and bending due to lateral spreading forces. Details of the failure can be found in Dash et al. (2009a, b).

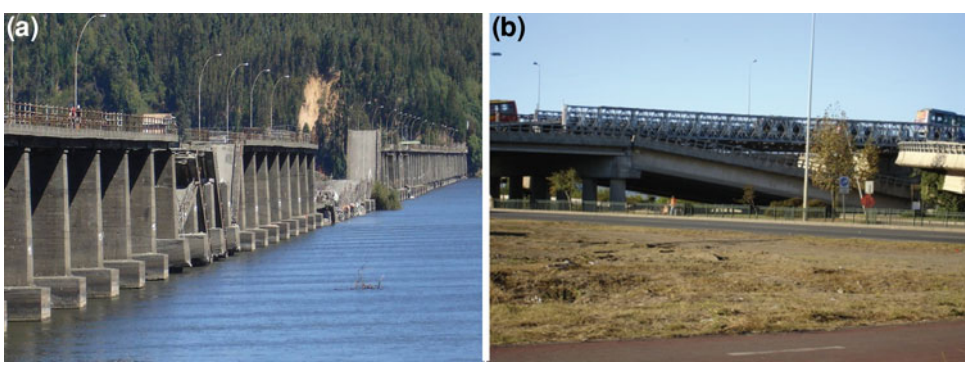

Fig. 3 Bridge damages during the 2010 Chile earthquake **a** Bio–Bio bridge **b** Llacolen bridge

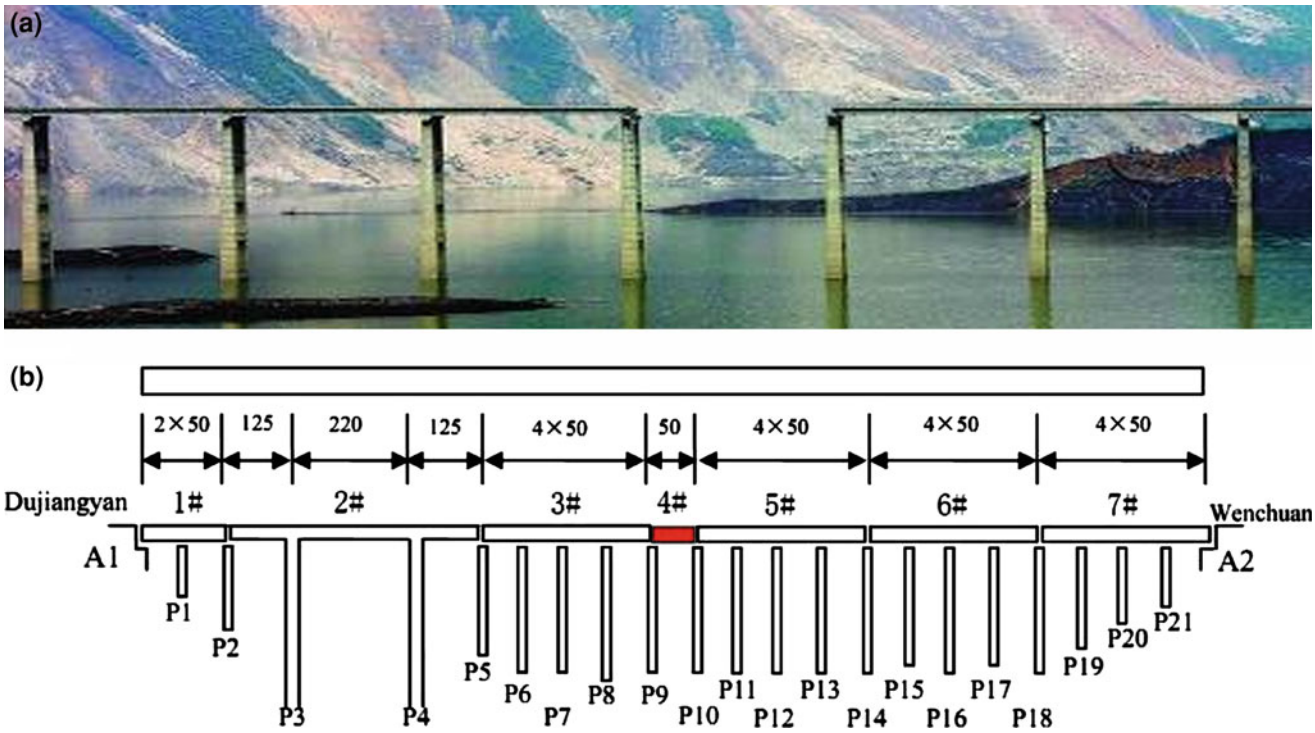

Fig. 4 **a** Photograph of the MPZ bridge following the 2008 Wenchuan earthquake **b** Schematic diagram of the bridge

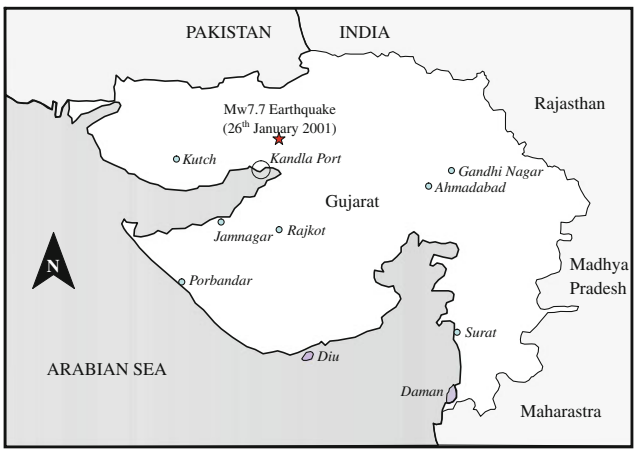

Fig. 5 Location map of Kandla port tower building along with the location of the epicentre

2.5 Kobe Earthquake 1995

The Kobe earthquake occurred on 17th January 1995 southern part of Hyogo Prefecture, Japan. It measured 6.8 on the moment magnitude scale (USGS). The tremors lasted for approximately 20 s. The focus of the earthquake was located 16 km beneath its epicenter, on the northern end of Awaji Island, 20 km away from the city of Kobe. Liquefaction caused damage to pile supported structures. Figure 7 shows two pile-supported building failures where the superstructures of the buildings are tilted due to the liquefaction of the subsoil. It may be mentioned that one of the buildings were founded on level ground and no lateral spreading was expected. Another building was on laterally spreading ground i.e. where the quay wall moved.

3 Observed Pile Damage from Detailed Field Investigations

As earthquakes are very rapid events and as much of the damage to piles occurs beneath the ground, it is hard to ascertain the failure mechanism unless deep excavation is carried out. Twenty years after the 1964 Niigata earthquake and also following the 1995 Kobe earthquake, investigations has been carried out to find the failure pattern of the piles, see Yoshida & Hamada (1990), BTL Committee (2000). Piles were excavated or extracted from the subsoil, borehole cameras were used to take photographs, and pile integrity tests were carried out. These studies hinted the location of the cracks and damage patterns for the piles. Of particular interest is the formation of plastic hinges in the piles. This indicates that the stresses in the pile during the earthquakes exceeded the yield stress of the material of the pile. As a result, design of pile foundation in seismically liquefiable areas still remains a constant source of attention to the earthquake geotechnical engineering community. The main observations are:

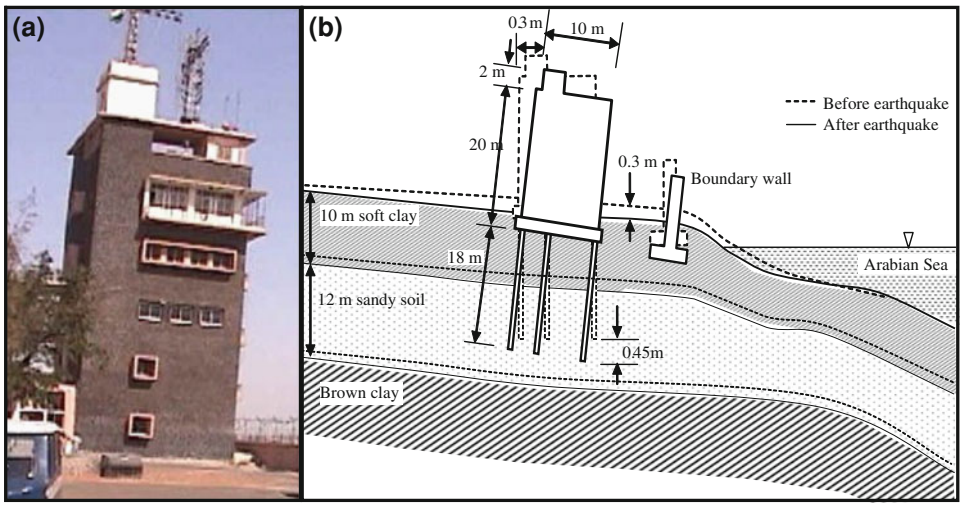

Fig. 6 **a** Kandla Port tower after the 2001 Bhuj earthquake **b** Plausible settlement mechanism of failure showing the tilting the Tower assuming there is no structural failure of piles

Fig. 7 Building failures after the 1995 Kobe earthquake

1. The failure of foundations not only occurred in laterally spreading grounds but also was observed in level grounds where no lateral spreading would be anticipated. This has been demonstrated through the building damages in Fig. 7. The failure patterns of the buildings in level ground and in laterally spreading ground are similar i.e. the buildings tilt considerably, see for example Fig. 7. In most cases, the superstructure remains undamaged. Therefore, by considering the building failure alone, it is difficult to ascertain the type of ground i.e. whether lateral spreading ground or level ground.
2. Figure 8 shows several examples of pile damage along which the soil profiles and the damage pattern. Cracks were observed near the bottom and top boundaries between liquefied and non-liquefied layers. Often cracks were observed at the pile head. More details can be found in Bhattacharya & Madabhushi (2008). The authors showed that plastic hinges also formed not only at the boundaries of the liquefiable and non-liquefiable layers but also at various depths. There are few cases where plastic hinges formed at the middle of the liquefied layer, see for example Fig. 8b. It has been reported, Yoshida et al. (2005) that this damage was observed when the structure was very close to the quay wall which moved towards the sea significantly.
3. Horizontal displacement of the piles were measured in some cases of pile failure, see for example Yoshida and Hamada (1990), Hamada & O'Rourke (1992). In some

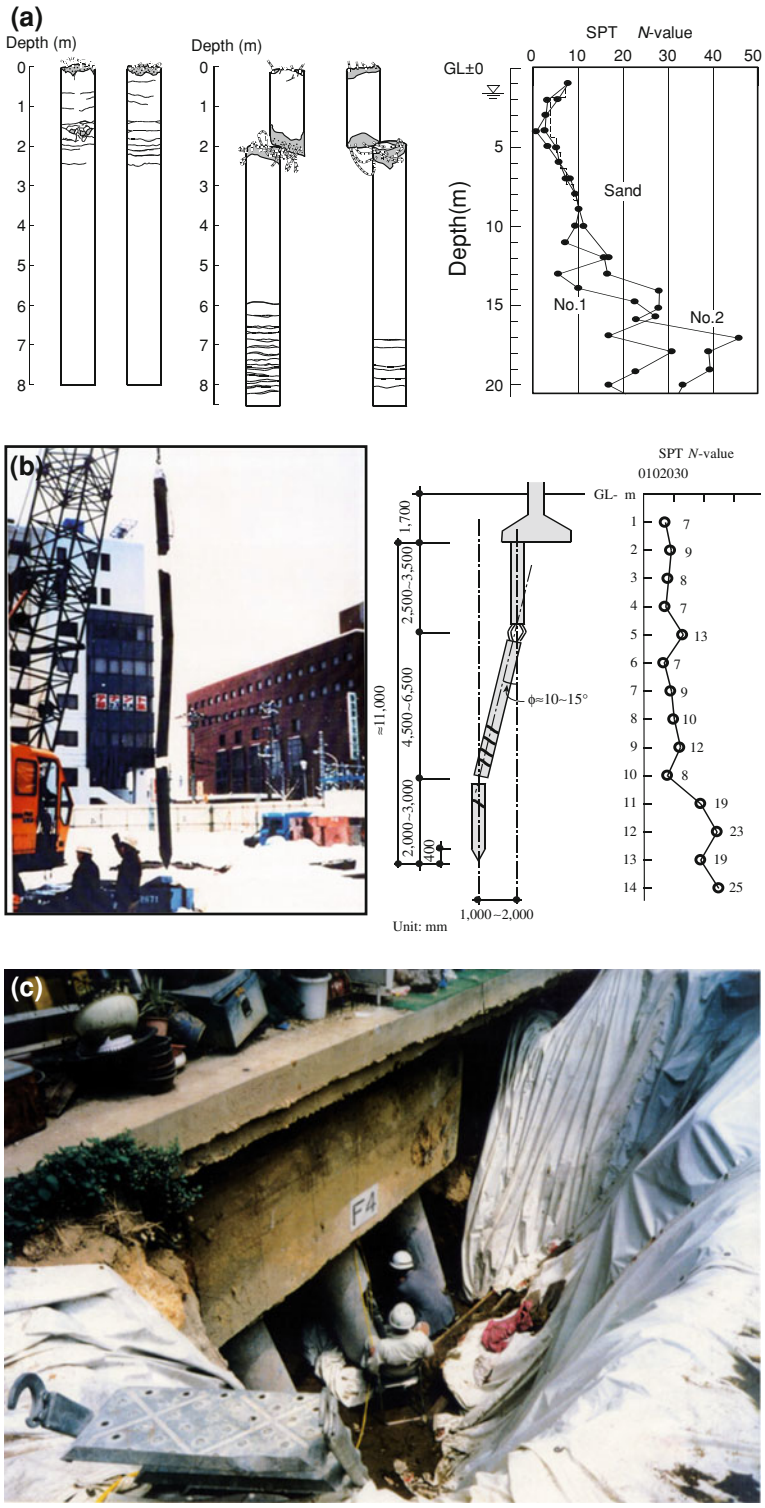

Fig. 8 **a** Building in Niigata city (Yoshida & Hamada 1990) **b** Building in Niigata city (Kawamura et al. 1985) **c** Damage to pile building during Kobe earthquake (Photo courtesy Dr Takashi Tazoh)

cases, the displacement of the piles was found to agree with the horizontal displacement of the ground.

4. It has been observed that large diameter piles performed well during the earthquake. For example, the older jetties of the Kandla port which were supported on 0.5 m diameter RCC piles suffered cracking during the 2001 Bhuj earthquake. In contrast, in the same area, the 1.0 m diameter RCC piles on the newer jetties and the concrete-filled-steel tubular piles performed well.

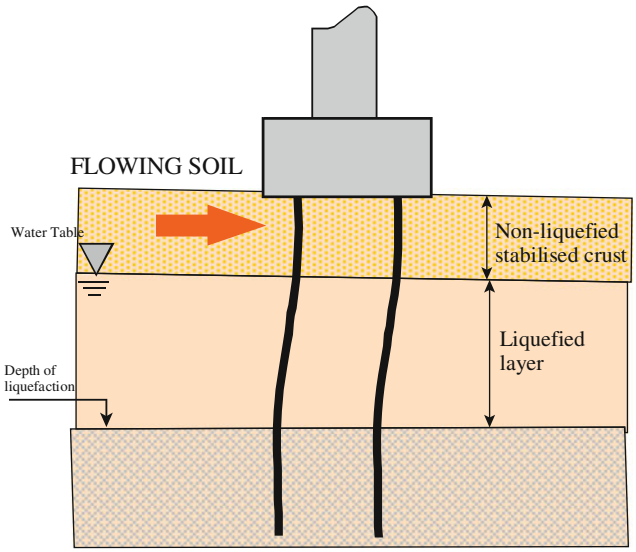

Fig. 9 Failure mechanism based on lateral spreading

4 Failure Mechanisms for Pile Foundations in Liquefiable Soils

It is generally acknowledged that the failure of the structures was caused by the lateral earth pressure applied by the laterally spreading liquefied sand and any non-liquefied stabilized crust resting on the top of the liquefied soil. Figure 9 explains the hypothesis of failure. This mechanism is therefore based on flexure of the pile causing a **bending failure** of the pile foundation.

However, recent research by Bhattacharya et al. (2004) suggested an alternative explanation recognizing the fact that pile foundations are normally carrying significant axial loads at the time of the earthquake. When the soil around the pile liquefies it loses much of its stiffness and strength, so the piles now act as unsupported long slender columns, and simply buckles under the action of the axial (superstructure) loads. The stress in the pile section will initially be within the elastic range, and the buckling length will be the entire 'unsupported' length in the liquefied soil. Lateral loading, due to slope movement, inertia or any out-of-alignment eccentricities will increase lateral deflections. When the pile suffers sufficient lateral deflections plastic hinges can form, reducing the buckling load, and promoting more rapid collapse. Therefore, this hypothesis is based on a **buckling failure** of the pile foundation.

There are two plausible failure mechanisms that can explain pile failure in liquefiable soils:

1. Bending mechanism where the piles are treated as beams. The lateral loads on the piles are due to inertial effects from the superstructure and kinematic effects due to ground movement.
2. Buckling instability where the piles are treated as beam-columns i.e. axially loaded slender columns carrying lateral loads. The piles are treated as unsupported columns in the liquefiable zones.

The next section describes each of these mechanisms in more detail.

4.1 Bending Mechanism

Tokimatsu et al. (1998) schematically described the soil-pile structure interaction in liquefiable soil as shown in Fig. 10a. The assumptions are:

1. Prior to the development of pore water pressure, the inertia force from the superstructure may dominate. This is referred to as stage I in Fig. 3.
2. Kinematic forces from the liquefied soil start acting with increasing pore pressure. This is referred to as stage II in Fig. 11a.
3. Towards the end of shaking, kinematic forces would dominate and have a significant effect on pile performance particularly when permanent displacements occur in laterally spreading soil.

Ishihara (1997) summarized the seismically induced loading on the pile by introducing the concepts of 'top down effect' and 'bottom up effect'. These are described below:

4.1.1 Top-Down Effect

At the onset of shaking, the inertia forces of superstructure are transferred to the top of the pile and ultimately to the soil. He assumes that during the main shaking, sandy soils in a deposit have not softened significantly due to liquefaction and that the relative movement between the piles and ground are small. However, he postulates that if ground motion is sufficiently high such that the induced bending moment in the piles exceeds the limiting value, the piles may fail. Since the horizontal load comes from the inertia force of superstructure, it is referred to as 'top down effect'. He concludes that the observed failure of a pile in the upper portion after an earthquake may be attributed to this effect.

Ishihara (1997) also reports: "It has been known that onset of liquefaction takes place approximately at the same time as the instant when peak acceleration occurs in the course of seismic load application having an irregular time history".

4.1.2 Bottom-Up Effect

In sloping grounds, the softened ground will start to move horizontally following the onset of liquefaction. Under this condition, lateral forces would be applied to the pile body embedded in the ground, leading to deformation of the pile in the direction of the slope. He assumes that seismic motion has already passed the peak but the shaking may still

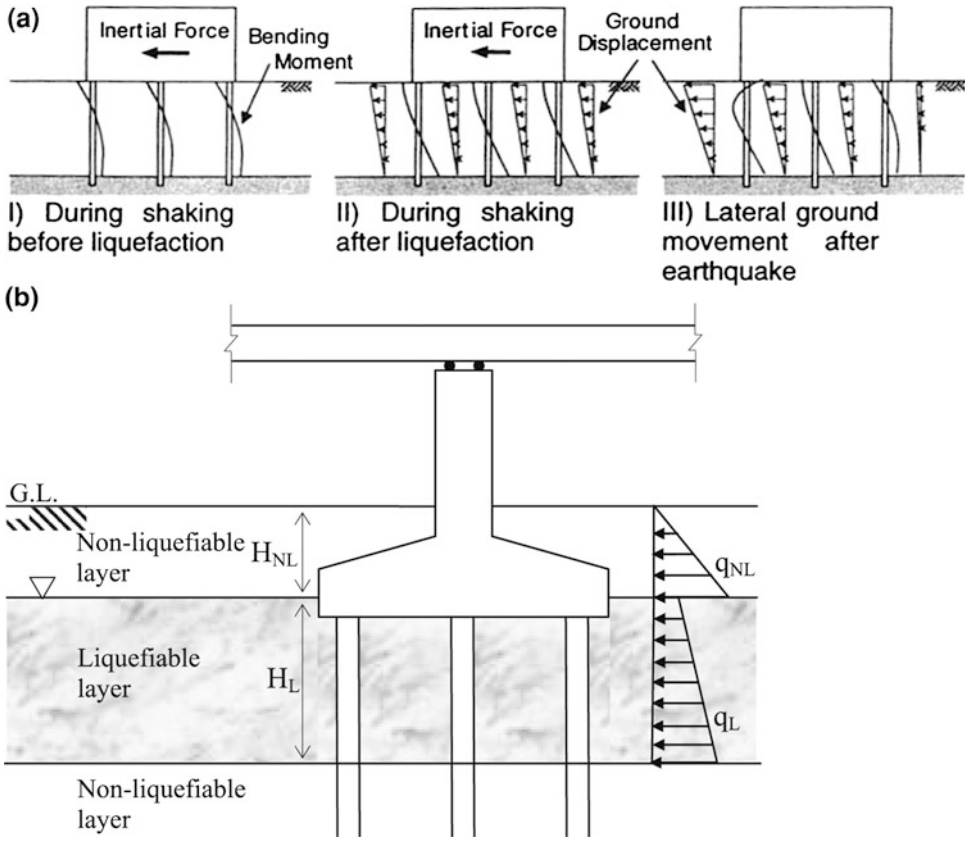

Fig. 10 **a** Schematic diagram showing the pile failure (after Tokimatsu et al. 1998) **b** JRA (1996) code of practice showing the idealisation for seismic design of bridge foundation

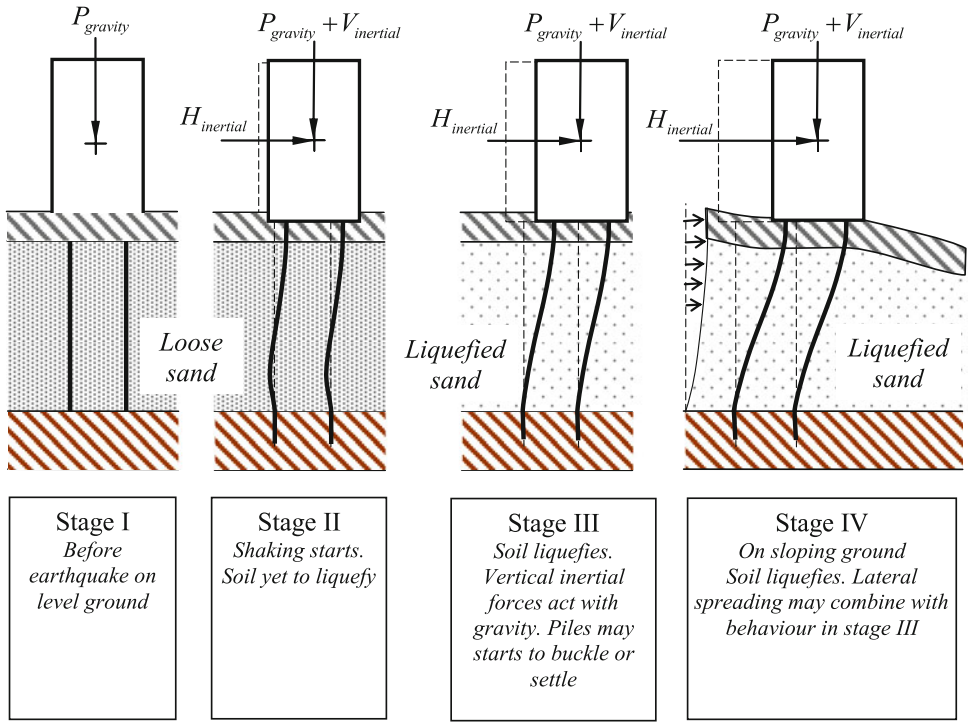

Fig. 11 Different loading regimes

be persistent with lesser intensity and therefore the inertia force transmitted from the superstructure will be small. Under such a loading condition, the maximum bending moment induced by the pile may not occur near the pile head but at a lower portion at some depth and this is referred to as, 'bottom-up effect'.

4.1.3 Japanese Highway Code of practice (JRA 1996 and 2002 edition)

The Japanese Highway code of practice (JRA 1996) has incorporated the concept as of "TOP-DOWN" and "BOTTOM-UP" effects as shown in Fig. 10a. The code advises practising engineers to design piles against bending failure assuming that the non-liquefied crust exerts passive earth pressure on the pile and the liquefied soil offers 30 % of total overburden pressure. Many researchers, as will be discussed later on have verified their experimental results against such pressure distribution. The code also advises designers to check against bending failure due to kinematic forces and inertia separately, i.e. a check against bending failure due to the combination of the two loads (Inertial and Kinematic) is not encouraged. The basis of such clauses can be well understood from the "Ishihara's top down and bottom up concepts".

4.2 Buckling Mechanism

Bhattacharya (2003), Bhattacharya et al. (2004, 2009) and Adhikari and Bhattacharya (2008) argues that piles become laterally unsupported in the liquefiable zone during strong shaking which may led to buckling type instability failure mechanism under the action of axial load acting on the pile at all times. Essentially, the soil around the pile liquefies and loses much of its stiffness and strength, so the piles now act as unsupported long slender columns, and simply buckles under the action of the vertical superstructure (building) loads. The stress in the pile section will initially be within the elastic range, and the buckling length will be the entire length in the liquefied soil. Lateral loading, due to slope movement, inertia or out-of-line straightness, will increase lateral deflections, which in turn can cause plastic hinge to form, reducing the buckling load, and promoting more rapid collapse. This theory has later been verified by other researchers; see for example Lin et al. (2005), Kimura & Tokimatsu (2007), Shanker et al. (2007), Knappett & Madabhushi (2005). Figure 11 shows the various loading regimes that affect the pile stresses and further details can be found in Bhattacharya et al. (2008).

The next section of the paper details few methods of analysis of pile foundations in liquefiable soils.

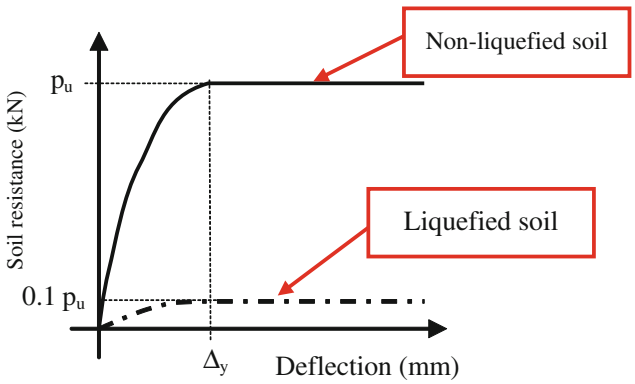

Fig. 12 p–y curve for non-liquefied soil and liquefied using p-multiplier

5 Analysis Procedures

Piles in liquefiable soil may be modeled by following two major analysis procedures:

1. Modeling by Beam on Nonlinear Winkler Foundation (BNWF)
2. Modeling considering Continuum

5.1 Winkler Models for Liquefied Soil

Beams on Non-linear Winkler Foundation (BNWF) of p–y method is commonly used to analyze piles API (2000). In "p–y" method, the soil is modeled as non-linear springs where 'p' refers to the lateral soil pressure per unit length of pile and the 'y' refers to the lateral deflection. Figure 12 shows a particular p-y model for non-liquefied soil and its corresponding liquefied condition based on an empirical method. The reduction of strength can be carried out using p-multiplier and typical values of this multiplier can be found in AIJ (2001), RTRI (1999), Liu & Dobry (1995). It may be noted that the initial stiffness (i.e. the initial slope of p–y curve) degrades when the soil transforms from being solid to fluid. A detailed discussion on the shape of p–y curves for liquefied soil can be found in Bhattacharya et al. (2009), Dash (2010).

However, analysis of the full-scale tests such as Rollins et al. (2005), centrifuge tests such as Bhattacharya et al. (2005), laboratory tests on liquefied soil by Yasuda et al. (1998), 1-g pipe pulling tests, Takahashi et al. (2002) suggests that the shape of the "p–y" curve for liquefied soil should look like a S-curve. Figure 13 shows the change of "p–y" curves when the soil is transformed from being solid to fluid-like medium. Figure 14 shows the shape following Dash et al. (2008).

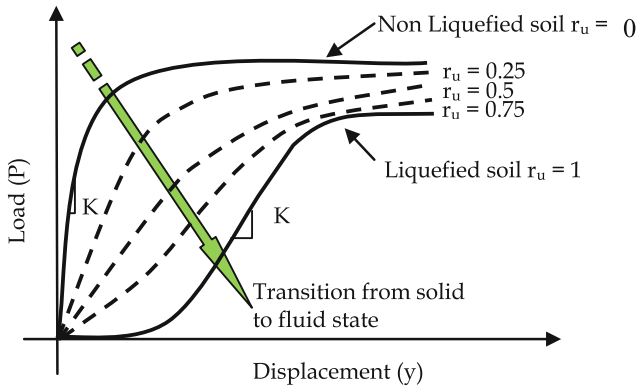

Fig. 13 p–y curve for saturated sandy soil during the process of liquefaction

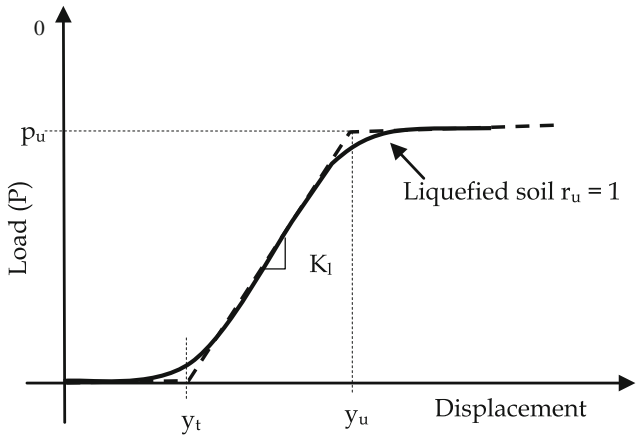

Fig. 14 Simplified p–y curve for liquefied soil, Bhattacharya et al. (2009), Dash et al. (2008), Dash (2010)

Figure 15 shows the implications of "p–y" curve on the small-vibration analysis of a pile-supported structure. The main parameters of a load–displacement (p–y curve) relationship are the stiffness and strength of liquefied soil. The stiffness of the soil i.e. the initial tangent stiffness of "p–y" curve is the resistance of soil to unit pile deformation. Under non-liquefied condition, when the differential soil-pile movement is small (i.e., the soil is not pushed to its full capacity), the resistance on pile depends on the initial stiffness of the soil and the value of deflection (Fig. 15a). In contrast, the strength of soil is an important parameter while dealing with high amplitude soil-pile interaction. In other words, when the differential soil-pile movement is large, the resistance offered by soil over pile is governed by the ultimate strength of the soil (Fig. 15a). For liquefied soil (see Fig. 15b), the pile response will be different for small and large amplitude vibrations. The lack of initial stiffness and strength of the liquefied soil will increase the P-delta effect for small amplitude vibration, and may promote buckling mode of failure of piles.

Reasonable accurate analyses can be carried out using BNWF model and examples of such analysis can be found in Dash et al. (2010) where both force based or displacement based loads can be applied. In displacement based analysis, relative pile-ground movement can be applied to the end of the springs. Figure 8 shows a typical plot where normalized pile head deflection are plotted against normalized force or ground displacement. It may be observed that with the combined action of axial load and lateral load/ground displacement, the pile head deflection becomes infinite suddenly (essentially instability). This shows the importance of considering the axial load in the analysis.

5.2 Continuum Modeling

With the advent of high end computers soil-pile system may also be modeled as continuum system with the standard finite element/finite difference software packages. These analyses can consider two/three dimensional behavior of the soil-pile system especially under dynamic condition. Advanced soil plasticity models can be employed in these analyses. Bentley & El Naggar (2000) have reported nonlinear analysis for single piles with a particular reference to Loma Prieta Earthquake (1989) time history for sandy soil. The separation between the soil and pile was simulated by using contact element at the interface of the soil and pile. Wu & Finn (1997a) proposed a quasi three dimensional finite element method of analysis for the dynamic response of the pile foundations feasible for practical applications. The method was presented for elastic response and was validated against Kaynia & Kausel (1982), Novak et al. (1990) and Fan et al. (1991). Responses were also validated with low-amplitude field vibration tests. Study was performed for single pile as well as 2 × 2 pile groups. Wu & Finn (1997b) extended the study for dynamic nonlinear analysis for pile foundations in the time domain. The analyses were performed for strain dependent modulus and damping. The analysis is validated using data from centrifuge tests on a single pile and a 2 × 2 pile group under simulated earthquake loading. The analysis demonstrated the importance of the inertial interaction between the foundation and structure. Time variation of dynamic impedances of the pile foundations during shaking is presented. Sarkar & Maheshwari (2012) and Maheshwari & Sarkar (2011) investigated the three-dimensional behaviour of single pile and pile groups considering liquefaction of the soil medium with work hardening Drucker-Prager soil model. This soil model effectively simulates the stress–strain-pore pressure response of fluid saturated granular materials (Baladi & Rohani 1979).

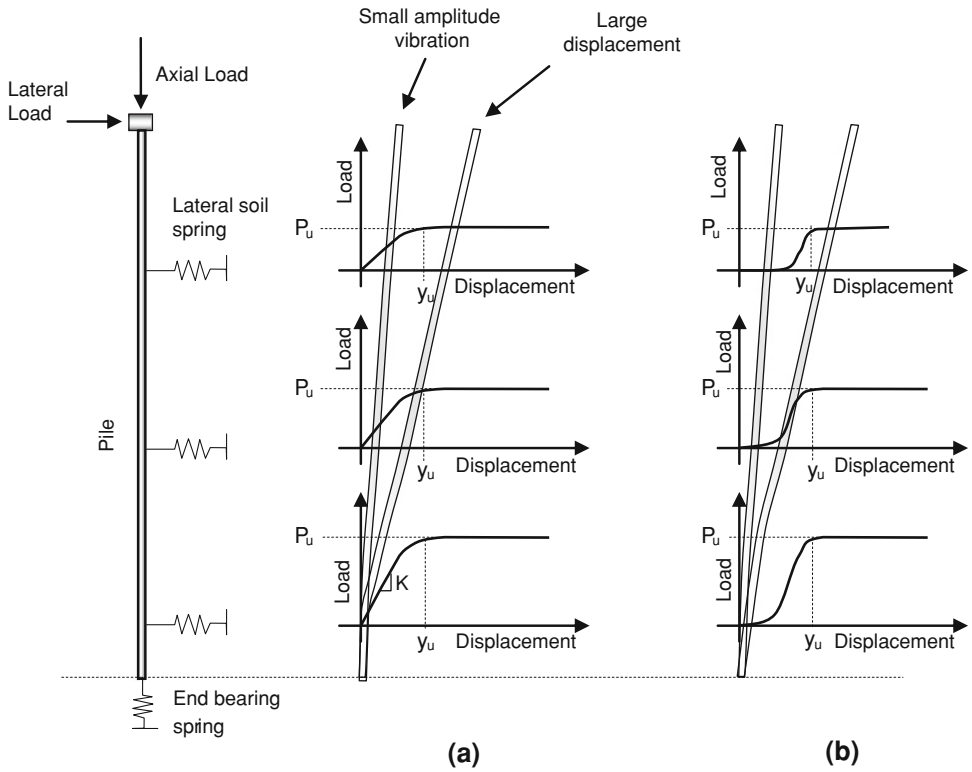

Fig. 15 Soil-pile interactions for two types of p–y curves: **a** for non-liquefied case; **b** for liquefied case

5.2.1 Liquefaction Model

Effective stress approach is used for simulating saturated condition. The soil medium is considered as two phase continuum consisting of a solid skeleton and pore fluid, the normal stress components should be divided into two parts: (1) The stress carried by the solid structures, referred to as effective stress; and (2) the stress carried by the pore fluid, referred to as pore-water pressure. The total stress can be written as

$$\sigma_{ij} = \sigma'_{ij} + u\delta_{ij} \tag{1}$$

where σ_{ij} = total stress tensor; σ'_{ij} = effective stress tensor; u = pore water pressure; δ_{ij} = Kronecker delta. The pore pressure is allowed to develop in the material by considering undrained condition.

The pore pressure may build up considerably in sands during cyclic shear loading. Eventually, this process may lead to liquefaction when the effective stress approaches zero. The pore water pressures that develop in saturated undrained sands during seismic loading are caused by plastic volumetric strains generated by slips at grain contacts (Martin et al. 1975; Finn 1982). This pressure reduces the effective stress regime in the sand and allows the sand skeleton to rebound elastically. The pore pressure model described by Martin et al. (1975) is given by the following incremental equation.

$$\Delta\varepsilon_v = C_1(\gamma - C_2\varepsilon_v) + C_3\varepsilon_v^2/(\gamma + C_4\varepsilon_v) \tag{2}$$

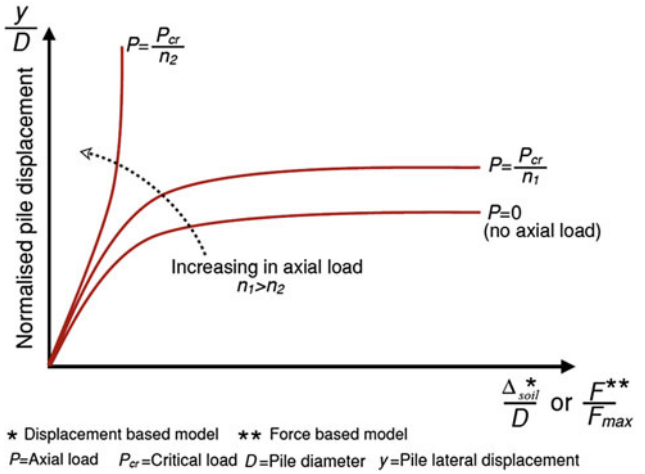

Fig. 16 Plot of normalised pile head displacement and normalised force/ground displacement

Where C_1, C_2, C_3 and C_4 are constants for a given sand at a given density, ε_v = accumulated irrecoverable volumetric strain, $\Delta\varepsilon_v$ = increment in volumetric strain, γ = current shear strain amplitude. $\Delta\varepsilon_v$, ε_v and γ are expressed in percentages.

Simplified version of that described in the Eq. (2) is given by the following incremental equation (Byrne 1991).

$$\frac{\Delta\varepsilon_v}{\gamma} = B_1 \exp\left(-B_2\left(\frac{\varepsilon_v}{\gamma}\right)\right) \tag{3}$$

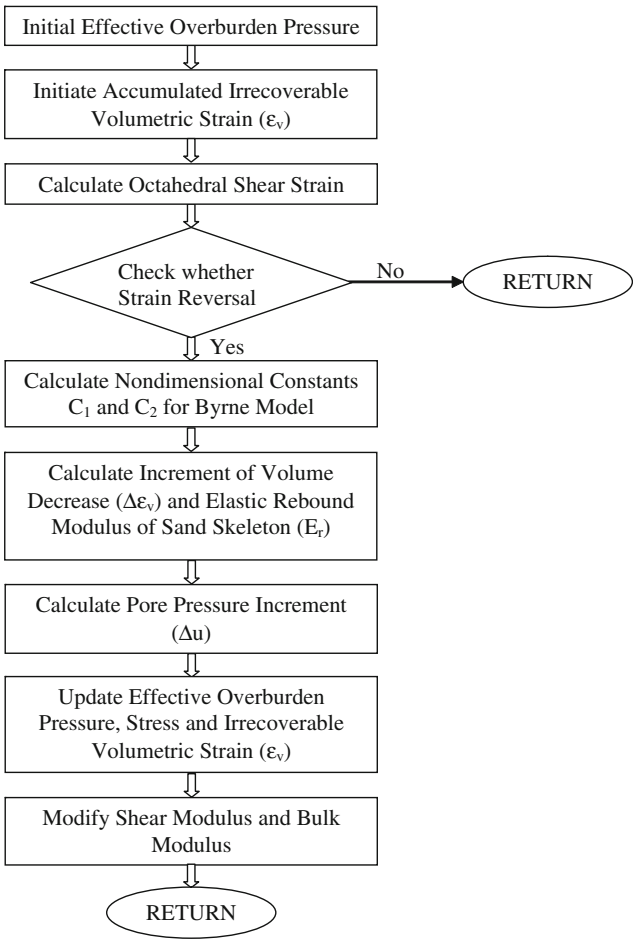

Fig. 17 Algorithm for pore pressure generation model

where and B_1, B_2 are constants for a given sand at a given density. The non dimensional constants C_1 and C_2, can be derived as follows

$$B_1 = 7600(D_r)^{-2.5} \tag{4}$$

$$B_2 = 0.4/B_1 \tag{5}$$

where D_r is the relative density and is expressed in percentage. For undrained behaviour the increase of pore water pressure is computed as follows (Martin et al. 1975)

$$\Delta u = E_r \, \Delta \varepsilon_v \tag{6}$$

in which Δu = increment in pore water pressure, E_r = rebound modulus of sand skeleton.

The rebound modulus E_r at an effective stress level σ'_v is given by

$$E_r = \frac{(\sigma'_v)^{1-m}}{mk_2(\sigma'_{v0})^{n-m}} \tag{7}$$

where σ'_{v0} is the initial value of effective overburden pressure at that level; and k_2, m and n are experimental constants for a given sand. The current shear modulus and bulk modulus is modified progressively for changing effective stresses in each time interval as follows (Martin & Seed 1979; Arduino et al. 2002)

$$G = G_{max}\left(\frac{\sigma'_v}{\sigma'_{vo}}\right)^{0.5}; \quad K = K_{max}\left(\frac{\sigma'_v}{\sigma'_{vo}}\right)^{0.5} \tag{8}$$

where G_{max} and K_{max} are initial shear and bulk modulus respectively. For the cases where due to rise in pore water pressure, effective stress becomes zero (complete liquefaction), to maintain stability in the calculations, shear modulus equal to 3 % of initial shear modulus (G_{max}) is generally retained. The algorithm for pore water pressure generation is presented below in Figs. 16 and 17. This algorithm is capable to consider pore pressure generation with advanced plastic soil models.

Acknowledgments The authors acknowledge the funding received from National Science Foundation (China) and Royal Society (U.K). This work was supported by the National Natural Science Foundation of China through the Grant No 41111130205.

References

Adhikari, S., & Bhattacharya, S. (2008). Dynamic instability of pile-supported structures in liquefiable soils during earthquakes. *Shock and Vibration, 15*(6), 665–685.

AIJ. (2001). Recommendations for design of building foundations. Architectural Institute of Japan, (in Japanese).

API. (2000). American Petroleum Institute. Recommended practice for planning designing and constructing fixed offshore platforms.

Arduino P, Kramer S. L, Li P., & Baska DA (2002). Dynamic stiffness of piles in liquefiable soils. Research report. Department of Civil and Environmental Engineering, University of Washington, Washington.

Baladi G. Y., & Rohani B. (1979). Elastic-plastic model for saturated sand. *Journal of Geotechnical Engineering Division, ASCE 105*(GT4), 465–480.

Bentley, K. J., & El Naggar, M. H. (2000). Numerical analysis of kinematic response of single piles. *Canadian Geotechnical Journal, 37*, 1368–1382.

Bhattacharya, S. (2003). *Pile instability during earthquake liquefaction*. PhD thesis, University of Cambridge, UK.

Bhattacharya, S., & Madabhushi, S. P. G. (2008). A critical review of methods for pile design in seismically liquefiable soils. *Bulletin of Earthquake Engineering, 6*, 407–446.

Bhattacharya, S., Madabhushi, S. P. G., & Bolton, M. D. (2004). An alternative mechanism of pile failure in liquefiable deposits during earthquakes. *Geotechnique, 54*(3), 203–213.

Bhattacharya, S., Bolton, M. D., & Madabhushi, S. P. G. (2005). A reconsideration of the safety of the piled bridge foundations in liquefiable soils. *Soils and Foundations, 45*(4), 13–26.

Bhattacharya, S., Dash, S. R., & Adhikari, S. (2008). On the mechanics of failure of pile-supported structures in liquefiable deposits during earthquakes. *Current Science, 94*(5), 605–611.

Bhattacharya, S., Adhikari, S., & Alexander, N. A. (2009). A simplified method for unified buckling and free vibration analysis of pile-supported structures in seismically liquefiable soils. *Soil Dynamics and Earthquake Engineering, 29*, 1220–1235.

Bhattacharya, S., Hyodo, M., Goda, K., Tazoh, T., & Taylor, C. A. (2011). Liquefaction of soil in the Tokyo Bay Area from the 2011 Tohoku (Japan) Earthquake. *Soil Dynamics and Earthquake Engineering, 31*, 1618–1628.

BTL Committee. (2000). Study on liquefaction and lateral spreading in the 1995 Hyogoken-Nambu earthquake. Building Research Report No 138, Building Research Institute, Ministry of Construction, Japan (in Japanese).

Byrne, P. M. (1991). A cyclic shear-volume coupling and pore pressure model for sand. *Proceedings of the 2nd International Conference on Recent Advances in Geotechnical Earthquake Engineering and Soil Dynamics.* St Louis, Report 1.24 (pp. 47–56).

Dash, S. R. (2010). *Lateral pile-soil interaction in liquefiable soils*. PhD thesis, University of Oxford, UK.

Dash, S. R., Bhattacharya, S., Blakeborough, A., & Hyodo, M. (2008). P-Y curve to model lateral response of pile foundations in liquefied soils. Paper number 04-01-0089, *Proceedings of the 14th World Conference on Earthquake Engineering*, October 12–17, 2008, Beijing.

Dash, S. R., Bhattacharya, S., & Blakeborough, A. (2009a). A study of p-y curves for liquefiable soils. *Proceedings of the International Conference on Performance-based Design in Earthquake Geotechnical Engineering. IS- Tokyo 2009*, CRC Press (Balkema) Taylor & Francis Group Book and CD-ROM ISBN 978-0-415-55614-9.

Dash, S. R., Govindaraju, L., & Bhattacharya, S. (2009b). A case study of damages of the Kandla Port and Customs Office tower supported on a mat-pile foundation in liquefied soils under the 2001 Bhuj earthquake. *Soil Dynamics and Earthquake Engineering, 29*(2), 333–346.

Dash, S. R., Bhattacharya, S., & Blakeborough, A. (2010). Bending-buckling interaction as a failure mechanism of piles in liquefiable soils. *Soil Dynamics and Earthquake Engineering, 30*, 32–39.

Fan, K., Gazetas, G., Kaynia, A. M., Kausel, E., & Shahid, A. (1991). Kinematic seismic response of single piles and pile groups. *Journal of Geotechnical Engineering ASCE, 117*(12), 1860–1879.

Finn, W. D. L. (1982). Dynamic response analysis of saturated sands. In: G. N. Pande, & O. C. Zienkiewicz (Eds.), *Soil mechanics—transient and cyclic loads.* NewYork: John Wiley & Sons Ltd.

Gobindraju, L., & Bhattacharya, S. (2012). Site-specific earthquake response study for hazard assessment in Kolkata city, India. *Natural Hazards, 61*(3), 943–965

Hamada, M., & O'Rourke, T. D. (Eds.). (1992). Case studies of liquefaction and lifeline performance during past earthquakes (vol. 1). Japanese case studies, Technical Report NCEER-92-0001.

Ishihara, K. (1997). Terzaghi oration: Geotechnical aspects of the 1995 Kobe earthquake. *Proceedings of ICSMFE*, (pp. 2047–2073). Hamburg.

JRA. (2002, 1996). Japanese Road Association. Specification for Highway Bridges, Part V, Seismic Design.

Kawamura, S., Nishizawa, T., & Wada, H. (1985).Damage to piles due to liquefaction found by excavation twenty years after earthquake. Nikkei Architecture (pp. 130–134).

Kaynia, A. M., & Kausel, E. (1982), Dynamic stiffness and seismic response of pile groups. Research Report R82-03, Order No. 718, Cambridge, Massachusetts.

Kimura, Y., & Tokimatsu, K. (2007). Buckling stress of slender pile with lateral displacement at the pile head in liquefied soils. *Journal of Structural and Construction Engineering, AIJ (Architectural Institute of Japan) 617*, 169–175.

Knappett, J. A., Madabhushi, S. P. G. (2005). Modelling of Liquefaction-induced Instability in pile groups. In: Boulanger and Tokimatsu (Eds.), *ASCE Geotechnical special publication No 145 on seismic performance and simulation of pile foundations in liquefied and laterally spreading ground* (pp. 255–267).

Lin, S. S., Tseng, Y. J., Chiang C. C., & Huang, C. L. (2005). Damage of piles caused by lateral spreading—Back study of three cases. In: R.W. Boulanger and K. Tokimatsu (Eds.), *ASCE Geotechnical special publication no 145 on seismic performance and simulation of pile foundations in liquefied and laterally spreading ground* (pp. 121–133).

Liu, L., & Dobry, R. (1995). Effect of liquefaction on lateral response of piles by centrifuge model tests. NCEER report to FHWA. *NCEER Bulletin, 9*(1), 7–11.

Maheshwari, B. K., & Sarkar, R. (2011). Seismic behaviour of soil-pile-structure interaction in liquefiable soils: A parametric study. *International Journal of Geomechanics, ASCE, 11*(4), 335–347.

Martin, P.P., & Seed, H. B. (1979). Simplified procedure for effective stress analysis of ground response. *Journal of Geotechnical Engineering Division, ASCE 105*(GT6), 739–758.

Martin, G. R., Finn, W. D. L., & Seed, H. B. (1975). Fundamentals of liquefaction under cyclic loading. *Journal of Geotechnical Engineering Division, ASCE 101*(GT5), 423–438.

Novak, M., Sheta, M., El-Hifnawy, L., El-Marsafawi, H., & Ramadan, O. (1990). *DYNA3: A computer program for calculation of foundation response to dynamic loads*. London: Geotechnical Research Centre University of Western Ontario.

Rollins, K. M., Gerber, T. M., Lane, J. D., & Ashford, S. A. (2005). Lateral resistance of a full-scale pile group in liquefied sand. *Journal of Geotechnical and Geoenvironmental Engineering, ASCE, 131*, 115–125.

RTRI. (1999). Design standard for railway facilities-seismic design. Tokyo: Railway Technical Research Institute.

Sarkar, R., & Maheshwari, B. K. (2012). Effects of separation on the behaviour of soil-pile interaction in liquefiable soils. *International Journal of Geomechanics, ASCE, 12*(1), 1–13.

Shanker, K., Basudhar, P. K., & Patra, N. R. (2007). Buckling of piles under liquefied soil condition. *Geotechnical and Geological Engineering, 25*(3), 303–313.

Takahashi, A., Kuwano, Y., & Yano, A. (2002) Lateral resistance of buried cylinder in liquefied sand. *Proceedings of the International Conference on physical modelling in geotechnics, ICPMG-02*, St. John's, Newfoundland, Canada.

Tokimatsu, K., Oh-oka, H., Satake, K., Shamoto, Y., & Asaka, Y. (1998). Effects of lateral ground movements on failure patterns of piles in the 1995 Hyogoken-Nambu earthquake. *Proceedings of a speciality conference, geotechnical earthquake engineering and soil dynamics III*, ASCE Geotechnical Special publication No 75 (pp. 1175–1186).

Wu, G., & Finn, W. D. L. (1997a). Dynamic elastic analysis of pile foundations using finite element method in the frequency domain. *Canadian Geotechnical Journal, 34*, 34–43.

Wu, G., & Finn, W. D. L. (1997b). Dynamic nonlinear analysis of pile foundations using finite element method in the time domain. *Canadian Geotechnical Journal, 34*, 44–52.

Yasuda, S., Terauchi, T., Morimoto, M., Erken, A., & Yoshida, N. (1998). Post liquefaction behavior of several sand. *Proceedings of the 11th European Conference on Earthquake Engineering*, Balkema, Rotterdam.

Yoshida, N., & Hamada, M. (1990). Damage to foundation piles and deformation pattern of ground due to liquefaction-induced permanent ground deformation. *Proceedings of 3rd Japan-US Workshop on Earthquake resistant Design of Lifeline Facilities and Countermeasures for Soil Liquefaction* (pp. 147–161).

Yoshida, N., Towahata, I., Yasuda, S., & Kanatani, M. (2005). Discussion to the paper by Bhattacharya et al. (2004) on "An alternative mechanism of pile failure in liquefiable deposits during earthquakes". *Geotechnique 55*(3), 259–263.

A New Method for Predicting Consolidation Settlement of Soft Ground Reinforced with Preloading Technique

G. B. Ye, X. An, and J. Wu

Abstract

Preloading technique provides an efficient and economic solution to the problem of improving soft soils. The main focus of this paper is to present a new method for predicting the ultimate consolidation settlement of soft ground reinforced with preloading technique. This method is based on the linear relationship between settlement and settlement rate that derived from the theoretical solution to average consolidation degree of ground under various drainage boundary conditions. Furthermore, the ultimate settlement of a ground cell improved by the technique of vacuum preloading combined with fill surcharge has been determined using this method as well as the non-linear curve fitting method with the model of negative exponential function according to the field monitoring data of surface settlement. The results of the two methods turn out to be very close, especially when the data with relatively larger time spacing are selected for calculation. And, the present method is of higher practicability since there is no need for complicated non-linear curve fitting.

Keywords

Settlement prediction • Preloading technique • Ultimate settlement

1 Introduction

Preloading technique is widely used for reducing the long-term settlement of highways and buildings constructed on soft soils. Ultimate settlement of the improved ground can be predicted according to the surface settlement data observed during construction period. Several methods have been proposed for settlement prediction, including Three-point Method, Hyperbolic Function Method, the Method of Asaoka (Asaoka 1978), Curve Fitting Method (Pan et al. 2004), Gray Model Prediction Method (Zhou et al. 2002) and Artificial Neural Network Prediction Method (Liu 2000) etc. However, the Three-point Method is unable to eliminate the influence of random error of field data. Gu et al. (2010) argued that, when using the Asaoka method to predict settlement, a constant-loading period of at least 4 months is generally required and the predicted settlement increases as constant-loading continues. Most of the other existing methods have been established simply according to the mathematical similarity instead of consolidation theory. Currently, a well-accepted predicting method is absent.

In this study, a new simple method based on the linear relationship between settlement and settlement rate is proposed and presented. This method can predict the ultimate settlement of the ground reinforced with preloading technique and the results have been compared with that of

G. B. Ye · X. An
Department of Geotechnical Engineering,
Tongji University, Shanghai 200092, China

G. B. Ye · X. An (✉)
Key Laboratory of Geotechnical and Underground Engineering
of Ministry of Education, Tongji University,
Shanghai 200092, China
e-mail: xin_an@163.com

J. Wu
Lend Lease Project Management and Construction (Shanghai)
Co., Ltd, Shanghai 200031, China

Y. Huang et al. (eds.), *New Frontiers in Engineering Geology and the Environment*,
DOI: 10.1007/978-3-642-31671-5_4,

Table 1 Physical and mechanical parameters of strata

No.	Soil	Modulus of compressibility Es (MPa)	Cohesion c (kPa)	Internal friction angle φ (°)	Void ratio e	Coefficient of permeability K (10^{-6}cm/s)
②	Mucky clay	1.73	3.1	2.3	1.794	0.734
③[1]	Silty clay	3.98	23.3	21.8	0.870	1.109

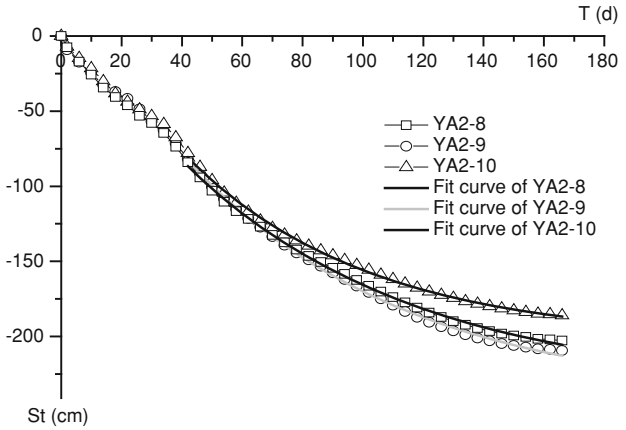

Fig. 1 Settlement-time curves of YA2-8, YA2-9 and YA2-10

Non-linear Curve Fitting Method to investigate its accuracy and validity.

2 Prediction Model Analysis

2.1 Linear Relationship Between Settlement and Settlement Rate

In various drainage boundary conditions, the general formula of the theoretical solution to the average consolidation degree $\bar{U}$ (Zeng and Yang 1959) is given by:

$$\bar{U} = 1 - \alpha e^{-\beta t} \tag{1}$$

.

where, α and β are parameters related to drainage boundary conditions and consolidation properties of the ground.

As a result, settlement s_t and settlement rate $\frac{ds_t}{dt}$ at the time of t can be expressed as:

$$s_t = s_\infty - \alpha(s_\infty - s_d)e^{-\beta t} \tag{2}$$

$$\frac{ds_t}{dt} = \alpha\beta(s_\infty - s_d)e^{-\beta t} \tag{3}$$

.

where, s_d and s_∞ are instant settlement and ultimate settlement of the ground respectively.

Substituting Eq. 3 into Eq. 2 gives:

$$s_t = s_\infty - \frac{1}{\beta}\frac{ds_t}{dt} \tag{4}$$

By transforming Eq. 4, we have:

$$\frac{ds_t}{dt} = \beta(s_\infty - s_t) \tag{5}$$

Eq. 4 describes the linear relationship between settlement and settlement rate. In addition, it is indicated in Eq. 5 that settlement rate is β times of the residual settlement at the time of t.

2.2 Settlement Rate Calculation

Three points $(t_{n-1},\ s_{t_{n-1}})$, $(t_n,\ s_{t_n})$, $(t_{n+1},\ s_{t_{n+1}})$ with equal time spacing in the observed settlement-time curve are selected to form three equations in accordance with Eq. 2. The solution of the equation group can be given as:

$$\begin{cases} \beta_n = \dfrac{1}{t_n - t_{n-1}} \ln\left(\dfrac{s_{t_n} - s_{t_{n-1}}}{s_{t_{n+1}} - s_{t_n}}\right) \\ s_{\infty n} = \dfrac{s_{t_{n+1}}(s_{t_n} - s_{t_{n-1}}) - s_{t_n}(s_{t_{n+1}} - s_{t_n})}{(s_{t_n} - s_{t_{n-1}}) - (s_{t_{n+1}} - s_{t_n})} \end{cases} \tag{6}$$

where, β_n and $s_{\infty n}$ are the value of β and s_∞ determined by three points in the time section of $(t_{n-1},\ t_{n+1})$, respectively.

According to Eq. 5, settlement rate at the time of t_n can be expressed as:

$$\left(\frac{ds_t}{dt}\right)_{t_n} = \beta_n(s_{\infty n} - s_{t_n}) \tag{7}$$

.

2.3 Ultimate settlement prediction

As to $n+1$ groups of settlement-time data (t_0, s_{t_0}), $(t_1, s_{t_1}) \cdots (t_n, s_{t_n})$ observed during the constant-loading period, corresponding $n-1$ groups of settlement–settlement rate data $\left(\left(\frac{ds_t}{dt}\right)_{t_1}, s_{t_1}\right)$, $\left(\left(\frac{ds_t}{dt}\right)_{t_2}, s_{t_2}\right) \cdots \left(\left(\frac{ds_t}{dt}\right)_{t_{n-1}}, s_{t_{n-1}}\right)$ can be

Table 2 Predicted results with the present method

Time spacing	YA2-8		YA2-9		YA2-10	
	s_∞/cm	β	s_∞/cm	β	s_∞/cm	β
4d	−219.5	0.016	−229.8	0.016	−194.8	0.020
8d	−225.1	0.015	−234.2	0.015	−196.2	0.019
16d	−233.6	0.013	−242.1	0.014	−199.4	0.018

Table 3 Predicted results with the non-linear curve fitting method

Settlement plate	s_∞/cm	β
YA2-8	−233.9	0.013
YA2-9	−241.7	0.014
YA2-10	−201.9	0.017

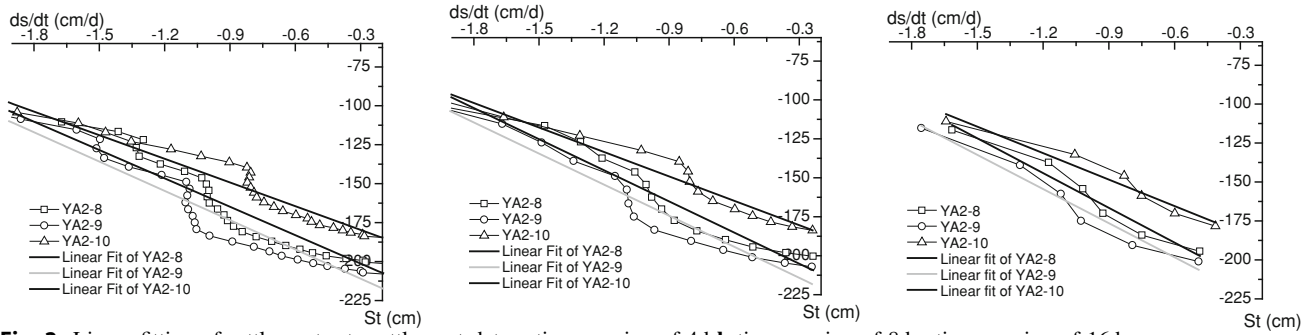

Fig. 2 Linear fitting of settlement rate-settlement data **a** time spacing of 4d **b** time spacing of 8d **c** time spacing of 16d

calculated based on Eqs. 6 and 7 and linear fitting can be conducted using Eq. 4 to determine the ultimate settlement s_∞ and parameter β.

3 Application of Model to Case History

3.1 Project Introduction

The 1st phase of a proposed chemical plant located in Guangdong province, China covers an area of 270000 m^2. Vacuum preloading method combined with fill surcharge was adopted for improving the widespread mucky soil layer; 3.9–28.70 m in thickness with an average of 18.24 m. Table 1 presents the physical and mechanical parameters of the mucky soil layer and the underlying layer of silty clay.

3.2 Settlement monitoring results

The whole site was divided into nine ground cells, namely YA1-YA9. Surface settlement monitoring has been carried out in all cells during the construction period. For instance, there were totally 18 settlement plates in ground cell YA2 with YA2-8, YA2-9 and YA2-10 in the central area. And, the observed settlement-time curves of YA2-8, YA2-9 and YA2-10 are illustrated in Fig. 1.

3.3 Ultimate Settlement Prediction and Analysis

Table 2 presents the predicted results obtained with this new method using the settlement-time data with time spacing of 4d, 8d and 16d.

As the fitting curves illustrated in Fig. 1, the Non-linear Curve Fitting Method with the negative exponential function model of Eq. 2 is also used to predict the ultimate settlement of YA2-8, YA2-9 and YA2-10, of which the results are shown in Table 3.

Comparison between Table 2 and 3 shows that predicted settlements of the two methods turn out to be very close, especially when the data with relatively larger time spacing are selected for calculation.

Figure 2 illustrates the fitting line of settlement–settlement rate. It is shown that there is nice linear relationship between settlement and settlement rate. R-squared value of the fitting is greater than 0.9 and increases as time spacing rises.

4 Conclusions

Based on the linear relationship between settlement and settlement rate, a new method for settlement prediction is established in this paper. The comparison between predicted results obtained with this new method and the Non-linear Curve Fitting Method shows that the two methods are in good agreement but the present method gains more practicability since there is no need for complicated non-linear fitting.

References

Asaoka, A. (1978). Observational procedure of settlement prediction. *Soils and Foundations, 18*(4), 87–92.

Gu, S. F., Liu, Y. S., & Liu, S. S. (2010). Study of application of Asaoka method to settlement prediction. *Rock and Soil Mechanics, 31*(7), 2238–2240.

Liu, Y. J. (2000). Prediction of Ultimate Settlements of Soft Ground for Expressway by Using Artificial Neural Networks. *Journal of Highway and Transportation Research and Development, 17*(6), 15–18.

Pan, L. Y., & Xie, X. Y. (2004). Observational settlement prediction by curve fitting methods. *Rock and Soil Mechanics, 25*(7), 1053–1058.

Zeng, G. X., & Yang, X. L. (1959). Settlement analysis of sand-drained ground. *Journal of Zhejiang University (Engineering Science), 3*, 34–72.

Zhou, Q. N., & Wang, X. (2002). The Use of the Gray Theory in the Prediction of Settlement. *Soil Engineering and Foundation, 16*(4), 31–33.

An Approach to Identify a Linked Spatial Network for Large Mammal Conservation on Yellow Sea Coast

S. B. Fang, Z. Tian, Y. G. Sun, and C. S. Yin

Abstract

On the coastal region how to protect the natural ecosystems is an urgent issue. In this study, taking the Elaphurus Davidianus as a case, a framework has been proposed to identify an ecological spatial network for the conservation of large mammals, which could be finished in two steps: ecological naturalness assessments and human-induced ecological risks assessments. Through the naturalness assessments regions to be conserved is identified, which are regions that having high ecological value; and through the human-induced risks assessments, a spatial network that is linked by regions with low human induced ecological impacts is identified. The analysis shows that this approach is an efficient solution through which the ecological risks can be infiltrated and ranked, and the efficient ecological conservation could be realized by prioritizing the management efforts.

Keywords

Ecological security • Ecosystem management • Ecological naturalness assessment • Ecological risks assessment • Coastal region

1 Purpose

How to prioritize the ecosystem for conservation purpose at landscape scale on coastal region is the question we want to discuss in this study. Landscape scale is the most reasonable scale to realize the ecosystem management for human actions acted at this scale.

S. B. Fang (✉) · Z. Tian (✉) · C. S. Yin (✉)
College of Fisheries and Life Science,
Shanghai Ocean University, Shanghai 201306 China
e-mail: bsfang@sina.com

C. S. Yin
e-mail: csyin@shou.edu.cn

Y. G. Sun
National Marine Environmental Monitoring Center,
Dalian, 116023 China

S. B. Fang
Environmental Science and Engineering Department, Fudan University, Shanghai 200433 China

2 An Approach to Identify a Spatial Network for Ecosystem Management

2.1 Ecosystem's Naturalness Assessment

Naturalness indicates the wildness, least human disturbed or pristine condition of an ecosystem. A high naturalness ecosystem generally is low human disturbed, providing more ecological welfare, and being the habitat of more wild species. This naturalness assessment is more to reflect the ecosystem's inherent character as much as possible.

The national nature conserve, the large area of native vegetations, forests, and other low human disturbed places, might be conserved first (Noss 1987).

2.2 Ecological Risks Assessment

From the ecological assessment, places with high naturalness and low risks should be prioritized to manage.

Y. Huang et al. (eds.), *New Frontiers in Engineering Geology and the Environment*,
DOI: 10.1007/978-3-642-31671-5_5,

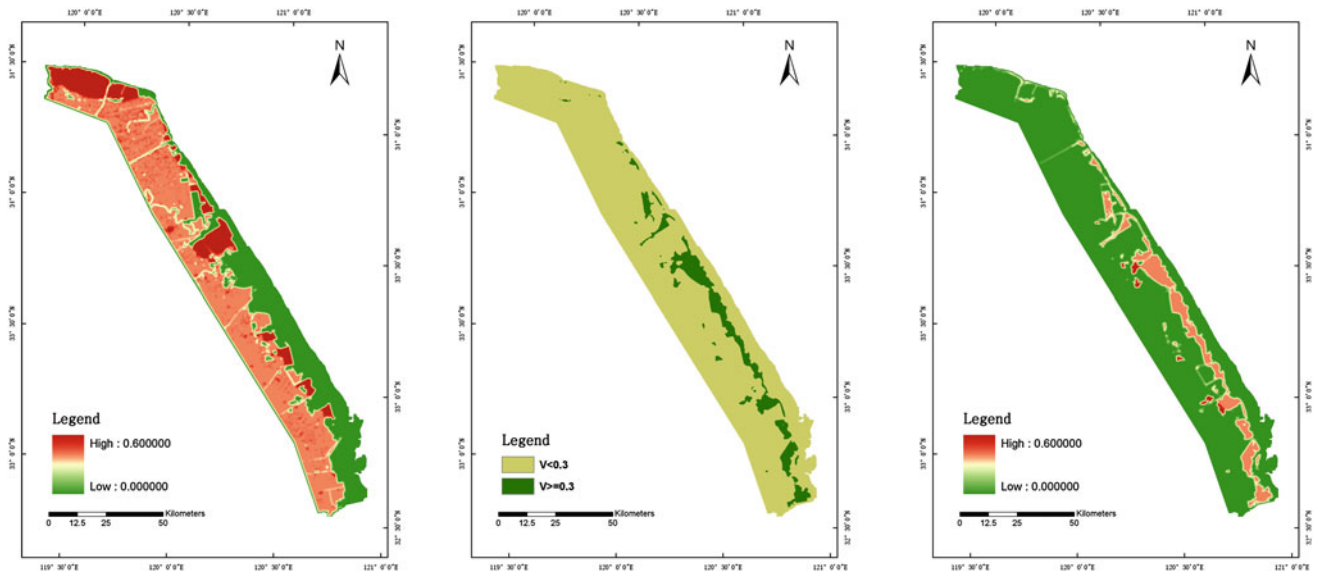

Fig. 1 **a** Ecological naturalness assessments. The suitable region, which is mainly located in the southeastern coast, has become more fragmented in recent time; **b** ecological risks assessments. The region with high R value has been enlarged in recent times, and the region has sprawled from the inland to the coast; **c** the areas with a value both $V > 0.3$ and $R < 0.3$ are computed. These regions are relatively more suitable for Milu population

The places with high naturalness could be called ecological hotspots. Ecological hotspot has been understood as "an anomaly, aberration, outbreak, elevated cluster, critical resource area and so on" (Patil et al. 2001). In this study we refer the ecological hotspots to the areas critical in affecting certain ecological process, such as areas important for birds' migration, areas as habitats of some endangered species such as Red-crowned Crane, Père David′s deer (Myers 1990; Myers et al. 2000).

2.3 Identification of the Ecological Conservation Spatial Network

The area with high ecological naturalness and low or moderate risks should be first conserved. For the same reason as the areas with moderate naturalness and risks, the areas with both high naturalness and risks are taken as mid-level security.

3 Identification of an Ecological Conservation Spatial Network on Chinese Coast

3.1 The Study Site

The wetlands on the Yancheng coast are an appropriate region to establish a wild Milu population (Ding 2005). Milu originated from middle and eastern China, inhabiting the plain and marshlands in the Huang River basin and the Yangtze River basin. Historically, because of the intensifying human pressures in the inner mainland, Milu migrated to the coastal region south of Huang River, from the west and north. They lived in this region until they became extinct in China.

3.2 Ecological Naturalness Assessment

According to Dafeng Milu's behavioral ecology research, we define a suitability index V to evaluate the potential habitat suitability for Milu. This index mainly reflects Milu's preferred habitat choice, where they can get food and shelter. According to the behavioral research in Dafeng, food, water and shelter are the most critical elements for a suitable Milu habitat (Ding 2005). Taken not only as food but also as shelter, the vegetation landuse is used to identify suitable habitat areas for Milu (Ding 2005). Within our landuse data, only the forests lands type and the high grasslands type could reflect the Milu's favorite habitat choice, so we choose the forest and the high cover grassland as the land cover type which we analyze as follows to get index values (Miller and Wardrop 2006). We define V as suitability index value, which was:

$$V = W_F P_F + W_G P_G$$

where W_F and W_G are the weights of landcover forest and high cover grassland, respectively, and PF and PG is the percentage of the forest and high cover grassland area, respectively, in each statistics cell. The cell is 1 km × 1 km, and in this size we do the spatial neighborhood analysis,

after transferring the vector form landuse data into raster form. We analyze 3 year's S index spatial distribution, 1987, 1995, and 2000, using the available data (Fig. 1a). According to Dafeng Milu research report, forest land cover is more important to Milu than grassland in its life history. So in the analysis, according to the experts' opinion, we determine that WF is 0.6, and WG 0.4.

We could found that appreciate region suitable for Milu has been fragmented more and more in recent years. And the region mainly locates on the south-eastern Yancheng coastal region.

3.3 Ecological Risks Assessment

On the Yancheng coast, agriculture and other intensive human disturbance activities, including salt field development, aquaculture development, harbor building and industrial factory building are the main human activities causing negative impacts on the coastal environment. These activities always fragment the potential habitat and destroy the ecosystems' integrity. In this study we take the land cover types agriculture and building land as the data with which we do the risk assessment (Ding 2005). We define R as the risk index value, which was:

$$R = W_A P_A + W_B P_B$$

where W_A and W_B are the weights of landcover farm lands and building lands, respectively, and P_A and P_B are the percentage of farm land and building land areas, respectively, in each cell. In the same size of the cell as the index V, we also compute R in 1987, 1995, and 2000, in the same process as V computing (Fig. 1b). For the risk assessment, given that it is less harmful to Milu compared with other building activities such as industrial and aquiculture, W_A is determined as 0.4, and W_B 0.6, according to experts' opinion.

The region with high R index value is increased more and more, and sprawl from inland to the coast.

4 Discussions

Two questions could be answered in the Milu example study: how to assess the Chinese Yancheng coastal region, integrating the landscape assessment and the Milu population research, and what region should be conserved according our assessment. Our ultimate aim is to restore the Milu metapopulation on the Yancheng coast. This work is to highlight the urgency that some priority coastal region should be reserved for Milu reintroduction. The main management issue for Milu reintroduction is the trade-off between development and Milu protection. Two levels of security patterns (SP) give us some information how urgent it is to reserve lands for conservation. If high level ecological SP is the aim, the economy might develop slower. Scenario analysis, with the involvement of policy-makers, native farmers, scientists and investors should be an effective way to resolve this issue (Peterson et al. 2003). This should be done in the near future.

It should be pointed out that this study for Milu habitat choice is not enough. It is just a theoretical discussion on how to use the coarse landuse data to assess a region and determine a possible ecological SP. More research should continue, and proposing issues are: the accurate threshold level that makes the habitat unacceptable to the deer, which could be measurable by the indices we provide. If it could be realized we could give more accurate and plausible spatial strategy for Milu reintroduction; in this study, only the food and shelter needs for Milu are considered. In fact, Milu need different detailed habitats in their life history (Ding 2005). So if with the detailed landcover map through the high resolution image interpretation, information that what kinds of vegetation are selected as food at different time of the year could be gotten, the more accurate and convincingly results for Milu conservation could be realized. Research on the issue of Milu's habitat choosing process in its life history should continue (Ding 2005).

References

Ding, Y. (2005). *Milu research in China*. Changchun, Jilin: Jilin Science and Technology Press (in Chinese).

Miller, S., & Wardrop, D. (2006). Adapting the floristic quality assessment index to indicate anthropogenic disturbance in central Pennsylvania wetlands. *Ecological Indicators, 6*, 313–326.

Myers, N. (1990). The biodiversity challenge: expanded hot-spots analysis. *The Environmentalist, 10*, 243–256.

Myers, N., Mittermeier, R., Mittermeier, C., Gustavo, AB., da Fonseca, GA., Kent, J. (2000). Biodiversity hotspots for conservation priorities. *Nature, 403*, 853–858.

Noss, R. (1987). From plant communities to landscapes in conservation inventories: a look at the nature conservancy (U.S.A). *Biological Conservation, 41*, 11–37.

Patil, G., Brooks, R., Myers, W., et al. (2001). Ecosystem health and its measurement at landscape scale: toward the next generation of quantitative assessments. *Ecosystem Health, 7*, 307–316.

Peterson, G., Cumming, G., & Carpenter, S. (2003). Scenario planning: a tool for conservation in an uncertain world. *Conservation Biology, 17*, 358–366.

Analysis of Waterfront Excavation Adjacent to Pile-Supported Wharves

Z. K. Cheng, D. G. Wang, Y. C. Ding, J. Z. Hang, Q. Gu, and J. H. Wang

Abstract
The two-dimensional numerical simulations were carried out to investigate the performances of the diaphragm wall scheme and the composite steel sheet pile wall scheme for a waterfront braced excavation adjacent to the pile-supported wharves, of which the lateral displacement as well as the safety factor of stability of the two retaining structures were analyzed. The results reveal that the composite steel sheet pile wall can exert the greater global bending stiffness and reduce the lateral soil pressure. Therefore, the maximum lateral displacement of the composite steel sheet pile wall is only one-third that of the diaphragm wall and the safety factor against basal heave is higher than the diaphragm wall.

Keywords
Waterfront excavation • Diaphragm wall • Composite steel sheet pile • Pile-supported wharf

1 Introduction

Rapid economic development of estuaries and costal regions in east China leads to increasing occurrences of waterfront excavation projects in coastal and offshore engineering (Li et al. 2006). These waterfront excavation projects are more easily influenced by currents, waves, sediments, reclamation and excavation, owing to their locations at inter-junction areas between sea, river and land or just in deep water areas (Ding and Wang 2008). Therefore, stability, anti-seepage measures, and deformation control issues become the most concerned challenges for engineers during design and construction of these projects (Ding et al. 2009).

Z. K. Cheng · D. G. Wang · Y. C. Ding (✉) · J. Z. Hang · Q. Gu
CCCC Third Harbor Consultants Co., Ltd,
200032 Shanghai, China
e-mail: ycding@163.com

J. H. Wang
Department of Civil Engineering, Shanghai Jiaotong University,
200240 Shanghai, China

In this paper, the two-dimensional finite element method (FEM) numerical simulations are carried out to compare the lateral displacement and the safety factor against basal heave of the two retaining structure schemes, the diaphragm wall and the composite steel sheet pile wall, for a waterfront excavation adjacent to the pile-supported wharves.

2 Project Descriptions

The site of the excavation is in water presently with the south boundary adjacent to the planned cruise wharves. The structural types of the mail steamer wharves are concrete frame structures consisting of beams and slabs supported by piles. According to the preliminary design scheme, the horizontal distance between the boundary of the excavation and the front edge of the south cruise wharves is 40 m. There are two feasible retaining structure schemes preliminarily considered at the schematic design stage of this excavation project. The first retaining structure scheme is the conventional diaphragm wall commonly adopted for onshore or overland foundation pit excavation projects. The second retaining structure scheme is the double-row

Y. Huang et al. (eds.), *New Frontiers in Engineering Geology and the Environment*,
DOI: 10.1007/978-3-642-31671-5_6,

Table 1 Physical and mechanical parameters of strata

Strata	γ (kN m^{-3})	c (kPa)	φ (°)	$E_{s0.1-0.2}$ (MPa)	E_{50}^{ref} (MPa)	E_{oed}^{ref} (MPa)	E_{ur}^{ref} (MPa)
II1	14.7	2.3	3.9	1.46			
III1	19.1	27.9	12.9	5.27	26.4	13.2	131.7
IV1	18.9	17.5	11.1	5.20	26.0	13.0	130.0
IV2	17.5	14.5	8.8	3.69	18.5	9.3	92.3
VI2	20.0	50.0	25.6	50.0			

composite steel sheet pile wall proposed for this waterfront excavation project.

The subsurface soil strata are mainly composed of a sequence of marine deposits, alluvia and underlying in situ rocks. The initial seabed level is about −12.5 m near the south pile-supported wharves, and the corresponding strata distributions can be described as: II1 marine mud, III1 silty clay, IV1 silty clay, IV2 mucky silt, and VI2 weathered granite. The physical and mechanical parameters of the strata are shown in Table 1, and some stiffness parameters are used by the constitutive model. The strength properties are obtained from the laboratory direct shear tests with consolidated and drained conditions.

The waterfront excavation project is located at the east bank of Zhujiang River estuary, with the annual average tidal difference from 0.97 to 1.7 m. The design tide levels are based on the mean sea level of Huanghai, and the design high and low tide level with return period of 50 years are 1.59 m and −0.91 m, respectively.

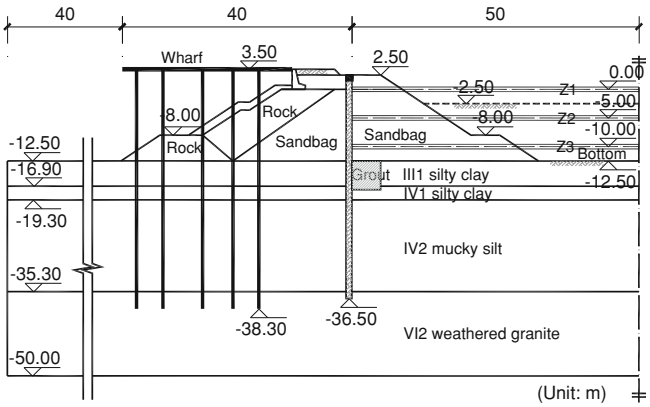

Fig. 1 Cross section of diaphragm wall scheme

Table 2 Calculation steps of diaphragm wall scheme

Step	Construction conditions
1	Build front wharves and embankment, fill sand to −2.5 m
2	Install diaphragm wall (displacement is set to zero after calculation)
3	Dewater to −3.5 m inside excavation and locally excavate to 0.0 m
4	Install the first level struts (Z1), dewater to −6.0 m and excavate to −5.0 m
5	Install the second level struts (Z2), dewater to −11.0 m and excavate to -10.0 m
6	Install the third level struts (Z3), dewater to −13.5 m and excavate to -12.5 m

3 FEM Modeling

The two-dimensional FEM geotechnical program Plaxis is employed to predict the mechanical performance of the retaining structures as well as the soils. The Harding-Soil constitutive model is used to describe the stress–strain relationship for the strata in light of its capability of dealing with the effects of shear hardening and compression hardening. The property parameters can be obtained and calibrated by laboratory triaxial compression test and oedometer test (Table 1).

The diaphragm wall with thickness of 1 m and length of 39 m are adopted for the diaphragm wall scheme. The pile-supported wharves and the land-connecting rubble mound embankment should be built first; meanwhile, the original full rubble stone filled embankment must be partially replaced by sandbags to satisfy the construction requirements of the concrete diaphragm panels. The piles and the transverse beams of the pile-supported wharves as well as the diaphragm wall are modeled by the elastic plate elements, and the interface elements are adopted to account for the sliding as well as the falling-off effects among soils, piles and diaphragm wall. The horizontal struts are modeled by the anchored bar elements only considered the uniaxial stiffness. The Mohr–Coulomb constitutive model is used to describe the strength characteristics and the deformation behavior of the reclaimed strata (Gong 2000). The cross section diagram of the diaphragm wall scheme is shown in Fig. 1, and the calculation steps of the scheme are presented in Table 2.

The double-row steel sheet piles with transverse spacing of 1.5 m and the filled concrete with strength grade of C30 are adopted to exert the combined bending stiffness for the composite steel sheet pile wall scheme. The both roots of the double-row steel sheet piles are inserted into VI2 weathered granite layer to be fixed. The rubble mound foot-

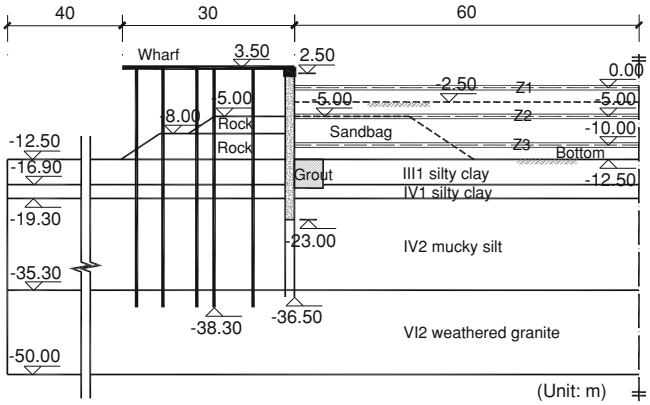

Fig. 2 Cross section of composite steel sheet pile wall scheme

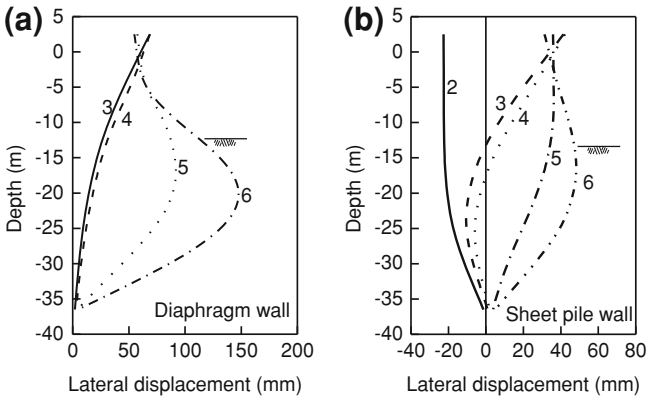

Fig. 3 Lateral displacement of retaining wall

Table 3 Calculation steps of composite steel sheet pile wall scheme

Step	Construction conditions
1	Build front wharves and composite steel sheet pile wall, fill berm to −5.0 m (displacement is set to zero after calculation)
2	Fill sand to −2.5 m
3	Dewater to −3.5 m inside excavation
4	Install the first level struts (Z1), dewater to −6.0 m and excavate to −5.0 m
5	Install the second level struts (Z2), dewater to −11.0 m and excavate to −10.0 m
6	Install the third level struts (Z3), dewater to −13.5 m and excavate to −12.5 m

protection berm outside the retaining structure is used to protect the steel sheet pile wall, and the sandbag berm inside the excavation is used to ensure the balanced vertical loading.

The global bending stiffness of the composite steel sheet pile wall is combined by the stiffness of side steel sheets and the filled concrete above the level of −23 m and is only taken into account the stiffness of the side steel sheets around the centerline of the steel sheets below the level of −23 m. The other property parameters of the structures and strata are identical to those adopted for the diaphragm wall scheme. The cross section diagram of the composite steel sheet pile wall scheme is shown in Fig. 2, and the calculation steps of the scheme are presented in Table 3.

4 Numerical Results and Discussion

The lateral displacement curves along depth of the diaphragm wall at different construction stages are shown in Fig. 3a. The shape of the lateral displacement curve of the diaphragm wall is like cantilever beam with the maximum displacement of 68.8 mm at the top under step 3 and 4, and the curve gradually shows the characteristic of deep-level bulge with the increase of excavation depth; meanwhile, the elevation of the maximum lateral displacement point also lowers with the succeeding excavating. The maximum lateral displacement of the diaphragm wall is 147.7 mm with the depth of −20.0 m at step 6. The diaphragm wall reveals excessive lateral displacement with the maximum relative displacement about 1 % at step 6. The diaphragm wall must independently sustain the hydrostatic water pressure with height difference of 16.19 m induced by the drops of groundwater head and the soil pressure induced by the rubble mound filling as well as the live loading on the embankment. Consequently, the displacement of the diaphragm wall outranges the allowance criteria of 0.5 % for the design.

The lateral displacement curves along depth of the composite steel sheet pile wall at different construction stages are shown in Fig. 3b. The sheet pile wall moves toward the sea due to the lateral soil pressure induced by inside sand filling at step 2, with the maximum lateral displacement of −22.3 mm at the top and the obvious built-in effects at the toe. The upper part of the wall inversely moves toward the land with inside excavating and dewatering under step 3 and 4, with the maximum lateral displacement of 42.2 mm at step 4. The deep-level lateral displacement of the wall increases gradually with inside excavating and dewatering, and the deformation curve shape of the wall also transforms from cantilever beam to deep-level bulge. The maximum lateral displacement of the composite steel sheet pile wall is 48.2 mm and just near to the excavation bottom at step 6, which is only about one-third the displacement value of the diaphragm wall.

The empirical relationship between the maximum relative lateral displacement of retaining structure and the safety factor against basal heave can be established according to the published literatures (Mana and Clough 1981; Clough and O'Rourke 1990), which shows that the maximum relative lateral displacement will decrease with

the enhancement of retaining structure stiffness. The maximum bending stiffness of the composite steel sheet pile wall is about 6.8 times that of the diaphragm wall, while the maximum lateral displacement of the composite steel sheet pile wall is only one-third that of the diaphragm wall at the most disadvantageous construction stage. The safety factor against basal heave around the lowest strut is 2.9 for the composite steel sheet pile wall scheme, and the value is only 2.5 for the diaphragm wall scheme.

5 Conclusions

Based on the results of the present study, the following conclusions can be drawn:

(1) The composite steel sheet pile wall can be constructed simultaneously with the front pile-supported wharves. This will reduce the lateral soil pressure acting on the retaining wall during inside excavating and dewatering.
(2) The composite steel sheet pile wall can exert the global bending stiffness from both the double-row steel sheets and the filled concrete, correspondingly, the maximum lateral displacement of the composite steel sheet pile wall is only one-third that of the diaphragm wall.
(3) The safety factor against basal heave of the composite steel sheet pile wall is higher than that of the diaphragm wall, owing to the greater global bending stiffness and the reduced lateral as well as vertical soil pressure.

References

Clough, G. W., & O'Rourke, T. D. (1990). Construction induced movements of in situ walls. In: *ASCE conference on design and performance of earth retaining structures* (pp. 439–470). New York: America.

Ding, Y. C., & Wang, J. H. (2008). Numerical modeling of ground response during diaphragm wall construction. *Journal of Shanghai Jiaotong University (Science), 13*(4), 1–6.

Ding, Y. C., Wang, J. H., & Xu, B. (2009). Three-dimensional numerical analysis of braced excavation based on FLAC3D. *Journal of Shanghai Jiaotong University, 43*(6), 976–980 (in Chinese).

Gong, X. N. (2000). *Ground improvement manual* (2nd ed.). Beijing: China Architecture and Building Press (in Chinese).

Li, X. J., Chen, Y. H., & Xuan, L. J. (2006). Creative design of super large dry-dock head construction by means of deep steel sheet piling excavation in water area. *Chinese Journal of Geotechnical Engineering, 28*(S1), 1560–1564 (in Chinese).

Mana, A. I., & Clough, G. W. (1981). Prediction of movements for braced cuts in clay. *Journal of Geotechnical Engineering, ASCE, 107*(6), 759–777.

Deformation Behavior of Braced Excavation and Its Influence on Adjacent Piles

Y. C. Ding, Z. K. Cheng, G. H. Li, and J. H. Wang

Abstract
A three-dimensional numerical modeling combined with in-situ measurements was performed to investigate the deformation behavior of a braced excavation for construction of underground metro station and its influence on the adjacent piles. The computed lateral deformation of the retaining wall agrees well with those of the field monitoring, indicating that it is feasible to use numerical model to predict the deformation of the embedded piles, which can not be acquired at the site. The study reveals that the design and construction countermeasures adopted in this project restrict the deformation of the retaining structures as well as the embedded piles, and ensure the safety of the structures effectively.

Keywords
Excavation • Metro station • Soft soil • Deformation control • Reclamation

1 Introduction

The soft deposit in Shanghai is well known for its high water content, high compressibility, high plasticity, low permeability and low strength. Nevertheless, there continuously comes up many deep excavation projects in crowded areas of Shanghai during the past decades, which are used for construction of underground metro station of public transportation networks. Deformation control and environment protection countermeasures are becoming the most concerned consideration during plan, design and construction of underground metro stations in geotechnical and structural engineering (Liu et al. 2005; Finno et al. 2007; Ou and Hsieh 2011).

Y. C. Ding (✉) · Z. K. Cheng · G. H. Li
CCCC Third Harbor Consultants Co., Ltd., Shanghai 200032, China
e-mail: ycding@163.com

J. H. Wang
Department of Civil Engineering, Shanghai Jiaotong University, Shanghai 200240, China

In this paper, a three-dimensional numerical simulation combined with in-situ monitoring was carried out to study the deformation of a metro station excavation and its influence on the adjacent pile foundations of the elevated bridge and to discuss the effectiveness of deformation control countermeasures.

2 Project Description

2.1 Project Profile and Retaining Scheme

The South Xizang Road Transfer Station of Shanghai Metro Line 8 is located at the crossroads between the South Xizang Road and the South Zhongshan Road in Huangpu district. The metro station is under-crossing the elevated bridge of South Zhongshan Road, and the layout is along north–south direction, as illustrated in Fig. 1. The major structure type of the underground metro station is composed of a 2-storey and 3-span concrete frame structure with length of 302 m and width of 22 m, of which the part with axial number from 23 to 28 is the underpass beneath the elevated bridge of South Zhongshan Road (noted as Zone 6

Y. Huang et al. (eds.), *New Frontiers in Engineering Geology and the Environment*,
DOI: 10.1007/978-3-642-31671-5_7,

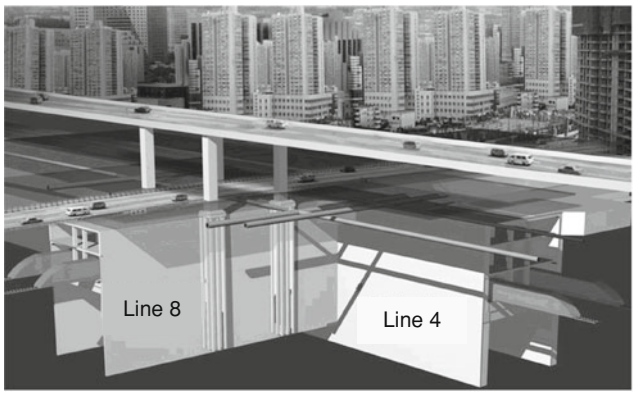

Fig. 1 Perspective of South Xizang road transfer station

in the following context). The excavation depth in Zone 6 is about 15.8 m with dimension of 36 × 22 m in horizontal plan.

The type of the bridge foundation is embedded pile-supported concrete abutment. The length of each pile shaft is 28 m and consists of two single piles connected by welding steel hoops at ends, and the depth of joints ranges from 13 to 16 m. The commonly used diaphragm wall retaining scheme is inapplicable for this excavation owing to its slurry trenching and concreting construction requirements, and corresponding stress relief as well as disturbance effects of the ground (Ding and Wang 2008). Meanwhile, the vertical clearance between the upper bridge structures and the ground can't ensure smooth operation of the trenching machines. Therefore, the contiguous cast-in-place bored piles combined with jet grouting cutoff curtains with specific directions are employed to retain soils and to cut off groundwater seepage.

2.2 Ground Conditions

The subsurface soil strata are mainly composed of a sequence of Quaternary marine deposits and alluvia. The initial ground surface level of the construction site is about 3.8 m and the corresponding geological stratification can be described as: I miscellaneous fill, II silty clay, III silty clay, IV muddy clay, V_1 clay, V_3 silty clay, VI silty clay and VII_2 fine sand. The average groundwater level is about 0.5 to 0.7 m below the ground surface. The main physical and mechanical parameters of the strata are given in Table 1.

2.3 Numerical Modeling

The numerical model, taking into account the interaction among soil, retaining structures and the adjacent pile foundations, was established based on the geotechnical program FLAC3D. The strata, the reclaimed ground and the abutments of the bridge were modeled with solid zones, the cast-in-place bored piles as well as the jet grouting cutoff curtains were model with liner structural element, the inner struts were modeled with beam structural elements, the local pre-installed middle concrete slab was modeled with shell structural element, and the outside piles were modeled with pile structural elements. The modified Cam-clay constitutive model was employed to describe the deformation behavior of soil (Potts and Zdravkovic 2001) according to the empirical data in Shanghai soft soil deposits. The calculation steps of the numerical model are presented in Table 2.

3 Lateral Displacement Behavior

The comparison between the computed and the measured lateral displacements of the retaining structure at monitoring point Q8 when the pit is excavated to the bottom (Step 6) are illustrated in Fig. 2a. The maximum calculated lateral displacement at point Q8 is 27.7 mm, while the maximum measured value at point Q8 is 29.3 mm. It can be shown that the calculated lateral displacement curve agrees well with the measured one, and the maximum lateral displacement point appears close to the base face when the pit is excavated to the bottom. The lateral displacement behavior of the retaining structures is well predicted by the numerical model; therefore, the numerical model can be adopted to investigate the deformation pattern and tendency of the embedded piles dynamically, which can not be acquired at the site because these piles are buried beneath the bridge abutments and shielded by them.

The lateral displacement curves of the pile at point P8 beneath the abutment during different construction stages are illustrated in Fig. 2b. There is almost no lateral displacement increment of the pile top when the pit is excavated to the second level struts (Step 2), indicating that the lateral deformation of the abutment has stabilized after this construction step. Nevertheless, the maximum lateral displacement of the pile increases with the succeeding excavating and dewatering; meanwhile, the deformation profile of the pile also changes with the construction. The depth range of the inside jet grouting ground reclamation is from 3 m below to 1 m above the final excavation bottom (with depth from 14.8 to 18.8 m), the depth of the connection joints of the piles are also from 13 to 16 m. The reclaimed ground inside the excavation serves as a giant block propping system during the excavating and dewatering process owing to its large deformation stiffness and high strength characteristics, resulting in the lateral displacements of the piles around depth range of the reclaimed ground being restricted effectively. The maximum lateral displacement of the pile at point P8 is 16 mm and located at

Table 1 Physical and mechanical parameters of strata

Strata	Thickness (m)	Unit weight (kN · m^{-3})	e_0	c_{cu} (kPa)	φ_{cu} (°)	λ	κ
II	3.0	18.3	0.73	20	20	0.090	0.007
III	4.5	17.5	1.32	11	18	0.133	0.01
IV	9.5	16.6	1.24	13	11	0.103	0.009
V_1	7.2	17.6	0.76	16	14	0.088	0.007
V_3	7.3	18	0.88	16	21	0.096	0.007
VI	3	19.2	0.93	44	21.5	0.058	0.005
VII_2	/	19.0	0.72	4	31.5	0.025	0.002

Table 2 Calculation steps of excavation in Zone 6

Step	Construction conditions
0	Calculate the initial ground stress considering pile foundations and retaining structures (displacement is set to zero after calculation)
1	Excavate and dewater to bottom of the first level struts and install the first level struts (Z1)
2	Excavate and dewater to bottom of the second level struts and install the second level struts (Z2)
3	Excavate and dewater to bottom of the third level struts and install the third level struts (Z3)
4	Install the middle concrete slab, excavate and dewater to bottom of the fourth level struts and install the fourth level struts (Z4)
5	Excavate and dewater to bottom of the fifth level struts and install the fifth level struts (Z5)
6	Excavate to final level and concrete the bottom slab

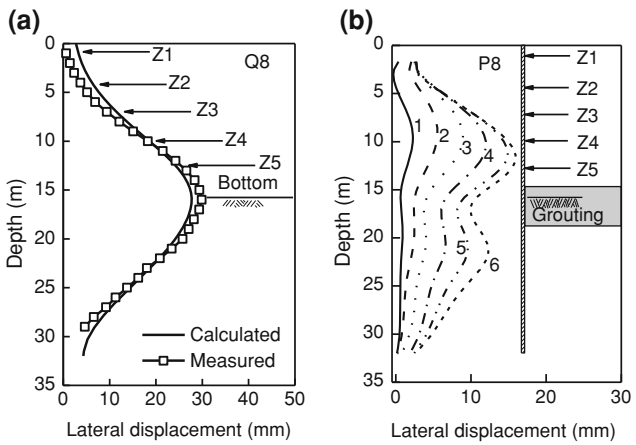

Fig. 2 Lateral displacement of retaining structure and pile

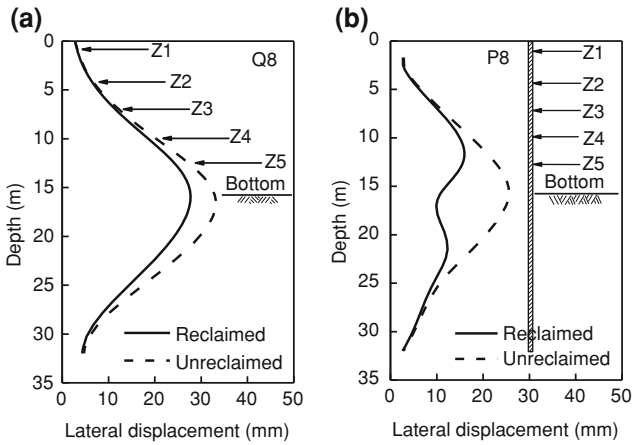

Fig. 3 Influence of inside grouting reclamation on structure displacement

depth of 11.4 m when the pit is excavated to the bottom (Step 6), while the maximum lateral displacement of the pile top is only 2.7 mm. The overall deformation shape of the pile at point P8 is like "M", with which the relative large values appear at the depth of 11.4 and 21.5 m respectively.

The influence of the jet grouting ground reclamation inside the excavation on the lateral displacement of the retaining structure at point Q8 and the pile at point P8 are shown in Fig. 3. The maximum lateral displacement of the retaining structure at point Q8 decreases from 33.2 to 27.7 mm with inside jet grouting when the pit is excavated to the bottom (Step 6), while the value of the pile at point P8 decreases from 25.6 to 16.0 mm. The influence of inside jet grouting on the deformation of the pile is more pronounced than that on the retaining structures, due to the greater overall bending stiffness of the contiguous cast-in-place bored piles combined with the jet grouting cutoff curtains.

4 Conclusions

Based on the results of the present study, the following conclusions can be drawn:

(1) The three-dimensional numerical model based on FLAC3D can dynamically compute the deformation behavior of the retaining structures at different construction stages and predict the lateral deformation of the embedded piles.
(2) The contiguous cast-in-place bored piles combined with jet grouting cutoff curtains with specific jet angle can exert great overall bending stiffness, cut off the transfer of ground deformation and the seepage of the groundwater effectively.
(3) The inside jet grouting ground reclamation can serve as a giant block propping system during the dewatering and excavating periods, and restrict the lateral displacement of the adjacent piles.

Acknowledgments The research is sponsored by the National Natural Science Foundation of China (No. 50679041) and the Shanghai Leading Academic Discipline Project (No. B208).

References

Ding, Y. C., & Wang, J. H. (2008). Numerical modeling of ground response during diaphragm wall construction. *Journal of Shanghai Jiaotong University (Science), 13*(4), 1–6.

Finno, R. J., Blackburn, J. T., & Roboski, J. F. (2007). Three-dimensional effects for supported excavations in clay. *Journal of Geotechnical and Geoenvironmental Engineering, ASCE, 133*(1), 30–36.

Liu, G. B., Ng, C. W. W., & Wang, Z. W. (2005). Observed performance of a deep multistrutted excavation in Shanghai soft clays. *Journal of Geotechnical and Geoenvironmental Engineering, ASCE, 131*(8), 1004–1013.

Ou, C. Y., & Hsieh, P. G. (2011). A simplified method for predicting ground settlement profiles induced by excavation in soft clay. *Computers and Geotechnics, 38*(8), 987–997.

Potts, D. M., & Zdravkovic, L. (2001). *Finite element analysis in geotechnical engineering: Application*. London: Thomas Telford Ltd.

Numerical Analysis on Deformation of Braced Excavation with Top-down Method

Y. C. Ding, D. G. Wang, J. C. Liu, K. H. Gu, Z. K. Cheng, and J. H. Wang

Abstract
A three-dimensional simulation based on FLAC3D was carried out to investigate the deformation characteristics of a braced excavation with top-down method in typical Shanghai soft soil deposits. The lateral displacement of the retaining wall, the ground surface settlement, and the subsoil movement outside the excavation were studied in detail. The predicted ground surface settlement curves agree well with the empirical ones, therefore, the reliability of the calculated results is verified, which can provide a useful guidance for engineers in design and analysis of similar excavation projects with top-down method.

Keywords
Numerical simulation • Braced excavation • Top-down method • Deformation • FLAC3D

1 Introduction

Overall stability and safety of retaining structures are the most concerned issues during design and construction of deep excavation of underground basement foundations and other public infrastructures, but in some circumstances especially in heavily congested metropolitan areas, deformation of retaining structures and movement of ground around the excavation should be determined first to appraise the environmental impacts of excavation on the surroundings appropriately (Mana and Clough 1981; Liu et al. 2005).

This paper presents a three-dimensional numerical simulation of a square braced excavation with the top-down construction method in typical Shanghai soft soil deposits based on FLAC3D. The modified Cam-clay constitutive model is used to describe the stress–strain relationship of the soils and the staged excavating as well as the propping processes are dynamically modeled in the numerical model. The lateral displacement of the retaining wall, the ground surface settlement and the ground movement around the excavation are analyzed and discussed.

Y. C. Ding (✉) · D. G. Wang · J. C. Liu · K. H. Gu · Z. K. Cheng
CCCC Third Harbor Consultants Co., Ltd.,
Shanghai 200032, China
e-mail: ycding@163.com

J. H. Wang
Department of Civil Engineering, Shanghai Jiaotong University,
Shanghai 200240, China

2 Numerical Modeling

The braced excavation is square in plan with dimension of 56 × 56 m, and only one quarter of the model is established and modeled regarding the symmetry of the excavation. The maximum excavation depth H_{max} is 20 m, which is divided into five excavation steps with excavation depth of 4 m within each step. The whole dimension of the numerical model is 128 × 128 × 100 m as illustrated in Fig. 1. The strata are modeled with 8-node and 6-face brick elements. The outer cut boundary faces are fixed in normal direction, the central symmetric faces are fixed with symmetric condition, and the base face of the model is fixed in three directions.

The modified Cam-clay constitutive model is employed to describe the deformation behavior of soil, and the variation of groundwater levels is simulated appropriately by

Y. Huang et al. (eds.), *New Frontiers in Engineering Geology and the Environment*,
DOI: 10.1007/978-3-642-31671-5_8,

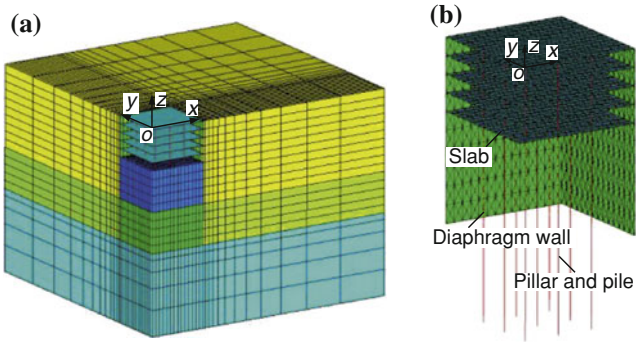

Fig. 1 Mesh of numerical model. **a** Overall model, **b** Retaining structures

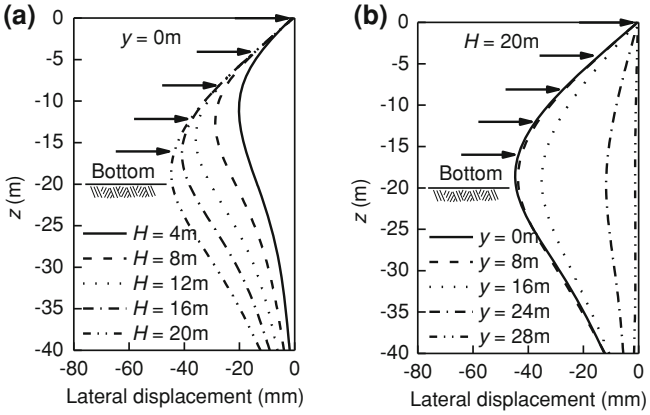

Fig. 2 Lateral displacement of retaining wall

adjusting the location of phreatic surfaces (Potts and Zdravkovic 2001; Wood 1990). The effects of stratification and consolidation are not taken into account in the numerical model, and the property parameters with effective stress conditions are adopted in the analysis. The initial groundwater level is located at 1 m below the ground surface, and the groundwater inside the excavation is drawn to 1 m beneath the excavation bottom during each excavation step. The physical and mechanical parameters of the soils are listed as: the unit weight $\gamma = 17.15\text{kN/m}^3$, the void ratio $e = 1.2$, the lateral at-rest soil pressure coefficient $K_0 = 0.5$, the slope of normal compression line in υ-ln$p$ plan $\lambda = 0.14$, the slope of swelling line in υ-ln$p$ plan $\kappa = 0.01$, the slope of critical state line in p'-q plan $M = 1.2$, the poisson's ratio $\mu = 0.35$ and the overconsolidation ratio $OCR = 1.0$. These property parameters are similar to those for III1 silty clay of Shanghai soft soil deposits.

The horizontal slab struts are modeled with shell elements with equivalent axial stiffness, the retaining walls are modeled with liner elements, and the pillars as well as the piles are modeled with pile elements. The concrete strength grade of C30 is adopted for all retaining walls, struts, pillars and piles, with only 80 percent of strength taken into account regarding the impacts of construction conditions. There are two rows of perpendicular diaphragm walls at $x = 28$ m and $y = 28$ m with depth of 40 m as well as thickness of 1.0 m. There are five levels of horizontal struts with vertical spacing of 4 m and thickness of 0.12 m.

3 Numerical Results and Discussion

3.1 Lateral Displacement of Retaining Wall

The lateral displacement curves of the retaining wall with different excavation depths and at different sections are shown in Fig. 2. The maximum lateral displacement of the retaining wall is −45.3 mm (the negative value indicates that the walls move towards excavation) when the pit is excavated to the bottom. The first level slab strut is installed prior to the excavation of superficial soils within depth of 4 m, resulting in the top of the retaining wall nearly being fixed in horizontal direction during the succeeding excavating processes. The maximum lateral displacements increase gradually with the excavation depth, and the elevations of the maximum lateral displacement points also lower with the excavation depth. The location of the maximum lateral displacement point is near to the excavation bottom face when the pit is excavated to the bottom. The increment of the maximum lateral displacement during each construction stage lowers down with the excavation depth due to the massive axial stiffness of the horizontal slab struts.

There exists a pronounced three-dimensional spatial deformation effect for the retaining wall, with the maximum lateral displacement appearing at the central symmetric section while the minimum value at the corner section, owing to the orthogonal propping effects between the perpendicular diaphragm walls with right-angle intersection.

3.2 Ground Surface Settlement

The ground surface settlement curves with different excavation depths at the symmetric face $y = 0$ m are shown in Fig. 3a. Ground surface upheaval does not appear due to the slipping and the falling-off effects between the retaining wall and the soils modeled with the liner structural elements combined with the interface elements. The maximum upheaval displacement of the retaining wall is 15 mm, while the ground surface settles during all excavation stages. The maximum settlement point occurs near to the excavation boundary when the superficial soils are excavated, then the distance between the maximum settlement

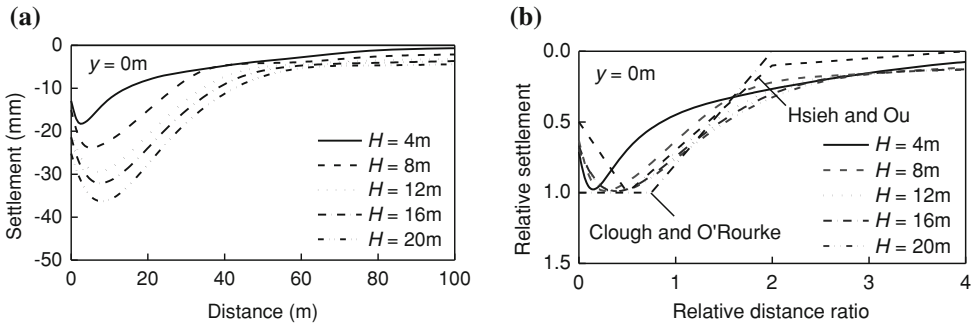

Fig. 3 Ground surface settlement. **a** Absolute settlement, **b** Non-dimensional settlement

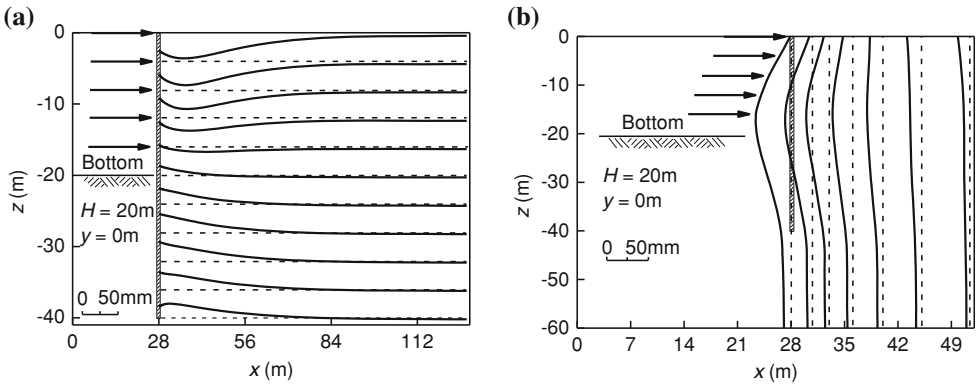

Fig. 4 Soil movement outside excavation. **a** Vertical movement, **b** Horizontal movement

point and the excavation boundary gradually increases with the succeeding excavating. The location of the maximum settlement point almost does not move outward when the excavation depth reaches 12 m.

There also exists a pronounced three-dimensional spatial settlement effect for the ground surface with obvious settlement trough around the middle part of the retaining wall along its longitudinal direction. The maximum ground surface settlement occurs near the central symmetric plane of the excavation with the value of −36.3 mm, while the settlement is much smaller near the corner of the excavation with the value of −16.4 mm. It can be inferred that the settlement of the ground surface and the lateral displacement of the retaining wall are relevant to each other, owing to the same three-dimensional load-bearing and deformation transferring mechanism.

The comparison between the non-dimensional settlement curves of the ground surface versus the relative distance ratio and the empirical envelop curves (Clough and O'Rourke 1990; Hsieh and Ou 1998) is shown in Fig. 3b. The calculated relative settlement curves agree well with the empirical ones, while there are some distinctions when the relative distance ratio is greater than two. The main reasons can be ascribed to: Firstly, the simplified displacement restrictions of the cut boundaries result in the fixed lateral displacement and the free vertical displacement conditions. Secondly, the modified Cam-clay constitutive model can not account for the large stiffness effects when the soils are under small strain state. The more reasonable cut boundary conditions as well as the accurate advanced constitutive models such as Hardening-soil model with Small Strain (HSS model) (Atkinson 2000) are more suitable to predict ground surface settlement characteristic.

3.3 Soil Movement Outside Excavation

The distributions of vertical and horizontal movements of the soils around the retaining wall at the central symmetric plane when the pit is excavated to the bottom are illustrated in Fig. 4. Settlement movements occur for the superficial soils with the maximum settlement points appearing at a short distance to the excavation boundary, while upheaval movements occur for the subsoils with the maximum upheaval points appearing just on the interfaces between the retaining wall and the surrounding soils. The horizontal movements of the ground near the retaining wall are similar to those of the retaining wall, showing a characteristic of deep-level bulge with the maximum lateral displacement adjacent to the excavation bottom face. The elevations of the maximum lateral displacement points for the outer soils

gradually rise with the increase of the distance from the retaining wall, and these points locate at the ground surface eventually.

4 Conclusions

Based on the results of the present study, the following conclusions can be drawn:

(1) The calculated ground surface settlement curves agree well with the published empirical data, indicating the established numerical model can predict the deformation characteristic of the braced excavation with top-down method reasonably and effectively.
(2) The lateral displacement of the retaining wall, the ground surface settlement, and the soil movement around the excavation all interact with each other and combine together to exhibit a pronounced three-dimensional spatial deformation characteristic.
(3) Some calculation conditions are simplified in the numerical model, including simplification of stratification, taking no account of seepage and consolidation due to dewatering. These issues are to be solved in the following studies.

Acknowledgments The research is sponsored by the National Natural Science Foundation of China (No. 50679041) and the Shanghai Leading Academic Discipline Project (No. B208).

References

Atkinson, J. H. (2000). Non-linear soil stiffness in routine design. *Geotechnique, 50*(5), 487–508.

Clough, G. W. & O'Rourke, T. D. (1990). Construction induced movements of in situ walls. In: *ASCE Conference on Design and Performance of Earth Retaining Structures* (pp. 439–470). New York: ASCE.

Hsieh, P. G., & Ou, C. Y. (1998). Shape of ground surface settlement profiles caused by excavation. *Canadian Geotechnical Journal, 35*(6), 1004–1017.

Liu, G. B., Ng, C. W. W., & Wang, Z. W. (2005). Observed performance of a deep multistrutted excavation in Shanghai soft clays. *Journal of Geotechnical and Geoenvironmental Engineering, ASCE, 131*(8), 1004–1013.

Mana, A. I., & Clough, G. W. (1981). Prediction of movements for braced cuts in clay. *Journal of Geotechnical Engineering, ASCE, 107*(6), 759–777.

Potts, D. M., & Zdravkovic, L. (2001). *Finite element analysis in geotechnical engineering: Application*. London: Thomas Telford Ltd.

Wood, D. M. (1990). *Soil behaviour and critical state soil mechanics*. Cambridge: Cambridge University Press.

Analysis of Engineering Geology Condition for Qingdao Tongan Area

D. W. Lv, W. F. Ning, B. B. Liu, H. Y. Liu, and J. P. Liang

Abstract

As economies develop dramatically fast, more and more engineering projects are being constructed near Qingdao Tongan areas. This issue is written to harmonize engineering activities with geo-environment and avoid occurrence of geological hazards and damages of environment, as well as to provide reliable fundamental data for the exploitation and utilization of Qingdao Tongan areas. This paper is supported by the engineering geological condition of the Qingdao Tongan. Many methods are applied to gain detailed original data, including engineering geological drilling, in situ tests in seabed soil, side sonar measurement, taking superficial soil samples and column soil samples. Many years' engineering reconnaissance data of Qingdao Tongan and research results are also combined in this paper. We study many aspects of this area, such as, regional geology, topography and geomorphy, lithostratigraphy, geological structure, hydrogeologic condition, soil mechanical characteristics and existing major engineering geo-environmental problems. On the basis of the study, we find out the types, regularities distribution, development tendency, hazard level of bad geological process in the study area, and then, offer some advices to manage it. Find out the types, depth, distribution, engineering properties of rock and soil bed in this study area and analyse and evaluate the stability, homogeneity and bearing capacity of ground base. Evaluate the seismic effects of this area. According to characteristics of the proposed building and site engineering geological conditions, select the appropriate foundation bearing stratum, and made a economic, reasonable suggestion.

Keywords

Engineering geology • Geological structure • Layer

D. W. Lv (✉) · W. F. Ning · H. Y. Liu
College of Geological Science and Engineering, Shandong University of Science and Technology, Qingdao 266510, Shangdong, China
e-mail: lvdawei95@126.com

D. W. Lv · H. Y. Liu
Key Laboratory of Depositional Mineralization and Sedimentary Mineral (SDUST), Qingdao 266510, Shandong, China

B. B. Liu
School of Ocean and Earth Science, Tongji University, Shanghai 200092, China

J. P. Liang
Geological Institute of Shandong Province, Jinan 250013, Shandong, China

1 Introduction

Tongan region is significant to the development of Qingdao economic zone, in this region, the construction of engineering structure is urgent to realize the engineering geological environment exactly, so realizing the geological environment and human engineering activities of mutual coordination, avoiding geological disaster.

Y. Huang et al. (eds.), *New Frontiers in Engineering Geology and the Environment*,
DOI: 10.1007/978-3-642-31671-5_9,

2 Geological Condition Analysis

2.1 Lithology

Qingdao region assise is consist of Laiyang Gr. Qingshan Gr. Wangshi Gr. and Quaternary strata (Jia & Tan 1995). Laiyang Gr. is not integrated above Jurassic system, integrated in a set of fluvialite facies and lacustrine facies clasolite which under the Baikui system Qingshan Gr. Lithology varies considerably from place to place. Qingshan Gr. is located in Laiyang Gr.,Wangshi Gr. or a set of volcanic series which under the Daqun Gr. The development of this group varies from place to place, Ludong develops more stratigraphic regionalizations, The mafic volcanic rock and acid volcanic alternate with appear. Wangshi Gr. which located above the Kq and Dasheng Gr. and under a set of red tertiary clasolite mainly distribute in Ludong stratigraphic regionalizations, Luxi develops less stratigraphic regionalizations, only in the local area in the distribution. Quaternary system develops along the river, the river and jiaozhou bay on both sides and the surrounding. By the features and the influence of different subsidence of Quaternary, thickness changes greatly, according to the present data, its thickness is commonly 0–30 m.

2.2 Geological Structure

According to the regional geological data (Jia & Tan 1995), proposed site which lies in Qingdao–Haiyang fault block heave Grade V tectonic element, since the upper Proterozoic has been in long-term, slow, steady rise the uplift state, in the Mesozoic tectonic activity strongly, with massive invasion of magmatic rocks, to form stable granite batholith. In the long-term weathering, erosion, accumulation and fluvial deposits, granite batholith forms different thickness,and the larger slope rock weathering bed and covered with a certain thickness of the Quaternary overburden.

Survey area is located among the Pishikou–Fushansuo fracture and Wanggezhuang–Shandongtou fracture.

3 The Geotechnical Engineering Evaluation

The proposed construction project covers an area of 5600.0 m^2, total construction area 26040 m, floor area ration 20.6 %. There are 24 floors in proposed 1#building, two floors garage on the bottom of this building, project $\pm 0.00 = 44.60$ m, underground garage bottom elevation is 33.00 m, embedded depth of foundation is about 11.6 m, this project is used to box shear structure, single footing, building specific loads and the deformation requirement is unknown; There are 21 floors in proposed 2, 3#building, two floors garage on the bottom of this building project $\pm 0.00 = 44.60$ m, underground garage bottom elevation is 33.00 m, embedded depth Of foundation is about 13.1 m, the actual completion of the workload: exploratory hole: 25, geologic section: 13, Fig. 1.

3.1 Aquifers with Engineering Analysis and Evaluation

According to field drilling data, Within the scope of proposed site survey depth, the main geotechnical layer are Quaternary plain filling and strong, middle weathering bedrock, aquifers with engineering analysis and evaluation as follow :

1. Quaternary

The first level miscellaneous fill soil backfill in the short time, belong to consolidation of soil, the thickness of the stratum is larger, the structure is loose, uniformity is poor, low intensity, and permeable layer is strong. After the foundation pit excavation the most is excavated. Combined with experience in comprehensive analysis, Natural severe γ take 18.0 KN/m3,stick together force c take 0.0 kPa, be like internal friction Angle φ take 20 °C.

2. Bed rock

The 16th strong weathered granite: by the strong weathering or structure effect, rock broken—very broken, joints and fissures development, rock loose, the mineral links between power is low, close-grained loose medium body, with the compressibility and weak rock foundation engineering characteristics, treat water to soften, is not stable grade V of rock mass, the slope rock mass easy to have the local instability collapse when excavating. On the basis of "Standard for classification of engineering rock masses" GB 50218—94 of relevant provisions, combining with the drilling situation, Qualitative discrimination: rock belong to soft rock, very broken-broken, the basic quality level of the rock is grade V.

Combined with experience in comprehensive analysis, the natural severe γ take 23.0 KN/m^3, stick together force c take 0.0 kPa, equivalent internal friction Angle φ take 45 degrees, the characteristic value of subgrade bearing capacity f_{ak} take 800 kPa, deformation modulus E0 take 45.0 MPa.

The 17th weathered granite: This layer is difficult to drill, the most of the core are fragments form, the exposing period of rock mass index averaged 0.68, BQ for 397.97. This layer of rock mass elasto-plastic material with characteristics, structure surface mainly for structural joints, followed by weathering fracture, joint plane micro opened. Rock have high bearing capacity, good stability, which is

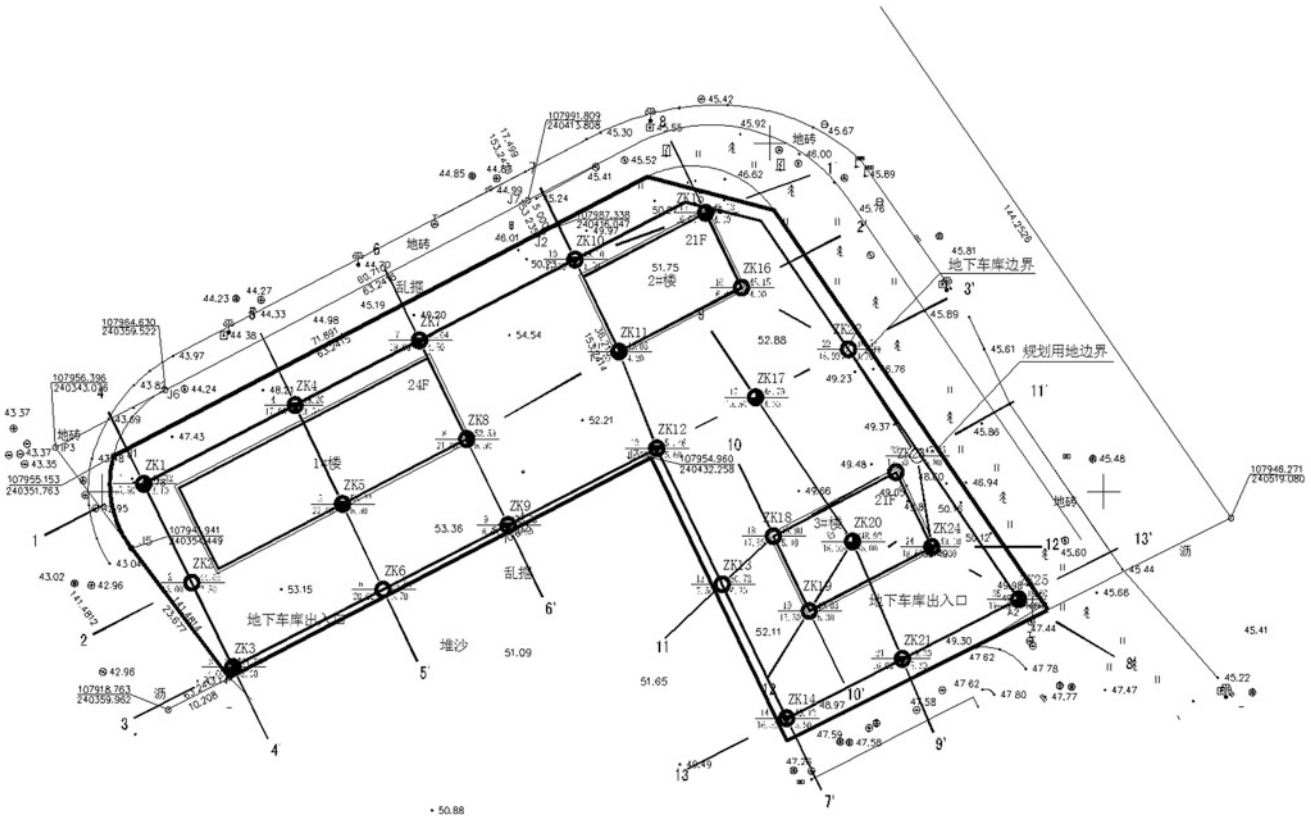

Fig. 1 Site workload schemes

good natural foundation and good building foundation next lie layer, but during the foundation pit excavation rock mass easy collapse or cavingalong the joints surfaces, which belong to III level of rock mass. On the basis of Tables 3 and 4 in chapter "Large Deformation Analysis for Costal Geo-Disasters Using Continuum and Discrete Modeling" shows statistical result and "Standard for classification of engineering rockmasses" GB 50218-94 of relevant provisions, calculation and analysis and judgement: the rock is more stronger, rock mass is more complete, the basic quality level of rock mass is III.

Combined with experience in comprehensive analysis, the natural severe γ take 25.0 KN/m^3, stick together force c take 0.0 kPa, equivalent internal friction Angle φ take 55 degrees, characteristic value of subgrade bearing capacity f_{ak} take 2000 kPa, elastic modulus E take 5×10^3 MPa.

The 18th low weathered granite: This layer of diamond drilling tools must be adopted to drilling, most of cores are cylindrical, the period of exposing rock mass integrity index averaged 0.74 kV, BQ for 501.23. Joints development—agensis, Joint surface closed, breakthrough sex of fracture is poorer, Core is short column shape, groundwater activities weak. The whole strength of the rock mass is high, good integrity, present elastic material characteristic, in certain vertical load can be regarded as incompressible body, the stability of rock mass is good natural foundation and foundation of the lie. On the basis of Tables 3 and 5 in chapter "Large Deformation Analysis for Costal Geo-Disasters Using Continuum and Discrete Modeling" shows statistical result and "Standard for classification of engineering rock masses" GB 50218-94 of relevant provisions, calculation and analysis and judgement: the rock is more stronger, rock mass is more complete, the basic quality level of rock mass is II.

Combined with experience in comprehensive analysis, the natural severe γ take 26.7 KN/m^3, stick together force c take 0.0 kPa, equivalent internal friction Angle φ take 65 degrees, characteristic value of subgrade bearing capacity f_{ak} take 5000, elastic modulus E take 25×10^3 MPa.

3. Each layer (body) geotechnical engineering property index

According to the above the layer of geotechnical engineering evaluation, concluding the engineering characteristics above data induction together, drawing up the engineering properties list. Then each layer (body) geotechnical engineering property index suggested value see Table 1 (the geotechnical engineering parameters of list).

Table 1 The geotechnical engineering parameters of the list

Tiernumber	Solum	Base of bed level (m)		Thick degree(m)		q_{sik} (kPa)	Severe γ (kN/m^3)	Cohesion C (kPa)	Internal friction angle φ	Modulus (MPa)	Load bearing f_{ak} (kPa)
		Min	Max	Min	Max						
①	Plain fill	43.3	49.3	0.4	4.9	20	18.0	0.0	20.0	–	–
(16)	High weathering granite	37.8	45.5	3.7	7.4	150	23.0	0.0	45.0	45/E0	800
(17)	Middle weathering granite	32.7	42.8	1.8	5.4	250	25.0	0.0	55.0	5×10^3/E	2000
(18)	Low weathering granite	Not penetrate				550	26.7	0.0	65.0	25×10^3/E	5000

f_{ak} characteristic value of subgrade bearing capacity, E_0 modulus of deformation, E modulus of elasticity, q_{sik} soil and the anchor solid limit friction standard values, γ natural severe, C cohesion, φ internal friction angle

4 Conclusion

1. In the proposed site, the geomorphy is simple and the stratal configuration is clear. Moreover, the regional tectonic background is steady so it's not easy to develop bad geological process.
2. In Qingdao, the seismic fortification intensity is 6 and this area is in the design earthquake group 2. The buildingyard category of the proposed site is I, and its eigen period is 0.30 s, which means that it is seismic favorable area.
3. There are no hidden riverway, channel, grave, air-raid shelter or boulder found in the reconnaissance process of the site.
4. The underground water of this area can erode the concrete structure. To reinforcement in the reinforced concrete structures, it has no effect in long-term water environment and slight effect in alternating wet and dry environment (Cheng & Hao 2002; Dong 2009). Furthermore, there's fine-grained granite dike in the proposed site.

References

Cheng, H. & Hao, J. (2002). Analysis of the effect of water on poor engineering geology. *Geology of Anhui 12*(4), 298–301.

Dong, Q. (2009). Engineering geological investigation in the influence of the hydrological geological problems. *Science and Technology Innovation Herald 10*, 81.

Jia, Y. & Tan, C. (1995). Qingdao city engineering geology, Qingdao.

Simulation of Tidal Flat Terrain Based on Landform Feature Lines of Tidal Basin

Y. Y. Kang and X. R. Ding

Abstract

Starting from tidal basin, we focus on obtaining the tidal flat digital terrain quickly and efficiently from remote sensing images which can be acquired in real-time. Three parts were illustrated in this paper. Firstly, the landform features of tidal basin were analyzed. The tidal creeks and the watershed beach ridges were considered as the main skeleton structure which could control the whole tidal basin terrain. Secondly, the tidal flat terrain was simulated. This part can be divided into three steps. ① The 2D layout of tidal creeks and watershed beach ridges were obtained from remote sensing images. ② 3D model of tidal creeks and watershed beach ridges was established based on inflection points just like tidal creeks intersections or measuring points on the cross-sections. ③ The terrain of tidal basin was simulated based on 3D elevation of tidal creeks and watershed beach ridges. "ANUDEM" was the main interpolation method. Finally, error analysis was made between the simulated terrain data and the actual measurement data. The result showed that 97 % of errors were between ±0.4 m. The simulated terrain data would be suitable for the further interrelated research within certain precision limitation. It has great significance for evolution research and reclamation of tidal flat in Jiangsu province China.

Keywords

Tidal basin • Tidal creek • Watershed beach ridge • Terrain simulation

1 Introduction

"Master Plan for the Development and Utilization of the Coastal Tidal Flat in Jiangsu" has been officially released in August 2010.180,000 hectares tidal flat will be reclaimed before 2020 (Ding & Kang 2011). In this big backdrop, basic research just like digital terrain model on tidal flat is particularly important. In general, terrain data are obtained by topographic survey. However, terrain change so quickly that the survey data are often delayed in tidal flat area. Additionally, it needs a lot of work and a large amount of human and material resources with field artificial method.

Along with the development of remote sensing technology, the retrieval of underwater terrain was accepted gradually. Polcyn (1973) and Mgengel (1991) presented quantitative water depth analysis respectively from MSS and TM images. Spitzer (1987) described several algorithms about RS-fathoming based on two-way flow radiative transfer model. Wei Ji (1992) developed a RS-fathoming model based on water backscatter, which was useful for the deep and relatively turbidity waters. Kang (2011) established a tidal basin terrain simulation model to interpret the whole tidal flat' terrain in Jiangsu coastal; The Previous researchers had made a lot of research on terrain

Y. Y. Kang (✉)
College of Harbor, Coastal and Offshore Engineering, Hohai University, No. 1 Xikang Road, Nanjng 210098, China
e-mail: kangyanyan850214@126.com

X. R. Ding
College of Hydrology and Water Resources, Hohai University, No. 1 Xikang Road, Nanjng 210098, China

Y. Huang et al. (eds.), *New Frontiers in Engineering Geology and the Environment*,
DOI: 10.1007/978-3-642-31671-5_10,

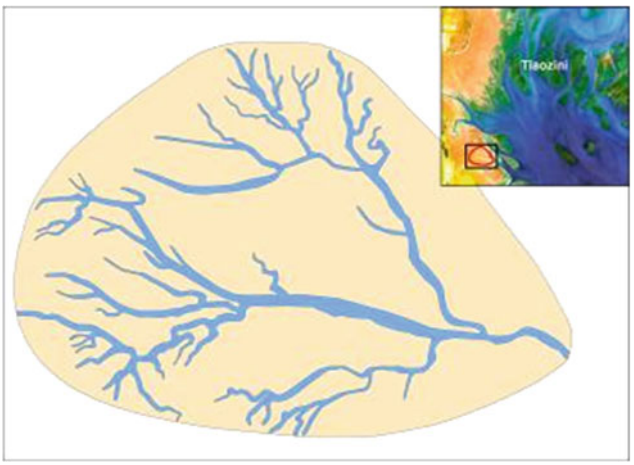

Fig. 1 Tidal basin (study area)

Fig. 2 Tidal creek

retrieval and obtain many valuable achievements. But so far, the interpret technique is not yet mature. The result often was affected by phase, tide, and image quality.

In this paper, unlike many of the existing methods, our solution involved two aspects: physiognomy and remote sensing. Landform features (water edges, tidal creek centerlines and watershed beach ridges) as the main input source were extracted from remote sensing images. The 3D information of feature lines was obtained, and then the tidal basin terrain was simulated quickly and efficiently.

2 Terrain Rules of Tidal Basin

Tidal basin (Fig. 1) is a basic landform unit on tidal flat. At high tide, the tidewater rushes into the flat surface which is made up of loose silty sand. At low tide, the tidewater flow along the lower-lying area, and gradually converges to form a line creek. Tidal water is back and forth for a long time, at last, lots of line small creeks will join together to form a bigger tidal creek. With the tidewater converging from the tidal flat, a catchment, like a dustpan will appear. Moreover, the boundary of catchment is considered as watershed beach ridge. Obviously, tidal creek and watershed beach ridge are the most important geomorphic units and skeleton lines of tidal basin.

Tidal creek (Fig. 2) is a relatively straight flow path which is formed by tidewater constantly converging from tidal flat (Ding & Zhu 1984). It also is the most important motivation factor to shape tidal flat terrain. The shape of tidal creek presents plumed or dendritic. In this paper, we selected ten tidal creek centerlines (longitudinal profile) for statistical analysis. The result (Fig. 3a) showed that tidal creek centerlines' elevation basically presented linear growth from downstream to upstream, and the shape changed through the bifurcation points.

Normally, between the two tidal creek systems, the tidewater flow to both sides owned by the adjacent tidal creeks. The dividing line is called watershed beach ridge. Usually watershed beach ridges are used to divide the different tidal basin controlled by different tide creek systems. In a typical tidal basin (Fig. 1), from high flat to low flat, the longitudinal profile presents first going down slowly, then dropping rapidly (an up-convex curve) (Fig. 3b).

3 Terrain Simulation and Analysis

3.1 Extraction of Feature Lines

Water edge can be easily extracted from real-time remote sensing image (TM, MSS, etc.) using thresholding, edge detection, etc. Based on water edges, tidal creek centerlines and watershed beach ridges were generated using the method of Thiessen polygon (Fig. 4).

- Water edges of the tidal creek were broken into points and the pitch intervals were 1 m.
- Voronoi diagrams (Thiessen polygons) were generated by discrete points.
- Thiessen polygons in the same line were merged, and then the centerlines of tidal creeks and the watershed beach ridges were extracted.

3.2 3D Simulation of Tidal Creek

Based on the bifurcation points' elevation information which have known in advance, piecewise linear interpolation method was used to simulate the tidal creeks centerlines' terrain. Firstly, the tidal creek centerlines were divided into lots of independent small segments by the bifurcation points from upstream to downstream. Secondly, the segments were broken into points those interval was

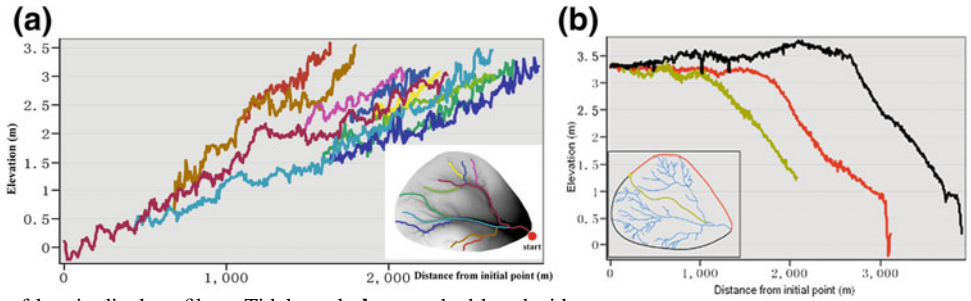

Fig. 3 Characters of longitudinal profile. **a** Tidal creek, **b** watershed beach ridge

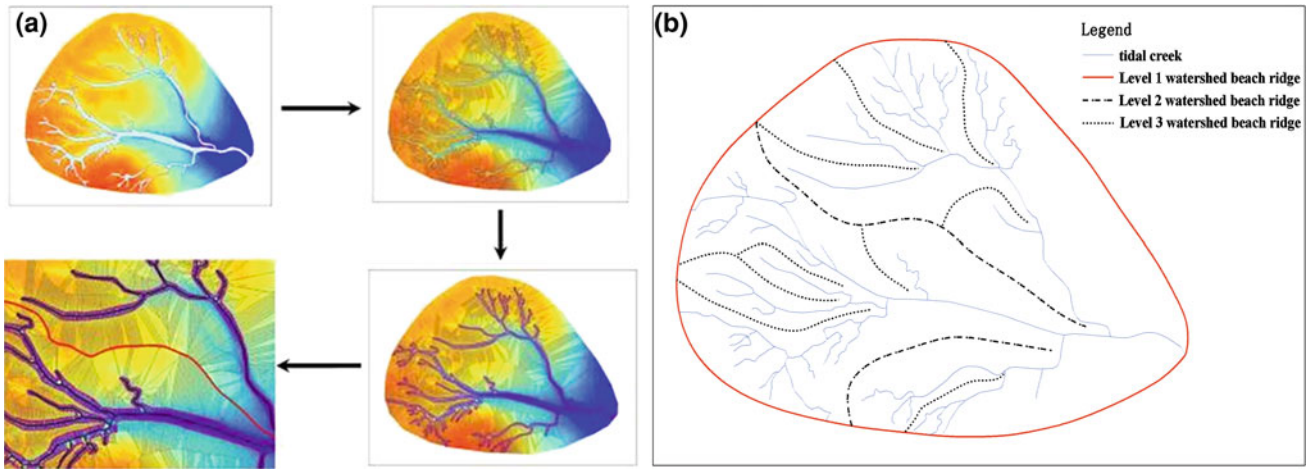

Fig. 4 Extraction of tidal creek centerline and watershed beach ridge. **a** Extract process, **b** extract result

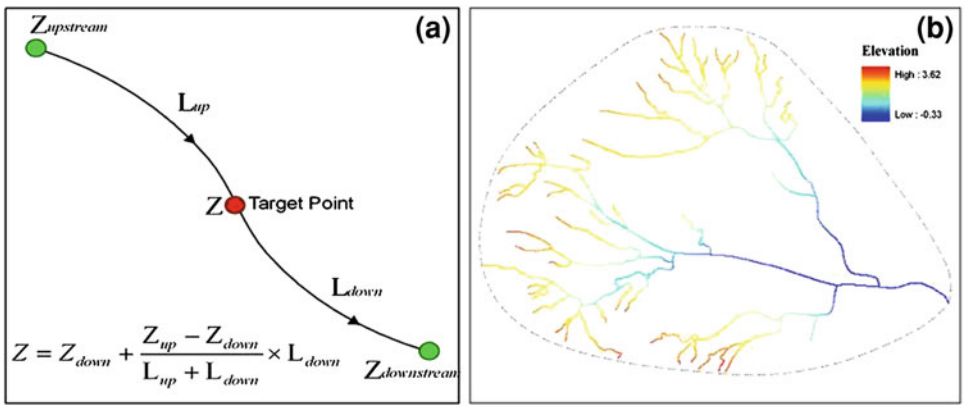

Fig. 5 Schematic diagram of the elevation calculation (tidal creek). **a** Counting principle, **b** digital elevation model of tidal creek

1 m. According to each point, L_{up} and L_{down} were calculated and together Z_{up} and Z_{down} were written in attributes list. Each point's elevation (Z) was calculated using the formula (Fig. 5a). At last, based on the elevation of each point, 5 m × 5 m raster was generated using "point to raster" transform method (Fig. 5b).

3.3 3D Simulation of Watershed Beach Ridge

Some measured points and inflection points (intersection points of watershed beach ridge, tidal basin boundary lines, contours and tidal creel centerlines) had been known. Set these points' elevation as input; Used the piecewise cubic

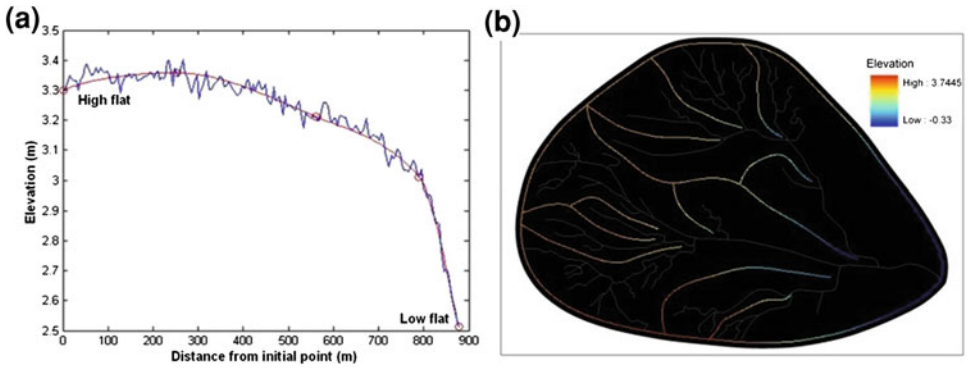

Fig. 6 Schematic diagram of the elevation calculation (watershed beach ridge). **a** Piecewise cubic interpolation, **b** DEM of watershed beach ridges

Fig. 7 Terrain simulation results of tidal basin

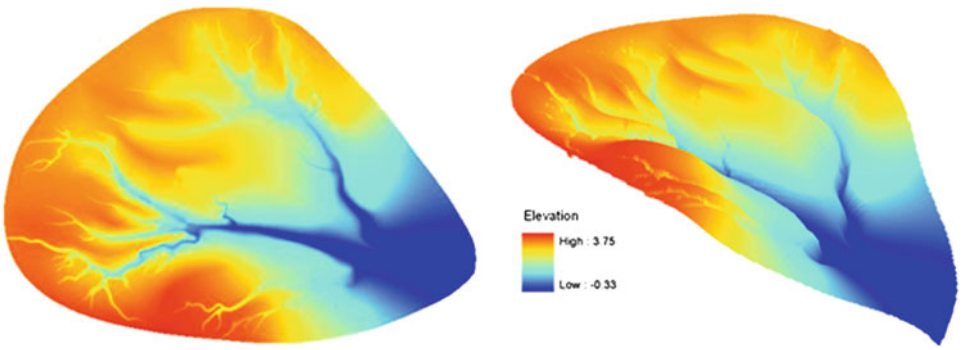

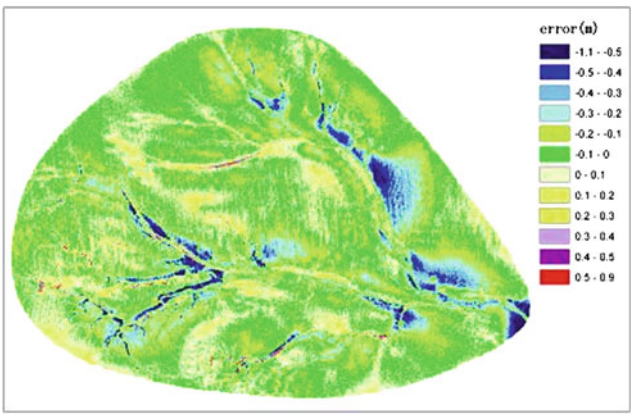

Fig. 8 Error distribution map

interpolation method (Fig. 6a) to calculate 3D elevation information of watershed beach ridges (Fig. 6).

3.4 Terrain Simulation of Tidal Basin

ANUDEM (thin-plate spline interpolation) is a long-term research result of professor Hutchinson State University of Australia. Its main characteristic is to maximize the retention important hydrological geomorphologic features especially erosion. Undoubtedly, tidal basin can be regarded as basic landform unit which is eroded by tidal creek. Therefore, ANUDEM is suitable for terrain simulation of tidal flat. In this paper, we set 3D information of watershed beach ridges and tidal creek centerlines as input, set the boundary of tidal basin, and then calculated the terrain elevation of the whole tidal basin using ANUDEM method. Model parameter: the maximum number of iterations: 50; the roughness factor: 0.5; grid size: 5 m× 5 m. Result maps are shown below (Fig. 7).

3.5 Error Analysis

The error distribution map (Fig. 8) (cell size: 5 m × 5 m) and the error statistical map (Fig. 9) were obtained by subtracting the result digital elevation and the measured LIDAR data. Root mean square error was 0.152. It can be seen from the figure that errors are overall small, 97 % of the errors were between ± 0.4 m. But the errors distributed around tidal creeks were bigger than other area. It also proved that the area around the tidal creek were terrain instability zone.

4 Conclusions and Feature Work

In this paper, Point–Line–Polygon–Body (2D–3D) transformation was implemented. Three-dimensional tidal basin terrain was simulated based on inflection points and

class	error range	pixel number	percentage
1	-1.1 ~ -0.5	1445	1.02
2	-0.5 ~ -0.4	2300	1.63
3	-0.4 ~ -0.3	4709	3.33
4	-0.3 ~ -0.2	9231	6.54
5	-0.2 ~ -0.1	25907	18.34
6	-0.1 ~ 0	54722	38.74
7	0 ~ 0.1	31871	22.57
8	0.1 ~ 0.2	8206	5.81
9	0.2 ~ 0.3	1859	1.32
10	0.3 ~ 0.4	668	0.47
11	0.4 ~ 0.5	236	0.17
12	0.5 ~ 0.9	86	0.06
	total	141240	100

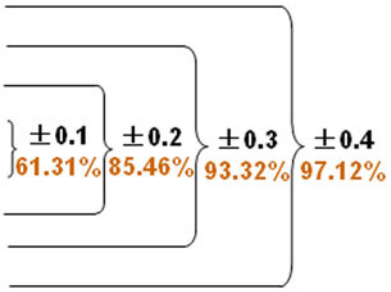

Fig. 9 Error statistical map

landform feature lines (2D). The simulation method was simple and efficient, and also the simulation result is credible. The simulation model can be extended to other tidal-type coast. Well, tidal basin is only a small landform unit of tidal flat. Another question is how to join the huge number of tidal basins and obtain the terrain of the whole tidal flat. According to the question, the terrain mosaicing technology between adjacent tidal basins will be studied in the future.

References

Ding, X., & Kang, Y. (2011). Tidal flat evolution analysis using remote sensing on tiaozini flat of the radial sand ridges. *Journal of Hohai University (Natural Science), 39*(2), 231–236.

Ding, X., & Zhu, D. (1984). *Characteristics of tidal flows and development of geomorphology in tidal flat creeks, Southern coast of Jiangsu Province. Seminar collection of hydrology and coastal engineering* (pp. 135–143). Beijing: China Ocean Press.

Kang, Y. (2011). Terrain modeling of tidal creek based on GIS&RS. In *3rd International Conference on Information Science and Engineering (ICISE2011)* Yangzhou, China. (pp. 2124–2128).

Mgengel, V., & Spitzer, R. J. (1991). Application of remote sensing data to mapping of shallow sea-floor near by Netherlands. *International Journal of Remote Sensing, 7*, 473–479.

Polcyn, F. C., & Lyzenga, D. R. (1973). Calculations of water depth from ERTS-MSS Data. *Symposium of significant results from ERTS-1*. NASA Spec, Publ-SP-327. (pp 1433–1436).

Spitzer, D., & Dirks, R. W. J. (1987). Bottom influence on the reflectance of the sea. *International Journal of Remote Sensing, 8*, 279–290.

Wei, J. (1992). Satellite remote bathymetry: a new mechanism for modeling. *Photogrammetric Engineering & Remote Sensing, 58*(5), 545–549.

Test and Control Methods for On-Site Compaction of Fine Sand Subgrade on Coastal Regions

J. S. Qian, H. L. Wang, and P. Wang

Abstract

This paper presents convenient methods and control index of on-site quality testing methods for compactness, aiming at the compaction quality problems of subgrade filled with fine sand from coastal regions in practical engineering. The analysis is based on the field test in Chonqi Channel project by means of sand replacement method, cutting ring method, PFWD method and bearing plate method. The research shows: (1) cutting ring method and sand replacement method, as the common compaction test methods in field, the former is easy and convenient while the latter tedious relatively. (2) PFWD is used to test the resilient of the subgrade, and easy to operate. The test data is discrete when PFWD is directly used in fine sand subgrade, while stable when top sealing layer paved. (3) Bearing plate is used to test the static resilient modulus of the subgrade, and the test result shows that the modulus of the cement and lime soil subgrade follow the standard. However, the application of bearing plate is complex.

Keywords

Subgrade engineering • Sand subgrade • Compaction degree • Resilient modulus • Test method

1 Introduction

Fine sand has already been used in high-grade road engineering in China, the Chongqi channel for instance (Xia & Huang 2009; Zhang et al. 2008). The reserve is rich of fine sand at the mouth of the Changjiang River (Yang 1994). It has positive effect on the saving of the soil resources on coastal regions (Zhang 2002).

The engineering experiences on fine sand subgradeis not mature at home and abroad (Bastian & Alleman 1998; Yoon et al. 2006). There are no related contents about compaction characteristics inspection and control method for on-site compactness in specifications. The existing research is not detailed and systemic. Compared to common subgrade, fine sand subgrade has low viscosity and easily become loose, which brings some problems on compactness inspection and control during instruction.

The group of the Changjiang River sand is mainly fine sand, in other words, the particle, whose size is larger than 0.075 mm, and represents more than 75 % of the total mass; In addition, the fine sand group is made up of silt and clay, whose content is <20 %. The single size and bad gradation go against on-site compactness. Therefore, it is necessary to perform thorough research on inspection and control method for on-site compactness quality of fine sand subgrade (Xia & Huang 2009; Zhang et al. 2008).

The paper is related to the project Chongqi Channel, in order to solve the problems in the practice engineering. According to the construction conditions, four field testing methods were taken, including: sand replacement method, cutting ring method, portable falling weight deflectometer (PFWD) and bearing plate method, thus applicability and

J. S. Qian · H. L. Wang (✉) · P. Wang
Key Laboratory of Road and Traffic Engineering of Ministry of Education, Tongji University, Shanghai 201804, China
e-mail: whltongji@163.com

Y. Huang et al. (eds.), *New Frontiers in Engineering Geology and the Environment*,
DOI: 10.1007/978-3-642-31671-5_11,

Table 1 Test methods

Test items	Detection method
Compaction degree	Cutting ring
	Sand replacement
Resilient modulus	PFWD
	Bearing plate

correlation of four methods emphatically analyzed, finally convenient and rapid inspection and control method for on-site compactness quality proposed.

2 Testing Methods of Compaction

The inspection is very important to construction and long-term performance of subgrade (Yuan & Wang 2007). Compaction degree and resilient modulus used as inspection index, following four field test methods are introduced.

(1) Cutting ring method: according to "Test Methods of Soils for Highway Engineering (JTG E40-2007)", cutting ring method is used to detect the compactness of the fine soil which does not contain gravel. Because of being simple and rapid, this method is widely adopted in the interior and outdoor inspection (Ministry of Communications of the People's Republic of China 2004, 2007).

(2) Sand replacement method: this method is used for inspection compactness of the fine soil, sand and gravel in the field test. In general case the maximum paticle-size is <15 mm, and the depth is 150–200 mm (Ministry of Communications of the People's Republic of China 2004, 2007).

(3) PFWD method: PFWD is widely used to test strength of the pavement and subgrade instruction, without any damage. Compared with other methods, PFWD is more safe and reliable, with high precision, portable, easy to operate, and can simulate the vehicle load.

(4) Bearing plate method: with this method resilient deformation of each stage load can be tested on the surface of the subgrade, then resilient modulus is obtained through conversion (Ministry of Communications of the People's Republic of China 2007). (Table 1).

3 Test Results and Analysis

3.1 Cutting Ring Method

A section, whose degree supposed to be 96.0 %, was chosen to carry out the compaction test. Test data showed that the dry density of the soil was between 1.52 and 1.54 g/cm^3. The maximum dry density was 1.59 g/cm^3,which was from the indoor experiment. The degree of the compaction was obtained. Figure 1 showed that the average of the degree was about 95.8 %; this is in consistent with the standard of the subgrade construction.

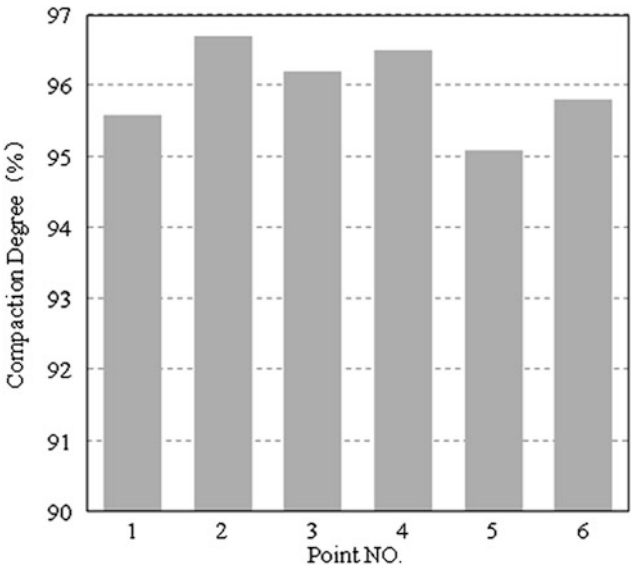

Fig. 1 Compaction degree

3.2 Sand Replacement Method

A section whose degree supposed to be 96.0 % was chosen to test compaction with sand replacement method. As shown in Table 2, the dry density of two kinds soil from site measurement was 1.52 and 1.51 g/cm^3. The maximum dry density was 1.59 g/cm^3, which was from the indoor experiment. The degree of the compaction was 95.6 and 95.0 %. It showed that the two test results were basically agree with the design values.

3.3 PFWD Method

Two subgrade sections (fine sand subgrade and fine sand subgrade with top-sealing layer) were chosen to test resilient modulus with PFWD. As shown in Fig. 2, 10 test points, where the surface was flat and easy to work, were chosen in each section. As for PFWD, the diameter of the bearing plate was 30 m, and the falling height was 85 cm.

3.3.1 Measurements at the Top of Sand Subgrade

As shown in Fig. 3, the resilient modulus of fine sand and cement subgrade was unstable, which means PFWD was not proper when directly used in sand subgrade.

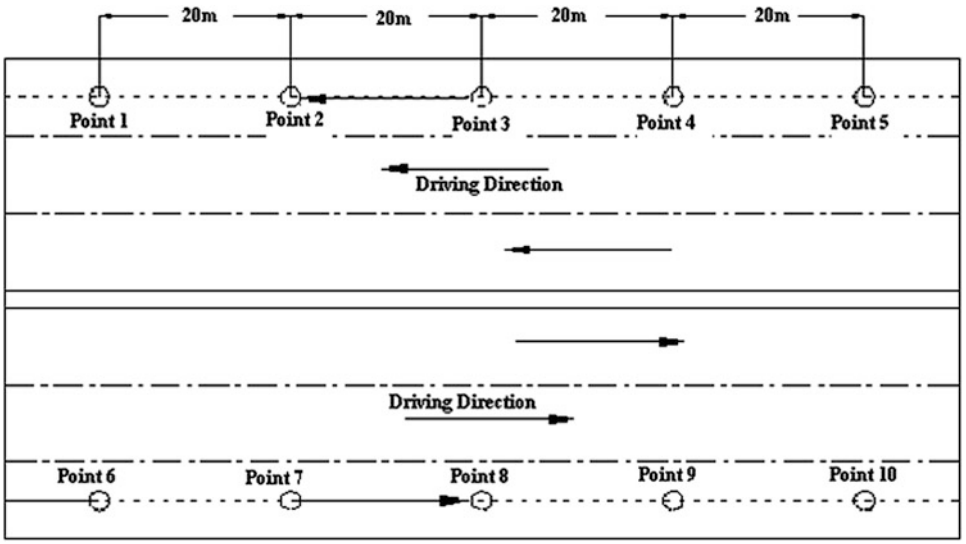

Fig. 2 Testing points in fields

Table 2 Degree of compaction

NO.	Standard sand density (g/cm^3)	Standard sand mass (g)	Fine sand mass (g)	Fine sand dry mass (g)	Wet density (g/cm^3)	Dry density (g/cm^3)	Compaction degree (%)
1	1.48	3008.9	3258.8	3088.5	1.60	1.52	95.6
2	1.48	3150.8	3554.7	3212.2	1.67	1.51	95.0

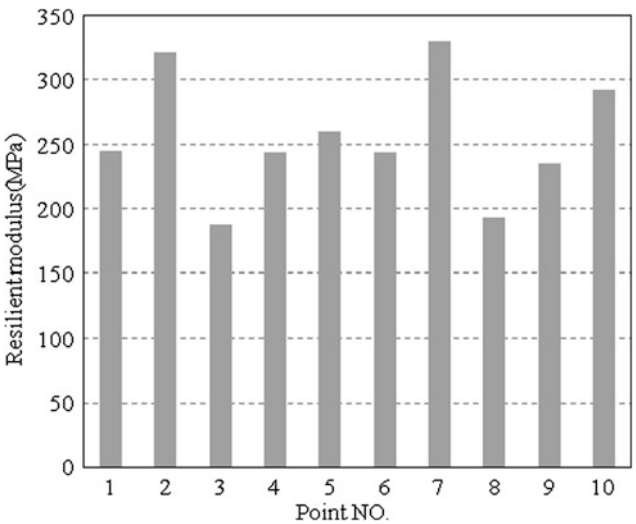

Fig. 3 Fine sand subgrade resilient modulus

3.3.2 Measurements at the Top Sealing Layer

Five percent lime was mixed into the sand of the top sealing layer. The first layer was paved on May 15th, and the second on 17th, then cement stabilized base was paved after the maintenance by 22th. From 16th to 22nd the resilient modulus was tested with PFWD every day except 17th.

Table 3 Resilient modulus of the top sealing layer (MPa)

No.	1	2	3	4	5	6	7	8	9	10
May 16th	92	209	108	100	96	117	202	165	200	203
May 18th	165	162	190	194	173	152	157	100	148	162
May 19th	127	174	197	144	165	154	153	131	143	182
May 20th	179	143	134	228	141	147	208	141	162	164
May 21th	207	187	156	168	169	134	158	197	114	162
May 22th	154	224	176	225	122	154	168	174	172	189

Various factors may influence the test results. However, as shown in Table 3, the average data of each point had a tendency to increase, and changed in a range between 150 and 200 MPa. This showed that the test result accorded with standard and the PFWD was reasonable in this case.

3.4 Bearing Plate Method

Two sections were chosen to test the static resilient modulus: cement and lime soil subgrade. The resilient modulus

of the cement soil subgrade was 82.6 MPa, and the lime 110.0 MPa. This indicated that the test result in this method was reliable.

4 Conclusions

The main conclusions in this paper are as follows.

(1) Cutting ring and Sand replacement methods are most commonly used in testing compaction degree of the subgrade. The former is easy to operate and convenient. The test result through this method is stable and reliable. Meanwhile, the test data of the latter is also reasonable. Comparatively, sand replacement is complex, thus bringing unfavorable effect on test result.

(2) PFWD is used to test the resilient of the subgrade, and easy to operate. The test data is discrete when PFWD is directly used in fine sand subgrade, while stable when top sealing layer paved.

(3) Bearing plate is used to test the static resilient modulus of the subgrade. The test result shows that the modulus of the cement and lime soil subgrade follow the standard. However, the application of bearing plate is complex.

References

Bastian, K. C., & Alleman, J. E. (1998). Microtox (TM) characterization of foundry sand residuals. *Waste Management, 18*(4), 227–234.

Ministry of Communications of the People's Republic of China. (2004). *Specification for design of highway subgrades*. Beijing: China Communication Press.

Ministry of Communications of the People's Republic of China. (2007). Test methods of soils for highway engineering. Beijing: China Communication Press.

Xia, N., & Huang, Q. (2009). The Experimental research of the capillarity water rising height of Changjiang delta fine sand. *Fly Ash Comprehensive Utilization, 6*, 3–5.

Yang, S. (1994). Statistic features for grain-size parameters of the Yangtze river estuary and their hydrodynamic explanation. *Journal of Sediment Research, 3*, 23–31.

Yoon, S., Prezzi, M., & Siddiki, N. Z. (2006). Construction of a test embankment using a sand-tire shred mixture as fill material. *Waste Management, 26*(9), 1033–1044.

Yuan, Y., & Wang, X. (2007). Experimental research on compaction characteristics of aeolian sand. *Chinese Journal of Geotechnical Engineering, 29*(3), 360–365.

Zhang, D. (2002). Application of fine sand at mouth of the Changjiang River in high grade road engineering. *Urban Roads Bridges & Flood Control, 4*, 33–37.

Zhang, H., Ling, J., & Jiang, X. (2008). Experimental investigations of highway performance of fine sand of the long river estuary. *Highway Engineering, 33*(3), 142–146.

Strength and Permeability of Biostabilized Sand

E. Yee, J. H. Lee, Y. S. Kim, S. R. Chung, H. Y. Kim, and B. S. Chun

Abstract
Shallow backshore sands in the coastal zone are continually left in a relatively loose state due to coastal processes and human behavior. Because of this, backshore construction usually involves some form of soil improvement or alternative foundation design. To address these issues, an investigation into the application of an eco-friendly organic acid for soil improvement is conducted. Test results show the organic acid focuses on the proliferation of local microbes to cement and restructure the sand matrix, thus making the application a more sustainable option. Unconfined compression, California bearing ratio, and permeability tests were performed to assess the degree to which the sample sand was improved. After 96 days, results showed compressive strength to increase by at least 60 % and a decrease in permeability of at least 49 %. California bearing ratios increased modestly. The results are promising and shed some light into the application of an organic acid for soil improvement.

Keywords
Backshore • Sand • Soil improvement • Foundations • Microbes

1 Introduction

The coastal areas of many countries are typically densely populated with permanent and recreational residents. Living or visiting coastal areas continues to grow and developments to service and manage so many visitors face many challenges (Crossett et al. 2004). One such challenge is the development of onshore infrastructure, more specifically the construction of structures or pipelines in sandy backshore regions.

Sandy coastal systems in well developed areas typically house loose sands at shallow depths. This is primarily due to Aeolian processes and human recreational behavior. These loose sands show good permeability but are prone to erosion and are not ideal for certain structural foundations. As an example, the first author was on a project where helical piles were used for the beach foundation as other foundation types were not suitable. Typically, such soils are stabilized to improve their engineering properties for construction.

This investigation explores the use of an alternative biological soil stabilization technique. This technique uses an organic acid to stimulate general microbe growth and encourage biological cementation. The effects of the organically induced cementation are identified through unconfined compression, California bearing ratio, and permeability tests.

E. Yee (✉) · J. H. Lee · S. R. Chung · B. S. Chun
Department of Civil end Environmental Engineering,
HanYang University, 17 Haengdang-dong, Seongdong-gu,
Seoul 133-791, South Korea
e-mail: mailericyee@gmail.com

Y. S. Kim
P.I.A. Co., Ltd, Seoul, 461-360, South Korea

H. Y. Kim
Construction Industry Research Institute,
Seoul, 121-841, South Korea

Y. Huang et al. (eds.), *New Frontiers in Engineering Geology and the Environment*,
DOI: 10.1007/978-3-642-31671-5_12,

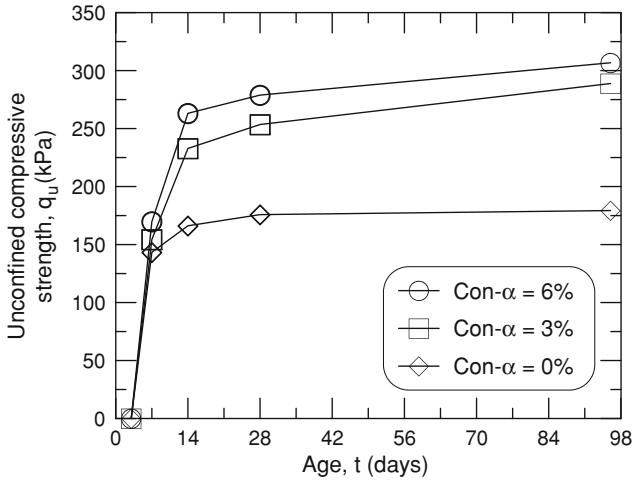

Fig. 1 Unconfined compressive strength of sand samples mixed with Con-α

2 Soil Stabilization

Two methods are commonly used for soil stabilization: mechanical or chemical. Mechanical soil stabilization techniques generally involve some sort of compaction or reinforcement. There are a variety of approaches to soil compaction, some of which include compaction rollers, vibroflotation, dynamic compaction, blasting and compaction grouting (e.g. Narsilio et al. 2009; Rollins and Kim 2010; El-Kelesh et al. 2012).

On the other hand, chemical stabilization techniques typically involve adding or mixing chemicals or additives, such as cementitious materials, into the soil. Some of these cementitious materials include cement, lime, fly ash, coal ash, silica fume, and even rice husks, with a wealth of research on their use and performance (e.g. Akbulut and Saglamer 2003; Lin et al. 2007). Although chemical stabilization techniques are great for increasing soil strength, there is some concern over the toxicity and sustainability of the more commonly used cementitious materials (Mohanty and Chugh 2006; Dombrowski et al. 2010).

In addressing these concerns, a recent alternative method in soil stabilization is the use of microorganisms to biologically treat soils. DeJong et al. (2006) and Dove et al. (2011) showed microbially induced calcite precipitation (MICP) to produce substantial increases in strength, while Van Paassen et al. (2010) applied a similar MICP approach to develop a bio-grout.

3 Organic Acid

An organic acid material produced by Osaki Corporation was considered for this study. This material, Con-α, is a mixture of different types of organic acids and plant extracts in powder form.

According to Osaki Corporation (2011), when Con-α is mixed with water and soil, inherent microbes such as aerobic and anaerobic bacteria will be able to proliferate due to the availability of a new energy source. The increase in the number of microbes follows with an increase in microbe-related by-products, one of which is believed to be microbially induced cementation. Instead of focusing on specific types of microbes (i.e. DeJong et al. 2006), the use of Con-α allows a variety of microbes to grow.

4 Materials and Preparation

A granitic clean sand from the southern part of the Korean peninsula was used to conduct our testing. The coefficient of uniformity, $C_u = 7.8$ and the coefficient of curvature, $C_c = 1.1$. This soil was classified as a well-graded sand, SW, according to USCS.

To prepare specimens for testing, the powder form of Con-α was simply spread over the sand in a pan and mixed with water until it appeared visually well distributed. Batches of 3 and 6 % of Con-α, by total weight, with a water content of 10 % were used. Mixing took a few hours and the pan was allowed to rest outdoors a few hours before samples were taken for biological and image analyses. While curing, 500 ml of water was supplied to the batch.

The mixed sand was also placed in three different test molds. One mold was 200 mm in height and 100 mm in diameter. These samples were compacted in accordance with ASTM D1557, using a 2.5 kg hammer in 10 layers and 36–37 blows per layer giving an estimated compaction energy of 2,700 kN-m/m^3. These samples were used for unconfined compression strength (UCS) testing in accordance with and ASTM D2166. Another mold measuring 150 mm in diameter and 170 mm in height was used to estimate the California Bearing Ratio (CBR) using the method outlined in ASTM D1883. The other mold was for triaxial permeability testing and measured 100 mm in height and 50 mm in diameter in accordance with ASTM D5084.

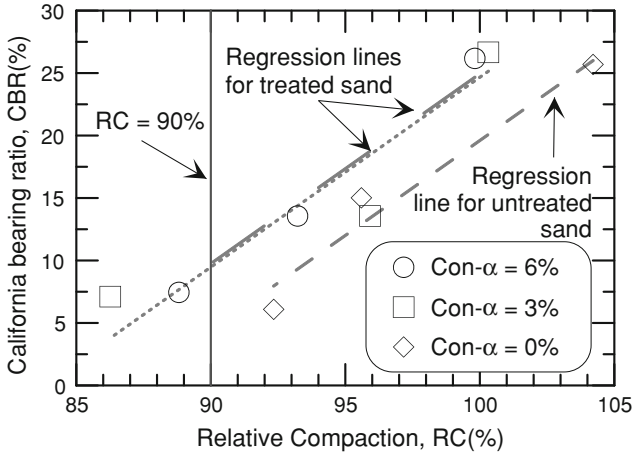

Fig. 2 CBR of sand samples mixed with Con-α

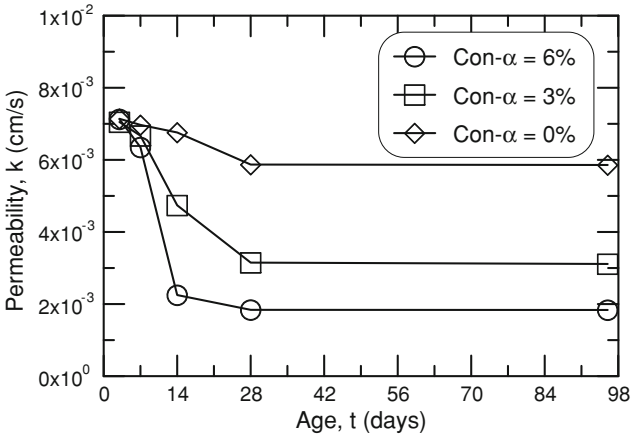

Fig. 3 Permeability of sand samples mixed with Con-α

5 Results

5.1 Unconfined Compressive Strength

Specimens aged 3, 7, 14, 28, and 96 days were tested for unconfined compressive strength, q_u. Three specimens from each age duration were tested and the average for each duration is plotted in Fig. 1.

Figure 1 shows an obvious improvement in unconfined compressive strength when Con-α is added and marginal increases in strength when Con-α concentration is increased. After 96 days, the untreated granitic sand had a $q_u = 179$ kPa, while 3 and 6 % Con-α concentrations yielded $q_u = 289$ and 307 kPa respectively, which is a 61 and 72 % increase in unconfined compressive strength respectively. Figure 1 also shows this strength increase to be gradual, with a majority of the strength attained after 28 day. We surmise this gradual strength increase is due to the process of cementation and perhaps a decrease in microbial activity because of less Con-α.

Additionally, all sand specimens aged 3 days were unable to develop the cohesion needed to stand unconfined and thus were unable to be tested.

5.2 California Bearing Ratio

CBR tests are conducted to estimate the bearing capacity and mechanical strength of subgrade soil for pavement design. Tests were performed on samples aged 28 days and their results are presented in Fig. 2. Figure 2 shows CBR = 4 for the untreated sand at a relative compaction, RC = 90 %. When treated with Con-α, the CBR modestly increases to about 10.

5.3 Permeability

Triaxial permeability tests were also conducted on specimens aged 3, 7, 14, 28, and 96 days, with the results shown in Fig. 3. Results also indicate permeability to stabilize after about 28 days. Figure 3 indicates the non-treated sand to have a coefficient of permeability, $k = 6 \times 10^{-3}$ cm/s after 96 days while the 3 and 6 % Con-α concentrations yielded $k = 3 \times 10^{-3}$ and 2×10^{-3} c,/s respectively, which is a 49 and 69 % decrease respectively.

6 Conclusions

The backshore region in many sandy coastal areas remains undeveloped. Natural coastal processes and human recreational behavior render the sand unsuitable for supporting a foundation. Tests were conducted to evaluate the engineering effects of using Con-α as a biological soil stabilization technique. Results showed unconfined compression to increase 61–72 %, CBR to increase from 4 to 10, and permeability to decrease 49–69 % for the concentration levels tested.

Acknowledgments Special thanks is given to Osaki Corp. for their support with the Con-α product.

References

Akbulut1 S., Saglamer A. (2003) Evaluation of fly ash and clay in soil grouting. *Proceedings of 3rd International specialty conference on grouting and ground treatment (GSP 120), ASCE* (pp 1192–1199). Louisiana: New Orleans.

Crossett, K. M., Culliton, T. J., Wiley, P. C., & Goodspeed, T. R. (2004). *Population trends along the coastal United States: 1980–2008*. Washington, DC: NOAA.

DeJong, J. T., Fritzges, M. B., Nüsslein, K. (2006) Microbial induced cementation to control sand response to undrained shear. *Journal of Geotechnical and Geoenvironmental Engineering, ASCE*, *132*(11), 1381–1392.

Dombrowski, F. J., Ramme, B. W., Okwadha, G. D. O., Kollakowsky, D. (2010) Evaluation of surface water runoff from fly ash–stabilized and nonstabilized soil surfaces. *Journal of Environmental Engineerng*, ASCE, *136*(9), 939–951.

Dove, J. E., Shillaber, C. M., Becker, T. S., Wallace, A. F., Dove, P. M. (2010) Biologically inspired silicification process for improving mechanical properties of sand. *Journal of Geotechnical and Geoenvironmental Engineering,* ASCE, *137*(10), 949–957.

El-Kelesh, A. M., Matsui, T., Tokida, K. (2012) Field investigation into effectiveness of compaction grouting. *Journal of Geotechnical and Geoenvironmental Engineering , ASCE.*

Lin, D. F., Lin, K. L., Hung, M. J., & Luo, H. L. (2007). Sludge ash/hydrated lime on the geotechnical properties of soft soil. *Journal of Hazardous Materials, 145*(1–2), 58–64.

Mohanty, S., & Chugh, Y. (2006). Postconstruction environmental monitoring of a fly ash-based road subbase. *Practice Periodical on Structural Design and Construction, ASCE, 11*(4), 238–246.

Narsilio, G. A., Santamarina, J. C., Hebeler, T., Bachus, R. (2009) Blast densification: multi-instrumented case history. *Journal of Geotechnical and Geoenvironmental Enginering, ASCE*, *135*(6), 723-734.

Osaki Corporation (2011) Construction manual for con-α (translated from Japanese). Osaki Corporation. http://www.osaki-c.co.jp. Accessed 1 February 2011.

Rollins, K. M., Kim, J. (2010) Dynamic compaction of collapsible soils based on u.s. case histories. *Journal of Geotechnical and Geoenvironmental Engineering, ASCE*, *136*(9), 1178–1186.

Van Paassen, L. A., Ghose, R., van der Linden, T. J. M., van der Star, W. R. L., van Loosdrecht, M. C. M. (2010) Quantifying biomediated groundiImprovement by ureolysis: large-scale biogrout experiment *Journal of Geotechnical and Geoenvironmental Engineering , ASCE*, *136*(12), 1721–1728.

Numerical Study on the Full-Range Consolidation Characteristics of a New Dredger Fill Foundation

F. F. Ren, Q. Xu, C. Xu, X. H. Xu, and H. Z. Wang

Abstract

Basing on the foundation treatment project of the beach area of Baosteel and considering the effect of dredger fill and miscellaneous fill on the consolidation behavior, the whole consolidation process of the foundation was studied with Plaxis program, and the results were validated by the monitor data. It is concluded that the excess pore pressure (EPP) of the underlying soft soil has not been dissipated completely before the foundation treatment, so the negative EPP value is caused in the following monitoring. Early settlement is mainly composed of the transient settlement due to the poor permeability of the foundation. In addition, early settlement is mainly consisted of the upper dredger fill, and there is an apparent deformation in the underlying stratum after inserting PVDs and preloading. The results are significant not only for understanding the consolidation history of new dredger fill foundation, but also for post-processing and monitoring work.

Keywords

Dredger fill • Preloading • Soft soil • Consolidation characteristics

1 Introduction

Differential settlement and low bearing capacity are usually caused during the period of building construction and operation by the characteristics of the soft soil, such as high void ratio, high water content, high compressibility, low strength and poor permeability. The prefabricated vertical drain (PVD) with preloading method is one of the most effective ways to deal with the soft clay foundation.

Many studies have been conducted to simulate the drainage performance of PVD, mainly through three methods of the equivalent permeability method (Chai et al. 2001), the equivalent sand wall method (Kim and Lee 1997; Zhao et al. 1998) and the PVD element method (Chai and Miura 1999; Yu and Li 2010). However, most of these studies are focused on normally consolidated soil under simple loading conditions other than the under-consolidated soil under complicated loading condition, especially for the large thickness under-consolidated soil, its behavior is much more complicated than the normal soil. This study will carry out a numerical study on a large thickness under-consolidated soil foundation, which is from a practical engineering of new dredger fill foundation in Baosteel Company.

F. F. Ren (✉) · C. Xu
Key Laboratory of Geotechnical Engineering, Tongji University, Shanghai 200092, China
e-mail: feifan_ren@tongji.edu.cn

F. F. Ren · C. Xu
Department of Geotechnical Engineering, Tongji University, Shanghai 200092, China

F. F. Ren · Q. Xu
State Key Laboratory of Geohazard Prevention and Geoenvironment Protection, Chengdu University of Technology, Chengdu 610059, China

X. H. Xu · H. Z. Wang
Baoshan Iron and Steel Co., Ltd, Shanghai 201900, China

Y. Huang et al. (eds.), *New Frontiers in Engineering Geology and the Environment*,
DOI: 10.1007/978-3-642-31671-5_13,

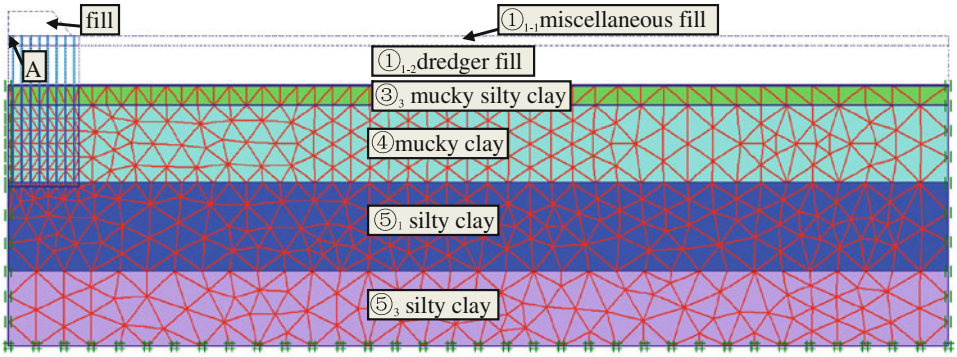

Fig. 1 Finite element model

Table 1 Physical and mechanical parameters of all soil stratums

Stratum	Depth	Density	Cohesion	Frictional angle	Elasticity modulus	Poisson's ratio	E_{50}^{ref}	E_{oed}^{ref}	E_{ur}^{ref}	Compressive modulus
	m	kN/m^3	kPa	°	kPa		kPa			MPa
Fill	–	19.0	5	25.0	12,000	0.27	–	–	–	–
①$_{1-1}$	1.5	17.2	10	10.0	4,193	0.30	–	–	–	–
①$_{1-2}$	7.9	18.8	4	29.5	4,193	0.30	–	–	–	15.45
③$_3$	11.0	17.4	9	31.0	–	–	2454	1963	18070	3.53
④	23.3	16.6	11	25.0	–	–	1881	1505	12040	2.69
⑤$_1$	37.3	17.8	21	19.5	–	–	2506	2005	20210	4.72
⑤$_3$	49.3	18.0	19	20.5	–	–	2697	2157	19090	5.56

2 Engineering and Geological Survey

Weiqi Road, which is distributed along the north Baosteel beach, is taken as an example. To meet the requirements of settlement and bearing capacity of building roads, the foundation was treated by the surcharge preloading method, with PVD 24 m length, spacing of 1.4 m and square layout. Soil layers are shown from top to bottom as follows: (1) miscellaneous fill (①$_{1-1}$); (2) dredger fill (①$_{1-2}$), with loose structure, and low strength; (3) mucky silty clay (③$_3$) and mucky clay (④), the two layers, with high water content, high compressibility and low strength, are the typical saturated soft soil in Shanghai. The underlying strata of silty clay (⑤$_1$, ⑤$_3$) have good mechanical properties.

3 Numerical Model

3.1 Establishment of Model

A symmetrical model is used to analyze the consolidation characteristics of Weiqi Road. Considering soil conditions and boundary effect, the model is 150 m in width, 49.3 m in depth, and the height of the preloading fill is 4 m. 15-node coupled plane strain elements are applied to model the soil units (Fig. 1). Bottom boundary conditions is taken as the horizontal and vertical displacement constraints, left boundary is the symmetrical horizontal displacement constraint, and the right is the horizontal displacement constraint, the top is free displacement boundary and free drainage boundary. In the numerical model, taking into account the physical and mechanical properties of the soil layers, the layers of ①$_{1-1}$, ①$_{1-2}$ and fill use Mohr–Coulomb model, ③$_3$, ④, ⑤$_1$ and ⑤$_3$ use the hardening soil model, the material parameters of the soil layers are shown in Table 1.

3.2 Simplified Method for PVD

The equivalent sand wall method is used to deal with PVD drainage in this paper, the bi-directional flow isostrain consolidation theory and Barron's axisymmetric consolidation theoretical solution were compared to derive equivalent equations between the plane strain state and axisymmetric state under the conditions of the constant average degree of consolidation or the constant average pore pressure in the same depth.

Table 2 Permeability coefficient and its equivalent value of all soil stratums

Stratum	Permeability coefficient (m/d)		Equivalent permeability coefficient (m/d)	
	k_{za}	k_{ra}	k_{zp}	k_{xp}
①$_{1-1}$	2.59E-01	2.59E-01	2.25E-01	1.49E-02
①$_{1-2}$	4.36E-01	5.32E-01	3.78E-01	3.07E-02
③$_3$	1.55E-03	3.13E-03	1.34E-03	1.80E-04
④	1.55E-04	2.31E-04	1.34E-04	1.33E-05
⑤$_1$	1.85E-03	4.08E-04	1.60E-03	2.35E-05
⑤$_3$	2.05E-03	5.10E-04	–	–

$$\begin{aligned} k_{xp} &= D_x k_{ra} \quad (\texttt{Horizontal}) \\ kx_{zp} &= D_z k_{za} \quad (\texttt{Vertical}) \end{aligned} \tag{1}$$

where k_{xp}, k_{zp} are the equivalent horizontal and vertical permeability coefficients of sand wall respectively, k_{ra},k_{za} are the horizontal and vertical permeability coefficients of the foundation soil respectively, D_x, D_z are the horizontal and vertical adjustment factors respectively, which can be expressed as:

$$\begin{aligned} D_x &= \frac{4\left(n_p - s_p\right)^2 (1+v) L^2}{9n_p^2 \mu_a - 12\beta L^2 \left(n_p - s_p\right)\left(s_p - 1\right)(1+v)} \\ D_z &= \frac{2(1+v)}{3} \end{aligned} \tag{2}$$

where L is the magnification coefficient of sand well spacing, $L = B/r_e$ (B is 1/2 sand well spacing, r_e is the effective drainage radius of sand well), $n_p = B/r_{wp}$ (r_{wp} is 1/2 sand well thickness), $s_p = r_{sp}/r_{wp}$ (r_{sp} is the distance from outer edge of the smear zone to the sand well center), $\beta = k_{ra}/k_{sp}$ (k_{sp} is the permeability coefficient of the smear zone), $\mu_a = \frac{n^2}{n^2-s^2}\ln\frac{n}{s} - \frac{3n^2-s^2}{4n^2} + \frac{k_{ra}}{k_{sp}}\frac{n^2-s^2}{n^2}\ln s$, n is the well diameter ratio, i.e. $n = r_e/r_{wa}$ (r_{wa} is the radius of sand well), $s = r_s/r_{wa}$ (r_s is the smear radius of sand well), v is Poisson's ratio.

In this paper, the spacing of sand wells is 1.4 m ($B = 0.7$ m), $v = 0.3$, $s = 3$, $s_p = 3$, $\beta = 5$, $r_{wa} = 0.012$ m, $r_e = 1.128B$, from Eq. (2), we can get that $D_x = 0.058$,$D_z = 0.867$. Therefore, equivalent permeability coefficients of all strata can be obtained from Eq. (1) (Table 2).

3.3 Calculation Process

The simulation processes are in full accordance with the actual construction stages, and take full account of the various processes' effect on foundation consolidation characteristics. According to the above construction process, the calculation processes are as follows. Process 1: geostatic stress balance, Process 2: dredger fill (①$_{1-2}$) is filled for 183 days, and the groundwater table rises to the top of ①$_{1-2}$, Process 3: miscellaneous soil is filled for 61 days, and the groundwater table rises to the top of ①$_{1-1}$, Process 4: foundation soil consolidates for 550 days under the load of ①$_{1-1}$ and ①$_{1-2}$, Process 5: construction of PVD, reset the displacement to 0 for intuitively comparing the consolidation settlements of before and after inserting PVD, and then applying the 4 m height preloading, Process 6: ground consolidation of 180 days.

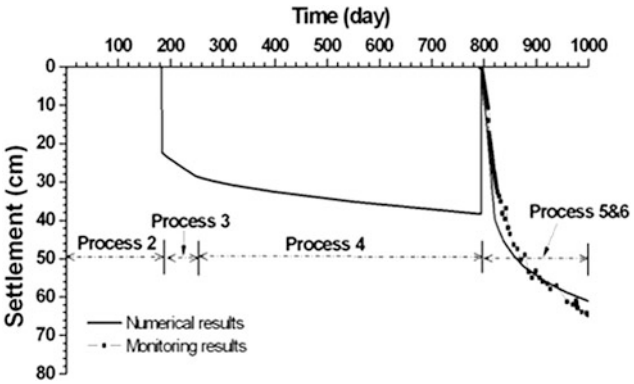

Fig. 2 Temporal changing curves of the surface settlement

4 Results and Discussion

4.1 Total Settlement

Figure 2 shows the settlement curve of point A (marked in Fig. 1) under various construction processes. The settlement is 0 during the period of process 2 due to the absence of point A. As of the process 3, there is a substantial instantaneous settlement of 22.4 cm, then with the self-weight consolidation of ①$_{1-1}$ and its effect on the underlying strata, the settlement increases at a small rate, and reaches 38.4 cm at the end of process 4. After entering the process 5, with the PVDs' insert, the drainage performance, especially the layers of ③$_3$ and ④, has been improved greatly. Under the preloading effect, the settlement rate increases significantly and stabilizes to 61.1 cm at the end of process 6. So the total settlement reaches 99.5 cm. To verify the reliability of

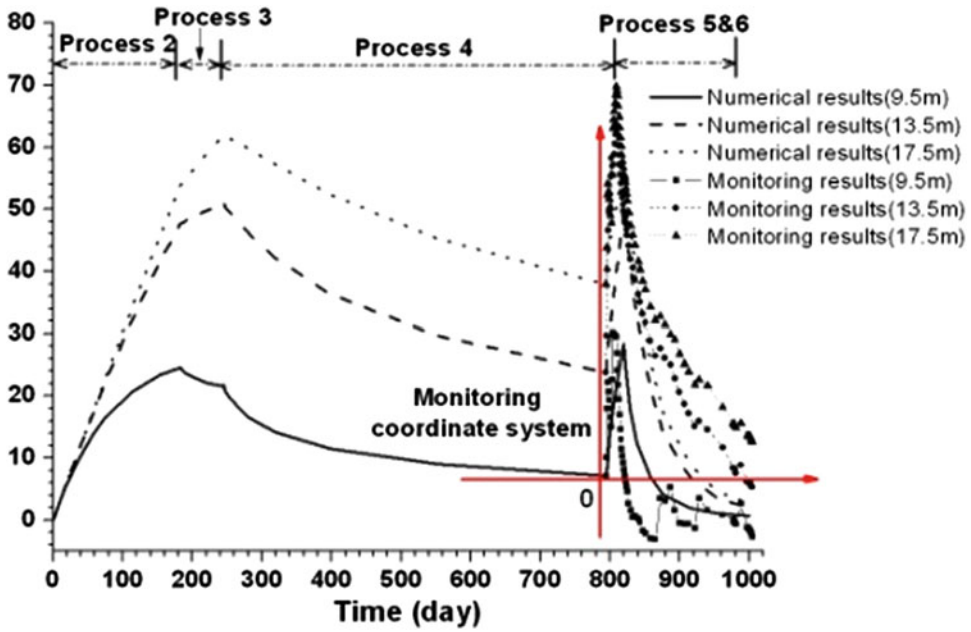

Fig. 3 Temporal changing curves of the EPP at different depths

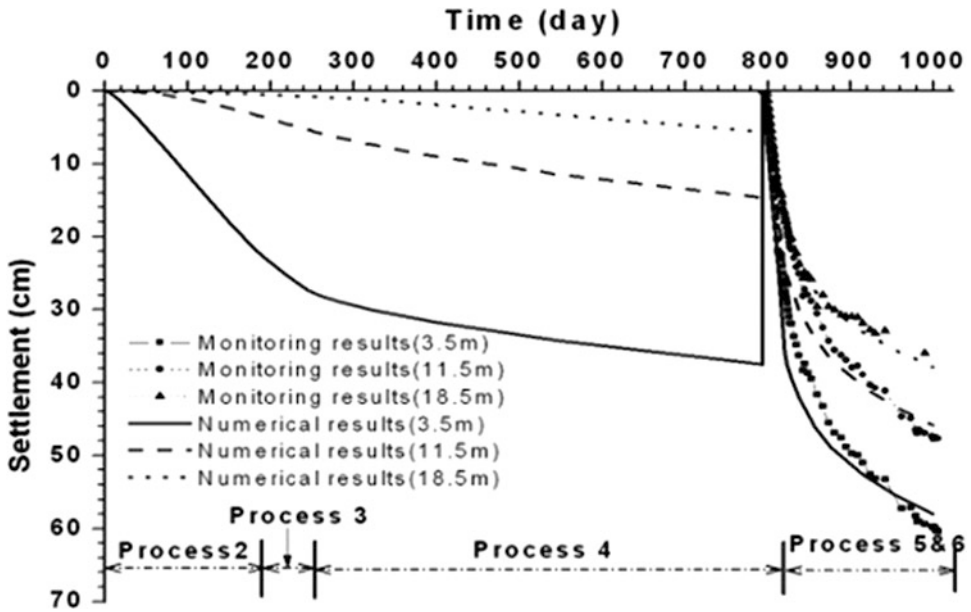

Fig. 4 Temporal changing curves of the settlement at different depths

numerical results, the results are compared with monitoring values and they are in good agreement (Fig. 2). It is concluded that the effect of the foundation treatment is very obvious.

4.2 Excess Pore Pressure

Figure 3 shows the excess pore pressure (EPP) curves at different depths during various processes. EPPs increase quickly during processes 2 and 3 because of poor foundation permeability, especially the strata of ③$_3$ and ④, then EPPs decrease slowly with the foundation's consolidation. Before the foundation treatment, the degrees of the consolidation (U) at the depth of 9.5 m, 13.5 m and 17.5 m are 71.3 %, 53.5 % and 38.9 % respectively. After the treatment, EPPs increase quickly first and then decreases rapidly due to the permeability improvement, finally the EPPs of various depths almost dissipate after 180 days. The numerical results are verified with monitoring results and

get a good agreement. In addition, the reason for negative EPP, which is usually met in the monitoring process of under-consolidated soil and cause the inconvenience of data processing, is figured out. Under the load of ①$_{1-2}$' ①$_{1-1}$, the EPPs does not dissipate completely, and the minimum degree of consolidation is 38.9 %, however, the starting pore press is artificially set to 0 in the monitoring (marked with monitoring coordinate system in Fig. 3), so the negative EPP is got at later consolidation stage, and it can be adjusted using the indoor consolidation test and consolidation theory.

4.3 Layered Settlement

Figure 4 shows settlement curves at different depths during various processes. There is a fast and large instantaneous settlement during processes 2 and 3. The settlements at the depth of 3.5, 11.5 and 18.5 m are 27.2 cm, 5.3 cm and 0.7 m, so the total settlement at that moment is mainly composed of the dredger fill's compression. Before the treatment, the average settlement in process 4 is only 8.2 cm in 550 days because of the poor permeability. After inserting PVD and preloading, the average settlement during the processes 5 and 6 reaches 47.3 cm quickly in 200 days, which is almost 6 times that before and mainly comes from underlying soft strata's compression. To certify the effect of the numerical model, monitoring data are used to compare with numerical results, and get a good agreement.

5 Conclusions

Taking the foundation improvement in Baosteel beach area as an example, and considering the effect of early dredger fill and miscellaneous soil, the consolidation characteristics of the under-consolidated soil foundation is systematically analyzed using Plaxis program, in which PVDs are simplified to the sand wall and hardening soil model is employed. The results of the total settlement, EPP and layered settlement are compared with the monitoring data and get a good agreement. The results are significant not only for understanding the consolidation history of new dredger fill foundation, but also for post-processing and monitoring work.

Acknowledgments This work was supported by the Opening fund of State Key Laboratory of Geohazard Prevention and Geoenvironment Protection, Chengdu University of Technology (SKLGP2012K017), the National Natural Science Foundation of China (41072200), Program for Young Excellent Talents in Tongji University (2010KJ046), and Kwang-Hua Fund for College of Civil Engineering, Tongji University.

References

Chai, J. C., Shen, S. L., Miura N. et al (2001) Simple method of modeling pvdimproved subsoil[J]. *Journal of Geotechnical and Geoenvironmental Engineering*, *127*(11), 965–972.

Kim, Y. T., & Lee, S. R. (1997). An equivalent model and back-analysis technique for modelling in situ consolidation behavior of drainage-installed soft deposits[J]. *Computers and Geotechnics, 20*(2), 125–142.

Zhao, W., Chen, Y., & Gong, Y. (1998). A methodology for modeling sand-drain ground in plain strain analysis[J]. *Shuili Xuebao, 1998*(6), 53–57. (In Chinese).

Chai, J. C., & Miura, N. (1999). Investigation of factors affecting vertical drain behavior[J]. *Journal of Geotechnical and Geoenvironmental Engineering, 125*(3), 216–226.

Yu, C., & Li, J. (2010). Fluid-solid coupling simulation of settlement process in soft ground based on drainage consolidation method with sand well. *Rock and Soil Mechanics, 31*(3), 939–943. (In Chinese).

Centrifuge Modeling of Embedment Effects on Eccentrically Loaded Shallow Foundation on Sand

M. Cocjin, T. Fujita, O. Kusakabe, and M. Kitazume

Abstract
Results of a series of centrifuge tests addressing the effect of embedment on the capacity of a shallow rectangular foundation on dense sand under eccentric vertical loads are reported. Vertical and overturning moment load capacities are assessed, where overall load capacity is expressed as a failure envelope in vertical and moment load space. Distribution of lateral earth pressure along the embedded depth of the footing is measured and resulting collapse mechanism for the soil is compared to a case involving surface loading. Results account for a general enhancement of footing capacity with increasing embedment, where observed enhancement is expressed as a function of embedment ratio.

Keywords
Centrifuge modeling • Shallow foundations • Embedment • Load eccentricity

1 Introduction

The use of footing embedment generally enhances the vertical load capacity (bearing capacity) of shallow foundations. This enhancement is accounted for by depth factors (Table 1) which scale the effect of initial embedment in the estimation of bearing capacity (Meyerhof 1963; Brinch Hansen 1970). For cohesionless soils, these factors depend on soil friction angle, ϕ_f and are typically increasing in influence with increasing embedment ratio, D/B, where D is depth of embedment and B is footing breadth. However, few documented experimental studies carried out on sand have directly assessed the effect of embedment other than those involved with purely vertical loading.

Studies involved with general loading of shallow foundations redefine and interpret the bearing capacity in terms of a failure envelope in vertical (V), horizontal (H) and moment (M/B) load space. Such an envelope, which marks the plastic collapse of a foundation, is presented within a strain-hardening, plasticity-based framework. By defining a force-resultant model that is said to be load-path independent (Ticof 1977), a unifying approach in understanding failure conditions of shallow foundations is made possible. A number of physical modeling studies observed under laboratory floor conditions (1 g) and which involved a variety of loading mechanisms have tackled bearing capacity problems within this framework, for example: Georgiadis and Butterfield (1988), Georgiadis (1993), Gottardi and Butterfield (1995) on eccentric and inclined loading; or Gottardi et al. (1999) and Byrne and Houlsby (1999) on direct swipe and probe test. From these studies, a failure envelope can be obtained for failure envelope can be obtained for any incurred plastic vertical footing penetration (Houlsby and Cassidy 2002; Cassidy et al. 2002), and can be expressed mathematically as:

M. Cocjin (✉) · T. Fujita · M. Kitazume
Department of Civil Engineering, Tokyo Institute of Technology, 2-12-1-M1-9, Ookayama, Meguro-ku, Tokyo 152-8550, Japan
e-mail: cocjin.m.aa@m.titech.ac.jp

O. Kusakabe
Office of the President, Ibaraki National College of Technology, 866 Nakane, Hitachinaka-shi, Ibaraki-ken 312-8508, Japan

Y. Huang et al. (eds.), *New Frontiers in Engineering Geology and the Environment*,
DOI: 10.1007/978-3-642-31671-5_14,

Table 1 Depth factors for embedment ratio, $D/B \leq 1.0$ and $\phi_f > 10°$

	$d_q = 1 + n(D/B)$	d_γ
Meyerhof (1963)	$n = 0.1\tan(45 + 0.5\phi_f)$	$d_q = d_\gamma$
Brinch Hansen (1970)	$n = 2.0\tan\phi_f(1\text{-}\sin\phi_f)^2$	$d_\gamma = 1.0$

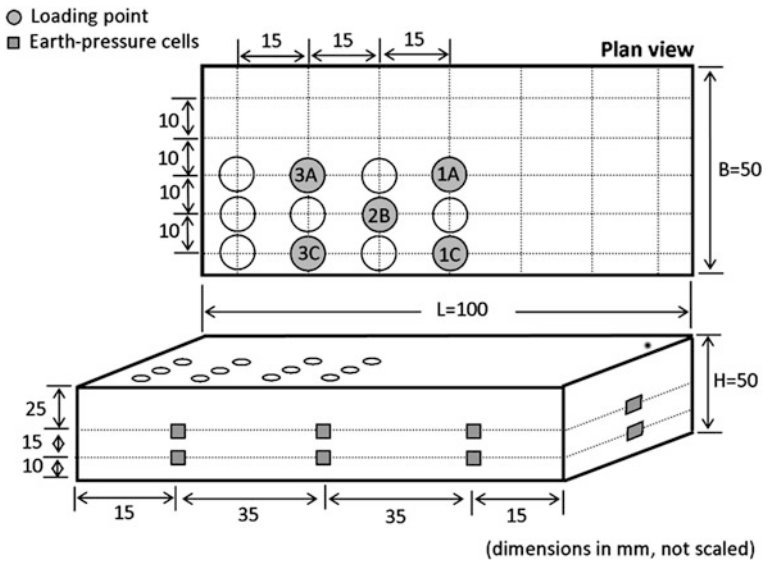

Fig. 1 Model footing

$$f(V,H,M/B) = \left(\frac{H}{V_o h_o}\right)^2 + \left(\frac{M/B}{V_o m_o}\right)^2 - 2a\frac{H}{V_o h_o}\frac{M/B}{V_o m_o} - \left\{\left[\frac{(\beta_1+\beta_2)^{(\beta_1+\beta_2)}}{\beta_1^{\beta_1}\beta_2^{\beta_2}}\right]\left(\frac{V}{V_o}\right)^{\beta_1}\left(1-\frac{V}{V_o}\right)^{\beta_2}\right\}^2 = 0 \quad (1)$$

where V_o corresponds to the largest vertical load of a given envelope. Existing parametric values on Eq. 1 for dense sand as proposed by Gottardi et al. (1999) and Houlsby and Cassidy (2002) based on 1 g experimental observations on circular footing are given as $m_o = 0.090$, $h_o = 0.121$, $a = -0.223$, and $\beta_1 = \beta_2 = 1.0$.

Recent centrifuge tests on dense sands have confirmed however, that a failure envelope obtained from loading tests with different initial footing embedment may vary with respect to Eq. 1 (*e.g.* Cassidy 2007, Govoni et al. 2010). These studies implicated that an overburden pressure due to embedment, which becomes more pronounced under an enhanced gravitational field, may generally enhance the footing capacity and consequently affect an additional expansion to a normalised failure envelope. Previous small-scale model tests on loose sand (Byrne and Houlsby 2001) have also shown that the size of failure envelope normalised by vertical load V_o, increases with increasing initial embedment. An opposite tendency has been observed on dense sand (Byrne and Houlsby 1999), though the contraction of said envelope was rather interpreted in relation to the peak bearing capacity. Nevertheless, these differing experimental observations put forward the need to assess the effect of initial embedment on the capacity of shallow foundations under large deviatoric loads.

In this study, the increase of footing capacity owing to initial footing embedment is investigated under a properly-scaled stress field using a perfectly-drained loading condition. Rectangular model footing initialised at various embedment depths on dense sand is subjected to central and eccentric vertical loads. Failure loads are interpreted using a force-resultant model. In addition, the mechanism of load enhancement due to embedment, particularly involving the lateral earth pressure mobilised along the embedded depth of the footing, is investigated by directly measuring the lateral contact pressure. Collapse mechanisms exhibited by formation of failure slip-lines are also presented and compared for surface and embedded footings.

2 Model Footing Tests

A rectangular footing (50 mm × 100 mm) with rough base was loaded vertically with various eccentricities using a loading test set-up described by Bando et al. (2011), for different embedment ratios of 0, 0.4 and 0.8.

Vertical load was applied to the top surface of the footing through half-spherical indentions carved at pre-determined points as shown in Fig. 1. These contact points provide eccentricities, e obtained as,

Table 2 Test program

Loading point	*D/B*	e_B (mm)	e_L (mm)	*e/B'*
1A	0	0	0	0
2B	0	10	15	0.25
3A	0	0	30	0.30
1C	0	20	0	0.40
3C	0	20	30	0.50
1A	0.4	0	0	0
2B	0.4	10	15	0.25
3A	0.4	0	30	0.30
1C	0.4	20	0	0.40
3C	0.4	20	30	0.50
1A	0.8	0	0	0
2B	0.8	10	15	0.25
3A	0.8	0	30	0.30
1C	0.8	20	0	0.40
3C	0.8	20	30	0.50

Table 3 Properties of Toyoura sand

Type	Values
Specific gravity	2.65
D_{50} (mm)	0.19
D_{30} (mm)	0.16
D_{10} (mm)	0.14
Coefficient of uniformity	1.62
Coefficient of curvature	1.05
Maximum void ratio, e_{max}	0.97
Minimum void ratio, e_{min}	0.61
Dry unit weight, γ_d (kN/m^3) at Dr = 80 %	15.4

Fig. 2 Mark III Centrifuge at Tokyo Institute of Technology

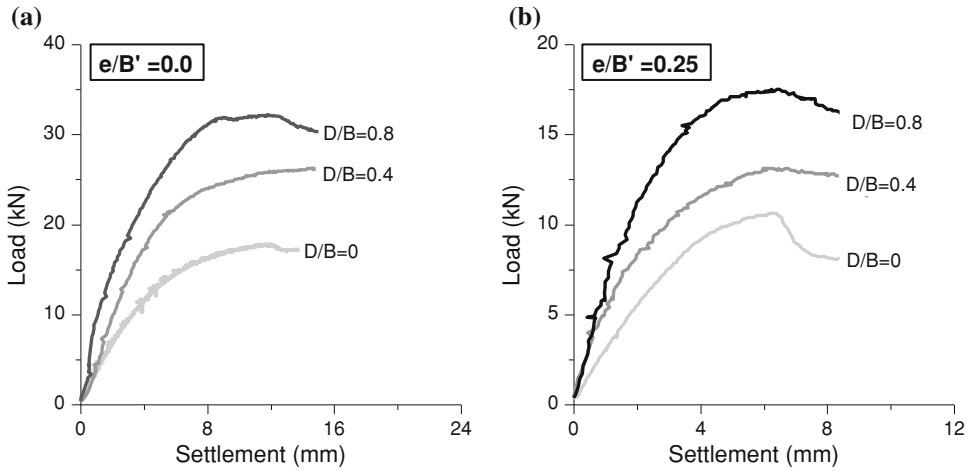

Fig. 3 Load and settlement of footings with various embedments: **a** central loading and **b** eccentric loading

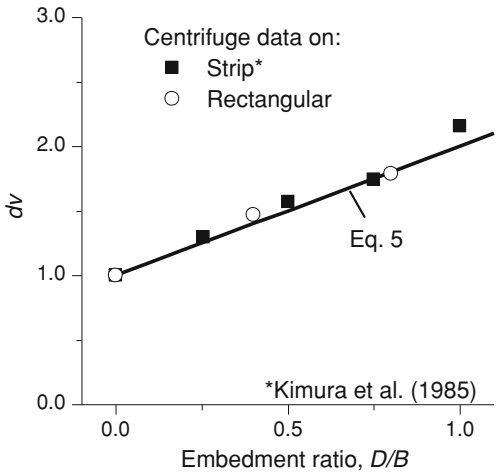

Fig. 4 Increase of vertical load capacity with embedment ratio on dense sand

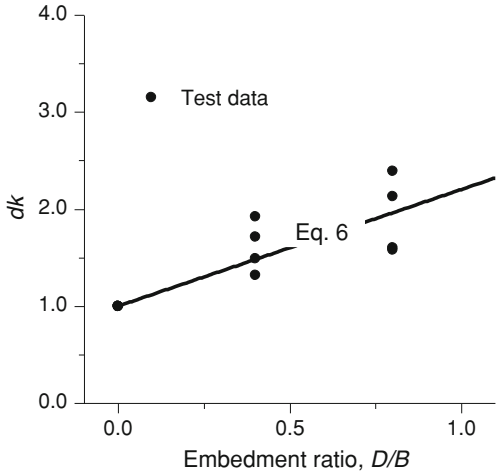

Fig. 5 Vertical stiffness parameter as a function of embedment ratio

$$e = B'\sqrt{\left(\frac{e_B}{B}\right)^2 + \left(\frac{e_L^2}{L}\right)} \quad (2)$$

where e_B and e_L are the eccentricities along the short (B) and long (L) axis of the footing respectively, and $B' = (B^2 + L^2)^{0.5}$. Values of e/B' are given in Table 2.

An unrestrained rotational condition was observed during the eccentric vertical loading. This was made possible by complimenting the concave spheres of loading points with a loading rod constructed with a semi-spherical cap with a diameter of 7 mm (Bando et al. 2011).

To measure the earth pressures on the lateral side of the model footing, a total of 16 small-sized, high-capacity earth pressure cells were embedded on each side of the footing, arranged in upper and lower rows as illustrated in Fig. 1.

The model ground was constructed from dry Toyoura sand, rained through a hoisted hopper with a pre-determined pouring height relative to the soil surface maintained throughout the preparation. The ground was set inside a circular steel container with internal diameter of 586 mm and depth of 400 mm, and was given a final height of 200 mm. A target relative density, Dr = 80 % was maintained all throughout different model tests. Plane-strain shear tests and triaxial tests conducted by Yamaguchi et al. (1976) have estimated that dense sample of Toyoura sand with $80 < \mathrm{Dr} < 86$ % has a maximum angle of shearing stress in the range of $40° < \phi_f < 46°$. The material properties of said sand are provided in Table 3.

All tests were conducted under a gravitational field equal to 50 g using the Mark III centrifuge of Tokyo Institute of Technology (Fig. 2).

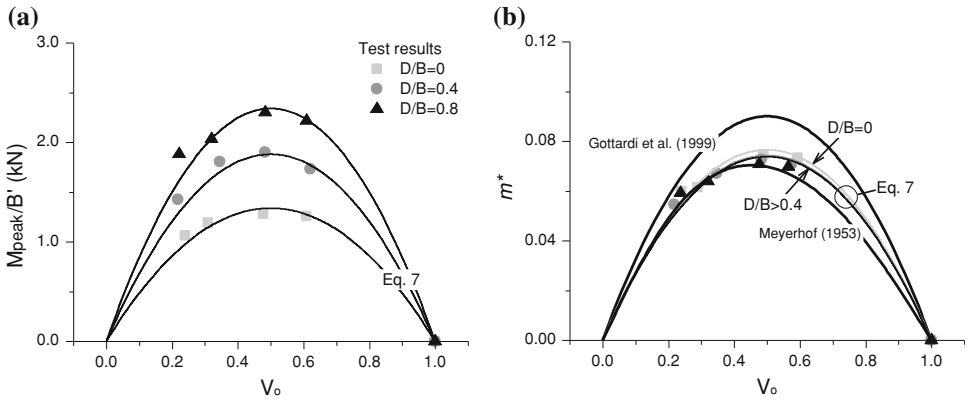

Fig. 6 Vertical moment load interaction

3 Results and Discussions

3.1 Vertical Load Capacity

Load-settlement curve for (a) central and (b) eccentric vertical loading with different initial footing embedment is shown in Fig. 3. The peak of this curve is used to define load failure, where a general increase in the said load is observed with increasing embedment.

To directly estimate the vertical load capacity of embedded footings, a vertical load ratio, *dv*, is defined as,

$$dv = \frac{V_{peak(D)}}{V_{peak(S)}} \tag{3}$$

where $V_{peak(D)}$ and $V_{peak(S)}$ are the failure loads obtained for embedded and surface footings, respectively. By conventional bearing capacity formulae (Meyerhof 1963), *dv* in above equation can also be expressed as:

$$dv = 1.0 + 2.0\left(\frac{N_q}{N_\gamma}\right)\left(\frac{d_q}{d_\gamma}\right)\left(\frac{D}{B}\right) \tag{4}$$

By applying the recommended depth factors given in Table 1 on Eq. 4, a quadratic and a linear relationship for the vertical load enhancement and embedment ratio is correspondingly derived following Brinch Hansen (1970) and Meyerhof (1963). For the case of Brinch Hansen (1970), the parameter *n* in Table 1 determines the coefficient of an additional variable *D/B* in Eq. 4. This parameter diminishes in value with increasing ϕ_f. Thus, for soil exhibiting high strength, the second-order term for *D/B* in Eq. 4 as defined by Brinch Hansen (1970) consequently reduces. In addition, for $40° < \phi_f < 50°$, the bearing capacity factor N_γ can be approximated as nearly twice in value of N_q. Under these conditions, Eq. 4 simplifies into a linear expression of *D/B* (Meyerhof 1963). The vertical load capacity of embedded footing can then be estimated as,

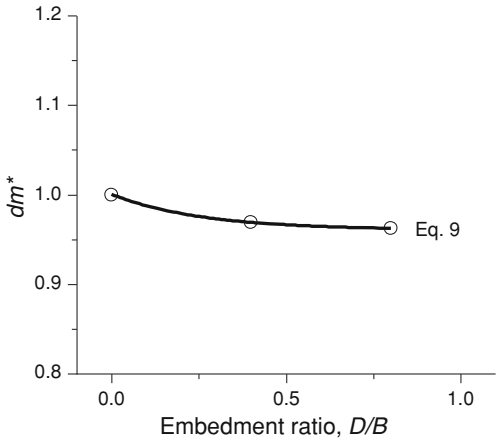

Fig. 7 Decrease in normalised moment load capacity with embedment

$$V_{peak(D)} = V_{peak(S)}\left(1.0 + \frac{D}{B}\right) \tag{5}$$

As seen in Fig. 4, the relationship given by Eq. 5 holds true for recorded *dv* of centrally-loaded rectangular footings on dense dry sand within $D/B < 1.0$.

This equation is also found to give a good representation to an observed load enhancement involving an embedded strip footing on dry Toyoura sand with Dr = 86 % (Kimura et al. 1985).

3.2 Vertical Stiffness Response

From the load-settlement results, a vertical loading stiffness parameter k_V was obtained by taking the ratio of the vertical load and footing settlement at failure. The $k_{V(D)}$ response for a footing with embedment is scaled to the k_V response of an

equivalent surface footing, and are plotted as a function of the embedment ratio in Fig. 5. A generally increasing vertical stiffness response with embedment is observed as shown, where $k_{V(D)}$ can be approximated as,

$$k_{V(D)} = k_{V(S)}\left(1 + 1.2\frac{D}{B}\right) \tag{6}$$

Above equation is validated for $0 < D/B < 0.8$. The parameter $k_{V(S)}$, which represents the k response for vertical loading of a surface footing, is obtained approximately equal to1.5 kN/mm in current loading tests (equivalently the initial loading stiffness). It is noted that $k_{V(D)}$ increases with embedment ratio at a larger rate compared to $V_{peak(D)}$ which suggests that failure settlement correspondingly reduces with increasing embedment (Kimura et al. 1985; Georgiadis 1993).

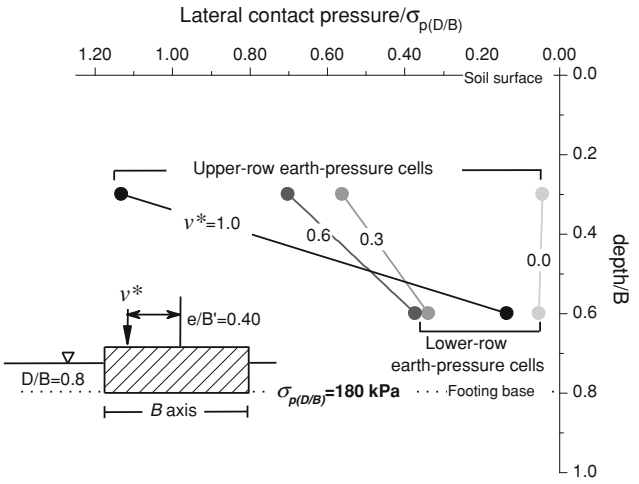

Fig. 8 Distribution of lateral earth pressure along embedded depth obtained at different levels of V_{peak} with $D/B = 0.8$, for case 1C ($e/B' = 0.40$)

3.3 Overturning Moment Load Capacity

The interaction of vertical and overturning moment load capacity is presented in a parabolic form following Ticof (1977) and Gottardi et al. (1999). This interaction is generally expressed as,

$$\frac{M_{peak}}{B'} = m_{(D)}V_o(1 - V_o) \tag{7}$$

where $M_{peak} = eV_{peak(e)}$ is the peak moment load determined by an eccentric vertical load, $V_{peak(e)}$ with eccentricity e. Equation 7 is a projection of Eq. 1 on V/V_o-M/BV_o load plane, where for a given embedment, the ratio of $V_{peak(e)}$ to failure load of a centrally-loaded footing, $V_{peak(c)}$ would correspond to V_o.

Equation 7 is correlated to current set of data as presented in Fig. 6a. By directly plotting the parameter $m_{(D)}$ with embedment ratio, moment load capacity of an embedded footing can then be approximated as,

$$m_{(D)} = m_{(S)}\left[1 + 0.95\left(\frac{D}{B}\right)\right] \tag{8}$$

where an $m_{(S)} = 1.34$ kN was obtained for the peak moment load of an equivalent surface footing. The expansion of failure envelope as given by Eq. 8 indicates the increased load-carrying capacity available with increased embedment ratio (Fig. 6a), and is found proportional to the increase in vertical load capacity with increasing embedment (Eq. 5). However, by normalising the moment load capacity to $V_{peak(c)}$, it is seen that a failure envelope determined by $m^* = M_{peak}/B'V_{peak(c)}$ decreases slightly in size with increasing D/B (Fig. 6b), though such a variation becomes minimal for $D/B > 0.4$. This observed decrease in normalised moment load capacity, dm^*, with increasing embedment ratio is illustrated in Fig. 7, where such a decrease was expressed as a power function of D/B given as,

$$m^*_{(D)} = m^*_{(S)}\left[0.96 + 0.04 \times 0.02^{\left(\frac{D}{B}\right)}\right] \tag{9}$$

The parameters $m^*_{(D)}$ and $m^*_{(S)}$ are the normalised moment load capacity for embedded and surface footings respectively. From present set of data, $m^*_{(S)} = 0.080$ is comparable to normalised moment load capacity, $m_o = 0.090$ obtained for circular and rectangular footings on dense sand by Gottardi et al. (1999) and Gottardi and Butterfield (1993), respectively.

In Fig. 6b, a more conservative set of failure loads is projected by Eq. 1 following parametric values obtained for circular footings (Gottardi et al. 1999) compared to an envelope presently obtained using rectangular footings. However, a failure envelope following effective-width assumptions of Meyerhof (1953) provides a closer estimation to present observation.

3.4 Lateral Contact Pressures

Figure 8 shows the lateral earth pressure developing for one-sided, eccentric vertical loading (case 1C) with $D/B = 0.8$. Shown in the said figure is the average pressure

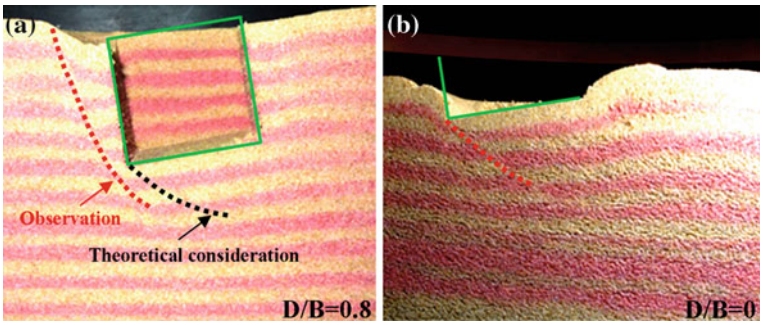

Fig. 9 Failure slip-line after eccentric loading along short-axis: **a** embedded, and **b** surface (after Bando et al. 2011)

recorded for each row of earth pressure cells on the side of long axis (side of eccentricity along the short axis), taken at different levels of peak load, $v^* = V_{(e)}/V_{peak(e)}$. In the said figure, lateral resistance offered by soil backfill in passive side increases in significance at the upper part of embedment with increasing overturning moment (increasing v^*). A sudden decrease of lateral contact pressure at the lower parts of the embedded footing is found when imposed vertical load reaches failure. Assuming a full lateral contact along *D/B*, observed distribution of lateral earth pressure on the footing suggests that a portion of soil backfill undergoes yielding when v^* approaches 1.0. This implies that overturning capacity of foundation would also depend on the strength of backfill soil. In the same figure, it is seen that the passive lateral earth pressure determined by embedment depth ($\sigma_{p(D/B)} = K_p\sigma_{v(D/B)}$) is completely mobilised at load failure, further confirming that increase in load capacity with embedment, in addition to the contribution of overburden, is also given by a yielding capacity of soil backfill.

3.5 Failure Slip-Line

Figure 9 shows a comparison of the failure slip-line for surface and embedded footings after an eccentric vertical loading along the footing's short axis (case 1C). Relative to a surface footing, the failure slip-line for an embedded footing is seen to form at a much larger angle with respect to the footing base. In addition, the observed slip-line under the said footing is seen to extend beyond the footing base, observed to be continuing from the local slip-line fully developed within the passive, back-fill soil. Such an observation has a strong implication to theoretical considerations of calculating load capacity for embedded footings, wherein a theoretical slip-line is often assumed to occur directly from the embedded footing base, and follows the form of a slip-line representing a surface footing with an equivalent surcharge γD.

4 Conclusions

The effect of embedment on the capacity of a shallow, rectangular footing on dense sand is investigated through centrifuge modeling. By scaling the embedment ratio, *D/B* to the recorded load capacity, it is found that a similar increase in vertical load capacity with increasing embedment can be expected for rectangular and strip footings.

Observations on dense sand, made under a properly-scaled stress field, show that increase in vertical and moment load capacity follows an almost linear relationship with embedment ratio.

Failure condition for eccentric vertical loading is expressed by a failure envelope in *V-M* load space. A failure envelope is represented for each embedment determined by the failure load of a centrally-loaded footing, wherein with respect to this failure load, a normalised envelope is found to be slightly dependent on the embedment ratio. The normalised envelope is found to reduce with increasing embedment ratio, though such reduction becomes insignificant for $D/B > 0.5$. Under increasing overturning moment, embedment effect is given by the increasing resistance offered by the upper portions of the soil backfill. Yielding of the backfill soil results to a failure slip-line forming at depths far deeper than a slip-line currently taken into account in theoretical calculation of embedded footing capacity.

References

Bando, R., Izawa, J., & Kusakabe, O. (2011). Rectangular footing on sand subjected to double eccentric load. *International Journal of Physical Modelling in Geotechnics, 11*(1), 33–49.

Brinch Hansen, J. (1970). A revised and extended formula for bearing capacity. *Danish Geotechnical Institute Bulletin, 28*, 5–11.

Byrne B & Houlsby G. (1999) Drained behavior of suction caissons on very dense sand. *Proceedings of the Offshore Technology Conference*. Houston, TX. Paper No OTC 10994.

Byrne, B., & Houlsby, G. (2001). Observations of footing behavior on loose carbonate sands. *Géotechnique, 51*(5), 463–466.

Cassidy, M., Byrne, B., & Houlsby, G. (2002). Modelling the behavior of circular footings under combined loading on loose carbonate sand. *Géotechnique, 52*(10), 705–712.

Cassidy, M. (2007). Experimental observations of the combined loading behaviour of circular footings on loose silica sand. *Géotechnique, 57*(4), 397–401.

Georgiadis, M., & Butterfield, R. (1988). Displacements of footings on sand under eccentric and inclined loads. *Canadian Geotechnical Journal, 25*, 199–212.

Georgiadis, M. (1993). Settlement and rotation of footings embedded in sand. *Soils and Foundations, 33*(1), 169–175.

Gottardi, G., & Butterfield, R. (1993). On the bearing capacity of surface footings on sand under general planar loads. *Soils and Foundations, 33*(3), 68–79.

Gottardi, G., & Butterfield, R. (1995). The displacement of a model rigid surface footing on dense sand under general planar loading. *Soils and Foundations, 35*(3), 71–82.

Gottardi, G., Houlsby, G., & Butterfield, R. (1999). Plastic response of circular footings on sand under general planar loading. *Géotechnique, 49*(4), 453–469.

Govoni, L., Gourvenec, S., & Gottardi, G. (2010). Centrifuge modeling of circular shallow foundations on sand. *International Journal of Physical Modelling in Geotechnics,*. doi:101680/ijpmg201010235.

Houlsby, G., & Cassidy, M. (2002). A plasticity model for the behaviour of footing on sand under combined loading. *Géotechnique, 52*(2), 117–129.

Kimura, T., Kusakabe, O., & Saitoh, K. (1985). Geotechnical model test of bearing capacity problems in a centrifuge. *Geotechnique, 35*(1), 33–45.

Meyerhof G. (1953) The bearing capacity of foundations under eccentric and inclined loads. *Proceedings of the 3rd ICSMFE* (Vol.1, pp. 440–445).

Meyerhof, G. (1963). Some recent research on the bearing capacity of foundations. *Canadian Geotechnical Journal, 1*, 16–26.

Ticof J. (1977) Surface footings on sand under general planar loads (Doctoral dissertation, University of Southampton, UK, 1977).

Yamaguchi, H., Kimura, T., & Fuji-i, N. (1976). On the influence of progressive failure on the bearing capacity of shallow foundations in dense sand. *Soils and Foundations, 16*(4), 11–22.

An Investigation on Stress–Strain Relationship of on Eucalyptus Saligna by Pull-Out Method Based on Regression Analysis

F. Chen, X. B. Xiong, S. Tan, R. L. Chen, and C. Gu

Abstract

With the rapid development of the construction of expressway and the increasing sense of environment protection of mankind at coastal areas in eastern China, the bio-engineering techniques for slope protection are becoming more and more important and being used widely in the construction of expressway. In this paper, several laboratory uniaxial tests with pull-out method were carried out to obtain the stress-strain relationship of single root of *Eucalyptus saligna*. In addition, mathematical model of experience for root tensile strength by regression analysis were obtained. The results of regression analysis show that the parabolic-curve model has good fitting precision and good generalization ability to describe the relationship of stress-strain. A uniform constitutive relation can be used to describe the stress-strain relationship of different root systems. It can be a conclusion that the pull-out method may determine the strength of tree root very well. Meanwhile, to attain the ultimate pull-out resistance of each single root and some engineering properties parameters. This kind root and its parameters do have a great impact on root mechanical properties, such as the maximum tensile strength and pull-out strengths. The plant is well suited to the large-scale demands for the practices in coastal areas.

Keywords

Pull-out method • Ultimate pull-out resistance • Root tensile strength • Properties of roots • Regression analysis • Measure curve of strength

1 Introduction

With the rapid development of Chinese infrastructure construction, especially highway and railway engineering, plenty of earthwork and stonework destroyed the original vegetation of mankind at coastal areas in eastern China. It causes soil erosion, slope instability and many other natural disasters, which lead to the severe deterioration of ecological environment and serious damage to economy development. Thereforth, it is extremely necessary to investigate soil and water conservation and vegetation restoration. Actually, roots increase soil shear strength by anchoring a soil layer and by modifying soil structure, which improve the stability of slopes and the erosion resistance ability of soil.(Comino and Marengo 2010) Furthermore, vegetation slope protection also correspond to the concept of harmonious development by using natural plants and soil engineering materials in slopes. For the advantage of making up the defects of the traditional engineering protection method, slope protection with vegetation is the most economic and reasonable method to stabilize slopes today.

F. Chen · X. B. Xiong · S. Tan · R. L. Chen · C. Gu
School of Architecture and Civil Engineering,
Nantong University, Seyuan Road,
Nantong 226019, China

X. B. Xiong (✉)
School of Engineering, Jinggangshan University,
Ji'an 343009, China
e-mail: thongtao2006@163.com

Y. Huang et al. (eds.), *New Frontiers in Engineering Geology and the Environment*,
DOI: 10.1007/978-3-642-31671-5_15,

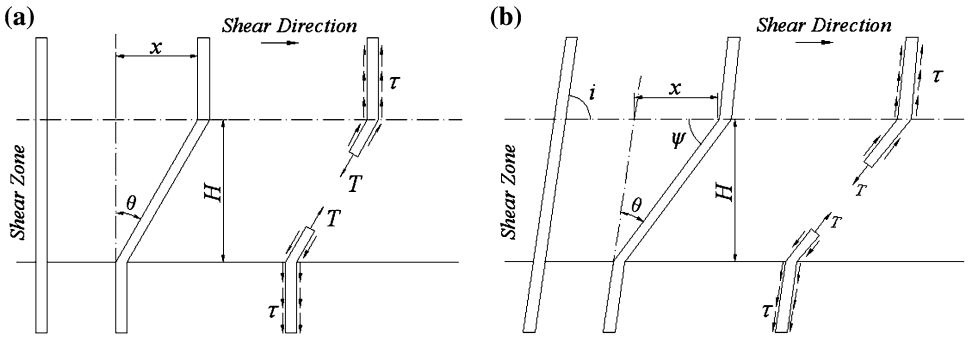

Fig. 1 Single root on the reinforced soil mechanics model (**a**) Orthogonal station; (**b**) Oblique station

Fig. 2 The equipment used for the determination of tensile strength of the root of *arbor*

During recent two decades, several scholars have attached considerable importance to the significance of plant root systems and have carried on plenty surveys to study the root reinforcement of soils, though the effects of root tensile strength need more study. The results of many researchers show that root tensile strength tends to decrease with the increase of diameter, which is the key factor of improving the stability of slopes. By analyzing root tensile strength and its distribution, a simple perpendicular root model was developed by Wu et al. (1979) to estimate the increment of soil shear strength. This model corresponds to the value measured well, which has been widely used in soil reinforcement studies(Csilla Hudek and Rey 2010). According to the characteristics of stress–strain relations, Pinghua Wang et al. (2011) fixed an empirical model of single root by investigating *Betula platyphylla* in north China. Chunjuan Lv et al. (2011) conducted single root tensile tests on five kinds of arbor, and their results showed that the root tensile strength and its diameter represents as a negative correlation, which can be described by power function.

Nowadays, two methods are widely adopted to investigate the tensile strength of root, which are in situ shear tests and individual root pull-out tests in laboratory. And more sophisticated models based on root tensile tests have been developed. A dynamic fiber bundle model was developed by Pollen and Simon (2005) to account for the progressive manner of root breaking. Chen (2007) established hyperbola model and parabolic model of root-soil, and the results of practical application show that quadratic parabola model describes the root tensile stress–strain relations better than the hyperbola one.

The tensile strength of roots depends on the plant species, root density, the diameter of roots and their distribution and orientation in the soil, as well as any seasonal variations that take place(Csilla Hudek and Rey 2010). However, the tensile strength of the whole root mainly depends on the tensile properties of single toot and its distribution(Chunjuan Lv et al. 2011). And it is also confirmed by Docker and Hubble (2008), which pointed out that *A. floribunda* has a relatively high tensile strength with more branches and fine roots, while the strength of *E. amplifolia* is lower for its relatively less fine roots.

In general, *arbor* has a prominent capacity in soil and water conservation. And the tensile strength of root is a key indicator. By individual root pull-out tests in laboratory, the diameter and the maximum tensile force and strength of single root were measured. These statistics are fitted by Origin 8.0 software, and the functional relationship was achieved. The systematic research in this paper shows that the larger the diameter, the greater the tensile force is, while the tensile strength is inverse.

2 Materials, Experiment and Methods

A model of the interaction between root and soil needs to be established to analyse the reinforced function of plant roots quantitatively. And the model of a single root on reinforced earth is showed in Fig. 1. Figure 1a represents the extension direction of the root is orthogonal with the shear zone, while Fig. 1b illustrates the oblique case.

By simple mechanical analysis, the increment of the soil shear strength is deduced. When the root is at orthogonal station, τ_R can be determined by:

$$\tau_R = \frac{T}{a}\sin\theta + \frac{T}{a}\cos\theta\tan\varphi \tag{1}$$

And for the oblique case, τ_R is showed as:

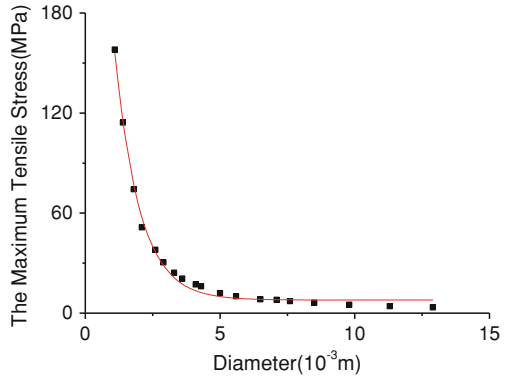

Fig. 3 Curve of root tensile stress (P)

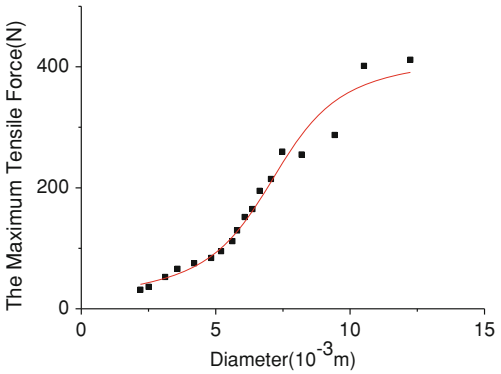

Fig. 4 Curve of root tensile force (F)

Table1 The tensile strength of the root

N (Tab.1)	D/10^{-3}m	TMTF/N	TMTS/MPa
1	1.1	143.1	158.07
2	1.4	159.7	114.32
3	1.8	175.4	74.25
4	2.1	186.2	51.46
5	2.6	194.0	38.05
6	2.9	200.9	30.42
7	3.3	206.8	24.22
8	3.6	213.6	20.72
9	4.1	227.4	17.21
10	4.3	233.2	16.08
11	5.0	241.1	12.01
12	5.6	251.9	10.12
13	6.5	262.6	8.24
14	7.1	318.5	7.97
15	7.6	340.1	7.18
16	8.5	360.6	6.31
17	9.8	388.1	5.07
18	11.3	410.6	4.11
19	12.9	434.1	3.48
Ave	5.34	260.39	32.07

Note Diameter (D); Length (L); The maximum tensile force (F); The maximum tensile stress (P)

$$\tau_R = \frac{T}{a}\sin(90^\circ - \psi) + \frac{T}{a}\cos(90^\circ - \psi)\tan\varphi \quad (2)$$

Where τ_R is the increment of soil shear strength; T is the tensile strength of single root (N); a is single effect of soil area; θ is shear deformation angle; φ is soil internal friction angle; ψ is the angle between the shear plane and the direction of root in shear zone, which has deformed by shear strength. It is represented as:

$$\psi = \tan^{-1}\left[\frac{1}{k + (\tan^{-1}\ i)^{-1}}\right] \quad (3)$$

where i is the angle between the oblique direction of root and the shear plane; k is shear ratio, $k = x/H$; H is the thickness of shear zone.

Bischetti et al. (2005) conducted tensile strength tests. The roots were subjected to a constant movement of the tangent screw at a speed of 10 mm/min. Then a maximum force of 200 N could be exerted. The following function was adopted to calculate the tensile strength of root.

$$P = \frac{4F_{\max}}{\pi D^2} \quad (4)$$

Table 2 The tensile and pull strength of the root

NO	D/10^{-3}m	L/cm	F/N	P/MPa
1	1.89	77.6	23.32	8.58
2	2.20	80.5	31.46	8.10
3	2.51	86.0	36.26	7.39
4	3.12	91.5	52.43	6.78
5	3.58	92.3	66.05	6.52
6	4.20	92.0	75.17	5.56
7	4.83	90.6	84.08	4.63
8	5.20	93.0	95.06	4.32
9	5.62	98.5	111.72	4.78
10	5.80	104	129.56	4.91
11	6.08	107	151.51	5.13
12	6.37	112	164.84	5.03
13	6.64	115	194.82	5.46
14	7.06	119.8	214.62	5.38
15	7.48	126	259.70	5.83
16	8.20	127	254.90	5.12
17	9.43	126.5	287.14	4.17
18	10.52	131.8	401.60	4.32
19	12.24	129	411.60	4.20
Ave	5.95	105.27	160.33	5.59

Note Diameter (D); Length (L); The maximum tensile force (F); The maximum tensile stress (P)

Table 3 The relationships between root tensile strength (T_r) and root diameter (D) for different plant species and different studies

Plant name	Equation	Reference
Arbor	$F_{max} = 10.499 - 6.138x + 1.566x^2 - 0.696x^3$	This article
Arbor	$P_{max} = 492.55^{-x/0.915} + 7.855$	This article
Rosmarinus officinalis	$T_r = 34.66D^{-0.78}$	Operstein (2000)
Atriplex halimus	$T_r = 72.97D^{-0.60}$	Mattia et al. (2005)

Where P is the root tensile strength (MPa), $F_{max}$is the maximum tensile strength in calculation of P(N), D is the average diameter of roots (mm).

The stress is determined by:

$$\sigma = \frac{4F}{\pi D^2} \tag{5}$$

where σ is the stress (MPa) and its ultimate value is equal to P, F is the tensile strength in calculation of P (N).

The experiment was performed using following equipment shown in Fig. 2.

3 Data and Discussion

By carrying out the experiments of the samples, 38 different kinds of diameter of arbor roots were acquired. They were divided into two groups and measured respectively. And four column data were obtained by the test, which are the diameter (D), the length (L), the maximum tensile strength (TMTS) and the maximum tensile force (TMTF). The statistics of the test are shown in Table 1 and Table 2.

The decrease in root tensile strength with increasing root diameter was explained by Marie et al. (2005). In order to determine the relationship between tensile strength and diameter, they carried out tensile tests on roots 0.2–12.0 mm in diameter of three conifer and two broadleaf species (such as Pinus pinaster Ait. and Castanea sativa Mill.), which are corresponding to Table 1.

From Table 1, with an increase in root diameter, it shows that the maximum tensile strength of single root represents increasing trend, while the maximum tensile force of single root decreasing obviously. And the decreasing trend reduces faster and faster, which is showed by Fig. 3.

The nonlinearity model of root diameter and the maximum tensile strength is acquired, which is expressed as:

$$P_{\max} = 492.55^{-x/0.9154} + 7.855 \quad (6)$$

where x is the diameter of the single root of an arbor, and the trend is shown in Fig. 3.

The trend of data is found by the same test, which is the diameter of roots, the force and strength have the same increasing trend, while the length is inversely, which is showed in Table 2.

Operstein (2000) and Mattia et al. (2005) also developed their models, which is listed in Table 3. By fitting the data, the cubic model of root diameter and the maximum tensile strength is acquired, whose function is determined by:

$$F_{\max} = 10.499 - 6.138x + 1.566x^2 - 0.696x^3 \quad (7)$$

Meanwhile, Fig. 4 shows the trends of the diameter and the maximum force.

4 Conclusion

(1) Vegetation improves slope stability mainly by increasing the shear strength of the soil through root reinforcement and via a buttressing effect from well anchored stems. The mechanical or reinforcing effect of plant roots can be described and accounted for in a systematic manner. The root tensile strength decreased with diameter increasing according to a power function, the parabolic function of third order can well reflect the basic characteristics of measured stress–strain curve, and its expression is $F_{\max} = 10.499 - 6.138x + 1.566x^2 - 0.696x^3$.

(2) The tensile strength of arbor roots has a negative correlation with root diameter and that they are in a power function relationship, and its expression is $P_{\max} = 492.555e^{-x/0.9154} + 7.855$. The tensile resistance of the root system has a positive correlation with root diameter, and they also present a relationship of power function.

Acknowledgments "Project 40962005 supported by National Natural Science Foundation of China." and this work was also supported by Opening Fund of State Key Laboratory of Geohazard Prevention and Geoenvironment Protection (Chengdu University of Technology) (Grant No. GZ2007-09).

References

Bischetti, G. B., Enrico, A. C., Tommaso, S., et al. (2005). Root strength and root area ratio of forest species in Lombardy (Northern Italy). *Plant and Soil, 278*, 11–22.

Docker, B. B. & Hubble, T. C. T. (2008). Quantifying root-reinforcement of river bank soils by four Australian tree species. *Geomorphology 100*, 18.

Chen, L. (2007). Study on the constitutive relation of forest root system. *Journal of Mountain Science, 25*(2), 224–228. (In Chinese).

Csilla Hudek, M. B., & Rey, Freddy. (2010). Root system traits of *Mahonia aquifolium* and its potential use in soil reinforcement in mountain horticultural practices. *Scientia Horticulturae, 125*, 8.

Comino, E. & Marengo, P. (2010). Root tensile strength of three shrub species: *Rosa canina*, *Cotoneaster dammeri* and *Juniperus horizontalis* soil reinforcement estimation by laboratory tests. *Catena*, (82), 227–235.

Lv, C., Chen, L., Zhou, S. et al. (2011) Root mechanical characteristics of different tree species. *Transactions of the CSAE*, *27*(S1): 329–335. (In Chinese).

Marie, G., Alexia, S., Salin, F., et al. (2005). The influence of cellulose content on tensile strength in tree roots. *Plant and Soil*, *278*, 1–9.

Mattia, C., et al. (2005). Biotechnical characteristics of root systems of typical Mediterranean species. *Plant and Soil, 278*, 23–32.

Operstein, V. (2000). The influence of vegetation on soil strength. *Ground Improve, 4*, 81–89.

Pollen, N., & Simon, A. (2005). Estimating the mechanical effects of riparian vegetation on stream bank stability using a fiber bundle model. *Water Resource Research, 41*, 1–11.

Wang, P., Fang, R., Chen, L., et al. (2011). Mechanical characteristics of tensile strength for *Betula platyphylla* Single Root. *Hunan Agricultural Sciences, 15*, 138–142. (In Chinese).

Wu, T., McKinnell, W. P., Swanston, D. N. (1979)Strength of tree roots and landslides on Prince of Wales Island Alaska. *Canadian Geotechnical Journal*, *16*, 19–33. (In Chinese).

Detection of Submerged Sand Bars in the Ebro Delta Using ASTER Images

R. Rodríguez-Martín and I. Rodríguez-Santalla

Abstract
Deltas are complex systems that can be affected by the alteration of any factors that interfere in their dynamic. Knowledge of these systems allows managers and scientists to model and establish the ecosystem state. This study is focused on the sand bars located in the Ebro delta coast. These sand bars constitute a natural sediment deposit to protect the beaches from wave erosion. Over the last 20 years, their detection has been based on the record of the maximum intensity shown by waves breaking over them. The methodology uses satellite images to detect the sand bars depending on the pixel value. Although is not possible to validate the results, their coherence allows where new investigation lines to be explored. The methodology used will allow increased frequency of monitoring in large areas while reducing costs.

Keywords
Submerged bars • Ebro delta • ASTER • Remote sensing

1 Introduction

Delta coasts are dynamic sedimentary formations found in the transition from terrestrial to marine environments. As a result delta coasts are affected by processes related to this environmental transition giving the delta coast an importance from environmental and economical aspects.

The bars are accumulations of submerged sediments and represent sedimentary formations located off the coastline, less than 10 m deep with a very dynamic morphology. The bars are formed by the action of intense waves that create effective return currents.

R. Rodríguez-Martín (✉)
Department of Geography, Alcalá University, C/Colegios, 2.Alcalá de Henares, 28801 Madrid, Spain
e-mail: rodrigo.rodriguez.martin@gmail.com

I. Rodríguez-Santalla
Department of Biology and Geology, Rey Juan Carlos University, C/Tulipán s/n. Mostoles, 28933 Madrid, Spain
e-mail: inmaculada.rodriguez@urjc.es

The importance of the bars is that they are a reserve of sediment which protects the coastline against erosion from storms. It is important to know their characteristics for the study of the hydrodynamics of the surf zone, for the beach morphology study and for the protection of the coast (Ojeda et al. 2008).

Lippman and Holman (1989) pioneered the use of video cameras for the detection of submerged bars. This was done taking advantage of the high light intensity that waves produce breaking over the crest of sand bars. This technique has been widely used, studied and improved. With this technique it has been established that the relationship between the position of the bars and the maximum intensity varies with the studied area (Ribas et al. 2010). This relationship depends on the tide level, the significant wave height (Ojeda et al. 2008) and the beach profile (Plant and Holman 1998). The best results are obtained with the average of images taken every second over 10 min (Lippman and Holman 1989). This approach lacks the synoptic view of satellite sensors and in addition requires study in situ and

Y. Huang et al. (eds.), *New Frontiers in Engineering Geology and the Environment*,
DOI: 10.1007/978-3-642-31671-5_16,

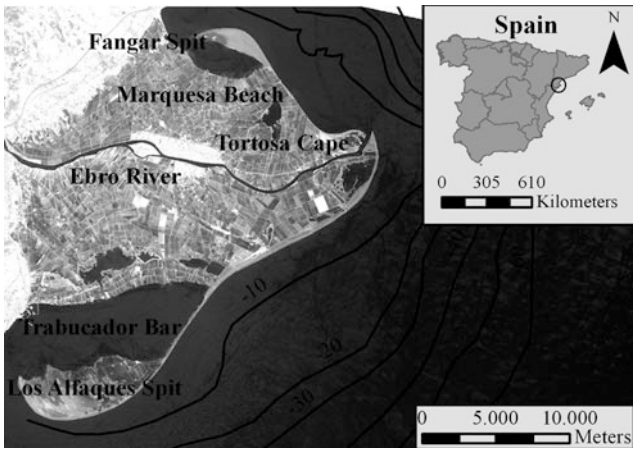

Fig. 1 Location map of the ebro delta. ASTER image

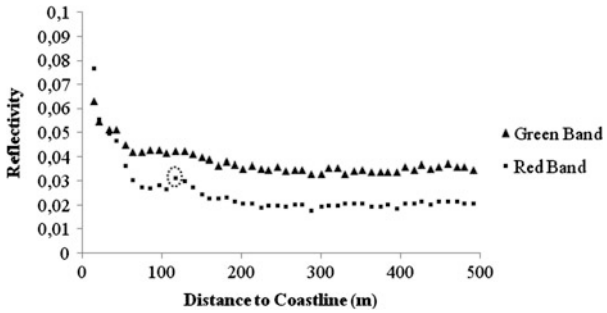

Fig. 2 Profile No. 43 of ASTER image of 2006, bands of red and green. The re-marked point has the highest intensity in the area where the bar is expected to be found

maintenance of video recording equipment, which leads to high cost.

On the other hand, the signal received by a satellite sensor in the coastal zone has low reflectivity in the visible range (Chuvieco 2010). The reflectivity increase due to the foam generated by breaking waves and also by the influence of the sea floor, especially where there are sand bars (Gould and Arnone 1997).

2 Field Site and Data

The Ebro Delta is on the Mediterranean coast of the *Comunidad Autónoma de Cataluña* (Spain) (Fig. 1). It is the most important coastal delta of the Iberian Peninsula, and is a microtidal delta currently dominated by waves (Jiménez and Sánchez-Arcilla 1993).

The most intense waves occur from October to March. The main incident wave comes from the east, and diverges at the Cape of Tortosa, creating two currents: one to the North and the other to the South (Garcia 1982). The longitudinal transport allows the formation of beach ridges that favor the growth of spits. The greatest erosion is concentrated in Cape Tortosa, while the main deposition is located at the end of El Fangar spit situated in the north hemidelta, and in the Los Alfaques spit, in the south hemidelta (Rodriguez 1999).

In this analysis four ASTER images are used which cover the area of the Ebro Delta: 07/06/2003, 01/07/2006, 08/10/2007 and 7/28/2010. The images of 2003, 2006, and 2010 correspond to the period in which the waves were less energetic, whereas, the image of 2007 includes the result of strong waves.

3 Methodology

The methodology seeks to transfer the experience acquired from the use of video cameras to the satellite images. This presents a set of problems and limitations. Satellite images show the state of the sea surface in a single instant; therefore it is impossible to have an average of 600 images for a 10 min period. This may not be a great problem taking into account that the spatial resolution of ASTER is 15 m and the fluctuations due to changes in wave height with the actual position of the bar's crest can be collected at the same pixel, or adjacent. The column of water between sensors and ground can be five times higher with a video camera than with ASTER because the angle of incidence of a video camera is around 80 and 21.3° in ASTER (Abrams and Hook 2007).

Due to the lack of accurate bathymetry, we could not validate the results. Therefore, we should consider this project as an exploratory technique.

3.1 Preprocessing and Processing

The preprocessing was carried out following instructions from Abrams and Hook (2007). The image of 2003 was georeferenced over an orthophoto of PNOA (Plan Nacional de Ortografía Aérea). The other took as a reference the 2003 image. A mask was done using the NIR band, with the goal of using only the sea within 500 m of the coast.

Bars were digitized visually for each date. Subsequently, lines perpendicular to the coastline were generated obtaining profiles according to the red and green bands. The position of the sand bar was assigned repeating the same steps in each profile: (1) observing the area where it was expected; and (2)

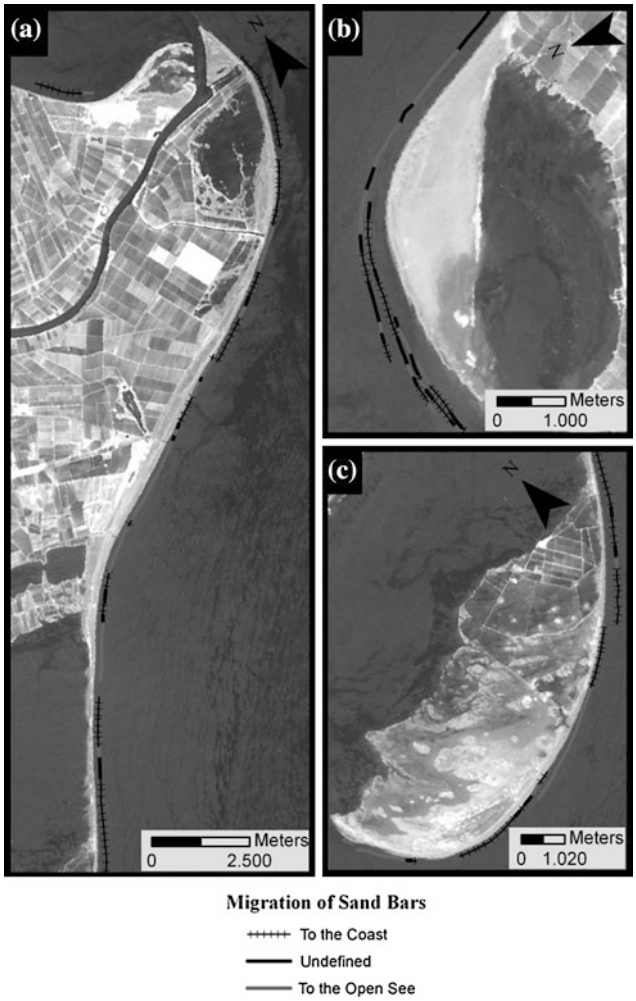

Fig. 3 Direction of migration of the bars. **a** Cape Tortosa and Trabucador Bar (2003–2006), **b** Spit of the Fangar (2006–2007) and **c** Spit Alfaques (2007–2010)

choosing the maximum relative point (Fig. 2). These points were used to digitalize the bars.

4 Results and Discussion

Fourteen bars were digitalized manually and are present in each of the four images. For their detection 247 lines perpendicular to the coastline were generated at irregular intervals (median: 204 m, maximum: 1223 m and minimum 15 m).

Visual analysis of 988 profiles showed that it was easier to select maximum reflectivity points with the red band (Fig. 2). The percentage of common points was relatively high (62.0–75.8 %).

The extension of the sand bars is very irregular (9–558 m). Their presence is not constant for the four dates as a consequence of the complex dynamic of the bars.

The positions of the bars, for each date, were compared with those closer in time. The RMS (Root Mean Square) of the differences, using the results of the red or green bands, was very low (0.47–0.59). The results of the migration of the bars are very similar and given that the visual analysis of the profiles showed greater variability with the red band, the results showed from now on will be exclusively for this band.

The magnitude of the movements of the sand bars has an error derived from the geometric correction: 3, 7 and 8 m for the periods 2003–2006, 2006–2007 and 2007–2010 respectively, this being the sum of the RMS of the images compared, except for the period 2003–2006, in which the error is due only to the image of 2006 and so the image of 2003 was taken as reference. There is no guarantee that differences of less than the error for each interval are actually due to changes in the position of the bar.

From 2003 to 2006, submerged bars migrated to the shore on an average of 8 m along the Ebro Delta. This general movement was not observed in some bars, such as Alfaques Spit, Cape Tortosa or the Trabucador bar (Fig. 3a). The highest specific migration to the coast (higher than the standard deviation minus the mean, < -60 m), occurred in the Tortosa Cape and Trabucador bar meanwhile the bars that move away from the coast are mostly situated in Los Alfaques spit.

From 2006 to 2007 average migration for the entire study area was 7 m to open sea. Only in three bars situated on the spits of the Alfaques and Fangar (Fig. 3b) was the mean motion towards the coast. The highest specific migration to the coast (< -23 m) in this period was found in the two spits and in Trabucador bar.

Among the images of 2007 and 2010 (Fig. 3c), half of the bars have an average of movement toward open sea of low intensity. The general computer shows a widespread retreat of 9 m.

Annual rates of migration were calculated to compare the intervals. It is relevant to remember that migration is not a unidirectional process. In Ojeda et al. (2008) variations of the same magnitude as in this study can be found, even occurring in a few days. There are movements of up to 69.8 m in 9.7 days (7.2 m/day) after a heavy wave storm. In the medium or long term rates may indicate a trend which can show the presence of a causal factor and its intensity.

The annual migration rates in intervals 2003–2006 and 2007–2010, for the whole Ebro Delta, are of the same intensity and direction, -3 m/year. On the other hand, for 2006–2007 the rate is doubled and changes direction 6 m/year. Images of 2003, 2006, and 2010 correspond to the low wave station, while the 2007 image has already been affected by high energy waves, which move the bar seaward, explaining the positive sign of the migration rate and that its magnitude was more than twice other intervals.

Jimenez (1996) and Rodriguez (1999) have observed how the redistribution of the sediments differs from an inflection point in the direction of both spits depending on the predominant wave direction. Aside from the inflection point, erosion is the dominant process and the bars recess of the bars while on the other side, the opposite phenomenon occurs. This phenomenon can be observed in the periods 2003–2006 and 2007–2010, while it is reversed for 2006–2007 due to the influence of strong waves. For the interval 2003–2006, in El Fangar spit this trend is not observed and there is a general advance of the bars to the coast, possibly due to the retention of sediments after the construction of a breakwater at the beginning of the spit.

The bars, present in front of the Marquesa Beach, Cape Tortosa and Trabucador Bar (Fig. 3a) have a similar behavior to the rest of areas of marine events. In Cape Tortosa, the bars show a tendency to back away due to the predominant wave incidence. Submerged bars in front of the Trabucador Bar tend to move to the continental body which was noted by Rodriguez (1999) from 1957 to 1998.

5 Conclusions

The sensitivity of the results of analysis is a function of (1) RMS of the geometric correction (2) spatial resolution (3) number of profiles obtained and (4) satellite trajectory, due to the assignation of the bar location to the center of the pixel.

The results of migration of the sand bars show how sensitive they are to coastal dynamics and human influence.

To establish a criterion to choose the dates of images and the sensor is the objective of the study and the timescale. ASTER provides a good cost-resolution ratio. However, the spatial resolution could be insufficient in short term studies, unless there are important changes between the two images.

Although results have not yet been validated, the analysis of literature that uses the methodology and consistency of results opens up new lines of research aimed at validating and improving the process, and also increases the knowledge in the subject matter. Repeating the methodology in a coastal area for which we have an accurate bathymetry could be the answer to: What wavelength and width of images give the best results? What proportion of high reflectivity values is to be fount on the bars, due to (1) a lower water column, to (2) the foam, to (3) the suspended sediments and to (4) the roughness of the waves? Is it possible to develop a computer program that automates the process?

Verifying the methodology would not be too expensive if an already existing accurate bathymetry were used, having only to buy the satellite image closest to the bathymetric survey. This minimal investment could help to reduce future costs, giving a synoptic view and generate fundamental information rapidly for coastal managers and scientists.

Acknowledgments This work was carried out under the project "Determination of morphodynamic relationships and sediment transfer mechanisms in the beach-dune system and its variation under different climatic scenarios. Application to the Ebro River delta system" funded by the Ministry of Science and Technology of the Spanish State.

References

Abrams, M. & Hook, S. (2007). Earth Remote Sensing Data Analysis Center. Aster User's Guide. Part II Version 5.1. p. 68.

Chuvieco, E. (2010). Teledetección ambiental: La observación de la tierra desde el espacio. Ariel. p. 576.

García, M. A. (1982). Aproximación al comportamiento estadístico del viento en el Delta del Ebro. Estudio de la velocidad escalar. *Investigación Pesquera*, *46* (3), 349–377.

Gould, R. W., & Arnone, R. A. (1997). Remote sensing estimates of inherent optical properties in a coastal environment. *Remote Sensing of Environment, 61*, 290–301.

Jiménez, J. A., & Sánchez-Arcilla, A. (1993). Medium –term coastal response at the Ebro delta, Spain. *Marine Geology, 114*, 105–118.

Jiménez, J. A. (1996). Evolución costera en el Delta del Ebro. Un proceso a diferentes escalas de tiempo y espacio. PhD, Universidad Politécnica de Cataluña; p. 274.

Lippman, T. C. & Holman, R. A. (1989). Quantification of sand bar morphology: A video technique based on wave dissipation, *Journal of Geophysical Research*, *94* (C1), 995–1011.

Ojeda, E., Guillén, J., & Ribas, F. (2008). Cambios morfológicos en barras sumergidas de playas artificiales. *Territoris, 7*, 7–19.

Plant, N. G. & Holman, R. A. (1998). Extracting morphologic information from field data. In *Proceedinds of the 26th International Conference on Coastal Engineering*, (pp. 2773–2784).

Ribas, F., Ojeda, E., Price, T. D., & Guillén, J. (2010). Assessing the suitability of video imaging for studying the dynamics of nearshore sandbars in tideless beaches. *IEEE Transactions on Geoscience and Remote Sensing, 48*(6), 2482–2497.

Rodríguez, I. (1999). *Evolución geomorfológica del Delta del Ebro y prognosis de su Evolución* (p. 200). Alcalá de Henares: Universidad de Alcalá de Henares. PhD.

A Brief Review of Actual Dune Dynamics Modeling: Applicability to El Fangar Dune System (Ebro Delta-Spain)

F. Barrio-Parra, I. Rodríguez-Santalla, M. Sánchez-García, and I. Montoya-Montes

Abstract

Dune systems have a complex dynamics which is difficult to model purely physical due to the no linearity of the wind shear stress estimation, the complexity of the dune systems geomorphology and the difficult to obtain real world field data to test them. Cellular models offer an interesting alternative approach with simple data entry requirements and very good reproduction of dynamic processes observed in the real world. These models can be an useful tool in the study of the dynamics of the El Fangar spit dune system. The application of these models to the dune system data will help to predict morphological evolution, identify sediment sources and sinks, study the importance of formation factors and analyze possible future scenarios focused on climate change risk assessment. The actual cellular models had not been widely applied to real world dune systems so some improvements must to be taken into account in an attempt to approximate them more closely to complex real systems: integration of wind data as the driving force of the sand saltation process, introduce the possibility of study the system dynamics under a direction and velocity changing wind regime and couple a sand supply model to the dune dynamic model.

Keywords

Sand dunes dynamics • Cellular models review

1 Brief Review of Actual Cellular Models

There are several approximations for modeling the sand dunes behavior. The physic study of this dynamics models the aerodynamic mechanisms to explain how sediment moves due to wind action (Bagnold 1941) and how the shear stress is transmitted to the dune surface and then explaining the interaction between morphology, wind and sand flux (Kroy et al. 2002a, b; Herrmann 2006). The differential equations that govern these processes are difficult to solve in a 3D real dune field, and the time and space scales are more detailed than the erosion and deposition processes that change the surface of the dune and determines the dune field dynamics. Because of these, stationary solutions for the wind field and sand flux are entered in these models (Herrmann 2006). The data demand to set up a physic model to reproduce the entire conditions of a dune field would be very exigent. Alternatively to the purely physical approach, the cellular models describe the dunes dynamics in a behavior oriented frame offering an interesting tool to geomorphologists (Werner 1995; Castro 1995; Nishimori and Tanaka 2003; Katsuki et al. 2011; Katsuki and Kikuchi 2011). These models apply a simplified algorithm whereby a height of sand is removed from each cell in an elevation array and is reallocated in other cell based on several rules.

F. Barrio-Parra (✉) · I. Rodríguez-Santalla · M. Sánchez-García · I. Montoya-Montes
Department of Biology and Geology, Rey Juan Carlos University, C/Tulipán s/n, 28933 Mostoles (Madrid), Spain
e-mail: fernando.barrio@urjc.es

Y. Huang et al. (eds.), *New Frontiers in Engineering Geology and the Environment*,
DOI: 10.1007/978-3-642-31671-5_17,

The cellular models described by Werner (1995) and de Castro (1995) consider the transport of a fixed sand mass (q_s) into downwind direction and decides if it is deposited or not at a fixed length in each iteration via generation of random numbers and comparing it with the probability of deposition (that is a model parameter).The separation bubble formed by aerodynamic processes at the leeward side of the dune is considered by the "shadow rule". This rule marks the leeward cells sheltered of wind action by higher ones under geometrical criteria. If q_s is moved to a shadow zone the probability of deposition of the sand mass increase to 1. Momiji and Warren (2000) described this process, in a physical view through the definition of the sand trapping efficiency (T_E) that is the proportion of moving sand trapped by the dune slip face. This depends on wind shear velocity on the level surface ($u_*(-\infty)$), the dune height and the sand grain diameter, but this approach could not predict the windward surface of the migrating dune by itself. This concept can be compared to the height dependence of the saltation length shown in Katsuki et al. (2011) too. Narteau et al. (2006) presented a different cellular model approach. Their model employs Poison process to domain the state of each cell in relation with its neighborhoods cells in an overall mechanism that can be regarded as a Markov chain. Nishimori and Tanaka (2003), Katsuki and Kikuchi (2011) and Katsuki et al. (2011) employs cellular models conceptually similar to the models of Werner (1995) and de Castro (1995) but these models avoid employing probabilistic parameters, so the sand mass is transported deterministically to a transport length (L_s) from the upstream face. The Eqs. 1 and 2 describes how cell height ($h(x,y)$) varies in a timestep (t). The simulations of Katsuki et al. (2011) with a constant transport length failed to create a realistic barchans with sharp horns, so a nonlinear height dependence of transport length was introduced by these authors. This dependence is in agreement with the wind speed up and sand flux saturation predicted by the purely physical models (Kroy et al. 2002b).

$$h(x,y,t) \rightarrow h(x,y,t+1) - q_s \quad (1)$$

$$h(x+L_s,y,t) \rightarrow h(x+L_s,y,t+1) + q_s \quad (2)$$

All the cellular models reviewed, except the model of Narteau et al. (2006), have an avalanche algorithm. This algorithm represents the slide down processes that occur when a repose angle is exceeded. When the local slope exceeds the repose angle, the highest and the lowest cell are located under neighborhood criteria. Then the sand volume that produces an unstable slope in the highest cell is reallocated to the nearest lowest cells in order to obtain a slope that not exceeds the repose angle. The role of vegetation cover has been introduced in cellular models as deterministic (Nishimori and Tanaka 2003) and probabilistic (Castro 1995; Pelletier et al. 2009) algorithms.

There are not very much examples of application of these models to real dune systems. Pelletier et al. (2009) applied a modified version of the Werner (1995) model to real elevation data of an aeolian dune field to explain and predict its evolution under several vegetation conditions. The results showed the power of this models to predict the dune field evolution with management proposes and to obtain quantitative and qualitative information of how the system response to different management actions (not to reproduce the exact details of the evolution of the dune system). The cellular models have demonstrated its capacity to produce almost all forms of dunes (Werner 1995; Castro 1995; Narteau et al. 2006; Barchyn and Hugenholtz 2011). The models of Katsuki et al. (2011) and Katsuki and Kikuchi (2011) have reproduced a variety of collision patterns of barchans dunes, the development of a barchans corridor from a punctual sand source (that showed the lateral migration of a sand dune due to the relative position of the sand source with respect the dune) and assessed the changes in morphology of the dunes due to the sediment mass balance. The cellular models approach for the description of these processes lacks in parameters that relate the sand transport capacity with wind data. Examples of available software of the Werner (1995) model could be found in Barchyn and Hugenholtz (2011) and in Elder (2012).

2 Applicability of Dune Models to El Fangar Dune System

El Fangar dune system is placed on the north hemidelta at the Ebro Delta (Tarragona, Spain) (Fig. 1). El Fangar spit formation is due to the transport and sedimentation of eroded material from old deltaic lobules. The Ebro Delta sedimentary dynamics and morphological evolution studies [i.e. Jimenez (1996); Jimenez et al. (1997); Rodríguez-Santalla (1999, 2000)] shows a reshaping trend with significant accretion at the end on the spit and a continued erosion in the middle-south joined to the deltaic body. El Fangar dune system is composed by 6 km of active barchan dunes. The dune field formation is related to the coast orientation and a predominant wind direction of greater intensity and frequency form 315°. The aeolian transport quantification of Serra et al. (1998) estimates an net transport of 10,000 m^3/year to the south east. This flux is incorporated to the littoral drift in the northwest direction (near one third of the drift transport).

Sánchez-García (2008) compiled temporal series of the dune field evolution via high resolution digital terrain models. This information linked with a wind data source

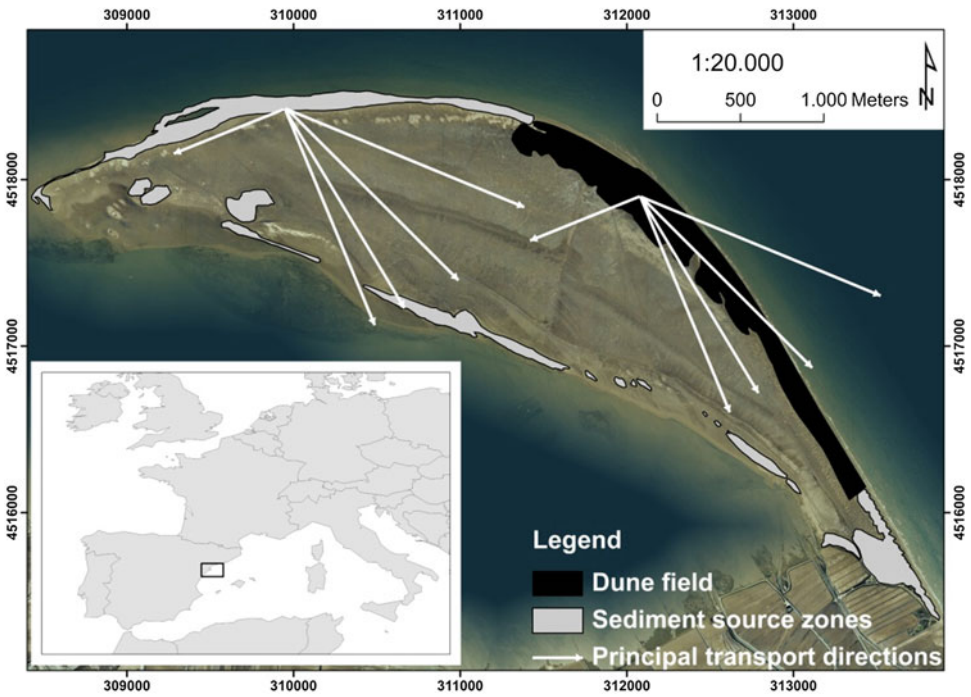

Fig. 1 El Fangar dune field location, sediment sources and principal aeolian transport directions (Sánchez-García 2008)

could be employed to set up a cellular model. These models can be a very useful tool in order to analyze the dune field behavior and to establish the sedimentary relationships among the sediment littoral transport, the assessment of the importance of sediment sources and sinks and the beach-dune interactions, as well as to identify the spit evolution key factors. This will help to establish future scenarios focused on climate change risk assessment. The existing models are not directly applicable due to the variable transport directions, the spatial configuration of the sediment source zones (Fig. 1) and the lack of an algorithm that allow to relate directly the wind data with an observed dune movement, sand catchment and erosion.

3 Improvements Needed to a "Real World Dune" Modeling

In order to apply the cellular models to a real world dune field, these should (1) introduce the variability of the sand flux with the dune height due to the shear stress changes produced in the windward dune profile by aerodynamic processes (Kroy et al. 2002a, b) introducing q_s as a function of the initial height and the shear velocity on a level surface (Momiji and Warren 2000; Herrmann 2006). The cellular models should (2) to evaluate when a cell is exposed to a wind or not due to its relative aspect to the incident wind, (3) to introduce the speed up effect (Momiji and Warren 2000) as a saltation length [function of the dune height (Katsuki et al. 2011; Katsuki and Kikuchi 2011)] and (4) as a function of the shear velocity on a level surface x and y components. The Eqs. 3 and 4 show our proposal of the saltation algorithm modification (Eqs. 1 and 2) that incorporates the improvements (1), (3) and (4) mentioned above.

$$h(x,y,t) \rightarrow h(x,y,t+1) - q_s(h(x,y,t), u_*(-\infty)) \quad (3)$$

$$h\left(x + L_{sx}(u_{*_x}(-\infty)), y + L_{sy}\left(u_{*_y}(-\infty)\right), t\right) \rightarrow h\left(x + L_{sx}, y + L_{sy}, t+1\right) + q_s \quad (4)$$

The models need to incorporate a sand influx model as a non-stationary boundary condition. An applied approach of the estimation of sediment supply from the beach to the dune can be seen in Bauer and Davidson-Arnott (2002), Bauer et al. (2009) and Delgado-Fernandez (2010, 2011).

4 Conclusions

This review shows that the existing models can reproduce the movement of sand dune fields but it is necessary to incorporate parameters to relate wind data with the sand saltation process under variable wind regimes and couple it with existing sand supply models in order to predict the movement of real sand dune fields.

Acknowledgments This work was carried out under the project "Determination of morphodynamic relationships and sediment transfer mechanisms in the beach-dune system and its variation under different climate scenarios. Application to the Ebro River delta system" funded by the Ministry of Science and Technology of Spanish State.

References

Bagnold, R. (1941). *The physics of blown sand and desert dunes*. London: Methuen.

Barchyn, T., & Hugenholtz, C. (2011). A new tool for modeling dune field evolution based on an accessible, GUI version of the Werner dune model. *Geomorphology, 138*(1), 415–419.

Bauer, B., & Davidson-Arnott, R. (2002). A general framework for modeling sediment supply to coastal dunes including wind angle, beach geometry, and fetch effects. *Geomorphology, 49*(1–2), 89–108.

Bauer, B., Davidson-Arnott, R., Hesp, P., et al. (2009). Aeolian sediment transport on a beach: Surface moisture, wind fetch, and mean transport. *Geomorphology, 105*(1–2), 106–116.

Castro, F. (1995). Computer simulation of the dynamics of a dune system. *Ecological Modelling, 78*(3), 205–217.

Delgado-Fernandez, I. (2010). A review of the application of the fetch effect to modelling sand supply to coastal foredunes. *Aeolian Research, 2*(2–3), 61–70.

Delgado-Fernandez, I. (2011). Meso-scale modelling of aeolian sediment input to coastal dunes. *Geomorphology, 130*(3–4), 230–243.

Elder, J. (2012). Models of dune field morphology. Retrieved February 20, 2012, from http://web.ncf.ca/jim/sand/dunefieldMorphology/index.html

Herrmann, H. (2006). Pattern formation of dunes. *Nonlinear Dynamics, 44*(1–4), 315–317.

Jimenez, J. (1996). Evolución costera en el Delta del Ebro. Un proceso a diferentes escalas de tiempo y espacio. PhD thesis, Univ Technol Barcelona, Barcelona (Spain).

Jimenez, J., Sánchez-Arcilla, A., Valdemoro, H., et al. (1997). Processes reshaping the Ebro delta. *Marine Geology, 144*(1–3), 59–79.

Katsuki, A. & Kikuchi, M. (2011). Simulation of barchan dynamics with inter-dune sand streams. *New Journal of Physics 13*(6), 063049 8.

Katsuki, A., Kikuchi, M., Nishimori, H., et al. (2011). Cellular model for sand dunes with saltation, avalanche and strong erosion: Collisional simulation of barchans. *Earth Surface Processes and Landforms, 36*(3), 372–382.

Kroy, K., Sauermann, G., & Herrmann, H. (2002a). Minimal model for sand dunes. *Physical Review Letters, 88*(5), 054301.

Kroy, K., Sauermann, G., & Herrmann, H. (2002b). Minimal model for aeolian sand dunes. *Physical Review E—Statistical, Nonlinear and Soft Matter Physics, 66*(3 Pt 1), 031302.

Momiji, H., & Warren, A. (2000). Relations of sand trapping efficiency and migration speed of transverse dunes to wind velocity. *Earth Surface Processes and Landforms, 25*(10), 1069–1084.

Narteau, C., Lajeunesse, E. & Métivier, F. et al (2006). Modelling of dune patterns by short range interactions. River, Coastal and Estuarine Morphodynamics, *2*,1035–1046.

Nishimori, H., & Tanaka, H. (2003). *Simple model for the complex dynamics of dunes* (pp. 87–100). : Concepts and Modelling in Geomorphology International Perspectives.

Pelletier, J., Mitasova, H., Harmon, R., et al. (2009). The effects of interdune vegetation changes on eolian dune field evolution: a Numerical-modeling case study at Jockey's Ridge North. *Earth Surface Processes and Landforms, 1254*, 1245–1254.

Rodríguez-Santalla, I. (1999). Evolución geomorfológica del delta del Ebro y prognosis de su evolución. PhD thesis, Departamento de Geografía, Universidad de Alcalá de Henares, Alcalá de Henares (Spain).

Rodríguez-Santalla, I. (2000). Proyecto de actuación medioambiental en el entrono de la península del Fangar, Playa de la Marquesa y Playa de Pal en el Delta del Ebro. Estudio de Impacto Ambiental, Madrid (Spain).

Serra, J., Maia, L. & Bautista, R. (1998). Aeolian contribution to the sediment budget along the coast of the Ebro delta. *In 15th International Congress of Sedimentology*, Alicante, Spain.

Sánchez-García, M. (2008). Evolución y análisis morfodinámico del campo dunar de la Flecha del Fangar (Delta del Ebro). PhD thesis, Departamento de Biología y Geología, Universidad Rey Juan Carlos, Madrid (Spain).

Werner, B. (1995). Eolian dunes: Computer simulations and attractor interpretation. *Geology, 23*, 1107–1110.

Transportation of Huanghe River-Discharged-Suspended Sediments in Nearshore of Huanghe River Delta in Conditions of Different Estuary Channels

X. H. Xue, G . S. Li, and L. Y. Yuan

Abstract

Periodical estuary-channel diversion, which intensely affects the coastal environment near Huanghe River Delta (HRD), is an important character of Huanghe River. To understand the differences in Huanghe river-suspended sediments (HRSS) transport in the nearshore of HRD under different estuary-channel conditions, Transportations of HRSS in conditions of two estuary channels were compared by numerical simulations. Results showed that longshore-transport pathways of HRSS, and thus the primarily HRSS-influenced coastal waters, were extremely varied in two estuary-channel conditions, that the dispersion area and distance of HRSS in condition of Diaokou Channel was larger and longer than that in condition of Qingshuigou Channel, and that HRSS transported from estuary to outer offshore was stronger in condition of Diaokou Channel than that in condition of Qingshuigou Channel. HRSS transport along longshore-transport pathways was also stronger in condition of Diaokou Channel than that in condition of Qingshuigou Channel.

Keywords

Estuary channel diversion • Sediment transport • The Huanghe River • The Bohai Sea

1 Introduction

Channel change is an important aspect of geomorphologic evolution in large alluvial rivers (Thad et al. 2004). The estuary channel of Huanghe River has experienced 50 times of shift ever since it re-entered the Bohai Sea in 1855 (Pang and Si 1979). Researchers has pointed out that the service life of every estuary channel of Huanghe River is limited (Wang et al. 2001), and that large-scale shift is unavoidable in the long term(Li et al. 2007). Frequent and large-scale shifts of estuary channel can deeply affects the coastal environment along Huanghe River Delta (HRD). One important factor is variation in the transport of Huanghe River-suspended sediment (HRSS) under conditions of different estuary channels. Although some studies have noted these problems, a clear knowledge on them, such as changes in transport direction, transport pathways, dispersion range and transport capacity, is unavailable.

The differences of hydrodynamics at different estuary and adjacent nearshore (Li 1990; Xue et al. 2011) make it possible for HRSS transport to be varied if estuary channel is changed (Ren & Shi 1991; Ren 2006). Studies in many fields, such as erosion and deposition (Li et al. 2002; Zhao 2006), remote sensing images (Huang et al. 2005), suspended materials content (Yang et al. 1991) and distribution of Huanghe River-diluted water (Shen and Le 1993), have also indentified those variations. But a detailed description on them is still needed.

Taking two typical estuary channels (Diaokou Channel and Qingshuigou Channel, which respectively entered the Bohai Sea at the north and the west of HRD) in their early

X. H. Xue (✉) · L. Y. Yuan
Department of Gardening and Horticultural, Yangtze University, No.88, Jingmi Road, Jingzhou 434025, China

G .S. Li
Institute of Geographic Sciences and Natural Resources Research, CAS, Beijing 100101, China

Y. Huang et al. (eds.), *New Frontiers in Engineering Geology and the Environment*,
DOI: 10.1007/978-3-642-31671-5_18,

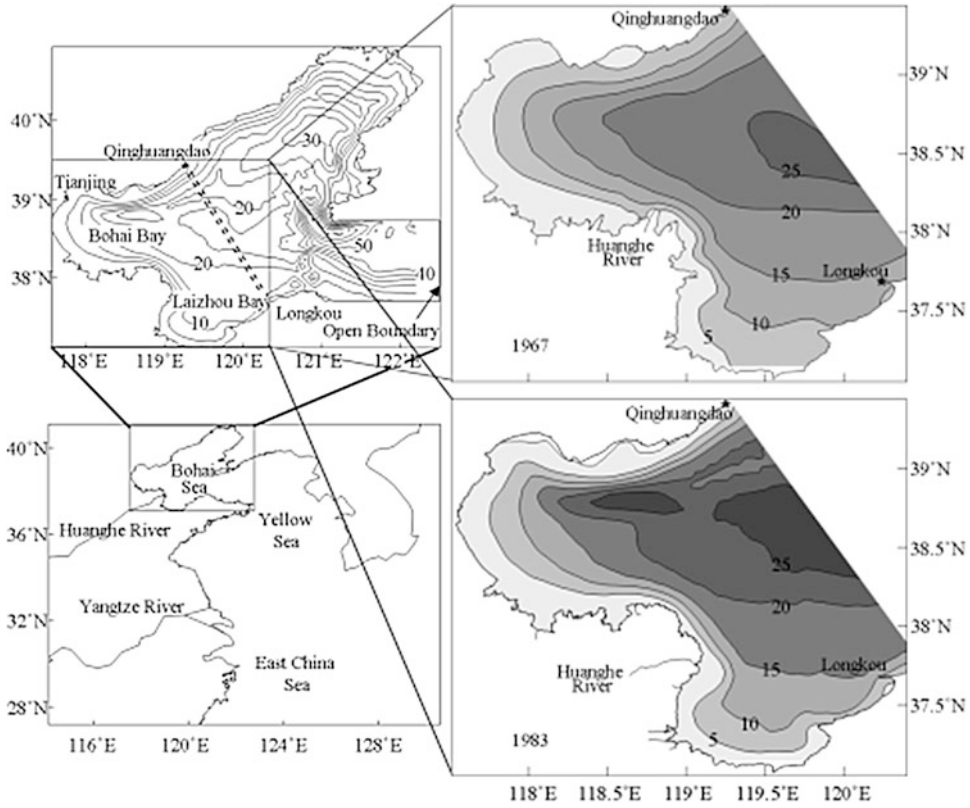

Fig. 1 Study area and its subaqueous landform

serving periods as an example, this paper compared HRSS transport in the nearshore of HRD by two numerical comparative tests.

2 Methods and Model Validation

2.1 Method

Two comparative numerical tests, in accordance with the boundary conditions of Diaokou Channel and Qingshuigou Channel, were designed: (1) as to coastline and coastal subaqueous landform (Fig. 1), the 1:50,000 topographic map in 1967 was used for condition of Diaokou Channel (test A), and water-depth data surveyed in 1983 was used for condition of Qingshuigou Channel (test B); (2) the location of river mouth in test A and B were respectively set at Diaokou (118.81°E, 38.15°N) and Qingshuigou (119.09°E, 37.74°N); (3) other model conditions and parameters were the same and detailed in the following section.

2.2 Data and Model Settings

Based on the Coastal Ocean Model with Sediment Transport (ECOMSED) model (Blumberg and Mellor 1987), test A and B for the simulation of hydrodynamics field and sediment transport were run. Study area in this paper is the nearshore along HRD (Fig. 1). But the modeling area contained the entire Bohai Sea, and the open boundary was set at the Bohai Strait to avoid the bad effect of imprecise water-level, velocity and temperature at open boundary on sediment transport.

Boundary and initial conditions for numerical calculation were achieved as follows: (1)sea surface forcing fields 1982–1984, including wind and heat flux, were got from NCEP/NCAR Reanalysis2 dataset (NOAA/OAR/ESRLPSD 2008); (2) the runoff and sediment load measured at Lijin Hydrometric Station (118°18′E, 37°31′N) during 1982–1984 was used as the Huanghe River flow and sediments delivered into the Bohai Sea, and the raw sediment data was amended by multiplying 70 %; (3) salt and temperature conditions were achieved from the "Marine Atlas of Bohai Sea, Yellow Sea and East China Sea" (Editorial Board for Marine Atlas 1993); (4) water level at open boundary was calculated from tidal parameters of 6 tidal components, including S_2, M_2, N_2, K_1, P_1 and O_1.

By using researches in study area (Lü et al. 2003; Gu et al. 2005) for reference and by adjustment calculation, parameters of bottom friction coefficient, horizontal mixing coefficient, vertical mixing coefficient and bottom roughness were respectively set to 0.0036, 0.1, 0.000001 and

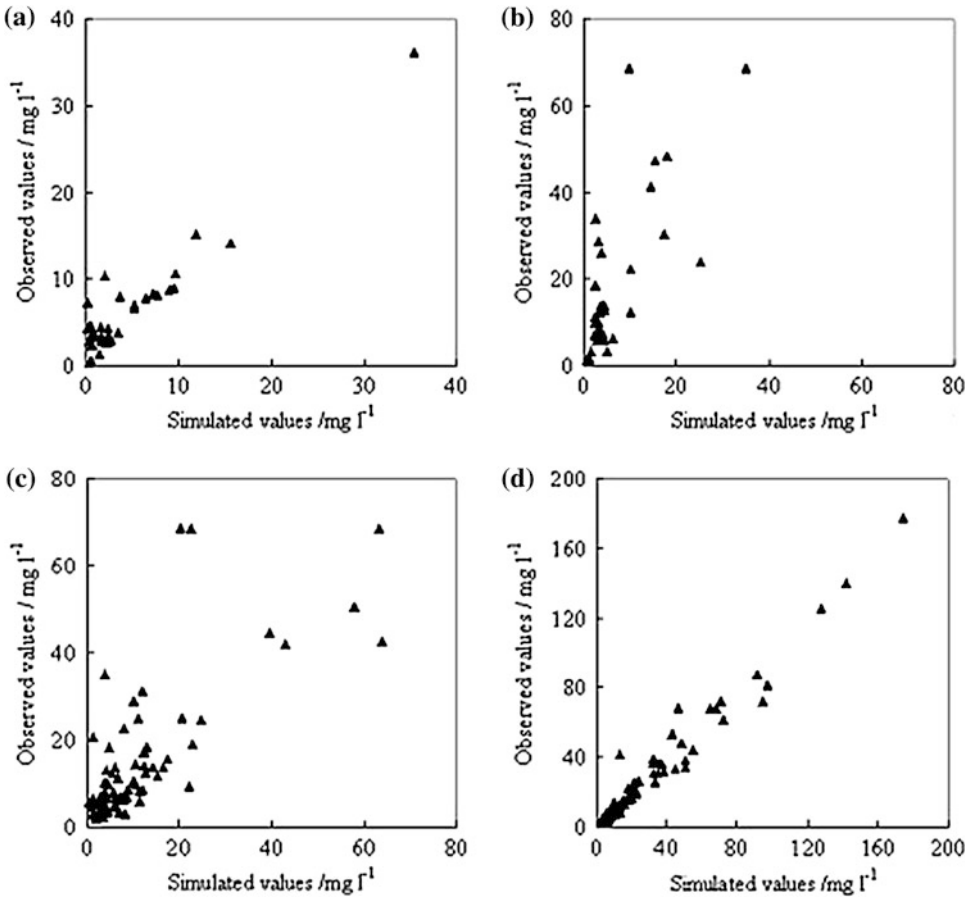

Fig. 2 Validation for sediment-concentration (a) at surface layer in Aug. and Sep., (b) at surface layer in Jan., (c) at middle layer, and (d) at bottom layer

0.0001 m. Reid and Bodine boundary condition was used as open boundary condition. Horizontal mixing process was calculated by Smagorinsky equation.

Parameters for the simulation of cohesive sediment flocculation and settling involving constants α, β, and minimum bottom shear stress $\tau_{b,\min}$ were respectively set to 2.42, 0.22 and 1 dynes cm^{-2}. In cohesive-sediment resuspension calculation, τ_c(critical shear stress for erosion) from first to the seventh layer were 1.1, 2.0, 3.0, 4.0, 5.0, 6.0 and 8.0 dynes cm^{-2}; the dry density of sediment bed was 1.1 g cm^{-3}; values of a_0, *m and n* were respectively 2.0, 0.5 and 2.0; bottom friction coefficient of cohesive sediment and bottom roughness were set to 0.0036 and 0.001 m.

2.3 Model Validation

Validation for tide and tidal current in modeling area has carried out in previous work (Li et al. 2005; Xue et al. 2011) which identified the effectiveness of numerical hydrodynamic model used in this paper.

Sediment data transformed from turbidity which was measured at 73 stations in the summer of 2000 and in the winter of 2001 was used for suspended sediment concentration (SSC) validation. Using conditions of runoff discharge, sediment, coastal landform and wind field during 1999-2001, a numerical test for sediment-validation was run. Fig. 2 shows that there is good agreement between the simulated and the observed values. For SSC at surface layer, the simulated results in August and September have good consistence with the observed (Fig. 2a), but have less consistence in January (Fig. 2b). Correlation coefficient for bottom layer (Fig. 2d) amounts to 98.8 % with $R^2 = 0.96$. Correlation coefficient for middle layer (Fig. 2c) is 76 % with $R^2 = 0.57$.

3 Results and Discussion

3.1 Comparisons on the Pathways and Ranges of HRSS-transport in the Nearshore of Huanghe River Delta

As shown in Fig. 3, HRSS mainly moves to the two sides of river mouth and then transport along the longshore of HRD in both estuary-channel conditions. Sediment transport at the direction of river discharge is weak and not far. There are two basic longshore-transport pathways in the two

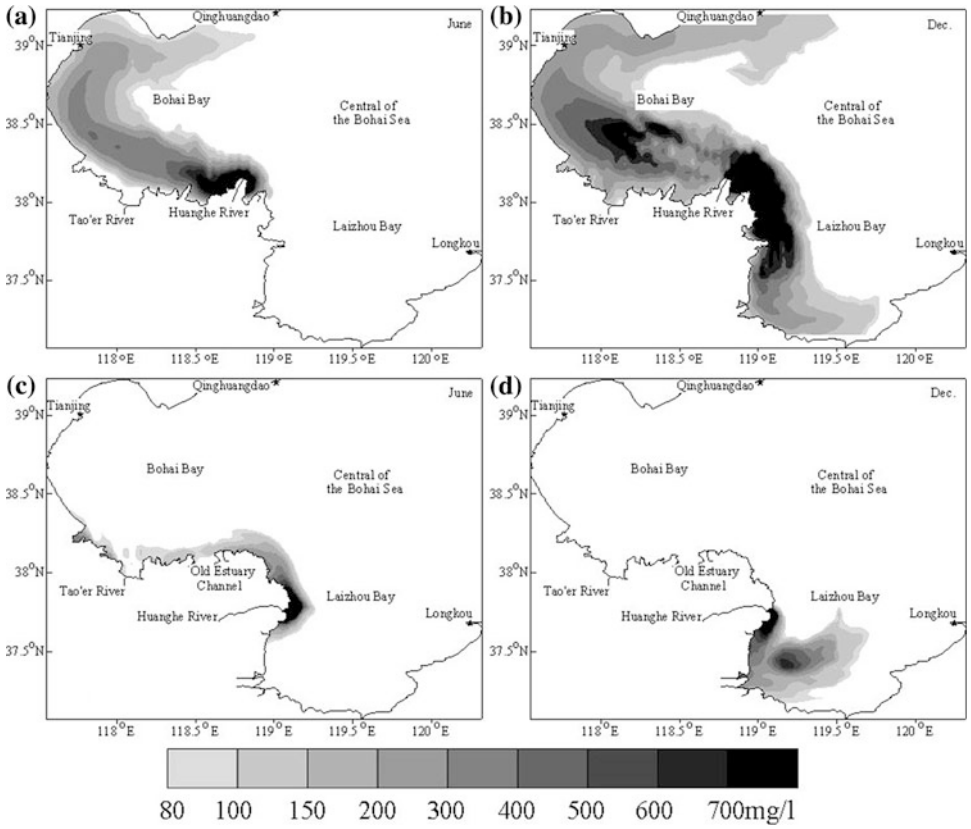

Fig. 3 Sediment distribution at middle layer of study area under condition of Diaokou Channel (a ~ b) and Qingshuigou Channel (c ~ d)

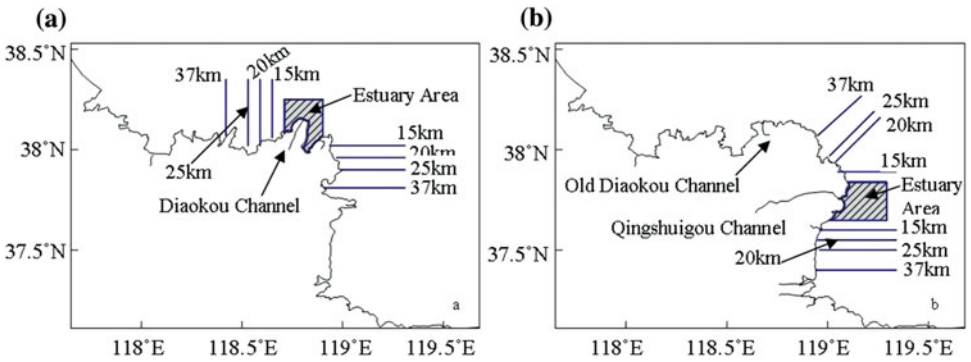

Fig. 4 Sections for the comparison of HRSS-transport capacity (a) in condition of Diaokou Channel and (b) in condition of Qingshuigou Channel

different conditions, respectively. Change of the location of river mouth leads to large difference in transport pathway and transport distance, which results in variation of HRSS-affected zone.

In condition of Diaokou Channel, HRSS moves to the west side of river mouth and then transports along south shore of Bohai Bay in summer (Fig. 3a), that is the longshore transport pathway along Bohai Bay (LTPBB). By another longshore transport pathway along west shore of Laizhou Bay (LTPWLB), HRSS moves to the east side of river mouth and then transports southward along the west shore of Laizhou Bay in winter (Fig. 3b).

In condition of Qingshuigou Channel, HRSS moves northeastward and then turns northwest in summer(Fig. 3c), that is, the longshore transport pathway at north of river mouth (LTPNRM). Partial HRSS can enter the Bohai Bay and move westward along the south shore of Bohai Bay. By another longshore transport pathway at south of river mouth (LTPSRM), HRSS moves to the south side of river mouth and transports southward along the west shore of Laizhou Bay. But after a non-far southward transport, sediments turn northeast.

The above transport patterns of HRSS shows that influence of HRSS on the Bohai Bay is much larger than that on the Laizhou Bay in condition of Diaokou Channel. Contrarily, HRSS, most of which disperses in the Laizhou Bay, has littler effect on the Laizhou Bay. In addition, the dispersion area of HRSS in condition of Diaokou Channel is

much broader than that in condition of Qingshuigou Channel. But their differences in sediment offshore-dispersion distance are not obvious. Therefore, the longshore-transport distance of HRSS in condition of Diaokou Channel is much longer than that in condition of Qinghshuigou Channel.

3.2 Comparisons on the Transport Capacities of HRSS in the Nearshore of Huanghe River Delta

To understand differences in HRSS transport capacity between conditions of two different estuary channels, their differences at estuary area and offshore along transport-pathway are separately discussed. Estuary area is defined by a section (20 km from river mouth) perpendicular to direction of run-off flowing and by two cross sections (10 km from river mouth) at two sides of river mouth (Fig. 4). To quantify the transport capacities along pathways, four cross sections which are respectively 15, 20, 25 and 37 km from river mouth are set(Fig. 4).

As to transport capacity in estuary area, HRSS transported out estuary area in condition of Diaokou Channel amounts to 35.2 % of sediment discharge, but it is only 14.7 % in condition of Qingshuigou Channel. In condition of Diaokou Channel, HRSS transported to west side of river mouth is much larger than that transported to east side of river mouth. In condition of Qingshuigou Channel, there is no evident difference between amounts of HRSS transported to south and north sides of river mouth.

As to transport capacities along longshore-transport pathways, the total transport capacity along two basic longshore-transport pathways in condition of Diaokou Channel is much stronger than that in condition of Qingshuigou Channel, but their difference decreases with increase of transport distance. In condition of Diaokou Channel, 74.7 % of HRSS that move out estuary are transported through the cross-section that is 15 km from river mouth, but it is only 50 % in condition of Qingshuigou Channel. HRSS transported through four sections that are separately 15, 20, 25 and 37 km from river mouth in condition of Diaokou Channel is respectively 2.7, 2.3, 2.3 and 1.7 times that in Qingshuigou Channel condition.

HRSS-transport along the Bohai Bay (LTPBB) plays a dominant role in condition of Diaokou Channel, transportation along west shore of Laizhou Bay (LTWLB) is much weaker. Amounts of HRSS transported through four cross-sections, which are set at pathway of LTPBB and are separately 15, 20, 25 and 37 km from river mouth, are 4.5, 3.9, 3.0 and 1.1 times that along LTWLB, respectively. In condition of Qingshuigou Channel, difference in the transport capacities between two basic pathways is much less.

4 Conclusions

Differences in the transportation of Huanghe River-suspended sediments discharged by different estuary channels are important for understanding influence of estuary-channel shift on coastal environment. Numerical simulation for Diaokou Channel and Qingshuigou Channel evidently revealed these differences in the transport pathway, dispersion range and transport capacity.

Transportation along south shore of Bohai Bay and transportation along west shore of Laizhou Bay are the two longshore-transport pathways of HRSS in condition of Diaokou Channel. Northward transport along west shore of Laizhou Bay and another pathway by which HRSS turns northeast after a non-far southward movement are the two longshore-transport pathways for condition of Qingshuigou Channel. Influence of HRSS on the Bohai Bay is larger than on the Laizhou Bay in condition of Diaokou Channel. Contrarily, influence of HRSS on the Laizhou Bay is primary in Qingshuigou condition. The dispersion area and transport distance of HRSS in condition of Diaokou Channel is much larger than that in condition of Qingshuigou Channel.HRSS transported from estuary to outer offshore in condition of Diaokou Channel is much more than that in condition of Qingshuigou Channel. The transport capacity along longshore-transport pathways in condition of Diaokou Channel is also stronger than that in condition of Qingshuigou Channel.

Acknowledgments This work was sponsored by Yangtze University Start-up Foundation (Grant No. CJDX-D2010196) and the National Natural Science Foundation, China (No. 40771030, No. 40571020 and No. 31170400).

References

Blumberg, A. F., & Mellor, G. L. (1987). A description of a three-dimensional coastal ocean circulation model. In N. Heaps (Ed.), *Three-Dimensional Coastal Ocean Models*. Washington: Coastal and Estuarine Sciences, American Geophysical Union.

Editorial Board for Marine Atlas. (1993). *Marine atlas of Bohai Sea, Yellow Sea and East China Sea (Hydrology sub-atlas)*. Beijing (In Chinese): China Ocean Press.

Gu, Y., Wu, Z. K., Lü, X. Q. (2005). Estimation of bottom friction coefficient for a 2-D nonlinear tidal model of the Bohai Sea by the adjoint method. *Transaction of Oceanology and Limnology,* (3), 1–7(In Chinese).

Huang, H. J., Li, F., Pang, J. Z., et al. (2005). *Study on the interaction between Huanghe River and Bohai Sea and Yellow Sea*. Beijing (In Chinese): Science Press.

Li, F. Y., Gao, S., Jia, J. J. (2002). Contemporary deposition rates of fine-grained sediment in the Bohai and Yellow seas. *Oceanologia Et Limnologia Sinica*, *33*(4), 364–369 (In Chinese).

Li, G. S., Wang, H. L., & Li, B. L. (2005). A model study on seasonal spatial-temporal variability of the Lagrangian residual circulation in the Bohai Sea. *Journal of Geographical Sciences, 15*(3), 273–285.

Li, Z. G. (1990) Flow field outside estuary of the Yellow River and its characteristics. *Yellow River*, *12(*4), 31–36 (In Chinese).

Li, Y. F., Wu, C. P., Wang, D. C., et al. (2007) Analysis on estuary regulation of Yellow River. *Water Resources and Hydropower Engineering*, *38*(10), 21–23 (In Chinese).

Lü, X. Q., Tian, J. W., & Wu, Z. K. (2003). The bottom friction coefficients of the Bohai Sea and the Huanghai Sea. *Acta Mechanica Sinica, 35*(4), 465–468.

NOAA/OAR/ESRLPSD, Boulder, Colorado, USA (2008). http://www.esrl.noaa.gov/psd/data/gridded/data.ncep.ranalysis2.html. Accessed: 20 June 2008.

Pang, J. Z., Si, S. H. (1979). The estuary changes of Huanghe River I: changes in modern time. *Oceanologia Et Limnologia Sinica*, *10*(2), 136–142 (In Chinese).

Ren, M. E. (2006). Sediment discharge of the Yellow River, China: Past, Present and Future—A Synthesis. *Advances in Earth Science*, *21*(6), 551–563 (In Chinese).

Ren, M. E., & Shi, Y. L. (1991). Sediment discharge of the Huanghe River and its effect on sedimentation of the Bohai Sea and the Yellow Sea. *Chinese Geographical Science, 1*(1), 1–18.

Shen, Z. L., Le, K. T. (1993). Effects of the Yellow River estuary location changes on its hydrochemical environment. *Studia Marina Sinica* (34), 93–105 (In Chinese).

Thad, A. W., Shawn, A., & Liu, P. S. (2004). Geomorphic context of channel locational probabilities along the Lower Mississippi River. *USA. Geomorphology, 63*(3–4), 145–158.

Wang, K. R., Yao, W. Y., Zhang, X. F., et al. (2001). Status and harness of the Yellow River estuary. *Marine Sciences, 25*(10), 52–54.

Xue, X. H., Li, G. S., & Wang, H. L. (2011). A numerical comparative study on residual currents along the Yellow River Delta during two different estuary channel: a typical case of early periods of Diaokou and Qingshuigou channel. *Marine Science Bulletin, 30*(2), 141–150.

Yang, G. F., Li, P., & Zhang, J. Y. (1991). *Deposition along the Huanghe River Delta and Dispersion of Huanghe River-Delivered Sediments* (pp. 195–206). Beijing: Geology Press.

Zhao, G. L. (2006). Study on the longshore sediment transport and coastal erosion situation in the modern Yellow River Delta area. *Coastal Engineering, 25*(2), 29–38.

3D Sediment Physical Model Test Study for PLTU 2 JATENG 1 × 660 MW Adipala, Cilacap, Indonesia

F. Gao, H. B. Chen, and Y. Luo

Abstract

Adipala 1 × 660 MW power plant stands between Serayu River mouth and Bengawan River mouth, about 15 km east of Cilacap city, south Java Island, Indonesia. Marine structures constructed for the coal-fired power plant, include unloading wharf, breakwaters, C. W inlet, C. W outlet and other relevant structures. In order to improve and optimize design plane layout, it is necessary to forecast sediment movement. According to the Hydro-meteorology, sediment survey data and design option, based on the results of wave, current numerical models and sediment movement analysis, the siltation mechanism of harbor basin is analyzed. On the basis of verifying the siltation of opening channel and harbor basin on S2P CFPP (nearby this project), the siltation after project constructed and the effect of alongshore sediment is tested. Because of weakly tidal current (maximum velocity of field survey is less than 0.30 cm/s) and sediment concentration (less than 0.01 kg/m^3), the movable-seabed physical model(Horizontal scale is 120, vertical scale is 60) test is carried out under the wave action due to the strong swell and long wave period (exceed 10 s). The results shows that siltation thickness is about 0.02–1.91 m/a (the average value is 0.52 m/a) and the deposition volume is about 16.8 × 104 m^3/a in harbor basin after project constructed. And, siltation happened at the root of west breakwater, but it will be more than 30 years when the long-shore sediment transport around the breakwater's head.

Keywords

Sediment • Physical model • Deposition • Wave

1 Introduction

Adipala 1 × 660 MW power plant stands between Serayu River mouth and Bengawan River mouth, about 15 km east of Cilacap city, south Java Island, Indonesia (see in Fig. 1).

Marine structures constructed for the coal-fired power plant, include unloading wharf, breakwaters, C.W inlet, C.W outlet and other relevant structures. In order to verify the design plane layout, it is necessary to forecast sediment movement. Based on survey data and analysis on the characteristic of sediment in project area, moveable-bed physical model test have been carried out to simulate the sedimentation in dredged navigation channel and harbor basin.

F. Gao (✉) · H. B. Chen
Key Laboratory of Engineering Sediment of Ministry of Communications, Research Institute for Water Transport Engineering, Tianjin 300456, China
e-mail: seal326@163.com

Y. Luo
China National Technical Import and Export Corp, Beijing 100055, China

Y. Huang et al. (eds.), *New Frontiers in Engineering Geology and the Environment*,
DOI: 10.1007/978-3-642-31671-5_19,

Fig. 1 Location of Adipala power plant project

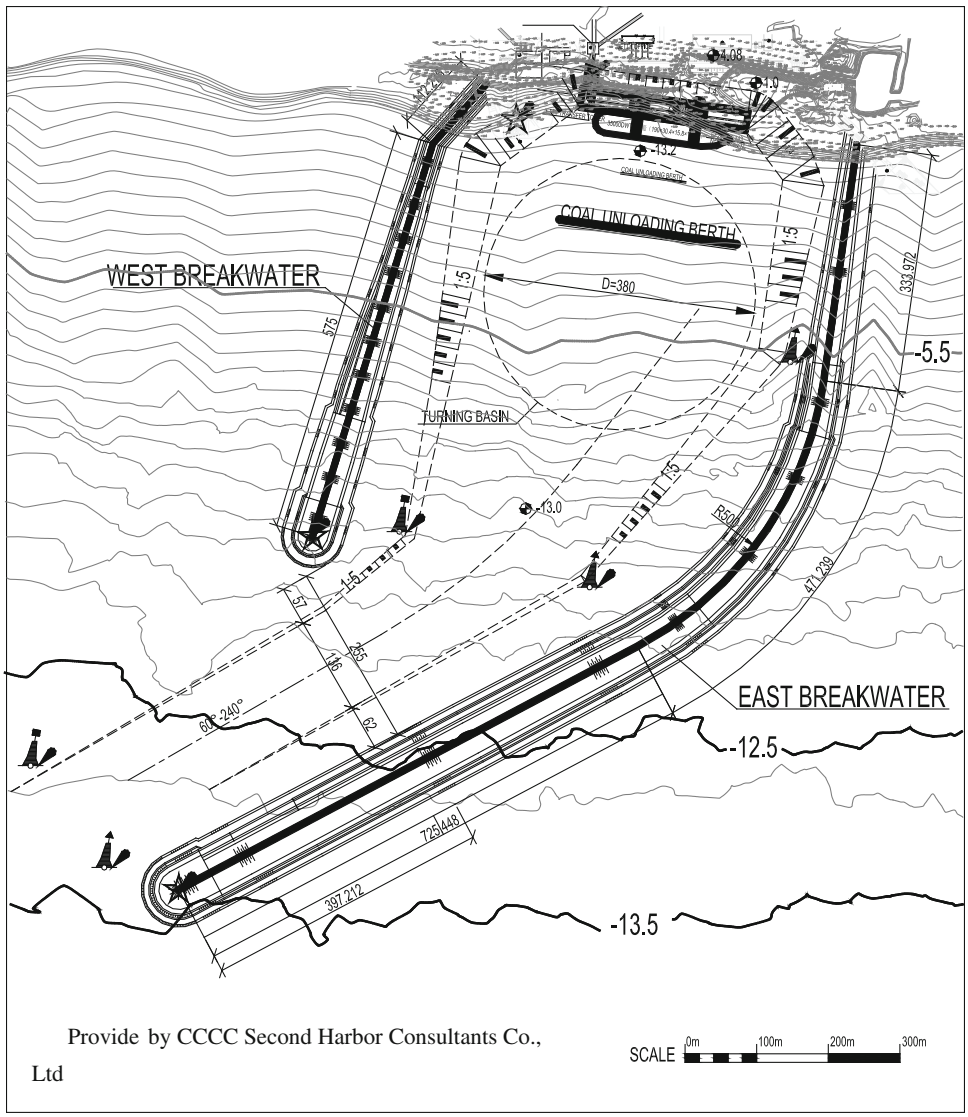

Fig. 2 Plane layout of design

Table 1 The eigenvalue on tidal level

Design water level(m)		Remarks
Design high water level	1.18	10 % high water frequency + storm surge
Design low water level	−0.83	90 % low water frequency
Mean sea level	0.00	MSL
Mean high water level	0.47	MHWL
Mean low water level	−0.52	MLWL
Mean tidal range	1.00	–

Table 2 The wave result at point of −40 m isobathe

Return period	$H_{13\ \%}$(m)	T_s(s)
Design wave	7.07	18.30
Ordinary wave	4.24	15.19

2 Foundation of Test Study

2.1 Plane Layout of Design

On the basis of former work, one plane layout is recommended, see Fig. 2. The design wharf berth is 35,000 DWT, the channel direction is 60–240°and the width is 136 m.The bottom elevation of channel is −13.0 m, the west breakwater(575 m long) head lies in −10.5 m, and east breakwater(1530 m long) head is −13.3 m. The inlet is located at harbor basin and outfall is located at the eastern of east breakwater foot.

2.2 Natural Condition

2.2.1 Tide and Current

According to the analysis on the tidal level of two stations (Dec. 2009–Jan. 2010), the result indicates that the tidal type is mixed tide with mainly semidiurnal tide. There are two high levels and two low levels during one day. And the diurnal inequality is obvious. Average flood tide duration is 6.3 h and average ebb tide duration is 6.2 h. Important water level result for project design is shown in Table 1. The maximum current speed is 0.26 m/s, and average flood velocity is 0.10–0.11 m/s, ebb velocity is 0.08 m/s.

2.2.2 Wave

According to the forecast data of national weather station and the description of local fisherman, the wave height in rainy season is small and those in dry season is strong, especially July and August. The maximum wave height can reach to 4.0–5.0 m. The survey (January. 2010) data shows the average wave height in project area is about 3.0–4.0 m. These indicate the wave is strong in project area. According to the result of wave numerical model, wave height and wave period of different return period at −40 m isobath is shown in Table 2.

2.2.3 Sediment

The sediment source mainly includes three parts, the first comes from the river nearby the project; the second comes from wave and current action; the third comes from ocean transportation and people activity. The SSC was measured during the site survey in Dec. The value is 0.0028–0.0074 kg/m^3 in projecr area, and 0.591–11.258 kg/m^3 in the area of estuary and wave breaking zone in offshore. The bottom material samples are analyzed by PW4400/40X ray fluorescence spectrometer in laboratory. Sea-bed sediments in this area contain SiO_2, Al_2O_3, CaO, MgO, K_2O, Na_2O, TiO_2, P_2O_5, MnO and TFe_2O_3 and other components, in which SiO_2 and TFe_2O_3 is the main component. The content of TFe_2O_3 of beach samples is up to 40 %, thus the density of sediment in this area reaches 2.77–2.96 g/cm^3.The density is more heavy than nature quartz sand (2.65 g/cm^3). The range of median grain size (D_{50}) is 0.0063–0.2502 mm in project area, and the average value is 0.0926 mm. The main component of samplings in this area is sand, and the proportion is about 68.1 %. Clay is about 27.1 %, and gravel is about 4.8 %. The range of median grain size (d_{50}) is 0.1312–0.7788 mm in breaking zone, and the average value is 0.3123 mm. The main component of samplings in this area is sand, and the proportion is about 93.7 %. Silt is about 3.9 %, and clay is about 1.7 %. The range of median grain size (d_{50}) is 0.0732–0.7838 mm at Searyu river, and the average value is 0.3484 mm. The main component of samplings is sand, and the proportion is about 93.4 %. Silt is about 5.2 %, clay is about 0.7 %.

3 Movable Bed Physical Model

3.1 Model Design

3.1.1 Scale and Layout

According to the test ground and the requirement of wave physical model test, the plane scale (λ_l) is confirmed as 120,

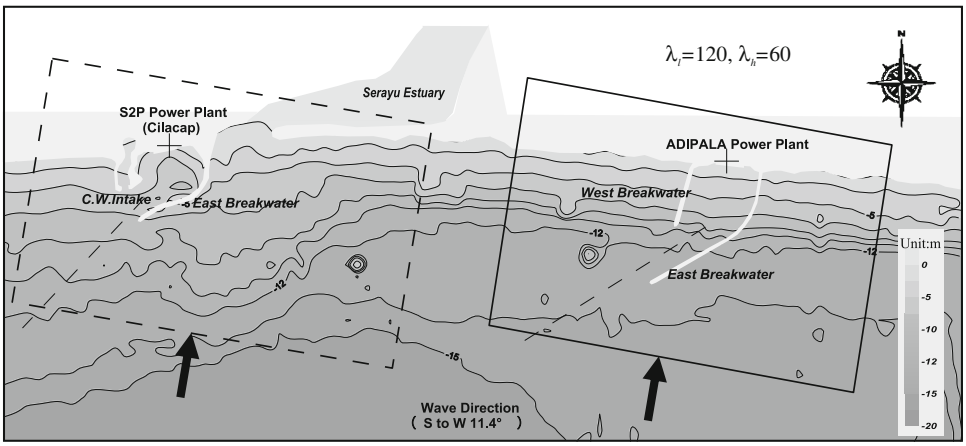

Fig. 3 The model range and plane layout

Table 3 The main scale relation in physical model test

Scale item	Sign	Calculate value	Adopt value
Horizontal	λ_l	/	120
Vertical	λ_h	/	60
Wave lengh	λ_L	/	60
Wave period	λ_T	$\sqrt{60}$	$\sqrt{60}$
Wave velocity	λ_C	$\sqrt{60}$	$\sqrt{60}$
Track velocity	λ_u	$\sqrt{60}$	$\sqrt{60}$
Grain density	$\lambda_{\rho s}$	1.93	1.93
Grain size	λ_D	1.022	1.0
Settling velocity	λ_ω	3.87	2.0

the vertical scale (λ_h) is 60, the rate is two, less than five (Wave model test regulation 2001). The model design plane layout is shown in Fig. 3. Model sediment selection is the key step to moveable physical model test.

3.1.2 Model Sediment Selection

According to the sediment median grain diameter of project area and similarity criterion (Technical regulation of modelling for tide-current and sediment on coast and estuary 2010; China professional committee 1992), the different model sediment grain diameter scale satisfied with initiating similarity and scouring and siltation location similarity synchronously(Cao 1992; Dou 2001) had been calculated. Bakelite powder (the density is1.45 g/cm^3) can satisfy with initiating similarity and scouring and siltation location similarity and sedimentation similarity. So, bakelite powder is confirmed as model sediment, the average grain diameter scale is 1.0. Of course, the above confirmed scale is primary, it will be modified and verified in the final test according to the model sediment transportation.

The final scale relation for physical model is shown in Table 3.

3.1.3 Simulation

- Wave: irregular wave is adopted in wave sediment physical model test (see in Fig. 4). The representing wave direction is 11.4 (from south to west),the representing wave height of this area is 1.75 m. Known from the calculating results of initiating wave height, when the wave height is 0.5 m (the wave period is 12 s),the sedimentation at the location of 7.5 m water depth can initiate. So wave is the main hydrodynamic factor, the above representing wave height calculated can satisfy with the requirement of initiating.
- Estuary: according to the analyzing results of numerical model, the flow dynamic of project area is feeble, the sediment coming from the estuary will disperse like fan shape under wave action, after project constructed, the sediment volume of long-shore transportation will change and the sand dam will be clashed out. Thus, the sediment coming from the Serayu River will disperse to the project area quickly, more earlier than before the sand dam clashed out. So, the estuary of Serayu will be simulated in the physical model test. The flux, sand dam and bottom material of Serayu River have been considered.

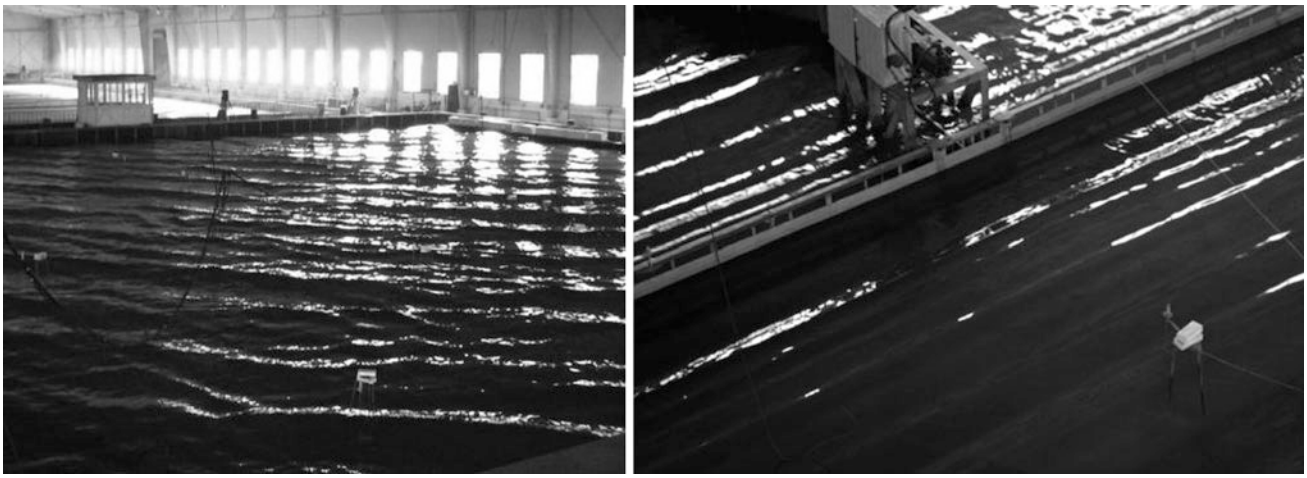

Fig. 4 Irregular wave generator in physical model test basin

- Sediment: The model sediment have been paved up at the range from the surf zone to the mouth of breakwater. So, two prototype bottom materials are considered in the physical model. They are: (1) The representing grain diameter near shore (including estuary and surf zone) is 0.15 mm (the average median grain diameter). (2) The representing grain diameter of project area (including mouth and navigation channel) is 0.08 mm (the average median grain diameter).
- The flux of C. W inlet and outfall: Two cases are considered in the model test, Adipala power plant (this new project) is 31.0 m^3/s (1 × 660 MW) and S2P power plant (exist) is 24.85 m^3/s (2 × 300 MW).

3.2 Verification Test of Movable Bed

The project of Adipala power plant locates in the parallel-straight coastline of silt-sandy beach. The breakwater would destroy the equilibrium sediment transport, if the layout of harbor plan is not reasonable (Yan 2002), serious sedimentation would happen in harbor basin such as deposition problem in water intake and basin of S2P power plant (nearby this project). According to the bed-load taken from the basin of S2P harbor, D_{50} is the range of 0.1–0.15 mm, the result shows that the grain size of sediment is more difference to estuary of Serayu river (0.03–0.06 mm). But the sediment is the same as that of outside area of basin. This phenomena show that the sediments came from bed load which transported by joint actions of wave and current, instead of suspended sediment from estuary directly, and the sediment concentration is low assuredly. So, the main deposition composition is bed-load.

Based on previous analysis, the water level alternation also had been considered in order to simulate the tidal prism, and to realize the change tendency of the coast from sediment stating off by wave and transporting by tidal current. And the process of silt in reality is just like this mechanism. There are about 160,000 m^3 sediment in water intake of S2P power plant. So, the sediment transport rate is about 51.1 t/h according to the average density of sediment in prototype (2.8 t/m^3). The physical model replays the deposition process of harbor basin and water intake of S2P power plant. The result shows that the siltation intensity and distribution are closed, and they are satisfied with the similarity relation ($i_l = 60$). So, the selection of dynamic condition and model sediment is reasonable, the result of verification test is perfect.

3.3 Deposition of Adipala Projects

Based on the result of verification test, the harbor of Adipala power plant was simulated in homologous position. The Adipala projects used same hydrodynamic condition which used in verification test (S2P). The breakwaters are designed to extend beyond the surf zone of 5.4 m wave height from E.L.W.L to +1.83 m water level which avoids the effect of active sediment movement, such as long-shore sediment transport and transverse transport. Because the opening area of basin and breakwater head had extend beyond of zone of sediment turbidity (<0.01 kg/m^3), so the deposition of basin expressed relative limitation. Physical model simulated one year (12 months) in prototype, continuously. The result shows that the sediment deposition occurred in the area of approach channel, opening zone and in front of pier, and the distribution of erosion and deposition is shown in Fig. 5. Siltation thickness in basin and channel of physical model is about 0.02–1.91 m/a (Ave. = 0.52 m/a) after 12 months in prototype, siltation

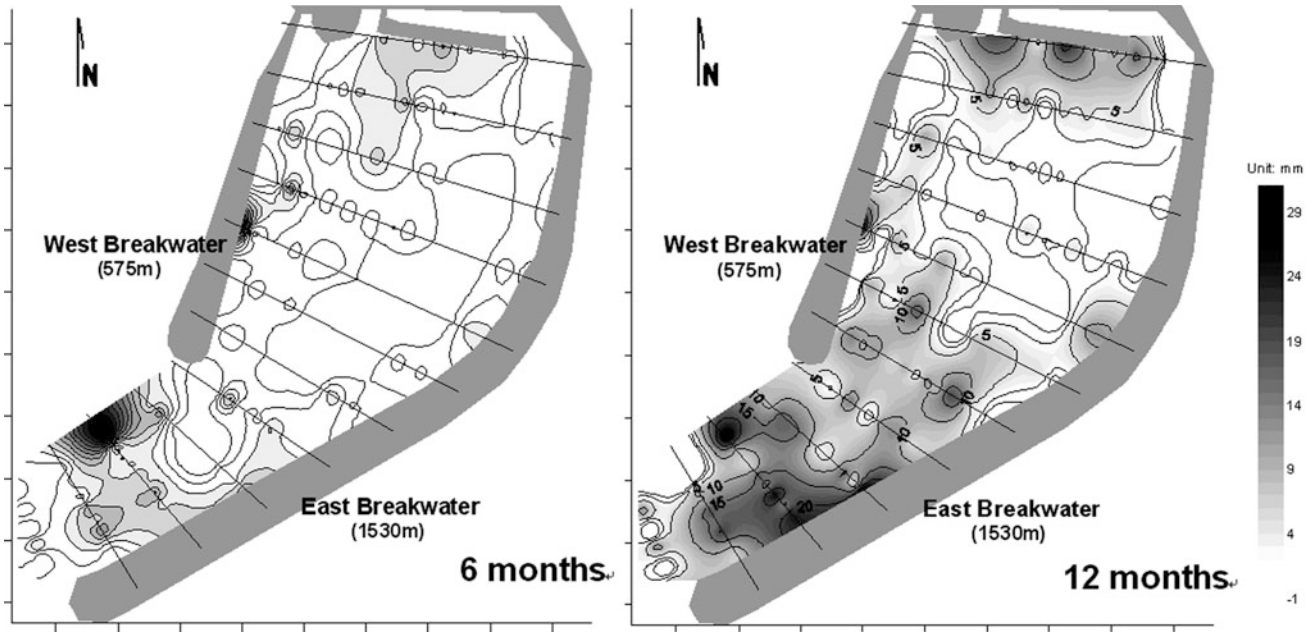

Fig. 5 Distribution of sediment deposition in harbor basin and approach channel9

Table 4 Result of physical model test

Item	Survey value in prototype by physical model test
Deposition thickness (m/a)	0.02–1.91(Ave. = 0.52)
Siltation volume(m^3/a)	16.8×10^4

volume is about 16.8×10^4 m^3/a, the results are shown in Table 4.

It should be mentioned that the maximum deposition is at inner side of and close to east breakwater, then occurs at the extend area of west breakwater. The navigation channel is between the two areas, and about half of maximum value. It shows the navigation channel direction is perfect. As the same time, there are siltation at the root of west breakwater. By calculate, it will be more than 30 years when the alongshore sediment transport around the breakwater head.

4 Conclusion

1. The siltation thickness is about 0.02–1.91 m/a (the average value is 0.52 m/a)and the deposition volume is about 16.8×10^4 m^3/a in harbor basin after project constructed.
2. When the deposition occurred in harbor basin, the alongshore sediment transport happened in the surf zone of near shore. But the sediment transportation had been blocked off by breakwaters because they all extended beyond of surf zone. And, the siltation at the root of east breakwater were more light than west breakwater due to the runoff of estuary.

References

Cao, Z. (1992). Bedload transport under the combined action of waves and tidal currents. *Journal of Waterway and Harbor*.

Dou, G. (2001). Starting law of silting of wave-induced. *Science in China, Series E, 41,* 566–573.

Sediment manual, issued by China professional committee. (1992). Beijing: China Environment Press.

Technical regulation of modelling for tide-current and sediment on coast and estuary (JTS/T 231-2-2010). (2010). Beijing: People's Republic of China.

Wave model test regulation (JTJ/T 234-2001). (2001). Beijing: People's Republic of China.

Yan, K. (2002). *Coast engineering*. China: Ocean Publishing Company.

Compression Behaviors of Marine Clay for Coastal Reclamation in Dalian, China

M. J. Jiang, N. Zhang, and J. D. Liu

Abstract

In the offshore areas of Dalian, China, a coastal reclamation project is ongoing for building an international airport. In the project, the possible excess settlement due to consolidation and creep of soil is one of the main concerns. In this paper, three series laboratory tests, i.e., conventional consolidation and rebounding tests, one-dimensional creep tests and triaxial creep tests were carried out to study the compression behaviors of the marine clay. All these tests were performed on undisturbed samples procured from the depth of 10 and 18 m below the seabed of Jinzhou Bay seabed. The compression and swelling indexes obtained from the conventional compression and rebounding tests show that marine clay presents much higher compressibility and special attention should be paid to the settlements in the project construction. The results of both one-dimensional and triaxial creep tests show that the creep deformation of soils increases with elapsed time and stress level. In addition, failure of soil hardly occurs in the process of creep and the soil deformation could eventually stabilize at any given stress level even in triaxial tests. At last, the stress-strain-time relationships were simulated to estimate the time-dependent behaviors of the marine clay.

Keywords

Marine clay • Compressibility • Creep • Stress-strain-time relationship

1 Introduction

In past decades, the coastal reclamation becomes more and more common in coastal area out of various purposes. These man-made lands directly rest on the marine deposits which are often featured by high water content, large void ratio, high compressibility and poor strength. Hence, the settlement and the stability are usually the main concerns in coastal reclamation projects. Actually, settlements often cause much more serious problems in marine engineering because the settlements may have exceeded the permissible limits when the soil is still strong enough to resist shear failure. Thus, in the design of the foundation treatment, the settlement always needs special attention.

It has been realized that there are two aspects involved in foundation settlements: consolidation and creep induced compression in soil. The former associates with increasing effective stress and pore water drainage. Terzaghi's theory and effective stress principle have been widely accepted in the evaluation of soil consolidation. And correspondingly, the layerwise summation method is generally used to estimate the foundation settlement in engineering. On the other hand, creep induced compression relates to the time-dependent behaviors of soil. The creep behaviors of soil have also been studied when the long term settlements of constructions

M. J. Jiang · N. Zhang · J. D. Liu
Department of Geotechnical Engineering, Tongji University, 1239 Siping Road, Shanghai 200092, China

M. J. Jiang (✉) · N. Zhang · J. D. Liu
Key Laboratory of Geotechnical and Underground Engineering of Ministry of Education, Tongji University, 1239 Siping Road, Shanghai 200092, China
e-mail: mingjing.jiang@tongji.edu.cn

Y. Huang et al. (eds.), *New Frontiers in Engineering Geology and the Environment*,
DOI: 10.1007/978-3-642-31671-5_20,

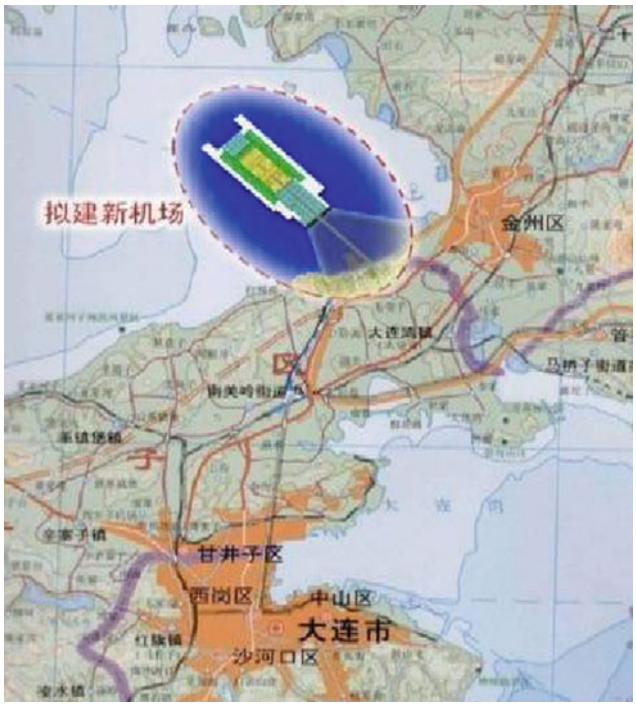

Fig. 1 The pictorial sketch of the coastal reclamation project

resting on soft clay (Bjerrum 1967; Leroueil et al. 1985; Mesri et al. 1997; Yin 1999) and reclaimed coastal (Miao 2008; Liu et al 2011; Chung 2002; Suneel 2008) was investigated. Developing a stress-strain-time relationship is the key problem in the estimation of the creep deformation which is still a controversial issue despite of the various attempts. So far, Singh-Mitchell creep model and Mesri creep model (Li 2001) are mostly used in geotechnical engineering. The differences between the two models lies in the description of stress-strain relationships. Singh-Mitchell model uses an exponential stress-strain relationship while Mesri model uses a hyperbolic relationship. The rheology tends to establish stress-strain-time relationship using element theory.

An ongoing coastal reclamation project locating in Dalian, China, is carried out for the construction of an offshore airport in the short run. It is for the first time that China constructs such an offshore airport independently. As shown in Fig. 1, the reclaimed land occupied about 22.89 km^2, with the length of 6540 m and the width of 3500 m, and the revetment is about 21440 m. The design altitude for the man-made land is 3.1 m, with the design high sea level of 1.06 m and the hundred-year extreme high sea level of 2.15 m. It is expected that the backfilled soil and rock could be as much as 17,368 m^3. This makes it one of the largest offshore airport projects worldwide, consequently raising quite a lot of geotechnical problems including stability and settlement.

In this paper, we investigate the compression behaviors of Dalican marine clay by consolidation tests and creep tests in laboratory. The stress-strain-time relationships for Dalian clay are developed using Mesri creep model based on the testing results. It should be pointed out that the native seawater with the salinity concentration of 0.05 g/ml was used in all tests in case of the influence of pore water system on soil compressibility.

2 Test Program and Soils Examined

2.1 Test Program

In laboratory, the soil compression behaviors were investigated by consolidation tests, and creep tests. The testing procedures are described in detail as follows.

Consolidation tests: The oedeometers were used to study the compressibility of soils due to consolidation by performing conventional 24 h consolidation tests. The consolidation loading increased from 50 to 1600 kPa in steps with the incremental ratio of 1.0.

Creep tests: One-dimensional and triaxial creep tests were carried out to study the time-dependent behaviors of soils. The specimens were also multi-stage loaded in both types creep tests. The one-dimensional creep tests were performed in oedometer and the loading was in the range of 50 to 1600 kPa with incremental ratio of 1.0. At each stage, the specimen deformation would observed until it was less than 0.01 mm in 24 h when the loading was increased to the following stage. The stress-path controlled instrument was used for the triaxial creep tests in which the specimens were firstly consolidated at the confining pressure of 100, 200, 400, 800 kPa respectively before creep testing. Triaxial creep tests were done under the drainage conditions. The specimen was first continuously loaded until the pre-designed deviator stress was attained. Then the axial strain and the volume change would be observed at this stress level until the axial deformation in 6 h was less than 0.01 mm when the deviator stress could increase to the next stage. In triaxial creep tests, the specimen would be loaded until the failure was observed in either loading or creep process.

Note that all the tests were done at the temperature of 20 ± 1 °C in case of the influence of temperature variation on soil creep behaviors.

2.2 Samples

Table 1 presents the general geological information of the area where the coastal reclamation project locates. The overlay mainly consists of sea shore facies, intermediate

Table 1 Hydrological engineering geology for clay in Dalian, China

Chronologic	Lithologic characters	Depth (m)	Thickness (m)	Formation
Holocene	Muddy silty clay	0−10	0−10	Sea shore facies
	Gray mild clay	11−22	0−12	

Table 2 Physical and basic mechanical parameters of Dalian clay

No.	Description	ω/%	ρ_d/g cm^{-3}	Liquid limit/%	Plastic limit/%	Void ratio	C_c	C_e
C10	Muddy silty clay	63.90	1.66	64.30	20.50	1.666	0.50	0.0749
C18	Clay	44.67	1.75	46.17	24.46	1.232	0.33	0.0880

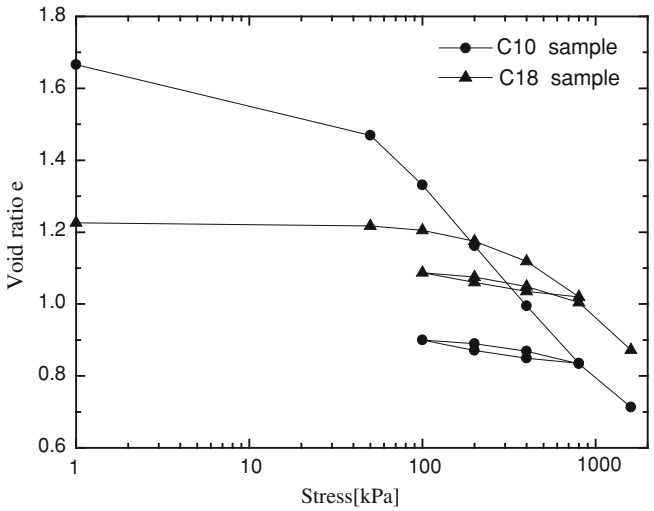

Fig. 2 The *e-lgp* curves for clay at different depth

facies and fluvial facies, indicating that it was formed in the process of marine transgression.

The laboratory tests were carried out on undisturbed samples to obtain reliable mechanical parameters for project design. Two different samplers have been used to procure the undisturbed samples from Jinzhou bay: the thin wall stationary piston and the fixed piston sampler. The thin wall stationary piston was used for the soft marine clay up to 12 m below seabed, while the fixed piston sampler for deeper soils. All the samples were immediately sealed on-site to maintain their native states and then carefully trimmed into specimens for testing. The general physical properties of these samples, as shown in Table 2, were also tested in laboratory.

3 Test Results

3.1 Conventional Consolidation Tests

Figure 2 presents the *e*-lg*p* curves obtained for clay at different depth below seabed by consolidation-rebound tests and the corresponding compression and swelling indexes were given in Table 2. It can be seen that the *e*-lg*p* curve for C10 sample is linear at normally consolidated state, while the curve for C18 sample is generally featured by global non-linearity. This observation indicates the stress dependent compressibility of C18 sample. The compression index for Dalian clay is found linearly related to their initial void ratio. Generally, the compression index can be estimated by the relation of $C_c = 0.283 \times (e_0 + 0.039)$.

3.2 One-Dimensional Creep Test Results

Figure 3 provides the variation of void ratio with elapsed time in terms of e-lgt curves. It can be seen that the compression curves for both samples are general in "S" shape as described in the text on soil mechanics, indicating the deformation of soil due to primary and secondary consolidation in the creep tests. Secondary consolidation is clearly observed in a rather long-term under a constant effective stress after primary consolidation. When the consolidation pressure is small, the secondary consolidation is hardly observed in three days after the application of load. When the stress is large enough, however, the deformation due to

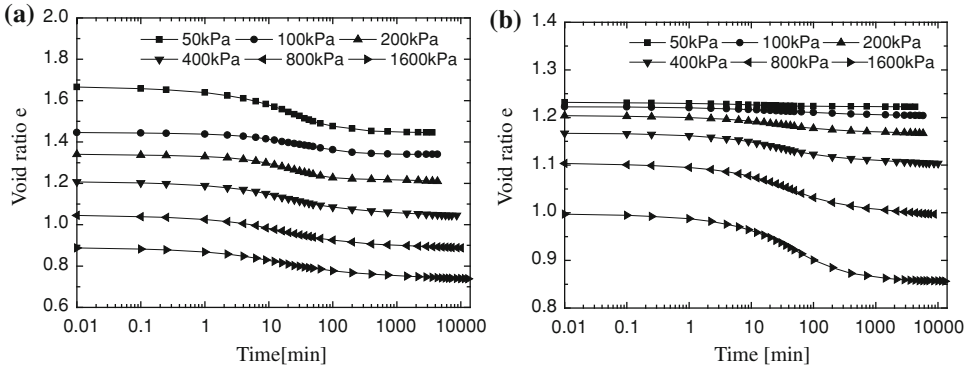

Fig. 3 The *e-lgt* curves obtained under one-dimensional conditions **a** C10 sample **b** C18 sample

secondary consolidation is still significant even 4 or 5 days after applying the consolidation pressure. It has been reported that secondary consolidation occurs with the soil structure adjustment at the particulate level (Jiang et al. 2009; Mesri and Castro 1987) and the diffusion of double layer (Fang et al. 2007). Both the processes are characterized by stress-dependent and time consuming. Hence the secondary consolidation often increases with the elapse of time and sustains much longer due to the increase of consolidation pressure.

In addition to the above-mentioned common features, some differences in the deformation of the marine clay are also worth mentioning here. It can observed that the strain induced by incremental stress at each loading stage for the upper marine remains the same more or less when the consolidation pressure becomes 200 kPa for C10 sample. The corresponding incremental strain for C18 sample, however, becomes larger and larger with increasing pressure.

The secondary consolidation coefficient defined by Eq. (1) was used to evaluate the creep property of Dalian clay.

$$C_\alpha = (e_1 - e_2)/\lg(t_2/t_1) \quad (1)$$

where t_1, t_2 are the time when creep deformation is observed and e_1, e_2 are the void ratio corresponding to t_1 and t_2.

Figure 4 presents the variation of secondary consolidation coefficients with increasing consolidation pressure. As shown in Fig. 4, a dramatic increase in the secondary consolidation coefficient can be observed when the consolidation pressure increases. The secondary consolidation coefficients for both samples eventually stabilized when consolidation pressure becomes larger enough. As mentioned above, creep property describing soil deformation at a constant effective stress connects with the particle rearrangement and structure alteration. The structure usually changes more significantly when the effective stress increases until the inherent structure has been totally damaged. Thus, the secondary consolidation coefficient of soil is observed increasing with effective stress when the soil is over-consolidated, and being almost steady at normally consolidated state (Shao, 2008).

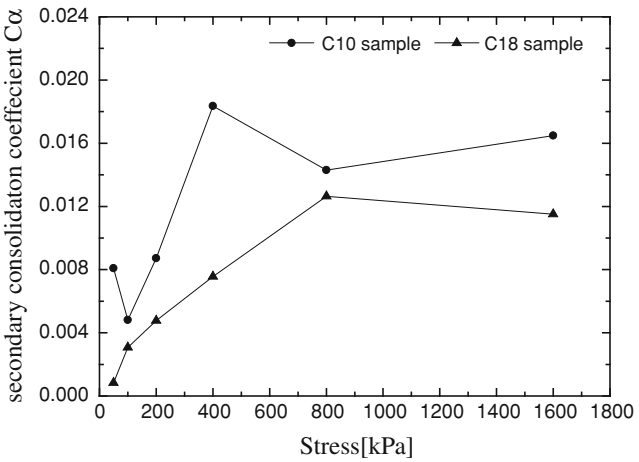

Fig. 4 Variation of secondary consolidation coefficient with effective stress

3.3 Triaxial Creep Tests

The observations of creep behaviors of Dalian marine clay obtained by triaxial creep tests under different confining pressures were quite similar, thus only the results from the confining pressure of 400 kPa are discussed here.

3.3.1 Time-Strain Curves

Fig. 5 presents the variation of axial strain with elapsed time for Dalian clay at different stress level. For both samples, the creep deformation increases greatly in a rather short run after the deviator stress was loaded, and in a fairly long run the creep develops at an attenuating rate which would becomes too small to contribute the deformation of soil. Consequently, the failure of soil was always observed in the loading period instead of the creep stage. This may be accounted for by soil deformation mechanism. Just like in one-dimensional creep tests, soil deformation in drained triaxial test also results from primary and secondary consolidation. The former relates to the drainage of pore water and the soil skeleton alteration due to increasing effective stress, while the latter relates to the further particle

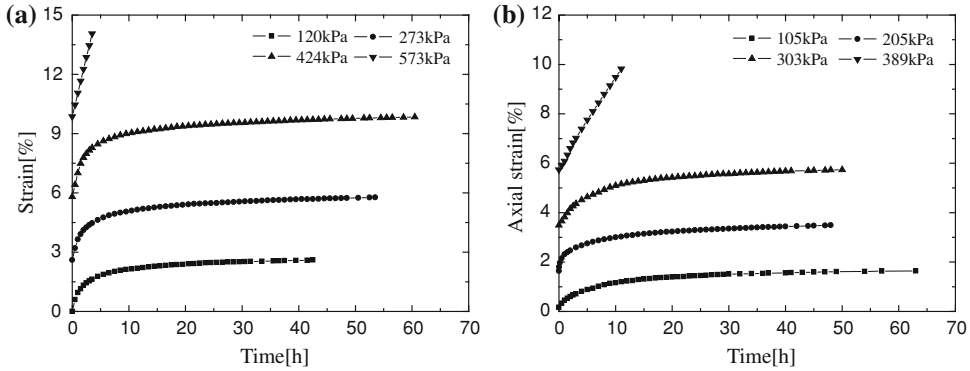

Fig. 5 Strain-time curves for Dalian clay **a** C10 sample **b** C18 sample

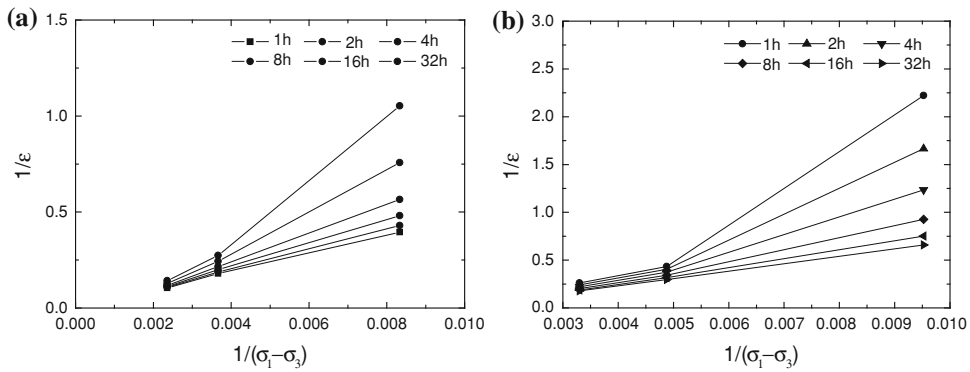

Fig. 6 Stress-strain relationship for typical Dalian clay **a** C10 sample **b** C18 sample

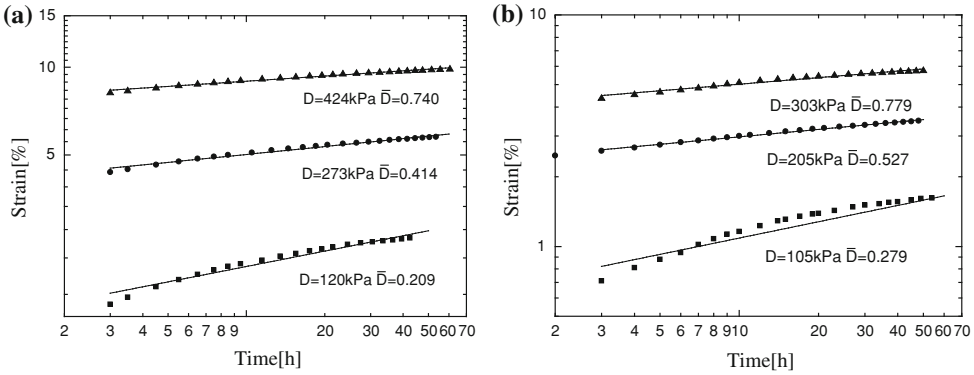

Fig. 7 Simulating curves of the Mesri creep model **a** C10 sample **b** C18 sample

rearrangement at a constant effective stress. Under drainage condition, soil particles arrange tighter and weak absorption layer turns thinner due to the drainage of pore water and the compression of soil skeleton in primary consolidation. These effects undoubtedly strengthen the soil structure and weaken the subsequent creep.

Note that, the soil creep deformation may develop fast after loading and then leads to soil failure, especially at high stress level, under undrained condition. In fact, foundation resting on soft clay may collapses due to accumulated creep under poor drainage condition. Thus, it had better to enhance the drainage capability of soil to prevent the creep induced failure.

4 Stress-Strain-Time Relationship and Model for the Soil

The stress-strain-time relationship was firstly raised by Singh and Mitchell (1968):

$$\varepsilon = Be^{\beta\bar{D}}\left(\frac{t}{t_1}\right)^{\lambda} \tag{2}$$

As mentioned above, Mesri described the stress-strain relationship using the hyperbolic equation proposed by Konder (1963). According to the hyperbolic equation, the stress-strain relationship can be expressed as:

Table 3 The parameters of Mesri creep model

No.	E_u/S_u	$\bar{D}$	R_f	λ	No.	E_u/S_u	$\bar{D}$	R_f	λ
C10	0.373	0.209	0.919	0.175	C18	1.134	0.270	0.926	0.234
	0.326	0.414	0.912	0.090		0.880	0.527	0.920	0.107
	0.587	0.74	0.915	0.059		1.356	0.779	0.919	0.094

$$\varepsilon/(\sigma_1 - \sigma_3) = a + b\varepsilon \tag{3}$$

Figure 6 presents some typical stress-strain isochrones for Dalian clay in cartesian coordinates with ordinate axis of $\varepsilon/(\sigma_1 - \sigma_3)$. It can be seen the linear relationships for these isochrones in the new coordinates. Hence, we develop the stress-strain-time relationship for Dalian clay using Mesri model here.

The initial tangential modulus E_{u} can be derived from Eq. (3) as,

$$E_{\mathrm{u}} = \left.\frac{d(\sigma_1 - \sigma_3)}{d\varepsilon}\right|_{\varepsilon=0} = \frac{1}{a} \tag{4}$$

The ultimate deviator stress $(\sigma_1 - \sigma_3)_f$ can be derived from Eq. (3) as,

$$(\sigma_1 - \sigma_3)_{ult} = \lim_{\varepsilon\to\infty} \frac{\varepsilon}{a + b\varepsilon} = \frac{1}{b} \tag{5}$$

It can be seen that $(\sigma_1 - \sigma_3)_{ult}$ is the deviator stress when the axial strain of specimen becomes infinite. Actually, the axial strain cannot be infinite and the soil usually fails at a certain strain of ε_f rather than the infinite strain. Here the failure stress ratio is used,

$$R_f = \frac{(\sigma_1 - \sigma_3)_f}{(\sigma_1 - \sigma_3)_{ult}} = \frac{(\sigma_1 - \sigma_3)_f}{1/b} \tag{6}$$

where $(\sigma_1 - \sigma_3)_f$ is the failure stress at the strain of ε_f.

Substitute Eqs. (4–6) into (3), and then the axial strain can be expressed as:

$$\varepsilon = \frac{(\sigma_1 - \sigma_3)_f}{E_u} \frac{\bar{D}}{1 - R_f\bar{D}} \tag{7}$$

where $\bar{D} = (\sigma_1 - \sigma_3)/(\sigma_1 - \sigma_3)_f$ is the stress level.

Thus, the Mesri model can be expressed as:

$$\varepsilon = \frac{2}{E_u/S_u} \frac{\bar{D}_1}{1 - (R_f)_1\bar{D}_1} \left(\frac{t}{t_1}\right)^{\lambda} \tag{8}$$

where $S_u = (\sigma_1 - \sigma_3)_f \big/ 2$.

So Eu/Su, Rf and λ are the parameters involved in Mesri creep model (Mesri et al. 1981).

Figure 7 provides the simulation results for Dalian clay by Mesri creep model and the parameters were given in Table 3.

It can be seen that when the strain does not increase with time in the initial period when the stress level is high or low, and thus there is some deviation between testing and simulation results. However, Mesri creep model can generally well describe the creep deformation of Dalian clay at most stress level. Thus, it can be used to estimate the long term settlement of foundation due to soil creep.

5 Conclusion

Foundation settlement is one of the major concerns in coastal reclamation project, especially the long term settlement due to soil creep. This paper investigated the compression behaviors of Dalian marine clay involved in an ongoing coastal reclamation project in Dalian, China. The main conclusion can be made as follows:

1. The *e*-lg*p* curves for Dalian marine clay could either be linear or nonlinear at normally consolidated state, indicating the stress dependency in compressibility of such a marine clay, which should be paid specific attention in the design.
2. Creep tests results show that the deformation of Dalian clay usually lasts in a fairly long run, especially under high stress level. Note that both one-dimensional and triaxial creep tests presented in this paper were performed under completely drainage condition, thus the soil hardly fails due to creep which is often observed in undrained condition.
3. Under one-dimensional condition, the secondary consolidation coefficient increases with effective stress when the soil is over-consolidated. The variation of the secondary consolidation coefficient can be nearly neglected at the normally consolidated state.
4. The creep of Dalian marine clay characterizes nonlinearity and can be expressed by hyperbolic equation. Thus the stress-strain-time relationship based on the Mesri creep model can well describe the time-dependent deformation of Dalian clay and be used to estimate the foundation settlement in the long run.

Acknowledgments This research was funded by China National Funds for Distinguished Young Scientists (Grant No. 51025932), the Doctoral Program of Higher Education (Grant No. 20100072110048) and the Changjiang Scholars and Innovative Research Team in University (Grant No. IRT1029).

References

Bjerrum, L. (1967). Engineering geology of Norwegian normally consolidated marine clays as related to the settlements of buildings. *Geotechnique, 17*(2), 83–118.

Chung, S., Giao, P., Nagaraj, T., & Kwag, J. (2002). Characterization of estuarine marine clay for coastal reclamation in Pusan, Korea. *Marine Georesources and Geotechnology, 20*, 237–254.

Fang, J., Gu, Z., Liu, C. et al. (2007). Cr removal from aqueous solution by activated carbon coated with quaternized poly. *Environmental Scientific Technology*, *41*(13), 4748–4753.

Jiang, M., Peng, L., Zhu, H., et al. (2009). Macro and micro properties of two natural marine clays in China. *China Ocean Engineering, 2*, 329–344.

Konder, R. (1963). Hyperbolic stress-strain response cohesive soils. *Journal of Soil Mechanics and Foundation Engineering, 89*(1), 115–143.

Leroueil, S., Kabbaj, M., Tavenas, F., et al. (1985). Stress-strain-strain rate relation for the compressibility of sensitive natural clays. *Geotechnique, 35*(2), 159–180.

Li, S., & Sun, J. (2001). Mesri's creep model for Shanghai silt-clay. *China Civil Engineering Journal, 34*(6), 74–79.

Liu, S., Shao, G., Du, Y., et al. (2011). Depositional and geotechnical properties of marine clays in Lianyungang, China. *Engineering Geology, 121*, 66–74.

Mesri, G., & Castro, A. (1987). Cα and Cc concept and K0 during secondary compression. *Journal of Geotechnical Engineering*, *113*(3), 230–247.

Mesri, G., Febres-Cordero, E., Shield, D., et al. (1981). Shear stress-strain-time behavior of clay. *Geotechnique, 31*(4), 537–552.

Mesri, G., Stark, T., Ajlouni, M., et al. (1997). Secondary compression of peat with or without surcharging. *Journal of Geotechnology and Geoenvironment Engineering, 123*(5), 411–421.

Miao, L., Zhang, J., Wang, F., et al. (2008). Time-dependent deformation behavior of Jiangsu marine clay. *Marine Georesources and Geotechnology, 26*(2), 86–100.

Shao, G., & Liu, S. (2008). Research on secondary consolidation of structural marine clay. *Rock and Soil Mechanics, 29*(8), 2057–2062.

Singh, A., & Mitchell, J. (1968). General stress-strain-time function for soils. *Journal of Soil Mechanics*, *94*(1), 21–46.

Suneel, M., Lee, K., & Jong, C. (2008). Compressibility characteristics of Korean Marine Clay. *Marine Georesources and Geotechnology, 26*(2), 111–127.

Yin, J. (1999). Non-linear creep of soils in oedometer tests. *Geotechnique, 49*(5), 699–707.

Numerical Modeling of Tidal Effects on Groundwater in the Coastal Aquifer of Donghai Island

P. P. Zhou, G. M. Li, M. Li, and Y. H. Dong

Abstract

In coastal region, tide takes an important role to affect the dynamics of the groundwater flow and saltwater transport. To analyze tidal effects on groundwater flow and saltwater transport in the unconfined coastal aquifer of Donghai Island, we develop a two-dimensional, finite-difference groundwater model. The model which is based on density-dependent fluid flow theory considers dynamic tidal boundary conditions and sloping beach surface. We simulated groundwater flow and the salt concentration distribution which forms the salt wedge in the coastal aquifer, as well as analyzed the dynamic characteristics of the groundwater flow and the salt concentration distribution during the flood-and-ebb process. Simulations indicate that fluid velocity in freshwater is greater than that in saltwater. Velocity decreases with depth, but increases along the freshwater-saltwater interface or dispersion zone in the coastal aquifer. Tidal action drives seawater recirculation through the intertidal beach zone, thereby creating an upper saline plume in the aquifer. And the water table in the upper saline plume area is higher than that in the freshwater area.

Keywords

Tidal effects • Groundwater flow • Salt concentration distribution

1 Introduction

In coastal aquifers, both groundwater flow and saltwater transport occur at the same time. The coastal aquifer discharges fresh groundwater to the sea, meanwhile the seawater intrudes into the fresh groundwater through the bottom of the aquifer. Finally a salt wedge area forms in the aquifer. And a freshwater-saltwater interface or dispersion zone occurs between the fresh groundwater area and salt wedge area in the aquifer. The salt concentration distribution depend on several factors, including the shape of the aquifer, parameters such as hydraulic conductivity, human activities, and tidal oscillations of sea level. Groundwater flow pattern is also influenced by these factors. In our research, the tidal effects on the dynamic characteristics of the groundwater flow pattern and salt concentration distribution is the main aim.

Numerous researchers have theoretically studied tidal effects on seawater intrusion and contaminant transport in coastal aquifers; in these works, numerical simulation methods were used as primary tools of investigation (Ataie-Ashtiani et al. 1999; Robinson et al. 2007; Robinson et al. 2009). Using actual area conditions, some scholars used actual area conditions in numerical simulations of seawater intrusion to analyze the influence of rainfall recharge, groundwater withdrawals through pumping, aquifer parameters, and tidal oscillations on seawater intrusion (Narayan et al. 2007; Yakirevich et al. 1998). And some

P. P. Zhou · G. M. Li (✉) · M. Li · Y. H. Dong
China Academy of Sciences, Institute of Geology and Geophysics, NO. 19 Beitucheng West Road, Chaoyang District, Beijing 100029, China
e-mail: guominli@mail.iggcas.ac.cn

P. P. Zhou
e-mail: zhoupengpeng@mail.iggcas.ac.cn

Y. Huang et al. (eds.), *New Frontiers in Engineering Geology and the Environment*,
DOI: 10.1007/978-3-642-31671-5_21,

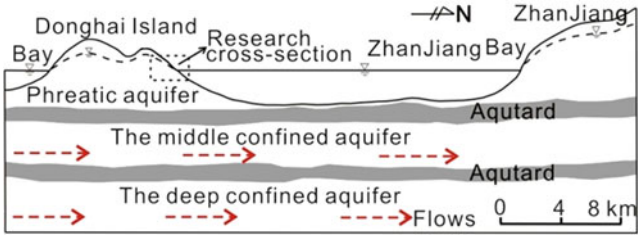

Fig. 1 Cross-section of Donghai Island

researchers have launched experimental study to observe the tidal effects on the groundwater (Zhang 2005).

The coastal phreatic aquifer of Donghai Island is vulnerable to seawater intrusion, but no effort has thus far been made to carry out numerical simulations of tidal effects on the groundwater flow and salt transport in this island. Understanding the effects of tidal oscillations is necessary.

2 Site Description and General Hydrogeology

Donghai Island is located south of Zhanjiang City. The sedimentary cover of the island consists of thick Cenozoic interbeddings of loose sand and soft clay. The Cenozoic sediments lie atop Cretaceous stratum and basement. The sedimentary rocks form three aquifers, including two confined aquifers, which are consistent with the confined aquifers of the mainland. The Zhanjiang Bay and two aquitards separate the island's phreatic aquifer from that of the mainland. Donghai Island is classified as a continental island. Our research cross-section is located in the north coastal area of this island. The profile of the island is shown in Fig. 1.

The groundwater in the phreatic aquifer receives rainfall recharge, flows radially from watershed to ocean and is discharged in the form of evaporation and runoff. The groundwater in the confined aquifers receive runoff–recharge from the south; flow to the mainland and are discharged by pumping and runoff.

3 Numerical Simulations

3.1 SEAWAT Model

The governing equation for density-dependent groundwater flow is

$$\nabla\left[\rho K_f\left(\nabla h_f+\frac{\rho-\rho_f}{\rho_f}\right)\right]=\rho S_f\frac{\partial hf}{\partial t}+\theta\frac{\partial\rho}{\partial C}\frac{\partial C}{\partial t}-\bar{\rho}q_s \tag{1}$$

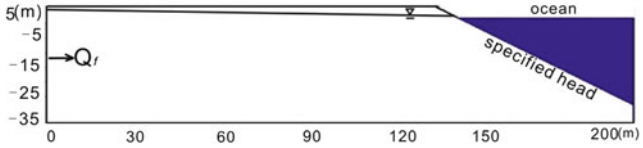

Fig. 2 Model domain and boundary conditions

Where ρ ρ_f, and $\bar{\rho}[ML^{-3}]$ are the fluid density, freshwater density, and source or sink fluid density, respectively; $K_f[LT^{-1}]$ is the equivalent freshwater hydraulic conductivity; h_f [L] is the equivalent freshwater head; $S_f[L^{-1}]$ denotes the equivalent freshwater storage coefficient; t[T] is the time; θ is the effective porosity; q_s [T^{-1}] is the flow rate per unit volume of the aquifer of the source or sink; and $C[ML^{-3}]$ is the salt concentration.

The governing equation for multi-species conservative transport is

$$\frac{\partial C}{\partial t}=\nabla\left(D\nabla C\right)-\nabla\left(\vec{v}C\right)-\frac{q_s}{\theta}Cs+\sum_{k=1}^{N}Rk \tag{2}$$

where $D[L^2T^{-1}]$ is the hydrodynamic dispersion coefficient; $\vec{v}$ represents the fluid velocity [LT^{-1}]; Cs is the solute concentration of water entering from sources or sinks [ML^{-3}]; and R_k(k = 1, …, N) denotes the rate of solute production or decay in reaction k of N different reactions [$ML^{-3}T^{-1}$] (Guo and Langevin 2002).

3.2 Model Discretization, Boundary Conditions, and Parameters

To simulate tidal effects on the coastal phreatic aquifer, we take a cross-section along the groundwater flow direction as an example. The cross-section is 200 long, 40 deep, and 5 m thick. The model area was discretized to 64,000 quadrilateral cells (400 columns, 160 layers, and 1 row). The details of the model with boundary conditions are shown in Fig. 2.

In the model, a freshwater source was set along the inner landward boundary. The boundary condition on the aquifer–ocean interface was set as a specified head boundary. Because a layer of very-low-permeability clay exists on the bottom of the phreatic aquifer, we incorporated a no-flow boundary on the base of the model domain. The simulation time in transient simulation processes is very slow (74.5 h); thus, we obtained minimal influence of rainfall in our research. To address this problem, we incorporated the no-flow boundary at the top of the model domain. A constant chlorine concentration boundary (16,000 mg/L, chlorine concentration of seawater) was established for the aquifer–ocean interface. The initial salinity of groundwater was 0 mg/L.

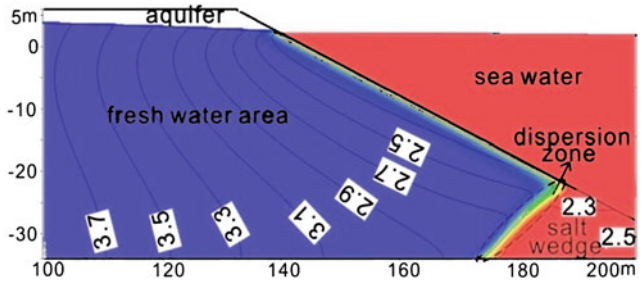

Fig. 3 Salt concentration (*colored*) and head equivalent (*contours*) without tidal effects

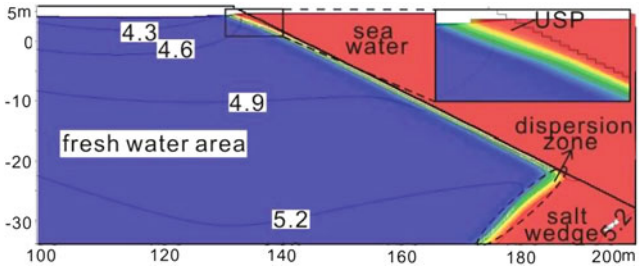

Fig. 4 Salt concentration (*colored area*) and head equivalent (*contours*) at high tide

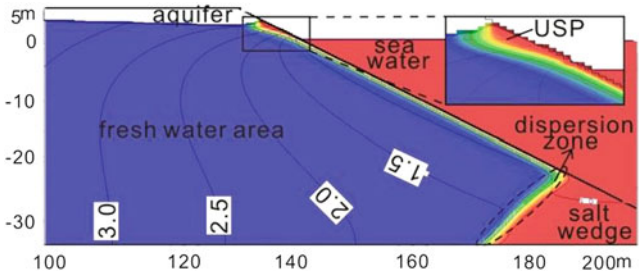

Fig. 5 Salt concentration (*colored area*) and head equivalent (*contours*) at low tide

The hydraulic conductivity (K) chosen for this model was 5 m/day, obtained from the pumping test. The longitudinal dispersivity (α_L) was 10 and the transverse dispersivity (α_T) was 2 m. These values were taken from previous research (Ranganathan and Hanor 1988).

4 Simulation Results

We conducted simulations with and without tidal effects, for which we assigned a time-varying head (an irregular semidiurnal tide) and a constant head (2.01 m, mean seawater level) as the boundary conditions on the aquifer–ocean interface, respectively.

4.1 Characteristics of Groundwater without Tidal Effects

The results of the simulation without tidal effects show the salt concentration distribution and groundwater flow pattern. The results are shown in Fig. 3.

The comprehensive effects of density gradient, salt concentration gradient, and hydrodynamic dispersion create salt concentration distribution which forms the salt wedge that is separated with fresh water by dispersion zone in the aquifer (Fig. 3). The maximum length of the salt wedge is approximately 25, and the width of the dispersion zone is 5.4 m.

In salt wedge, saltwater flows into aquifer along the landward direction. Then, saltwater flows back to the ocean along the dispersion zone. In the freshwater zone, fresh groundwater is discharged to the ocean along the dispersion zone. The results indicate that fluid velocity in the freshwater zone decreases with depth but increases along the dispersion zone. The salt wedge dynamics exhibit regularity, but the fluid velocity is lower than that in the freshwater zone.

In this situation, the salt concentration distribution and groundwater flow pattern is at a steady state.

4.2 Characteristics of Groundwater with Tidal Effects

The numerical simulation results for high sea level are shown in Fig. 4, and those for low tide are illustrated in Fig. 5. In the figures, the shortening of the upper saline plume is denoted by "UPS."

Compared with the results of the simulations without tidal effects, those of the simulations with tidal effects indicate that tidal oscillations have significant influence on the salt concentration distribution in the aquifer. In the flood tide process, the sea level is higher than the water table of the aquifer. The hydraulic gradient causes seawater to flow through the intertidal beach zone into the upper area of the aquifer near the aquifer–ocean interface, thereby forming the upper saline plume. At low tide, the upper saline plume continues to exist. The shape of the upper saline plume depends on factors, including the tidal amplitude, fresh groundwater flux (Robinson et al. 2007), and physical characteristics of the aquifer.

Tide considerably affects groundwater flow pattern. As tide rises, the rate at which sea level increases is faster than that at which the water table of the coastal phreatic aquifer rises. The hydraulic gradient causes seawater to flow into the upper area of the aquifer. By contrast, as tide falls, the aquifer which has a water table elevated to above sea level gradually releases groundwater which then flows to the ocean. And the water table in the upper saline plume is at a higher level than that of freshwater. And in the upper saline

plume area, groundwater flows vertically, and then seaward to the ocean.

In summary, tide significantly affects the salt concentration distribution and groundwater flow pattern. Tidal action drives seawater recirculation through the intertidal beach zone, thereby creating the upper saline plume.

5 Conclusion

In this study, a two-dimensional variable-density groundwater flow and solute transport model was developed to simulate the tidal effects on groundwater in Donghai Island. The model simulated the variation patterns of the groundwater flow and salt concentration distribution during the flood-and-ebb tide process, and deepened understanding to the tidal effects on coastal aquifer.

Without tide oscillations, the groundwater flow pattern and salt concentration distribution remain at a steady state. The fluid velocity in the aquifer decreases with depth but increases along the dispersion zone. And the fluid velocity in the freshwater area is greater than that in the saltwater area. Compared with the results without tidal effects, the tide significantly changed the groundwater flow pattern and salt concentration distribution. Tidal action drives the formation of the upper saline plume.

References

Ataie-Ashtiani, B., Volker, R., & Lockington, D. (1999). Tidal effects on sea water intrusion in unconfined aquifers. *J Hydrol, 216*, 17–31.

Guo W, Langevin C (2002) User's guide to SEAWAT: a computer program for simulation of three-dimensional variable-density groundwater flow. In: U.S. geological survey techniques of water-resources investigations, Florida

Narayan, K., Schleeberger, C., & Bristow, K. (2007). Modelling seawater intrusion in the Burdekin Delta Irrigation Area, North Queensland, Australia. *Agricultural Water Management, 89*, 217–228.

Ranganathan, V., & Hanor, J. (1988). Density-driven groundwater flow near salt domes. *Chem Geol, 74*, 173–188.

Robinson, C., Li, L., & Barry, D. (2007). Effect of tidal forcing on a subterranean estuary. *Adv Water Res, 30*, 851–865.

Robinson, C., Brovelli, A., Barry, D., et al. (2009). Tidal influence on BTEX biodegradation in sandy coastal aquifers. *Adv Water Res, 32*, 16–28.

Yakirevich, A., Melloul, A., Sorek, S., et al. (1998). Simulation of seawater intrusion into the Khan Yunis area of the Gaza Strip coastal aquifer. *Hydrogeol J, 6*, 549–559.

Zhang, Q. (2005). An experimental study of seawater intrusion. *Hydrogeol Eng Geol, 4*, 43–47.

Engineering Geological Assessment of the Anzali Coastal Region (North Iran, South Caspian Coast) to Sustain Urban Planning and Development

M. Hashemi, M. R. Nikoudel, N. Hafezi Moghaddas, and M. Khamehchiyan

Abstract

In this research a broad assessment of the geological, sedimentological and geotechnical characteristics of the coastal Holocene sediments of the Anzali Area was made and three engineering geological units as Upper Sandy Zone (USZ), Middle Clayey Zone (MCZ) and Lower Sandy Zone (LSZ) were identified. These units are the consequences of rapid sea-level fluctuations of the Caspian Sea in the Holocene. The engineering geological characteristics of these units were analyzed and the main engineering geological problems associated with sediments of each unit were identified. The results show that USZ has high liquefaction potential, low bearing capacity, settlement susceptibility and excavation problem. MCZ has low bearing capacity, high settlement susceptibility and excavation problem. LSZ that has good geotechnical properties poses few problems.

Keywords

Anzali coastal region • Holocene sediments • Engineering geological problems

1 Introduction

Anzali port is one of the most important ports in north of Iran along Caspian Sea coast (Fig. 1). This area is subjected to rapid urbanization and development. More recently growing population in addition to increasing tourism has lead to major construction in the study area, including development of buildings, roads, railroads, sewer networks and related infrastructures. These civil engineering activities upon coastal sediments having unfavorable engineering geological conditions have lead to (or will lead to) rising some engineering geological problems.

In this research the geo-environmental problems of the study area were assessed via a broad engineering geological investigation to provide the prerequisites for urban planning and development of the Anzali Area.

2 Geology and Engineering Geology

The recent deposits of the Caspian coast include beach and dune sands and swamp sediments. In addition a number of deltaic fans extend across the coastal plain to the sea (Clark et al. 1975; Annells et al. 1975). Figure 2 presents the geological map of the study area. As can be seen, the study area mainly consists of Holocene marine deposits and organo-detritic deposits. These sediments are the consequence of rapid sea-level changes of the Caspian Sea in the Holocene (Kazanci et al. 2004; Lahijani et al. 2009).

By characterizing the sediments of the study area, land units with similar behavior were defined. The data used for characterization were obtained from various geotechnical reports from both private and public projects across the

M. Hashemi (✉) · M. R. Nikoudel · M. Khamehchiyan
Department of Engineering Geology,
Tarbiat Modares University, Tehran, Iran
e-mail: M.hashemi@modares.ac.ir

N. H. Moghaddas
Geosciences Faculty, Shahrood University of Technology,
Shahrood, Iran

Y. Huang et al. (eds.), *New Frontiers in Engineering Geology and the Environment*,
DOI: 10.1007/978-3-642-31671-5_22,

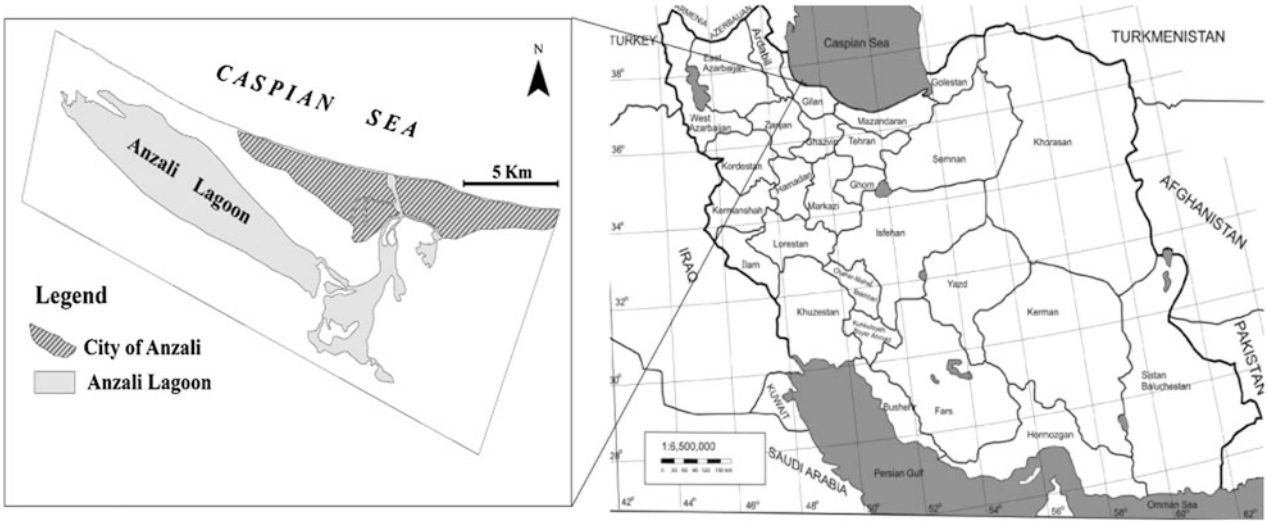

Fig. 1 Location map of the study area

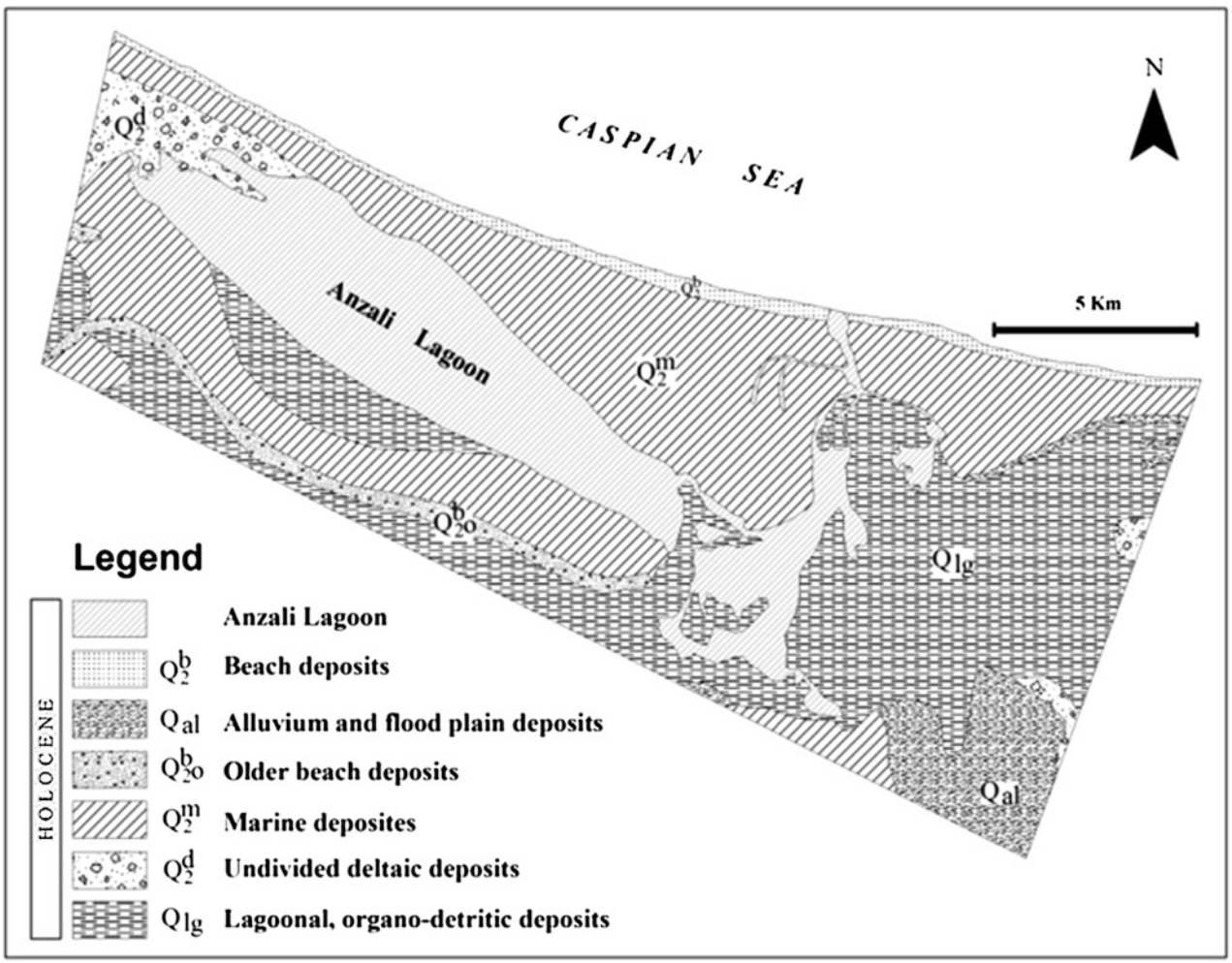

Fig. 2 Geological map of the study area

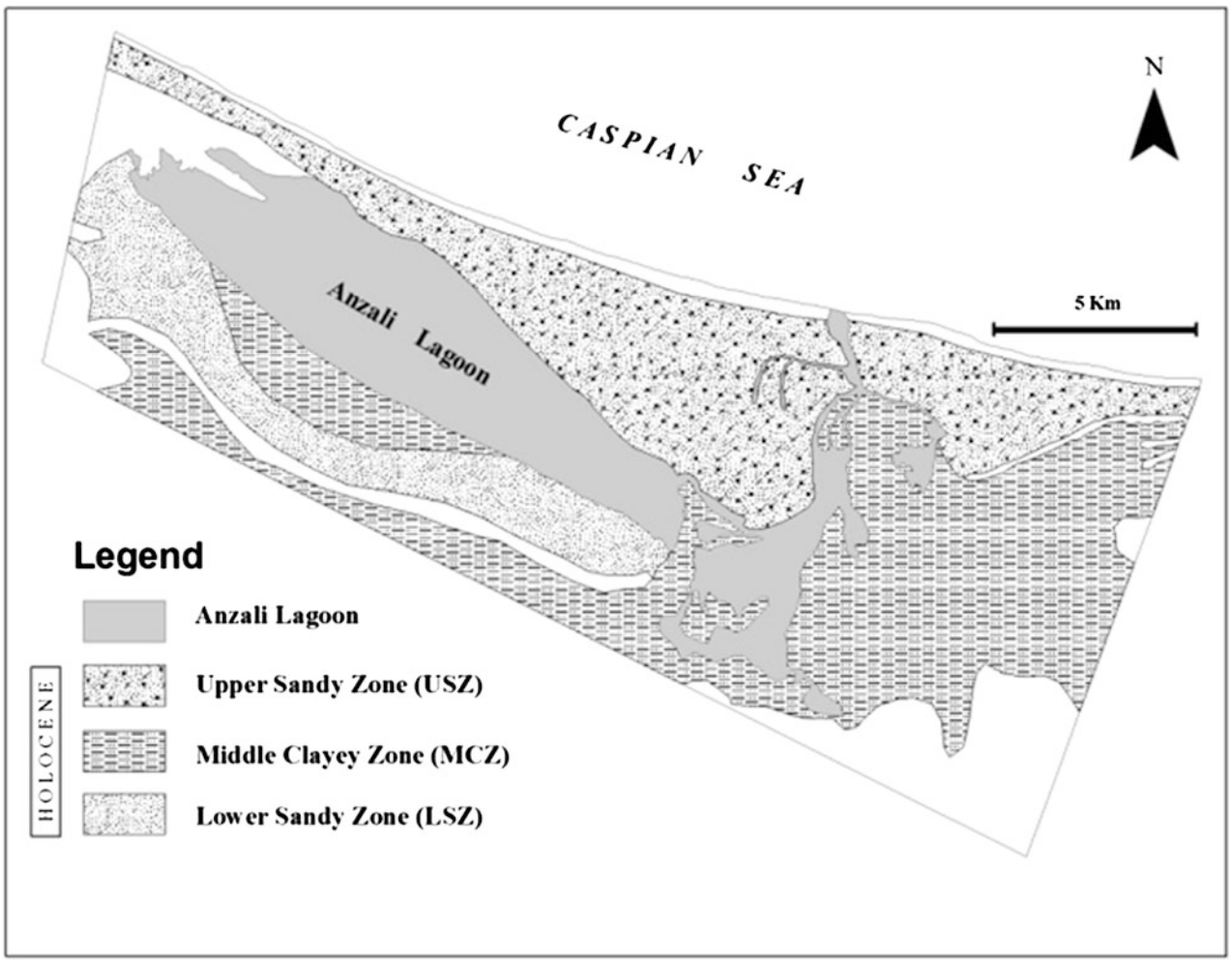

Fig. 3 Distribution of zones defined in this research

study area. Moreover, nine dynamic cone penetrometer (DCP) tests were conducted to determine geotechnical properties of sandy soils up to 10 m in depth below ground surface.

Based on geotechnical data and sedimentological studies, the sediments of the study area can be divided to three units including USZ, MCZ and LSZ as Fig. 3. The LSZ and USZ are consequences of highstands of the Caspian Sea in Early and Late Holocene respectively and the MCZ has been deposited during lowstans of Caspian Sea in Middle Holocene in a lagoon environment. Main geotechnical properties of soils of these three units are given in Table 1.

3 Problems Associated With the Sediments

Saturated Holocene sediments of the Anzali Area with generally poor geotechnical properties like low shear strength and low density are associated with some problems including excavation problems, low bearing capacity, high settlement susceptibility and liquefaction potential. These problems are mainly associated with USZ and MCZ.

3.1 Excavation Problems

Loose sandy soils and low strength clayey soils in addition to shallow water table cause rising problems during excavations in USZ and MCZ. The groundwater table in the city of Anzali lies between 1.0 and 2.0 m. During the rainy season, the water table is higher than 1.0 m. Construction activities, therefore, often involve excavations of considerable depth underwater. The development of underground civil constructions in USZ below the water table requires rigorous and careful planning. The unforeseen events during the excavation works in saturated loose sandy soils of USZ can lead to serious problems, posing at risk surrounding buildings. One example of soil-related failures of underground structures built below the water table in USZ

Table 1 Main geotechnical properties of soils of engineering geological units

Soil parameters	USZ	MCZ	LSZ
Gravel (%)	0–5	0	0–3
Sand (%)	60–96	2–49	52–90
Silt and clay (%)	0–40	51–98	10–48
Median particle size (mm)	0.11–0.27	0.0015–0.06	0.095–0.22
Natural moisture content (%)	6.2–53	29–92.4	14.5–66.4
Liquid limit (%)	–	25–75	–
Plasticity index (%)	–	7–36	–
Specific gravity of soil solids	–	2.51–2.78	–
Soil density (kN/m^3)	17.65–18.64	15.7–17.16	19.13–20.6
Void ratio	0.46–1.72	0.81–1.99	0.42–1.1
SPT blow count (N)	2–>50	4–34	26–>50
Cohesion (kPa) UU	–	18–51	–
Friction angle (deg.) UU	–	0–4	–
Cohesion (kPa) CD	0	0.05–0.25	0
Friction angle (deg.) CD	28–33	18–27	34–36
Unconfined shear strength (kPa)	–	24.3–142	–

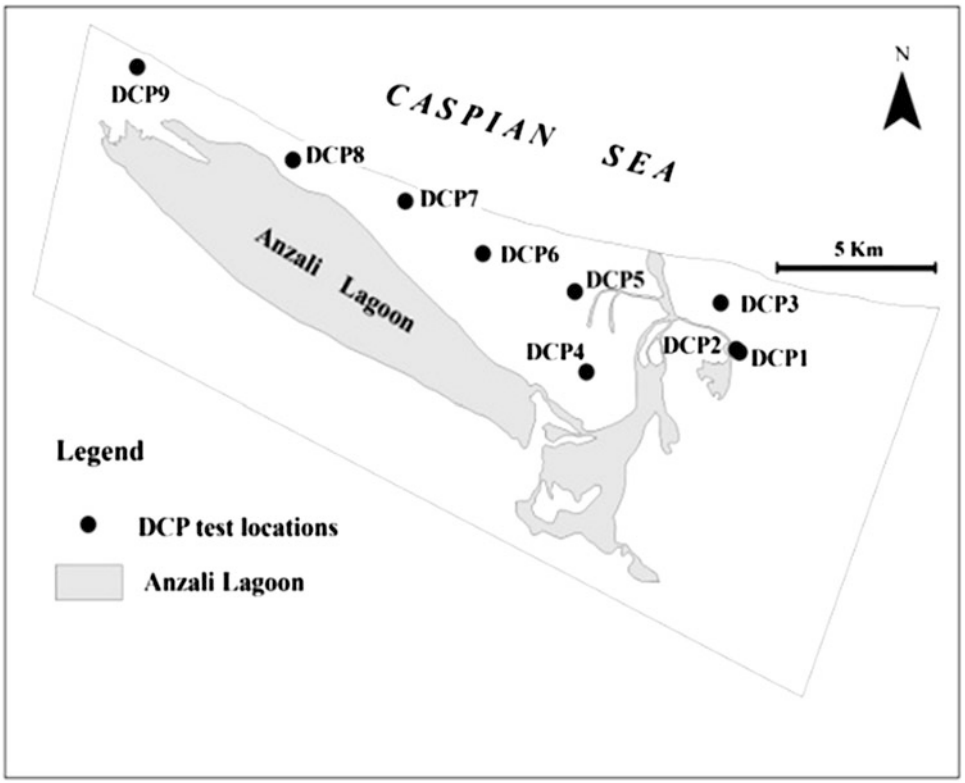

Fig. 4 Location map of DCP tests

includes the excavation failure during micro-tunneling in fine sands in a sewer line project in the city of Anzali (Jebelli et al. 2010). In this case micro-tunneling in saturated sandy soil has led to partial soil loss due to short stand-up time and high groundwater pressure. Because excavations lead to unstable situations, thus it is often imperative to adopt bracing systems and lower the groundwater table. Invasion of water from both Caspian Sea and Anzali Lagoon to the sandy soils of USZ, make dewatering difficult in this unit.

Table 2 Liquefaction potential index of USZ soils based on DCP test results

Location	Depth of investigation (m)	Liquefaction potential index	Liquefaction potential
DCP1	9.5	17	Very high
DCP2	10	22	Very high
DCP3	9	21	Very high
DCP4	6	12.75	High
DCP5	6.5	6	High
DCP6	4	4.5	Moderate
DCP7	7	13	High
DCP8	7	19.5	Very high
DCP9	7	16	Very high

3.2 Low Bearing Capacity

Superficial (up to 5 m in depth) sandy soils of USZ are not competent and have weak nature and low bearing capacity. As shown in Table 1, low SPT "N" values indicate low shear strength and low density of these soils that this fact in return demonstrates low bearing capacity of soils. In the case of heavy loads and high rise buildings up on USZ, pile foundations supported principally by end bearing would be required. Based on the depth of LSZ, the length of piles varies between 20 and 35 m from east to west parts.

Since the MCZ soils are very soft and have low bearing capacity, any structures up on these soils (in south and southeast of the City of Anzali) should be founded on pile foundations. Depth of competent sand stratum is relatively shallower in this area so pile foundation with maximum 15 m in length would be required.

LSZ appears at the ground surface in small parts in south of Anzali Lagoon. Based on the better geotechnical properties of the LSZ soils like higher SPT values, greater unit weight, and larger angle of internal friction, it appears that shallow foundation of any types at depths of 1.0–2.0 m would be suitable for most applications.

3.3 Settlement Susceptibility

Settlement susceptibility is mainly related to compressible nature of the clayey soils of MCZ. Evaluation of compressibility of MCZ soils was made based on the results of oedometer tests. The e-log p relationship does not show any definite overconsolidation. Moreover high natural moisture contents in comparison with liquid limits of the clayey soils of MCZ indicate that these soils are normally consolidated. The coefficient of compressibility (Cc), extracted from the record, ranged between 0.14 and 1.1 (Table 1). The high Cc values (>0.25) are attributed to high in situ void ratios and moisture contents. These values are indicative of their vulnerability to excessive settlements under applied loads.

3.4 Liquefaction Potential

USZ soils are young and comprising sandy material with low relative density that occurring in saturated conditions. Moreover, the southern Caspian Sea region is seismically active based on many historical and instrumental records of earthquakes (Jackson et al. 2002). Considering abovementioned conditions, it can be deduced that the sandy soils of USZ have high liquefaction potential. In this regard, the factor of safety (FS) of USZ against liquefaction was determined based on the SPT data (Youd and Idriss 2001). For determination of FS, a peak horizontal acceleration (a_{max}) of 0.35 g and an earthquake magnitude of M7.5 were considered for the area based on Nogol-e-Sadat (1991). Based on determined FS against liquefaction, in many cases the USZ soils have high liquefaction potential (the FS less than one).

Another evaluation of liquefaction potential was made based on DCP test results. In this case, Liquefaction Potential Index (LPI) of USZ was determined for each DCP test location (Fig. 4) based on Luna and Frost (1998) and Sonmez (2003). For determination of FS (needed for determination of LPI), a peak horizontal acceleration (a_{max}) of 0.35 g, an earthquake magnitude of M7.5 and mean value of 15 % for fine contents of the USZ soils were considered. Table 2 shows the liquefaction potential index of USZ soils based on DCP test results and their liquefaction potential classification. As shown in Table 2, USZ soils have mainly high and very high liquefaction potential based on DCP test results.

4 Conclusions

In this research the engineering geological conditions of Holocene sediments of the Anazli area were investigated based on geological and sedimentological studies, DCP test results and geotechnical data collected over the study area. The results show that the sediments of the study area have

high degree of engineering geological problems that should be taken into account during planning and construction of infrastructures in the Anzali area. The results of this study could be used for prediction of geological conditions in new foundation sites in the study area. With this information, the planners are able to coordinate urban development plans with unfavorable engineering geological conditions to achieve a sustainable development of the study area.

References

Annells, R., Arthurton, R., Bazley, R. et al. (1975) *Explanatory text of the Qazvin and Rasht Quadrangles Map 1:250000*. Geological survey of Iran.

Clark, G., Davies, R., Hamzepour, B., et al. (1975) *Explanatory text of the Bandar-e-Anzali Quadrangle Map 1:250000*. Geological survey of Iran.

Jackson, J., Priestley, K., Allen, M., et al. (2002). Active tectonic of the south Caspian basin. *Geophysical Journal International, 148*, 214–245.

Jebelli, J., Meguid, M., & Sedghinejad, M. (2010). Excavation failure during micro-tunneling in fine sands: A case study. *Tunneling and Underground Space Technology, 25*, 811–818.

Kazancı, N., Gulbabazadeh, T., Leroyd, S., et al. (2004). Sedimentary and environmental characteristics of the Gilan–Mazenderan plain, northern Iran: influence of long- and short-term Caspian water level fluctuations on geomorphology. *Marine Systems, 46*, 145–168.

Lahijani, H. A. K., Rahimpour-Bonab, H., Tavakoli, V., et al. (2009). Evidence for late Holocene highstands in Central Guilan–East Mazanderan, South Caspian coast. *Iran. Quaternary International, 197*, 55–71.

Luna, R., & Frost, J. (1998). Spatial liquefaction analysis system. *Journal of Computing in Civil Engineering, 12*(1), 48–56.

Sonmez, H. (2003). Modification of the liquefaction potential index and liquefaction susceptibility mapping for a liquefaction-prone area (Inegol, Turkey). *Environmental Geology, 44*(7), 862–871.

Nogol-e-Sadat, M. (1991). *Comprehensive geological studies of Guilan Province*. Guilan: Governmental office of Guilan Province.

Youd, T., & Idriss, I. (2001). Liquefaction resistance of soils: summary report from the 1996 NCEER and 1998 NCEER/NSF workshop on evaluation of Liquefaction resistance of soils. *Journal of Geotechnical and Geo-environmental Engineering, 127*(10), 817–833.

Evaluation of Engineering Geological Condition in Shanghai Coastal Area

Y. J. Shi, X. X. Yan, J. H. Wang, Z. Fang, and B. Li

Abstract

Shanghai coastal area, as the leading development region of Shanghai, has been constructed more and more engineering projects in recent years. However, its engineering geological conditions are complicated and not been well understood by far, as many geological problems occurred during project construction. Therefore, it is quite necessary for project designers and decision-makers to have a reasonable evaluation results on the engineering geological condition of this area. With the information of about 1,000 boreholes and almost 100 years' underwater topographic maps of Shanghai coastal area, this paper aims to assess the suitability of building project, underground engineer, and underwater pipe lines construction by analyzing the engineering geological condition, summarizing the character of environmental geological problems, and establishing an engineering geological stratigraphic sequence.

Keywords

Evaluation • Engineering geological condition • Environmental geological problem • Special soil • Suitability

1 Introduction

Shanghai coastal area has played an important and active role in economic development. As the economic center of Yangtze River Delta, Shanghai plans to quicken the infrastructure construction of new cities and towns located in coastal area and Yangtze River bank.

With the construction of a number of projects, the complicated engineering conditions, together with many geological problems are confronted by the designers and engineers, their existence directly influence the layout and planning of new building, bridge, pipeline, etc. (Wang 2011). Moreover, coastal erosion and deposition, land subsidence, and other environmental geological problems are definitely influencing the safe operation of major projects, so we must find out their situation and future trend, more important; present the feasibility evaluation for different projects according to the engineering geological conditions, as they are vital for insuring construction safety and saving cost from engineering maintenance.

2 Features of Engineering Geological Stratum

Based on the analysis of 1,000 engineering geological boreholes (Fig. 1), and the research result of Quaternary deposition evolvement environment (Li et al. 2000); (Qiu et al. 2007), this paper establishes the engineering geological stratigraphic framework of Shanghai coastal area covering both land and water areas. In total, nine

Y. J. Shi (✉) · J. H. Wang
Shanghai Jiaotong University, Shanghai 200240, China
e-mail: shiyujin1976@163.com

Y. J. Shi · X. X. Yan · Z. Fang · B. Li
Shanghai Institute of Geological Survey, Shanghai 200072, China

Y. Huang et al. (eds.), *New Frontiers in Engineering Geology and the Environment*,
DOI: 10.1007/978-3-642-31671-5_23,

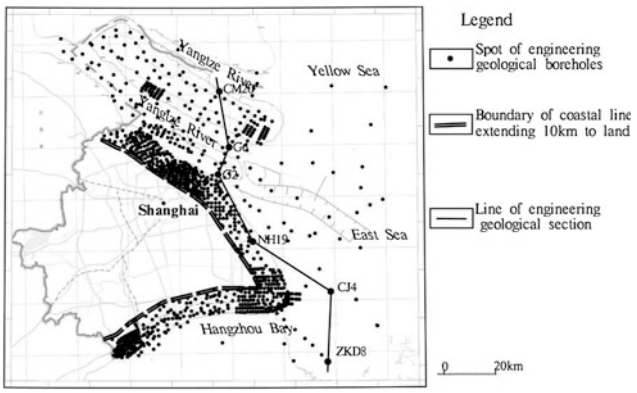

Fig. 1 Sketch map showing the distribution of engineering geological boreholes in Shanghai coastal area

Soft soil, mainly composed of muddy cohesive soil, spreads all over the coastal area of Shanghai except part of Chongming island. Its upper layer is muddy silty clay, and lower layer is muddy clay. The soft soil are characterized by poor physical and mechanical properties, such as high water content, big pore ratio, high compressibility, and lower strength, and are the main subsidence layer under additional load. Moreover, because of rheological and thixotropy features, soft soil can induce long-term deformation of foundation and pit slope failure.

In the coastal area, liquefacient sand soil are majorly gray silt or sandsilt of layer ②$_3$, ⑤$_2$, and ⑦. Layer ②$_3$ is shallow buried with big thickness, widely distributed in land and water area. Layer ⑤$_2$ is characterized by greatly various depth and thickness, it can only be found in part of Chongming island and its adjacent area. layer ⑦, as the first confined aquifer in Shanghai area, is widely spread in Hangzhou Bay area. On account of the high groundwater level of these liquefacient sand soil layers, shifting sand and sand boiling often occur during the construction of excavation engineering.

Fig. 2 Cross section of engineering geological strata

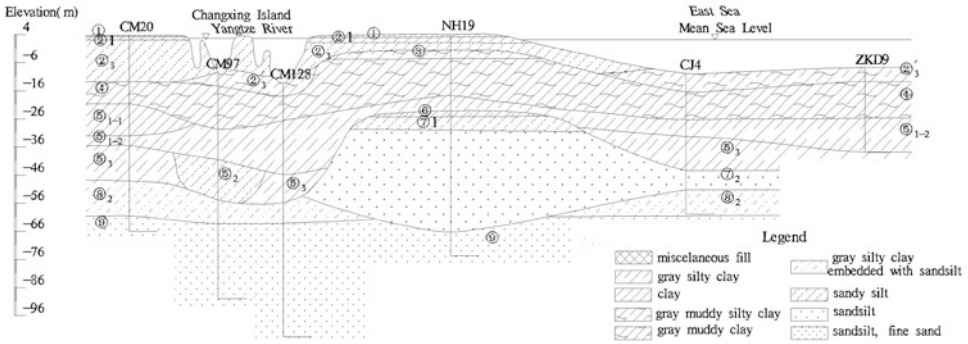

engineering geological layers and 40 sub-layers are determined within 100 m in depth below surface (Fig. 2, Table 1) (Yan & Shi 2006). The main layers are Holocene littoral-estuarine shallow sand soil layer (layer number is ②$_3$), littoral-neritic soft soil layers (③, ④), littoral or downed valley cohesive soil layer embedded with sand soil (⑤), late Pleistocene lake-swamp cohesive soil layer (⑥), estuarine-littoral sand soil layer (⑦), littoral-neritic cohesive soil layer (⑧), and fluvial sand soil layer (⑨).

3 Special Soils

Rinse fill, soft soil, and liquefacient sand soil are the main special soils in Shanghai coastal area. They have poor engineering geological features for engineering construction.

Rinse fill, varying from cohesive soil to sandy silt lithologically, is widely distributed in the new land area along the Yangtze River and sea. It can't be the natural subgrade bearing stratum due to lower natural bearing capacity of foundation, it is also the main poor geological phenomenon during the construction of metro, anti-flood bank, and pipeline. Additionally, the sandy silt rinse fill is liquefacient soil, and vibration liquefaction seepage liquefaction could probably occur during the construction of underground project.

4 Suitability Assessments of Engineering Geological Conditions for Construction

There are main three project types in Shanghai coastal area, shallow foundation, pile foundation, and underground engineer. Generally, pile foundation is adopted in bridges, buildings, and docks, shallow foundation is adopted in pipelines and lower buildings, whereas underground foundation is adopted in metro and crossing river tunnel projects. Based on the analysis of engineering geological conditions and project types, we can assess the suitability for these projects.

4.1 Pile Foundation Project

For assessing the suitability of engineering geological conditions for pile foundation projects, landform is the first

Table 1 Brief table of engineering geological stratum of Shanghai coastal area

Geological era		Layer no	Layer name	Top elevation (m)	Thickness(m)	Genetical type	State or compactness
Holo-cene Qh	Qh_3	$①_1$	Miscelaneous fill		0.4–2.7	Man-made	Loose
		$①_3$	Rinse fill	5.5–0.8	0.4–6.0	Man-made	Loose
		$②_1$	Brown-yellow cohesive soil	4.4–0.7	0.5–3.4	Littoral-estuarine	Plastic state to incompetent plastic
		$②_3$	Gray silt, sandsilt	3.5 to −20.0	0.9–29.4	Littoral-estuarine	Loose to sparse
		$②_3'$	Gray muddy silty clay	−0.3 to −14.5	1.0–13.9	Littoral-estuarine	Flow plastic
	Qh_2	③	Gray muddy silty clay	1.6 to −4.7	2.8–9.0	Littoral-neritic	Flow plastic
		④	Gray muddy clay	−2.5 to −29.4	1.2–22.3	Littoral-neritic	Flow plastic
	Qh_1	$⑤_{1-1}$	Gray clay	−11.1 to −33.7	1.0–15.9	Littoral, swamp	Flow to incompetent plastic
		$⑤_{1-2}$	Gray silty clay	−13.5 to −38.1	1.4–31.0	Littoral, swamp	Incompetent plastic to plastic state
		$⑤_2$	Gray silt, sandsilt	−19.5 to −50.2	3.0–19.2	Littoral, swamp	Sparse to mederate dense
		$⑤_3$	Gray silty clay	−21.8 to −53.8	1.2–27.0	Drowned valley	Plastic state
		$⑤_4$	Gray-green silty clay	−27.3 to −53.6	1.0–5.7	Drowned valley	Plastic state to competent plastic
Late Pleist-ocene Qp_3	Qp_3^2	⑥	Dark green silty clay	−10.7 to −31.8	1.4–4.8	Estuarine-littoral	Competent plastic
		$⑦_1$	Yellow sandy silt	−13.1 to −32.8	2.0–10.8	Estuarine-lake-swamp	Mederate dense to dense
		$⑦_2$	Gray-yellow sandsilt	−28.1 to −56.1	2.8–36.0	Estuarine-littoral	Dense
		$⑧_{1-1}$	Gray clay	−19.0 to −59.3	2.5–16.7	Littoral-neritic	Plastic state
		$⑧_{1-2}$	Gray silty clay	−30.4 to −58.9	4.5–12.0	Littoral-neritic	Plastic state
		$⑧_2$	Gray silty clay	−32.3 to −60.4	2.5–26.5	Littoral-neritic	Plastic state
	Qp_3^1	⑨	Gray sandsilt, fine sand	−57.0 to −77.8	10–30.0	Fluvial	Dense

factor to be considered. There exists difference between land area and water area in the conditions and the suitability. According to the distribution of bearing stratum, layer ⑦, of pile foundation, we can detailedly partition subdivision. In land area, the suitability where the top surface of layer ⑦ is higher than −27 m in elevation and the thickness exceeds 30 m is better than other regions. In water area, the suitability where top surface of layer ⑦ is higher than −37 m in elevation is better than other regions. So we can make out four divisions in the coastal area. They are very good, good, ordinary, and little worse suitable area (Fig. 3).

4.2 Underground Engineering

Due to the big difference between land area and water area in geological conditions and construction technique, the partition principles vary from one another (Sun 2011).

In the land area, excavations and tunnels are the main underground engineers. During the construction, we will be confronted with shifting sand induced by rinse fill or sand soil, foundation deformation induce by soft soil, and water and soil piping of foundation pit induced by high groundwater level. The division factors are the distribution situation of layers $②_3$, $⑤_2$, and⑦, because these sand soil layers

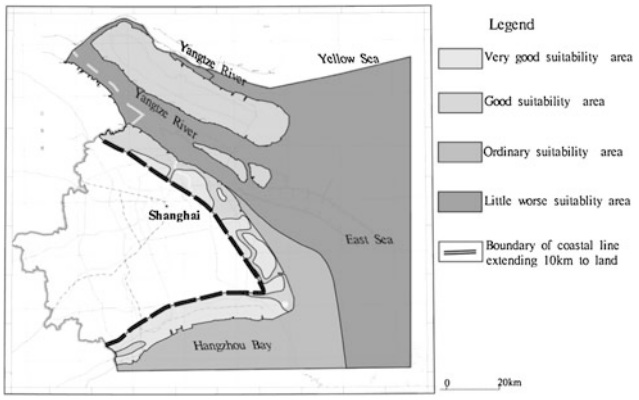

Fig. 3 Sketch map showing the suitability of pile foundation projects

are respective phreatic aquifer, shallow confined aquifer, and the first confined aquifer, moreover, the distribution of soft soil layer is related to them. According to that, the suitability of most places in land area is ordinary, and north coastal zone of Hangzhou Bay is the little worse suitable area.

In water area, except the engineering geological problems of shifting sand and soft foundation deformation, coastal erosion and deposition should be considered as well. The result of suitable partition indicates that Hangzhou bay is good suitable area for the underground engineer and the Yangtze River Estuary is basic little worse suitable area.

4.3 Pipeline Under the Sea

Generally, fiber optic cable and electric cable crossing sea or river are located under the water. Some of them are laid on the top of seabed, and some are under the seabed. During the construction of pipelines, we should take account of bedforms, shallow soil properties, etc. Main engineering geological problems are sand liquefaction, soft foundation deformation, erosion and deposition of seabed and riverbed, and underwater landslide.

According to that, we can determine the suitability in the coastal area. (1) In the Nanhui beach, and east Chongming Island and Hengsha riffle regions, there is only one kind of engineering geological problem, liquefaction sand or soft deformation, therefore, the suitability is very good; (2) In the region where two kind of engineering geological problems occur simultaneously,among sand liquefaction, soft foundation deformation, erosion and deposition of seabed and riverbed, the suitability varies from good to ordinary; (3) Sometimes three kinds of engineering geological problems including water bottom landslide may simultaneously come out in some regions, where the suitability is poorer.

5 Conclusions

The following results are concluded from this paper:

(1) There are total nine engineering geological layers and 40 sub-layers in Shanghai coastal area within 100 m in depth below surface, in which Holocene late Pleistocene sand soil, soft soil and cohesive soil are included; (2) In Shanghai coastal area the main special soils are rinse fill, soft soil, and liquefacient sand soil, they are characterized by poor engineering geological specificity during construction;(3) the construction suitability vary from one another due to different construction technique of shallow foundation, pile foundation, and underground engineer, and different engineering geological conditions in Shanghai coastal area. The designers and builders should take reasonable plan and construction according to the result of suitable division.

Through the evaluation of engineering geological conditions in Shanghai coastal area, this paper gets the suitable division for different project type, and presents the assessment results. Even though, further survey and assessment are required for specific project since the engineering geological conditions vary complicatedly, and the investigation scale is not big.

Acknowledgments I would express my gratitude to Ministry of Land and Resources of China, and China Geological Survey, who sponsored geological investigation in Shanghai coastal, so that we can get so much geological information. I gratefully acknowledge the help of my supervisors in my university and institute. I do appreciate their patience, encouragement, and professional instructions during my writing. In addition, I deeply appreciate the contribution to this paper made in various ways by my colleagues.

References

Li, C., Chen, Q., Zhang, J., et al. (2000). Stratigraphy and paleoenvironmental changes in the Yangtze Delta during the late Quaternary. *Journal of Asian Earth Sciences, 18*, 453–469.

Qiu. J., & Li, X. (2007). *The Quaternary strata and sedimentary environment* (1st edn). Shanghai: Shanghai Science and Technology Press.

Sun, J. (2011). Prevention and control of the environmental geotechnical problems in development and utilization of urban underground space. *Shanghai land and Resources, 32*(4), 1–11.

Wang, P. (2011). Earth science research in Shanghai: From Yangtze estuary to deep ocean. *Shanghai land and Resources, 32*(3), 1–6.

Yan, X., & Shi, Y. (2006). Structure characteristic of engineering geology in Shanghai. *Shanghai Geology 27*(4):19–24.

Study of Optimum Building Spacing of Dense High-Rise Building Group in Shanghai Based on Centrifugal Model Test

Y. Q. Tang, C. S. Sun, S. P. Song, Q. Yang, and J. Li

Abstract

Facing the problem of soaring urban population caused by accelerated urbanization in China, more cities choose dense high-rise building groups to release pressure of tremendous land requirement, which is proved effective. However, those building groups could also induce over-standard engineering land subsidence, which can be a catastrophe especially to low-altitude cities. Land subsidence had been well controlled by limiting the excavation of groundwater in Shanghai, but the continuing urban construction made the effort not as useful as before, engineering-environmental effect caused by dense high-rise building group had become a main form of land subsidence in Lujiazui, Shanghai, the chosen area in this paper. Through the model test by Tongji University TLJ-150 geotechnical centrifuge, this paper studies the influence of three different building spacing on the land subsidence of dense high-rise building group. Through data analysis base on simplification of viscoelastic foundation, if displacement is considered only, the optimum building spacing of dense high-rise building group in Shanghai Lujiazui is attained as 34 m. The paper also deduces the displacement–time (S–t) equation from displacement–time curve and the displacement-distance (S–L) equation.

Keywords

Soft soil • Dense high-rise building group • Engineering land subsidence • Optimum building spacing • Centrifugal model test

1 Introduction

Since it's first recorded in Mexico City in 1891, land subsidence has gradually become a worldwide engineering problem (Guerrero et al. 2008). The early stage work, which mainly focused on the displacement caused by excessive extraction of groundwater or the load of single building, had attained abundant achievement (Cui and Tang 2007). Nowadays, with the dramatically increase of urban population, dense high-rise building groups have become popular to rapid urbanization. Till the end of 2009, there were 3,827 buildings over 19 floors and 975 buildings over 30 floors in Shanghai. Relative researches showed that engineering environmental land subsidence caused by construction of high-dense building groups had accounted for majority of land subsidence in soft soil area. In this case, a rational layout for new coming dense high-rise building group is crucial to the fast development field like Shanghai Pudong Lujiazui area.

Common land subsidence observation is easily influenced by observe conditions or some other factors, it's difficult to conduct a long-term and accurate observation test. In this paper, a small spatial scale and short time scale model test is applied to replace the large spatial scale and long time scale prototype test.

Y. Q. Tang (✉)
Key Laboratory of Geotechnical and Underground Engineering of Ministry of Education, Tongji University, No.1239, Siping road, Shanghai 200092, China
e-mail: tangyiqun2@mail.tongji.edu.cn

Y. Q. Tang · C. S. Sun · S. P. Song · Q. Yang · J. Li
Department of Geotechnical Engineering, Tongji University, No.1239, Siping road, Shanghai 200092, China

Y. Huang et al. (eds.), *New Frontiers in Engineering Geology and the Environment*,
DOI: 10.1007/978-3-642-31671-5_24,

Table 1 Physical properties of main model soil

Layer number	Water content w (%)	Dry density(g/cm^3)	Natural void ratio e_0	Compress modulus$E_{s0.1-0.2}$ (MPa)	Cohesionc(kPa)	Angle of internal friction φ(°)	Coefficient of permeability k(m/s)
④	41.7	3.09	1.42	2.12	14.44	20.16	1.45×10^{-7}
⑦	27.8	3.45	0.77	11.95	3.77	34.59	3.51×10^{-4}
⑧	33.7	2.75	0.93	5.49	13.57	21.62	4.79×10^{-6}

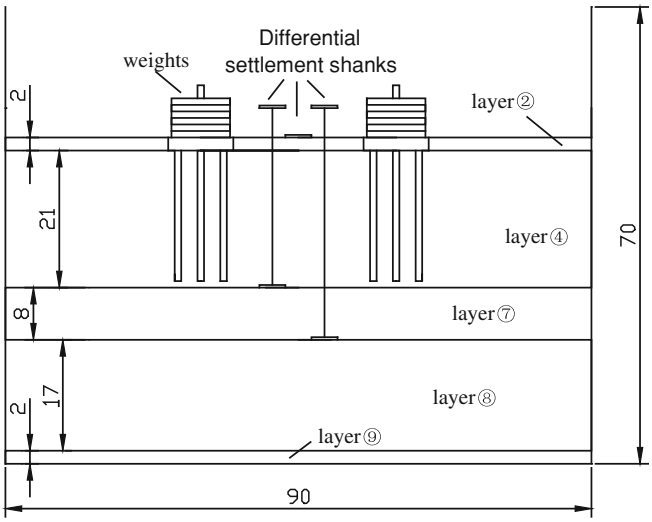

Fig. 1 Section figure of model (unit: cm)

Due the complexity of soft soil mechanical structure, suitable materials were barely found to replace it in model test. The model soil can only be made with natural soil, which means mechanical similarity ratio in the model test is 1 (Zuo 1984). Definite E_S as the soil modulus of compression, the relationship between stress (σ) and displacement (ε) can be expressed as:

$$\sigma = E_s \varepsilon \tag{1}$$

From the similarity theory (Yuan 1998):

$$C_{E_s} = C_\gamma C_L = C_\rho C_g C_L \tag{2}$$

When model soil is same to prototype soil, $C_{E_s} = C_\rho = 1$. Then:

$$C_g C_L = 1 \tag{3}$$

In model test, the prototype material is used in the model, it means that if $C_L \neq 1$, then $C_g \neq 1$, the influence of unit weight should be sufficiently considered—geotechnical centrifugal model test is specifically applied in this condition (Xing and Xing 2005).

2 Centrifugal Model Test Design

Tongji University TLJ-150 geotechnical centrifuge is applied in this model test. The machine's capacity is 150 gt and its effective radius is 3 m. The size of model box is 0.9 m × 0.7 m × 0.7 m (L × W × H), and the mass of the model box is 572 kg.

According to the typical engineering geological conditions of Shanghai Pudong Lujiazui area, following undisturbed soil samples were selected as soil models: the ②layer of brown-yellow clay layer; the ④layer of silt clay layer; the ⑦layer of silt layer; the ⑧layer of silt clay layer and the ⑨layer of silt layer (Tang and Cui 2008). Physical properties of main soil layers are shown in Table 1.

The chosen geometric similarity ratio is decided as 120, the height of model box is 70 cm and the total thickness of the model soil is 50 cm. The sectional and plane figures of the model box are shown in Figs. 1 and 2.

Piles foundation is chosen as the building model foundation. Considering the impact of the size effect, this paper selects pile diameter $d = 6$ mm and pile length $L_P = 20$ cm, the number of piles is determined by the bearing capacity of single pile test.

In prototype, there are four building, the size of each building is 12 m × 12 m, the number of floor layers is 18, and three different building spacing are chosen as 18, 24 and 30 m.

Additional stress can be figured out from the weight of single building via the formula (4).

$$P = \gamma_0 \alpha \omega N_s \tag{4}$$

Where

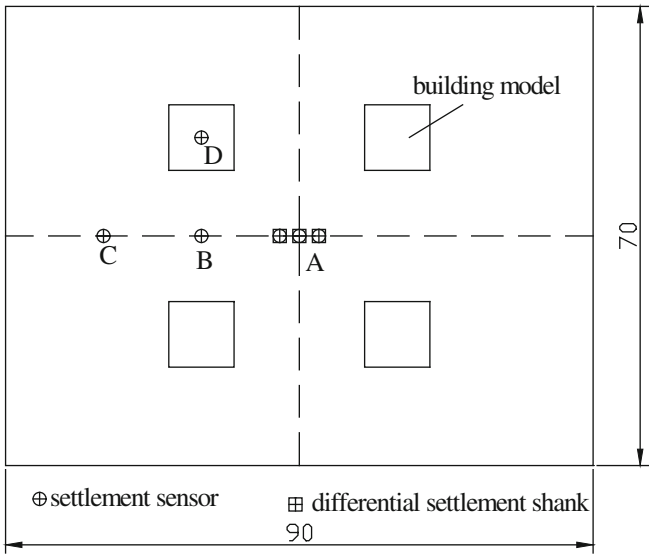

Fig. 2 Plane figure of model (unit: cm)

P additional stress;
γ_0 sub-vertical load coefficient, taking 1.2;
α amplification coefficient when consider the axial force caused by earthquake, taking 1.05–1.1 when 7° and 1.1–1.05 when 8°;
ω the vertical load of unit building area, taking 12–14 KN/m^2 when frame structure and frame-wall structures and 14–16 KN/m^2 when shear walls and tube structure;
N_s column section above the floor layer;

So the additional stress P in prototype is:

$$\mathrm{P} = 1.2 \times 1.05 \times 14 \times 18 = 317.52\ \mathrm{kN/m^2};$$

And the additional stress $\mathrm{P_m}$ and upper building load $\mathrm{F_m}$ in model test are:

$$\mathrm{P_m}{=}317.52\ \mathrm{kN/m^2};$$

$$\mathrm{F_m} = \mathrm{PS_m} = 317.52 \times 0.1 \times 0.1 = 3.18\ \mathrm{KN};$$

The mass of single model building $\mathrm{m} = \mathrm{F} \div (120\ \mathrm{g}) = 2.65$ Kg, mass of 'piles + platform' solid is 0.85 kg, the number of upper weights is 6, and mass of single weight is 0.3 kg.

Table 2 is the model parameters of different building spacing in centrifugal model test:

3 Test Data Analysis

The building load will generate an additional stress field around the building foundation. This paper hypothesizes: (1) the horizontal additional stress σ_H is linear with the vertical additional stress σ_V, and $\sigma_H = K_0\sigma_V$, where K_0 is the coefficient of "at-rest" pressure; (2) Before the foundation damagements, soil foundation doesn't produce horizontal displacement (or horizontal displacement is very tiny), so on any vertical annular in different distance to single building's center, the total horizontal additional stress acts is a constant: $\sum \sigma_{\mathrm{H}} = \text{constant}$; (3) The soil is a viscoelastic body, and its integrated soil spring coefficient of the model soils is K, integrated damping coefficient is C. The solution of viscoelastic model equation is:

$$S(t) = \frac{\sigma_0}{K}\left(1 - e^{-\frac{K}{C}t}\right) \tag{5}$$

At the first 30 min of this test, the centrifuge is in its loading phase, the additional building load and the soil itself is changing, therefore, we can only consider the following displacement when dealing with the data, and add a constant w on Eq. 5 to denote the displacement of first 30 min. So the equation can be rewritten as:

$$S(t) = \frac{\sigma_0}{K}\left(1 - e^{-\frac{K}{C}t}\right) + w \tag{6}$$

From the similarity theory, some other equations will be attained:

$$S(t)_m = \frac{\sigma_0}{K_m}\left(1 - e^{-\frac{K_m}{C_m}t_m}\right) + w_m = ns \tag{7}$$

$$K_m = \frac{1}{n}K \tag{8}$$

$$C_m = \frac{1}{n^3}C \tag{9}$$

$$t_m = \frac{1}{n^2}t \tag{10}$$

$$\begin{aligned} s = \frac{1}{2}S(t)_m &= \frac{1}{n}\frac{\sigma_0}{\frac{1}{n}K}\left(1 - e^{-\frac{\left(\frac{1}{n}K\right)}{\left(\frac{1}{n^3}C\right)}\times\frac{1}{n^2}t}\right) + \frac{1}{n}w_m \\ &= \frac{\sigma_0}{K}\left(1 - e^{-\frac{K}{C}t}\right) + w = S(t) \end{aligned} \tag{11}$$

Table 2 Model parameters of different building spacing in centrifugal model test

Spacing (cm)	Number of floor layers	Size of platform	Mass of single model building (kg)	Mass of 'piles + platform' solid (kg)	Weights number	Mass of single weight (kg)
15	18	10 cm × 10 cm	2.65	0.85	6	0.3
20	18	10 cm × 10 cm	2.65	0.85	6	0.3
25	18	10 cm × 10 cm	2.65	0.85	6	0.3

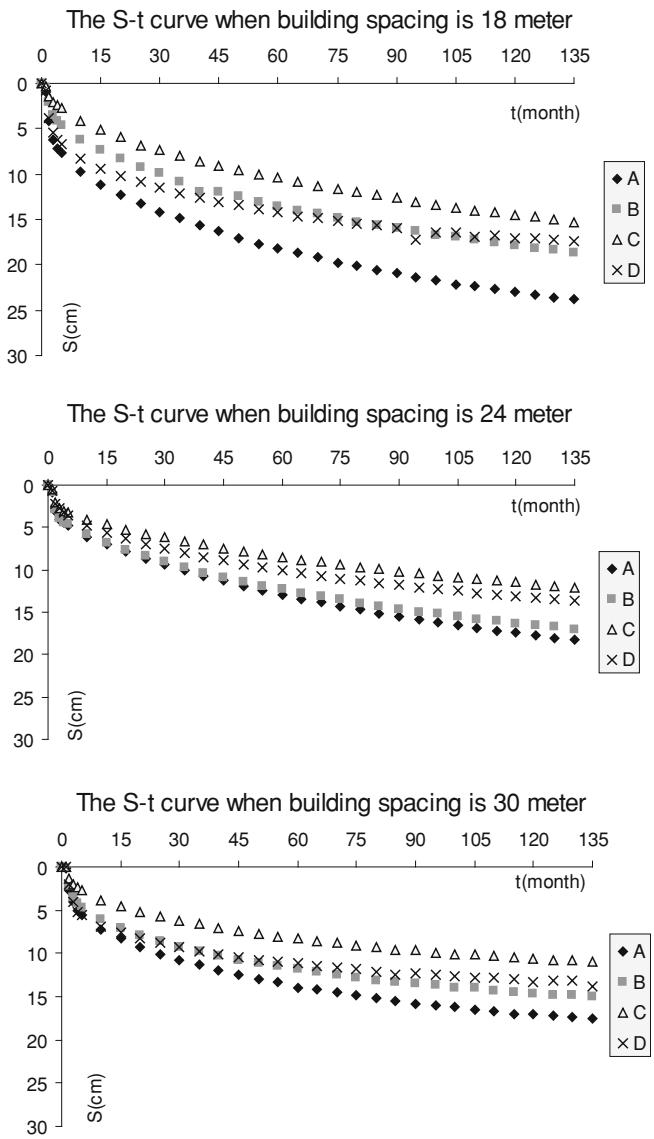

Fig. 3 Displacement-time curves of observation points in three different building spacing

Where n denotes the geometric similarity ratio; s denotes the measure value of the displacement.

Formula (11) shows the measuring value of displacement in the centrifugal model test equals to the displacement in natural world. In this centrifugal model test, similarity ratio of time is the square of lengths'. The geometric similarity ratio is 1:120; therefore, the time similarity ratio is 1:14,400, which means 1 s in centrifugal field equals 4 h of the natural world. The prototype displacement–time (S–t) curves of observational points in three different building spacing are shown in Fig. 3.

Defining $v = \frac{\sigma_0}{K}$, $u = \frac{K}{C}$. In practical projects, u, v, w indeed have special significance, v reflects the building's land subsidence of post-construction; u relates to the building's land subsidence during construction. Fit Eq. 6 in those data and the related model parameter are shown in Table 3.

Table 3 Statistics of the model parameter

Spacing = 18 m	Point A	Point B	Point C	Point D
U(month^{-1})	0.013	0.011	0.012	0.017
v(cm)	19.15	17.16	15.35	11.7
w(cm)	7.77	4.51	2.65	6.7
Spacing = 24 m	Point A	Point B	Point C	Point D
u (month^{-1})	0.01	0.012	0.01	0.013
v (cm)	17.71	16	11.32	12.18
w(cm)	4.3	4.24	2.79	3.59
Spacing = 30 m	Point A	Point B	Point C	Point D
u (month^{-1})	0.016	0.016	0.015	0.02
v (cm)	13.95	12.9	9.14	8.28
w (cm)	5.53	5.27	2.61	5.49

Table 4 Part data of the spacing-subsidence relationship

Spacing (m)	21	25.5	29.7	47.4	56.9	66.4
Displacement (cm)	6.77	5.51	4.87	2.27	1.55	1.01

Table 5 Part data of the spacing-subsidence relationship

Spacing (m)	6.77	15	18	21	21.2	25.5	29.7	47.4	56.9	66.4
Displacement(cm)	6.74	6.95	7.13	6.77	6.73	5.51	4.87	2.27	1.55	1.01

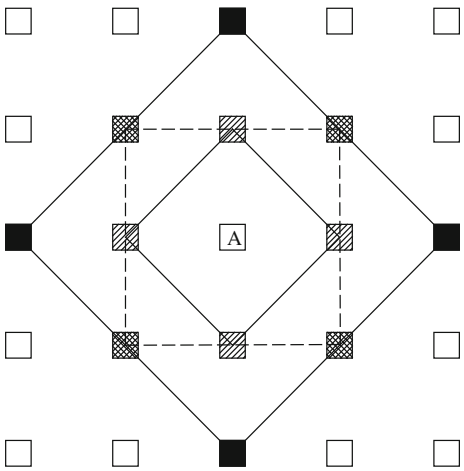

Fig. 4 A n × n dense building group

Table 3 shows that compared with three other points at the same spacing, there is a 25 % increase in the u value of point D, which means that there are great differences in soils' elasticity and damping between pile-soil foundation and soil foundation.

Defining $H(x)$ as the vertical stress effective depth, $\because \sum \sigma_{\mathrm{H}} = \text{constant}$, $\sigma_H = K_0\sigma_V$, $\sigma_V = KS(x)$ then:

$$2\pi x[H(x) - S(x)]\sigma_H = 2\pi x[H(x) - S(x)]K_0KS(x) = \text{constant t} \quad (12)$$

$$x[H(x) - S(x)]S(x) = a \quad (13)$$

Where a is a constant. The solution of Eq. 13 is:

$$S(x) = 0.5H(x) - \sqrt{0.25H^2(x) - \frac{a}{x}} \quad (14)$$

For simplifying the solution, $H(x)$ can be treated as a constant. From superimposition principle, when the building spacing is L:

$$S(\frac{\sqrt{2}}{2}(L + 12)) = 0.25S_A \quad (15)$$

$$S(\frac{\sqrt{10}}{2}(L + 12)) = 0.5(S_C - 0.5S_A) \quad (16)$$

Then Table 4 is got:

Fit Eq. 14 in those data. It's found that the calculated data of equation is little deviation with the measuring data: when $8 < x < 15$, the calculated data is a little larger than the measuring data, and little smaller when $x > 40$. Therefore, a correction factor should be added:

$$S(x) = (0.5H - \sqrt{0.25H^2 - \frac{a}{x}})(b^x + c) \quad (17)$$

Fit Eq. 17 in the data of Table 4 adopting Quasi-Newton (BFGS) method:

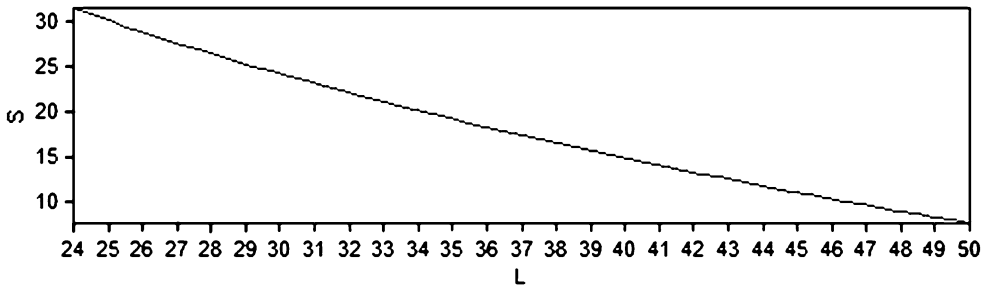

Fig. 5 Land subsidence-building spacing (S-L) curve of dense building group

$$S(x) = (14.62 - \sqrt{213.75 + \frac{5544.62}{x}})(1.0085^x - 2.13) \tag{18}$$

When $L = 18$, 24 and 30, the corresponding $S_D = 18.4$, 16.77 and 13.77, Eq. 19 gives out three different value of $S(r)$: 6.67, 6.73 and 6.81, fluctuate of the result is acceptable, and $S(r)$ is chosen as average (6.67, 6.73, 6.81): $S(r) = 6.74$.

$$S_D = S(r) + 2S(L + 12) + S(\sqrt{2}(L + 12)) \tag{19}$$

$$S_B = 2S(\frac{\sqrt{5}}{2}(0.5L + 6)) + 2S(0.5L + 6) \tag{20}$$

From Eq. 20:

$$S(15) = 0.5 \times (17.16 + 4.51) - S(33.54) = 6.95$$
$$S(18) = 0.5 \times (16 + 4.24) - S(40.25) = 7.13$$
$$S(21) = 0.5 \times (12.9 + 5.27) - S(46.95) = 6.77$$

Table 5 shows that there is a distinct difference between the curve of $x > 20$ and $x < 20$. Eq. 6 shows that the final displacement $S(x) = \frac{\sigma_0}{K} + w$. When $x > 20$, the influence of pile foundation can be ignored, $S(x)$ is simply relevant to σ_0 and w. When $x < 20$, K is changing frequently with the increase of x, and $S(x)$ is relevant to all its parameters.

In a boundless site, when the building density reaches its maximum, as it's shown in Fig. 4, when the building spacing $L \geq 24$ m, there are only 12 shadow building and building A itself contribute to the displacement of building A. From the superimposition principle, the final displacement S of building A is:

$$S = S(r) + 4S(L + 12) + 4S(\sqrt{2L} + 16.97) + 4S(2L + 24) \tag{21}$$

Where

L the building spacing;
r the equivalent round radius of building foundation

Figure 5 is the land subsidence-building spacing (S–L) curve of dense building group.

According to "DGJ08-11-2010 J11595-2010", the displacement of high-rise building should be below 20 cm. If $S = 20$, then $L = 34$. It means that if displacement is considered only, the optimum building spacing of dense high-rise building group in Lujiazui Shanghai is 34 m.

Most of the high-rise building foundation form is pile foundation in Lujiazui, and the thickness of the layers in this model test is chosen through a large number of prospect data, it means that the conclusion is trusty.

In this condition, the building plat ratio is 1.22; the habitation is in a superior building environment (Yan and Gong 2002). Generally, if the displacement environment of building is not as terrible as building A in Fig. 5, the suitable building spacing is less than 34 meter and it can be calculated through Eq. 18 through the superimposition principle.

On practical project, the optimum building spacing of dense high-rise building group is not a constant, some other standard should be also considered, according to the "Technical Code of Shanghai Urban Planning and Management", when high residential building arranged in parallel with others, the spacing between them should obey:

(a) If one building's orientation is north–south, the spacing between them should not be less than 0.5 times of the south building height, and its minimum value is: 24 m within the Inner Ring area in Puxi, and 30 m in other areas.
(b) If one building's orientation is east–west, the spacing between them should not be less than 0.4 times of the higher building height, and its minimum value is 24 m.

4 Conclusions

According model tests of three different building spacing by Tongji University TLJ-150 geotechnical centrifuge and data analysis, this paper achieves some general rules of land subsidence in dense high-rise building group. Results as follows:

(1) Through the geotechnical centrifuge tests, this paper attains dense high-rise building group S–t (displacement–time) curve and equation, dense high-rise building group S–L (displacement-spacing) equation;

(2) If displacement is considered only, through the superimposition principle, this paper attains that the optimum building spacing of dense high-rise building group in Lujiazui Shanghai is 34 m, and the corresponding building plat ratio is 1.22;

Acknowledgments This work is supported by Subject of National Science and Technology Supporting Plan (2012BAJ11B04), National Nature Science Foundation of China (40872178 & 41072204) and Shanghai Leading Academic Discipline Project (project No.B308).

References

Cui, Z., & Tang, Y. (2007). Present situation and study of domestic and foreign land subsidence (in Chinese). *Northwestern Seismological Journal, 3*, 275–278.

Zuo, D. (1984). *Theory and method of model test (in Chinese)*. Beijing: China WaterPower Press.

Guerrero, O., Rudolph, D., & Cherry, J. (2008). Analysis of long-term land subsidence near Mexico City: field investigations and predicative modeling. *Water Resources Research, 35*(11), 3327–3341.

Tang, Y., & Cui, Z. (2008) Model test study of land subsidence caused by the high-rise building group. *Bulletin of Engineering Geology and Environment, 67(2)*, P173–P179.

Yan, X., & Gong, S. (2002). The relationship between the Shanghai city proper building density and land subsidence (in Chinese). *Hydrogeology and Engineering Geology, 6*, 21–25.

Yuan, W. (1998). *Similarity theory and statics model test (in Chinese)*. Chengdu: Southwest Jiao tong University Press.

Xing, Y., & Xing, J. (2005). Progress and thoughts about centrifugal model test study (in Chinese). *Journal of Water Resources architecture Engineering, 3*(1), 28–31.

THM Simulation for Real-Scale Field Test

Y. L. Xiong, F. Zhang, T. Nishimura, and Y. Kurimoto

Abstract
In deep geological disposal for high level radioactive waste, one of the most important factors is to study the thermo-hydraulic-mechanical (THM) behavior of natural barrier, that is, host rock during heat process and hydraulic environment change. In this paper, a program of finite element method called as SOFT, using finite element-finite difference method in soil–water-heat coupling problem has been developed to simulate the above-mentioned THM behavior of geological disposal based on a thermo-elasto-viscoplastic constitutive model. In order to verify the availability of the program, a real-scale field heating test reported by Gens et al. (2007) is simulated by the proposed THM-FEM program. The material parameters of the rock involved in the constitutive model are determined based on element tests for the rock. It is shown from the figures that the proposed program can well describe the THM behavior observed in the heating test such as temperature and excessive pore water pressure (EPWP).

Keywords
THM • FEM • Temperature • Heating test

1 Introduction

In considering the problem about deep geologic disposal for high level radioactive waste, not only artificial barrier, but also the thermo-hydro- mechanical (THM) behavior of natural barrier, most of which is sedimentary rock or granite, is also a very important factor to be studied. High radioactive substance might permeate with water through barrier systems to biosphere. The temperature emitting from nuclear waste canisters also requests the study of temperature effect on soft sedimentary rock. The water may induce swelling phenomenon which can yield to a damage of the nuclear waste containers due to the generated temperature. All the above phenomena need to be well understood in order to guarantee the safety and the efficiency of the waste sealing construction.

In this paper, a program of finite element method (FEM) named as SOFT, considering soil–water-heat coupling problem, has been developed to simulate the above-mentioned THM behavior of geological disposal based on a thermo-elasto -viscoplastic model (Zhang and Zhang 2009). In order to verify the availability of the program, a real-scale field test reported by Gens et.al (2007) is simulated by the proposed numerical method. The material parameters of the rock involved in the constitutive model are determined based on element tests for the rock.

2 Brief Description of Modified Thermo-Elasto-Viscoplastic Model

A simple thermo-elasto-viscoplastic model for soft sedimentary rock has been proposed by Zhang & Zhang (2009), which can not only describe properly the thermodynamic

Y. L. Xiong · F. Zhang (✉) · T. Nishimura · Y. Kurimoto
Department of Civil Engineering, Nagoya Institute of Technology, Nagoya 466-0851, Japan
e-mail: cho.ho@nitech.ac.jp

Y. Huang et al. (eds.), *New Frontiers in Engineering Geology and the Environment*,
DOI: 10.1007/978-3-642-31671-5_25,

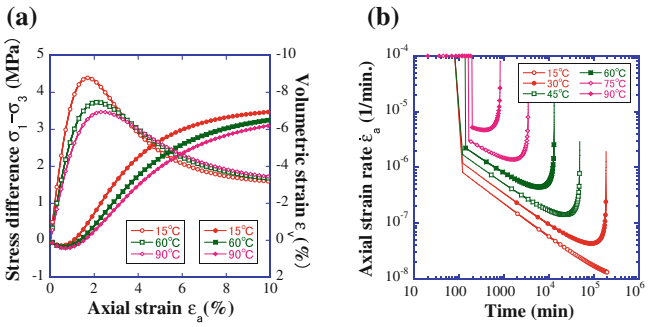

Fig. 1 Theoretical prediction of host rock by the proposed model **a** triaxial compression test **b** triaxial creep test

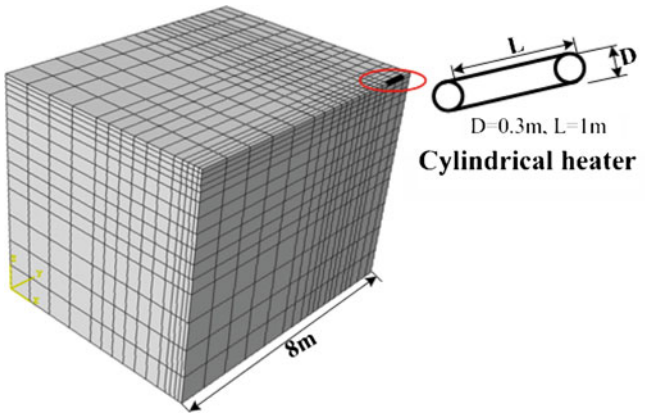

Fig. 2 3D FEM mesh

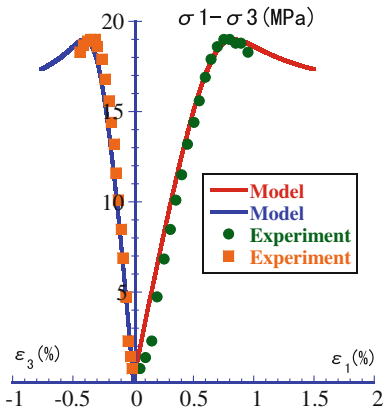

Fig. 3 Simulation of triaxial test Confining pressure of 8 MPa for Opalinus clay

behavior, but also overconsolidated and time-dependent behavior of soft sedimentary rocks. In order to take into account the influence of intermediate stress on the deformation and strength of geomaterials, modified stress t_{ij} is introduced into it.

Figure 1 shows the theoretical predictions of host rock for triaxial compression tests and creep tests under different constant temperature respectively. Table 1 shows the parameters involved in the model. It is known from the results that the shear strength in the compression tests under constant temperature and the failure time under creep tests all show good agreements with the results of element tests that have been reported in some delicate experiments by Okada (2005, 2006).

3 Description of FE-FD Mathematical Formulation

In the present paper, a FEM-FDM scheme, proposed by Oka et al. (1994), is adopted to formulate the THM coupling relation, in which finite element method (FEM) is used for spatial discretization of equilibrium equation and energy conservation equation, and finite difference method (FDM) is used for the spatial discretization of continuity equation. The temperature, displacement and pore water pressure are unknown variables in the program. The governing equations involved in the program are listed in the following:

(a) **Energy conservation equation**

$$\rho c \frac{\partial T}{\partial t} = k_t \frac{\partial^2 T}{\partial x_i \partial x_i} + Q \tag{1}$$

(b) **Equilibrium equation**

$$\frac{\partial \sigma_{ij}}{\partial x_j} + \rho b_i = 0 \tag{2}$$

(c) **Continuity equation**

$$\frac{\dot{\varepsilon}_{ii}^s}{n} - \frac{k}{\gamma_w} \frac{\partial^2 p_d}{\partial x_i \partial x_i} - \frac{1}{K^w} \dot{p}_d - 3\alpha_T^w \dot{T} = 0 \tag{3}$$

It is worth noting that the influence of the convection of water flow is not considered in the present paper, because compared with heat conduction, the maximum velocity of pore water is very small, usually less than 10^{-10} m/s within rock and can be neglected.

4 Simulation of a Real-Scale Field Test

A field test of heating process (HE-D), carried out in a soft rock called as Opalinus clay by Mont Terri underground laboratory (Gens et al., 2007), is simulated with the SOFT. For simplicity, only the case with symmetric condition is considered in this paper. Compared to the simulation by

Table 1 Parameters involved in the model

σ'_{30} (MPa)	E (MPa)	E_p	a	α	β	C_n	v	R_f	α_T	e_0	OCR
0.3	900	0.04	500	0.7	1.5	0.025	0.0804	6.0	8.0×10^{-6}	0.72	100

Table 2 Physical properties and material parameters of rock

Parameters			Physical properties		
	Young's modulus $\boldsymbol{E}$(MPa)	9800.0		Preconsolidation pressure (MPa)	900
	Poisson's ratio	0.295		Thermal expansion coefficient α_T (1/K)	8.0×10^{-6}
	Stress ratio at critical $\boldsymbol{R}_{CS}^{(=\sigma 1/\sigma 3)}$	3.0		α_{water}(1/K)	2.1×10^{-4}
	Plastic stiffness $\boldsymbol{E}_p$	0.002		Permeability $\boldsymbol{k}$ (m/s)	4×10^{-12}
	Potential shape parameter	1.5		Thermal conductivity $\boldsymbol{K}_t$(kJ m^{-1} $K^{-1}Min^{-1}$)	0.18
	Time dependent parameter	1.5		Specific heat $\boldsymbol{C}$ (kJ Mg^{-1} K^{-1})	840
	Time dependent parameter C_n	0.005		Heat transfer coefficient of air boundary	
	Over consolidation parameter **a**	8000		α_c((kJ m^{-2} K^{-1} Min^{-1})	230
	Reference void ratio e_O (at σm0=98kPa	0.159		Specific heat of water $\boldsymbol{C}_{water}$ (kJ Mg^{-1} K^{-1})	4184

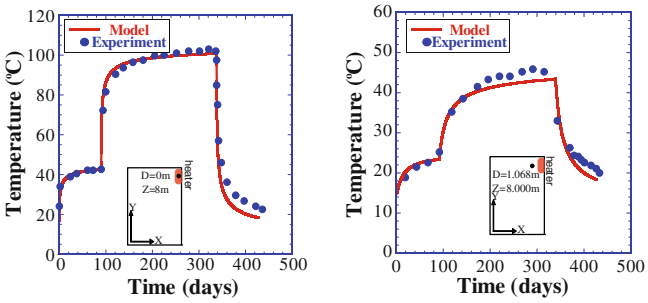

Fig. 4 Change of temperature at different position

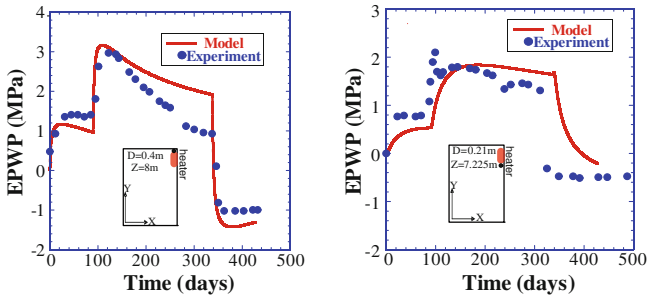

Fig. 5 Variation of EPWP at different position

Gens et al. (2007), only 1/8 area is considered. Figure 2 shows 3D mesh that consisted of 4275 cubic isoparametric elements.

In order to investigate the mechanical behavior of the rock near HE-D experiment site, triaxial compression test under confining pressure of 8 MPa was conducted by Jia et al. (2007), whose results are first simulated by the proposed model and the results are shown in Fig. 3. By this simulation, the parameters of the rock are determined and listed in Table 2. It can be seen that the proposed model can well describe the behavior of test rock.

Figure 4 shows the change of temperature at the center of heater. The temperature reached about 40° at first heating phase, and then increased very sharply at the second heating phase up to the highest temperature of about 100°. When the power of heater is switched off, the temperature decreased sharply. It also can be seen that the calculated result can well describe the experimental data. Figure 4 also shows the change of temperatures at different position. On the whole, the THM-FEM analysis can well describe the HE-D experiment.

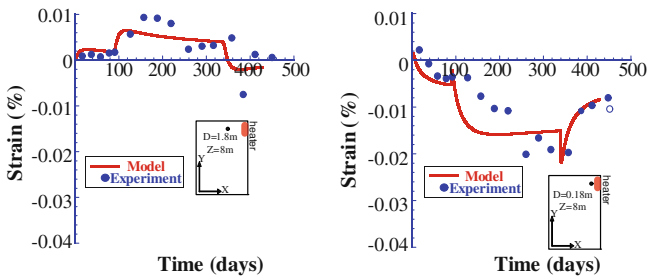

Fig. 6 Variation of deformation at different position

The evolution of EPWP with time is depicted in Fig. 5 at the different sites. It is found that the EPWP increases sharply when temperature rises up suddenly, and then it will decrease with time even though the temperature is increasing. The highest value of EPWP is up to 3 MPa. The increase of EPWP is due to the fact that thermal expansion coefficient of water is much higher than that of rock. Owing to the low permeability of rock, drainage is slow and the pore water expansion is impeded, resulting in the EPWP increase at the beginning. At later time, as mentioned

above, migration of water from the heat source is gradually accelerated due to the increase of permeability, allowing pore pressure to dissipate.

At the same time, heat-induced deformation is also investigated. Figure 6 shows the calculated and experimental results at different positions. It is found that the calculation can describe the change of the deformation qualitatively if compared with the test data. The deformation of the rock near the heater is expansive; while the deformation of the rock far away from the heater is contractive. It is very easy to understand that the rock may behave expansive due to the significant increase of temperature; nevertheless, the change of temperature at the places far away from the heater is rather. Therefore, the dilation of the rock far away from the heater is very small compared with the rock in the vicinity of the heater. As the results, swelling force caused by the expansion of the rock near the heater will cause contraction of the rock far away from the heater.

5 Conclusions

In the present paper, a program of finite element method (FEM) named as SOFT, considering soil–water-heat coupling problem, has been developed to simulate THM behavior of geological disposal based on the modified thermo–elasto- viscoplastic model which can take into consideration the influence of temperature and stress at the same time on the deformation and strength of rock. And then a field test of heating process is simulated by the proposed program. It is found that the proposed numerical method can well describe the THM behavior, such as, the temperature change, the change of EPWP and the heat-induced deformation.

References

Gens, A., Vaunat, J., Garitte, B., & Wileveau, Y. (2007). In situ behavior of a stiff layered clay subject to thermal loading: observations and interpretation. *Geotechnique, 57*(2), 207–228.

Jia, Y., Wileveau, Y., Su, K., Duveau, G., & Shao, J. F. (2007). Thermo-hydro-mechanical modeling of a situ heating experiment. *Geotechnique, 57*(10), 845–855.

Oka, F., Yashima, A., Shimata, T. et al. (1994). FEM-FDM coupled liquefaction analysis of a porous soil using an elasto-plastic model. *Applied Scientific Research, 52*, 209–245.

Okada, T, (2005) Mechanical properties of sedimentary soft rock at high temperatures (part 1)-Evaluation of temperature dependency based on triaxial compression test. Civil Engineering Research Laboratory Report, No. N04026 (in Japanese).

Okada, T. (2006). Mechanical properties of sedimentary soft rock at high temperatures (Part 2)-Evaluation of temperature dependency of creep behavior based on unconfined compression test. Civil Engineering Research Laboratory Report, No. N05057 (in Japanese).

Zhang, S., & Zhang, F. (2009). A thermo-elasto- viscoplastic model for soft sedimentary rock. *Soils and Foundations, 49*(4), 583–595.

Cluster Analysis for Orientation Data Using DifFUZZY Method

J. Wu and Z. X. Zhang

Abstract
Fuzzy clustering techniques are often used in the study of high-dimensional data sets, such as orientation data. Several methods are used in finding groups within directional data, but traditional methods usually meet difficulties when dealing with some data sets. In this paper, a new DifFUZZY clustering method, which was proposed by Ornella Cominetti and Anastasios Matzavinos for the complex data sets, is firstly applied to cluster the orientation data. The results are compared with the FCM method and the real-life data.

Keywords
Cluster Analysis • Statistics • DifFUZZY • Orientation data

1 Introduction

Before stability analysis for underground structures in rock mass, structural geologists usually need to measure and analyze orientation data in rocks and then try to subgroup the orientation data to get a general results of dominated direction data, but how to get an effectively statistics analysis of sets of orientation data is still a great challenge for them.

Until now, several methods have been proposed to help the geologists to solve the clustering problem. For examples, Schmidt(1925) proposed a counting method for the visually classifying of the orientation data in stereographic plots; Shanley and Mahtab (1976) developed a clustering technique for orientation data with minimum constraint on resulting partitions. However, these methods strongly depend on the density of data points and their results are prone to the aforementioned sampling bias. This perhaps leads to incorrect results for clusters with a small dip angle, and may lead to a suboptimal solution. Furthermore, Hammah (1998) proposed a fuzzy K-means method, named FCM, to automatically identify the orientation data. But this method still had a weakness that is how to select a proper cluster number for the subgroup orientation data and the selected value will greatly affect the clustering results.

In this paper, a DifFUZZY method (Cominetti and Matzavinos 2010) is introduced to cluster the orientation data. Unlike the FCM, it can automatically return the cluster number. In this paper, the synthetic orientation data and in situ data are used to verify the effectiveness of this method and the clustering results based on the DifFUZZY method are compared to the results of FCM method and the method by Shanley and Mahtab, respectively.

2 Methods

The DifFUZZY method (Cominetti and Matzavinos 2010) is a fuzzy spectral clustering method for biological data originally. In this paper we will attempt to utilize this method to cluster direction data. However, the input data form was not defined in detail in the paper (Cominetti and

J. Wu · Z. X. Zhang
Department of Geotechnical Engineering, School of Civil Engineering, Tongji University, Shanghai 200092, China

J. Wu · Z. X. Zhang (✉)
Shanghai Urban Construction (Group) Corporation, Shanghai 200023, China
e-mail: zxzhang@tongji.edu.cn

Y. Huang et al. (eds.), *New Frontiers in Engineering Geology and the Environment*,
DOI: 10.1007/978-3-642-31671-5_26,

Table 1 Application of the new clustering method to an artificial data set

Cluster Symbol	Synthetic data	FCM	DifFUZZY
1 (*)	30/30 (k = 40, N = 100)	32.35/32.66 (N' = 102)	31.87/31.57 (N' = 100)
2 (+)	140/45 (k = 10, N = 60)	137.73/47.64 (N' = 63)	138.54/47.28 (N' = 61)
3 (o)	230/60 (k = 15, N = 30)	233.70/63.24 (N' = 27)	236.29/62.53 (N' = 25)
4 (.)	310/75 (k = 30, N = 30)	308.89/67.90 (N' = 28)	308.92/69.62 (N' = 26)

Matzavinos 2010), moreover the input form will affect the cluster results. So in this paper, the input orientation data form can be defined as follows:

$$D = \{(1, \alpha_1, \beta_1), (1, \alpha_2, \beta_2), \ldots, (1, \alpha_n, \beta_n)\} \quad (1)$$

Thus, the three-dimension spherical coordinates (1, α, β) can be projected onto a two-dimension equatorial equal-area plane coordinates, given by the Eq.2 (Priest 1985).

$$\alpha_n = \alpha_d \pm 180; (0^\circ \leq \alpha_n \leq 360^\circ)$$

$$\beta_n = 90^\circ - \beta_d$$

$$\begin{cases} x_i = r * \sqrt{2} * \sin \alpha_n * \cos(45 + \frac{\beta_n}{2}) \\ y_i = r * \sqrt{2} * \cos \alpha_n * \cos(45 + \frac{\beta_n}{2}) \end{cases} \quad (2)$$

$$X = \begin{bmatrix} x_1, x_2, \ldots, x_n \\ y_1, y_2, \ldots, y_n \end{bmatrix} \quad (3)$$

Where α_d and β_d are the trend and the plunge of a discontinuity, respectively; while α_n and β_n are the trend and plunge of the normal to this discontinuity, respectively; r is the radius of equatorial equal-area circle, n is the set number of orientation data and $X \in R^2$.

The algorithm of the DifFUZZY method can be summarized as follows:

Step1: nail the hard point as the core of each cluster.

Step2: label the soft data point;

Step3: assign membership values of the soft data points.

In the third step, firstly the whole field is diffused over by a given number of time steps, secondly the soft data point is moved to the nearest point, subsequently diffuse again, and then both of diffusion profiles is subtracted to get a measure of distance. Finally according to the measure distance, the membership value of each data point in each cluster is calculated.

In the whole procedure, there necessarily need another four parameters. One of them is an external and vital parameter, M, which is a integer number and represents the minimum number of data points in the clusters to be found, and the rests are the internal and optional parameters $\gamma 1$, $\gamma 2$ and $\gamma 3$, which can be adjusted by the experiences.

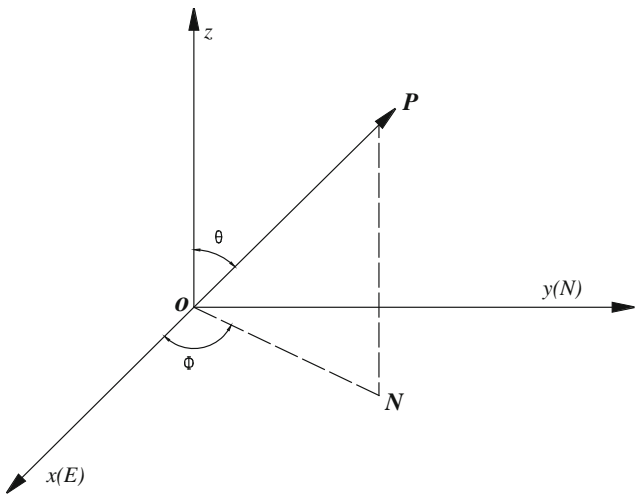

Fig. 1 The orientation vector coordinates (Yu et al. 2007)

3 A Case Study

Firstly, this method is applied to an artificial data set where the orientation data are advanced statistically in Fisher Distribution. Subsequently it is used to a real-life example of in situ data set, which is got from the San Manual copper mine, Arizona, USA (Hammah et al. 1998), compared to the results of Shanley and Mahtab and FCM method.

3.1 Fisher Distribution

In this section, the synthetic data is based on the Fisher Distribution. Figure 1 shows the orientation direction of a discontinuity and it is expressed in a unit normal vector system. OP is the unit normal vector of (α_s, β_s). Point N is the projection of Point P in XY PLANE. θ presents the clockwise angle between OP and Z-axis and φ is the anti-clockwise angle between ON and X-axis.

θ^* and φ^* correspond to the Fisher distribution, when the Z-axis rotate to the mean vector of (θ_m, φ_m). Then the two variables (θ^*, φ^*) can be expressed as follows (Yu et al. 2007):

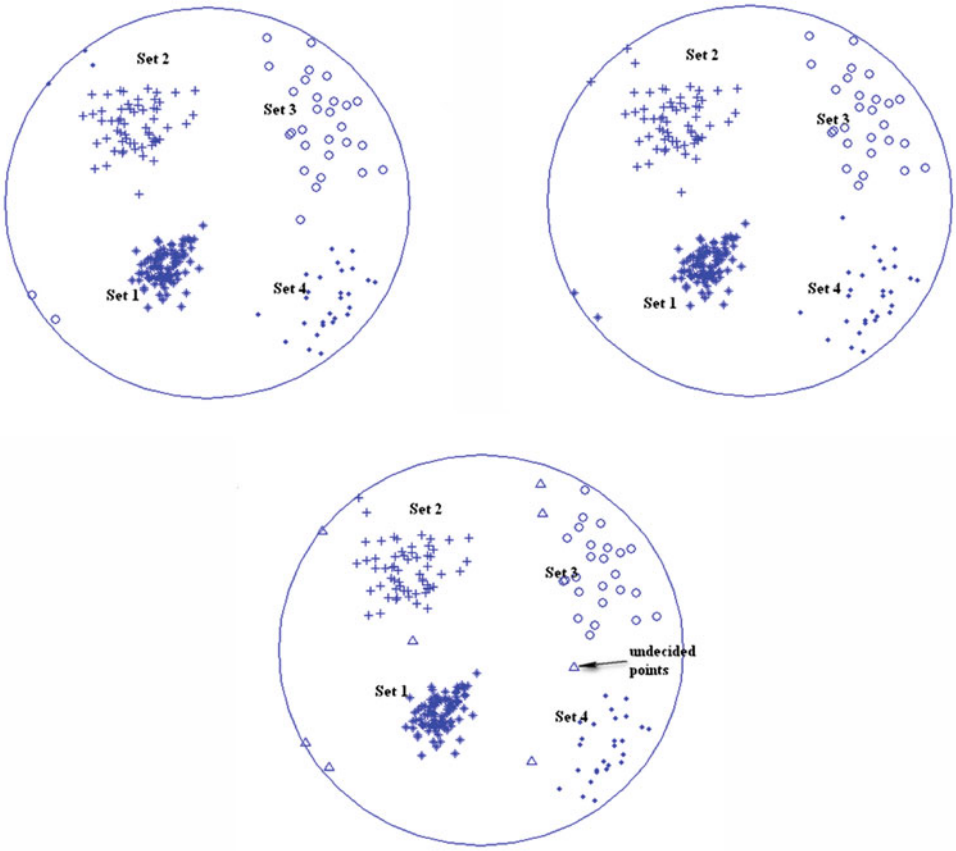

Fig. 2 Synthetic data and the cluster results of FCM and DifFUZZY in equal-area projection

Table 2 Application of the new clustering method to San Manual copper mine data sets

Cluster	Shanley and Mahtab	FCM	DifFUZZY
1 (*)	250/76	250.7374/68	258.59/73.70
2 (o)	350/73	245.10/75.87	346.72/76.60
3 (+)	128/26	118.9759/53.8795	127.74/26.45

$$f(\theta^*) = \frac{k \sin \theta^*}{2 \sinh k} e^{k \cos \theta^*}, 0 \le \theta^* \le \pi$$

$$f(\varphi^*) = \frac{1}{2\pi}, 0 \le \varphi^* \le 2\pi$$

Table 1 summaries four different artificial parameters based on Fisher Distribution of orientation data clusters and the results of FCM and DifFUZZY. From Table 1 and Fig. 2, the clustering results of FCM and DifFUZZY basically agree with the assuming data. There are only a few differences between the FCM and DifFUZZY. It seems that the values of DifFUZZY are slightly higher than the results of FCM, as shown in Fig. 2. There are some data points excluded from the clusters as the undecided points, and the rest data points belong to the cluster are closer to the synthetic cluster center points than the FCM.

3.2 Application to an In Situ Data Set

A real-life example of in situ data set, which includes 286 discontinuities sample from the San Manual copper mine, Arizona, USA (Hammah et al. 1998), is used to certify the DifFUZZY method. Figure 3 shows an equal-area stereographic projection of the data set and the density contour plot. There are three density peaks (250/76, 350/73 and 128/26, respectively) in the contour plot, it validate the expert's information of Shanley and Mahtab (Hammah et al. 1998).

Table 2 summaries the results of Shanley and Mahtab (Hammah et al. Hammah 1998), FCM method and DifFUZZY method. The values of each cluster data (α, β) obtained by Shanley and Mahtab's counting method were taken from (Hammah et al. 1998). The results of FCM method and DifFUZZY are computed by computer code.

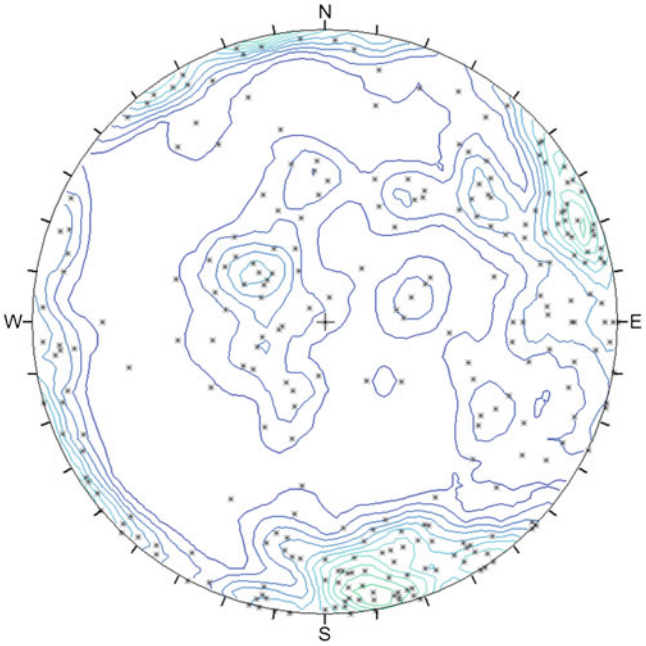

Fig. 3 An equal-area stereo graphic projection of the data set and the contour plot

The counting method of Shanley and Mahtab (Hammah et al. 1998) inevitably requires the construction of a density contour plot, and when the set number of orientation data is large, this progress will be time-consuming. This is not necessary for the FCM and the DifFUZZY, they can automatically separate the orientation data and save the time of constructing density contour plot and both of them need not to know a priori information of the orientation data. But FCM has to select a proper cluster number for the orientation data. The results by FCM method in cluster 2 shown in Fig. 4 deviate quite strongly from the results of the method by Shanley and Mahtab (Hammah et al. 1998). As the FCM method tries to subgroup the whole points into each cluster and it does not consider that some deviation data points that related to a cluster. DifFUZZY separates all three clusters very well compared to the density contour plot in Fig. 3. There is only a slight difference from the results obtained by the method of Shanley and Mahtab (Hammah et al. 1998) and it excludes some deviation data points from the clusters.

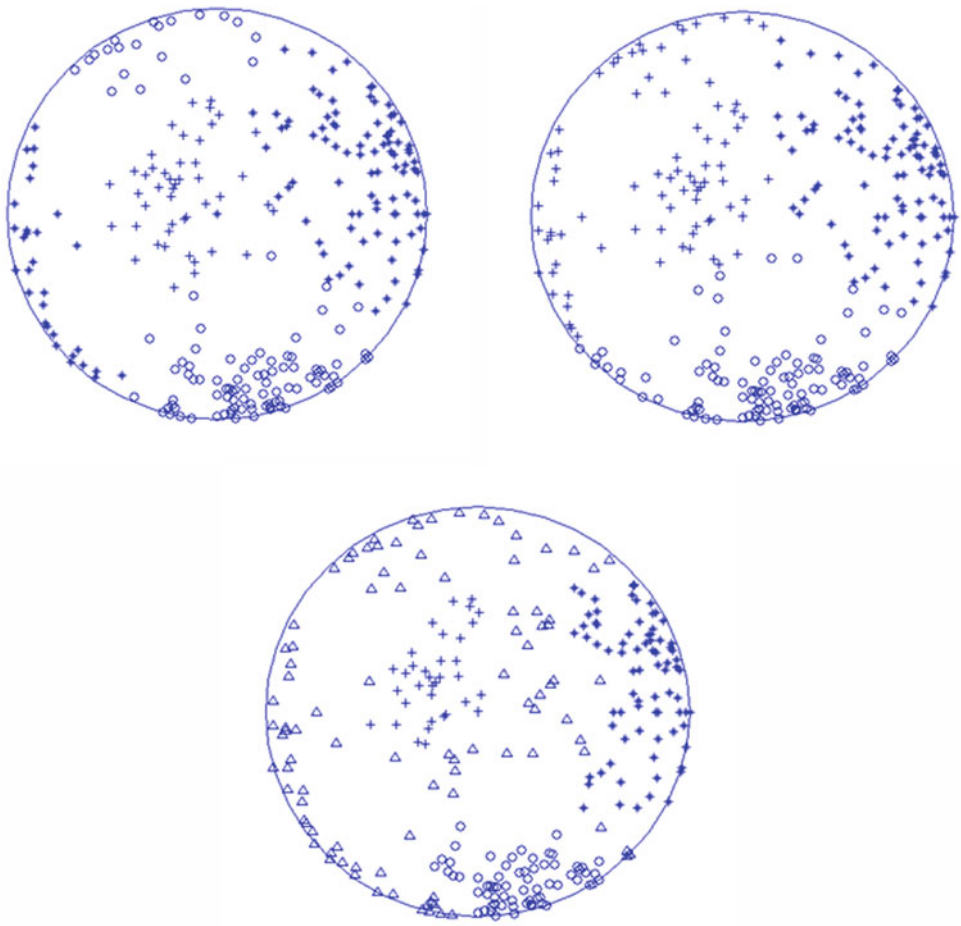

Fig. 4 Clustering results of Shanley and Mahtab and obtained by FCM and DifFUZZY

4 Conclusions

The DifFUZZY method presented in this paper is a new simple and powerful method, which can automatically separate directional data into distinct clusters and get the dominated value of orientation data as the FCM. Both of the FCM and DifFUZZY do not require any advanced information about the orientation data, and they just randomly select the initial values as the dominated orientation and then according to their own algorithm finally decide which points belong to a cluster and the finally dominated orientation values of the clusters. The difference between FCM and DifFUZZY is that FCM needs the cluster number and then it according to the cluster number automatically divides the whole point data. But there is a problem that the cluster number will great affect the cluster results and sometime because it never considers the deviation of the data points, so the cluster results will be distorted. However, the DifFUZZY can self-acting return the cluster number and on the principle of the membership value it can automatically decide the point lies in which cluster or not. The discrepancy between them leads the different results while there are some deviation data points from the density peak, as shown in Fig. 3, the contour plot certified the accuracy of DifFUZZY method. But there is still a problem about how to effectively select the minimum number, M, which is the essential part of the DifFUZZY. The different minimum value will lead different cluster number in the clustering. Further study will be carried out in the near future.

References

Schmidt, W. (1925). Gefugestatistik, Tschermaks Mineral. *Petrol Mitt*, *38*, 392–423.

Shanley, R., & Mahtab, M. (1976). Delineation and analysis of clusters in orientation data. *Mathematical Geology*, *1*, 9–23.

Hammah, R. (1998). Fuzzy cluster algorithm for the automatic identification of joint sets. *Rock Mechanics and Mining Sciences*, *35*(7), 889–905.

Cominetti, O., & Matzavinos, A. (2010). DifFUZZY: a fuzzy clustering algorithm for complex datasets. *International Journal of Computational Intelligence in Bioinformatics and Systems Biology*, *1*(4), 402–417.

Priest, S. (1985). *Hemispherical projection methods in rock mechanics*. London: George Allen & Unwin Ltd.

Yu, Q., Xue, G., & Chen, J. (2007). *Fractured rock mass block theory*. Beijing: China Water Power Press.

Research Progress and Trend of Geotechnical Environmental Problems in Large-Scale Reclamation Projects

F. S. Ma, R. L. Hu, J. H. Xiong, and Q. H. Deng

Abstract

We discussed a number of geotechnical engineering key problems in large-scale reclamation process, and proposed some new research ideas by analyzing the progress and development trend about the problems, which would have an important guiding significance to further study geotechnical environmental problems in large-scale reclamation projects.

Keywords

Coastal zone • Reclamation • Geotechnical environmental problems • Research progress • Research development trend

1 Introduction

The coastal zone has a location advantage in using lands and ocean resources. It's the center of human activity for its high productivity and convenient traffic conditions. More than half of the world's population, production and consumption activities are concentrated in coastal zones, which cover less than 10 % of the global area (Fig. 1) (Ibrahim and Shaw 2012). The densely populated coastal region faces with a land deficit problem, as a result, land reclamation has become the main way to resolve it. And people can benefit a lot from the land reclamation, such as new space for city development, increase in the food supply (if the new land of reclamation is used for agriculture), attracting more investment (if the new land is used for the development of industry), etc.

With the rapid development of world economy and growth of population, the demand for land is also increasing. Many countries, especially the coastal countries (such as the Netherlands, Japan, Singapore, South Korea, etc.), all put "Reclamation land" as a basic national policy for national survival and development, and the development trend are growing. Take the Netherlands as an example, it began large-scale reclamation since the thirteenth century. And now percent 20 of Dutch national territory was made by the artificial reclamation.

Since the 1950s, China has gone through three major reclamation booms. The first was in the early 1950s for salt production, saltworks were distributed in the 12 provinces, municipalities and autonomous regions which were all along the coasts from Liaodong Peninsula to Hainan Island. The environmental effect of the reclamation was the accelerating of beach siltation. The second large-scale reclamation was in the mid-1960s to the 1970s for expanding the agricultural land, whose environmental effect was mainly the disappearance of large areas of inshore shoals. The third large-scale reclamation happened in the late 1980s to late 1990s for beach aquaculture, whose environmental effects were mainly water eutrophication and marine ecological environmental problems. Because of these large-

F. S. Ma (✉) · R. L. Hu
Key laboratory of engineering geomechanics, Institute of geology and geophysics, Chinese Academy of Sciences, Beijing 100029, People's Republic of China
e-mail: fsma@mail.iggcas.ac.cn

J. H. Xiong
Key Laboratory of Geotechnical and Underground Engineering of Ministry of Education, Tongji University, Shanghai 200092, People's Republic of China

Q. H. Deng
Shandong University of Science and Technology, Qingdao 266590, People's Republic of China

Y. Huang et al. (eds.), *New Frontiers in Engineering Geology and the Environment*,
DOI: 10.1007/978-3-642-31671-5_27,

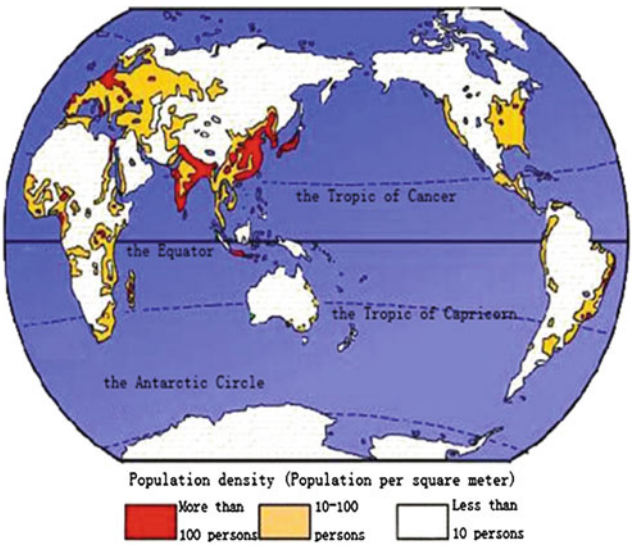

Fig. 1 Distribution of population density in global coastal zone

scale reclamations, about 1.2 million hectares of land area was increased, more than 1/2 of the existing beach area.

Enter the Twenty-first century, with rapid and sustained economic growth in China, a new round of large-scale reclamation booms. Since 2003, land reclamation movement develops rapidly with a speed several times higher than in the past in China. From the northeastern Liaoning Province to the southeast Guangxi Province, every coastal province is actively pursuing the reclamation work. The area of reclamation in 2003 was 2,123 hm^2, then increase to 5,352 hm^2 in 2004, and after the year 2005, it became more than 10,000 hm^2. The scale of the reclamation works are various, for example, in Coastal New area in Tianjin city, the sea reclamation land area will reach 30,000–40,000 hm^2 in 2020, and Caofeidian New area in Tangshan city, Hebei province, is planned to make 48,700 hm^2 artificial land from 2008 to 2020 year, including beach reclamation, salt field reclamation, and so on. The new round of reclamation land is aiming mainly at extending the construction land, which not only has a large-scale and significant impact on the offshore environment, but also should meet the higher quality of the reclamation requirements. Therefore, how to ensure these aspects effectively and minimize natural disasters becomes the hot topic in the geotechnical environment field.

2 Geotechnical Environmental Problems in Large-Scale Reclamation Project

Now, the main methods of reclamation are hydraulic fill and miscellaneous fill (Figs. 2, 3), and the key problems of geotechnical engineering caused by them are as follows.

(1) Material properties of miscellaneous fill venues are messy and their qualities are difficult to control. And the building capacity (bearing capacity and deformation) is also hard to assess accurately. Besides, the strength of reclaimed soil foundation is low and the consolidation time is long, a reasonable foundation treatment should be taken to meet the construction requirements.
(2) In the reclaimed lands, there are always group construction projects, which will lead to unevenly subsidence and properties heterogeneity. The problems are hard to predict and control effectively, so geological disasters are widespread, such as land subsidence, which will result in buildings lean, collapse or pavement cracking.
(3) Because of shallow groundwater level and complex soil situation, there are venues salinization and rather more pit problems, such as complex drainage conditions and process, pit support constrained by the heterogeneous filling, and poverty quality controlling standard.
(4) For the reclamation land near the sea are directly loaded on modern sediments, that of the outer edge is extremely uneven, and lack of effective support. Also the loading on the original less-consolidated soil may results the underwater landslide. It is understood that in Caofeidian Development Zone, there are some signs of underwater landslide. So if we don't prevent it effectively, it will be a direct threat to the Zone, especially the long-term stability of the port projects.

3 Research Progress of Geotechnical Environmental Problems in Reclamation Project

In order to protect the existing good ecological environment, researchers give long-term focus on the ecological and environmental problems of the reclamation land. They have studied deeply and comprehensively the environmental changes in aquatic ecosystems, accumulation in estuarine sediment, shoreline changes, riverbed remediation, harbor planning, biological protection and so on. That provides an adequately scientific support for using of reclamation land in early and medium term, including agriculture, animal husbandry, and fishery.

Since the 1950s, reclaimed land gradually shift to be used as the purpose of the expansion of building with the increasing scale and range, but the sites often could not meet the demand of the project construction, and triggered a series of problems. Among them, land subsidence is especially prominent, which restricts the sustainable development of construction projects in coastal areas, causing a great concern of scholars in many countries. Since 1969, seven international conferences of land subsidence have been held in five countries, including Japan,

Fig. 2 Hydraulic fill site in Tianjin Tanggu

Fig. 3 Miscellaneous fill site in Weihai, Shandong province

the United States, Italy, the Netherlands and China. Land subsidence has been a major worldwide disaster. It is estimated that at the end of last century, the loss caused by land subsidence and the cost for controlling land subsidence in the United States each year were more than one hundred million dollars. In view of this, people carried out extensive researches on subsidence monitoring, and applied constantly new technologies and theories in monitoring land subsidence. They included soil and rock compression test (Yang et al. 2010), radioactive hierarchical standard monitoring techniques (Baù et al. 2002), interferometer synthetic aperture radar technology (INSAR) (Zhang 2011), GPS technology (Huang and Kuang 2000) and GIS technology (Cao et al. 2007). The INSAR and the subsequent development of interferometer synthetic aperture radar (D-InSAR) technology will be one of the main technologies used for monitoring land subsidence in future. In foreign countries, INSAR technique was applied relatively early in monitoring land subsidence. For example, Poland, United States, Italy and France had carried out a large number of empirical studies, and had achieved the ideal results. In China, the research of INSAR technique using for monitoring land subsidence began in recent years and applied mainly in the city.

Since the 1990s, the settlement issues induced by engineering construction have been more common. On the one hand, they would affect the operation of constructions. On the other hand, they also have an impact on the regional land subsidence. Engineered settlement problems could happen in many areas of the project, including land subsidence surrounding the project and foundation settlement problems caused by construction, settlement problems during the operation, differential settlement, regional land subsidence's impact on the project and so on. Now, most researches were concentrated on these problems, but less attention was paid to the cluster project settlement.

Land reclamation by hydraulic filling is the main way to expand the land area in the world. To meet the project construction requirements, it needs to be consolidated. Consolidation for hydraulic filling soil basically refers to the soft soil consolidation technology. Although there is a great similarity, compared to the soft soil, hydraulic filling soil has more disadvantages, including looser structure, lower intensity, more obvious rheological, greater consolidation difficulty and longer concretion cycle. So researchers are striving for finding some more economical, faster, and effective consolidation techniques and methods. Now main consolidation techniques and methods include the combination of plastic drainage plate and vacuum dewatering (Zhang and Chen 1992), low vacuum method (Wu et al. 2007), the thin layer of sand and clay interbedded filling method (Lee et al. 1987), horizontal drainage blanket (Kim and Hirokane 1995), the PTM method (Progressing Trenching Method) (Cao et al. 2011), consolidation in layers by the method of spatial vacuum drainage (Li et al. 2002) and dynamic drainage consolidation method (Xue and Li 2011). In order to meet the development needs of large-scale, high-speed construction projects, the fast forming shell technology and efficient deep reinforcement process are becoming the imperative breakthrough key technologies for geotechnical engineering in reclamation land area.

Saline soil as a special kind of soil is widely distributed in China, which includes inland saline soil, coastal saline soil and the secondary saline soil. Since the 1940s, some researchers began to study saline soil in former Soviet Union, and proposed a rather systematic and comprehensive theory. From the 1970s, researchers began to study saline soil in China, the contents including micro-structure and material composition of saline soil (Zhao et al. 2004), the dissolution subsidence of saline soil foundation (Zhang et al. 2008), salt-frost deformation (Yang et al. 2009), corrosion property (Zhong 2011) and so on. Moreover, great advances have been made in the evolution of saline soil, water and salt dynamics change (Zhang et al. 2000; Dong et al. 2005), and the saline soil amelioration. The amelioration methods include early dry salt drainage and current chemical amelioration, including lime, fly ash, SH and so on, and ecological engineering amelioration (Jiang and Zhang 2001). Among them the ecological improvement method has increasingly become one of main technologies.

4 Research Trends of Geotechnical Environmental Problems in Large-Scale Reclamation Project

To achieve the large-scale, high-speed, sustainable-development reclamation land project, higher demands in the geotechnical engineering are as follows.

(1) The heterogeneity problems of rock and soil. In the miscellaneous fill venues formed by large-scale reclamation, particle size varies largely, characters are messy and its physical and mechanical properties have been far beyond the capability of the traditional continuum mechanics. To understand its strength and the deformation characteristics, we should learn from a new perspective by innovating in terms of theory, methods, and detection technology.

The evaluation on strength and bearing capacity of miscellaneous fill has been puzzled by heterogeneity of the media. Now qualitative evaluation is mainly used instead of quantitative analysis, which makes the credibility of the evaluation results unable to be determined. In recent years, considerable progress had been made on research of the gravelly soil or rock mixture (Xu et al. 2007; Zhou et al. 2007), which was a great reference to the evaluation on miscellaneous fill. The problem of the stability evaluation on miscellaneous fill foundation can be properly solved through analyzing and simulating the mechanical behavior of granular media. Therefore, we propose the methods to evaluate the strength and bearing capacity of miscellaneous fill site, which are quantitative analysis the structural of the granular medium and large-scale field shearing test.

(2) The rapid consolidation of low-permeability hydraulic fill soil. The reclamation site is mostly composed by the sludge or silt soil with high water content, which generally can not directly reach the building foundation requirements, for its low intensity, obvious thixotropy and long rheology cycle, so consolidation is needed. Because of the poor permeability, it is difficult for pore water to discharge, so consolidation time is long, in normal conditions, the period will requires 1–3 years, which seriously affect the completion period. It is needed to find ways to accelerate the consolidation process, and rapidly increase the soil strength. There have been many patents on consolidated draining technology of hydraulic fill soil, but the problems are also long consolidation period and unstable effect. We will make great efforts to resolve the problem of quickly forming shell by taking the measures of combining three-dimensional drainage and surface plant reinforced. Therefore, we can study transfer mechanism of the loosely bound water in low permeability media and develop rapid consolidation patented technology by the expansion of seepage paths and reduction of penetration path.

(3) Subsidence prediction and control of cluster project. An important feature of modern construction projects in reclamation area is high-level and intensive. It demands not only higher strength of building foundation but also better control deformation technique. For the heterogeneous fill soil, there is not only the outstanding differences in settlement, but also highlight coupling deformation effect between the buildings. At the same time, its settlement calculation is different from separate building. At present, there are many settlement calculation methods for the engineering of single pile or a separate building (Liu 2002; Yang 2008), but poor understanding of settlement mechanism of cluster construction and no effective method of calculation and control standards. Therefore, through site subsidence monitoring network and some indoor large-scale physical simulation, we can study cluster project settlement mechanism and coupled deformation calculation method to reveal the superimposed effect of construction load, impact factors and distribution law of cluster settlement, and finally propose the corresponding prediction models and controlling method.

(4) Controlling drainage of sites and pit and ground salinization. There have been many productions and patented technologies of city pit drainage and support. However, there is great difference between reclamation land sites and inland environment. The drainage and support of pit are more difficult, and technical requirement are stricter, so it is needed to adjust the related technologies. We can revise the relevant technical standards, and make the corresponding design software and technical regulations through field trials

and large-scale physical simulation.

As reclamation land site is close to the sea, and groundwater is buried in shallow, so the problem of water gushing may be serious while excavating foundation pit, and ground salinization problems may exist. We can develop a pit drainage and optimized support system suitable in shallow water levels and high saturated foundation, and propose a integrated technology for preventing and treating saline soil, by indoor large-scale physical modeling, numerical simulation and a variety of modifiers contrast tests.

(5) Stability evaluation and protection of artificial coasts. The waterfront side of the fill site often constitutes a certain slope, in most cases, it lacks the necessary protection. Under the continuing effect of the waves and the pore water pressure, it is prone to bank slope landslide, causing a devastating impact on the shore construction. The technical difficulties of the subject are mainly material high heterogeneity, high-saturated water, prominent moving-hydrostatic pressure and the existence of lateral waves. Now, there have been no coastal landslide research records.

To understand the stress–strain relationship caused by the impact of waves on the soil and master the stability of the site, we can combine wave-water- soil interaction model and marine soft soil dynamic viscoelastic constitutive model, through field testing heterogeneous mechanical properties of reclamation land, physical simulation and numerical analysis, to establish stability analysis method for the bank slope under the wave loading and the underwater landslide criterion, and analyze the changing law of the shear strain rate, circulation weakening parameters and shear modulus in the soft clay under the wave cycling effect. At the same time, we can study the bank slope stability problems under coupling factors such as load weight, the wave force, penetration. All that will provide a theoretical basis for the slope protection methods and techniques.

5 Conclusions

While scientific and reasonable reclamation project is significant for the mitigation of the conflicts between people and land, and promoting the developments of social and economy, the contranatural disorder reclamation may have serious and permanent negative effects on resources, environment and society in coastal areas. From scientific point of geotechnical engineering, providing scientific and rational geotechnical engineering technologies are important ways to ensure the orderly development of the reclamation works. Therefore, about the geotechnical environmental problems encountered in large-scale reclamation process, it is necessary for us to carry out advanced, reliable technology research of reclamation land geotechnical engineering through the changing law analysis of geological environment caused by reclamation land, the theoretical analysis of the nonlinear mechanics characteristics of soil, field experiments and numerical simulation. The researches will provide important guarantee for sustainable development of large-scale reclamation.

Acknowledgments The research was funded by the Special Funds for National Basic Research Program of China (Grant No.2010CB428803) and the National Natural Science Foundation of China project (Grant No. 41172271).

References

Baù, D., Ferronato, M., Gambolati, G., et al. (2002). Basin-scale compressibility of the northern Adriatic by the radioactive marker technique. *Geotechnique, 52*(8), 605–616.

Cao, Y., Li, W., & Liu, T. (2011). Application of geotechnical drainage net to improvement of ultra-soft soil. *Port and Waterway Engineering, 11*, 237–240. (In Chinese).

Cao, X., Ruan, J., & Zheng, B., et al. (2007). Application of GIS technique in geological hazard information system. *The Chinese Journal of Geological Hazard and Control, 18*(3), 112–115 + 125. (In Chinese).

Dong, X., Jiang, H., Deng, M., et al. (2005). Study on the distribution and balance of the salt in the inland basin. *Advances in Water Science, 16*(5), 638–642. (In Chinese).

Huang, L., & Kuang, S. (2000). Possibility of application of GPSTechnique to vertical deformation measurement. *Crustal Deformation and Earthquake, 20*(1), 30–37. (In Chinese).

Ibrahim, H., & Shaw, D. (2012). Assessing progress toward integrated coastal zone management: Some lessons from Egypt. *Ocean and Coastal Management, 58*, 26–35.

Jiang, Y., & Zhang, Y. (2001). Ecological distribution, properties and amelioration of saline soil in Shenyang region. *Chinese Journal of Soil Science, 32*(S0), 124–127. (In Chinese).

Kim, H., & Hirokane, S. (1995). Consolidation behaviour of dredged clay ground improved by horizontal drain method[A].In H. Yoshikuni & G. Kusakabe (Eds.), Proceedings of the Compression and Consolidation of Clayey Soils, (Vol. 1, pp. 99–104).

Lee, S., Karunaratne, G., Yong, K., et al. (1987). Layered clay-sand scheme of land reclamation. *Journal of Geotechnical Engineering, 113*(9), 984–995.

Li, L., Wang, Q., Wang, N., et al. (2002). Research on the feasibility of consolidating hyd.raulic fill in layers by the method of spatial vacuum drainage. *Chinese Jounal of Geotechnical Engineering, 24*(4), 522–524. (In Chinese).

Liu, J. (2002). A summary of calculation methods for single pile settlement. *Journal of Zhuzhou Institute of Technology, 16*(1), 71–75. (In Chinese).

Wu, Y., Zhang, M., & Xu, S. (2007). Study on test of high vacuum compact method for reclaimed ground improvement. *Port Engineering Technology, 1*, 43–46. (In Chinese).

Xu, W., Hu, R., Yue, Z., et al. (2007). Mesostructural character and numerical simulation of mechanical properties of soil-rock mixtures. *Chinese Journal of Rock Mechanics and Engineering, 26*(2), 300–311. (In Chinese).

Xue, R., & Li, G. (2011). Study of model tests of soft soil foundation by dynamic drainage consolidation. *Rock and Soil Mechanics, 32*(11), 3242–3248. (In Chinese).

Yang, G. (2008). New computation method for soil foundation settlements. *Chinese Journal of Rock Mechanics and Engineering, 27*(4), 679–686. (In Chinese).

Yang, Y., Li, G., & Dou, Y., et al. (2010). Present situation and advance problems on the land subsidence caused by groundwater pumping. *Geotechnical Investigation and Surveying,* 11, 32–37 + 91–93.(In Chinese).

Yang, B., Liu, X., He, X., et al. (2009). Test study on saline soil subgrade salt-frost deformation. *Chinese Journal of Underground Space and Engineering, 5*(3), 594–603. (In Chinese).

Zhang, W. (2011). Analysis of mining ground deformation based on D-InSAR. *GNSS World of China, 3*, 62–66. (In Chinese).

Zhang, C., & Chen, X. (1992). Study on the vacuum method of drainage for reclaimed ground. *Port and Waterway Engineering,* 1, 37–42 + 49. (In Chinese).

Zhang, L., Feng, Y., Zhang, H., et al. (2000). Simulation study on role of water and salt movement of seashore saline soil. *Journal of Shandong Agricultural University (Natural Science), 31*(4), 381–384. (In Chinese).

Zhang, W., Zhang, B., & Shen, N. (2008). Research on geotechnical engineering characteristics of saline soil and advances. *Site Investigation Science and Technology, 3*, 7–11. (In Chinese).

Zhao, H., Han, W., & Zhang, Y. (2004). Research on engineering properties of salinized soil in littoral area. *Journal of Tianjin Institute of Urban Construction, 10*(3), 161–164. (In Chinese).

Zhong, D. (2011). Study on the distribution characteristics of the saline soil and the foundation treatment in Xining area. *Journal of Qinghai University* (*Nature Science*), *29*(2), 30–33. (In Chinese).

Zhou, Z., Fu, H., & Liu, B., (2007). Tan Hanhua and Long Wanxue. Artificial rainfall tests on a well-instrumented soil-rock-mixture slope. *Rock of Soil Mechanics, 28*(7), 1391–1396. (In Chinese).

Change Law of Vane Shear Strength of Soft Soil with Depth in Coastal City

P. Yang, T. Deng, Z. J. Zhou, Y. Q. Tang, and J. X. Wang

Abstract
The in situ vane shear test is one of the most common in situ tests to obtain the shear strength of soft soil. Based on the data of the in situ vane shear tests of mucky soft soil in Zhoushan, change law of vane shear strength of mucky soft soil with depth is analyzed. The test results show that vane shear strength of mucky soft soil increases nonlinearly with increasing of depth of soil. The relationship of vane shear strength and depth of soil was fitted by conic model.

Keywords
Soft soil • Vane shear test • Vane shear strength

1 Introduction

The in situ vane shear test is typically used for measuring the undrained shear strength of soft clay (Tian et al. 2004). When the blades of the vane reached the aimed depth of soil, the vane was rotated in a rate about point one degree in one second, and the corresponding torque was measured. The shear strength of soil was calculated by the maximum torque and the dimension of blades (Chen 2001). In the past decades, vane shear test has been proved that it is very useful for measuring shear strength of soft soil and it has been introduced into many countries (Yang and Zhao 2008; Eden and Law 1980; Tiesong and Bryant 1997). Most area of Zhoushan are typical soft soil, it is very important to establish reasonable and high precision predicting model to describe change law of vane shear strength of mucky soft soil with depth, based on the data of the in situ vane shear tests.

2 Physical and Mechanical Properties of Soft Soil

Due to the short time of consolidation and the low load in history, soft soil is characteristic with high water content, large void ratio, small permeability and high compressibility (Liu et al. 2004; Yan et al. 2007; Ma and Lu 2009; Liu and Chen 2005). In most costal area of Zhoushan, soil layer consists of the following several engineering geological layers. In general, about 1–2 m in thickness hard crust could be encountered near the ground surface. Underneath this crust is a approximately 4–5 m in thickness silt and followed by 5–6 m in thickness layer of silt with silty sand. At about 12 m below the ground surface, silt clay with silty sand and silt clay layers could be encountered. Besides, localised lens of floury soil and silty sand could be found in the silt clay layer. The physical and mechanical properties of soft soils are shown in Table 1.

P. Yang (✉) · Y. Q. Tang · J. X. Wang
Key Laboratory of Geotechnical and Underground Engineering of Ministry of Education, Tongji University, Shanghai 200092, China
e-mail: csuyangp@163.com

P. Yang · T. Deng (✉) · Y. Q. Tang · J. X. Wang
Department of Geotechnical Engineering, Tongji University, Shanghai 200092, China
e-mail: dengtao3@126.com

Z. J. Zhou
Department of Bridge Engineering, Tongji University, Shanghai 200092, China

Y. Huang et al. (eds.), *New Frontiers in Engineering Geology and the Environment*,
DOI: 10.1007/978-3-642-31671-5_28,

Table 1 Physical and mechanical properties of soft soil

Soil stratum	Silt	Silt with silty sand	Silt clay with silty sand	Silt clay
Water content (%)	52.0–68.8	42.1–56.7	40.6–54.1	40.9–58.4
Density (g/cm^3)	1.61–1.74	1.67–1.93	1.70–1.81	1.65–1.82
Void ratio	1.207–1.858	0.860–1.568	1.138–1.435	1.078–1.589
Modulus of compressibility (MPa)	1.61–2.07	1.22–2.90	2.00–2.83	1.65–2.67
Coefficient of compressibility (MPa^{-1})	1.060–1.586	0.771–2.572	0.762–1.176	0.811–1.552

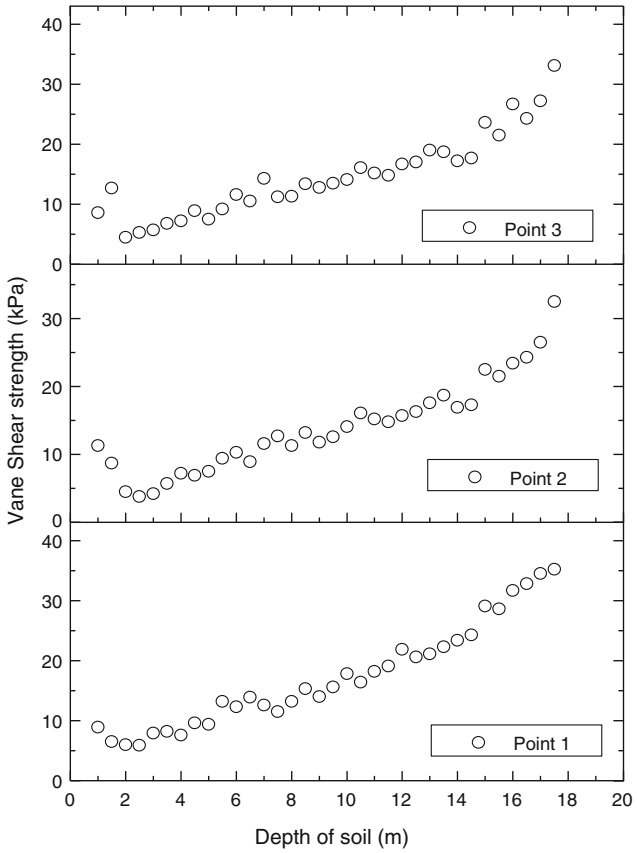

Fig. 1 Relationship of vane shear strength and depth in the in situ tests

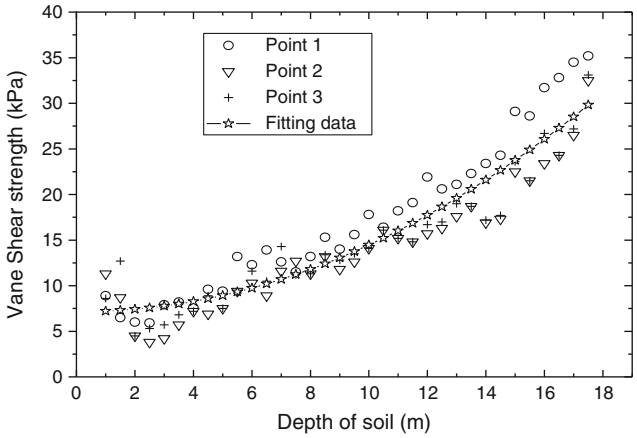

Fig. 2 Relationship of test data and fitting data

3 Analysis of Test Results

3.1 Relationship Between Vane Shear Strength and Depth of Soft Soil

Three in situ vane tests were conducted and data of three in situ vane shear tests are shown in Fig. 1.

Figure 1 shows that the vane shear strength of soft soil is larger than that of the underlying soil between 3–10 m due to the hard crust. Below the hard crust, vane shear strength increases almost linearly with increasing of depth of soft soil between 3–12 m. Below depth 12 m, vane shear strength increases nonlinearly with increasing of depth of soft soil. At the same time, the three curves have similar change law.

3.2 Change Law of Vane Shear Strength of Soft Soil with Depth

An empirical formulation was obtained by fitting the data of three points to describe the variation of vane shear strength with depth of soft soil:

$$\mathrm{Cu} = 0.0577\,\mathrm{d}^2 + 0.3422\,\mathrm{d} + 7.1623 \qquad (1)$$

$$R^2 = 0.9873$$

Where Cu is vane shear strength (kPa), d is depth of soft soil (m), R^2 is the correlation coefficient.

Figure 2 shows that the relativity of the test data and fitting data is quite good. Equation (1) is a good empirical relationship between the vane shear strength and depth of soft soil and it can be used to predict the vane shear strength of soft soil in this area, it will be useful for foundation treatment and engineering construction (Meng and Wang 2009; Cheng 2008; Deng et al. 2007; Ding et al. 2011; Wu and Liu 1998).

To verify the Eq. (1), the vane shear strength of soft soil at different place is predicted with Eq. (1). The result is plotted in Fig. 3. The Fig. 3 shows that there is a little difference, mostly within 15 % (see Fig. 4).

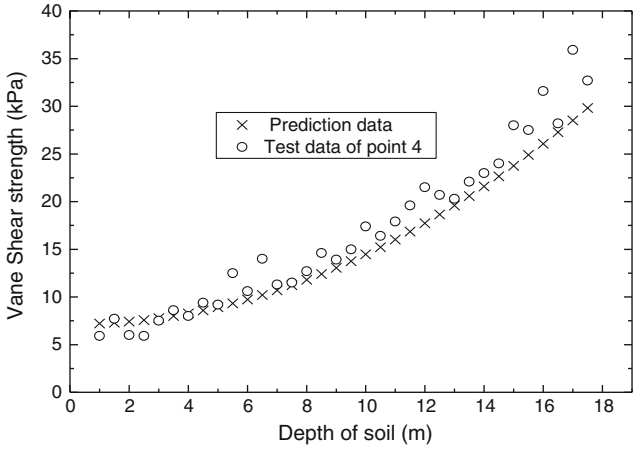

Fig. 3 Comparison of test data and prediction data at point 4

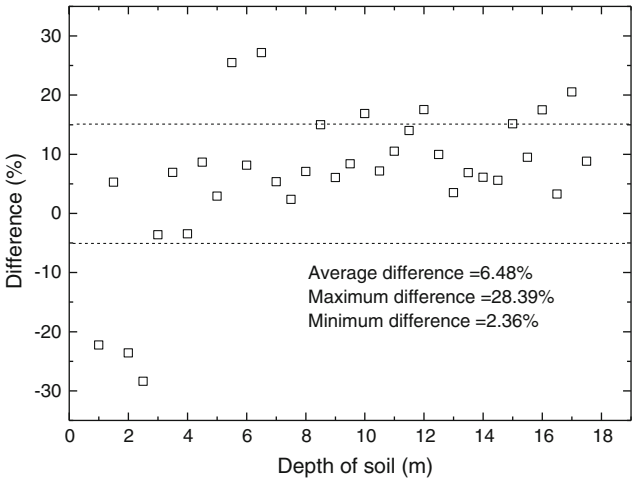

Fig. 4 Difference of test data and prediction data at point 4

Though the Eq. (1) obtained from fitting curve method is not rigorous, the method of using Eq. (1) to predict the vane shear strength of soft soil in this area is considered to be promising.

4 Conclusions

Vane shear strength of soft soil increases nonlinearly with the increasing of depth of soft soil.

The relationship between vane shear strength and depth of soft soil can be described with Eq. (1).

Equation (1) can be used to predict the vane shear strength of soft soil in this area.

Acknowledgments This investigation was supported by the National Natural Science Foundation of China, Project No. 41002093, Shanghai Leading Academic Discipline Project, Project No. B308 and the Program for Young Excellent Talents, Tongji University. The authors are deeply indebted to the three financial supporters.

References

Chen, C. (2001). *Evaluating undrained shear strength of Klang clay from cone penetration test*. Bali: International Conference on in situ Measurement of Soil Properties and Case Histories.

Cheng, J. (2008). The comprehensive application of vane shear tests. *Journal of Geotechnical and Surveying, 1*, 83–91.

Ding, L., Jiang, Y., Chen, D., et al. (2011). The analysis of guangzhou soft soil mechanics characteristics. *Railway Engineering, 10*, 75–78.

Deng, X., Lan, Y., Zhang, M., et al. (2007). The application of mathematical statistical methods of the vane shear test results. *Geotechnical Engineering World, 10*, 63–65.

Eden, W., & Law, K. (1980). Comparison of undrained shear strength results obtained by different test methods in soft clays. *Canadian Geotechnical Journal, 17*(3), 369–381.

Liu, J., & Chen, B. (2005). Analysis on engineering characters of coastal soft soil and its reinforcing result. *West-China Exploration Engineering, 9*, 8–9.

Liu, R., Yan, S., & Zhang, L. (2004). Vane shear strength based stability analysis of slopes in unconsolidated soft clay. *Transactions of Tianjin University, 10*(3), 195–200.

Ma, C., & Lu, W. (2009). The treatment method of coastal soft soil foundation. *Chinese hi-tech enterprise, 1*, 79–80.

Meng, L., & Wang, D. (2009). Study on shear strength test of muddy soil and silty interbeded soil [J]. *Port Engineering Technology, 46*(4), 51–52.

Tian, H., Note, S., & Io, C. C. (2004). Vane shear behavior of soft Bangkok clay. *Geotechnical Testing Journal, 27*(1), 57–66.

Tiesong, Lu, & Bryant, W. (1997). Comparison of vane shear and fall cone strengths of soft marine clay. *Marine Georesources and Geotechnology, 15*(1), 67–82.

Wu, Z., & Liu, Q. (1998). The correlation analysis of the relationship of cone penetration test and vane shear test in Shenzhen bay offshore soft soil. *Geotechnical Engineering Technique, 3*, 48–50.

Yan, C., Xia, W., & Dong, P. (2007). The study for engineering geological features and genetic types of soft-soil in the lower reaches of the Yangtze River. *Journal of Engineering Geology, 15*(1), 142–145.

Yang, J., & Zhao, J. (2008). Vane shear test in the treatment of soft clay. *Fujian Architecture and Construction, 15*, 53–55.

The Bearing Capacity of Flexible Piles Under Combined Loads in Dense Sand

M. Jian, C. Zhao, C. F. Zhao, and W. Z. Wang

Abstract
Pile foundations are often subjected to vertical and lateral loads and moments. The current design practices assume that the effect of these loads is independent of each other and hence the pile design is carried out separately for vertical and lateral loads. The ultimate bearing capacity of flexible single piles in sand has been researched by model test under various combinations of vertical load, horizontal load and moment. The results of the load test which contain of the curve of vertical load-settlement, horizontal load-displacement and the ultimate bearing capacity are presented in the form of Cartesian co-ordinates. The basic laws of the component of the combined loads are analyzed and the ultimate bearing capacity is compared with the theoretical estimates based on the test results. Reasonable agreement has been found between the observed and predicted ultimate bearing capacity of flexible piles.

Keywords
Flexible piles • Combined load • Ultimate bearing capacity

1 Introduction

The pile foundations of engineering structures such as bridges, high buildings, and offshore structures are frequently subjected to combined loads, which contain vertical and horizontal loads and moments. Extensive studies have been carried out by many researchers on the behavior of rigid and flexible piles and subjected to inclined load by theoretical and model methods (Koumoto et al. 1986; Meyerhof and Ghost 1989; Sastry and Meyerhof 1994, 1995). It was suggested (Meyerhof and Yalcin 1984; Meyerhof and Sastry 1985) that the behavior of flexible piles under eccentric and inclined loads can be estimated from that of rigid piles by using the concept of an effective embedment depth. A semi-empirical formula is presented for calculating the displacement of piles under both eccentric and inclined loads (Zhao and Li 2006).

Previous work was limited to inclined load which the component of the vertical and horizontal loads loaded at the pile top at the same time, and the ratio of vertical load-horizontal load was keeping constant. As a continuation, the bearing capacity of flexible piles in sand has been investigated by model test and the results are summarized below.

2 Experimental Investigation

The sand was poured into a concrete chamber of about 2.6 m width and 3.6 m length and 3 m height and was compacted every 15 cm thickness. The sample of sand was prepared from the chamber. The data of sand was got after many soil tests were done and is presented in Table 1.

M. Jian · C. Zhao (✉) · C. F. Zhao · W. Z. Wang
Department of Geotechnical Engineering, Tongji University, 1239 Siping Road, Shanghai 200092, People's Republic of China
e-mail: zhaocheng@tongji.edu.cn

C. Zhao · C. F. Zhao
Key laboratory of Geotechnical and Underground Engineering of Ministry of Education, Tongji University, 1239 Siping Road, Shanghai 200092, People's Republic of China

Y. Huang et al. (eds.), *New Frontiers in Engineering Geology and the Environment*,
DOI: 10.1007/978-3-642-31671-5_29,

Table 1 Soil parameter

ρ(g·cm-3)	ω(%)	e	φ(°)	ES1-2 (MPa)
1.86	29.6	0.853	25.2	12.45

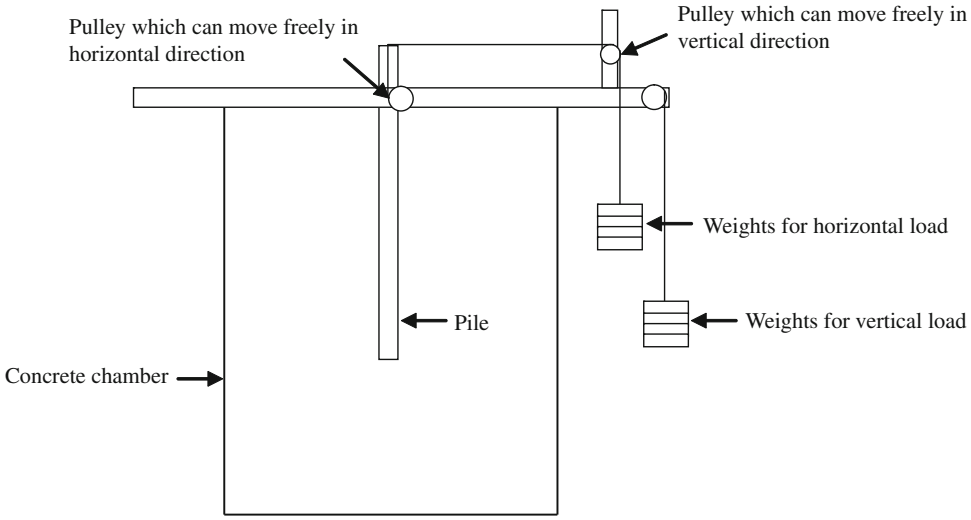

Fig. 1 Schematic diagram of test setup

Table 2 The loading plan of piles

Group	Piles	H(N)	H (m)	$M = H \times h$ (N·m)	V(N)
1	P11	0	0	0	V_u(2100)
2	P21	H_u(420)	0	0	0
3	P31	180/-180	0.2	36	V_u(2100)
	P32	180	0.2	36	V_u(2000)
	P33	240	0.15	36	V_u(2000)
	P34	360	0.1	36	V_u(1900)
4	P41	H_u(420)	0.1	$H_u \times h$	0
	P42	H_u(390)	0.2	$H_u \times h$	0
	P43	H_u(330)	0.3	$H_u \times h$	0
	P44	H_u(300)	0.4	$H_u \times h$	0

The model piles used in this investigation were made by fine aggregate concrete, and the embedded length and diameter were 1,840 and 46 mm, respectively (depth/diameter ratio = 40). The flexural rigidity EI of the pile was measured to be 2.133×10^3N·m^2. The relative stiffness *K*rs of the pile is given by (Banerjee and Davis 1978; Poulos and Davis 1980)

$$K_{rs} = \frac{E_p I_p}{E_h D^4} = 3.3 \times 10^{-5}$$

where E_h is the horizontal soil modulus at pile tip, E_p is the modulus of elasticity of pile, and Ip is the moment of inertia of pile. The values of Krs for the present piles is 3.3×10^{-5} and the piles are flexible piles because of $K_{rs} < 10^{-2}$.

Aim to research the bearing capacity of piles under vertical and horizontal loads independently loaded on the pile, loading device was manufactured (Fig. 1). There were four group piles. The first group had 1 pile (p11). It is subjected to vertical load only, and the ultimate vertical bearing capacity was got for all piles in the tests because the prosperities of all piles and soil were same. The second group had 1 pile (p21) which is subjected to horizontal load only and the ultimate horizontal bearing capacity was got. The third group had 4 piles (p31, p32, p33, p34), and the pile top was loaded horizontal loads H with different distance from the ground level e until soil failure. The details of the loading plan are presented in Table 2. The forth group had 4 piles (p41, p42, p43, p44), which were subjected to different horizontal loads

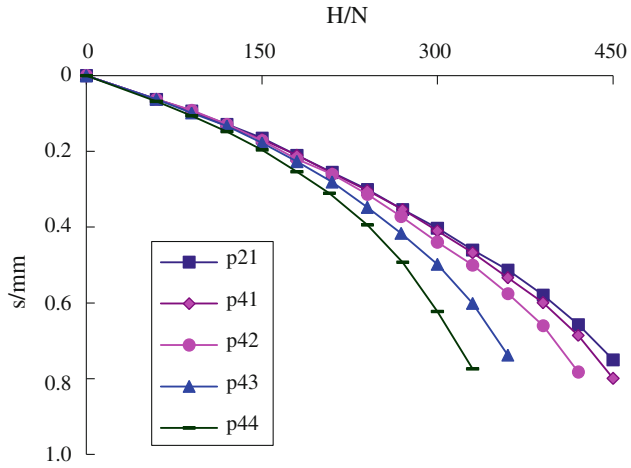

Fig. 2 The curve of H–s for single piles

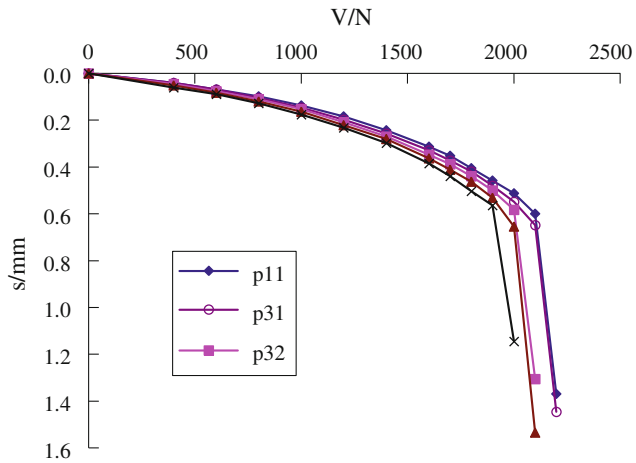

Fig. 3 The curve of V-s for single piles

H with different distance from the ground level e, but the moment $M = H \times e$ on the pile top was constant, then, the pile was subjected to vertical load V until soil failure.

The criterions of soil failure were as follows: Vertical: 1) the settlement was 2 times on a certain load than pervious load and was not stable in an hour; 2) the settlement was 5 times on a certain load than pervious load; Horizontal: the displacement of the pile on the ground line reached 6 mm, in order to insure no crack along the pile.

3 Experimental Results

The test results of the piles in sand under combined loads are plotted in Figs. 2 and 3, respectively.

Figure 2 indicates that the displacement increases with the increase of moment under horizontal load keeping invariably. The ultimate horizontal load decrease with the increase of the

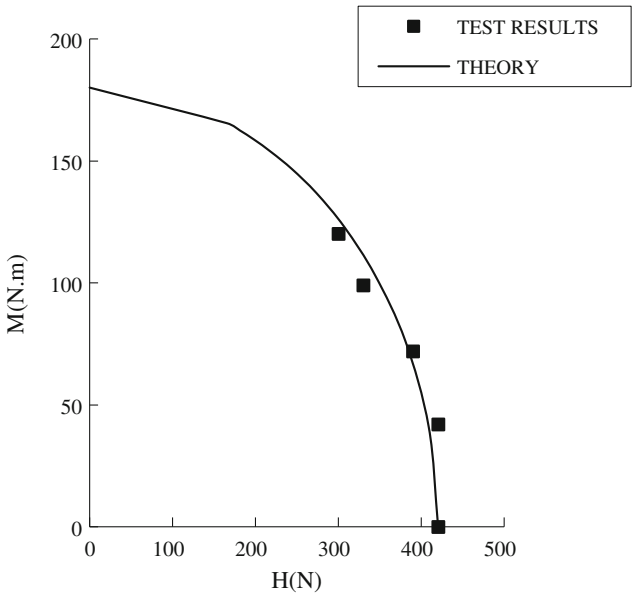

Fig. 4 UBC (horizontal load and moment)

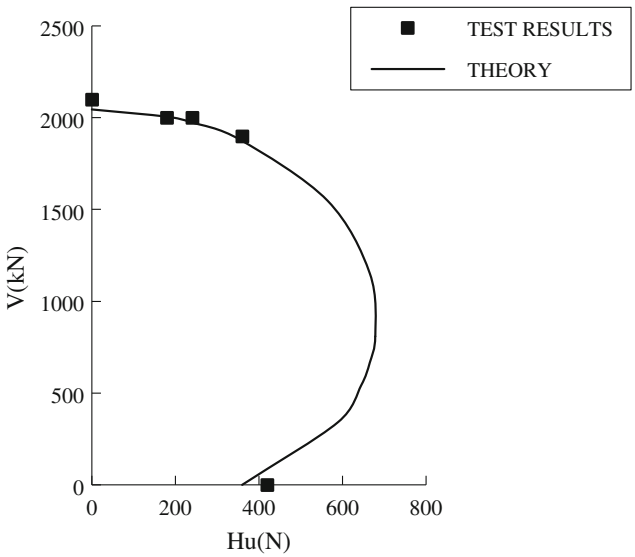

Fig. 5 UBC(horizontal and vertical load), Note: UBC means ultimate bearing capacity of piles

moment. The reason is obvious because in some ways, the horizontal load and moment on the pile top are equivalent.

Figure 3 indicates that the settlement increases slightly with the horizontal load increases if the vertical load and moment are no change. The vertical capacity of the pile consists of shaft resistance and tip resistance. When a pile is subjected to horizontal load and develops displacement along the pile, the lateral earth pressure around the pile changes and it induces the shaft resistance changes because there is direct proportion between them. The piles are flexible piles, so the tip resistance is not affected by

horizontal load. It says that the lateral resistance and the shaft resistance decrease with the horizontal load increases.

The ultimate bearing capacity for all piles is presented in brackets behind Vu or H_u in Table 2 and shown in Figs. 4 and 5. Although the test results are limited, the basic law is obvious. The ultimate vertical load decrease when the horizontal load increases and the ultimate horizontal load decrease when the moment increases at the pile top.

4 Conclusions

An extensive series of model tests has been carried out on flexible piles in sand under combined load. It was found that the ultimate vertical load, horizontal load and moment are influenced each other. The results of model tests on singles flexible piles under horizontal load and moment at the pile top show that the ultimate horizontal bearing capacity decreases with the increase of moment. The results of model tests on singles flexible piles under vertical and horizontal load and constant moment at the pile top show that the ultimate vertical bearing capacity decreases with the increase of horizontal load. But there is optimum vertical load which can increase the horizontal bearing capacity, and the optimum ratio of vertical $\kappa = 0.32$ for this tests. In addition, it indicates that the ultimate combined load envelope diagram of a single pile is an irregular ellipsoid in three-dimensional space.

The formulas which are listed in this paper can be reasonable reflect the test results. Although these proposed methods of analysis are approximately supported by the present model tests, field load test should be done on flexible piles for further investigation.

Acknowledgments The present study was supported by Shanghai Pujiang Program (11PJ1410100), Kwang-Hua Fund for College of Civil Engineering, Tongji University, Innovation Program of Tongji Younger Scholar (2010KJ047) and the National Natural Science Foundation Project (project number: 40972180). The entire staff at the Key Laboratory of Geotechnical and Underground Engineering of the Ministry of Education in Tongji University are gratefully acknowledged for their cooperation.

References

Koumoto, T., Meyerhof, G-G., & Sastry V-V (1986). Analysis of bearing capacity of rigid piles under eccentric and inclined loads. *Canadian Geotechnical Journal, 23*, 127–131.

Meyerhof, G–. G., & Ghost, D. P. (1989). Ultimate capacity of flexible piles under eccentric and inclined loads. *Canadian Geotechnical Journal, 26*, 34–42.

Sastry, V-V., & Meyerhof, G-G. (1994). Behavior of flexible piles in layered sands under eccentric and inclined loads. *Canadian Geotechnical Journal, 31*, 513–520.

Sastry, V-V., & Meyerhof, G-G. (1995) Behavior of flexible piles in layered clays under eccentric and inclined loads. *Canadian Geotechnical Journal, 32,* 387–396.

Meyerhof, G.-G., & Yalcin, A. S. (1984). Pile capacity for eccentric inclined load in clay. *Canadian Geotechnical Journal, 21*, 389–396.

Zhao, M. H., Li, W. Z. (2006). A model test study on displacement of piles under inclined and eccentric loads in layered soils. *China Civil Engineering Journal, 39*(12), 95–99.

Banerjee, P. K., & Davis, T. G. (1978). The behavior of axially and laterally loaded single piles embedded in homogeneous soils. *Geotechnique, 28*, 309–326.

Poulos, H. G., & Davis, (1980). *Pile foundation analysis and design*. New York: Wiley.

Meyerhof, G-G., & Sastry V-V. (1985). Bearing capacity of rigid piles under eccentric and inclined loads. *Canadian Geotechnical Journal, 22,* 267–276.

Foundation Design Challenges at Hunter Expressway Alliance Project in Australia

H. H. Zhang and B. Choi

Abstract
The Hunter Expressway is a road infrastructure project that will provide a 40 km four lane carriageway between the F3 Interchange at Newcastle and the New England Highway at Branxton, New South Wales Australia. It is due to be opened by the end of 2013. The Hunter Expressway Alliance (HEA), comprising Roads and Maritime Services (RMS), Thiess Pty Ltd, Parsons Brinckerhoff and Hyder Consulting is constructing one of two sections consisting of 13 km of new freeway and local road adjustments. Eight bridges (including three viaducts) are affected by mine subsidence due to past mine workings and future mining works. This chapter describes the foundation design challenges due to subsidence movements and innovative engineering solutions at one of the viaducts. In particular, the subsidence induced horizontal movements, strategies for managing subsidence risks, design methodologies for piled foundations and superstructure to accommodate the anticipated subsidence movements will be discussed. Rock socketed pile design using the Rowe and Armitage Method and pile group analysis will also be covered.

Keywords
Piled foundation • Mine subsidence • Rock socketed piles

1 Introduction

The Hunter Expressway is a new highway consisting of 13 km of new freeway construction with various local road adjustments, including 20 new bridges and three culverts to provide crossings across major valleys and creeks. Figure 1 shows the route of the Hunter Expressway.

Of the 20 bridges, eight bridges including three viaducts will be constructed in areas of prior mine workings and proposed mining works. Thus, one of the major issues and significant challenge of the project is to ensure the foundation of the bridges accommodates the anticipated mine subsidence effects.

This paper will present the design of one of the viaducts, BW010, a twin bridge with 3 piers and 4 spans. The foundation issues due to the mine subsidence effects, the innovative foundation designs and the outcome of the design.

2 Bridge Design Loads and Articulation

The design loads associated with the bridge structure consists of the design vehicular loading as specified by the Scope of Works Technical Criteria (SWTC) and in accordance with the Australian Standards AS5100. Construction loading was considered along with temporary loading associated with the delivery of precast segments and the launching of the erection gantry.

H. H. Zhang (✉) · B. Choi
Principal Geotechnical Engineer, Parsons Brinckerhoff, GPO Box 5394, Sydney, NSW 2001, Australia
e-mail: hezhang@pb.com.au

Y. Huang et al. (eds.), *New Frontiers in Engineering Geology and the Environment*,
DOI: 10.1007/978-3-642-31671-5_30,

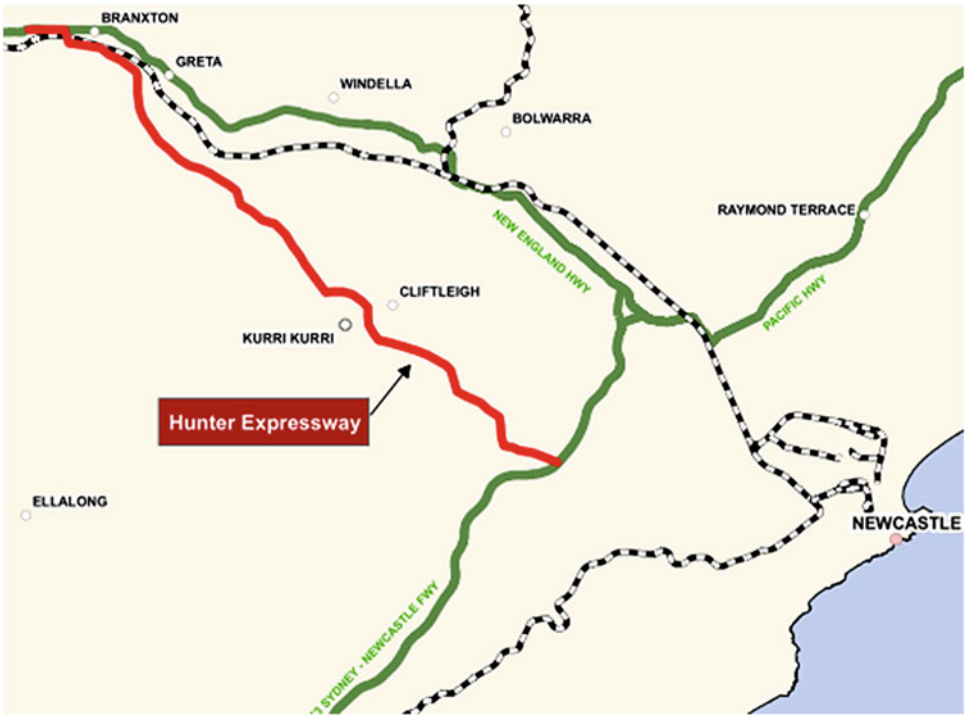

Fig. 1 Hunter expressway plan view

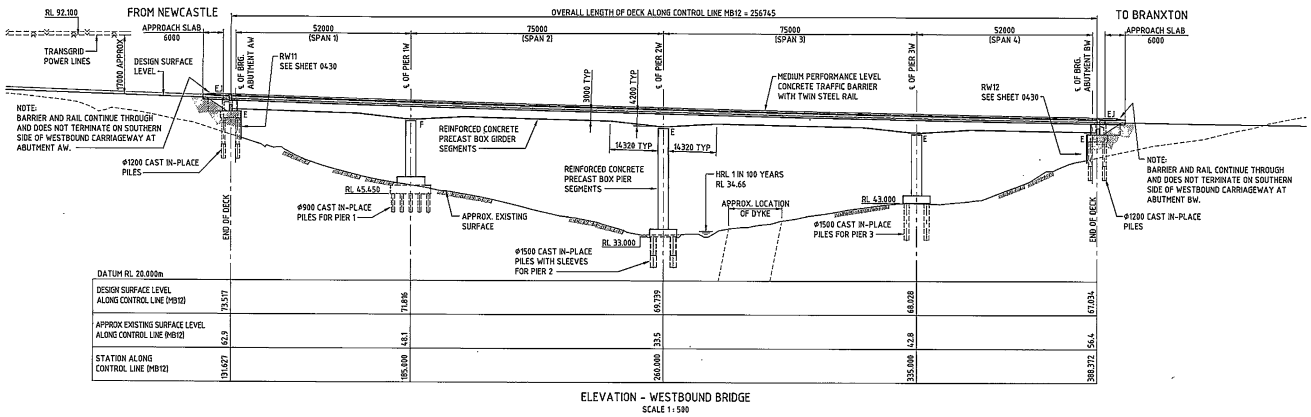

Fig. 2 BW010 cross section view

BW010 is classified as a Type III bridge for earthquake design in accordance with AS5100. The bridge earthquake design is categorised as BEDC-3, based on the acceleration coefficient and the site factor. Based on the SI data available and in accordance with AS1170.4, a site factor (S) of 1.0 is adopted for earthquake design and a ground acceleration coefficient (α) of 0.11 for the design of the structures. No SLS EQ load case was considered for the design of the structures.

BW010 is restrained horizontally by a fixed shear key at Pier 1 and a guided shear key at Pier 3. This allows rigid movement of the bridge deck during a horizontal mine subsidence event resulting in no additional stresses in the deck. All horizontal loads are transferred through shear keys only. All bearings are free sliding, transferring vertical load only (Fig. 2).

3 Foundation Design Challenges

There were two challenges for foundation engineers. The first was soil-structure interaction and the integration of superstructure and foundation design. Structural programs were used to determine the forces and behaviour of the whole bridges under various load combinations; however such programs are not good at soil-structural interaction and

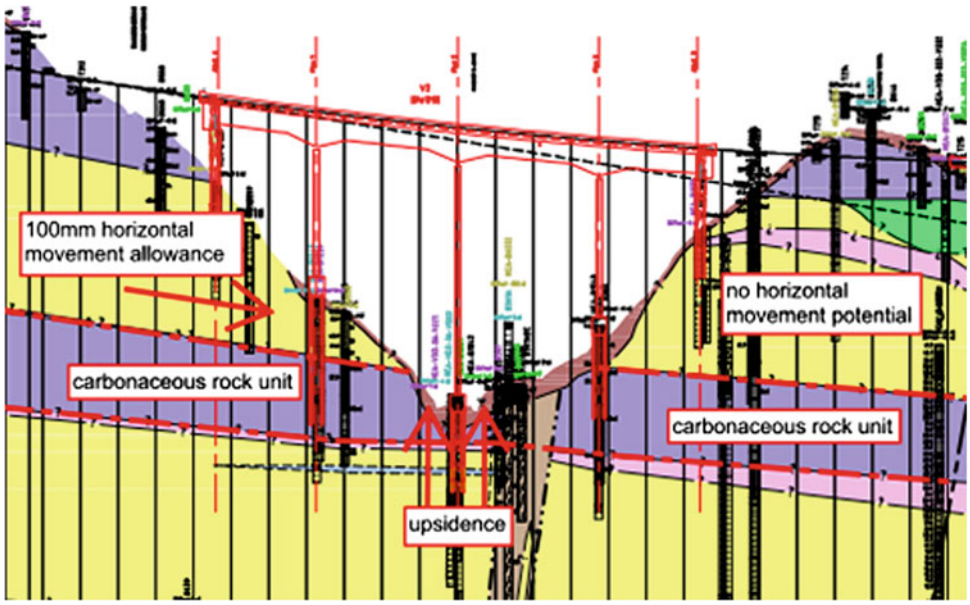

Fig. 3 Horizontal movements and carbonaceous rock unit for BW010

rely on simplified linear springs to simulate this effect. To overcome such limitations, geotechnical programs were adopted to assess soil-structure interaction and estimate the springs for superstructure model. Thus there was a gap between geotechnical analysis and structural analysis.

The second and the biggest challenge was the mine subsidence. Subsidence movements associated with the sudden collapse of old mine workings and proposed future mining have potential to impact on bridge BW010. Following the mine void grouting, the nominated ground movements for BW010 were as follows: (1) Vertical Movement = 25 mm differential settlement; (2) Tilt = < 1 mm/m; (3) Horizontal Movement (Abutment A, Pier 1 and Pier 2) = 100 mm; horizontal Movement (Abutment B and Pier 3) = 0 mm; (4) Upsidence Movement (Pier 2) = 75 mm.

Low strength bedding planes associated with tuffaceous claystone units within the carbonaceous rock unit occurs at and below the base of the valley which BW010 crosses. This carbonaceous rock unit or potential shearing zone is shown in purple in Fig. 3. The strata are dipping to the southwest which equates to a westerly dip along the alignment.

The mechanism and approach to assessing the mine subsidence movements are discussed in SCT Letter Report (2011) and are beyond the scope of this chapter.

4 Innovative Foundation Design

4.1 Soil-Structure Interaction Analysis

Repute 2.0 was adopted to analyze soil-structure interaction at all pier and abutment locations. Pile group effect under combined vertical, horizontal load and bending moment was analyzed for both serviceability and ultimate limit states. Other programs Plaxis 3D Foundation and Piglet were also used to calibrate the results from Repute. These three programs gave comparable results.

To close the gap between geotechnical analysis and structural analysis, the following procedure was adopted: step 1—preliminary soil/rock springs (=similar magnitude of Young's modulus) were used in structural program to determine forces of a pile group. Step 2—these forces were then input to Repute to calculate the pile movements and forces. Step 3—if the difference between two programs was acceptable (within 20 %) then stopped and used the highest loads form two programs to design the individual piles; otherwise repeated step 1 and 2 with springs back-calculated from Repute analysis until the difference was acceptable.

4.2 Individual Pile Geotechnical Design

Once the pile forces were determined, two checks were made: axial and lateral geotechnical capacity.

4.2.1 Pile Socket Design for Axial Load

Rowe and Arimitage (1987) Elastic Method was used to check the rock socket length. The ultimate bearing capacity was also checked against the criteria in AS2159-2009: $\phi_g R_{ug} \geq S^*$, ϕ_g was taken as 0.5 based on AS2159-2009. For piles under tension load, only the shaft resistance was considered; both piston pull-out failure and cone lift-out failures were checked.

4.2.2 Pile Socket Design for Lateral Load

Broms (1964) method was used to check pile lateral geotechnical capacity. Rocks were assumed as clay with ultimate lateral pressure of $9.0C_u$ (or $4.5q_u$), where Cu is undrained shear strength and q_u uniaxial compressive strength of intact rock.

4.3 Pile Solution for Mine Subsidence

The strategies adopted for managing the subsidence risk included both mine fill and bridge design components. The bridge structures have been designed to accommodate the low levels of vertical subsidence that could not be prevented by mine filling alone and the potentially horizontal ground movements caused by pillar collapse at adjacent areas.

The design philosophy for bridges subject to horizontal movement was to provide a flexible structure with the foundations isolated from the horizontal ground movements either through double-sleeving of piles that penetrate through the shear zone or footings founding above the potential shearing zone. The double-sleeving of piles provides an annulus of free space between the outer and inner sleeves to accommodate potential horizontal movements across the basal shear plane.

4.3.1 Pile Raft Solution at P1

The design of the foundation for Pier 1 consisted of a combined piled raft foundation that terminated above the potential shear zone. The 25 × 12 m thick raft slab is sat on a grid of 45, 0.9 m diameter piles and a 1.0 m nominal thick plain concrete layer. The piles were founded on the top of the potential shearing zone and on R4 rock. The raft slab was founded on plain concrete which transfers the compressive bearing stress through the residual soil layer to the top of the R5 rock. FE program Plaxis 2D and 3D were used to analyze the piled raft behavior and individual pile forces.

4.3.2 Sleeved Pile Solution at P2

Double sleeved piles were adopted for the P2 foundation to avoid the potential horizontal and vertical subsidence movements. P2 piles were founded in the R2 layer below the identified coal seams. The pile cap soffit level was located above the finished ground level to cater for potential upsidence movement.

4.3.3 P3 and Abutment B Piles

Pier P3 piles were founded in R2/R3 layer within the coal seam strata with no sleeves. At this location, evidence from the mine subsidence investigation and mine void grouting indicated that there was no potential for ground movement.

4.3.4 Abutment A Piles

The piles of this foundation were founded above the shear plane and not sleeved. It was assumed that during mine subsidence event, piles and pile cap would move with the surrounding ground.

4.3.5 Monitoring of Mine Subsidence

The monitoring system for double-sleeved pile foundations included inspection pipes installed within the pile caps to allow the inspection of piles sleeves via an endoscope camera. Inclinometers were installed at pier locations through the anticipated zone of shearing to monitor the horizontal movements.

5 Conclusion

A case history of bridge foundation design for mine subsidence is presented. Innovative engineering solutions for pile foundations to accommodate mine subsidence are presented: P1 piled raft foundation that terminated above the potential shear zone and double sleeved piles at P2 to avoid the potential horizontal movements. The incorporation of monitoring into foundation designs will permit detection and an appropriate response to movements should they occur.

Acknowledgments The authors would like to thank RMS for approval of publishing this paper. The views expressed in the paper are those of the authors and do not necessary reflect those of the supporting organizations.

References

Broms, B. (1964). The lateral resistance of piles in cohesive soils. *Journal of Soil Mechanics Found Division ASCE, 90*, 27–63.

Repute 2. www.geocentrix.co.uk/repute

Rowe, R. K., & Armitage, H. H. (1987). A design method for drilled piers in soft rock. *Canadian Geotechnical Journal, 24*, 126–142.

SCT Letter Report (2011). *Downward Revision of Horizontal Movements Predicted for Eastern End of Viaduct 3 (BW011) and Western End of Viaduct 2 (BW010)*. Reference PBA3631G dated 23 August 2011.

Analytical Solutions for Three-Dimensional Stability of Coastal Slope

C. Y. Han, X. H. Xia, and J. H. Wang

Abstract
The theory of limit analysis is presented for three-dimensional stability of coastal slope. In the frictional soils, the failure surface has the shape of logarithm helicoids, with outline defined by log-spirals. Dissipation rate and gravity power are obtained. By solving the energy balance equation, the expression of stability factor for coastal slope is obtained. The influences of the ratio of width and height and slope angle on the stability are evaluated. Numerical results are presented in the form of graphs. Some examples illustrate the practical use of the results.

Keywords
Stability • Landslides • Limit analysis • Coastal slope

1 Introduction

Coastal slope failures are major transport process from the upper slope to the ocean (Hutton and Syvitski 2004; Grilli et al. 2009; L'Heureux et al. 2010). Coastal slope failure can take different forms such as translational or rotational slides (Locat 2001). The different failure forms likely represent the different geotechnical and properties of the failed material, (Locat and Lee 2002; Tinti and Bortolucci 2000; Walters et al. 2006). In the absence of direct observations, scientists have made assumptions about failure institutions. The most common assumption is that a failure process is a cascade or an avalanche process (Densmore et al. 1998; Guzzetti et al. 2002; Malamud et al. 2004; McAdoo and Watts 2004; Lee and Stow 2007).

C. Y. Han (✉) · X. H. Xia · J. H. Wang
Department of Civil Engineering, Shanghai Jiaotong University, Shanghai 200240, China
e-mail: hanyu02@163.com

X. H. Xia · J. H. Wang
Center for Marine Geotechnical Engineering, Shanghai Jiaotong University, Shanghai 200240, China

The stability of coastal slope has been given little attention in the past, even though coastal landslides are common. All coastal slope failures are three-dimensional 3D in practical, but two-dimensional 2D model is usually adopted with very simple. However, when the dimensions of coastal slope are clearly limited by adjacent rock formations or existing structures, a three-dimensional analysis of safety may be more appropriate (Ten Brink et al. 2009; Krastel et al. 2001; Locat et al. 2010).

The upper bound solutions for the failure of coastal slope are presented. The soil is treated as a plastic material, satisfying the coulomb's yield criterion. The failure surface has the shape of logarithm helicoids, with outline defined by log-spirals. Examples are provided to illustrate the stability factor influenced by the angle of internal friction, the unit weight of the soil, distance from sea level to slope top and slope width.

2 Theoretical Formulation

The application of limit analysis to problems involving stability of earth slopes, first performed by Drucker and Prager (1952), involves determining a lower bound on the

Y. Huang et al. (eds.), *New Frontiers in Engineering Geology and the Environment*,
DOI: 10.1007/978-3-642-31671-5_31,

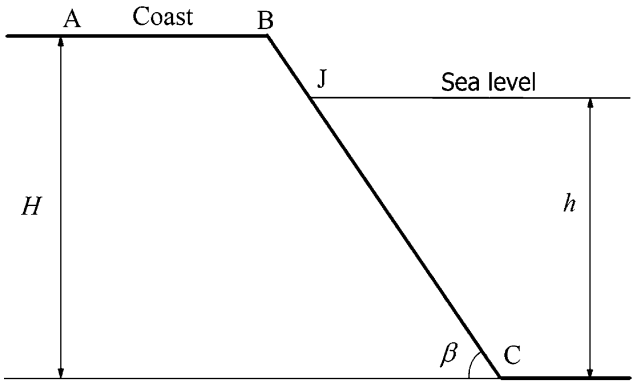

Fig. 1 Schematic diagram for coastal slope

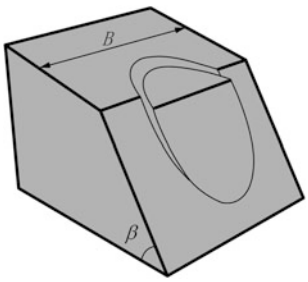

Fig. 2 Three-dimensional rotational mechanism

collapse load by assuming a stress field which satisfies equilibrium and does not violate the yield criterion at any point. An upper bound is obtained by a velocity field compatible with the flow rule in which the rate of work of the external forces equals or exceeds the rate of internal energy dissipation.

The problem considered here is the safety factor of coastal slope with angle β as shown in Figs. 1 and 2. The upper-bound theorem of limit analysis states that the coastal slope will collapse, for any assumed failure mechanism, the rate of work done by the soil weight exceeds the internal rate of dissipation. Equating external and internal energies for any such mechanism thus gives an upper bound on the safety factor.

A rotational discontinuity mechanism is shown in Fig. 3, in which the failure surface is assumed to pass through the top and the toe of the coastal slope. Similar shape of this mechanism is considered by Michalowski and Drescher (2009) for evaluating critical height of slope. Soil over the failure surface rotates about the center of rotation O (as yet undefined), while the materials below the failure surface static. Failure surface AC is the velocity discontinuous surface. Assumed mechanism can be specified completely by three variables. For the sake of convenience, we select the angles θ_0, θ_h and r_0'/r_0. Equation for the logarithmic spiral surface is given by:

$$r = r_0\, e^{(\theta-\theta_0)\tan\varphi},\ r' = r_0'\, e^{-(\theta-\theta_0)\tan\varphi} \tag{1}$$

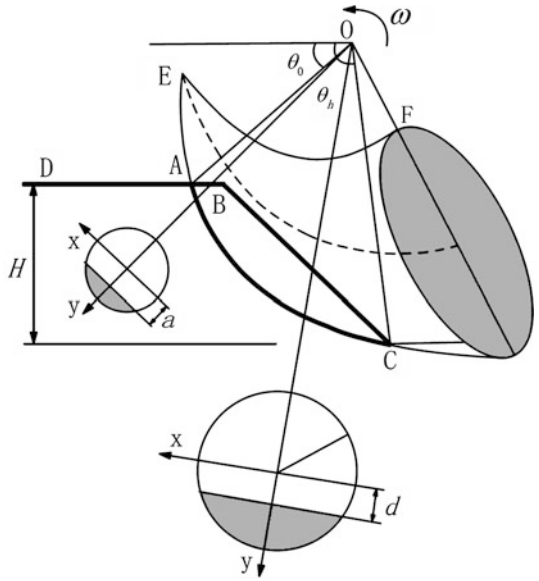

Fig. 3 Schematic diagram of the 3D mechanism

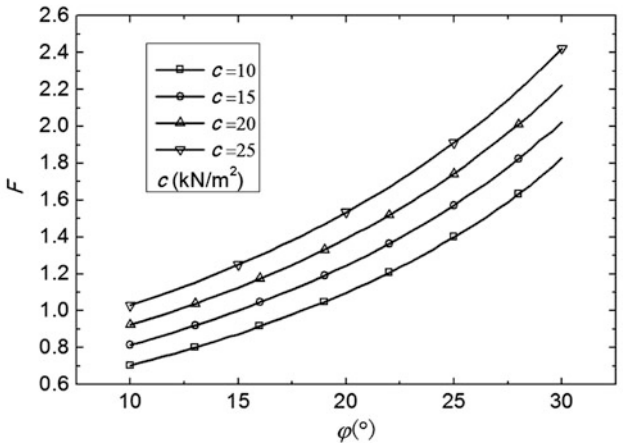

Fig. 4 Variation of safety factor F with the angle of internal friction

The rate of work of the external forces (weight) is:

$$W_\gamma = 2\omega\gamma\left[\int_{\theta_0}^{\theta_B}\int_0^{x_1^*}\int_a^{y*}(r_m+y)^2\cos\theta\, dydxd\theta + \int_{\theta_B}^{\theta_h}\int_0^{x_2^*}\int_d^{y*}(r_m+y)^2\cos\theta dydxd\theta\right] \tag{2}$$

where γ is unit weight of the soil, ω is angular velocity of the region ABC.

The total rate of external work due to the seawater pressure is.

$$W_{\mathrm{w}} = -2\omega\gamma_{\mathrm{w}}\int_{\theta_{\mathrm{w}}}^{\theta_h} r_{x_2}^2 h''\sqrt{R^2-d^2}\cot(\theta+\beta)d\theta \tag{3}$$

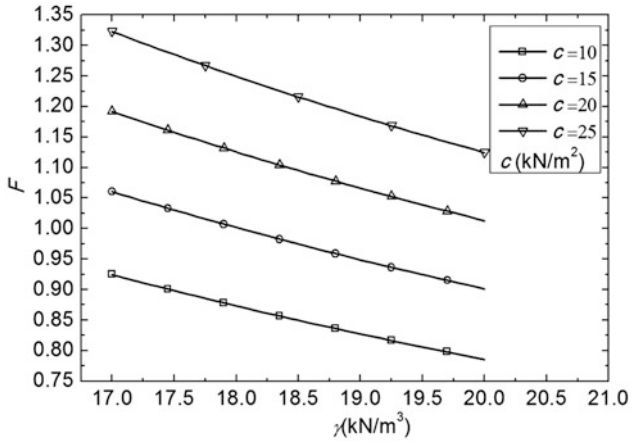

Fig. 5 Variation of safety factor F with the unit weight of the soil

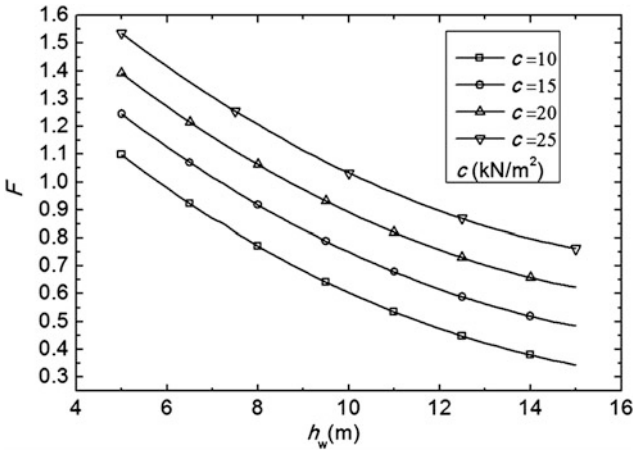

Fig. 6 Variation of safety factor F with distance from sea level to slope top

Internal dissipation of energy can be more specifically written as sum of integrals over top and surface of the coastal slope

$$D = D_{AB} + D_{BC} \tag{4}$$

where the functions D_{AB}, D_{BC} are defined as:

$$\frac{D_{AB}}{c\cot\varphi} = -2\omega r_0^2 \sin^2\theta_0 \int_{\theta_0}^{\theta_B} \frac{\cos\theta}{\sin^3\theta}\sqrt{R^2 - a^2}\,d\theta \tag{5}$$

$$\frac{D_{BC}}{c\cot\varphi} = -2\omega r_0^2 e^{2(\theta_h-\theta_0)\tan\varphi}\sin^2(\theta_h + \beta)\int_{\theta_B}^{\theta_h} \frac{\cos(\theta+\beta)}{\sin^3(\theta+\beta)}\sqrt{R^2 - d^2}\,d\theta \tag{6}$$

where functions r_m, R, x_1^*, x_2^*, y^*, a, d, θ_B, r_{x_1}, r_{x_2}, r_{x_B}, h'', θ_w are defined as:

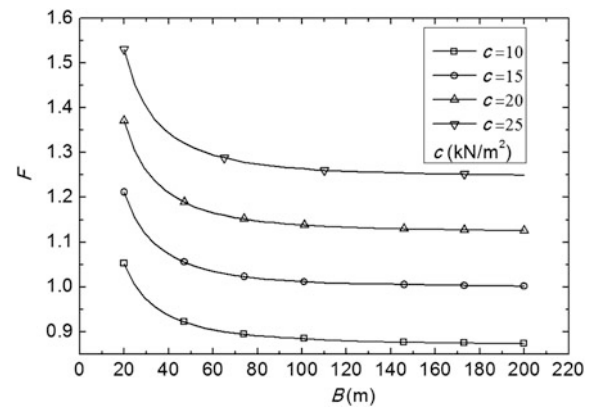

Fig. 7 Variation of safety factor F with slope width

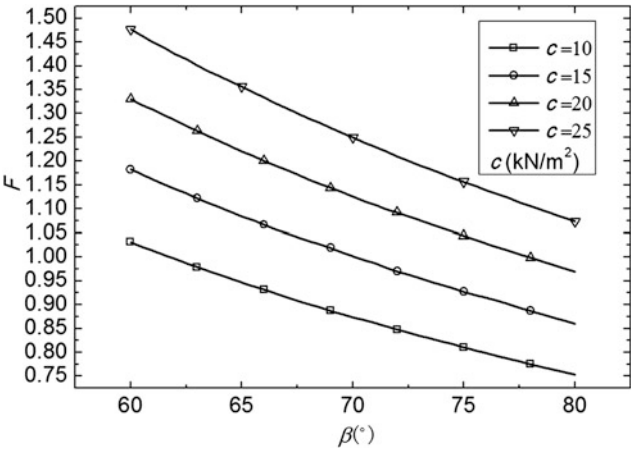

Fig. 8 Variation of safety factor F with slope angle

$$r_m = \frac{r+r'}{2}, R = \frac{r-r'}{2}, x_1^* = \sqrt{R^2 - a^2}, x_2^* = \sqrt{R^2 - d^2}, y^* = \sqrt{R^2 - x^2},$$

$$a = \frac{\sin\theta_0}{\sin\theta} r_0 - r_m,\ d = \frac{\sin(\beta+\theta_h)}{\sin(\beta+\theta)} r_0\, e^{(\theta_h-\theta_0)\tan\varphi} - r_m,$$

$$\theta_B = \arctan\frac{\sin\theta_0\sin\beta}{\sin(\theta_h+\beta)e^{(\theta_h-\theta_0)\tan\varphi} - \sin\theta_0\cos\beta}, r_{x_1} = \frac{\sin(\beta+\theta_h)}{\sin(\beta+\theta_w)} r_0\, e^{(\theta_h-\theta_0)\tan\varphi},$$

$$r_{x_2} = \frac{\sin(\beta+\theta_h)}{\sin(\beta+\theta)} r_0\, e^{(\theta_h-\theta_0)\tan\varphi}, r_{x_B} = \frac{\sin(\beta+\theta_h)}{\sin(\beta+\theta_B)} r_0\, e^{(\theta_h-\theta_0)\tan\varphi},$$

$$h'' = r_{x_2}\sin\theta - r_{x_1}\sin\theta_w, \frac{r_{x_B}}{H-h} = \frac{\sin(\theta_w+\beta)}{\sin\beta\sin(\theta_w-\theta_B)}$$

The factor of overall safety is calculated as

$$F = \frac{D + W_{\mathrm{w}}}{W_{\gamma}} \tag{7}$$

To avoid lengthy computations, these simultaneous equations may be solved by a numerical procedure. The minimum $F_{\min}$ is calculated with independent variable parameters θ_0, θ_h, r_0'/r_0.

3 Example

Calculations for parameters are performed using the mechanisms in Fig. 3. For three-dimensional mechanisms, independent variable in minimising F is θ_0, θ_h, r_0'/r_0. Finding the least value of F requires a numerical procedure. In the procedure for finding the minimum of safety factor F, the independent variables, θ_0, θ_h and r_0'/r_0 are changed sequentially by a single computational loop. The computational loop is repeated until the minimum is found.

The first example considers a coastal slope with the following parameters, slope depth 20 m, slope width 200 m, soil bulk density $\gamma = 18\,\mathrm{kN/m^3}$, sea water density $\gamma_{\mathrm{w}} = 10.22\,\mathrm{kN/m^3}$, distance from sea level to slope top 5 m, and slope angle 70°. Figure 4 shows plots of F versus the angle of internal friction. The factor of safety increases as φ increases.

Figure 5 shows plots of F versus the unit weight of the soil with the following parameters, slope depth 20 m, slope width 200 m, the angle of internal friction $\varphi = 15°$, sea water density $\gamma_{\mathrm{w}} = 10.22\ \mathrm{kN/m^3}$, distance from sea level to slope top 5 m, and slope angle $\beta = 70°$. The factor of safety decreases with increasing soil bulk density

Figure 6 shows plots of F versus distance from sea level to slope top with the following parameters, slope depth 20 m, slope width 200 m, the angle of internal friction $\varphi = 20°$, sea water density $\gamma_{\mathrm{w}} = 10.22\ \mathrm{kN/m^3}$, soil bulk density $\gamma = 18\ \mathrm{kN/m^3}$, and slope angle $\beta = 70°$. The factor of safety decreases with increasing h_{w}.

Figure 7 shows plots of F versus slope width with the following parameters, slope depth 20 m, soil bulk density $\gamma = 18\ \mathrm{kN/m^3}$, the angle of internal friction $\varphi = 15°$, sea water density $\gamma_{\mathrm{w}} = 10.22\ \mathrm{kN/m^3}$, distance from sea level to slope top 5 m, and slope angle $\beta = 70°$. The chart shows that F is affected by slope width. The factor of safety decreases with increasing slope width.

>>Figure 8 shows plots of F versus slope angle with the following parameters, slope depth 20 m, soil bulk density $\gamma = 18\ \mathrm{kN/m^3}$, the angle of internal friction $\varphi = 15°$, sea water density $\gamma_{\mathrm{w}} = 10.22\ \mathrm{kN/m^3}$, distance from sea level to slope top 5 m, and slope width 200 m. The factor of safety decreases with increasing slope angle.

4 Conclusions

The upper bound method for the three-dimensional analysis of coastal slope stability is presented in this paper for frictional/cohesive soil. Formulas for the stability analysis are obtained through theoretical derivation on the basis of limit analysis theory. Rotational mechanisms are presented for coastal slope stability. The failure surface has the shape of logarithm helicoids, with outline defined by log-spirals.

Examples are provided to illustrate variations of the stability factor with the angle of internal friction, the unit weight of the soil, distance from sea level to slope top and slope width. The stability factor increases with decreasing the soil bulk density, distance from sea level to slope top and slope width. The safety factor increases as φ increases.

Acknowledgments This study was substantially supported by the grant from the National Natural Science Foundation of China (Grant No. 41172251, 41002095).

References

Densmore, A. L., Ellis, M. A. et al. (1998). Landsliding and the evolution of normal-fault-bounded mountains. *Journal of Geophysical Research-Solid Earth, 103*(B7), 15203–15219.

Drucker, D. C., & Prager, W. (1952). Soil mechanics and plastic analysis or limit design. *Quarterly of Applied Mathematics, 10*(2), 157–165.

Grilli, S. T., Taylor, D. S., et al. (2009). A probabilistic approach for determining submarine landslide tsunami hazard along the upper east coast of the United States. *Marine Geology, 264*(1–2), 74–97.

Guzzetti, F., Malamud, B. D., et al. (2002). Power-law correlations of landslide areas in central Italy. *Earth and Planetary Science Letters, 195*(3–4), 169–183.

Hutton, E. W. H., & Syvitski, J. P. M. (2004). Advances in the numerical modeling of sediment failure during the development of a continental margin. *Marine Geology, 203*(3–4), 367–380.

Krastel, S., Schmincke, H. U. et al. (2001). Submarine landslides around the Canary Islands. *Journal of Geophysical Research-Solid Earth, 106*(B3), 3977–3997.

L'Heureux, J. S., Hansen, L., et al. (2010). A multidisciplinary study of submarine landslides at the Nidelva fjord delta, Central Norway—implications for geohazard assessment. *Norwegian Journal of Geology, 90*(1–2), 1–20.

Lee, S. H., & Stow, D. A. V. (2007). Laterally contiguous, concave-up basal shear surfaces of submarine land-slide deposits (Miocene), southern Cyprus: differential movement of sub-blocks within a single submarine landslide lobe. *Geosciences Journal, 11*(4), 315–321.

Locat, J. (2001). Instabilities along ocean margins: A geomorphological and geotechnical perspective. *Marine and Petroleum Geology, 18*(4), 503–512.

Locat, J., Brink, U. S. T. et al. (2010). The block composite submarine landslide, southern New England Slope, USA: A Morphological Analysis.

Locat, J., & Lee, H. J. (2002). Submarine landslides: advances and challenges. *Canadian Geotechnical Journal, 39*(1), 193–212.

Malamud, B. D., Turcotte, D. L., et al. (2004). Landslide inventories and their statistical properties. *Earth Surface Processes and Landforms, 29*(6), 687–711.

McAdoo, B. G., & Watts, P. (2004). Tsundami hazard from submarine landslides on the Oregon continental slope. *Marine Geology, 203*(3–4), 235–245.

Michalowski, R. L., & Drescher, A. (2009). Three-dimensional stability of slopes and excavations. *Geotechnique, 59*(10), 839–850.

Ten Brink, U. S., Barkan, R., et al. (2009). Size distributions and failure initiation of submarine and subaerial landslides. *Earth and Planetary Science Letters, 287*(1–2), 31–42.

Tinti, S., & Bortolucci, E. (2000). Energy of water waves induced by submarine landslides. *Pure and Applied Geophysics, 157*(3), 281–318.

Walters, R., Barnes, P., et al. (2006). Locally generated tsunami along the Kaikoura coastal margin: Part 2. Submarine landslides. *New Zealand Journal of Marine and Freshwater Research, 40*(1), 17–28.

NCEER Method and Application of an Embankment Slope with Liquefaction Problem in Coastal Area

G. L. Wang, H. Y. Liu, F. Q. Wu, and G. X. Yang

Abstract

Seismic liquefaction problems of embankment slope involve two different fields such as geotechnical engineering and engineering earthquake. It's an intersectant topic of the slope engineering and sand soil liquefaction. The embankment slope Liquefaction is a very common phenomenon in coastal area of Tangshan, China, where the ground water table is very shallow and the distribution of saturated sand soil is widespread. Adopting theoretical analysis method,the problem of seismic liquefaction for embankment slope has been studied in detail. According to the method of NCEER, the factor of safety against liquefaction is used to evaluate sand soil liquefaction for embankment slopes. Through calculating parameters of CSR (Cyclic Stress Ratio), MSF (Magnitude Scaling Factor) and $CRR_{7.5}$ (Cyclic Resistance Ratio for $M = 7.5$ earthquakes), the computation formula for factor of safety against liquefaction (FS) can be obtained. The index of FS is relatively convenient to be used in projects. As a case study, a typical embankment slope with three layers (the upper layer is fill, the middle layer is silty sand and the sub-layer is gravel soil) is used to prove the method of NCEER, and the result shows that liquefaction will occur in saturated sand soil. Finally, the NCEER method has better application for liquefaction assessment of embankment slope in coastal area.

Keywords

Embankment slope • Factor of safety against liquefaction • Seismic liquefaction • Saturated sand soil

1 Introduction

The coastal area of Tangshan in China belongs to high earthquake intensity region,where the ground water table is usually very shallow and the saturated sand is extensively developed. As a result, the embankment slopes in the coastal area is being confronted with great danger of earthquake liquefaction. The failure of embankment slopes triggered by earthquake is the most destructive phenomenon in nature (Chen et al. 2009; Zhou et al. 2009; Fu and Zeng 2005). When earthquake occurs, the powerful seismic force will cause severe destruction for the embankment slopes, on the other hand, the loss of shear strength due to liquefaction of saturated sand soil is also a most important reason (Seed and Idriss

G. L. Wang (✉)
Xi'an Center of Geological Survey, China Geological Survey, No. 438, East of Youyi Road, Beilin District, Xi'an 710054, China
e-mail: wang2006@mail.iggcas.ac.cn

H. Y. Liu
Shandong Provincial Key Laboratory of Depositional Mineralization and Sedimentary Minerals, Shandong University of Science and Technology, No. 579, Qianwangang Road, Economic and Technical Development Zone, Qingdao 266590, China

F. Q. Wu · G. X. Yang
Key Laboratory of Engineering Geo-Mechanics, Chinese Academy of Sciences, No. 19, Beitucheng Western Road, Chaoyang District, Beijing 100029, China

Y. Huang et al. (eds.), *New Frontiers in Engineering Geology and the Environment*,
DOI: 10.1007/978-3-642-31671-5_32,

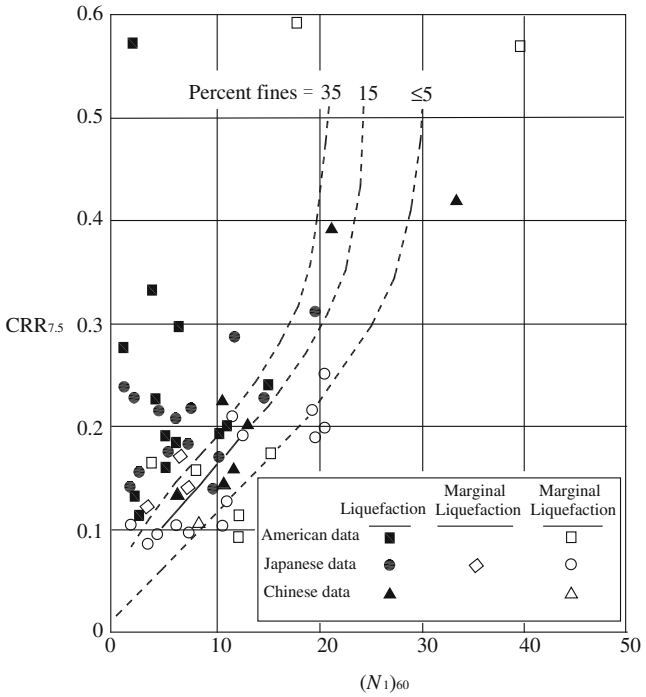

Fig. 1 Relationship between cyclic stress ratios causing liquefaction and(N1)60 values for silt sands in M = 7.5 Earthquakes(After Seed et al. 1985)

1971; Wang et al. 2010). Such as the 1995 Kobe earthquake in Japan, the liquefaction of embankment foundation caused severe damage along the Yodo-gawa River; the 1999 Chi-chi earthquake in Taiwan, the foundation liquefaction of embankment slopes resulted in a lot of surface cracks and sand boils in Nantou County. Both the 1975 Tangshan earthquake and the 2008 Wenchuan earthquake in China also caused severe damage to buildings, bridges and roads, due to liquefaction (Chen and Men 2002; Ren et al. 2007).

The method of NCEER (Youd and Idriss 1997) is applied to analyze the liquefaction problem of embankment slopes in coastal area in the paper. According to the approach, a factor of safety against liquefaction for the embankment slopes is put forward by the author. The results can not only deepen the liquefaction mechanism, but also provide basic theory of the prevention and treatment for embankment slopes in coastal area.

2 NCEER Method

2.1 Factor of Safety Against Liquefaction

When the foundation of embankment slopes has liquefiable soil layer (saturated sand soil), the analysis and evaluation of the liquefaction are needed. The NCEER is an internationally recognized evaluation method of soil liquefaction for the stratified foundation. The method is also appropriate

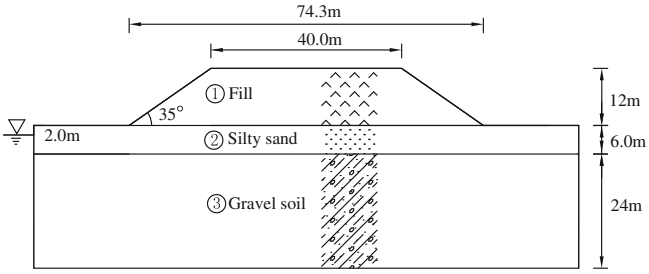

Fig. 2 Engineering geology cross section of embankment slope

to the problem of liquefaction for embankment slopes. The evaluation index is the factor of safety against liquefaction (FS). When using this method the equivalent cyclic stress ratio (CSR), magnitude scaling factor (MSF) and the circulation resistance radio when the magnitude is 7.5 ($CRR_{7.5}$) need to be calculated. The computation formula for factor of safety against liquefaction is expressed as:

$$\mathrm{Fs} = \frac{\mathrm{CRR}_{7.5} \times \mathrm{MSF}}{\mathrm{CSR}} \tag{1}$$

2.2 Cyclic Stress Ratio

CSR (Cyclic Stress Ratio), which is improved by Seed and Idriss (1971), is a simplified calculation method of sand liquefaction. CSR is given as:

$$\mathrm{CSR} = \frac{\tau_{\mathrm{av}}}{\sigma'_{\mathrm{v}}} = 0.65\,\frac{a_{\max}}{g}\frac{\sigma_{\mathrm{v}}}{\sigma'_{\mathrm{v}}}\gamma_d \tag{2}$$

where τ_{av} is uniform cyclic shear amplitude of the earthquake(kPa), $a_{\max}$ is the peak ground surface acceleration($\mathrm{m{\cdot}s^{-2}}$), g is the acceleration of gravity, σ_{v} is the total vertical stress(kPa), σ'_{v} is the vertical effective stress(kPa), and γ_d is the value of a stress reduction factor at the depth of interest. The value of stress reduction factor is given by:

$$\gamma_d = \frac{1.0 - 0.4113z^{0.5} + 0.04052z + 0.001753z^{1.5}}{1.0 - 0.4177z^{0.5} + 0.05729z - 0.006205z^{1.5} + 0.001210z^2} \tag{3}$$

2.3 Magnitude Scaling Factor

MSF(Magnitude Scaling Factor)is equal to 1 When $\mathrm{M_w} = 7.5$; and when $\mathrm{M_w} \neq 7.5$,MSF is given as:

$$\mathrm{MSF} = \left(\frac{\mathrm{M_w}}{7.5}\right)^{-2.56} = \frac{10^{2.24}}{\mathrm{M_w^{2.56}}} \tag{4}$$

where $\mathrm{M_w}$ is moment magnitude of earthquakes.

2.4 Cyclic Resistance Ratio

$CRR_{7.5}$(Cyclic Resistance Ratio for M = 7.5 earthquakes)is proposed by Seed in Fig. 1 which shows the relationship between $CRR_{7.5}$ and $(N_1)_{60}$. The experience computing formula of $CRR_{7.5}$ is given as:

$$CRR_{7.5} = \frac{a + cx + ex^2 + gx}{1 + bx + dx^2 + fx_3 + hx^4} \tag{5}$$

In the formula: a = 4.844E − 02, b = −1.248E − 01, c = −4.721E − 03, d = 9.578E − 03, e = 6.136E − 04, f = −3.285E − 04, g = −1.673E − 05 and h = 3.714E − 06. When $(N_1)_{60}$ is less than 30, the Eq. 5 is effective, but it is not suitable for the condition of $(N_1)_{60}$ less than 3.0. When $(N_1)_{60}$ is more than 30, $CRR_{7.5}$ is equal to 1.2.

In the Eq. 5, x is expressed as:

$$x = a + \beta(N_1)_{60} \tag{6}$$

where $(N_1)_{60}$ is the standard penetration test N value corrected for both field testing procedures and overburden pressure. The values of α and β are given by:

$$\begin{cases} \alpha = 0 & FC \le 5\,\% \\ \alpha = \exp[1.76 - (190/FC^2)] & 5\,\% < FC \le 35\,\% \\ \alpha = 5.0 & FC \ge 35\,\% \end{cases} \tag{7}$$

$$\begin{cases} \beta = 1.0 & FC \le 5\% \\ \beta = \exp[0.99 - (FC^{1.5}/1000)] & 5\% < FC \le 35\% \\ \beta = 1.2 & FC \ge 35\% \end{cases} \tag{8}$$

where FC is the content of fine particles (%) by the gradual test at the laboratory $(N_1)_{60}$ can be calculated as follows:

$$\begin{cases} (N_1)_{60} = C_N \cdot N \cdot (ER/60) \\ C_N = \sqrt{100/\sigma'_v} \end{cases} \tag{9}$$

where C_N is correction factor of overburden pressure. C_N is more than 2, which is equal to 2; C_N is less than 0.4, which is equal to 0.4. N is the value of measured standard penetration test. ER is the energy ratio of bore rod, which can be defined as follows:

$$\begin{cases} ER(\%) = 30 \times (Z_{liq}/11) + 50 & Z_{liq} \le 11m \\ ER(\%) = 80 & Z_{liq} \ge 11m \end{cases} \tag{10}$$

3 Examples Analysis

Figure 2 is the engineering geological cross section of an embankment slope. The embankment width is 40.0 m, the embankment foundation width is 74.3 m, and the embankment slope angle is 35°. The embankment is non-liquefiable fill which is 12 m in height. The foundation can be divided into two layers, the upper layer is silt of 6 m in thickness, which is liquefiable when earthquake occurs; the sub-layer is gravel soil of 24 m in thickness. The buried depth of the groundwater is 2.0 m. The parameters of soil are shown in Table 1.

Table 1 Parameters of soil

Layer number	Soil type	γ(kN/m^3)	c(kPa)	Φ(°)
①	Fill(ML)	20	9.8	25
②	Silty sand(SM)	19	0	28
③	Gravel soil(GM)	22	4.9	36

Table 2 Safety factor against liquefaction of the embankment slope

Depth(m)	CSR	MSF	$CRR_{7.5}$	FS
14.0	0.183	1.193	0.089	0.58
16.0	0.179	1.193	0.097	0.64
18.0	0.173	1.193	0.198	1.37

The magnitude of earthquake $M_w = 7.0$, the peak acceleration $a_{max} = 0.33$ g, energy radio of bore rod ER = 80 %, fine particles content FC = 25 %. The values of α, β are calculated to be 4.29, 1.12, by Substituting those parameters into Eqs. 7 and 8.

At the depth of 14, 16 and 18 m below the embankment, the corresponding standard penetration test N value are 4, 5 and 16, and corresponding $(N_1)_{60}$ are 3.35, 4.05 and 12.57 respectively. Based on the Eq. 3, the stress reduction factors at different depth are 0.79, 0.73 and 0.67 respectively.

Through the Eq. 1, the calculation results of safety factor against liquefaction in different depths can be obtained (see in Table 2). According to the results, the values of FS at depth of 14 and 16 m are less than 1.0, so liquefaction of saturated sand soil will occur. As a result, subsidence deformation after liquefaction also will happen.

4 Conclusion

Through calculating the parameters of equivalent cyclic stress ratio (CSR), magnitude scaling factor (MSF) and the circulation resistance radio when the magnitude is 7.5 ($CRR_{7.5}$), the factor of safety against liquefaction (FS) can be obtained according to NCEER method. The method has better application for liquefaction assessment of embankment slope in coastal area, and the safety factor against liquefaction (FS) is relatively convenient to be used in projects.

References

Chen, W., & Men, F. (2002). Study on FEM to simulate slip and seismic liquefaction of slope-field by theory of two phased dynamics. *Earthquake Engineering and Engineering Vibration, 22*(1), 132–140.

Chen, L., Yuan, X., Cao, Z., et al. (2009). Liquefaction macro phenomena in the great Wenchuan earthquake. *Earthquake Engineering and Engineering Vibration, 8*(2), 219–229.

Fu, L., & Zeng, X. (2005). Seismic rehabilitation and analysis of Chaohe Earthdam. *Earthquake Engineering and Engineering Vibration, 4*(2), 265–273.

Ren, H., Lv, X., & Li, P. (2007). Advances in liquefaction research on saturated soils. *Earthquake Engineering and Engineering vibration, 27*(6), 166–175.

Seed, H. B., & Idriss, I. M. (1971). Simplified procedure for evaluating soil liquefaction potential. *Journal of Soil Mechanics and Foundations Division, ASCE, 97*(9), 1249–1273.

Seed, H. B., Tokimatsu, K., Harder, L. F., et al. (1985). Influence of SPT procedures in soil liquefaction resistance evaluations. *Journal of Geotechnical Engineering, 111*(12), 1425–1445.

Wang, J., Yao, L., & Wu, W. (2010). Research on seismic dynamic mode and dynamic characteristics of road embankment. *Rock and Soil Mechanics, 31*(12), 3801–3808.

Youd T. L., Idriss I. M. (1997). *Proceedings of the NCEER workshop on evaluation of liquefaction resistance of soils.* Buffalo: National Center for Earthquake Engineering Research.

Zhou, Y., Chen, Y., & Ling, D. (2009). Shear wave velocity-based liquefaction evaluation in the great Wenchuan earthquake: a preliminary case study. *Earthquake Engineering and Engineering Vibration, 8*(2), 231–239.

Low-Order Lateral Buckling Analysis of Submarine Pipeline Under Thermal Stress

L. P. Guo, R. Liu, and S. W. Yan

Abstract
The lateral buckling is the main failure mode for unburied submarine pipelines. Buckling mode analysis shows that the second lateral buckling mode has greater probability of occurrence. Analytical solution to the second buckling mode is obtained based on small deformation theory and Hook's law. The relationships between the buckling temperature and the amplitude or the wavelength of the buckle segment are established as well. Analytical tools are applied to predict the occurrence and the consequence of in-service buckling of a heated pipeline in an oil field. The effects of temperature difference and properties of subsoil on the buckling mode are investigated. The analyzing results show that buckling will occur once the temperature difference exceeds the safe temperature and the larger the friction coefficients, the safer the submarine pipeline.

Keywords
Submarine pipeline • Lateral buckling • Analytical solution • Temperature difference • Subsoil friction resistance

1 Introduction

In-service hydrocarbons must be transported at high temperature and pressure to ease the flow and prevent solidification of the wax fraction. Thermal stress together with Poisson effect will cause the steel pipe to expand longitudinally. If such expansion is resisted, compressive axial stress will be set up in the pipe-wall. Once the value exceeds the constraint of foundation soil on the pipeline, sudden deformation will occur to release internal stress, and lateral or vertical buckling may occur. Studies show that lateral modes will be dominant in pipelines unless the line is trenched or buried. The earlier paper on pipeline thermal buckling in the open literature appeared in 1978. Based on achievements (Kerr 1978) on lateral buckling of continuously welded track, Hobbs, presented a summary of the basic models of buckling in a long pipeline in 1984(Hobbs 1984). Taylor and Gan provided analytical solutions to ideal submarine pipelines by considering the lateral soil resistance changes with its displacement (Taylor & Gan 1986a, b). Neil Taylor and Aik Ben Gan presented a set of analysis on analytical solutions which incorporate structural imperfections and deformation-dependent axial friction resistance (Taylor & Gan 1986a, b).

In this paper, based on analytical solutions to lateral buckling of ideal submarine pipelines, the second buckling mode is analyzed by establishing numerical method and practical project, and the effects of friction coefficients of foundation soil to pipeline is also presented. (Fig. 1)

L. P. Guo · R. Liu (✉) · S. W. Yan
State Key Laboratory of Hydraulic Engineering Simulation and Safety, Tianjin University,
92 Weijin Rd, Nankai District,
Tianjin 300072, China
e-mail: liurun@tju.edu.cn

Y. Huang et al. (eds.), *New Frontiers in Engineering Geology and the Environment*,
DOI: 10.1007/978-3-642-31671-5_33,

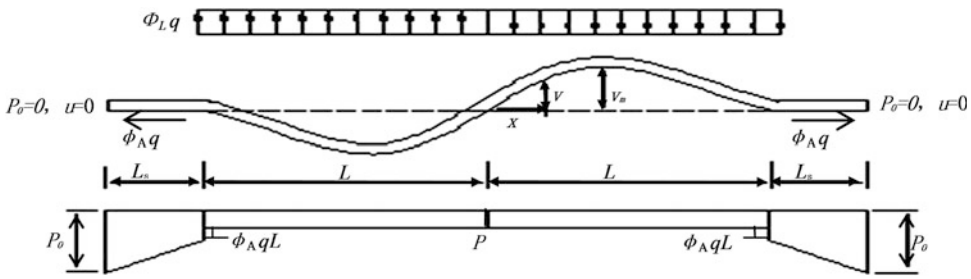

Fig. 1 Deformation and force distribution for the second lateral buckling mode

2 Analysis on the Second Lateral Buckling Mode

Since the second lateral buckling mode is an antisymmetric mode, a half of the buckled region can be analyzed for convenience.

General solution of the second lateral buckling mode can be written as:

$$v = A_1 \cos nx + A_2 \sin nx - \frac{\phi q}{2n^2 EI} x^2 + A_3 x + A_4 \qquad (1)$$

In which EI denotes flexural rigidity, m^4; v is the lateral deformation of the buckled zone, m; q is the self-weight of per unit length, kN; $P = n^2 EI$ is the axial force in the buckled region, kN; ϕ_L is the fully mobilized lateral friction coefficient of foundation soil to pipeline; L is the buckle length, m.

And the constants A_1 to A_4 can be obtained in accordance with boundary conditions:$v|_{x=0} = 0$, $v_{\backslash xx}|_{x=0} = 0$, $v|_{x=L} = 0$, $v_{\backslash x}|_{x=L} = 0$. Take those constants into Eq. (1), and employ the antisymmetrical condition $v_{\backslash xx}|_{x=L} = 0$, it can be obtained that:

$$\mathrm{nL} = 2\pi \qquad (2)$$

Use Eqs. (1–2), and the buckle deformation v can be obtained as:

$$v = \frac{\phi_L q L^4}{16\pi^4 EI}\left\{1 - \cos\frac{2\pi x}{L} + \pi \sin\frac{2\pi x}{L} + 2\pi^2\left[\frac{x}{L} - \left(\frac{x}{L}\right)^2\right]\right\} 0 \le \mathrm{x} \le \mathrm{L} \qquad (3)$$

$x = 0.3464L$, where there is the buckle amplitude, can be obtained from boundary condition $v_{\backslash x} = 0\,(x \in (0,\ L))$, and take value of this x into Eq. (3)

$$v_m = 5.5315 \times 10^{-3} \frac{\phi_L q L^4}{EI} \qquad (4)$$

Where v_m is the buckle amplitude in the buckled length.

The relationship of $(T + T')$ versus L can be obtained as:

$$AE\alpha(T+T') = 39.478\frac{EI}{L^2} + \phi_A qL\left\{\left[1.743 \times 10^{-4} qAE\phi_L\left(\frac{1}{EI}\right)L^5 - 1 + \left(1 - \frac{\phi_A}{\phi_L}\right)^2\right]^{\frac{1}{2}} + \left(1 - \frac{\phi_A}{\phi_L}\right)\right\} \qquad (5)$$

In which A denotes sectional area, m^2. The maximum bending moment M_m can be obtained at the place where the boundary condition is $v_{\backslash xxx} = 0$

$$M_m = EIv_{\backslash xx} = -0.1088\phi_L qL^2 \qquad (6)$$

3 Analysis of Project

3.1 General Conditions of the Project

The pipe considered has an outer diameter of 323.9 mm, and a wall thickness of 12.7 mm. The designed internal pressure and temperature difference are 4.60 MPa and 80 °C respectively. Parameters of pipeline and foundation soil have been presented in Table 1.

3.2 Results

The coefficient of foundation soil to pipeline is 0.4 according to the geology conditions. Figure 2 details the relationship of v_m and L versus ΔT respectively of the second lateral buckling mode.

It can be known from Fig. 2 that each curve is divided by "S" point. The temperature difference corresponding to the separation point is the safe temperature.

Equal the internal pressure into temperature difference, and the total temperature difference will be 85 °C. Figure 2 indicates that safe temperature of this lateral buckling mode is 30 °C, which is lower than the designed temperature difference. Therefore, this pipeline will occur lateral buckling.

Table 1 Properties of pipeline and subsoil

Parameters of pipeline									Parameters of foundation topsoil	
Young's modulus E/kPa	Poisson ratio v	Internal radius r/m	External radius r/m	Wall thickness t/m	Thermal coefficient a/ °C	Bulk density γ/(kN/m^3)	Sectional area A/m^2	Inertia moment I/m^4	Effective bulk density γ/(kN·m^{-3})	Internal friction angle φ/ °
2.06×10^8	0.3	0.149	0.162	0.0127	0.000011	7850	0.0124	0.000301	5.5	35

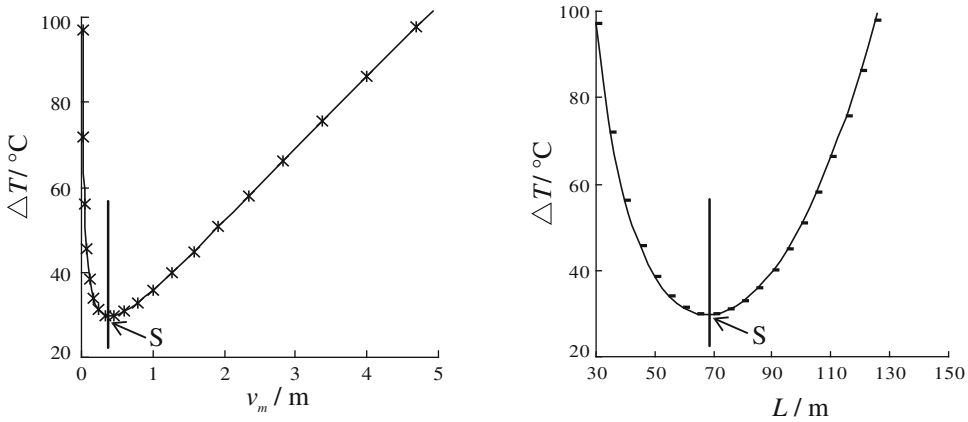

Fig. 2 Relationship between the buckle shape and the temperature difference

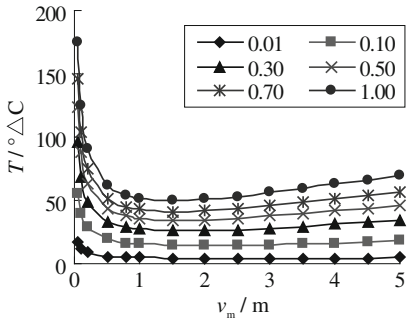

Fig. 3 Relationships of v_m versus $\triangle T$

3.3 Effects of Friction Coefficient on Buckling Shapes

In the analysis of buckling, friction coefficient is a parameter of vital importance. To know its effects on pipeline buckling, choose different friction coefficients: 0.01, 0.10, 0.30, 0.50, 0.70 and 1.00 to analyze. Figure 3 presents temperature difference $\triangle T$ against buckle amplitude v_m curves.

As to unburied pipelines, friction force is the only restraint to limit its deformation, which is showed as boundary condition in calculation. So condition of friction coefficient has great impact on buckling characteristics. Figure 3 details that the larger the friction coefficient, the less possibility of pipeline buckles. But calculation of stress indicates that the stress corresponding to a fixed temperature difference increases evidently with increasing of friction.

4 Conclusions

Lateral buckling of submarine pipelines under thermal stress is analogous to the buckling stability of a column. The temperature difference against buckle length and amplitude curves are both in "U" shape, which can be divided by "S" point into two buckling conditions. The first condition is an unstable buckling mode, and it's hard to occur; while the second condition is a stable buckling mode, which is easy to occur in practice. Since the friction between the pipeline and subsoil is only restraint to limit unburied pipelines to deform, the friction coefficient has a great impact on the lateral buckling characteristics. Generally, the larger the friction coefficient, the larger the restraint of foundation soil to the pipeline, and the higher the safe temperature.

Acknowledgments The work described in this paper was funded by Innovative Research Groups of the National Natural Science Foundation of China (51021004), China National Natural Science Foundation (40776055) and State Key Laboratory of Ocean Engineering Foundation (1002).

References

Kerr, A. D. (1978). Analysis of thermal track buckling in the lateral plane. *Acta Mechanica, 30*, 17–50.

Hobbs, R. E. (1984). In service buckling of heated pipelines. *Journal of Transportation Engineering, 110*(2), 175–189.

Taylor, N., & Gan, A. B. (1986a). Submarine pipeline buckling-imperfection studies. *Thin-Waleed Structures, 4*, 295–323.

Taylor, N., & Gan, A. B. (1986). Refined modeling for the lateral buckling of submarine pipeline. *Journal of Constructional Steel Research,* 143–162.

DEM Coupled SMAC Simulation on the Moving Process of Flow Like Landslide

A. Kondo, Y. Huang, and K. Maeda

Abstract

This study aims to simulate the flow-like landslides which caused by the Wenchuan earthquake 2008. For approaching this phenomenon, it is difficult to examine for simulation method based on continuum model that occurred in landslide body due to collision of granular materials and its effect. In this paper, we modeled this phenomenon as multi-phase flow, and simulated by discrete element method (DEM) and simplified maker and cell method (SMAC) with introducing simplified interaction. As for the verification of simulation especially for interaction, terminal settling velocity test is executed and shows quantitatively agreement. Moreover, through this simulation, moving process of the Tangjiashan landslides picked up as typical flow-like landslides. This landslide located beside the valley, and due to the landslides it held the mountain stream. Based on this simulation, depositional process is obtained.

Keywords

Discrete element method • Simplified marker and cell method • Interaction • Flow-like landslide • Moving process

1 Introduction

Recently, the considerable damage has been caused by the great earthquake that occurs frequently all over the world. The Wenchuan earthquake (Ms = 8.0; epicenter located at 31.0°N, 103.4°E, occurred in May 12, 2008) strongly reminds in our minds. During this earthquake, damage due to the earthquake is not only generated by the seismic motion, secondary disasters such as rock fall, landslide, debris flow, liquefaction also caused extensive damage. In the afterwards survey, some big landslides are flow-like type which flows extremely fast and seems to be triggered by the liquefaction due to the seismic wave (Huang and Jiang 2010).

Previously, these landslides are often treated in continuum scheme (Huang et al. 2011). However, front line of the landslides is hard to consider as continuum scheme, and it can expand damage like stony type debris flow. Because of these back ground, discrete element method (DEM) (Cundall and Strack 1979) are widely applied for these type phenomenon. According to the part of flow treated as particle assembles, it enables to consider the collision, flaking off and division, and estimate the effects for overall behavior caused by granular materials (Maeda and Hirabayashi 2006). In this study, we focused on the flow-like landslides occurred in Wenchuan earthquake, this phenomenon are modeled as multiphase flow, which landslide itself is treated as

A. Kondo · Y. Huang (✉)
Department of Geotechnical Engineering, Tongji University, Shanghai, 200092, People's Republic of China
e-mail: yhuang@tongji.edu.cn

A. Kondo
e-mail: akihiko1987@gmail.com

K. Maeda
Department of Civil Engineering, Nagoya Institute of Technology, Nagoya, 466-8555, Japan

Y. Huang et al. (eds.), *New Frontiers in Engineering Geology and the Environment*,
DOI: 10.1007/978-3-642-31671-5_34,

viscosity fluid and it also contains big gravel inside. Additionally, it can be possible to consider the moving process by introduced interaction between liquid phase and solid phase. Moreover, through the cross section analysis, arrival time and sliding distance are estimated.

2 Modeling of Landslide

In this study, landslide body is modeled as multiphase flow, which DEM as solid, and SMAC (Amsden and Harlow 1970) as liquid phase. To brief description, we focused on describing about interaction between soil and liquid phase in this chapter.

2.1 Interaction Between Soil and Liquid Phase

The interaction from fluid to particle is based on simplified equation of motion in a turbulent fluid (Tchen 1947), which omit the basset terms, Saffman lift term and Mugnus lift term for simplified expression. As for the rotation equation, the torque caused by the flow is also omitted. Interaction force is calculated through with relative velocity of each particle against flow velocity, following Eq. 1.

$$(\rho^s + \rho^w C_M)A_3 \frac{du_p}{dt} = \frac{1}{2} C_D \rho A_2 |u_w - u_p|(u_w - u_p) + \rho(1 + C_M)A_3 \frac{du}{dt} + (\rho^s - \rho^w)A_3 g \quad (1)$$

where, u_p is velocity of particles, u_w is velocity of fluid, A_3 is volume of particle, A_2 is projected area, C_D is drag coefficient, C_M is coefficient of additional mass, ρ^s is density of particle, ρ^w is density of liquid. Moreover, the drag coefficient is expressed as function of Reynolds number (Schiller and Naumann 1933).

$$C_D = \frac{24}{\mathrm{Re}}\left(1 + 0.15 R_e^{0.687}\right) : R_e < 1000, C_D = 0.4 \quad : 1000 \leq R_e, \; R_e = \frac{|u - u_p|d}{v} \quad (2)$$

where, d = diameter of particle. As for the interaction from solid to liquid, averaged cell density in which concerned soil mass calculated by overlapped particle area with cell adopts to density of pressure term in Navier–Stokes equation.

2.2 Verification

In this section, interaction is verified by comparison of terminal settling velocity, well known as Stokes's law and impact law. Moreover, approximate expression obtained by experimental test is also added to comparison (Gibbs et al. 1971).

Therefore, this settling velocity is estimated by changing DEM particle diameter in this verification study. The sizes of particle diameter are following: 0.003, 0.01, 0.02, 0.05, 0.1, 0.2, 0.5, and 1.0 cm. As for the simulation condition is

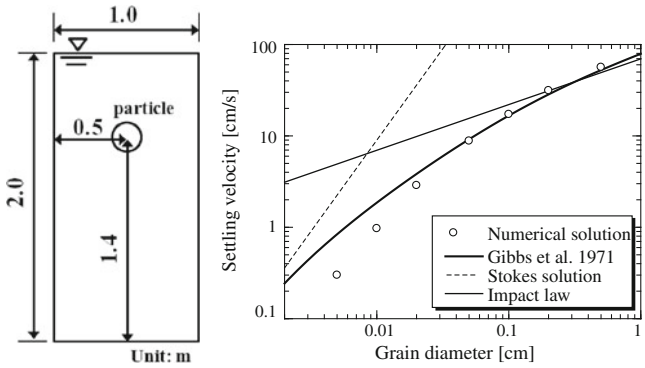

Fig. 1 Schematic illustration of verification analysis (*left*) and terminal settling velocity correspond to grain diameter (*right*)

Table 1 Analysis Parameter for Verification of settling terminal velocity test

Parameter Unit Value	Unit	Value
Time increment	s	1.0×10^{-5}
Particle element density	kg/m^3	2650.0
Water density	kg/m^3	1000.0
Coefficient of viscosity	m^2/s	1.0×10^{-3}
Height of water tank (division number)	m	2.0 (20)
Width of water tank (division number)	m	1.0 (10)

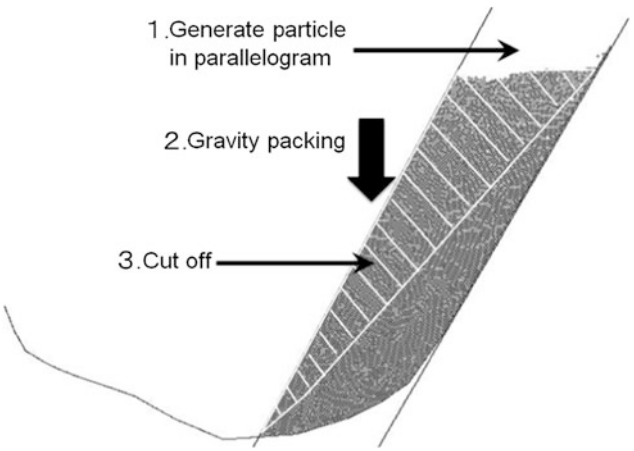

Fig. 2 Calculation process for constructing Landslide body and appearance of gravity packing

Table 2 Analysis Parameter of Tangjiashan landslide

Parameter Unit Value	Unit	Value
Time increment	s	1.0×10^{-3}
Particle radius	m	2.0
Particle density	kg/m^3	2650.0
Spring coefficient, normal direction	kN/m^3	1.0×10^8
Spring coefficient, shear direction	kN/m^3	2.5×10^7
Damping factor	–	1.0 (critical damping)
Friction angle	degree	20.0
Water density	kg/m^3	1000.0
Coefficient of viscosity	m^2/s	1.5×10^2
Height of water tank (division number)	m	890.0 (890)
Width of water tank (division number)	m	620.0 (620)

shown in Fig. 1 (left), and calculation parameter is followed in Table 1. Boundary condition is non-slip condition.

Figure 1 shows the comparison of settling velocity of numerical solution with above mentioned three relationships. Results are quantitatively corresponding well in large particle diameter, though in range of diameter smaller than 0.01 cm settling velocity becomes relatively small.

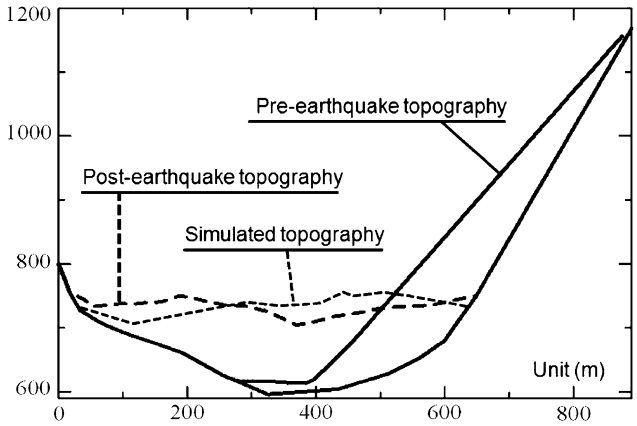

Fig. 3 Tangjiashan landslide simulation results, pre and post-earthquake topography

2.3 Modeling of Landslide in situ

In this study, landslide body and base slope are created by the assemblies of same size circular particle elements. As first step, slope particle set off along to slope shape, then, landslide particle generated in parallelogram area which is surrounded by non-frictional wall and slope particle as bottom. Secondly, deposit particle assembles is created under gravity of 9.8 m/s^2. Figure 2 shows the appearance of after gravity packing and this instruction. Thirdly, particles outside of pre-earthquake topography are removed after

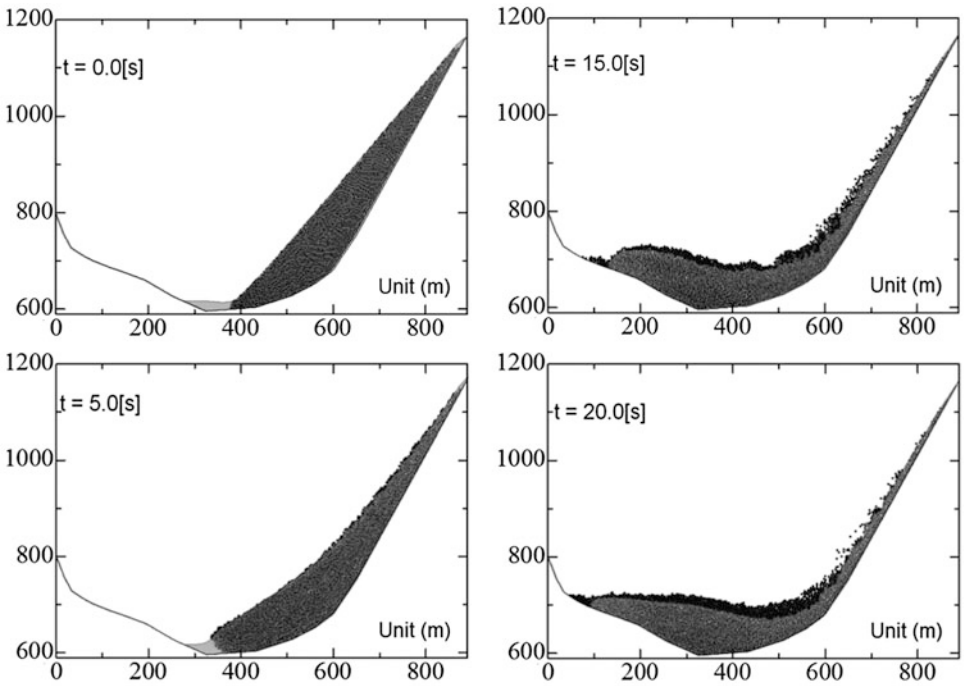

Fig. 4 Appearance of moving process

stopped particle moving in second step. Finally, create a liquid phase with mountain stream by same parameter without interaction. Table 2 shows analysis parameter of construction process and main calculation. Moreover, number of particle is 5208.

Figure 3 shows the comparison between numerical solution and post-earthquake topography with pre-earthquake topography. Though deposition shape is not same, but flowing distance, deposition height is almost same. Figure 4 shows flowing appearance at several time step. In this figure, black point indicate particle, and gray part means liquid area. Because of the front line shape is almost same, it can be assumed that flowing process are led by liquid phase. However, as a remarkable point, difference between this figure at t = 10.0 and 15.0 s, it can be seen a collection of soil particle around the front line. This process seems caused by slowdown of liquid due to rising slope. In addition, this collection remains till moving process is stopped.

3 Conclusions

In this study, we modeled Tangjiashan landslide as multi-phase flow which are DEM coupled with SMAC with interaction. As for deposition height and run up distance, it shows qualitatively well agreement. During the moving process, though liquid phase assume initiative role, after the slowdown in rising slope, collection of grain particle was observed.

Acknowledgments This work was supported by the National Basic Research Program of China (973 Program, Grant No. 2012CB719803), the National Natural Science Foundation of China (Grant Nos. 41211140042 and 41072202), the Program for New Century Excellent Talents in University (Grant No. NCET-11-0382) and the Kwang-Hua Fund for College of Civil Engineering, Tongji University.

References

Amsden, A. A., & Harlow, F. H. (1970). The SMAC method: A numerical technique for calculating incompressible flu-id flows, LA-4370.

Cundall, P. A., & Strack, O. D. L. (1979). A discrete model for granular assemblies. *Geotechnique, 29*(1), 47–65.

Gibbs, R. J., Matthews, M. D., & Link, D. A. (1971). The relationship between sphere size and settling velocity. *Journal of Sedimentary Petrology, 41*(1), 7–18.

Huang, Y., & Jiang, X. (2010). Field-observed phenomena of seismic liquefaction and subsidence during the 2008Wenchuan earthquake in China. *Natural Hazards, 54*, 839–850.

Huang, Y., Zhang, W., Xu, Q., Xie, P., & Hao, L. (2011). Run-out analysis of flow-like landslides triggered by the Ms 8.0 2008 Wenchuan earthquake using smoothed particle hydrodynamics, Landslides. doi 10.1007/s10346-0110285-5.

Maeda, K., & Hirabayashi, H. (2006). Influence of grain proper-ties on macro mechanical behaviors of granular media by DEM. *Journal of Applied Mechanics JSCE, 9*, 623–630.

Schiller, L., & Naumann, A. Z. (1933). Uber die grundlegenden berechungen bei der schwerkraftaufbereitung. *Ver. Deut. Ing., 77*, 318–321.

Tchen, C. (1947). Mean value and correlation problems connected with the motion of small particles suspended in a turbulent fluid (Doctoral dissertation, Techniche Hogeschool). Delft.

Risk Assessment for Coal Mining Under Sea Area

W. H. Sui and Z. M. Xu

Abstract

This paper presents a case study of risk assessment for coal mining under sea area in the Beizao Coalmine, Shandong Province, China. The coalmine is facing the risk of sea water inrush hazards because most of its panels are under the Bohai Sea. To forecast water disaster, three important factors, including efficient aquifuge, water flowing fractured zone and the water pressure bearing capacity of aquifuge, are considered to assess the mining safety situation for Panel H2301 in the Beizao Coalmine. The efficient aquifuge is identified by lithological analysis and water chemical comparison between sea water and groundwater. The water flowing fractured zone under different mining conditions is obtained by statistically analyzing the field measurements and numerical simulation. The safety mining condition under the Bohai Sea is assessed and the upper mining limit of Panel H2303 has been proposed.

Keywords

Underground coal mining • Mining under sea area • Risk assessment • Upper mining limit • Underground water inrush

1 Introduction

There are over 2.5 billion tons of coal resources located under surface water bodies in China. In recent years, China has been a rich experience of coal mining under water body such as lake, river and reservoir (Sun et al. 2008, 2009; Xu et al. 2010; Liu et al. 2010; Wu et al. 2009; Peng et al. 2011). Coal mining under surface water has been successfully carried out in some locations but there have also been many water-inrush disasters caused by the surface water when the overburden strata were damaged by the coal mining.

In addition, there are six countries having the experience of coal mining under the sea area all over the world, they are Britain, Australia, Chile, Japan, Canada and China. At the early 1980s, nearly 60 % of the coal production from 15000 of the underground coalmines in Britain was extracted from the sea area. Coal production from the sea area of Japan and Australia also accounts for a large proportion of the national coal production. In these countries, due to the special coal mining under the sea, mining activities were managed strictly by the government regulations and orders [John et al. 1982; Laxminarayan 1987; Niskovskiy and Vasianovich 1996; Sun 1999; Gill 2000; Singh and Jakeman 2001; Gandhe et al. 2005; Winter et al. 2008; Winter et al. 2008; Sun et al. (2008, 2009); Xu et al. 2010].

Current prediction methods for water flowing fractured zone are: field measurements, physical or numerical simulation and theoretical analysis (Liu 1995). There are many methods concerning the risk assessment for mine water inrush, such as Neural Network Method, Multi-sources

W. H. Sui (✉) · Z. M. Xu
State Key Laboratory for Geomechanics and Deep Underground Engineering, School of Resources and Geosciences, China University of Mining and Technology, Xuzhou 221116, China
e-mail: suiwanghua@cumt.edu.cn

Y. Huang et al. (eds.), *New Frontiers in Engineering Geology and the Environment*,
DOI: 10.1007/978-3-642-31671-5_35,

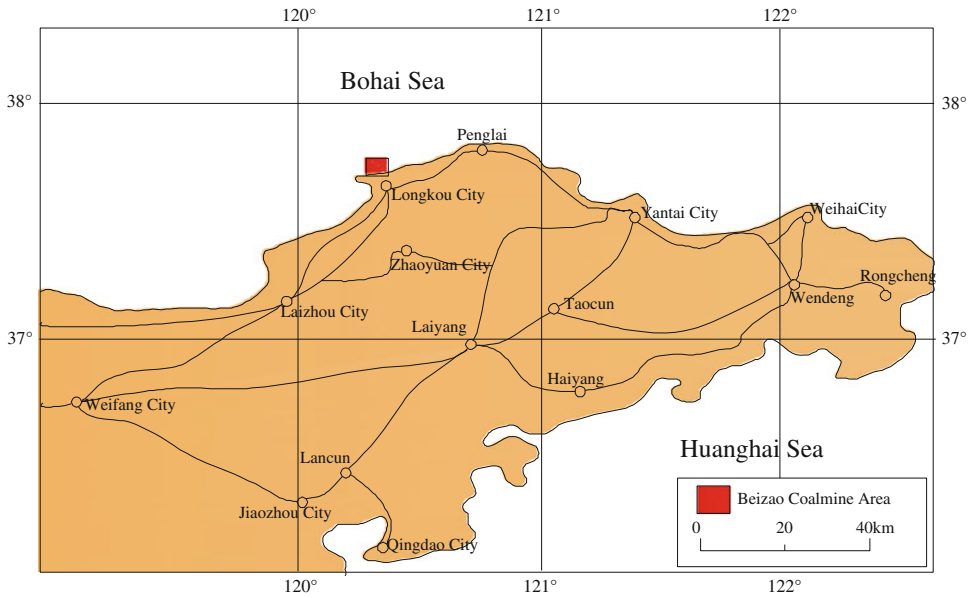

Fig. 1 The location of the Beizao Coalmine in Shandong Province

Information Fusion Method, Vulnerable Index Method and GIS (Sun et al. 2008).

This paper presents a case study of risk assessment for coal mining under sea area in the Beizao Coalmine, and deals with three key scientific problems: features of efficient aquifuge, height of the water flowing fractured zone and the water pressure bearing capacity of aquifuge, to present the water disaster forecasting results.

2 Geological Background

The Beizao Coalmine, which involves the first coal mining panel under the sea area in China, located in the northern part of Longkou city, Shandong Province, is facing a great risk of sea water inrush hazards. Fig. 1 shows the location of the Beizao Coalmine.

The major coal seam to be excavated in the Beizao Coalmine is Seam No.2 located in the Lower Tertiary System and the thickness ranges from 3.84 to 5.93 m. The overburden rock consists of mudstone, sandy mudstone, calcareous mudstone, oil mudstone and oil shale, which are easy to be expanded when mudding and have perfect water insulation. The inflow of mine water ranges from 25 to 30 m^3/h, among which the maximum is 42 m^3/h when the aquifer was exposed in the Beizao Coalmine.

The thickness of the overburden rock of Seam No. 2 is about 100 m, which can usually interrupt hydraulic connection between coal measures and the Quaternary aquifers. According to the observation in the Beizao and Liangjia Coalmine, the marl aquifers groundwater level is decreased by almost 30 m slowly, while the water level in the Quaternary unchanged. This result shows that there is not any significant hydraulic connection between the Quaternary and marl and marl-inter-bedded aquifers.

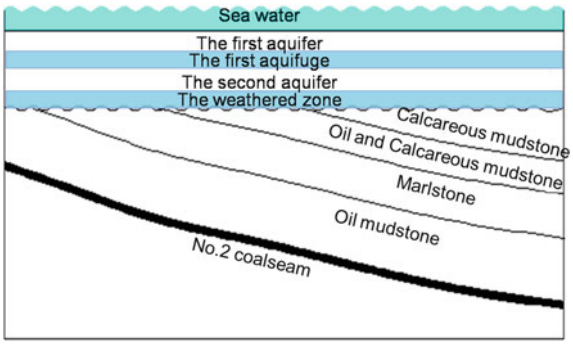

Fig. 2 The effective aquifuge in the Beizao Coalmine

3 Effective Aquifuge

The effective aquifuge is an impermeable seam which can prevent sea water from infiltrating into the coalmine. The impermeable clay layer of the first aquifuge of the Quaternary was determined to be an effective aquifuge (Fig. 2).

The first aquifuge, with the lithological composition of mainly clay and sandy clay, and a thickness about 20 m, effectively obstructs the hydraulic connection between the first and the second aquifer. The different chemical composition of the Quaternary groundwater, coal seam aquifer and sea water also show the effective aquifuge is reliable.

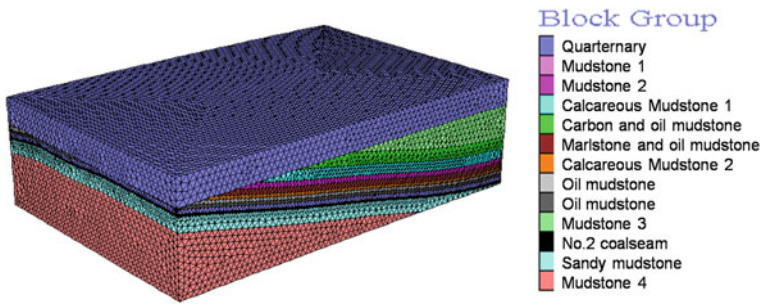

Fig. 3 Simulation model

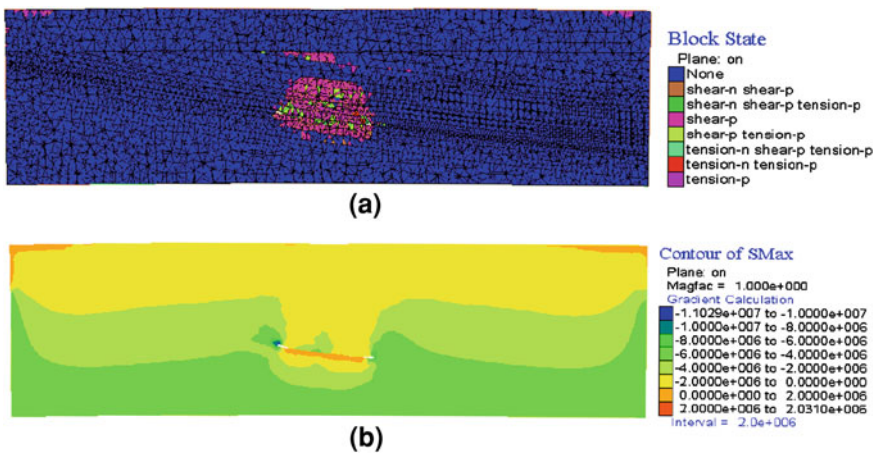

Fig. 4 Plastic zone and stress distribution **a** Plastic zone distribution. **b** Stress distribution

4 Water Flowing Fractured Zone

Studies of the failure process and range in the overburden rock after coal mining have been done. Numerical simulations are often the first choice for these studies. The plastic zone and the stress, which are often chosen when estimating the range of water-flow fractured zone. The Fast Lagrangian Analysis of Continua (FLAC) has been parameterized and used with some success (Sun et al. 2009; Xu et al. 2010).

A numerical model was created following the known structure of the overburden stratum of Panel H2303 of the Beizao Coalmine. The model for Panel H2303 is 1000 m × 660 m × 270 m in size and had 11 overburden strata (Fig. 3).

The simulation concentrated on the failure of the overburden rock. The height of the water flowing fractured zone was obtained by analyzing the plastic zone and the stress distribution.

Figures 4 a and b show that the changed plastic zone in the overburden rock, subsequent to coal mining, visually indicates the range of disturbance in the overburden. The plastic zone increases as the mined area moves when mining to 150 m the plastic zone increases continuously to reach a maximum of 55 m.

Then, the field measurements are used to validate the height of the water flowing fractured zone in this research. The field measurements method and the actual data showing the failure range under specific conditions in the four Coalmines, which have the similar geological and hydrological condition, at Longkou coalmining area, are shown in the manuscript (Xu and Sui 2012).

5 Water Pressure Bearing Capacity

The water pressure bearing capacity of the overburden rock was assessed with a certain thickness and properties, especially the bearing characteristics of the protective layer. Evaluation formula is as follow:

$$H = \frac{AL}{4K}\left(\sqrt{r^2L^2 + 8KP} + rL\right) \quad (1)$$

where H is the safety thickness of the aquifuge (m), P is water pressure (MPa), L is the width of the panel (m), K is the tensile strength of rock (MPa), r is the density of rock (kg/m^3) and A is the safety coefficient (ranges from 1.2 to 1.5).

The parameters of Panel H2303 are substituted into Eq. 1, the required minimum thickness of the security barrier under the current sea water head pressure is 7.6 m, which is

much smaller than the thickness of the effective water barrier 39 m. According to the level of the Quaternary bottom −76 m, it is determined that the upper mining limit for 6 m cutting height is −160 and −130 m when the cutting height decreased to 3 m.

6 Conclusions

(1) The effective aquifuge of sea water infiltration is the first aquifuge, an impermeable layer of clay in the Quaternary, which effectively obstructs hydraulic connection between the Bohai Sea and the overburden rock of Seam No.2 .
(2) The results of field measurements and numerical simulation show that the range of the overburden rock failure zone shows an exponential relation with the cutting height of seam.
(3) According to the overburden rock structures of Panel H2301, the level of the Quaternary bottom is −76 m. The safety mining condition under the Bohai Sea is assessed and the upper mining limit of Panel H2303 has been proposed.

Acknowledgments The authors want to acknowledge the financial support of the National Natural Science Foundation—Shenhua Group Jointly Funded Project under grant No. 51174286. This research was also supported by A Project Funded by the Priority Academic Program Development of Jiangsu Higher Education Institutions and the Fundamental Research Funds for the Central Universities (No.2010QNB35).

References

Gandhe, A., Venkateswarlu, V., & Gupta, R. N. (2005). Extraction of coal under a surface water body—a strata control investigation. *Rock Mechanics and Rock Engineering, 38*(5), 399–410.

Gill, D. R. (2000). Hydrogelogic analysis of streamflow. In *Relation to Underground Mining in Northern West Virginia. Morgantown*, West Virginia.

John, W., Donald, T., Kelvin, K. (1982). Some technical considerations when mining under bodies of water. West Virginia University, (pp. 241–248).

Laxminarayan, H. (1987). Design of mine working under surface waters in New South Wales. *Bulletin and Proceedings-Australasian Institute of Mining and Metallurgy, 3*, 45–50.

Liu, T. Q. (1995). Influence of mining activities on mine rock mass and control engineering. *Journal of China Coal Society, 2*, 1–5. (In Chinese).

Liu, C. Y., Liu, Y. J., Yang, Z. (2010). Caving thickness effects on stability of coal-rock pillar against water on steep coal seam mining under water. *ICMHPC—2010 International Conference on Mine Hazards Prevention and Control*, (pp. 356–363).

Niskovskiy, Y., Vasianovich, A. (1996). Investigation of possibility to apply untraditional and ecologically good methods of coal mining under sea bed. In *Proceedings of the International Offshore and Polar Engineering Conference, Los Angeles*, *ISOPE* , (51–53).

Peng, K., Li, X. B., & Peng, S. Q. (2011). Optimization of frame stope structure parameters based on response surface method in undersea mining. *Journal of Central South University (Science and Technology), 42*(8), 2417–2422. (In Chinese).

Singh, R. N., & Jakeman, M. (2001). Strata monitoring investigations around longwall panels beneath the cataract reservoir. *Mine Water and the Environment, 20*(2), 33–41.

Sun, H. X. (1999). The prospect for the coal mining under sea area in China. *China Coal, 25*(8), 34–36. (In Chinese).

Sun, Y. J., Xu, Z. M., & Dong, Q. H. (2008). Forecasting water disaster for a coal mine under the Xiaolangdi reservoir. *Journal of China University of Mining and Technology, 18*(4), 516–520.

Sun, Y. J., Xu, Z. M., & Dong, Q. H. (2009). Monitoring and simulation research on development of water flowing fracture for coal mining under the Xiaolangdi reservoir. *Chinese Journal of Rock Mechanics and Engineering, 28*(2), 238–245. (In Chinese).

Winter, T. C., Buso, D. C., & Shattuck, P. C. (2008). The effect of terrace geology on ground-water movement and on the interaction of ground water and surface water on a mountainside near Mirror Lake, New Hampshire. *USA Hydrological Processes, 22*(1), 21–32.

Wu, X., Wang, X. G., & Jiang, X. W. (2009). A study on coal mining under large reservoir areas. *Environmental Geology, 57*(3), 675–683.

Xu, Z. M., Sun, Y. J., & Dong, Q. H. (2010). Predicting the height of water-flow fractured zone during coal mining under the Xiaolangdi reservoir. *Mining Science and Technology, 20*(3), 434–438.

Xu, Z. M., Sui, W.H. (2012). Statistical prediction of overburden failure due to coal mining under sea area. In *New Frontiers in Engineering Geology and the Environment,* Springer-Verlag Berlin Heidelberg, (pp. 255–257).

Potential of Using Remote Sensing Data for Dike Inspection

S. L. Cundill, H. R. G. K. Hack, M. van der Meijde, J. S. van der Schrier and D. J. M. Ngan-Tillard

Abstract
Dikes are increasingly becoming structures of major importance in view of sea level changes. Dike inspectors monitor dikes visually whilst walking the dike. It has been proposed that remote sensing could be used to make dike inspection faster and cheaper. This paper presents the results of a study which investigates remote sensing for evaluating the soil moisture and dike grass cover quality. Correlations were found between soil moisture and thermal and multispectral remote sensing data, and between dike grass cover quality and multispectral remote sensing data. Remote sensing provides useful information for soil moisture and grass cover quality evaluation for dike inspection and may be useful for dike quality inspection.

Keywords
Dike • Remote sensing • RSDYK • Peat • Moisture content

1 Introduction

Due to the expected consequences of sea level changes, dikes (also levees, embankments or dams) are increasingly becoming more important. In many countries, dikes are inspected by a dike inspector walking the dike looking for irregularities (Givehchi et al. 2002; Moser and Zomer 2006; Swart 2007). It has been proposed that remote sensing is a possible tool for increasing the efficiency, objectivity and coverage of dike inspection with potential problematic areas being identified for further inspection (Givehchi et al. 2002; Hack et al. 2008; Swart 2007). This study is part of the RSDYK project for the Dutch Flood Control 2015 program. Two key features that dike inspectors evaluate are the quality of the dike covering and the soil moisture content of the dike (Moser and Zomer 2006; van Baars and van Kempen 2009). The covering of many dikes consists of grass. Multispectral, and more recently hyperspectral, remote sensing is used widely in vegetation studies (Blackburn 2007; Lillesand et al. 2008). This is because different vegetation types and qualities can be distinguished, particularly in the near-infrared part of the electromagnetic spectrum. Additionally, vegetation is highly responsive to changes in soil moisture (Hopkins and Hüner 2009). Remote sensing, especially hyperspectral and thermal, is actively researched for detection of water deficit stress in agricultural plants because this affects the quality and quantity of the harvest.

2 Materials and Methods

A grass covered dike in the Netherlands was selected as the study site since it is known to have problems along some areas of the dike. The surface of the dike has varying

S. L. Cundill (✉) · H. R. G. K. Hack · M. van der Meijde
Department of Earth Systems Analysis, ITC, University of Twente, P.O. Box 217, Enschede, 7500 AE, The Netherlands
e-mail: cundill@itc.nl

J. S. van der Schrier
Royal Haskoning, P.O. Box 151, Nijmegen, 6500 AD, The Netherlands

D. J. M. Ngan-Tillard
Department of Geotechnology, Delft University of Technology, P.O. Box 5048Delft, 2600 GA, The Netherlands

Y. Huang et al. (eds.), *New Frontiers in Engineering Geology and the Environment*,
DOI: 10.1007/978-3-642-31671-5_36,

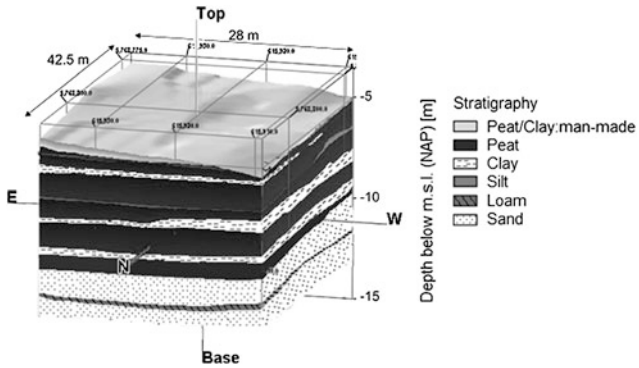

Fig. 1 3D model of the geology of the dike

consistency, with some locations considerably less stiff than others, probably indicating larger quantities of moisture. Further, the bottom of the dike shows signs of extruding water, which may come through the dike or from deeper layers. The dike is a 'peat dike', i.e. a natural barrier left in place around an excavated area to be able to drain the excavated area. The dike materials consist of the geology in the area, shown in Fig. 1.

A field campaign was carried out on 15–16 July 2010, when remote sensing and validation datasets were measured. Four types of remote sensing data were collected, namely thermal, visible, multi-spectral and hyperspectral. Two sets of validation data, namely soil moisture data and quality assessment of the grass cover of the dike, were collected. The soil moisture and hyperspectral instruments limited the study to point based measurements. Therefore the image-based remote sensing instruments for visible, multispectral and thermal measurements were averaged per location to obtain a single value per location. Measurements were recorded at 54 point locations on the west-facing side of the dike. The local weather conditions varied during the measurement period and included sunny, partly-cloudy and cloudy conditions and a trace amount of rain. There is a canal to the east of the dike top and its water level was less than 50 cm from the top of the dike at the time of measurement.

2.1 Remote Sensing Data

Thermal, visible, multispectral and hyperspectral remote sensing data were collected. Thermal images were taken for each location using the NEC TH9100 Thermal Tracer camera, which has a spectral range of 8–14 μm. Images were recorded almost every hour between 12 h00 on 15 July 2010 and 12 h00 on 16 July 2010. Visible light digital photographs were taken in RAW format using a Canon EOS 400D with a zoom lens EF-S 17-85 mm 1:4–5.6 IS USM. The photographs were taken at 18 h30 on 15 July. The images have three layers with data recorded in broad bands in the red, green and blue wavelengths.

Broadband multispectral images were taken for each location using the Tetracam agricultural camera, in the green, red and near-infrared (NIR) wavelengths. Images were recorded at 13 h00, 16 h20 and 19 h00 on 15 July 2010. For this paper, the results for the 16 h20 measurements will be shown. Hyperspectral reflectance spectra for each location were measured using the ASD Fieldspec Pro spectrometer, which has a spectral range of 350–2500 nm. An 8° fore-optic was used at a height of about 60 cm so as to obtain data that covers the same area as the image-based remote sensing instruments. Four sets of measurements were taken, namely 13 h00, 16 h00 and 17 h00 on 15 July 2010 and 10 h00 on 16 July 2010. The results for the 10 h00 measurements will be presented in this paper.

2.2 Validation Data

Soil moisture data and the quality of the grass cover of the dike were collected as validation data. Volumetric soil moisture for each location was measured using a Tetraprobe. Nine readings were taken at various times during a 24 h period at different point positions within the area covered by the image-based sensors. Since the soil moisture is expected to remain consistent during a 24 h period, and to reduce the effect of an anomalous patch of soil, the measurements were averaged per location. This soil moisture value was used for analysis. Evaluation criteria for the quality of grass cover include grass density, canopy cover and the presence and quantity of standing litter (dead plant material), flotsam and bare soil. The grass cover quality for each location was assessed and allocated to either a good, medium or poor quality class.

2.3 Analysis

Pearson correlation coefficients were calculated in PASW Statistics version 18 software (from IBM Corporation, Armonk, New York) to investigate the linear relationships between the datasets, excluding the hyperspectral data. Combinations of wavelength bands frequently provide more information than the bands on their own since the relative proportions of reflectance in different bands offer information on vegetation quality. The ratios NIR:red, NIR:green and green:red were therefore calculated and added as extra datasets in the analysis process. The NIR:red ratio provides information on overall vegetation quality and is sensitive to changes in chlorophyll concentration (Jensen 2007). The NIR:green ratio is useful for information on moisture content of vegetation and high amounts of standing litter (Asner 1998). The green:red ratio provides information on the appearance of the vegetation including the presence of standing litter and bare soil

Table 1 Selected pearson correlation coefficients showing relationships between the datasets

Dataset 1	Dataset 2	Correlation coefficient	Significance
Soil moisture	Thermal (15h00)	−0.668	**
Soil moisture	Near-infrared (multispec.)	0.614	**
Soil moisture	Green (multispec.)	0.610	**
Cover quality	Green:red ratio (Visual)	−0.671	**
Cover quality	NIR:red ratio (multispec.)	−0.627	**
Cover quality	Near-infrared (multispec.)	−0.617	**

** Significant at the 0.01 probability levels

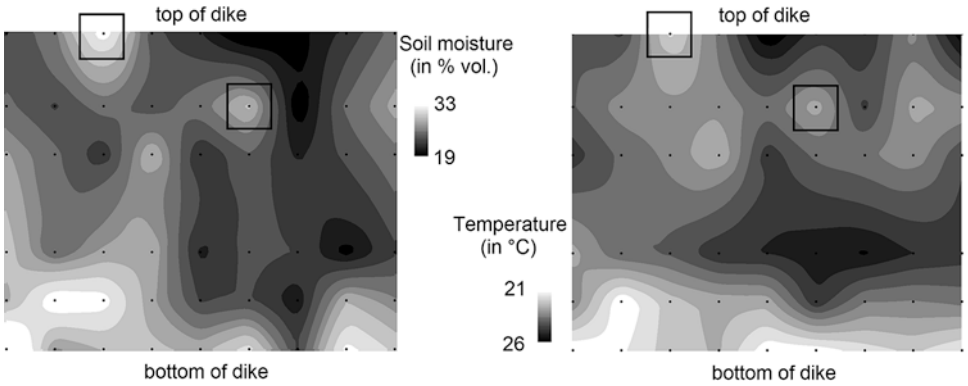

Fig. 2 The spatial distribution and patterns for the soil moisture (*left*) and 15h00 thermal data (*right*)

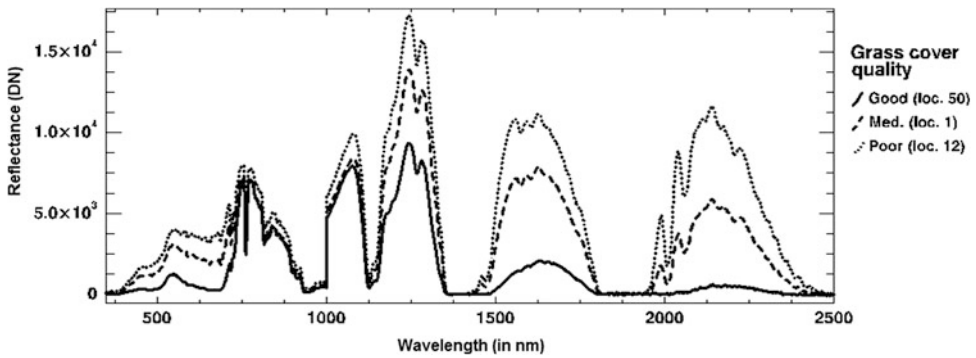

Fig. 3 The spectra signatures of good, medium and poor quality grass cover

(Asner 1998). To explore the spatial distribution and patterns of the data, the data were interpolated using the natural neighbor method.

3 Results

The significant correlation values above 0.600 are presented in Table 1. For soil moisture, three datasets showed significant correlation. Daytime thermal (specifically the 15 h00 measurements), near-infrared and green measurements correlated with the soil moisture values. For the dike grass cover quality, three datasets were significant, namely the green:red ratio, NIR:red ratio and near-infrared. In addition, soil moisture and grass cover quality were correlated, with a value of −0.533 (significant association at $P \leq 0.01$). The spatial distribution and patterns apparent in the soil moisture dataset were mirrored in the daytime thermal measurements, the multispectral near-infrared data and the visible green:red ratio data. Not only was an overall pattern visible but some anomalies that deviated from the overall pattern were also persistent. This is illustrated in Fig. 2, where the two anomalies are indicated with squares and the overall patterns are evident.

Locations with different grass cover quality displayed different hyperspectral spectral signatures. Examples of these are shown in Fig. 3. The good quality cover, location 50, has a typical signature of healthy vegetation (Asner 1998) with a peak

in the green (500–600 nm), high reflectance in the near-infrared (700–1300 nm) and low reflectance in the shortwave-infrared (1300–2500 nm). The medium quality cover, location 1, has a spectral signature which reveals that some standing litter is present (Asner 1998). There is an overall higher reflectance in both the visible wavelengths (400–700 nm) and shortwave-infrared. The poor quality cover, location 12, has some standing litter and some bare soil exposed (Asner 1998). This effect is visible in the spectral signature, with overall increased reflectance across the whole spectrum, as well as the flattening of the curve in the green to red wavelengths (500–700 nm).

4 Discussion and Conclusion

The results show that remote sensing data have strong relationships with both soil moisture and dike cover quality. These are also reflected in the spatial patterns. Thermal and multispectral remote sensing data are correlated with and show similar spatial patterns to soil moisture content. Visual, multispectral and hyperspectral remote sensing provide information on the quality of the dike's grass cover. From this study it is apparent that remote sensing provides useful information for dike inspection, for both soil moisture and grass cover quality and could be used to indicate the origin of the water as it would be likely that water seeping through the dike will extrude at higher locations than water originating from deeper sources below the dike.

References

Asner, G. P. (1998). Biophysical and biochemical sources of variability in canopy reflectance. *Remote Sensing of Environment, 64*(3), 234–253.

Blackburn, G. A. (2007). Hyperspectral remote sensing of plant pigments. *Journal of Experimental Botany, 58*(4), 855–867.

Givehchi, M., Vrijling, J. K., Hartmann, A., van Gelder, P. H. A. J. M., van Baars, S. (2002). Application of remotely sensed data for detection of seepage in dikes. *International Symposium on Resource and Environmental Monitoring, Hyderabad*, India, December 2002.

Hack, H. R. G. K., van der Meijde, M., van der Schrier, J. S., Awaju, J. H., Rupke, J., Barritt, S., van 't Hof, J., Maccabiani, J., Maresch, S., Calero, D. P., Reymer, A., Schweckendiek, T., Stoop, J., Wilbrinck, H., Zomer, W. (2008). Strength of peat dykes evaluated by remote sensing. *RSDYK2008*, Pro-gram Flood Control 2015 (FC2015). 15 December 2008.

Hopkins, W. G., & Hüner, N. P. A. (2009). *Introduction to Plant Physiology* (4th ed.). New York: Wiley.

Jensen, J. R. (2007). *Remote Sensing of the Environment* (2nd ed.). Upper Saddle River: Pearson Education.

Lillesand, T. M., Kiefer, R. W., & Chipman, J. W. (2008). *Remote Sensing and Image Interpretation* (6th ed.). New York: Wiley.

Moser, G. M., & Zomer, W. S. (2006). *Inspectie van Waterkeringen*. Zwijndrecht: STOWA.

Swart, L M Th. (2007). *Remote sensing voor inspectie van waterkeringen*. Nieuw-Vennep: Swartvast.

van Baars, S., van Kempen, I. M. (2009). The causes and mechanisms of historical dike failures in the Netherlands. *E-Water*. http://www.dwa.de/portale/ewa/ewa.nsf/home?readform&sub menu = _1_6_2 &objectid = 0AB6528C5177A8B7C12572B1004EF1C7. Accessed 18 May 2010.

Experimental Investigation for Water Flowing Fractured Zone Due to Coal Mining Under Sea Area

W. X. Wang, W. Hu, and Y. K. Liang

Abstract

This paper presents an experimental investigation of development of water flowing fractured zone due to coal mining under sea area by scaled model test. Two models are designed to simulate coal mining along the strike and the dip. In model 1, the thickness of the overburden varies from 74 to 124 m and coal seam dips at an angle of 8°, and model 2 with a overburden thickness of 90 m and a dip angle of 0°. The results indicate that the height of overburden caving and water flowing fractured zones both increase at first then decrease to a comparatively stable values with the mining distance increasing; the height of overburden water flowing fractured zone increases significantly with the thickness of the overburden increasing and the height of overburden caving zone does not. When the coal mining thickness is 6 m, the maximum height of overburden water flowing fractured zones is 64.16 m (in model 1) and 48.20 m (in model 2), the maximum height of overburden caving zones is 12.76 m (model 1) and 12.00 m (model 2), respectively. The research results provide a helpful basis for upper mining limit decision-making and risk assessment.

Keywords

Water flowing fractured zone • Experimental investigation • Mining under sea • Upper mining limit

1 Introduction

The observation methods of ultrasonic imaging, parallel network electricity method CT, physical simulation, numerical simulation, drilling hole for injecting water experiment and so on are used to observe the overburden fracture due to coal mining (Sun et al. 2009; Liu et al. 2011). The mechanism and prevention on quicksand hazards in underground coal mines has been studied by many researchers (Sui et al. 2007, 2008; Xia et al. 2008).

Until now, only few countries have had the experience in mining under sea, which are England, Australia, Chile, Japan, Canada and so on(Sun 1998; Peng et al. 2011). The minimum thickness of overburden for mining under sea is 46 m in Australia, 60 m in America and 60–100 m in Japan by longwall collapse mining, respectively.

The Beizao Coalmine is located in Shandong Province, China. It has about more than 10 millions tons coal resources under sea area with an overburden thickness of less than 105 m. With the coal mining thickness of 6 m the water flowing fractured zones may conduct the upper aquifer and most panels are facing water inrush hazards. A safety mining verification must be carried out when the thickness of overburden is between 80 and 105 m.

W. X. Wang (✉) · W. Hu · Y. K. Liang
State Key Laboratory for Geomechanics and Deep Underground Engineering, School of Resources and Geosciences, China University of Mining and Technology, Xuzhou 221008, China
e-mail: wang603698305@163.com

Y. Huang et al. (eds.), *New Frontiers in Engineering Geology and the Environment*,
DOI: 10.1007/978-3-642-31671-5_37,

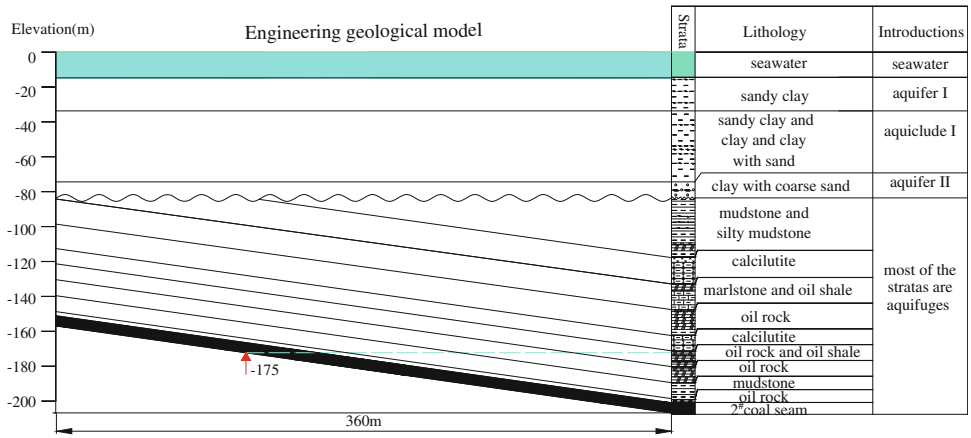

Fig. 1 Engineering geological model

2 Hydrogeoloical and Engineering Geological Conditions

The coalmine faces south coast of the Bohai sea and the No. 2 coal hides in the Tertiary strata with a dip angle of 8°and thickness of 6 m. The overburden strata are mainly mudstone, calcicutite, and oil shale, the uniaxial compressive strengths of which are mostly lower than 30 MPa. Most of the strata are aquifuges which can disconnect the hydraulic relationship between the aquifer I and No. 2 coal seam.

The Quaternary strata in this area encompass two aquifers inter-bedded by one aquifuge as shown in Fig. 1. The aquifer I with a maximum thickness of 17.83 m consists of sandy clay and has a specific capacity of 0.1186–3.713 L/s m. The aquifuge I with a minimum thickness of 31.79 m is composed by sandy clay and clay. It constitutes a regional aquifuge and disconnects the hydraulic relationship between the aquifer I and II. The aquifer II with a thickness of 10.07 m in maximum consists of clay with coarse sand and has a specific capacity of 0.249–1.094 L/s m.

3 The Experimental Model

In this paper, two models are designed to simulate coal mining along the strike and the dip of Panel H2303. The main purpose of the experiment is to investigate the overburden failure due to mining in an elevation of −175 m and deeper. In model 1, the thickness of the overburden varies from 74 to 124 m and coal seam dips at an angle of 8°, and model 2 with the overburden thickness of 90 m (where the elevation is −175 m) and a dip angle of 0°.

The scaled models designed should follow the laws of similarity, which is described as the follow formulas: $l_p : l_m = c_l,\ \gamma_p : \gamma_m = c_\gamma,\ t_p : t_m = c_t,$ here $l =$ geometric parameters, $\gamma =$ bulk density, $t =$ mining time, and subscript p represents real parameters, subscript m represents model parameters. c_l , c_γ , c_σ , c_t are similarity ratios and $c_l = 200$, $c_\gamma = 1$, $c_\sigma = 200$, $c_t = \sqrt{200}$.

In the models, the compensation of horizontal stress and vertical stress are 60 and 70 kPa separately according to earth stress measurements.

The two models' sizes both are 1.8 m × 0.3 m × 0.8 m. The materials used in the models are blancfixe, gypsum, calcium carbonate stone powder, quartz sand, glycerol, and we mixed them in different proportion to gain the suitable strength to every layer. Figure 2 shows the design of model 1.

In model 1, the open-off cut was set at the point that was correspond to the elevation of −175 m in actual as shown in Fig. 3. The coal seam with length of 1.6 cm and thickness of 3 cm would be mined in every 1.69 h from the open-off cut to the right side of model 1, the development of the water flowing fracture was observed by digital camera.

In model 2, the mining method is similar to model 1, the whole mining distance is 100 cm and 40 cm coal seam was left in two sides of model 2 to avoid the boundary effects.

4 Results and Discussions

The model 1 results indicate that when the mining distance is less than 60 m, the height of overburden caving and water flowing fractured zones are the same and increase with mining distance increasing. The height of overburden caving reaches the peak (12.76 m) at the mining distance 60 m and decreases to 8–12 m with the mining distance increasing. However, the height of water flowing fractured zones increase until the mining distance being 210 m when it reaches the peak (64.14 m), then it decreases to 54–64 m with the mining distance increasing which shows a "saddle shape", as shown in Fig. 3. In Model 2 the maximum height of overburden caving and water flowing fractured zones are 12.0 m at the mining distance 80 and 48.20 m at the mining distance 150 m, respectively.

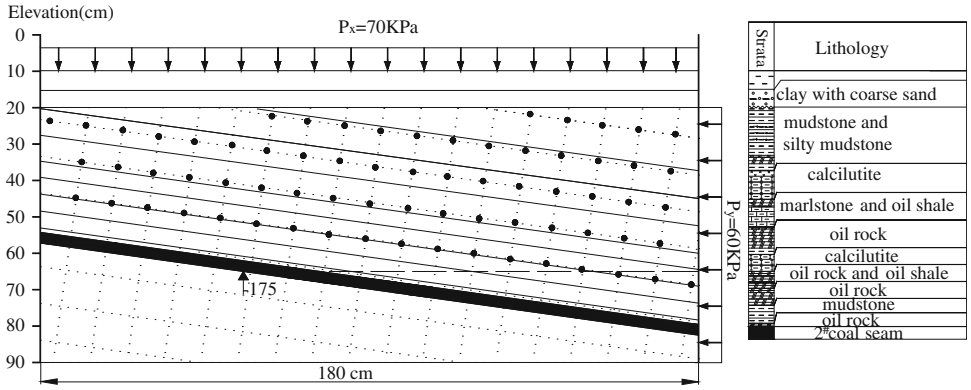

Fig. 2 The experimental model 1

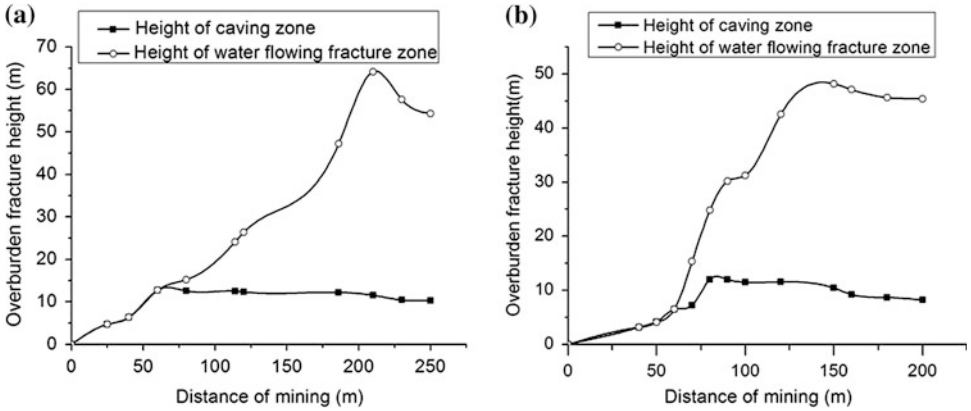

Fig. 3 Overburden failure height with distance of mining

The maximum height of overburden water flowing fracture is 64.16, according to Chinese coal mine of preventing water regulation, 3 times of coal mining thickness should be added for security considerations. It will be dangerous for mining when the overburden thickness is thinner than 82.16 m, and the upper mining limit determined at elevation of −175 m (overburden height is 90 m) should be safe.

5 Conclusions

a) The height of overburden caving and water flowing fractured zones both increase at first then decrease to a comparatively stable values with the mining distance increasing; the height of overburden water flowing fractured zone increases significantly with the thickness of the overburden increasing while the height of overburden caving zone does not.

b) The maximum height of overburden water flowing fracture is 64.16 m. with 3 times of coal mining thickness added, for much safer mining the overburden thickness must be thicker than 82.16 m, and the upper mining limit determined at elevation of −175 m (overburden height is 90 m) should be safe.

Acknowledgments The authors want to acknowledge the financial support of the National Natural Science Foundation—Shenhua Group Jointly Funded Project under grant No. 51174286. This research was also supported by A Project Funded by the Priority Academic Program Development of Jiangsu Higher Education Institutions and the Fundamental Research Funds for the Central Universities.

References

Liu, G., Liu, Z., Zhang, H., et al. (2011). Physical simulation of isolated pillar controlling role to overlying strata failure in conditions of fully-mechanized top-coal caving mining under Jing River. *Rock and Soil Mechanics, 32*(supp. 1), 433–437.

Peng, K., Li, X., Peng, S., et al. (2011). Ore-rock stability of frame stope hierarchical level filling mining method in seabed mining. *Journal of Central South University, 42*(11), 3452–3458.

Sui, W., Cai, G., & Dong, Q. (2007). Experimental research on critical percolation gradient of quicksand across overburden fissures due to coal mining near unconsolidated soil layers. *Chinese Journal of Rock Mechanics and Engineering, 26*(10), 2084–2091.

Sui, W., Dong, Q., Cai, G., et al. (2008). *Quicksand Hazards in Underground Coal Mines: Mechanism and Prevention*. Beijing: Geological Publishing House.

Sun, H. (1998). Prospect of mining under sea in China. *China Coal, 08*, 38–40.

Sun, Y., Xu, Z., & Dong, Q. (2009). Monitoring and simulation research on development of water flowing fractures for coalmining under Xiaolangdi Reservoir. *Chinese Journal of Rock Mechanics and Engineering, 28*(2), 238–245.

Xia, X., Sui, W., & Yang, W. (2008). Model test and numerical simulation of overburden failure process in multi-coal seam mining. *Journal of Engineering Geology, 16*(4), 528–532.

Geodisasteres Prevention and Reinforcement of the Sea Coast in Primorsko Town in Bulgaria

K. A. Anguelov

Abstract
The sea coast in Primorsko town in Bulgaria and specially the peninsula of the town was seriously damaged by costal geodynamic process—coastal abrasion in the zone covered by sedimentary rocks, landslides in the same sediments and rock falls in the volcanic rock zones. These processes seriously affected a number of the elements of the infrastructure of the town (roads, pipelines, power lines and a lot of private houses).All attempts to decrease individual hazardous processes in limited areas were unsuccessful because of the influence of the main factor of their activation—abrasion. This factor was the reasons for the landslides and rock falls. The fully solving the problem has been done during the period 2005–2007.Our team held engineering geological and hydro geological studies, which were used to compile the project for overall strengthening the sea coast. This project involved strengthening dams around the entire peninsula and was completed in 2007. Now all the processes of geodynamic are slacken and fortifying them is not a problem.

Keywords Landslides • Engineering geology • Hydrogeology • Geotechnical

1 Introduction

Black Sea is an inland sea with an area of 413 500 km2, whose shores are marine borders of Bulgaria, Romania, Ukraine, Georgia and Turkey. His name "black" is associated with terrible sea storms that killed thousands of people. These storms are caused by waves with a height of 4–6 m, but in some cases even reached 12 m (such a wave is measured in the city of Sochi in the winter of 1947). In such storms are measured pressures in the range of 2.50 × 105 Pa (Fig. 1).

Such unusual strong storms in the enclosed Black Sea causing huge waves that in turn determine the strong sea abrasion. It is determined by the energy of waves and geological structure of the coastal strip. In such complicated geodynamic conditions are destroyed dozens of reinforcement and harbor facilities on the beach in many coastal cities, not only in Bulgaria but also in other Black Sea countries.

2 Geological Conditions in the Area

This report covers the assessment of abrasion on the sea coast near the town of Primorsko (Fig. 2) and conditions for construction of retaining structures around the peninsula on which is built the old town.

As seen from the application fragment of geological map of Bulgaria (scale 1: 100,000) (Fig. 3), the sediments at the seashore area around the town of Primorsko, are part of Neogene system representing etc. Galatska Formation (gN1t-k):

This Formation is composed of oolitne and detrusive limestone, limy and sandy clays, well graded sandstones and sands. In layers less participate conglomerates such as lenses. Described sediments occur on Cretaceous volcanic rocks, which form the eastern peninsula.

K. A. Anguelov (✉)
Department of Hydrogeology and Engineering Geology,
University of Mining and Geology St. Ivan Rislki,
11 Str. Prof. George Zlatarsk, 1700, Sofia, Bulgaria
e-mail: angelov@bondys.bg

Y. Huang et al. (eds.), *New Frontiers in Engineering Geology and the Environment*,
DOI: 10.1007/978-3-642-31671-5_38,

Fig. 1 Satellite photo of the black sea

Upper Cretaceous volcanic rocks are presented of extremely interesting oval boulders of volcanic lava, cooled underwater. These oval rocks have a significantly higher strength characteristic of the Neogene sediments and of course are much more resistant to abrasion impact of the waves. And for that reason it is formed the most protruding part of the nose of Primorsko.

3 Engineering Geological Conditions and Engineering Geological Varieties

As can be seen from the topographic (Fig. 2) and geological maps (Fig. 3) heterogeneous geological base is exposed to abrasion impact of the waves. This geological diversity is the main factor that determines the different geodynamic phenomena on coastal slope - landslides, rock falls and abrasion destruction of the beach.

The Neogene sediments that build seashore are represented by dark brown clays with gravel inclusions and layers of fine graded lightly brown sands and fractured light limestone, with sandy-clay component. Aggregate physical and mechanical characteristics of these varieties are presented in Table 1.

4 Geodynamic Processes and Phenomena

4.1 Sea Abrasion

The Sea abrasion in the area of Primorsko peninsula is determined mainly by stormy northeast winds over 10 m/s and duration of 80 h or at a speed of 14 m/s and duration of 50 h. These winds (Rozhdestvensky 1980) are responsible for storm waves causing catastrophic violations of the coastline, such as the case with research area in the town of Primorsko near the landslide area "Bunkera"(Fig. 2). According to the comparison of topographic maps of Primorsko for about 20 years the coastline has moved on average by 1,5 m to the shore. In this section obviously processed by the sea abrasion masses are mainly from the heel of the landslide, which was formed in the clays, which occur over the Neogene sands and lime stones.

4.2 Landslide Processes and Phenomena

One of the main factors provoking particularly the development of landslides and roch falls processes and phenomena, is the morphology of the terrain. North Beach of Primorsko is a particularly steep and high coastal slope (cliff). The slope of the coast is around 30 degrees its height above the sea level an average of 9-11 m. All this leads to increased risk of gravity phenomena and processes. Formed in the base of the coastal slope of the wave surge niche activity additionally modify the tense state of the array, the probability of landslides and rock falls dramatically increased.

In this studied area, etc. "Bunkera" (Figs. 4 and 5) has clearly shaped landslide circus that is medium length of 6 m and width of 64 m (according a report for "Bunkera" made by company "Bondys" Ltd., Sofia city, 2007a year). The landslide is from delapsive type, i.e. the development of sliding

Fig. 2 Map of primorsko and the location of geodynamic phenomena

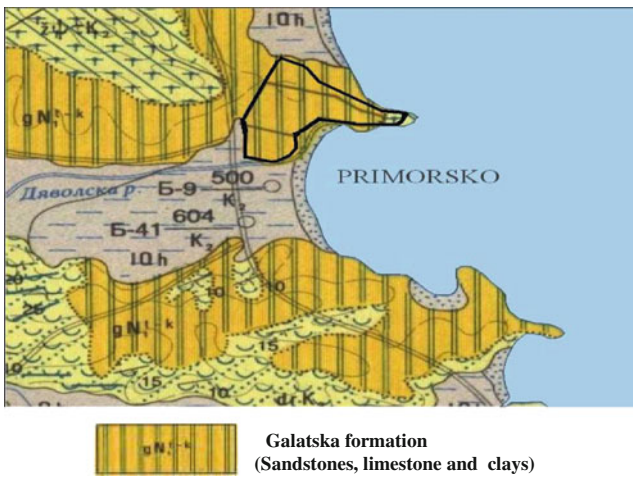

Fig. 3 Geological map sheet

processes is a "bottom–up" toward the progressive development of abrasion processes. The depth of sliding surface is shallow, in different shapes ranging from 3,0 m to 4,0 m.

The development of landslides in neighboring sections of the "Bunkera" is a circular cylindrical or near shallow slide surfaces which gradually affects part of the coast plateau, covered with clay varieties.

Activation of landslides is obviously related to the infiltration of surface rainfall water, abrasion and possible infiltration by the breakdown of water mains and sewers, located directly under roadway or next to the landslide. These processes affect both facilities on the plateau part of the beach and concrete stairs to the coast line. In general, all these facilities in and around the landslide have to be constantly repaired and their failure creates extreme discomfort for the whole region for the normal functioning of the tourist season.

4.3 Rock Falls

Such rock falls are typical for sections of the coastline, which are composed of pillow lava blocks - blocks of volcanic rock. This is primarily the most projecting part of the nose to the town of Primorsko, which has never been a beach strip. This indicates intense abrasion of the whole area (Fig. 6).

5 Strengthening the Coast Near the Town of Primorsko

To strengthening sea coast affected by a variety of geodynamic processes and phenomena - abrasion processes, landslides and rock falls was consisting project which foresees the construction of embankment block design shown in Fig. 7 (according a report for 33A made by company "Bondys" Ltd., Sofia city, 2007b year).

This embankment structure in combination with reinforced concrete alley increase the area of coastline with about 35–45 m in width and stabilize any landslide processes and rock falls. The effect of this enhancement could be seen in Fig. 8 made prior to construction and on Fig. 9 made after the construction of the facility (project for strengthening the peninsular part of Primorsko, 2004 year). From a socio ecological perspective these facilities have a tremendous effect on the resort town–most of the

Table 1 Table of aggregated physical and mechanical characteristics

Varieties	Bulk density	Specific gravity	Plasticity index	Water content	Effective cohesion		Residual strenght	
					Angle of friction	Cohesion	Angle of friction	Cohesion
	ρn [g/cm^3]	ρs [g/cm^3]	Ip[%]	W [%]	Φ[°]	c [*10^{5}Pa]	φ [°]	c [*10^{5}Pa]
Dark brown clays	1,96	2,69	17,83	27,76	19,95$_{норм.}$	0,35 $_{норм.}$	15,87$_{норм.}$	0,184$_{норм.}$
Light brown sandstones	2,07	2,68	14,74	19,09	31,00$_{норм.}$	0,23 $_{норм.}$	30,50$_{норм.}$	0,08$_{норм.}$
Limestone	98	2,71	13,20	20,53	Rn = 45 MPa	–	–	–
Pillow lava blocks					Rn = 120 MPa			

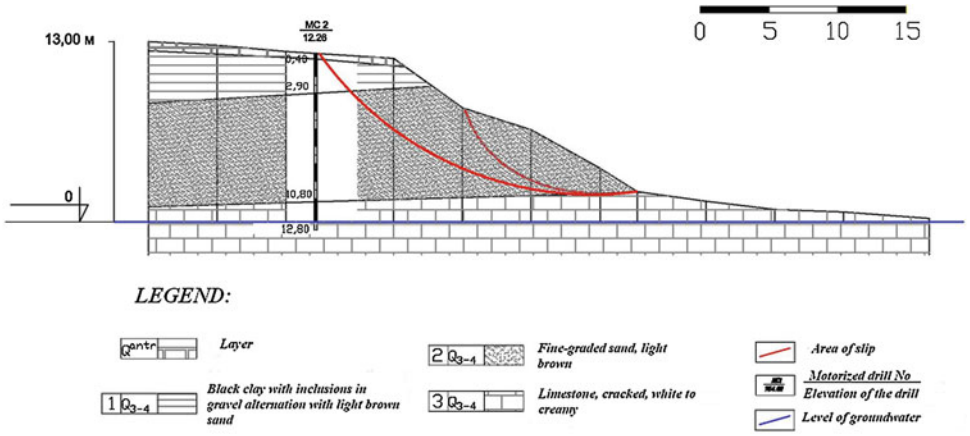

Fig. 4 Lithological profile of the landslide

Fig. 5 Common view of the landslides

Fig. 6 Zone of the abrasion

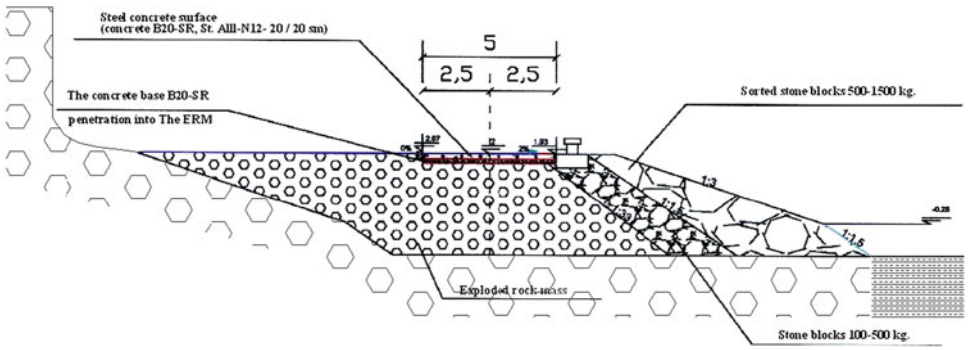

Fig. 7 Profile of the strengthening of the sea coast near town of Primorsko with embankment of exploded rocks

Fig. 8 Section of the north coast of Primorsko affected by landslides and rock falls before the construction of retaining structures

Fig. 9 The same section of the coast north of Primorsko after the construction retaining structures

vacationers prefer longer walks along the sea front alley on the reinforced concrete walking street in the old town.

6 Assessing Stability of the Constructed Facilities

In January 2012 near the town of Primorsko and more of a fortified part there was very strong sea storm that never until then not been registered. Waves reached 10 meters high and completely poured after breaking all constructed facilities. The impact of these waves lasted several days and then lull them bulk facilities proved practically unaffected. Only some boulders were "skipped" reinforced concrete path and some individual pillow lava blocks were loosed.

According to the experts who made an assessment of the status of all marine facilities after extreme storm, only those facilities in Primorsko were not affected by the huge waves.

Meanwhile, in neighbouring areas where no facilities constructed beach was unrecognizable-the sand of the beaches was totally taken to the sea and shoreline move by 3–4 m. These data show how important it is to make efficient equipment suitable form to stop the devastating impact of the waves.

7 Conclusion

The construction of a well dimensioned retaining structures on the coast, which are not always the most expensive (as in Primorsko), is especially important for successful combat the sea abrasion. These facilities except for versus erosion effect they do have also strengthening effect.

References

Engineering Geology Research and Technical Projects. (2007a). Engineering geology research and technical projects for strengthening landslide in the area of "Bunkera", Primorsko town—A report made by company "Bondys" Ltd, Sofia.

Engineering Geology Research and Technical Projects (2007b) Engineering geology research and technical projects for strengthening landslide in the area of Residential Estate 33A, Primorsko town—A report made by company "Bondys" Ltd., Sofia.

Project for strengthening the peninsular part of Primorsko, (2004).

Rozhdestvensky. (1980) Engineering Geodynamic (by V.D.Lomtadze, Leningrad).

Potential Tsunami Hazard Modelling of Black Sea Coastline, Turkey

Ö. Acır, V. I. Agoshkov, R. Aps, A. A. Danilov, and V. B. Zalesny

Abstract

Black Sea is one of the biggest inland seas in the world covering an area of 461.000 km^2 where six countries share a common coastline. Turkish portion of the Black Sea coastline has a length of 1650 km along with 15 cities where 9 million people live. The region is the main fishery resource of Turkey while hosting country's major ports, industrial facilities, specific regional agricultural products (tea, tobacco and nuts), offshore oil and gas production barges and a number of planned nuclear power plants. The coastline was prone to several big earthquakes, but went through three major tsunami events (Amasya 1598; Fatsa 1939; and Amasra 1968) in the past. Therefore the upcoming tsunami event in the future will be a major threat to the people of the region as well as economy of the country. In this study, a mixed discontinuous/continuous Galerkin finite element method is applied to solve the shallow water equations describing the long wave dynamics and representing a potential hazard modelling in the Black Sea. Discontinuous piecewise linear functions for velocity and continuous piecewise quadratic functions for sea level will be both utilized while the splitting method will be used with respect to time. Grid generator for Galerkin finite element method is based on unstructured triangular cells of variable size. The results of the simulation of the Black Sea level dynamics after initial shock suggest rather narrow alert/response time window of opportunity for the coastline of Turkey.

Keywords

Tsunami • Potential hazard • Modelling • Black Sea • Turkey

1 Introduction

Black Sea is one of the biggest inland seas in the world covering an area of 461.000 km^2 where six countries share a common coastline. Turkish portion of the Black Sea coastline has a length of 1650 km along with 15 cities where 9 million people live. The region is the main fishery resource of Turkey while hosting country's major ports, industrial facilities, specific regional agricultural products (tea, tobacco and nuts), offshore oil and gas production barges and a number of planned nuclear power plants.

Ö. Acır (✉)
Petrako Oil and Gas Exploration Ltd, Ankara, Turkey
e-mail: ozguracir@tr.net

R. Aps
Estonian Marine Institute, University of Tartu, Tartu, Estonia

V. I. Agoshkov · A. A. Danilov · V. B. Zalesny
Institute of Numerical Mathematics, Russian Academy of Sciences, Moscow, Russia

Y. Huang et al. (eds.), *New Frontiers in Engineering Geology and the Environment*,
DOI: 10.1007/978-3-642-31671-5_39,

Fig. 1 Tectonic features of Black Sea with significant earthquakes (M ≥ 5) occurred at the offshore and/or coastal areas

2 Geology and Seismicity of Black Sea

Geologically, Black Sea is an intra-continental sea occured with the combination of extensional and compressional tectonic regime during the closure of Tethyean Ocean. Many authors considered that Black Sea developed as a Cretaceous to Palaeogene back-arc basin (Zonenshain and Le Pichon 1986; Görür 1988; Dercourt et al. 1993; Okay et al. 1994; Robinson 1997; Nikishin et al. 2003). Current geomorphological features (i.e., shelves and coasts) of Black Sea basin have been controlled by the neotectonic regime, which is also the source of recent seismic activity. Major structural elements of the Black Sea basin are Western Black Sea Fault, North Anatolian Fault, West Crimean Fault and Cacaucasus Thrust Belt accordingly (Fig. 1).

The seismicity of Turkish Black Sea region was discussed by various authors in terms of neotectonic Anatolid-Pontide plate movements (McKenzie 1972; Alptekin 1973; Dewey 1976; Şengör 1979; Şengör and Caunitez 1982; Şengör et al., 1985) and mainly North Anatolian Fault (NAF) system. On the other hand, the seismic activity of off-shore Black Sea is generally considered as "weak to moderate" (Kuşcu et al. 2004) although Romanian coasts had many tsunami-type hazards in the past (Ranguelov 1996 and Oaie et al. 2006).

Historical records show that Turkish Black Sea coastline had produced significant earthquakes and also 3 major tsunami events (Amasya-1598, M:8; Fatsa-1939, M:8; and Amasra-1968, M:6.6) in the past (Altınok and Ersoy 2000) which all of them were examined and related with NAF as well (Kuran and Yalçıner 1993; Ambraseys and Finkel, 1995; Soysal et al., 1981; Şengör et al., 1983). Meanwhile it's notable that 1939 Fatsa tsunami was triggered by Erzincan earthquake (M:8) which the epicentre was more than 350 km in the *hinterland* from the tsunami observed coast.

As briefly mentioned above, Turkish Black Sea tsunami events are considered with NAF mechanism only. However off-shore Black Sea, specifically Ukrainian and Romanian coasts, have produced considerable big earthquakes (M ≥ 6.5) in the past so they also have a potential to produce tsunami prone earthquakes in the future. This study proposes a new mathematical approach to evaluate the potential tsunami risk for the Turkish Black Sea coasts.

3 Methodology

3.1 Galerkin Finite Element Method for Linear Shallow Water Equations

Discontinuous/continuous Galerkin finite element method is modification of the conventional Galerkin finite element method with the following basis functions: $P1_{DG}$—piecewise linear functions and P2—piecewise quadratic functions. In this study, continuous piecewise quadratic functions are used for sea level $\boldsymbol{h}$ and discontinuous piecewise linear functions are used for velocity $\boldsymbol{u}$ accordingly. This element pair has the property that all geostrophically balanced states which strongly satisfy the boundary conditions have discrete divergence equal to exactly zero and hence are exactly steady states of the discretized equations. This means that the finite element pair has excellent geostrophic balance properties. These numerical properties of the $P1_{DG}$–P2 finite element pair are presented in more detail (Cotter et al. 2009; Cotter and Ham 2011).

The linear shallow water equations for the domain Ω is defined as:

$$u_t + \frac{1}{\mathrm{Ro}} k \times u + \frac{1}{\mathrm{Fr}^2} \nabla \mathrm{h} = 0, \mathrm{u} = (\mathrm{u}_1, \cdots, \mathrm{u}_\mathrm{d}), \quad (1)$$

$$\mathrm{h}_t + \nabla u = 0, \quad (2)$$

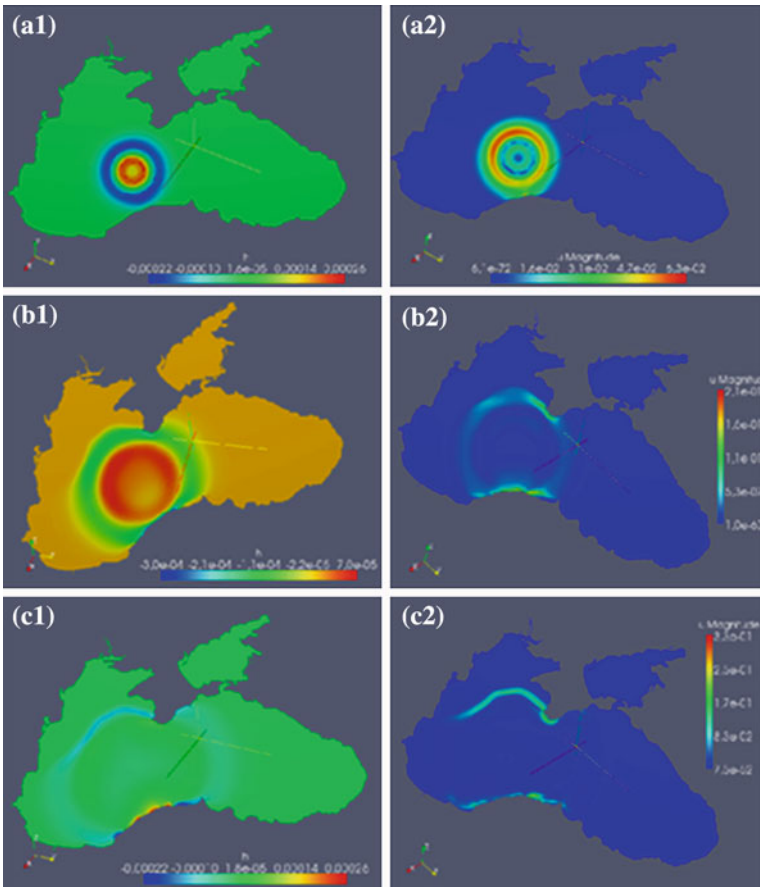

Fig. 2 Sea level displacement (1) and velocity magnitude field (2) in Black Sea (a) at $t = 10$ min; (b) $t = 20$ min. and (c) $t = 30$ min

where $\boldsymbol{u}$—velocity filed, h—sea level displacement, $\boldsymbol{k}$—unit vector along z axis,$Ro = \frac{u}{fL}$—Rossby number, $F\gamma = \sqrt{\frac{U}{gH}}$ Froude number, where U—characteristic velocity scale, L—characteristic space scale, H—average sea level, f—Coriolis parameter, and g—gravitational constant.

The boundary conditions are the following:

$$u \cdot n = 0 \quad \text{on} \quad \partial\Omega \tag{3}$$

where $\boldsymbol{n}$—outward unit normal vector.

When discontinuous/continuous Galerkin finite element method is used and Eq. (1) is multiplied by discontinuous test function $\boldsymbol{\omega}$ and Eq. (2) by continuous test function $\boldsymbol{\varphi}$, the integrated equation becomes:

$$\frac{d}{dt}\int_{\mathrm{E}} \omega \cdot u\mathrm{dv} + \frac{1}{Ro}\int_{\mathrm{E}} \omega \cdot k \times u\mathrm{dv} = -\frac{1}{Fr^2}\int_{\mathrm{E}} \omega \cdot \nabla h\mathrm{dV}, \tag{4}$$

$$\frac{d}{dt}\int_{\mathrm{E}} \phi \cdot hdV = -\int_{\mathrm{E}} \phi \cdot \nabla u\mathrm{dV}, \tag{5}$$

Now we integrate Eq. (5) by parts and consider Eq. (3) for boundary conditions, and we obtain the following system:

$$\frac{d}{dt}\int_{\mathrm{E}} \omega \cdot u\mathrm{dv} + \frac{1}{Ro}\int_{\mathrm{E}} \omega \cdot k \times u\mathrm{dv} = -\frac{1}{Fr^2}\int_{\mathrm{E}} \omega \cdot \nabla h\mathrm{dV}, \tag{6}$$

$$\frac{d}{dt}\int_{E} \phi \cdot hdV = \int_{E} \nabla\phi \cdot u\mathrm{dV} - \int_{\partial E/\partial\Omega} n \cdot \tilde{u} \cdot \phi\mathrm{dS}, \tag{7}$$

Where $\tilde{u}$—value of velocity field $\boldsymbol{u}$ on the element boundary, determined by the specific Galerkin scheme, and $\boldsymbol{n}$—outward unit normal vector to ∂E. Summing these equations over all mesh elements and canceling the boundary terms since $\boldsymbol{\phi}$ is a continuous function we obtain the finite element shallow water equation system:

$$\frac{d}{dt}\int_{\Omega} \omega \cdot u\mathrm{dv} + \frac{1}{Ro}\int_{\Omega} \omega \cdot k \times u\mathrm{dv} = -\frac{1}{Fr^2}\int_{\Omega} \omega \cdot \nabla h\mathrm{dV}, \tag{8}$$

$$\frac{d}{dt}\int_{\Omega}\phi\cdot h dV=\int_{\Omega}\nabla\phi\cdot u\mathrm{dV}, \tag{9}$$

Let us suppose, that functions $\boldsymbol{u}$ and $\boldsymbol{\omega}$ are approximated by discontinuous piecewise linear functions u^{δ} and ω^{δ} and functions $\boldsymbol{\phi}$ and h—by continuous piecewise quadratic functions h^{δ} and ϕ^{δ} Then our finite element discretization of a system (8, 9) will become:

$$\frac{d}{dt}\int_{\Omega}\omega^{\delta}\cdot u^{\delta}\mathrm{dv}+\frac{1}{Ro}\int_{\Omega}\omega^{\delta}\cdot k\times u^{\delta}\mathrm{dv}=-\frac{1}{Fr^{2}}\int_{\Omega}\omega^{\delta}\cdot\nabla h^{5}\mathrm{dV},$$

$$\frac{d}{dt}\int_{\Omega}\phi^{\delta}\cdot h\,dV=\int_{\Omega}\nabla\phi^{\delta}\cdot u^{\delta}\mathrm{dV}, \tag{10}$$

where test functions ϕ^{δ} and ω^{δ} belong to the corresponding special function spaces.

Complete discontinuous/continuous Galerkin finite element scheme, some numerical results for equation system (10), as well as the proof of several properties of this scheme are given by Cotter et al. (2009).

The C-code consists of standalone unstructured mesh generator, discrete solver for equation system (10) using unstructured grids, and the results visualization system. The input data is a boundary of the domain represented by a closed polyline and the mesh generator creates a discrete triangular mesh for the region inside the polyline. Two approaches are available: a quasi-uniform triangular mesh with a quasi-constant user-defined element size; and an automatic mesh size adaptation to the value $\sqrt{g\cdot H}$, where g—gravitational constant, and H—user-provided sea depth field. The second approach is more practical, since it provides the more dense mesh near the coastline, and hence the solution would be more accurate.

4 Results and Conclusion

The numerical experiment was run using the second module—finite element solver. Considering Black Sea area has a zero initial sea level displacement and zero velocity fields, an imaginary earthquake (supposed to be on the West Crimean Fault) was developed at longitude 32° East and latitude 43° North. Calculations were run for the first 30 min. The resulting sea level displacement field and velocity magnitude field are visualized by Paraview software and presented in Fig. 2.

Black Sea has a quite dynamic seismo-tectonic regime which has already originated significant earthquakes as well as tsunamis in the past. Considering this, results of the numerical experiments run by Discontinuous/continuous Galerkin finite element method show that such an event would lead narrow alert/response time window of opportunity (t < 30 min) for the coastline of Turkey.

References

Alptekin, Ö. (1973). Focal mechanism of earthquakes in western Turkey and their tectonic implications. *PhD thesis*, New Mexico Institute of Mining and Technology, USA.

Altinok, Y., & Ersoy, Ş. (2000). Tsunamis observed on and near the Turkish coast. *Natural Hazards, 21*, 185–205.

Ambraseys, N., Finkel, C. (1995). The seismicity of Turkey and adjacent areas. *A historical review, 1500–1800*, Istanbul: Eren Yayıncılık.

Cotter, C. J., Ham, D. A., & Pain, C. C. (2009). A mixed discontinuous/continuous finite element pair for shallow-water ocean modelling. *Ocean Modelling, 26*, 86–90.

Cotter, C. J., & Ham, D. A. (2011). Numerical wave propagation for the triangular P1DG–P2 finite element pair. *Journal of Computational Physics, 230*, 2806–2820.

Dercourt, J., Ricou, LE., Vrielynck, B. (Eds.) (1993). *Atlas Tethys, Paleoenvironmental Maps* (pp. 307). Paris: Gauthier-Villars. 14 maps, 1 pl.

Dewey, J. W. (1976). Seismicity of northern Anatolia. *Bulletin of Seismological Society of America, 3*, 843–868.

Görür, N. (1988). Timing of opening of the Black Sea basin. *Tectonophysics, 147*, 247–262.

Kuran, U., & Yalçıner, A. C. (1993). Crack propogations earthquakes and tsunamis in the vicinity of Anatolia. In S. Tinti (Ed.), *Fifteenth international tsunami symposium, 1991, Tsunamis in the world* (pp. 159–175). Holland: Kluwer Academic Publishers.

Kuşçu, İ., Parke, R. J., White, S. R., McKenzie, D., Anderson, A. G., Minshull, T. A., et al. (2004). Active slumping offshore Amasra (Southwest Black Sea) and its relation with regional tectonics. *Mineral Research and Exploration Bulletin, 128*, 27–47.

Nikishin, M., Korotae, M. V., Ershov, A. V., & Brunet, M. F. (2003). The Black Sea basin: tectonic history and Neogene–Quaternary rapid subsidence modelling. *Sedimentary Geology, 156*, 149–168.

McKenzie, D. (1972). Active tectonics of the Mediterranean region. *Geophysical Journal of Royal Astronomical Society, 30*, 109–185.

Oaie, G., Secrieru, D., Seghedi, A., Ioane, D., & Diaconescu, M. (2006). Preliminary assessment of the tsunami hazard for the Romanian Black Sea area: historical and paleotsunami data. Abstracts. *Geosciences, 200*, 300–302.

Okay, A., Sengör, A. M. C., & Görür, N. (1994). Kinematic history of the opening of the Black Sea and its effect on the surrounding regions. *Geology, 22*, 267–270.

Ranguelov, B. (1996). Earthquakes and tsunami hazards in the Black Sea. In *Abstract Book of the First Congress of the Balkan Geophysical Society* (pp. 44–45). 23–27 September, Athens.

Robinson, A. G. (Ed.) (1997). Regional and petroleum geology of the Black Sea and surrounding region (p 85). Vol. 68, Tulsa: American Association of Petroleum Geologists, Memoir.

Soysal, H., Sipahioğlu, S., Kolçak, D., Altınok, Y. (1981). Türkiye ve Çevresinin Tarihsel Deprem Kataloğu (MÖ 2100-MS 1900), Istanbul: Tubitak, TBAG Proje No. 341.

Şengör, A. M. C., Büyükaşıkoğlu, S., & Canıtez, N. (1983). Neotectonics of the Pontides: Implications for 'incompatible' structures along the North Anatolian Fault. *Journal of Structural Geology, 5*, 211–216.

Şengör, A. M. C. (1979). The North Anatolian transform fault: its age, offset and tectonic significance. *Journal of Geological Society of London, 136*, 269–282.

Şengör, A. M. C., Canıtez, N. (1982). The North Anatolian fault. In Berchemer, Hsu, K. (Eds.) *Alpine and mediterranean geodynamics* (pp. 205–216, Vol. 7). Washington: Geodynamical Series, American Geophysical Union.

Şengör, A. M. C., Görür, N., Şaroğlu, F. (1985). Strike-slip faulting and related basin formation in zones of tectonic escape: Turkey as a case study (pp. 227–264, Vol. 37). Ottawa: Mineralogists Special Publication.

Zonenshain, Le Pichon. (1986). Deep basins of the Black Sea and Caspian Sea as remnants of Mesozoic back-arc basins. *Tectonophysics, 123*, 181–211.

Alluvial Risk in the Costal Plain of Pesaro City, Northern Marche (Italy)

U. Gori, M. Mari, and R. W. Romeo

Abstract

Pesaro city (central Italy) stands on the alluvial plain of Foglia River, between foothills on the rear and the Adriatic Sea in the front of. On November 2005, an industrial area, as large as 12 ha, due to an intense rainfall event was flooded. Several damages to structures and infrastructures occurred, as well as property losses which blocked every economic activity for a long period of time, thus increasing the indirect losses due to the flooding. With the aim to ascertain whether or not the event could be forecasted, an in-depth search of the historically documented previous events was carried out and its result statistically analyzed. The statistical analysis allowed for detecting the return period of intense rainfall in the area spanning from recurrent to infrequent events ($2 < T < 100$ years). A comparison with the cumulative rainfall prior to the flooding event on November 2005, showed as the event is consistent with return periods of some to few tens of years, thus confirming that the event could be forecasted and properly accounted for in 20 how hydrological statistical analyses can contribute to solve questions arising from the responsibilities of evaluating and mitigating the natural hazards for a safer world.

Keywords

Flooding • Rainfall • Return periods • Alluvial risk

1 General Framework

The affected area by the alluvial flooding on November 2005 close to Pesaro city (central Italy, Fig. 1), lies across the end course of Foglia River, 2 km away from the outlet in the Adriatic sea. The event caused many damages to some industrial facilities located on an alluvial terrace developed in a wide meander on the right river bank. An embankment 3 m height separates the river thalweg from the terrace and it represents the only barrier against flooding.

The upstream river basin (Fig. 1) develops for about 700 km^2 in the WSW–ESE direction, sourcing from Apennines mountainous chain at an elevation of about 1,400 m a.s.l. The outcropping geological formations belong to the basin domain called Umbro-Marchigiana Sequence, made by limestone and marls, overlaid by Plio-pleistocene clayey deposits (Regione Marche 1991). The most recent stratigraphic units (Miocene to Olocene) made by sandy–clayey soils, alluvial deposits and colluvium, diffusely outcrop in the basin and influence the relationship between seepage and flooding. The Foglia River, whose course extends about 90 km from the source to the outlet, has an estimated run-off time of 16.6 h (Giandotti 1934).

U. Gori (✉) · M. Mari · R. W. Romeo
Dipartimento di Scienze della Terra della Vita e dell'Ambiente,
Urbino University Campus Scientifico Enrico Mattei
61029, Urbino, Italy
e-mail: umberto.gori@uniurb.it

Y. Huang et al. (eds.), *New Frontiers in Engineering Geology and the Environment*,
DOI: 10.1007/978-3-642-31671-5_40,

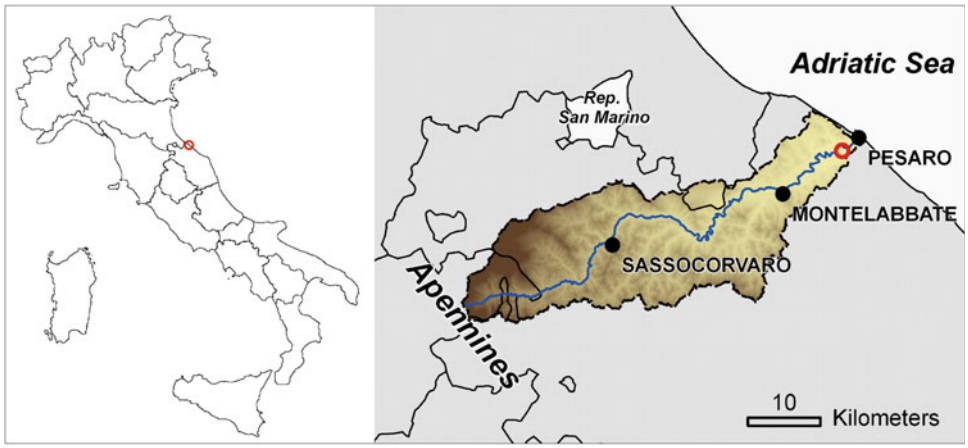

Fig. 1 Location of Pesaro city and boundary of the Foglia River Basin (the *circle* indicates the flooded area close to Pesaro city)

Fig. 2 Average annual rainfall in Marche Region (http://www.meteo.marche.it/)

2 Rainfall Data

There is an evident difference in the rainfall characteristics of the upper and lower river course. Rainfall data coming from three weather stations distributed along the river basins were used: Pesaro station, located close to the river outlet; Montelabbate station, located in the middle of the river basin; Sassocorvaro station located in the upstream.

Average rainfall increases from the sea coastline toward the mountains [Fig. 2, from Amici and Spina (2002)]. The recorded rainfall in Pesaro city since 1871 is shown in Fig. 3 along with the computed running average and the residuals. The rainfall recorded in the period July–November 2005, whose daily maximum occurred on September 18 (136.8 mm) and whose monthly maximum was November (146.7 mm), do not represent extraordinary events even if they may be still regarded as particularly significant.

Table 1 shows the maximum rainfall intensities in 12 and 24 h recorded on November 2005, which are representatives of the estimated run-off time for the basin (16.6 h).

3 Rainfall Analyses

Starting from the acquired data, the work consisted in analyzing the rainfall events occurred in the past to ascertain whether or not the rainfall event on November 2005 can be regarded as exceptional or, on the contrary, it could be forecasted and its consequences avoided. To this end we computed the rainfall probability distribution curves, in order to determine the return period of the rainfall (Tr). The probabilities were computed according to Gumbel distribution using the maximum rainfall intensities recorded at the weather stations in the period 1950–1989 (Fig. 4).

The rainfall probability curves shown in Fig. 4, related to Sassocorvaro, point out that neither the rainfall event occurred on November 26, nor the rainfall event occurred on October 8th, can be regarded as exceptional events, since they largely fall well below the rainfall probability curve with a return period of 10 years. Pesaro and Montelabbate weather stations show a very close behaviour.

Saccorvaro weather station shows an amount of rainfall close to the 10 years return period rainfall probability curve if one considers also the contribution coming from the snow fallen in the days before.

In relation to the rainfall recorded in the month of November during the period 1871–2005, the average monthly rainfall is 86.7 mm and though the rainfall event occurred on November 2005 largely exceeded this value, it can be observed that at least 13 events in the last 130 years were indeed larger than that occurred on November 2005. Applying the same statistical method used for the rainfall probability curves, the rainfall expected with different

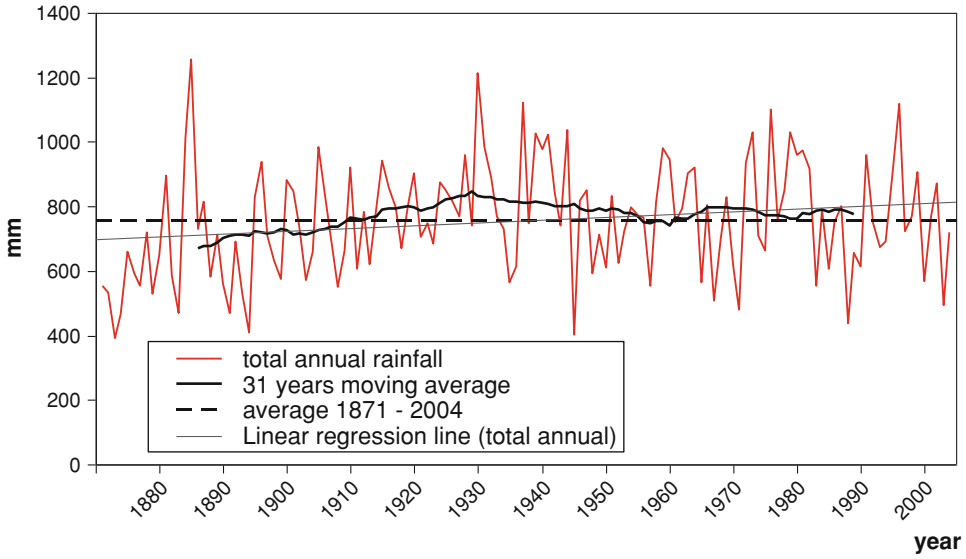

Fig. 3 Average yearly rainfall recorded by Pesaro weather station since 1871 A.D

Table 1 Maximum rainfall intensity recorded on November 2005

Weather station	12 h (mm)	24 h (mm)
Pesaro	16.8	25.2
Montelabbate	20.2	31.4
Sassocorvaro	30.8	50.4

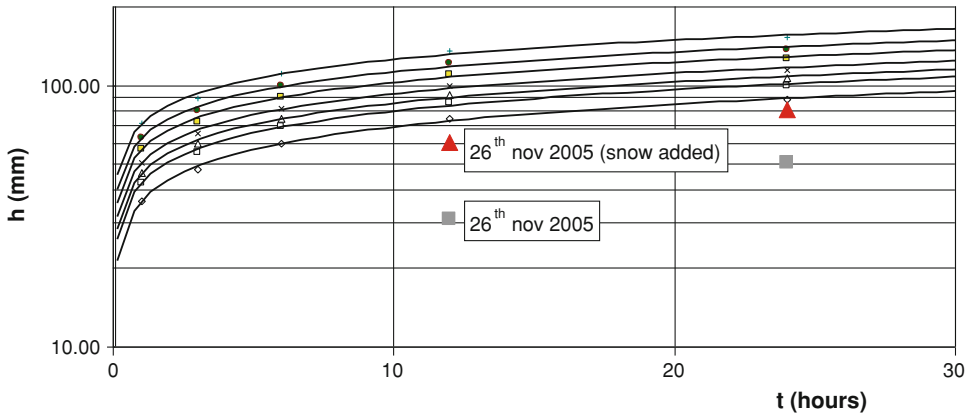

Fig. 4 Sassocorvaro weather station: rainfall probability curves for return periods of 10, 20, 30, 50, 100, 200 and 500 years (bottom to top). Squares are the rainfall intensities recorded on November 26th, triangles with the added snow fallen in the days before (about 40 mm)

return periods in the month of November is shown in Table 2.

The graphs show as the longer the observational period the more exceptional the rainfall event on November 2005 becomes. To test this hypothesis in Fig. 5 the cumulated rainfall in the days before the flooding event is compared with the rainfall probability curves with return periods ranging from 2 to 100 years, using the GEV-function (Jenkinson 1955; Hosking et al. 1984).

Within 2 months before the event, the cumulated rainfall does not exceed the rainfall probability curve with 2 years return period; only extending the cumulative period to 4 months prior the event, the cumulated rainfall reaches the rainfall probability curve with 20 years return period.

The same Meteorological Agency of the Marche Regional Government (Centro Funzionale Multirischi per la Meteorologia e l'Idrologia—Regione Marche Protezione Civile 2005) as well as other sources (Geologi Associati

Table 2 Pesaro weather station: monthly (November) rainfall within different return periods

Tr—return period (years)	Rainfall (November) (mm)	Tr—return period (years)	Rainfall (November) (mm)
10	182.68	100	304.40
20	219.97	200	340.44
30	241.42	500	387.98
50	268.23		

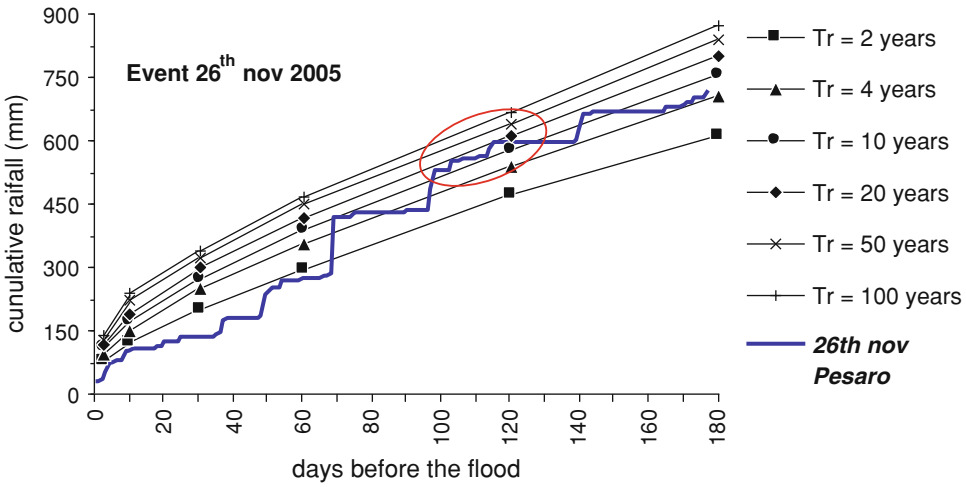

Fig. 5 Pesaro weather station: cumulated rainfall prior the November 26th rainfall event and rainfall probability curves with different return periods

Gennari-Mengarelli 1999), confirmed that the outflow discharge recorded on November 2005 was comparable to other similar events with return periods not longer than 5 years. Joining this information with the analyses carried out in this study, one can conclude that the event occurred on November 2005 was predictable with an estimated return period not longer than 10 years.

4 Conclusions

The main conclusions of this study can be summarized as follows:

(a) The rainfall on November 2005, though larger than the monthly average, had hourly intensities and cumulated values well below than those estimated with return period of 10 years, yet computable with the available rainfall data coming from local weather stations.
(b) Nor the snow fallen in the days before in the upstream course of the Foglia River can have significantly affected the amount of the flow discharge.
(c) The rainfall and outflow data yet available at the time of the event, made it predictable with a reasonable degree of reliability within return periods of some years, and thus suitable to be considered as a design value in any land planning or intervention devoted to the prevention and mitigation of natural disasters. Thus confirming again how only an in-depth knowledge and analysis of the natural phenomena can represent an effective prevention policy.

References

Amici, M., Spina, R. (2002). Centro di Ecologia e Climatologia OGS Macerata, Campo medio della precipitazione annuale e stagionale sulle Marche per il periodo 1950–2000.

Centro Funzionale Multirischi per la Meteorologia e l'Idrologia—Regione Marche Protezione Civile. (2005). Rapporto di Evento 25–27 novembre 2005.

Geologi Associati Gennari-Mengarelli. (1999). Studio per la individuazione delle aree a rischio idrogeologico–idraulico del Fiume Foglia con programmazione degli interventi di mitigazione e riqualificazione.

Giandotti, M. (1934). Previsione delle piene e delle magre dei corsi d'acqua. Istituto Poligrafico dello Stato, 8: pp. 107–117.

Hosking, J. R. M., Wallis, J. R., Wood, E. F. (1984). *Estimation of the generalized extreme value distribution by the method of probability weighted moments* (vol. 27, pp 251–261). Wallingford: Institute of Hydrology. (Report 89).

Jenkinson, A. F. (1955). The frequency distribution of the annual maximum (or mini-mum) values of meteorological elements. *Quarterly Journal Royal Meteorological Society, 81*, 158–171.

Regione Marche, G. R. (1991). *L'ambiente fisico delle Marche*. Firenze: SELCA s.r.l.

Analysis of the Carbon Monoxide Released Law Caused by Shield Construction in Shallow Stratum in Sea Reclamation District

J. X. Wang, B. P. Zou, X. J. Chen, J. Yi, and G. L. Kuang

Abstract

Carbon monoxide released in shallow stratum in sea reclamation district is a difficult problem in the process of shield construction. Based on carbon monoxide released in shallow stratum in the process of shield construction of Dengliang-Houhai section in Shenzhen Metro, this article analyzes the occurrence characteristics of carbon monoxide in shallow stratum from three respects in sea reclamation district, including geological conditions, reserving conditions, and occurrence structure. It also analyzes the disaster mechanism of carbon monoxide released in shallow stratum, and studies the carbon monoxide released law caused by shield construction from the dynamic and the static, including the rapid release, the slow release, the released volume concentration, and the pressure of gas bearing formation. The results show that the rapid release of carbon monoxide has a greater influence on the soil deformation compared with the slow release. The soil deformation is mainly elastic deformation, and the maximum occurs near the medial axis. The released volume concentration of carbon monoxide was relatively high from shield tail to trolley 5 under dynamic conditions, but it is large for internal soil chamber under static conditions.

Keywords

Sea reclamation district • Shield tunnel • Carbon monoxide • Soil deformation

1 Introduction

With the acceleration of the urbanization process in China, subway development is the key to solving the development problems of land resources, urban congestion. The shield, as a major subway construction engineering method, has been widely used in China. But it is facing many thorny problems in the course of shield construction, such as the sudden harmful gas in shallow stratum (Tang et al. 2003, 2007), the disturbed original formation and stress field (Nomoto et al. 1999; Ding et al. 2011).

For a long time, many scholars have studied soil deformation caused by shield construction from four respects, including the empirical formula, the theoretical analysis, the model test, the artificial neural network, has made prominent achievements (Peck 1969; Karakus 2007; Santos and Celestino 2008; Juneja et al. 2010). But these research, were

J. X. Wang (✉)
Key Laboratory of Geotechnical and Underground Engineering of Ministry of Education, Tongji University, Shanghai 200092, China
e-mail: wangjianxiu1971@gmail.com

J. X. Wang · B. P. Zou
Department of Geotechnical Engineering, Tongji University, Shanghai 200092, China

X. J. Chen
College of Civil Engineering, Guilin University of Technology, Guilin 541004, China

J. Yi · G. L. Kuang
China Tunnel Construction Co., Ltd., Guangzhou 510635, Guangdong, China

Y. Huang et al. (eds.), *New Frontiers in Engineering Geology and the Environment*,
DOI: 10.1007/978-3-642-31671-5_41,

only considered soil loss, groundwater level, grouting, and other factors. So far there has been little research on the harmful gas released law in the process of shield construction. The harmful gas is mainly to study the methane in shallow stratum, and mainly focuses on the following aspects such as the distribution, the mining, the utilization (Leonid and Valeriy 1996; Nagao et al. 1997; Tang et al. 2003, 2007; Gebhardt et al. 2009; Rodríguez and Lombardía 2010; Singh et al. 2010). However, there are no studies on the carbon monoxide in shallow stratum. Especially, there are no studies on the carbon monoxide released law of rich water tunnel in shallow stratum in sea reclamation district.

Shenzhen lies in Pearl River Delta plain, with its complex geology mostly in weak watery stratum. Moreover, a lot of sea reclamation projects have been carried out in Shenzhen during recent years. Therefore, it belongs to the typical sea reclamation district. Therefore, based on carbon monoxide released in shallow stratum in the process of shield construction of Dengliang-Houhai section in Shenzhen Metro, this article analyzes the occurrence characteristics of carbon monoxide in shallow stratum from three respects in sea reclamation district, including geological conditions, reserving conditions, and occurrence structure. It also analyzes the disaster mechanism of carbon monoxide released, and studies the carbon monoxide released law caused by shield construction from the dynamic and the static, including the rapid release, the slow release, the released volume concentration, and the pressure of gas bearing formation. This paper has significant referential function to the tunneling engineering disaster prevention, and to provide evidence for subsequent engineering prevention.

2 Occurrence Characteristics of Carbon Monoxide in Shallow Stratum in Sea Reclamation District

Taking Dengliang-Houhai section in Shenzhen Metro as example, it belongs to the typical sea reclamation district. This article analyzes the occurrence characteristics of carbon monoxide in shallow stratum from three respects in sea reclamation district, including geological conditions, reserving conditions, and occurrence structure. The mileage of Dengliang-Houhai section in Shenzhen Metro is YDK8 + 649.580–YDK9 + 409.140. The left line is 774.507 m, and the right line is 770.44 m. The section tunnels are built by shield method. The maximum curve radius of tunnel planes is 1000 m, and the minimum is 400 m. The tunnel width from left to right is 13.2–14.2 m. The maximum longitudinal slope of lines is 28 ‰, and the minimum is 2.0 ‰. The vertical curve radius is 5000 m, and the minimum is 3000 m. Vault is 10–15 m in buried depth.

2.1 Engineering Geology and Hydrogeology

2.1.1 Engineering Geological Conditions

The original landform of site is the littoral faces inter-tidal zone (tidal flat), the original elevation of which is −0.7 to 1.2 m. The site were formed from sea reclamation by soft foundation treatment, the ground elevation is 3.00–4.93 m. The tunnel body is divided into four strata in the process of shield construction.

The soil mechanical properties are listed in Table 1.

(1) Layer ⑤$_2$ is gravel sand, offwhite to light yellow. Its main component is quartz matrix. The mixed cohesive soil is about 10 %. It is slightly dense to medium dense, saturated and good gradation. Its sorting feature is poor. The layer thickness is from 2.0 to 6.8 m. (2) Layer ⑥$_2$ is grey black silt clay, wet to saturated, and soft-plastic to plastic. Its thickness is about 0.3–7.0 m. (3) Layer ⑥$_3$ is light yellow to offwhite clay. It is plastic. Its thickness is about 0.8–1.5 m. (4) Layer ⑥$_4$ is gravel sand, offwhite to brownish yellow. Its main component is quartz matrix. It is slightly dense to medium dense, saturated, and good gradation. Its sorting feature is poor. The layer thickness is from 0.8 to1.5 m.

2.1.2 Hydrogeological Conditions

The silt clay and the clay layer are aquifuges, and both the upper and lower ones are aquifers in the study area. The lower layer is a confined aquifer, but the upper layer is of phreatic water. The thickness of silt clay layer is big, low permeable. It is contribute to negligible change of the water level between the confined aquifer and the phreatic water. The thickness of gravel sand layer is big, evenly distributed, which has relation with seawater. Thus its aquosity is better, and groundwater level is very high. Therefore, the groundwater has great influence on the tunnel construction. It is easy to cause quicksand and water inflow.

2.2 Reserving Conditions of Carbon Monoxide in Shallow Stratum

The study area belongs to the typical sea reclamation district, and its soil mainly is silt clay with high sensitivity, high water content, high changeability and low strength. It belongs to under-consolidated saturated soft soil, and containing a lot of organic materials. At the suitable temperature and pressure, and in reducing environment of overlaying soil, the degradation of these organic materials produced carbon monoxide. There are two different carbon monoxide reservoir types; one part in which carbon monoxide closed in silt clay layer and the other where soil is overflow into adjacent gravel sand layer in the process of consolidation. The gravel sand layer is mainly of carbon

Table 1 Soil mechanical properties

Layer	Type	Natural water content (%)	Void ratio	Compression modulus (MPa)	Permeability coefficient (m/d)
⑤$_2$	Gravel sand	15.9	0.561	12	25
⑥$_2$	Silt clay	52.6	1.254	3	0.005
⑥$_3$	Clay	31.4	0.921	5	0.05
⑥$_4$	Gravel sand	14.2	0.525	15	30

(1) Layer ⑤$_2$ is gravel sand, offwhite to light yellow. Its main component is quartz matrix. The mixed cohesive soil is about 10 %. It is slightly dense to medium dense, saturated and good gradation. Its sorting feature is poor. The layer thickness is from 2.0 to 6.8 m. (2) Layer ⑥$_2$ is grey black silt clay, wet to saturated, and soft-plastic to plastic. Its thickness is about 0.3–7.0 m. (3) Layer ⑥$_3$ is light yellow to offwhite clay. It is plastic. Its thickness is about 0.8–1.5 m. (4) Layer ⑥$_4$ is gravel sand, offwhite to brownish yellow. Its main component is quartz matrix. It is slightly dense to medium dense, saturated, and good gradation. Its sorting feature is poor. The layer thickness is from 0.8 to1.5 m

monoxide reservoir, and is mainly from adjacent silt clay layer, and the minority is the decomposition of these organic materials.

2.3 Occurrence Structure of Carbon Monoxide in Shallow Stratum

Occurrence structure is divided into a closed water pore, a dual connected pore, a closed gas pore and a confined saturation zone combined with reserving conditions of carbon monoxide in shallow stratum. In the closed water pore, soil pore mainly is filled with carbon monoxide, and it is connected, but the pore is very few. Soil pore are connected between the carbon monoxide and the pore in the dual connected pore. In the closed gas pore, the pore is applied to segment the carbon monoxide. The confined saturation zone mainly is released carbon monoxide dissolved in solution when the pressure of gas bearing formation is decreased (Tang et al. 2003, 2007).

3 Disaster Mechanism of Carbon Monoxide Released

Carbon monoxide released in shallow stratum has great influence on the soil deformation in different speed. The effective stress of carbon monoxide layer is much lower than gravity stress under high gas pressure, and this is the underlying reason for causing loose soil structure. If carbon monoxide is released slowly, it will cause large soil deformation. But if the monoxide is released rapidly, together with engineering vibration of shield construction and soil thickness uneven distributed, the high pressure carbon monoxide can expose roof, and the fast flow will cause strong soil erosion. When the pressure of gas bearing formation is decreased, this must cause the migration of monoxide from gas–water interface to jet hole. Meanwhile, the groundwater flow will produce soil erosion, and this must cause soil deformation in the bigger range (Tang et al. 2003, 2007).

Therefore, the carbon monoxide is released rapidly, it will cause the soil violently disturbed, the soil and water loss. It is easy to cause quicksand, piping and soil collapse.

4 Analysis of the Carbon Monoxide Released Law Caused by Shield Construction in Shallow Stratum

It studies the carbon monoxide released law during shield construction, including the dynamic (the construction), the static (the stop construction). This paper has significant referential function to the tunneling engineering disaster prevention.

4.1 Dynamic Analysis

The six monitoring points such as trolley 5# (monitoring point 5), trolley 4# (monitoring point 4), trolley 3# (monitoring point 3), trolley 2# (monitoring point 2), trolley 1# (monitoring point 1), shield tail (monitoring point 0), segment 50R, segment 160R and segment 200R were set in the tunnel. Because the carbon monoxide of gas bearing formation mainly is released from shield head to screw conveyor in the process of excavated. This is the main way to enter the tunnel, which is the real factor to reflect soil deformation and carbon monoxide released law. Industrial Scientific M40 gas detector was used to monitor the carbon monoxide released for 24 h. In this study, the left tunnel was selected in mileage of Z9 + 010– Z8 + 890. Test data are monitored at 8'oclock everyday for 17 days, from December 11 to 27.

Figure 1a shows the carbon monoxide released law from shield tail to trolley 5#. Figure 1b shows the carbon monoxide released law from segment 50R to 200R. As seen, the released volume concentration of carbon monoxide was relatively high from shield tail to trolley 5#, but it was very low from segment 50R to segment 200R. The released volume concentration of carbon monoxide from shield tail

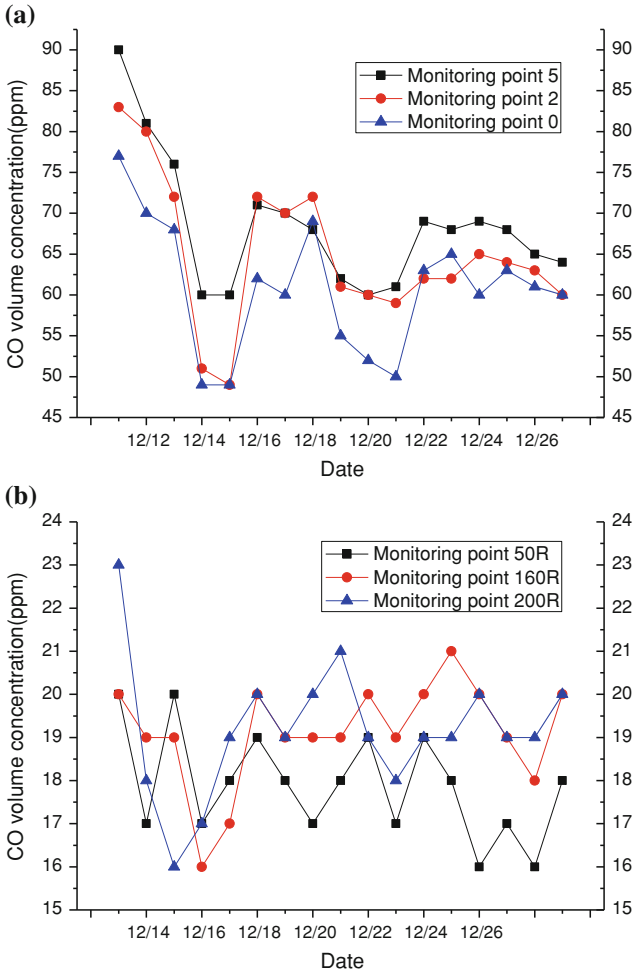

Fig. 1 Carbon monoxide released law under dynamic conditions

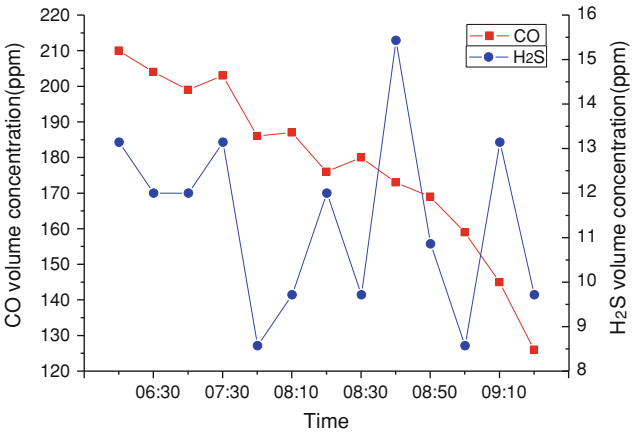

Fig. 2 Gas released law of the internal soil chamber under static conditions

to trolley 5# was gradually decreased, and experienced five steps, namely, the high steps, the low steps, the high steps, the low steps, the high steps. The released volume concentration of carbon monoxide is at 49–76 ppm. The maximum is the monitoring site 5 being 76 ppm and the minimum, monitoring site 0 being 49 ppm. Therefore, the released volume concentration of carbon monoxide is much larger than the normal (35 ppm). The released volume concentration of carbon monoxide from segment 50R to segment 200R was less than 23 ppm, and experienced five steps, namely, the high steps, the low steps, the high steps, the low steps, the high steps. It was gradually decreased from segment 200R to 50R. The monitoring site 5 is the excavation point, its released volume concentration were most, and experienced in different stages. This is because the carbon monoxide of gas bearing formation mainly is released from shield head to screw conveyor in the process of excavated, and its re-gather may have effect on it.

4.2 Static Analysis

The gas released law of the internal soil chamber [carbon monoxide, hydrogen sulfide (H_2S)] is divided into 13 time segments from 6:00 to 9:20 (see Fig. 2). Meanwhile, the carbon monoxide released law of the external soil chamber is monitored at 8'oclock by using the monitoring sites 5, 4, 3, 2, 1, L, 0 (see Fig. 3).

The released volume concentration of carbon monoxide, hydrogen sulfide is large, but the former is significantly larger than the latter. The released volume concentration of carbon monoxide is at 126–210 ppm, and had successively suffered two developing stages of high and low in the process of shield construction. The maximum difference volume concentration is 84 ppm. The released volume concentration of carbon monoxide is much larger than the normal (35 ppm) (see Fig. 2). It shows that the rapid release, the slow release, the released volume concentration, and the pressure of gas bearing formation may have effect on soil deformation in the process of shield construction. The released volume concentration of hydrogen sulfide is at 9–15 ppm, and had successively suffered four stages of high, low, high and low in the process of shield construction. The volume concentration is much larger than the normal (10 ppm), 85 % of the volume concentration is greater than10 ppm (see Fig. 3). On the contrary, the released volume concentration of the external soil chamber is at 20–30 ppm (see Fig. 3). It shows that the shield construction has great influence on the carbon monoxide release. The released volume concentration of carbon monoxide for internal soil chamber is large under static conditions, while the position of shield, trolley and tunnel has little effect on it.

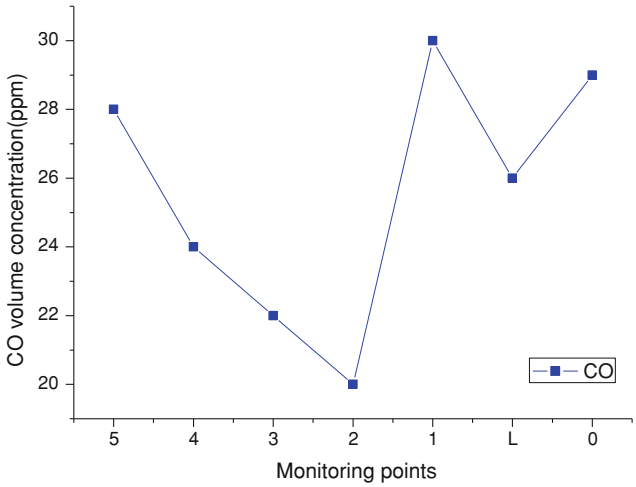

Fig. 3 Carbon monoxide released law of the external soil chamber under static conditions

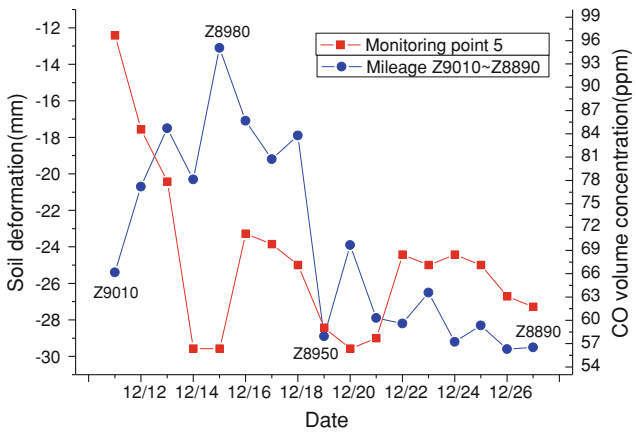

Fig. 4 Soil deformation and carbon monoxide released law caused by shield construction

5 Discussion

It is interesting to note that the relationship between the released volume concentration of carbon monoxide and the soil deformation. In this study, the monitoring site 5 was selected in mileage of Z9 + 010–Z8 + 890 by using the test data from December 11 to 27 (see Fig. 4). As seen, the released volume concentration of carbon monoxide is at 60–81 ppm during shield construction. When the maximum soil deformation is the monitoring site of Z8 + 895, being −29.5 mm, the released volume concentration of carbon monoxide is 65 ppm. When the minimum soil deformation is the monitoring site of Z8 + 980, being −13.1 mm, the released volume concentration of carbon monoxide is 60 ppm. 71 % of the soil deformation is −20 to −30 mm, 77 % of the released volume concentration of carbon monoxide is 60–80 ppm. In mileage of Z9 + 010–Z8 + 980, the soil deformation had successively suffered two developing stages of high and low. At this time, the released volume concentration of carbon monoxide was changed from 90 to 60 ppm, and it also had successively suffered two developing stages of high and low. It shows that the carbon monoxide had experienced two steps, namely, the rapid release, the slow release. The rapid release of carbon monoxide has a greater influence on the soil deformation compared with the slow release.

In mileage of Z8 + 980–Z8 + 950, the soil deformation increases rapidly, but the released volume concentration of carbon monoxide decreases gradually from high to low. It shows that the pressure of gas bearing formation, the slow release of carbon monoxide also has a greater influence on it. In mileage of Z8 + 950–Z8 + 890, the soil deformation present the trend of slow growth. When the soil deformation reached the maximum, and it has remained basically stable, the released volume concentration of carbon monoxide is basically stable from high to low. It shows that except for the elastic deformation, the plastic deformation is known in the process of carbon monoxide released with little deformation. In a word, the soil deformation had generally experienced three steps, namely, the high steps, the slow steps, the high steps. At this time, the released volume concentration of carbon monoxide also had successively suffered four developing stages of high, low, high and low. It shows that the maximum soil deformation is the medial axis, and the velocity of the carbon monoxide releasing directly affects it. Because soil contains a carbon monoxide, the squeezing properties of the soil was increased. Meanwhile, it destroys the framework structure of the soil. The stress concentration caused by the disturbance of shield construction in a carbon monoxide layer is an important cause that reduces the shear strength of soil. In the case of high pressure, the strong soil erosion is mainly related to the fast release of carbon monoxide. It is easy to cause soil deformation.

6 Conclusions

(1) The rapid release of carbon monoxide has a greater influence on the soil deformation compared with the slow release. Except for the elastic deformation, the plastic deformation is known in the process of carbon monoxide released with little deformation. The maximum soil deformation is the medial axis. The released volume concentration of carbon monoxide is at 60–81 ppm.

(2) It is suggested that the shield construction has great influence on the carbon monoxide release. The released volume concentration of carbon monoxide was relatively high from shield tail to trolley 5# under dynamic conditions. The carbon monoxide of gas bearing formation mainly is

released from shield head to screw conveyor in the process of excavated, and its re-gather may have effect on it. The released volume concentration of carbon monoxide for internal soil chamber is large under static conditions, while the position of shield, trolley and tunnel has little effect on it.

(3) The rapid release, the slow release, the released volume concentration, and the pressure of gas bearing formation were main influencing factors of soil deformation causing by carbon monoxide released.

(4) It is suggested that the closed water pore, the dual connected pore, the closed gas pore and the confined saturation zone is the main hazard factor of soil deformation causing by carbon monoxide released.

Acknowledgments The research work described herein is supported by the National Natural Science Foundation of China (No. 41072205, No.50579097), the Shanghai Natural Science Foundation of China (No. 10ZR1431500).

References

Ding, L., Ma, L., Luo, H., Yu, M., & Wu, X. (2011). Wavelet analysis for tunneling-induced ground settlement based on a stochastic model. *Tunnelling and Underground Space Technology, 26*, 619–628.

Gebhardt, S., Fleige, H., & Horn, R. (2009). Effect of compaction on pore functions of soils in a Saalean moraine landscape in North Germany. *Journal of Plant Nutrition and Soil Science, 172*, 688–695.

Juneja, A., Hegde, A., & Lee, F. H. (2010). Centrifuge modelling of tunnel face reinforcement using forepoling. *Tunnelling and Underground Space Technology, 25*(4), 377–381.

Karakus, M. (2007). Appraising the methods accounting for 3D tunnelling effects in 2D plane strain FE analysis. *Tunnelling and Underground Space Technology, 22*, 47–56.

Leonid, A., Valeriy, N. (1996). Main principles on analysis and design of buried ballasted pipelines on marshes. In *Proceedings of the International Pipeline Conference,* IPC (pp. 637–642).

Nagao, M., Takatori, T., Oono, T., Iwase, H., Iwadate, K., Yamada, Y., et al. (1997). Death due to a methane gas explosion in a tunnel on urban reclaimed land. *American Journal of Forensic Medicine & Pathology, 18*, 135–139.

Nomoto, T., Imamura, S., Hagiwara, T., Hagiwara, T., Kusakabe, O., & Fujii, N. (1999). Shield tunnel construction in centrifuge. *Journal of Geotechnical and Geoenvironmental Engineering, 125*(4), 289–300.

Peck, R. B. (1969). Deep excavations and tunnelling in soft ground. In *Proceedings of 7th International Conference on Soil Mechanics and Foundation Engineering* (pp. 225–290). Mexico City.

Rodríguez, R., & Lombardía, C. (2010). Analysis of methane emissions in a tunnel excavated through carboniferous strata based on underground coal mining experience. *Tunnelling and Underground Space Technology, 25*, 456–468.

Santos, O. J., & Celestino, T. B. (2008). Artificial neural networks analysis of Sao Paulo subway tunnel settlement data. *Tunnelling and Underground Space Technology, 23*, 481–491.

Singh, R., Senthil Kumar, J., Zlotnicki, J., & Kafatos, M. (2010). Satellite detection of carbon monoxide emission prior to the Gujarat earthquake of 26 January 2001. *Applied Geochemistry, 25*, 580–585.

Tang, Y., Ye, W., & Huang, Y. (2003). Marsh gas in shallow soils and safety measures for tunnel construction. *Engineering Geology, 67*, 373–378.

Tang, Y., Zhou, N., Wang, J., & Yan, X. (2007). Soft soil environment engineering geology (pp. 192–214). Beijing: China Communications Press (in Chinese).

Numerical Simulation of Seismic Responses of Asymmetric-Plan Reinforced Concrete Frame With Brbs

H. J. Sun and C. X. Li

Abstract

As a kind of prospective energy dissipation and vibration reduction component, buckling-restrained brace (BRB) overcomes the buckling characteristics of conventional braces. When subjected to the frequent earthquakes, the BRBs are in elastic state, providing the stiffness for the main structure; when subjected to the rare earthquakes, they are in elasto-plastic state in the structure, providing the energy-dissipation capacity. This paper presents a 6-story reinforced concrete asymmetric frame with BRBs. The comparison of the seismic effects of the retrofitted structure using response spectra analysis and time history analysis under the frequent earthquakes proves that the model is reasonable. And we compare the drift ratio between frame with and without BRBs using time history under rare earthquakes. The results show that the BRBs can effectively control the structure under the action of earthquakes. And force-displacement relationship of BRB is perfect. In addition, the results of nonlinear analyses will be use in the test of BRB and the structure design.

Keywords

Asymmetric-plan reinforced concrete frame • Buckling-restrained brace • Seismic analysis

1 Introduction

The earthquake is one of the main natural disasters which threats the safety of life and property of human. In order to mitigate the earthquake disasters, many scholars devoted to the research of enhancing the seismic performance of structure. The traditional seismic method is using the structure itself to resist the earthquake effects. But the structure will not meet seismic requirements in the sudden earthquake possibly, it is necessary for people to improve the lateral stiffness of the structure. In order to meet different degree of seismic requirements, more and more seismic design methods which dissipate earthquake energy with the nonstructural components are being applied in practice.

The buckling-restrained brace (BRB) is a kind of prospective energy dissipation and vibration reduction component, which has been widely used in recent years. It shows the same hysteretic performance and good capability of energy consumption when it sustains tension and compression. It can be yielded firstly under severe earthquake, then use the hysteretic behavior to consume earthquake energy, to protect the structure. This paper takes a reinforced concrete irregular frame with BRBs as an example to analyze the seismic response, which is based on ABAQUS software.

2 Description of the Project

This project is a school building which built in 1980s. It has six stories (seven stories locally), the height of the bottom storey is 4.5 m, the others are 3.6 m. The maximum

H. J. Sun (✉) · C. X. Li
Department of Civil Engineering, Shanghai University, 149 Yanchang Road, Zhabei, Shanghai 200072, China
e-mail: hjsuncivil@163.com

Y. Huang et al. (eds.), *New Frontiers in Engineering Geology and the Environment*,
DOI: 10.1007/978-3-642-31671-5_42,

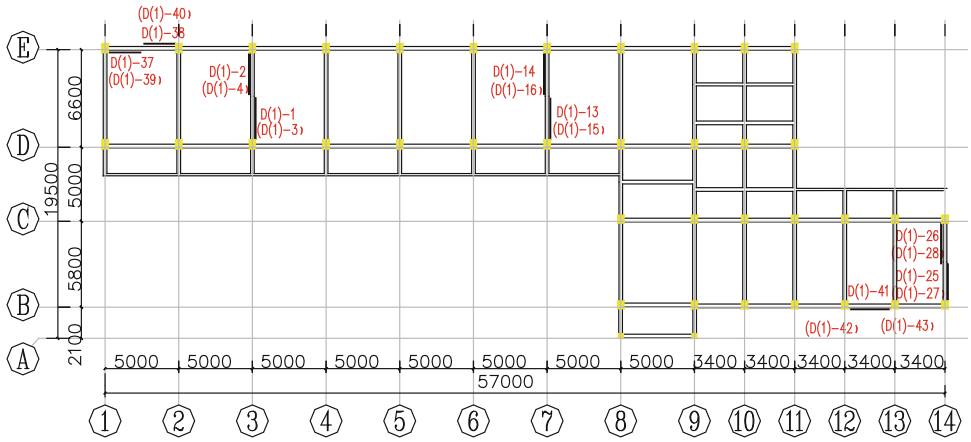

Fig. 1 Arrangement plan of BRBs

dimension in east–west is 57 m,and 19.5 m is the maximum dimension in north–south. The length outstanding plane locally is greater than the width and 30% of the total length, so according to the Chinese code (2010), it is called as asymmetric structure in plan. It is a reinforced concrete frame with precast floor slabs. The concrete strength of beams and column is 27.2 MPa, 22.3 MPa. The reinforcement is HRB335. The thickness of slab is 100 mm. The arrangement plan of BRB is in Fig. 1.

3 Three Dimensional Finite Element Model

ABAQUS was used to build finite element model and performed linear and nonlinear dynamic time history analyses. The beams and columns were modeled using a second-order 3D Timoshenko beam element (B32). The linear, reduced-integration, quadrilateral shell element (S4R) was used to model slabs. 3D truss element was employed to model the BRBs. We used *rebar to model each reinforcement bar separately in beams and columns. The connection between the structure and its foundation is treated to be fixed. Finally, the analysis modal is comprised of 4223 elements and 6727 nodes in all. According to Chinese code, the representative value of the gravity load of school building is taken as the sum of dead load and half of live load, and it is 44048.854KN.

4 Dynamic Characteristics of School Building

The Lanczos method is adopted to calculate the natural frequencies and mode shapes of school building in modal analysis. The periods of the building with BRBs and without BRBs are summarized in Table 1. Evidently, the period of the building with BRBs is smaller than the without one, it indicates that the stiffness of the building which was retrofitted is increasing. Mode 1 and mode 2 are two orthogonal translational modes. Mode 3 is the fundamental torsion mode. The ratio of the first torsion period to the first translational period is equal to 0.926612/1.24375 = 0.745, thus less than the code requirement, i.e., a minimum of 0.9.

5 Response Spectrum Analysis

The school building is located in Anqing, Anhui, where the seismic fortification intensity is 7°, the design basic accelerations of ground motion is 0.10 g, the design earthquake group is the group 1 and the construction field belongs to Site-class II.

In this study, the maximum of effect coefficient of horizontal earthquake under frequent earthquakes is 0.08; the feature period of the site is 0.3 s (2009); the damping ratio which concerns BRBs is assumed to be 0.045. The first 12 vibration modes are used to calculate the seismic responses of school building by the Complete Quadratic Combination rule on the basis of the response spectrum analysis. In the analysis, the seismic responses subjected to one horizontal ground motion component, two horizontal ground motion components, and two horizontal and one vertical ground motion components, respectively, are calculated accordingly. Table 2 presents the base shears and shear factors.

It is seen from Table 2 that the minimum of the shear factors is equal to 0.02822, which is greater than 0.016 and meets the code requirements. Likewise, the effect of vertical seismic action is generally little.

From Figs. 2 and 3, the results obtained using the response spectrum analysis indicate that the translational displacement of structure increases with the story increased, and it is shear deformation. The maximum drift ratio is equal to 1/1000 under the frequent earthquake, with

Table 1 The periods of structure

Period (s)	Without BRBs	With BRBs
T1	1.362897	1.243750
T2	1.261042	1.013654
T3	1.203916	0.926612

Table 2 Base shears and shear factors obtained using the response spectrum method

Condition	Base shears		Shear factors	
	Fx (kN)	Fy(kN)	X-direction	Y-direction
One horizontal ground motion component	1243.063	1428.272	0.02822	0.032425
Two horizontal ground motion components	1243.279	1428.46	0.028225	0.032429
Two horizontal and one vertical ground motion components	1243.28	1428.475	0.028225	0.032429

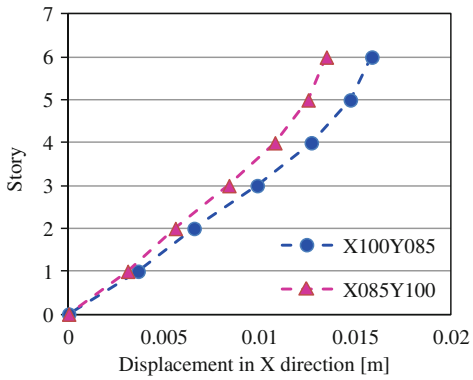

Fig. 2 X/Y translational displacements

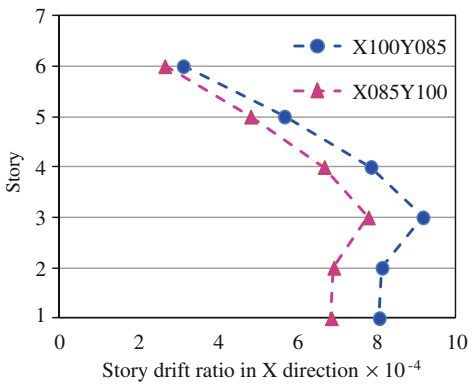

Fig. 3 X/Y inter-storey drift ratios

occurring at the 3 story, is less than the code requirement, i.e., a maximum of 1/550, which effectively means that the lateral stiffness is reasonable.

6 Dynamic Time-History Analysis

The response spectrum analysis conducted previously only considered the maximum amplitude of seismic effects, while the dynamic analysis in the time domain may provide more information for earthquake-resistant designs of structures. In the elastic time-history analysis, two recorded earthquake ground motions (PEER Strong Motion Database 2000): three components of the 1940 El-Centro Earthquake and three components of the 1952 Taft Earthquake. Likewise, one artificial earthquake ground motions is generated for the Anhui area with a probability of exceedance of 10% in 50 years, called RG. For each earthquake ground motion, the magnitude of the ground acceleration was scaled in the present analyses. The scaled ground accelerations have the peak ground accelerations (PGA) of 35 gal. The earthquake function duration is not less than 5–10 times the basic cycle of structure (T = 1.263096 s), so we take 15 s. Two orthogonal earthquake ground motions were inputted according to1:0.85, and the vertical earthquake ground motion was 0.65.

The obtained base shear forces from the elastic time-history method and response spectrum method are shown in Table 4. In the table, the RSM is short for the response spectrum method, the DTM is for the elastic dynamic time-history method, and the ADTM is for the average values of elastic dynamic time-history method.

It can be calculated from Table 3 that the obtained base shear force from each time-history curve is not less than 65% of that from the response spectrum method; the average value from the three time-history curves is not less than 80% of that from the response spectrum method. It is shown that the base shear force of the response spectrum method is a little greater than the average value of the time-history calculation results. Therefore, the response spectrum method is adopted for seismic calculation.

The materials of the finite element model were changed into elasto-plastic materials. The isotropic bilinear kinematics hardening model was used for reinforcement and

Table 3 Obtained base shears using both the dynamic time-history methodand response spectrum method

Earthquake	Base shear F_x (kN)			Base shear F_y (kN)		
	DTM	ADTM	RSM	DTM	ADTM	RSM
El-Centro	1122.0			1722.8		
Taft	1218.8	1234.2	1243.3	1262.4	1528.2	1614.4
RG	1361.7			1599.5		

Table 4 Properties of the steel

Steel grade	Yield stress (MPa)	Ultimate stress (Mpa)	Ultimate plastic strain	Modulus of elasticity (MPa)
HRB335	335	475	0.025	2.1E+5
Q235	235	340	0.025	2.1E+5

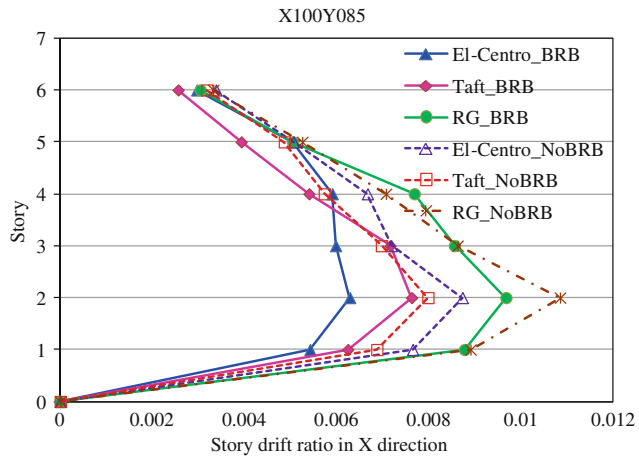

Fig. 4 Inter-storey drift ratios

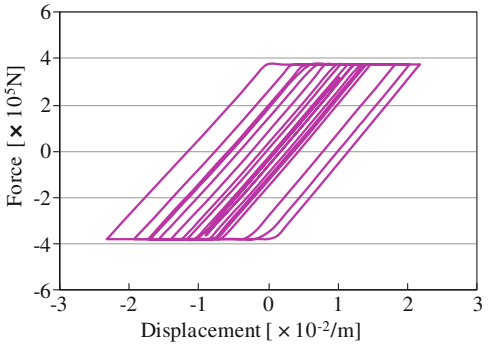

Fig. 5 Force-displacement relationship of BRB

BRB, in which Bauschinger effect was considered. The ultimate plastic strain corresponding to the ultimate stress was considered as 0.025. Check Table 4 for details.

Since there was no proper concrete material model available for B32 element in current ABAQUS edition, a user material subroutine was brought from the book(Lu et al. 2009). This user material(Qu 2011) uses the uniaxial concrete constitutive modal proposed by McKenna, and it is same to the Concrete02 model of Open SEES.

The damping ratio which concerns BRBs is assumed to be 0.05 in elasto-plastic dynamic time-history analysis. For each earthquake ground motion, the scaled ground accelerations have the peak ground accelerations (PGA) of 220 gal. In order to ensure that the nonlinear dynamic analysis is stable and converged, the biggest calculation time step takes 0.002 s. Likewise, P-Δ effect and large displacement are also taken into account.

Figure 4 shows the inter-story drift ratios of the structure with and without BRBs under the action of three seismic waves. We can see that the maximum drift ratios of the structure without BRBs decreased after it was retrofitted, and the maximum meets the allowable value 1/50 of Chinese code .

Take force–displacement relationship of a BRB under El-Centro in elasto-plastic dynamic time-history analysis for example, the hysteretic lop of energy consumption is perfect. It means that the BRBs work for energy dissipation very well (Fig. 5).

7 Conclusions

A 3D finite element model of the structure is established using the selected finite element types for the structural members. Detailed investigations on the dynamic characteristics and seismic responses of school building are carried out. The maximum story drift ratio of structure without BRBs was emerged in fourth story, while it decreased obviously after retrofitted. The simulation results of this research have demonstrated that it is able to guarantee the structural safety under seismic actions with the seismic fortification, as stipulated in the Chinese code for seismic design of buildings. In the elasto-plastic stage, the hysteretic curve is full. It means that BRB consumed energy very well. The conclusion of the research can be applied to the test of BRB and the structure design.

References

National Standard of the People's Republic of China. (2010). *Code for seismic design of buildings*. Beijing: China Architecture & Building Press.

National Standard of the People's Republic of China. (2009). *Standard for seismic appraisal of buildings*. Beijing: China Architecture & Building Press.

PEER Strong Motion Database. (2000). Regents of the University of California. Accessed September 12, 2011: http://peer.berkeley.edu/smcat/search.html

Lu, X. Z., Ye, L. P., Liao, Z. W. (2009). Elasto-plastic analysis of buildings against earthquake—theory, model and implementation on ABAQUS, MSC.MARC and SAP2000. Beijing: China Architecture & Building Press.

Qu, Z. (2011). PQFiber_Manual_v1.6. Accessed September 15, 2011: http://www.quzhe.net/PQFiber.htm

Seismic Analysis of Geosynthetic-Reinforced Quay-Wall Structure

J. F. Lu, B. Ye, and J. Nagaya

Abstract
A new kind of quay-wall structure using geosynthetics has been proposed for renovating existing sheet-pile quay-wall structures to increase their earthquake resistance capability. The proposed structure adopts the combined techniques of stabilized soil and geogrid for a quay wall, which is referred to simply as an 'SG-WALL'. This paper presented a numerical comparison study on quay-wall structures improved by SG-WALL method and the traditional anchor-pile reinforced method. The analysis results showed that SG-WALL method has a better effect to improve the seismic performance of a quay-wall structure than the traditional anchor-pile improvement method.

Keywords
Geogrid • Geosynthetics • Numerical simulation • Quay wall

1 Introduction

Sheet-pile quay wall structures with anchor piles, as show in Fig. 1, are widely used for port construction. During the 1995 Hyogo-ken Nanbu Earthquake in Japan, many quay-wall structures were damaged due to the strong ground motion (Kamon et al. 1996). To improve the earthquake resistance of port structures, a new technology for renovating existing sheet-pile quay-wall structures using geosynthetics has been proposed, as shown in Fig. 2. The proposed technology adopts the combined techniques of stabilized soil and geogrid for a quay wall (hereafter referred to simply as an SG-WALL). The stabilized soil is made of clay with cement additives, and the geogrid is made from polypropylene materials. Using SG-WALL technology, sheet-piles are supported by a combination of the geogrid and the stabilized soil instead of the anchor piles.

To investigate the seismic improvement effect of SG-WALL structure, comparison analyses were performed on quay-structures improved by SG-WALL method and the traditional anchor-pile method.

2 Description of the Simulated Quay-Wall Structures

Figure 3 shows the original quay-wall structure before improvement. It was a real structure that has been damaged during the 1995 Hyogo-ken Nanbu Earthquake. Two different improved plans were designed using the traditional anchor-pile method and SG-WALL technology respectively, as shown in Figs. 4 and 5. The two improvement designs have approximately the same construction cost. The simulation cases are shown in Table 1. The materials used in the design are listed in Table 2.

The input motion was Portland wave which was measured at Kobe during the 1995 Hyogo-ken Nanbu Earthquake. The acceleration wave is shown in Fig. 6.

J. F. Lu · B. Ye (✉)
Department of Geotechnical Engineering, Tongji University, Siping Road 1239, Shanghai 200092, People's Republic of China
e-mail: yebinmail1977@gmail.com

J. Nagaya
Engineering Department, Geo-Research Institute, 4-3-2 Itachibori Nishiku, Osaka 500-0012, Japan

Y. Huang et al. (eds.), *New Frontiers in Engineering Geology and the Environment*,
DOI: 10.1007/978-3-642-31671-5_43,

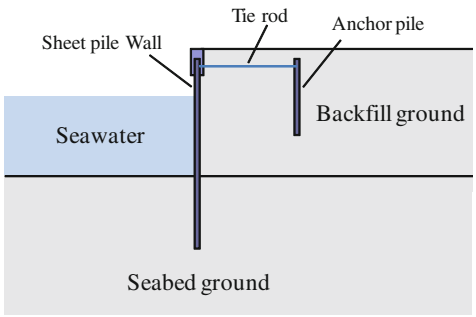

Fig. 1 Sheet-pile quay-wall with anchor piles

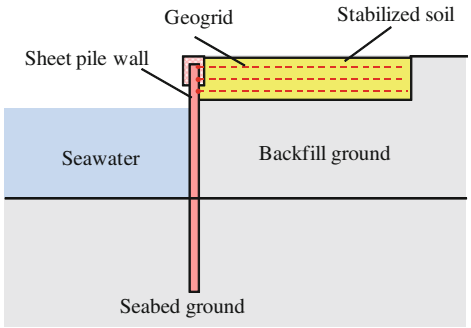

Fig. 2 SG-WALL structure

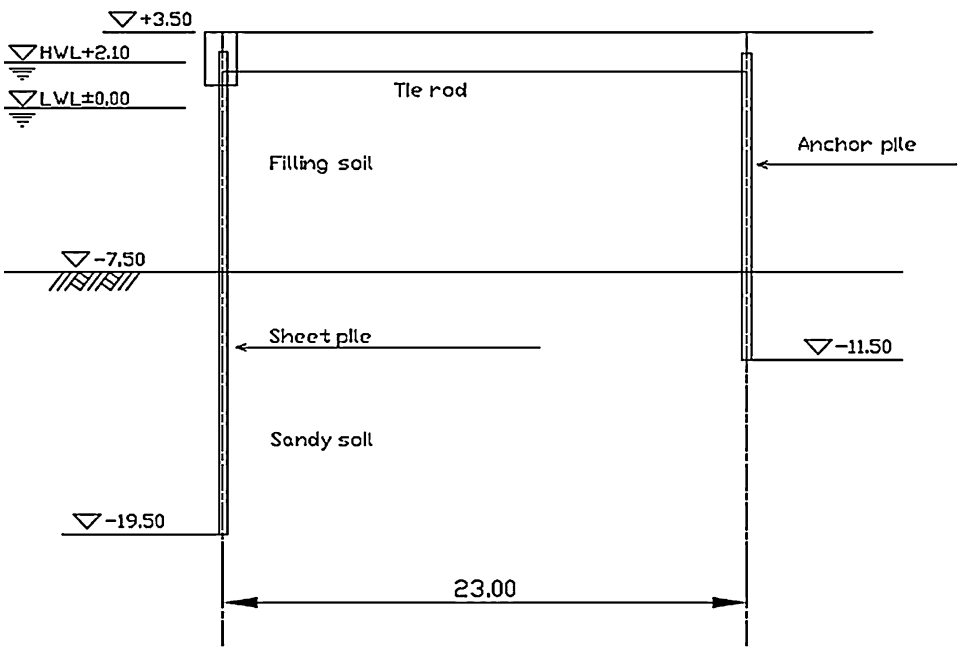

Fig. 3 The original quay-wall structure

3 Numerical Simulations

3.1 FEM Model

The numerical simulations were conducted using a FEM (Finite Element Method) program called FLIP, which has been widely used in design and analysis for port construction (e.g., Iai and Kameoka 1993, Iai et al. 1998). The FEM model of Case 3 is shown in Fig. 7. The FEM models of Cases 1&2 can be found in Fig. 8.

3.2 Modeling of Materials

3.2.1 Ground Soil

In the simulation, the ground soil was modeled by an elasto-plastic constitutive model proposed by Iai et al. (1992). Iai

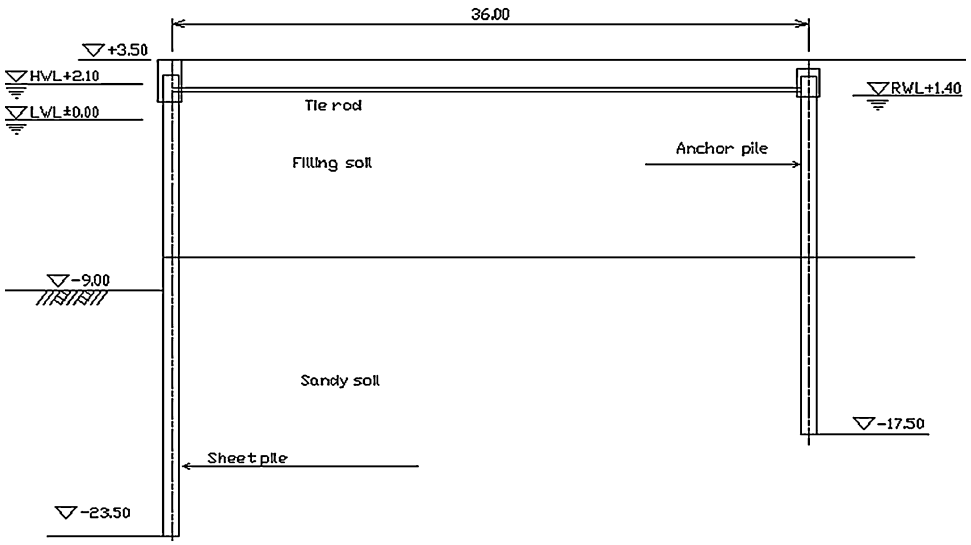

Fig. 4 The improved structure using traditional anchor-pile method

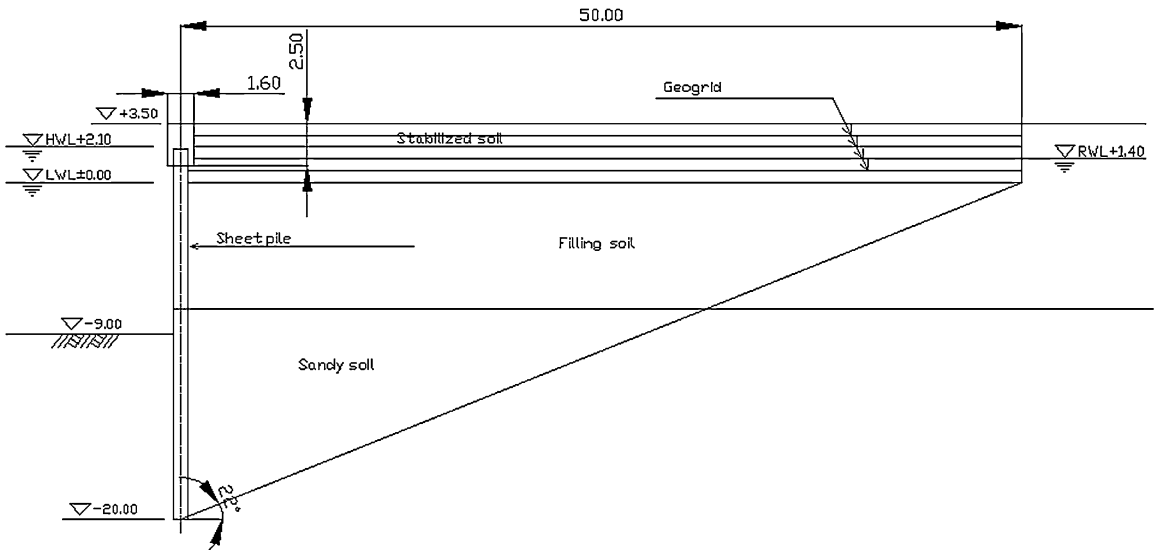

Fig. 5 The improved structure using SG-WALL method

Table 1 Analysis cases

Case 1	The original structure
Case 2	Renovation plan with anchor-piles
Case 3	Renovation plan using SG-WALL method

Table 2 Materials of the quay-wall structures

Material	Description
Stabilized soil	Kibushi clay with cement additive
Geogrid	Polypropylene grid
Sheet-pile wall	Steel pipe pile
Anchor pile	H-shaped steel pile and steel pipe pile
Tie rod	Steel bar of Φ55and Φ80

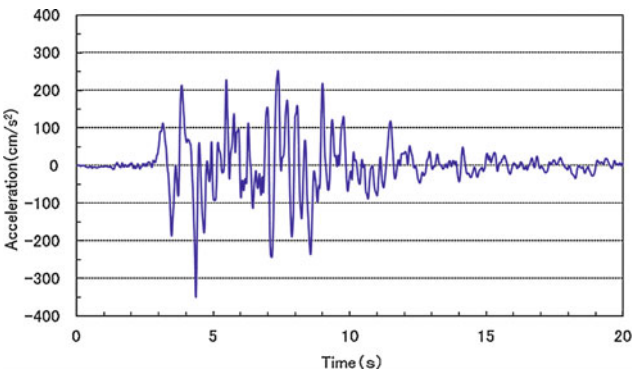

Fig. 6 The input Portland acceleration wave

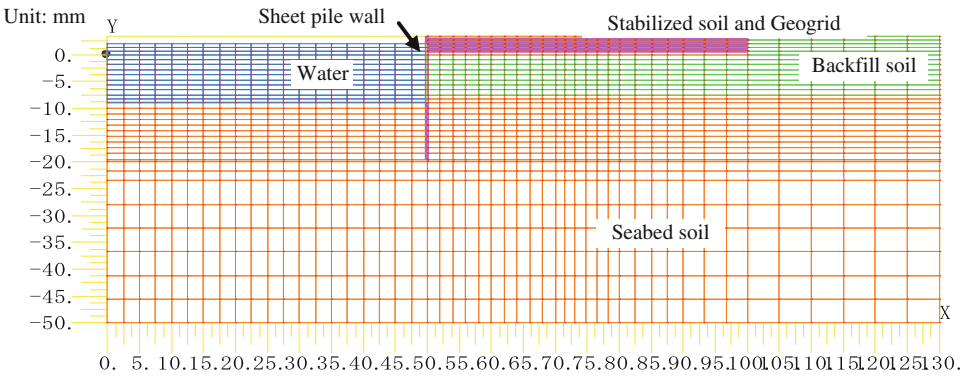

Fig. 7 FEM mesh of Case 3

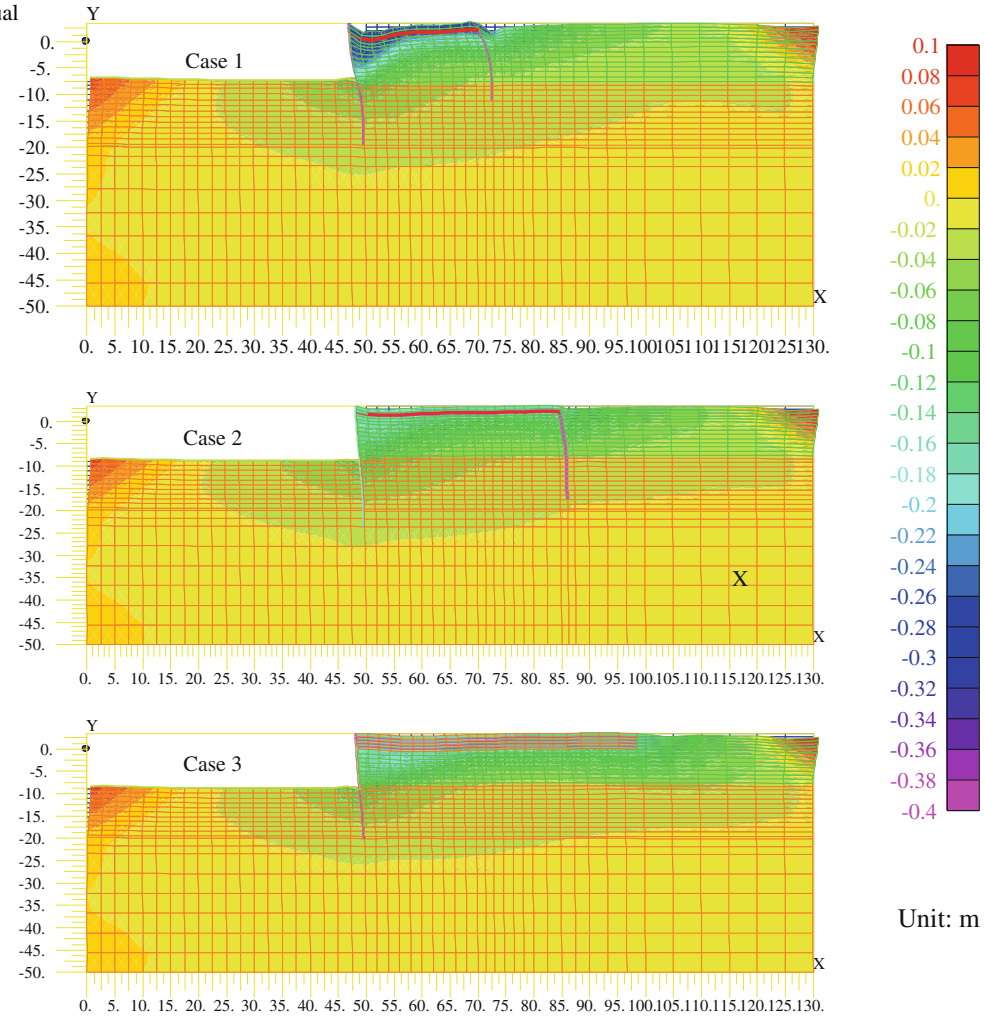

Fig. 8 Simulation results of residual deformation contour

et al. (1990) also provided an empirical method to determine the material parameters of the constitutive model. Using this method, the parameter values were determined and shown in Table 3.

3.2.2 Stabilized Soil

The previous study showed that the stabilized soil can be regard as a linear-elastic material within the range of its deformation (Ye et al. 2012). The material parameter values are shown in Table 4.

3.2.3 Geogrid

The geogrid was modeled as an elastic material with high tensile stiffness and very low compressive and flexural stiffness. The material parameters were converted to unit width, which are shown in Table 4.

Table 3 Material parameters of ground soil

Parameter	Value
Initial shear modulus, G_{ma} (kPa)	1.89×10^5
Bulk modulus, K_{ma} (kPa)	4.95×10^5
Normalized confining pressure, σ_{ma} (kPa)	98
Coefficient of confining pressure dependence, m	0.5
Density, ρ (g/cm^3)	1.8
Void ratio, n	0.45
Cohesion, c (kPa)	0
Shear resistance angle, φ_f (°)	43.31°
Poisson ratio, v	0.33

3.2.4 Other Material

Table 4 Material parameters of stabilized soil and geogrid

Parameter	Stabilized soil	Geogrid
Elasticity modulus, E (GPa)	3.0×10^4	2.46
Area of cross-section, A (m^2/m)	None	5.86×10^{-4}
Moment of inertia of cross-section, I (m^4/m)	None	1.95×10^{-12}
Density, ρ (g/cm^3)	1.4	0.34
Poison ratio, v	0.2	None

Table 5 Material parameters of other material

Material	Area of cross-section, A (m^2/m)	Moment of inertia of cross-section, I (m^4/m)
VL Sheet-pile in Case 1	2.67×10^{-2}	6.30×10^{-4}
Sheet-pile in Case 2	4.30×10^{-2}	5.26×10^{-3}
Sheet-pile in Case 3	4.35×10^{-2}	8.99×10^{-3}
Tie rod in Case 1	1.19×10^{-3}	2.24×10^{-7}
Tie rod in Case 2	2.35×10^{-3}	9.39×10^{-8}
Anchor pile in Case 1	1.11×10^{-2}	3.39×10^{-4}
Anchor pile in Case 2	3.7×10^{-2}	4.54×10^{-3}

The sheet pile and tie rod were modeled by a linear-elastic beam, and the material parameters value are shown in Table 5.

4 4 Analysis Results

The simulation results of the deformation contours after shaking are shown in Figs. 8, 9 demonstrates the horizontal displacement distributions of the sheet-piles along the elevation. By comparing the sheet-pile displacements in three cases, it can be seen that the improvement methods in Case 2 and Case 3 can reduce the displacement of the sheet-piles during earthquake. Moreover, the sheet-pile displacement in Case 3 is smaller than that in Case 2. This result confirms the seismic improvement effect of SG-WALL method.

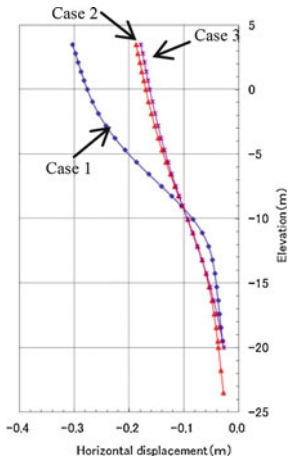

Fig. 9 Horizontal sheet-pile displacement along elevation

5 Conclusions

This paper presented a comparison analysis of two different renovation methods for quay-wall structure, i.e. the traditional anchor-pile method and the SG-WALL method. It was found that both improvement methods can reduce the seismic displacement of the quay-wall structures, but the SG-WALL method has a better improvement effect than the anchor-pile method.

Acknowledgments This work was supported by the Science Foundation of Key Laboratory of Engineering Geomechanics, Institute of Geology and Geophysics, Chinese Academy of Sciences (No. KLEG201108), the National Natural Science Foundation of China (Grant Nos. 41002094 and 41002097), and the Kwang-Hua Fund for College of Civil Engineering, Tongji University.

References

Iai, S., Matsunaga, Y., & Kameoka, T. (1990). Parameter identification for a cyclic mobility model. *Report of the Port and Harbour Research Institute, 29*(4), 57–83.

Iai, S., Matsunaga, Y., & Kameoka, T. (1992). Strain space plasticity model for cyclic mobility. *Soils and Foundations, 32*(2), 1–15.

Iai, S., & Kameoka, T. (1993). Finite element analysis of earthquake induced damage to anchored sheet pile quay-walls. *Soils and Foundations, 33*(1), 71–91.

Iai, S., Ichii, K., Liu, H., & Morita, T. (1998). Effective stress analyses of port structures. Soils and Foundations, Special issue on

geotechnical aspects of the January 17, 1995 Hyogoken–Nambu earthquake, pp. 97–114.

Kamon, M., Wako, T., Isemura, K., Sawa, K., Mimura, M., Tateyama, K., & Kobayashi, S. (1996). Geotechnical disasters on the waterfront. Soils and Foundations, Special issue on geotechnical aspects of the January 17, 1995 Hyogoken–Nambu earthquake, pp. 137–147.

Ye, B., Ye, G. L., Nagaya, J., & Sugano, T. (2012). Numerical simulation of shaking-table test on soil-stabilized, geosynthetic-reinforced quay-wall structures. *Geosynthetics International, 19*(1), 54–61.

Shape Effect on Active Earth Pressure Against a Sheet Pile Wall with Different Displacement Modes

F. Liu, G. Q. Zhang, M. J. Jiang, and H. Nakayama

Abstract

Steel sheet pile walls are widely used in coastal projects such as quay walls of ports. The corrugated shape of sheet piles could leads to a very different distribution of earth pressure in comparison with a planar retaining structure. Unfortunately such shape effect has not been fully understood and well quantified. This paper employed the finite element (FE) method to analyze the earth pressure distribution against a corrugated sheet pile wall. The FE model was first validated by numerically simulating a small-scale model test of a planar wall. The verified numerical model was then used to simulate a corrugated sheet pile wall and a planar wall subjected to pre-defined displacements away from the backfill. The results indicate that the sectional shape of the sheet piles affects the distribution of the transversal earth pressure against the wall. Little noticeable difference is found in the earth pressure at rest against the sheet pile wall and the planar wall, while prominent variation of the active earth pressure is found at the extruding portion and the dented portion when the wall translates or rotates.

Keywords

Steel sheet pile walls • Earth pressure • Shape effect • Retaining structures • Finite element

1 Introduction

Steel sheet pile walls are formed by sequentially connecting the joints of adjacent prefabricated steel sheet piles. They are widely used in coastal projects such as quay walls of ports in soft soils, partially attributed to their exceptional performance in space-saving and reusability.

The spatial distribution of the earth pressure against a sheet pile wall is critical for designing the wall. A few solutions were proposed for cantilever sheet pile walls and anchored or propped sheet pile walls based on the classic earth pressure theories derived from planar retaining structures, and they ignore the impact from the geometry of the pile profile (e.g., Kort 2002; Krabbenhoft et al. 2005; Zhai 2009). However, the actual earth pressure distributions along sheet pile walls could be rather different from that along planar retaining walls. For instance, DiBiagio (1977) reported the lateral earth pressure against a propped sheet pile wall was almost equal on the protruding and indented corrugations immediately after the installation of sheet piles, but later became different due to excavation. More recently, Tan and Paikowsky (2008) further confirmed the pressure difference between the inside and outside webs of sheet piles by conducting two-year field instrumentation.

The corrugated shape of sheet piles could leads to a distribution of earth pressure quite different from that against planar retaining structures. However such shape

F. Liu (✉) · G. Q. Zhang · M. J. Jiang
Department of Geotechnical Engineering, Tongji University, 1239 Siping Road, Shanghai 200092, China
e-mail: liufang@tongji.edu.cn

Key Laboratory of Geotechnical and Underground Engineering, Tongji University, Ministry of Education, 1239 Siping Road, Shanghai 200092, China

H. Nakayama
Nippon Steel Corporation, 20-1 Shintomi Futtsu, Chiba 293-8511, Japan

Y. Huang et al. (eds.), *New Frontiers in Engineering Geology and the Environment*,
DOI: 10.1007/978-3-642-31671-5_44,

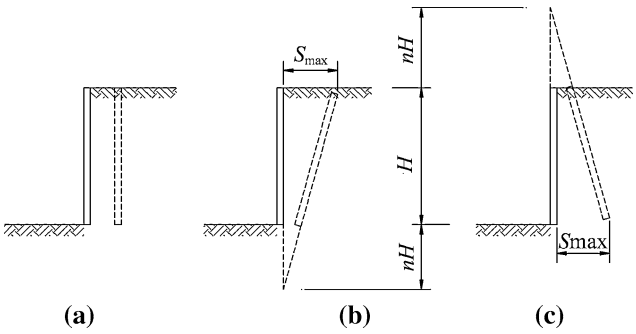

Fig. 1 Passive wall movements. **a** T mode. **b** RB mode. **c** RT mode

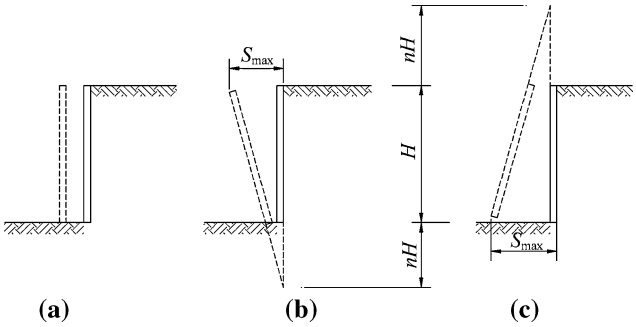

Fig. 2 Active wall movements. **a** T mode. **b** RB mode. **c** RT mode

effect remains unclear and hard to be quantified. This paper aims to investigate the impact of the corrugated profile of a typical sheet pile wall on the active earth pressure against the wall with the aid of numerical testing approaches. A finite element (FE) model was first validated through conducting a numerical simulation of a previous model test of a small-scale retaining wall. The verified model was then used to simulate a steel sheet pile wall and a planar wall displaced away from the backfill.

2 Model Validation

Fang et al. (1994) carried out a small-scale test on the passive earth pressure against a rigid retaining wall subjected to a variety of wall displacements. Air-dry Ottawa sand was placed in a 200 cm × 100 cm × 100 cm (length × width × height) soil container using the pluviation method, resulting in a unit weight of 15.5 kN/m^3 and an internal frictional angle of 30.9°. The movable wall was a steel plate embedded into the sand up to 50 cm. The wall-soil friction angle was 19.2°.

Figure 1 illustrates three displacement modes tested in the experiment: (1) translation (T mode); (2) rotation about a point below the wall base (RB mode); and (3) rotation about a point above the top (RT mode). In parallel, the wall can also

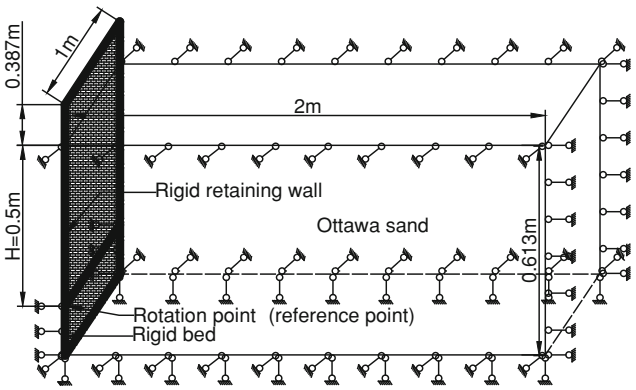

Fig. 3 FE model setup and boundary conditions

Table 1 Parameters in the numerical simulation

Wall-backfill frictional angle	Unit weight (kN/m^3)	Poisson ratio	Cohesion (kPa)	Friction angle	Young's modulus (MPa)
19.2°	15.5	0.30	0	30.9°	5

be displaced in the active modes as shown in Fig. 2. However Fang et al. (1994) only dealt with the passive state in their test.

Figure 3 shows the geometry and boundary conditions in the FE model used for simulating test conducted by Fang et al. (1994). The Mohr–Coulomb model was chosen for the backfill, and Table 1 tabulates the relevant model parameters. Contact pairs were set between the wall and the backfill.

Figure 4 compares the numerical results and testing results. The analytical solution based on Terzaghi earth pressure theory is superimposed in the figure for comparison. The distribution pattern of earth pressure distribution obtained from the FE simulation is in good agreement with experimental observation. It should be mentioned that the wall displacement required to mobilize the passive state is much smaller than that observed in the experiment. However the former falls into the range suggested in Brinch-Hansen (1953) and Matsuzawa and Hazarika (1996). Fang et al. (1994) also confirmed that their measurement could be impractical if the size of the wall was scaled up to a real problem.

3 Simulation of a Corrugated Sheet Pile Wall

The verified FE model was then employed to assess the performance of a simplified steel sheet pile wall formed by typical U-profile piles. The model dimension as illustrated in Fig. 3 was enlarged in order to simulate a wall with actual dimensions. Figure 5 illustrates the dimensions of the

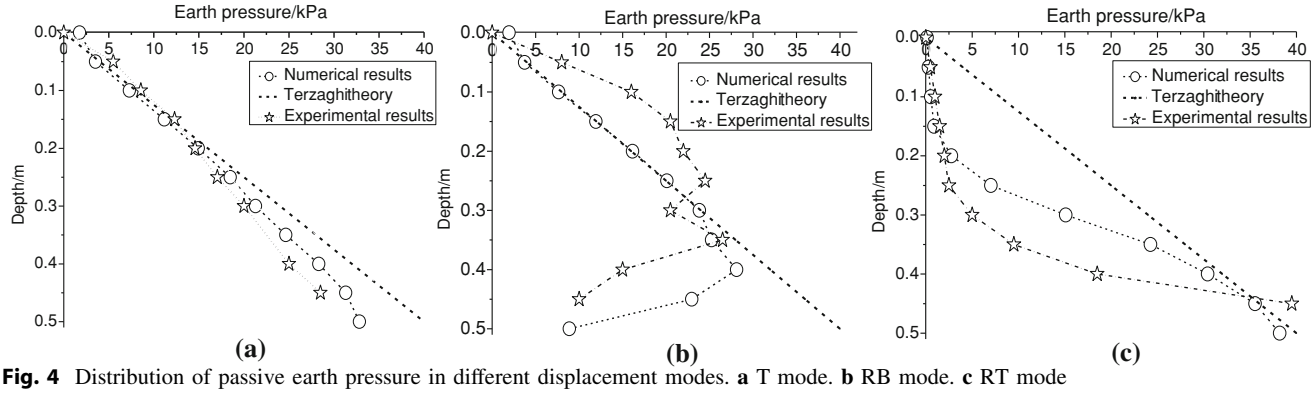

Fig. 4 Distribution of passive earth pressure in different displacement modes. **a** T mode. **b** RB mode. **c** RT mode

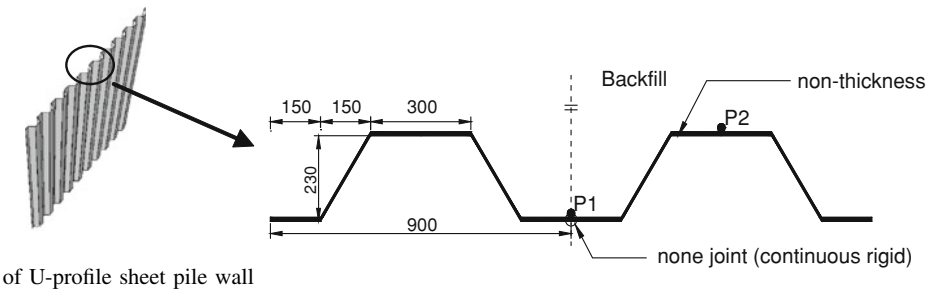

Fig. 5 Dimensions of U-profile sheet pile wall

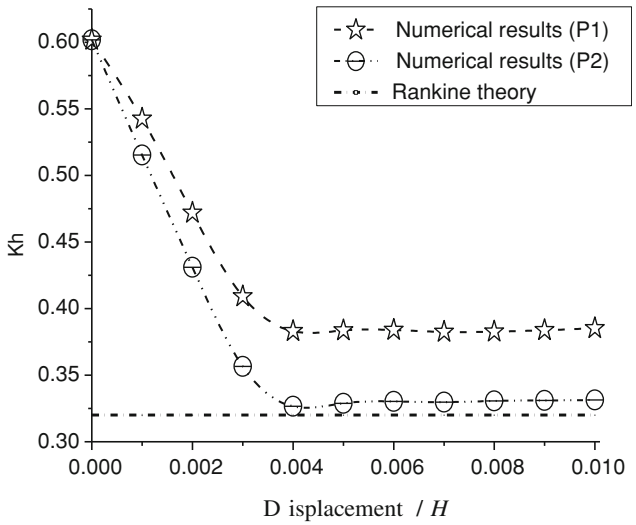

Fig. 6 Variation of K_h with wall displacement (P1 and P2 through the extruding portion and dented portion as shown in Fig. 5)

cross section of the wall, which are 12 m in height and 8.5 m in width consisting of nine U-profile steel sheet piles. The wall is assumed to be frictionless, non-thickness and rigid. The joints between piles are simplified as rigid connections in current model. The Young's Modulus of the backfill is 10 Mpa, and the rest of the model parameters remain the same as Table 1. For comparison a planar wall was also simulated in parallel.

4 Results

4.1 Translation Mode

Figure 6 illustrates relationship between the earth pressure coefficient K_h and the wall displacement when the wall is subjected to translational movement away from the backfill. K_h is defined as the ratio of the horizontal component of total thrust on a vertical slice to $\gamma H^2/2$, where γ and H is the unit weight of the backfill and the total height of the wall, respectively. K_h decreases with the wall displacement and approaches to the value calculated from Rankine's earth pressure theory when the wall displacement exceeds 0.4 % H. The total thrust at the slice through the extruding portion of the wall (i.e., P1 as shown in Fig. 5) is equal to the value at the slice through the dented portion of the wall (i.e., P2 as shown in Fig. 5) when the wall is at rest. However the total thrust varies at the two slices when the wall moves, and the variation is enlarged with the increase of the wall displacement. The active total thrust at the dented slice is in good agreement with the theoretical solution, however lower than the theoretical solution at the extruding slice.

Two horizontal planes were cut through the FE model at the depth of one-third and two-third of the wall height to examine the shape effect on the transversal earth pressure distribution. Figure 7 compares the transversal earth pressures obtained from the sheet pile wall and the planar wall. The two distribution curves superpose each other when the

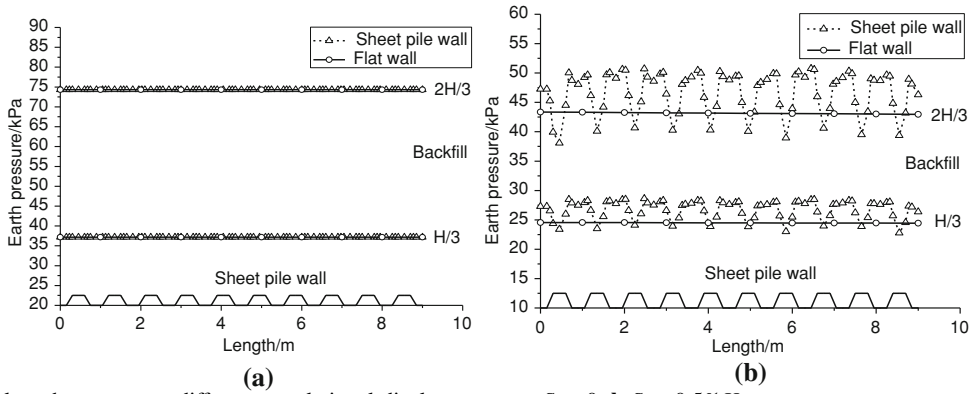

Fig. 7 Transversal earth pressure at different translational displacements. **a** $S = 0$. **b** $S = 0.5\%H$

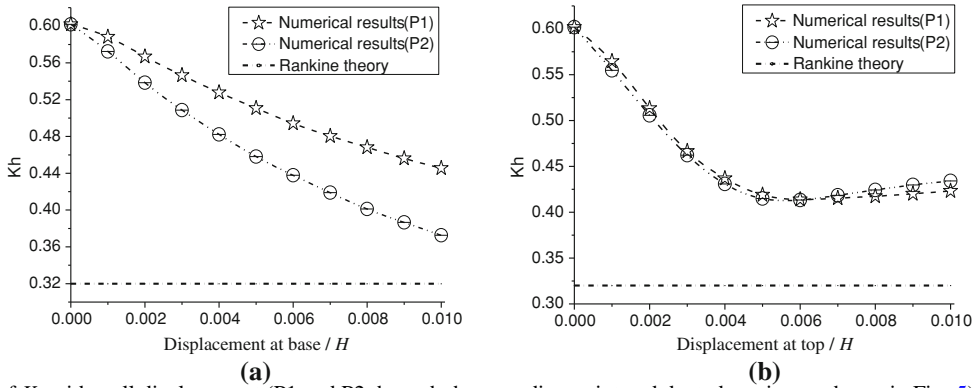

Fig. 8 Variation of K_h with wall displacement (P1 and P2 through the extruding point and dented portion as shown in Fig. 5). **a** RB mode, **b** RT mode

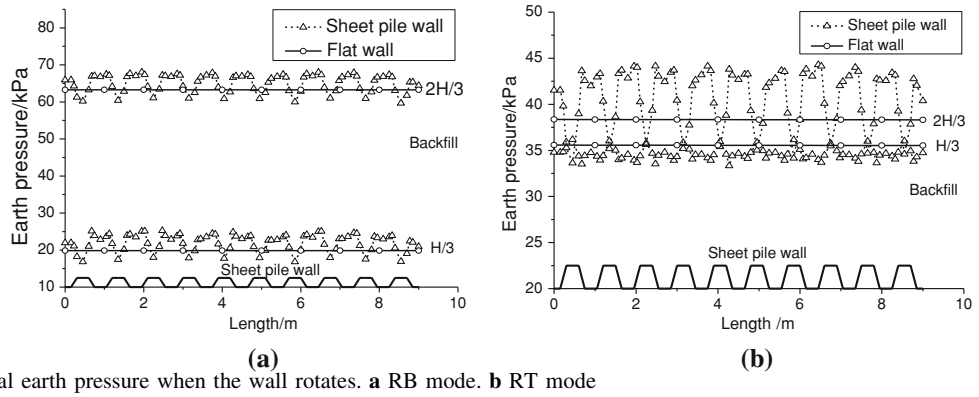

Fig. 9 Transversal earth pressure when the wall rotates. **a** RB mode. **b** RT mode

walls are at rest, while the distribution curve obtained from the sheet pile wall starts to vibrate up and down around the curve obtained from the planar wall when the wall displaces away from the backfill until the active earth pressure is mobilized. The amplitude of the vibration increases with increasing depth of the backfill.

4.2 Rotational Modes

Figure 8 illustrates the difference of K_h at the extruding portion and the dented portion of the sheet pile wall when the wall rotates around the base of the wall (RB mode) or around the top of the wall (i.e., RT mode). Similar to the T

mode as illustrated Fig. 6, pronounced difference in K_h is found at different vertical slices of the wall when the wall displaces in RB mode (see Fig. 8a), which however requires larger wall displacement to reach the active state (i.e., approximately 1 % H). On the contrary, K_h exhibits little difference at different slices for RT mode (see Fig. 8b).

Figure 9 compares the transversal earth pressures obtained from the sheet pile wall and the planar wall when the walls rotate. The earth pressure at the extruding portion is larger than that at the dented portion throughout the height of the wall in RB mode (see Fig. 9a). However the earth pressure at the extruding portion becomes lower than that at the dented portion in RT mode (see Fig. 9b) at the depth above one-third of the height of the wall, resulting in nearly equal value of K_h calculated from the vertical slices through the extruding portion and the dented portion of the wall.

5 Conclusions

This paper investigates the shape effect of a corrugated sheet pile wall on the active earth pressure against the wall using numerical tests. The major conclusions are as follows:

1. The corrugated shape of the wall has little noticeable effect on the earth pressure distribution when the wall is at rest.
2. The displacement of the wall mobilizes the variation of the transversal earth pressure against the corrugated wall. The geometry characteristics of the sheet pile wall could cause relative movement of the backfill adjacent to wall, resulting in soil arching and stress redistribution. This could be the reason causing different value of active earth pressure against the corrugated wall at the same depth.
3. The earth pressure acting on the extruding portion of the sheet pile wall is larger than that on the dented portion except in RT mode, and the deviation increases with the depth of the backfill and the displacement of the wall.

Acknowledgments The study is part of the collaboration project financially supported by Nippon Steel Corporation. Support from National Science Foundation of China (Grant No. 41102173) and Program for Changjiang Scholars and Innovative Research Team in University (PCSIRT, IRT1029) is also appreciated.

References

Brinch-Hansen, J. (1953). *Earth pressure calculation*. Copenhagen: Danish Technical Press.

DiBiagio, E. (1977). *Field instrumentation-a geotechnical tool* (vol. 115, pp. 29–40). Oslo: Norwegian Geotechnical Institute Publication.

Fang, Y. S., Chen, T. J., & Wu, B. F. (1994). Passive earth pressure with various wall movements. *Journal of Geotechnical Engineering, 120*(8), 1307–1323.

Kort, D. A. (2002). *Steel sheet pile walls in soft soils*. The Netherlands: Delft University of Technology.

Krabbenhoft, K., Damkilde, L., & Krabbenhoft, S. (2005). Ultimate limit state design of sheet pile walls by finite elements and nonlinear programming. *Computers and Structures, 83*, 383–393.

Matsuzawa, H., & Hazarika, H. (1996). Analyses of active earth pressure against rigid retaining walls subjected to different modes of movement. *Soils and Foundations, 36*(3), 51–65.

Tan, Y., & Paikowsky, S. G. (2008). Performance of sheet pile wall in peat. *Journal of Geotechnical and Geoenviromental Engineering, 4*, 445–458.

Zhai, E. (2009). *A comparison study of engineering approaches for seismic evaluation of anchored sheet pile walls. lifeline earthquake engineering in a multihazard environment*, pp. 1021–1030.

"Atlant" Anchor Pile Technology and Capacity Experimental Results

D. Malinin and A. Malinin

Abstract
In-situ tests and laboratory tests of "Atlant" anchor piles in comparison with other types of anchor piles are described in this article.

Keywords
Anchor • Pile • Drilling • In situ test • Laboratory test • Adhesion

1 Introduction

"Atlant" is a name of a type of anchor pile. It is based on using hollow high-strength drilling pipes. These drilling pipes are left in the borehole after drilling. The pipes play the role of pile reinforcing element or anchor bar. The bars are connected with each other by couplings with cone thread that provides high strength of connection in the surrounding cement stone.

2 In situ Tests

Some in situ tests were carried out to define "Atlant" anchor pile capacity. Underpinning works with the use of "Atlant" anchor piles were carried out by Construction Company InzhProektStroy in Yekaterinburg, Russia. 30 m long piles are constructed in clay with broken rock interlayer. The consistency of the clay varied from soft plastic to semi hard. Pile construction works were carried out in a basement. A bar Ø 73 mm (5.5 mm thickness) with smooth surface was used for these works. The bars of 1 m long each were connected with each other by couplings Ø 89 mm. Some in situ tests which included pile testing by pulling and jacking force were carried out before the works were started. The results of these tests are given in Table 1.

The in situ tests confirmed the possibility of using smooth surface bars to reach high capacity at jacking and pulling load. The maximum loads can be compared with the ultimate load at the yield point of steel.

The aim of another experiment was to compare "Atlant" anchors with "Titan" anchors. "Titan" anchors consist of hollow bars with rolled screw thread. During the reconstruction of intergateway waterfront structure of Volga-Baltic Channel some experimental works were carried out in order to check the ground anchor capacity during sheet pile wall construction (Fig. 1).

The results of anchor testing by compressive load show that "Atlant" anchor capacity in clay soil is higher than "Titan" anchor capacity (Table 2). This is caused by the use of homogenizers (special steel elements) which help to improve the drilling process as they increase the anchor body diameter during the process of drilling.

Sheeting works with the use of "Atlant" anchors were carried out during the construction of an administrative commercial building in Perm, Russia. Soil within the job site area consists of sand with filled soil at the top level.

Some experimental works, including pulling of 3 m long "Atlant" piles with different structural features, were carried out in order to define supplementary anchor element influence.

Experimental anchors differed from each other by drill bit diameter (114, 150, 180 mm) and type of reinforcement:

D. Malinin (✉) · A. Malinin
IPS Construction Company, Komsomolsky Avenue 34,
Office 105, Perm, Russia614000,
e-mail: info-ips@yandex.ru

Y. Huang et al. (eds.), *New Frontiers in Engineering Geology and the Environment*,
DOI: 10.1007/978-3-642-31671-5_45,

Table 1 Pile test results

Type of force	Quantity of tested piles	Average capacity (kN)
Jacking	3	565
Pulling	4	582

Fig. 1 Experimental works on Volga-Baltic Channel

Table 2 Anchor test results

№	Anchor type	Anchor length (m)	Soil type	Ultimate load (kN)
3	Titan 40/16	12	Sandy loam	534
A1	Atlant 89 × 6.5	12	Sandy loam	550
5	Titan 40/16	12	Clay	404
6	Titan 40/16	12	Clay	269
9	Titan 40/16	12	Clay	387
A2	Atlant 89 × 6.5	12	Clay	505
A3	Atlant 89 × 6.5	12	Clay	455

– "A" type—bar Ø 73 × 5.5 mm with smooth surface;
– "B" type—bar Ø 73 × 5.5 mm with special anchor element pieces welded pair wise at a distance along the full bar length.

Piles were tested by a pulling force. All piles were excavated later to measure the effective pile diameter. The results of these measurements are given in Table 3.

Analysis of the measurement results shows that the pile diameter is 5 % higher than the drill bit diameter when a smooth surface bar is used. The diameter is 21 % higher that the drill bit diameter when an anchor element bar is used.

The loading capacity of the different pile types is shown in Fig. 2. It is shown that an increase in drill bit diameter by 50 % increases the pile loading capacity 1.5–2 times.

Table 3 Effective diameter of "Atlant" anchor pile

Pile type	Drill bit diameter (mm)	Effective pile diameter (mm)	Diameter increase factor	Average diameter increase factor
A	127 150 180	128 162 192	1.01 1.08 1.07	1.05
B	127 150 180	178 172 196	1.40 1.15 1.09	1.21

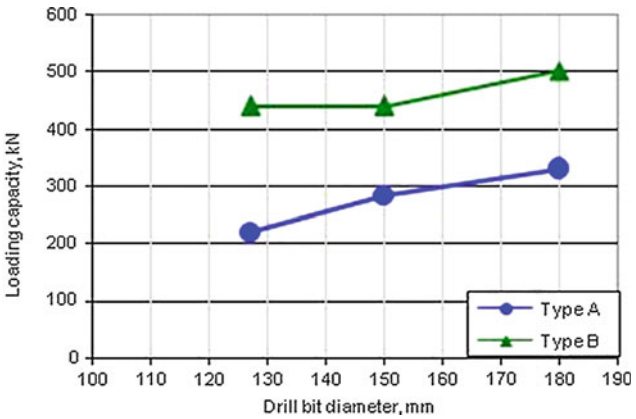

Fig. 2 Pile loading capacity as a function of drill bit diameter

"Atlant" piles with anchor element bars (B type) show a higher cement body diameter and loading capacity than "Atlant" piles with smooth surface bars (A type).

3 Laboratory Tests

Laboratory research on the contact strength between anchor bar and a cement sand body was carried out. It is presumed that adhesion influences the contact strength. Adhesion is caused by roughness and surface asperity of the reinforcing element. Cylindrically formed samples were made from cement. The anchor bar is installed in the centre of the sample.

Reinforcing bars of different types (new bar; corroded bar of secondary use; painted bar; bar with four welded steel elements Ø 10 mm; bar with rolled screw thread) were installed in the centre of cylindrical samples filled with cement-sand grout.

The diameter of the smooth reinforcing bar was 60 mm and the bar with rolled screw thread had a diameter of 57 mm. The height of the rolled screw thread was 108 mm. It was chosen according to the calculated area of contact between bar and cement, which accounted for 200 cm^2. The external diameter of the sample was 168 mm. It approximately

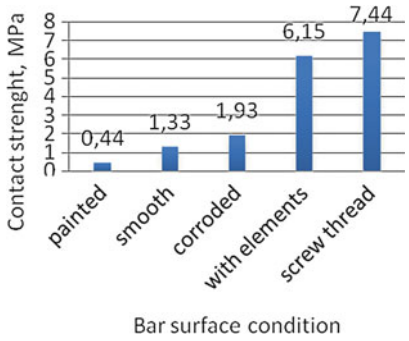

Fig. 3 Test results of contact strength of reinforcing element and cement stone

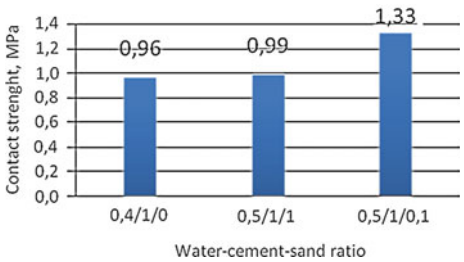

Fig. 4 Test results of contact strength with different water-cement-sand ratio

corresponded to diameter of real anchor pile. Portland cement 500, sand shifting and water mixed in the ratio 1:0.1:0.5 were used for grouting.

Three tests were carried out in order to investigate the influence of the cement-sand mixture. A new (smooth) bar is installed in these samples. The water-cement-sand ratio was varied (W/C/S = 0.4/1/0; 0.5/1/0.1; 0.5/1/1). Samples of all types are made in six fold in order to collect statistic values.

After filling, all samples were hardened for 28 days at room temperature 20° and in humid conditions. The contact strength, σ_a, is defined as the ratio between the breaking load, F_{lim}, and the contact area, S_k, of bar in cement body:

$$\sigma a = \text{Flim}/\ \text{Sk} \quad (1)$$

The test results are given in Figs. 3, 4, 5. Test results show:

- If cement-sand mix ratio is varied there is an insignificant influence of anchor cement body composition on adhesive characteristics.
- The contact strength considerably depends on characteristics of reinforcing element surface characteristics.
- The painted bar has the lowest results. The reason is smoothness of paintwork layer.
- Adhesion strength of bar with corroded surface is 1.5–2 times higher than adhesion strength of bar with smooth surface.

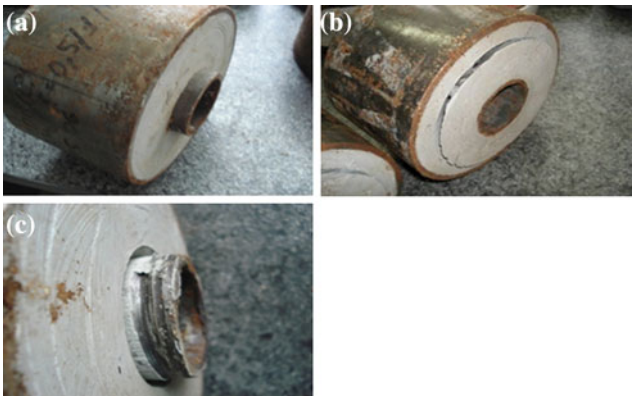

Fig. 5 Destruction character of contact between cement and bars. **a** bar with smooth surface. **b** bar with anchor elements. **c** bar with srew surface

- The contact strength increases significantly in the samples with the bar with rolled screw thread and welded reinforcing pieces. In these cases, the sample breaks within the cement body and not at the contact between the bar and the grout body.

To evaluate the results it is necessary to note that for example in clays the capacity of 1 meter of "Titan" or "Atlant" anchors with cement stone diameter 150 mm accounts for 30 kN according to DIN 1054–2005 calculations. According to in situ tests this loading capacity varies from 35 kN to 40 kN.

One meter of reinforcing bar Ø 89 mm has the contact area with cement equal to 0.28 m^2. Contact strength of corroded bar is 1.93 MPa. This implies that the capacity of one meter of contact with this pipe is 553 kN which is 18 times more than the in situ pile ground capacity. New bar reinforcement shows a contact strength which is almost 10 times higher than the soil loading capacity of an anchor. On the top of that the coupling diameter increases the bar diameter, which gives additional contact that is not taken into account in calculations.

4 Summary

In situ tests have shown the possibility of using anchor pile construction technology with a smooth bar surface. The technology has been successfully used at many job sites such as geotechnical shield construction, pile foundation construction for manufacturing machinery at some industrial enterprises, foundation pit anchoring, underpinning of buildings under the threat of collapse, etc.

Laboratory tests have shown when anchor pile is reinforced by different types of bars; a bar with screw surface and a bar with special anchor elements give the highest

contact strength with cement stone. A bar with smooth painted surface gives the lowest contact strength. However contact strength between cement and bar with smooth surface corresponds to the ground strength of anchors and micro piles.

Statistical Prediction of Overburden Failure Due to Coal Mining Under Sea Area

Z. M. Xu and W. H. Sui

Abstract

This paper presents a statistical prediction of the height of water flowing fractured zone due to coal mining under sea area. Some field measurement methods were used in the Beizao, Liangjia, Wali and Huangxian Coalmines in Shandong Province, China, to investigate the failure process and the maximum height of water flowing fractured zone under different mining and geological conditions. Then, a statistical method has been adopted in this paper for accurately predicting the height of the water flowing fractured zone from the field measurements. The results show that the height of water flowing fractured zone H_f is mainly determined by cutting thickness of seam m in a non-linear relationship, which can be expressed as $H_f = 58.26 \cdot (1 - e^{-0.3m})$. This result has been successfully used for coal mining decision-making of new panels in the Longkou coalmining area.

Keywords

Coal mining under sea area • Water flowing fractured zone • Statistical prediction • Underground water inrush

1 Introduction

Now, there are six countries having the experience of coal mining under the sea area all over the world, which are Britain, Australia, Chile, Japan, Canada and China. At the early 1980s, nearly 60 % of the coal production from 15,000 of the underground coalmines in Britain was extracted from the sea area. Coal production from the sea area of Japan and Australia also accounts for a large proportion of the national coal production. In these countries, due to the special coal mining under the sea, mining activities were managed strictly by the government regulations and orders (Sun HX 1999; Gandhe et al. 2005; Niskovskiy et al. 1996; Singh et al. 2001; Winter et al. 2008). In recent years, China has been a rich experience of coal mining under water body such as lake, river and reservoir (Compilation Commission 1997; Sun et al. 2008, 2009; Xu et al. 2010). Coal mining under surface water body has been successfully done in some locations but there are also many water inrush disasters caused by the surface water when the overburden strata were damaged by coal mining.

The Longkou coalmining area, which involves the first practical example of coal mining under the sea area in China, located in the northern part of Longkou city, Shandong Province, is facing a significant risk of sea water inrush hazards. Figure 1 shows the location of Longkou coalmining area.

In general, the main pathway for water inrush is the fractured zone (we usually call it water flowing fractured zone) formed when the overburden rock breaks during the coal mining. When dealing with the problems of coal mining under surface water, researchers usually consider whether the mining-induced fissures connect with each other and if the connected fissures affect the water body

Z. M. Xu (✉) · W. H. Sui
State Key Laboratory for Geomechanics and Deep Underground Engineering, School of Resources and Geosciences, China University of Mining & Technology, Xuzhou 221008, China
e-mail: xuzhimin@cumt.edu.cn

Y. Huang et al. (eds.), *New Frontiers in Engineering Geology and the Environment*,
DOI: 10.1007/978-3-642-31671-5_46,

Fig. 1 The location of the Longkou coalmining area in Shandong province

during and after coal mining. Therefore, it is necessary to study the development of the water flowing fractured zone (Sun et al. 2008, 2009; Xu et al. 2010).

Previous studies have elucidated the occurrence of overburden-rock failure and of water conduction through pathways arising from coal mining activities (Liu 1995; Kang et al. 2002). Current prediction methods for water flowing fractured zone are: field measurements, simulation experiments (physical simulations or numerical simulations) and theoretical analysis (Ding et al. 2005; Zhu et al. 2008).

This paper presents a statistical prediction of the height of water flowing fractured zone due to coal mining under sea area. Based on the field measurements of the failure process and the maximum height of water flowing fractured zone under different geological conditions in the Beizao, Liangjia, Wali and Huangxian Coalmines, a statistical method has been adopted in this paper for accurately predicting the height of the water flowing fractured zone. Then, a new predicting model from the statistical results is used to provide technological support for decision-making of new panels in the Longkou coalmining area.

2 Geological Background

The major coal seam to be excavated in the Longkou coalmining area is Seam No.2 in the Lower Tertiary System, which consists of Seam No.1, No.2, No.3 and No.4. The overburden rock consists of mudstone, sandy mudstone, calcareous mudstone, oil mudstone and oil shale, which are easy to expand in volume when mudding and have better performance of insulation.

The thickness of the overburden of Seam No.2 is about 100 m, which usually interrupts the hydraulic connection between coal seam and Quaternary aquifers or sea water. According to the hydrogeological observation in the Beizao and Liangjia Coalmines, the water level of marl mudstone aquifer is decreased by almost 30 m slowly, while the water level in Quaternary does not change. This result shows that there is not any significant hydraulic connection between the aquifers. The effective aquifuge between the aquifers is an impermeable seam which can prevent sea water from infiltrating into the coalmine.

3 Field Measurements of Overburden Failure

Coalmines mining under surface water body should determine or predict the height and range of water flowing fractured zone or caving zone before mining.

In the previous practice, Beizao and the nearby coalmines had determined the heights of water flowing fractured zone in many panels in the thin seam or slice mining of thick coal seam by using the "two-terminal plugging tool measurement method". Figure 2 shows the principle of the overburden failure measurement in the upward borehole. We measured the water loss within the borehole between the expansion rubbers after the high-pressure water injected into the rubbers by expansion console to obtain actual data showing the scope of rock failure.

The geological and hydrological conditions of the Liangjia, Wali and Huangxian Coalmines were basically similar to the Beizao Coalmine. During the past few years, some field

Table 1 The measured heights of water flowing fractured zone

Coalmine	Panel	Mining thickness (m)	Height of water flowing fractured zone (m)	Ratio of the height of the fractured zone to the mining thickness
Beizao	4,201	2.37	13.40	5.65
	1,101	2.12	25.10	11.80
	1,102	2.17	17.30	8.00
	1,202	4.51	38.50	8.50
	3,201	3.94	25.70	6.50
	3,207	2.23	24.40	10.90
	H2101	3.60	30.00	8.30
	H2106	4.40	41.90	9.52
Liangjia	2,106	4.00	38.80	9.70
Huangxian	1,211	1.61	23.60	14.60
		1.82	17.29	9.50
	1,201	1.40	16.53	11.80
		1.44	16.70	11.60
		1.44	17.14	11.90
		1.44	13.26	9.20

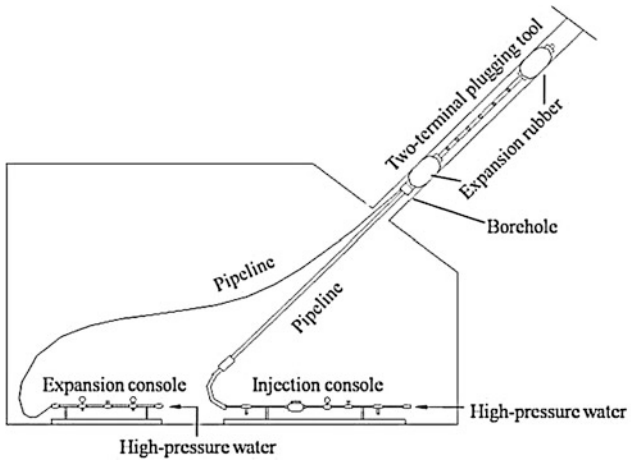

Fig. 2 Overburden failure measurement in the upward borehole

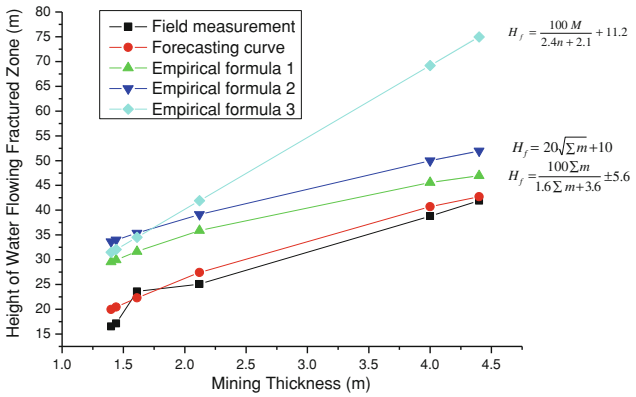

Fig. 3 Comparison of the fit formula and the empirical ones

measurements of the overburden failure were practiced in the above Coalmines, the mining thickness ranges from 1.40 to 4.93 m, and the field measurement height of the water flowing fractured zone is from 13.26 to 41.90 m, the ratio of the height of the fractured zone to the mining thickness is from 3.70 to 11.90 m. Table 1 shows the detail measured heights of the water flowing fractured zone in the four coalmines at Longkou coalmining area.

4 Statistical Prediction

We chose the code Origin to find a new formula to predict the height of the water flowing fractured zone. Origin has a perfect function in mathematical analysis, in addition, Origin itself provided many drawing model that you can select or make your' as you wish.

By analyzing the data of the field measurement, our prediction formula to calculate the maximum height of the water flowing fractured zone for the Beizao Coalmine was fitted as follows:

$$H_f = 58.26 \cdot (1 - e^{-0.3m}) \quad (1)$$

where m is the excavated coal thickness, m; H_f is the maximum height predicted for the water flowing fractured zone, m.

This model predicts that the height of the water flowing fractured zone increases non-linearly with the mining thickness. It is different from other empirical formulas (shows in Fig. 3) in the government regulations and is more applicable (and valid) for the geological condition and

overburden rock structure associated with the Beizao Coalmine. Figure 3 shows the trends in water flowing fractured zone height with increased mining thickness using four different formulas. The fit formula has a higher accuracy than the empirical ones, which have large errors.

5 Conclusions

(1) Field measurement is demonstrated to be effective at determining the height of the water flowing fractured zone, the "two-terminal plugging tool measurement method" was used to get the height of the water flowing fractured zone in the four coalmines at Longkou coalmining area in this research.
(2) By analyzing the data of the field measurement, a new prediction formula to calculate the maximum height of the water flowing fractured zone for the Beizao Coalmine was fitted. The results suggest that the height of the water flowing fractured zone shows an exponential relation to the mining thickness.
(3) A new prediction model has been created and successfully applied to decision making when coal mining under the Bohai Sea. This is a very important basis for predicting the sea water inrush disasters.

Acknowledgments The authors want to acknowledge the financial support of the National Natural Science Foundation—Shenhua Group Jointly Funded Project under grant No. 51174286. This research was also supported by A Project Funded by the Priority Academic Program Development of Jiangsu Higher Education Institutions and Fundamental Research Funds for the Central Universities (No.2010QNB35) for their financial supports.

References

Compilation Commission. (1997). *Mine water prevention experiences compilation of China*. Beijing: China Coal Industry Publishing House.

Ding, D. X., Wang, Y. G., & Zhang, Z. J. (2005). Research on the height of water fractured zone based on adaptive neural fuzzy inference. *Mining Technology, 18*(3), 15–18.

Gandhe, A., Venkateswarlu, V., & Gupta, R. N. (2005). Extraction of coal under a surface water body- a strata control investigation. *Rock Mechanics and Rock Engineering, 38*(5), 399–410.

Kang, J. R., & Wang, J. Z. (2002). The mechanical model of the overburden rock under mining and the broken condition analysis. *Journal of China Coal Society, 27*(1), 16–20.

Liu, T. Q. (1995). Influence of mining activities on mine rock mass and control engineering. *Journal of China Coal Society, 2*, 1–5.

Niskovskiy, Y., & Vasianovich, A. (1996). Investigation of possibility to apply untraditional and ecologicaly good methods of coal mining under sea bed. In *Proceedings of the International Offshore and Polar Engineering Conference* (pp. 51–53). Los Angeles: ISOPE.

Singh, R. N., & Jakeman, M. (2001). Strata monitoring investigations around longwall panels beneath the cataract reservoir. *Mine Water and the Environment, 20*(2), 33–41.

Sun, H. X. (1999). The prospect for the coal mining under sea area in China. *China Coal, 25*(8), 34–36.

Sun, Y. J., Xu, Z. M., & Dong, Q. H. (2008). Forecasting water disaster for a coal mine under the Xiaolangdi reservoir. *Journal of China University of Mining & Technology, 18*(4), 516–520.

Sun, Y. J., Xu, Z. M., & Dong, Q. H. (2009). Mornitoring and simulation research on development of water flowing fracture for coal mining under the Xiaolangdi reservoir. *Chinese Journal of Rock Mechanics and Engineering, 28*(2), 238–245.

Winter, T. C., Buso, D. C., & Shattuck, P. C. (2008). The effect of terrace geology on ground-water movement and on the interaction of ground water and surface water on a mountainside near Mirror Lake, New Hampshire, *USA. Hydrological Processes, 22*(1), 21–32.

Xu, Z. M., Sun, Y. J., & Dong, Q. H. (2010). Predicting the height of water-flow fractured zone during coal mining under the Xiaolangdi reservoir. *Mining Science and Technology, 20*(3), 434–438.

Zhu, Q. H., Feng, M. M., & Miao, X. X. (2008). Numerical analysis of water inrush from working-face floor during mining. *Journal of China University of Mining & Technology, 18*(2), 159–163.

Numerical Analysis for the Stability of Over-Length Trench Wall Based on a Novel Pre-supporting Excavation Method

Z. X. Zhang, C. H. Pan, and C. F. Duan

Abstract

Building enclosure and supporting system has been widely used for the construction of soft soil foundation. To improve the deformation of envelope system and stratum, this paper presents a novel pre-supporting excavation method (PEM). Unlike traditional construction methods, the new method proposes supporting system be installed completely before excavation and one of the key problems is the stability of over-length trench supported by slurry. Aiming at the stability analysis, this paper does an in-depth research by a numerical simulation analysis and a model of slurry-filled trench wall in the actual excavation environment is analyzed based on the elasto-plastic finite-element method (FEM). Various factors influencing on the stability of trench wall and the settlement of ground surface are considered, especially the groundwater as an important point is of key consideration. The analysis results show that the stability of over-length slurry trench could be ensured in the condition of dewatering under the bottom of foundation pit.

Keywords

Pre-supporting • Excavation • Pit foundation • FEM

1 Introduction

The excavation supporting systems, e.g. diaphragm wall and steel strut or diaphragm wall and cast reinforced concrete strut, have been widely used in soft clay excavation construction (Clough and Duncan 1971; Fen 2010; George et al. 2004; Liu and Lu 2005; Patrick 2004; Pavol et al. 2001). However, the aforementioned supporting systems have different characteristics and still exist some deficiencies due to the following main reasons:

(1) It is difficult to control the deformation of envelope system and stratum. The construction process is complicated and requires various corresponding personnel.
(2) Large number of cast-in-place reinforced concrete struts and temporary steel struts are required and a large amount of reinforced concrete struts are difficult to be dismantled and can not be recycled to reuse.
(3) It is impossible to achieve synchronization in excavation process of the whole plane. If existing pits are greater and deeper, the traditional supporting systems require increasingly demanding deformation control with tight schedule.

Therefore, the pre-supporting excavation method (PEM) as a novel rapid construction technology with micro disturbances to vicinity is proposed in this paper. PEM refers to that precast steel struts have been installed to the design position prior to the excavation of the pit as well as diaphragm wall construction. The method leads to the completion of supporting system before excavation and then the whole plane excavation, thus effectively reduces

Z. X. Zhang (✉) · C. H. Pan
Department of Geotechnical Engineering, School of Civil Engineering Tongji University, Shanghai 200092, China
e-mail: zxzhang@tongji.edu.cn

Z. X. Zhang · C. F. Duan
Shanghai Urban Construction (Group) Corporation, Shanghai 200023, China

Y. Huang et al. (eds.), *New Frontiers in Engineering Geology and the Environment*,
DOI: 10.1007/978-3-642-31671-5_47,

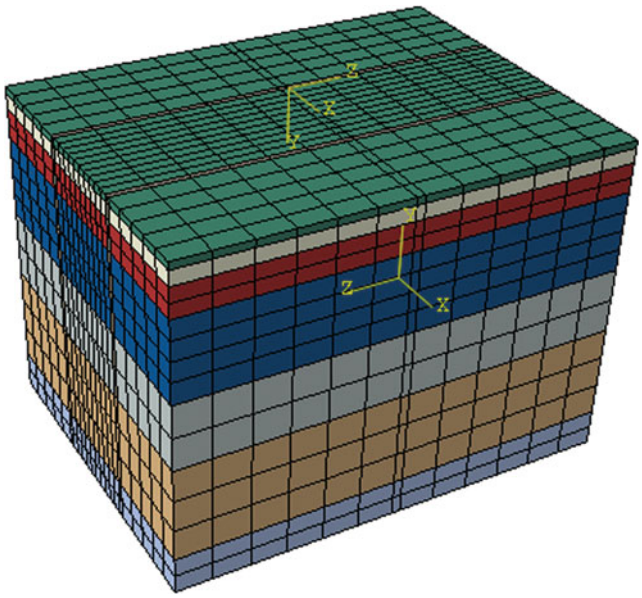

Fig. 1 FEM model for PEM

the settlement of the surrounding stratum and improves the efficiency of excavation construction.

In order to realize PEM smoothly, several technical difficulties should be resolved. One of the most important techniques is how to ensure the stability of the over-length trench (Shi and Zhang 2006; Tsai and Chang 1996; Zhang and Xia 2000; and Zhen 2007). Because PEM requires particular trench with corresponding length and depth to install the precast steel struts, and digging trench is a key process in diaphragm wall construction. The division of the unit trench length needs to consider various factors: geological conditions, ground surcharge, joint position, lifting capacity of crane, thus generally the length of the unit trench is 3−8 m in construction. It is noted that the factors of joint position and lifting capacity of crane in this simulation were neglected. Actually, the two factors may have some effects on the stability of over-length trench wall, and need to be further studied in the future.

In this paper, numerical simulations by finite element method for a typical excavation environment are developed to analyze the stability of over-length trench wall and the results of systematic sensitivity studies contained in this study will show the influence of the investigated parameters.

2 Finite Element Modeling of PEM in Soft Soil

2.1 Modeling of PEM Works

The investigated simulation combines with the soft soil in Shanghai and PEM in deep pit as the background. Using the ABAQUS finite element software as an analytical tool, the stability of over-length trench in construction conditions has been simulated with its influencing factors. The main issues in this study are as follows:

(1) With respect to soft soil in Shanghai, the length of diaphragm wall is generally less than 10 m. However, PEM requires trench with the length more than 20 m for installing the struts. Thus with the help of numerical simulation, the relationship of the length of the trench and its stability are analyzed.
(2) Slurry in the trench is used to balance the soil and groundwater forces on the trench wall, unit weight of which is an important factor to affect the stability of trench. The unit weight of the slurry in diaphragm construction is generally 10−13kN/m^3, therefore this study will try to explore the relationship of the unit weight and stability.
(3) Groundwater level has significant influence on the stability of the trench. In general, the groundwater pressure on the wall is an adverse factor, thus dewatering means reducing unfavorable loads. Meanwhile dewatering is conducive to the consolidation of soils, which can effectively enhance the stability of the trench. Some conclusions of the effects of dewatering are obtained through the finite element simulation.

The required FEM model is shown in Fig. 1 to simulate the working status of trench in soft soil. The ground water level is 1 m below the ground surface and the depth and width of the soil layers are 2–3 times the excavation depth. Both endpoints of the trench are supported by diaphragm wall as the pit enclosure. Considering the characteristic of soft soil in Shanghai, the soil behavior is assumed to be governed by an elastic perfectly-plastic constitutive relation based on the D-P criterion with a non-associative flow rule.

The soil mechanical parameters for FEM simulation are shown in Table 1

2.2 Numerical Results

As aforementioned, several factors will affect the stability of over-length trench by proposed PEM method, including the influence of dewatering condition, excavation depth and length, and slurry unit weight. In this section, the FEM is used for the above parametric studies.

(1) Dewatering condition

Figure 2 shows the deflection of the trench wall in different dewatering conditions. The wall deformation tends to outside the wall in the condition of non-dewatering and dewatering 5 m below the soil surface. However, the wall deformation tends to opposite direction in the condition of dewatering 10 m below and to the bottom. It shows that the trench wall has reached the failure limit in the first two

Table 1 Soil mechanical parameters for FEM modeling

Layer	Thickness (m)	Unit weight (kN/m^3)	C (kPa)	φ (°)	Compression modulus (MPa)	Poisson's ratio	Flow stress ratio
①$_1$	1	18	60.09	41.5	8	0.29	0.778
②$_1$	2.1	18	51.35	32.9	6.2	0.32	0.822
③	3.9	17.5	31.05	28.8	3.8	0.30	0.845
④	10.5	16	26.55	21.6	3.5	0.29	0.883
⑤$_1$	9	17.9	28.21	27.9	5	0.30	0.850
⑤$_3$	13	18	42.69	37.4	8	0.35	0.797
⑦	7	19.3	7.23	35.8	13	0.35	0.778

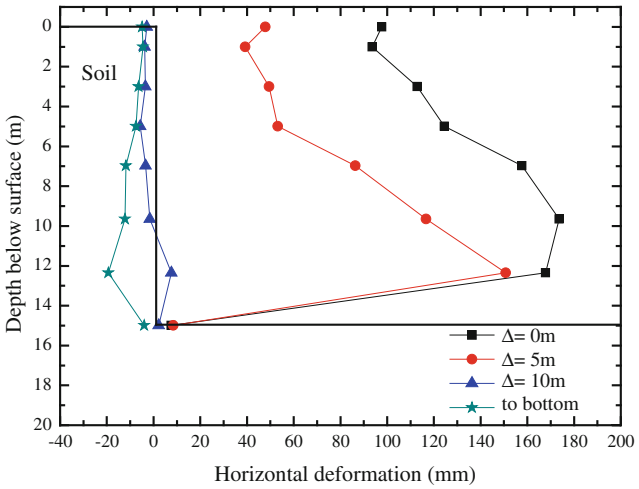

Fig. 2 Wall deformation in different dewatering conditions

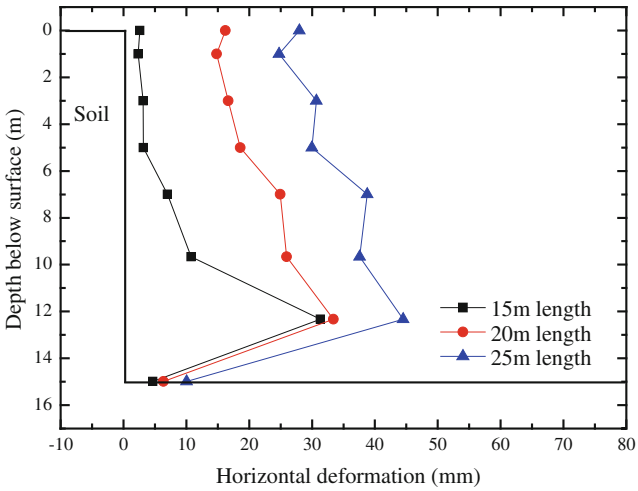

Fig. 4 Wall deformation in different excavation lengths

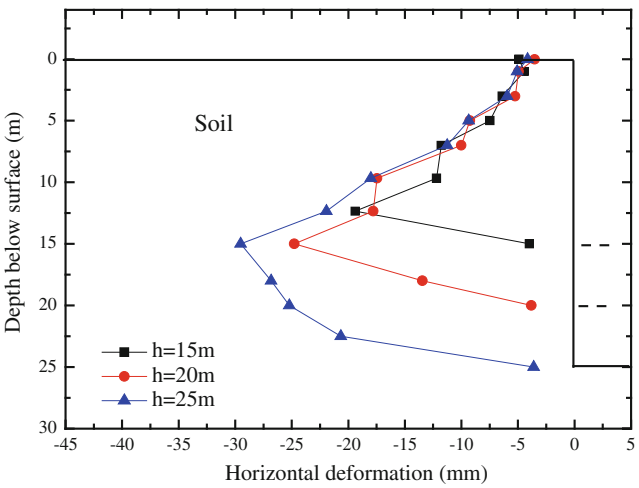

Fig. 3 Wall deformation in different excavation depths

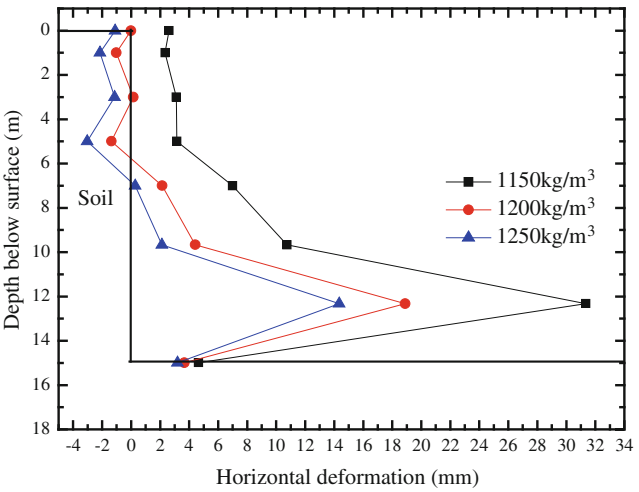

Fig. 5 Wall deformation in different slurry unit weights

conditions and the failure zone appears in the range of 9−12 m below the surface. Therefore, the effect of dewatering is significant and the deeper the depth of dewatering, the better the stability of the trench.

(2) Excavation depth and length

Figure 3 shows deflection of the trench wall influenced by three excavation depth levels, 15, 20 and 25 m, respectively. In the condition of 1150 kg/m^3 unit weight for slurry and completely dewatering, the deformation amplitude increases gradually with the increase of excavation depth. In

addition, the deformation near the bottom of the trench is obviously larger than the one in the range of 0−10 m. And the deformation is up to 30.6 mm when the depth of the trench reaches 25 m.

Figure 4 shows deflection of the trench wall influenced by three excavation length, 15 m, 20 m and 25 m, respectively. Obviously, in the conditions of 1150 kg/m^3 unit weight slurry, 15 m excavation depth and dewatering 7 m below the surface, the deformation gradually increases with the increasing excavation length which indicates the soil tends to be unstable.

(3) Unit weight of slurry

The unit weight of slurry has important influence on the stability of the trench wall. In the typical simulation, Fig. 5 shows the deflection of the trench wall influenced by different unit weights of slurry in the condition of excavation depth 15 m, excavation length 15 m and dewatering 7 m below the soil surface. Above the dewatering level, the upgrade unit weight of slurry will bring the reverse of the direction of displacement of the trench wall, which caused by the increasing horizontal pressure from improving slurry weight. Otherwise, the deformation amplitude from 1150 to 1200 kg/m^3 is much larger than the one from 1200 to 1250 kg/m^3, which indicates that the effect on the stability of the trench wall by improving the slurry unit weight to a certain extent is limited.

3 Conclusions

For the novel pre-supporting excavation method in soft soil below the ground water table, the influence of dewatering condition, excavation depth and length, and slurry unit weight has been analyzed by means of numerical sensitivity studies based on 3D finite element modeling. The results of presented in this study demonstrate the possibility of PEM. The findings on PEM are as follows:

(a) The control of dewatering depth is essential to the over-trench excavation. With respect to the specific study in soft soil, dewatering to the half of excavation depth would better benefit the stability of the over-length trench.
(b) The excavation depth of trench has small impact on the stability. However, if the excavation length is more than 20 m, the deformation of the over-length trench wall near surface increases substantially large.
(c) The upgrading of the slurry unit weight has smaller effect on the stability as it increases, thus the effect of improving slurry unit weight to maintain the stability of the trench in soft soil is limited.

Acknowledgments The financial support of this work by Shanghai Urban Construction Group is gratefully acknowledged by the authors.

References

Clough, G. W., & Duncan, J. M. (1971). Finite element analyses of retaining wall behavior. *Journal of Geotechnical Engineering, ASCE, 97*(12), 1657–1673.

Fen, Y. (2010). Diaphragm wall recessed into the wall stage slot wall stability and deformation of thress-dimensional numerical analysis. *Structure Construction, 32*(5), 415–418.

George, M. F., Tiffany, A., & Richard, R. D. (2004). Stability of long trenches in sand supported by Bentonite-water slurry. *Journal of Geotechnical and Geoenvironmental Engineering, ASCE, 130*(9), 915–921.

Liu, G., & Lu, H. (2005). Settlement study of diaphragm wall trench construction. *Journal of Geotechnical Engineering, 27*(2), 287–289.

Patrick, J. F. (2004). Analytical solutions for stability of slurry trench. *Journal of Geotechnical and Geoenvironmental Engineering, ASCE, 130*(7), 749–758.

Pavol, O., Keizo, U., Masaaki, K., et al. (2001). A design method for slurry trench wall stability in sandy ground based on the elasto-plastic FEM. *Computers and Geotechnics, 28*(2001), 145–159.

Shi, S., & Zhang, W. (2006). Stability study in deep pit diaphragm slurry trench. *Journal of Geotechnical Engineering, 28*, 1418–1421.

Tsai, J. S., & Chang, J. C. (1996). Three-dimensional stability analysis for slurry-filled trench wall in cohesionless soil. *Canadian Geotechnical Journal, 33*, 798–808.

Zhang, H., & Xia, M. (2000). Three-dimensional analysis of stability in diaphragm wall slurry trench construction. *Journal of Civil Engineering, 33*(1), 73–76.

Zhen, Y. (2007). Stability study of diaphragm wall trench. *Geotechnical Engineering, 21*(1), 36–38.

Estimating the Effects of Shield Tunnelling on Buried Pipelines Based on a Kerr Foundation Model

H. Zhang and Z. X. Zhang

Abstract

Based on a Kerr-type three-parameter elastic foundation model, a two-stage analytical method for estimating the longitudinal deflection and internal forces of existing pipelines is presented in this paper. With respect to the first stage, the Loganathan and Poulos analytical solution is used to estimate the free-soil settlement caused by shield tunnelling at the existing pipeline's position; in the second stage, the free-soil settlement is imposed to the existing pipeline, which is simplified as an infinite beam on a Kerr foundation. The governing differential equations of the pipe are formulated and analytically solved, and the deformation and internal forces of the pipeline are obtained. Foundation model parameters are determined by the simplifying elastic continuum method. The superiority of the Kerr foundation model, compared to Winkler foundation model, is verified by numerical results and a real-life case.

Keywords

Shield tunnelling • Buried pipeline • Kerr foundation model • Deflection • Analytical solution

1 Introduction

Shield tunnelling method is of great popularity in megacity to solve the traffic problems, but existing pipelines are often affected by the inevitable ground movements during shield tunnelling. In recent years, increasing attention has been paid to the effects of shield tunnelling on buried pipelines and the assess of the complex pipe-soil interaction problem usually rely on analytical solutions based on Winkler foundation model (Attwell et al. 1986; Vorster et al. 2005; Klar et al. 2005; Wang et al. 2006; Zhang et al. 2009). However, Winkler foundation model (Fig. 1a) could not always give accurate predictions because its inherent defect that not able to reflect the foundation continuity. Large errors may be produced especially when dense thick soil foundation or whole rock foundation is encountered (Winkler 1867; Selvadurai 1979). In order to overcome this weakness of Winkler model and get better results, a shear layer is added to the model to provide mechanical interaction among spring elements, like Pasternak foundation model (Pasternak 1954) (Fig. 1b). Kerr (1964, 1965) presents a more accurate three-parameter foundation model as an attempt to produce a generalization of the Pasternak model, by introducing another spring element layer to the two-parameter foundation model. The Kerr foundation model consists of two linear elastic spring layers of constants c [kN/m^3] and k [kN/m^3] respectively, interconnected by a unit thickness shear layer of constant G [kN/m] (Fig. 1c) (Avramidis & Morfidis 2006).

H. Zhang · Z. X. Zhang (✉)
Key Laboratory of Geotechnical and Underground Engineering of Ministry of Education, Tongji University, Shanghai 200092, China
e-mail: zxzhang@tongji.edu.cn

H. Zhang
Department of Geotechnical Engineering, Tongji University, Shanghai 200092, China

Y. Huang et al. (eds.), *New Frontiers in Engineering Geology and the Environment*,
DOI: 10.1007/978-3-642-31671-5_48,

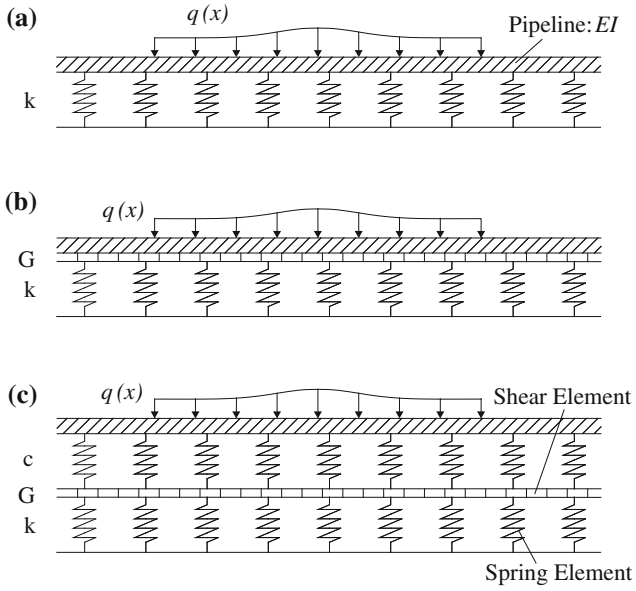

Fig. 1 Three types of foundation models (**a**–**c**)

In this paper, based on a Kerr-type three-parameter elastic foundation model, a two-stage analytical method for estimating the longitudinal deflection and internal forces of existing pipelines is presented. With respect to the first stage, the Loganathan and Poulos analytical solution is used to estimate the free-soil settlement caused by shield tunnelling at the existing pipeline's position; in the second stage, the free-soil settlement is imposed to the existing pipeline, which is simplified as an infinite beam on a Kerr foundation. The governing differential equations of the pipe are formulated and analytically solved, and the deformation and internal forces of the pipeline are obtained as well. In addition, foundation model parameters can be determined by simplifying elastic continuum method. The superiority of the Kerr foundation model, compared to Winkler foundation model, is verified by numerical results and a real-life case.

2 Analytical Solution Based on a Kerr Foundation Model

2.1 Additional Stress Acting on a Pipeline Due to Shield Tunnelling

The schematic diagram of the problem is shown in Fig. 2, in which a new tunnel is excavated under an existing pipe. According to existing results (Attwell et al. 1986; Vorster et al. 2005; Klar et al. 2005; Huang et al. 2012), the problem is discussed under some key assumptions as follows:

(1) A continuous elastic homogenous pipeline is buried in homogenous soil, (2) The pipe is always in contact with the soil, (3) The pipe is smooth and friction between the pipe and the soil is not considered.

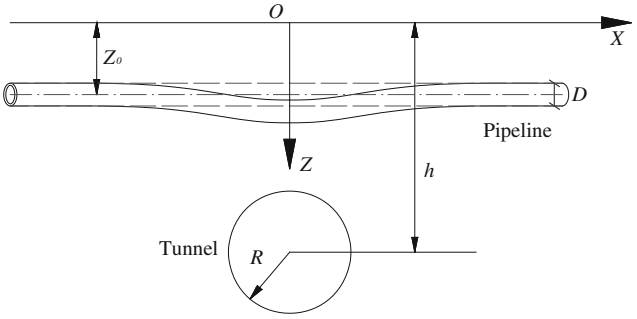

Fig. 2 Schematic representation of the problem

Loganathan & Poulos (1998) proposed that the ground deformation pattern around tunnel is not uniform but oval shaped and the ground settlement due to tunnelling could be illustrated as

$$u(x)=\varepsilon_0 R^2\left\{-\frac{z_0-h}{x^2+(z_0-h)^2}+\frac{(3-4v)h(z_0+h)}{x^2+(z_0+h)^2}-\frac{2z_0\left[x^2-(z_0+h)^2\right]}{\left[x^2+(z_0+h)^2\right]^2}\right\}h \exp\left[\frac{-1.38x^2}{(h+R)^2}-\frac{0.69z_0^2}{h^2}\right] \tag{1}$$

Where R = radius of the tunnel; z_0 = depth of the existing pipeline from the ground surface; h = depth of the tunnel from the ground surface; v = soil Poisson's ratio; ε_0 = equivalent undrained ground loss; x = lateral distance from the tunnel axis.

Considering the Kerr foundation, the free-soil settlement $u(x)$ satisfies the following equation as

$$u(x)=u_1(x)+u_2(x) \tag{2}$$

Where $u_1(x)$ is the deformation of the upper spring layer and $u_2(x)$ is the total deformation of the shear layer and the lower spring layer (Fig. 3).

Assuming that the stress under the soil is $q_1(x)$and the stress under the shear layer is $q_2(x)$, then

$$q_1(x)=cu_1(x)=c(u(x)-u_2(x)) \tag{3}$$

$$q_2(x)=ku_2(x) \tag{4}$$

When considering both the shear layer and the lower spring layer, we have

$$q_1(x)=-G\frac{d^2u_2(x)}{dx^2}+ku_2(x) \tag{5}$$

Where c = stiffness of the upper spring layer, G = the shear stiffness, and k = stiffness of the lower spring layer.

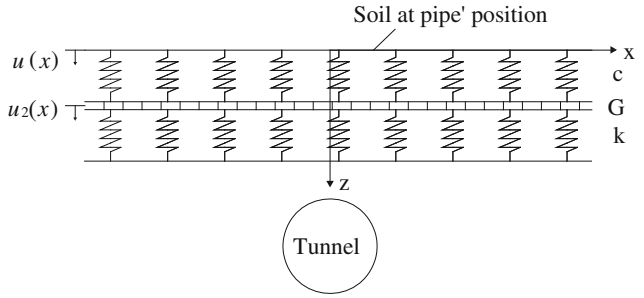

Fig. 3 Free-soil settlement due to shield tunnelling

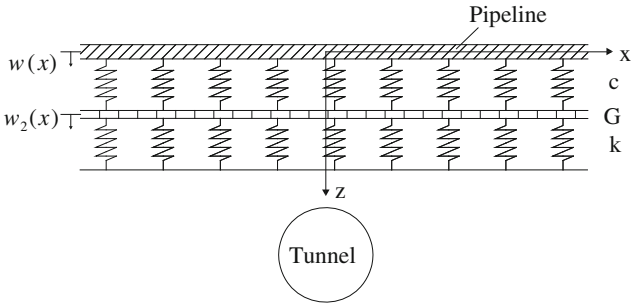

Fig. 4 Pipeline under shield tunnelling

By introducing Eq. (5) into Eq. (3) the following relation can be obtained as

$$u(x) = \left(1 + \frac{k}{c}\right)u_2(x) - \frac{G}{c}\frac{d^2u_2(x)}{dx^2} \tag{6}$$

Where $u_2(x)$ can be gained by solving Eq. (6) and then $q_1(x)$ can be obtained by taking $u_2(x)$ into Eq. (5) combined with following boundary conditions.

$$w_2\Big|_{x=\infty} = 0; \frac{dw_2}{dx}\Big|_{x=0} = 0 \tag{7}$$

2.2 Governing Differential Equation of a Pipe and its General Solution

Assuming that the stiffness of the existing pipe is EI and its deflection under $q_1(x)$ can be expressed as

$$w(x) = w_1(x) + w_2(x) \tag{8}$$

Where $w_1(x)$ is the deformation of the upper spring layer, $w_2(x)$ is the total deformation of the shear layer and the lower spring layer (Fig. 4).

Assuming that the stress under the pipe is $p_1(x)$ and the stress under the shear layer is $p_2(x)$, similarly, the equations for $p_1(x)$ and $p_2(x)$ can also be obtained as

$$p_1(x) = cw_1(x) = c(w(x) - w_2(x)) \tag{9}$$

$$p_2(x) = kw_2(x) \tag{10}$$

$$p_1(x) = -G\frac{d^2w_2(x)}{dx^2} + kw_2(x) \tag{11}$$

$$w(x) = \left(1 + \frac{k}{c}\right)w_2(x) - \frac{G}{c}\frac{d^2w_2(x)}{dx^2} \tag{12}$$

Then, the governing differential equations of a pipe can be expressed as

$$EI\frac{d^4w(x)}{d(x^4)} + p_1(x)D = q_1(x)D \tag{13}$$

Where EI = the stiffness of the pipe and D = the diameter of the pipe.

By Eqs. (11) and (12), the Eq. (13) can be changed into

$$\frac{d^6w_2(x)}{dx^6} - \frac{c+k}{G}\frac{d^4w_2(x)}{dx^4} + \frac{Dc}{EI}\frac{d^2w_2(x)}{dx^2} - \frac{Dck}{EIG}w_2(x) = -\frac{Dc}{EIG}\left(-G\frac{d^2u_2(x)}{dx^2} + ku_2(x)\right) \tag{14}$$

In fact, Eq. (14) is a differential equation of six orders with $w_2(x)$ as unknown variables, and $w(x)$ can be obtained by substituting $w_2(x)$ into Eq. (12) when $w_2(x)$ being worked out (Avramidis & Morfidis 2006).

First of all, efforts are made to get the general solution of Eq. (14), we have

$$\frac{d^6w_2(x)}{dx^6} - \frac{c+k}{G}\frac{d^4w_2(x)}{dx^4} + \frac{Dc}{EI}\frac{d^2w_2(x)}{dx^2} - \frac{Dck}{EIG}w_2(x) = 0 \tag{15}$$

Noted that the characteristic equation of Eq. (15) can be expressed as

$$r^6 - \frac{c+k}{G}r^4 + \frac{Dc}{EI}r^2 - \frac{Dck}{EIG} = 0 \tag{16}$$

Then, we obtain

$$\left(r^2 - \psi_1\right)\left(r^2 - \psi_2\right)\left(r^2 - \psi_3\right) = 0 \tag{17}$$

Considering that the expand form of Eq. (17) is identically equal to Eq. (16), the following relations can be obtained as

$$\begin{cases} \psi_1 + \psi_2 + \psi_3 = (c+k)/G \\ \psi_1\psi_2 + \psi_2\psi_3 + \psi_1\psi_3 = Dc/EI \\ \psi_1\psi_2\psi_3 = Dck/EIG \end{cases} \tag{18}$$

By analyzing Eq. (18), it's found that ψ_1, ψ_2 and ψ_3 are the three roots of Eq. (19).

Hence,

$$\psi^3 - \frac{c+k}{G}\psi^2 + \frac{Dc}{EI}\psi - \frac{Dck}{EIG} = 0 \tag{19}$$

Making $a = 1$, $b = -\frac{c+k}{G}$, $e = \frac{Dc}{EI}$, $d = -\frac{Dck}{EIG}$ and $S = 9abe - 2b^2 - 27a^2d$, $\mathrm{T} = 4(3ae - \mathrm{b}^2)^3$.

According to the traditional approach to solve the univariate cubic equation, the three roots of Eq. (19) can be obtained as

$$\psi_1 = -\frac{c+k}{G} + \frac{1}{3}\left[\sqrt[3]{\frac{1}{2}(S + \sqrt{S^2+T}} + \sqrt[3]{\frac{1}{2}(S - \sqrt{S^2+T}}\right] \tag{20}$$

$$\psi_{2,3} = -\frac{c+k}{3G} - \frac{1}{6}\left[\sqrt[3]{\frac{1}{2}(S + \sqrt{S^2+T}} + \sqrt[3]{\frac{1}{2}(S - \sqrt{S^2+T}}\right] \pm \frac{\sqrt{3}}{6}i\left[\sqrt[3]{\frac{1}{2}(S + \sqrt{S^2+T}} - \sqrt[3]{\frac{1}{2}(S - \sqrt{S^2+T}}\right] \tag{21}$$

Thus, considering Eq. (17), the six roots of Eq. (16) are

$$r_{1,2} = \pm\sqrt{\psi_1} = \pm\alpha;\ r_{3,4,5,6} = \pm(M \pm Ni) \tag{22}$$

Where M and N can be calculated by extraction of ψ_2 and ψ_3.

$w_2(x)$ can be thus expressed as

$$w_2(x) = A_1e^{-ax} + A_2e^{ax} + e^{-Mx}(A_3\cos Nx + A_4\sin Nx) + e^{Mx}(A_5\cos Nx + A_6\sin Nx) \tag{23}$$

In fact, $w_2(x)$ must be equal to zero when x approaches to infinity, and thus Eq. (23) can be converted into

$$w_2(x) = A_1e^{-ax} + e^{-Mx}(A_3\cos Nx + A_4\sin Nx) \tag{24}$$

2.3 Pipeline Deformation Under a Concentrated Load

(1) Traditional Winkler model

The governing differential equation of a pipe on a Winkler foundation is

$$EI\frac{d^4w(x)}{dx^4} + k_ww(x)D = q(x)D \tag{25}$$

For a concentrated load condition, we have

$$w_w(x) = P\lambda e^{-\lambda x}(\cos\lambda x + \sin\lambda x)/2k_w \tag{26}$$

Where $\lambda = \sqrt[4]{k_wD/4EI}$

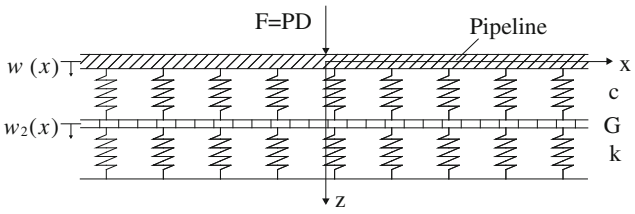

Fig. 5 Pipeline under concentrated load

(2) Kerr model

In order to get A_1, A_2 and A_3 in Eq. (24), the deflection of a pipe under a concentrated load should be worked out first (Fig. 5).

The particular solution of Eq. (14) under a concentrated load is $w_2^* = 0$, and the boundary conditions are as follows

$$\left.\frac{dw}{dx}\right|_{x=0} = 0;\ \left.\frac{dw_2}{dx}\right|_{x=0} = 0;\ -EI\left.\frac{d^3w}{dx^3}\right|_{x=0} = -PD/2 \tag{27}$$

According to the boundary conditions, the expression of $w_2(x)$ can be obtained and then $w(x)$ can be calculated by Eq. (12).

Hence,

$$w(x) = B_1e^{-ax} + e^{-Mx}(B_3\cos Nx + B_4\sin Nx) \tag{28}$$

The bending moment of the pipe can be resolved by means of Eq. (28), then

$$M(x) = -EI\frac{d^2w}{dx^2} \tag{29}$$

Based on simplified elastic space method, foundation parameters can be expressed as the function of foundation depth H, elastic modulus of soil E_0 and Poisson's ratio v (Kerr 1985; Avramidis & Morfidis 2006).

$$\mathrm{kw} = \mathrm{E0/H},\ k = \frac{4E_0}{3H},\ c = 7k,\ G = \frac{4G_0H}{9} \tag{30}$$

Where $G_0 = \frac{E_0}{2(1+v)}$

2.4 Pipeline Deformation Due to Shield Tunnelling

With respect to any point on the axis of the pipe, assuming that the additional load at this point derived from shield tunnelling is $F(\xi)\mathrm{d}\xi$. According to Eq. (28), the deflection $\mathrm{d}w(x)$ caused by $F(\xi)\mathrm{d}\xi$ at another point x on the axis of the pipe can be described as

$$dw(x) = B_1e^{-\rho|x-\xi|}d\xi + e^{-M|x-\xi|}\hbar(B_3\cos N|x-\xi| + B_4\sin N|x-\xi|)\,d\xi \tag{31}$$

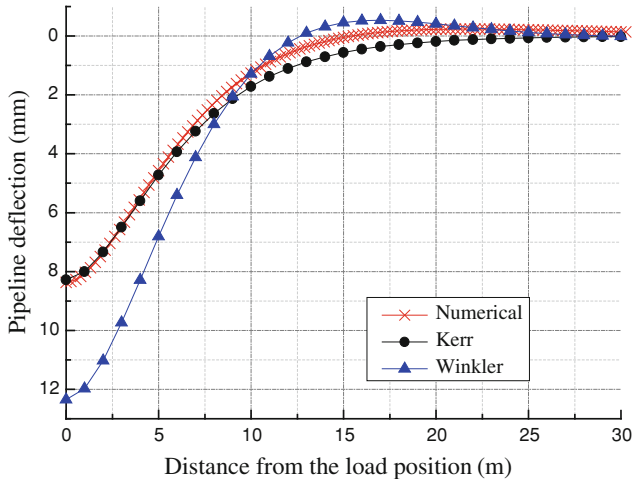

Fig. 6 Pipeline deformation under concentrated load

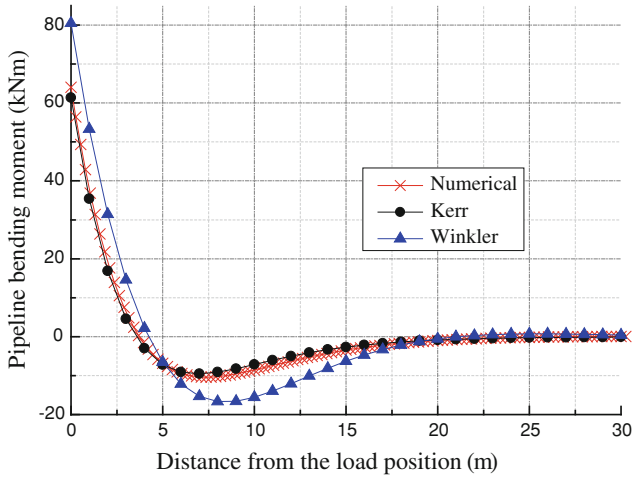

Fig. 7 Pipeline moment under concentrated load

and the deflection of a pipe due to shield tunnelling can be obtained by integration of Eq. (31) in infinite range, then

$$w(x) = \int_{-\infty}^{+\infty} dw(x) \tag{32}$$

3 Case Study

The Dapu shield–driven tunnel in Shanghai is 1,462 m long and its diameter is 11.22 m. The tunnel passes through a sewage pipe and its overburden soil is 19.8 m. The sewage pipe is 1.8 m in diameter and buried 15 m in depth above the tunnel.

Table 1 Calculation parameters

H/m	E_0/kPa	v	D/m	EI/kN m^2	P/(kN/m)
15	11312.1	0.32	0.6	93851.5	100

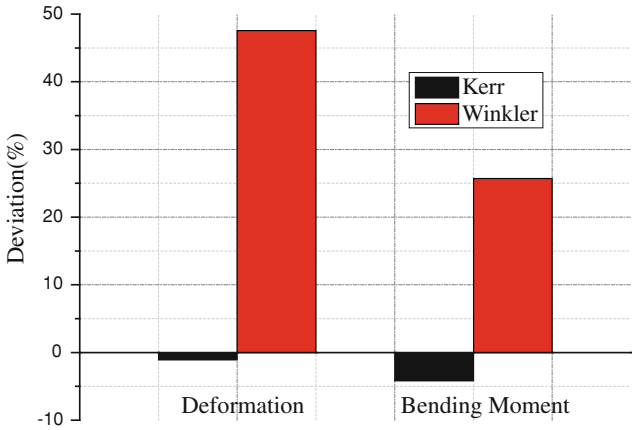

Fig. 8 Deviation between analytical and FEM results

3.1 Comparison Between Kerr and Winkler Foundation Model Under a Concentrated Load

Based on the proposed method, the deflection and bending moment of the pipeline under a concentrated load is calculated and a comparison is made as shown in Figs. 6 and 7. It is noted that the calculating parameters are shown in Table 1

Obviously, the deflection and bending moment of the pipe calculated based on Kerr foundation model are better in agreement with numerical results.

Furthermore, if a definition is given as

$$\text{Deviation} = (\text{Analytical results} - \text{Numerical results})/\text{Numerical results} \tag{33}$$

Then, the deviation of maximum deflection for Kerr and Winkler model is −1.05 and 47.55 %, respectively; and the deviation of maximum bending moment is 4.7 and 25.7 % respectively (as shown in Fig. 8).

3.2 Pipeline Deformation of Dapu Road Tunnel in Shanghai

In this section, the pipeline deflection due to shield tunnelling can be calculated using the proposed method in this paper. The calculating parameters are shown in Table 2.

Table 2 Calculation parameters

R/m	h/m	Z_0/m	ε_0	H/m	E_0/kPa	v	D/m	EI/kN m^2	E_0/kPa
5.5	25.5	3.9	0.005	21.5	11,312	0.3	1.8	4,837,562.5	11312

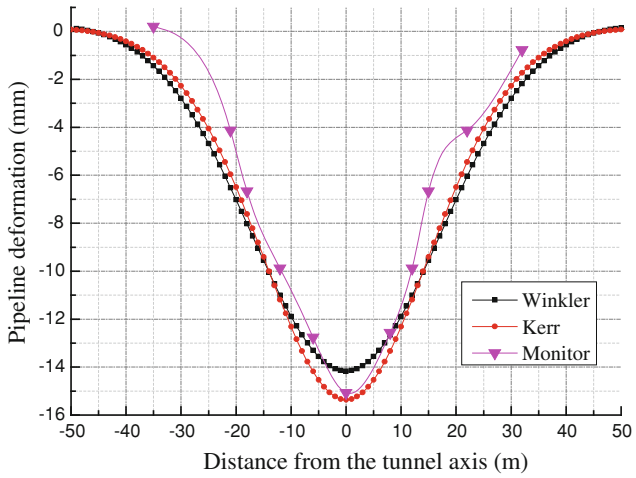

Fig. 9 Pipeline deformation due to shield tunneling

Figure 9 shows the monitoring results and analytical solutions based on Winkler model and Kerr model. It is noted that Kerr foundation model gives a better prediction on the deflection of the pipeline.

4 Conclusions

(1) The two-stage analytical method is a reasonable and effective way to estimate the pipe's response due to shield tunnelling as long as appropriate free-soil settlements and foundation model are adopted.

(2) The Kerr-type three-parameter elastic foundation model has an advantage in estimating the pipe's deflection and bending moments caused by shield tunnelling compared to Winkler foundation model as it could reflect the continuity of the foundation.

(3) Simplified elastic space method is a shortcut to obtain foundation parameters for its concise and convenience.

References

Attwell, P. B., Yeates, J., & Selby, A. R. (1986). *Soil movements induced by tunneling and their effects on pipelines and structures*. London: Blackie & Son Ltd.

Avramidis, I. E., & Morfidis, K. (2006). Bending of beams on three-parameter elastic foundation. *International Journal of Solids and Structures, 43*, 357–375.

Huang, X., Huang, H., & Zhang, D. (2012) Longitudinal deflection of existing shield tunnel due to above deep excavation. *Chinese Journal of Geotechnical Engineering,* (accepted for publication)

Kerr, A. D. (1964). Elastic and viscoelastic foundation models. *Journal of Applied Mechanics, 31*, 491–498.

Kerr, A. D. (1965). A study of a new foundation model. *Acta Mechanica, 1*(2), 135–147.

Kerr, A. D. (1985). On the determination of foundation model parameters. *Journal of Geotechnical Engineering, 111*(11), 1334–1340.

Klar, A., Vorster, T. E. B., Soga, K., et al. (2005). Soil-pipe interaction due to tunnelling: comparison between Winkler and elastic continuum solutions. *Geotechnique, 55*(6), 461–466.

Loganathan, N., & Poulos, H. G. (1998). Analytical prediction for tunneling-induced ground movements in clays. *Journal of Geotechnical and Geoenvironmental Engineering, 124*(9), 846–856.

Pasternak, P. L. (1954). *On a new method of analysis of an elastic foundation by means of two-constants*. Moscow: Gosudarstvennoe Izdatelstvo Literaturi po Stroitelstvu I Arkhitecture.

Selvadurai, A. P. S. (1979). *Elastic analysis of soil-foundation interaction*. NewYork: Elsevier Scientific Publishing Co.

Vorster, T. E. B., Klar, A., Soga, K., et al. (2005). Estimating the effects of tunneling on existing pipelines. *Journal of Geotechnical and Geoenvironmental Engineering, 131*(11), 1399–1410.

Wang, T., Wei, G., & Xu, R. (2006). Prediction for influence of tunneling on adjacent pipelines. *Rock and Soil Mechanics, 27*(s), 483–486.

Winkler, E. (1867). Die lehre von der elastizitat und festigkeit. Prague.

Zhang, Z., Huang, M., & Wang, W. (2009). Responses of existing tunnels induced by adjacent excavation in soft soils. *Rock and Soil Mechanics, 30*(5), 1373–1380.

Depositional History and Geotechnical Properties of Shanghai Clays

C. J. Wu, G. L. Ye, J. R. Sheng, and J. H. Wang

Abstract
Shanghai locates in the Yangtze River delta facing the East Sea. Shanghai clays (layer ②–⑥) has an average thickness of 30–40 m. They are sensitive marine clays with high water content and large void ratio. Almost all the underground structures are constructed within these soft clays. A re-summary of their depositional history and an investigation on their geotechnical properties will be useful for the deeper understand of the Shanghai clays. In this paper, the depositional process and environment of each layer of Shanghai clays is re-summarized first. Then the physical, mineralogy and mechanical properties of different layers are investigated by a series of laboratory tests. A comparison with the famous Asian clays, Japan Ariake clay and Bangkok clay is carried out. It is found that although three clays were deposited in the similar period, they show significant different properties.

Keywords
Soft clay • Depositional history • Geotechnical properties • Laboratory tests

1 Introduction

Shanghai locates in the Yangtze River delta facing the East Sea (Fig. 1). The quaternary sediment in Shanghai region has a depth of 200–400 m. The so-called Shanghai soft clays are the upper part of this sediment. Their average thickness is about 30–40 m. During the depositional process, Shanghai soft clays underwent the influences of the transgression-regression cycles and the Yangtze River that carries 464 million tons sediments every year. Due to the unique depositional environment, although they are classified as marine clays, they show different engineering characteristics from other famous Asian marine clays, e.g. Japan Ariake clay and Bangkok clay.

In recent years, many infrastructures such as metro lines, underground highways and municipal facilities are constructed within these soft clays. Most researches focused on the geotechnical properties of clays. There are few literatures describing the geological properties and the relation between the depositional history and the geotechnical properties. In this paper, an analysis on the relation between the depositional history and the geotechnical properties will be carried out to better understand the Shanghai clays.

2 Geological Setting

Shanghai area can be classified to four types of geomorphological units: tidal flat, estuarine-spit-sandy island, coastal plain, and lake-marshy plain, as shown in Fig. 1. The urban area and most of the rural area belong to the coastal plain.

Figure 2 shows cross profiles of the quaternary sediment in Shanghai region. Positions of these two profiles are shown in Fig. 1. The quaternary sediment has a depth of 200–400 m. It can be divided into four series in a sequence from the

C. J. Wu · G. L. Ye (✉) · J. R. Sheng · J. H. Wang
Department of Civil Engineering, Shanghai Jiao Tong University, Shanghai 200240, China
e-mail: ygl@sjtu.edu.cn

Y. Huang et al. (eds.), *New Frontiers in Engineering Geology and the Environment*,
DOI: 10.1007/978-3-642-31671-5_49,

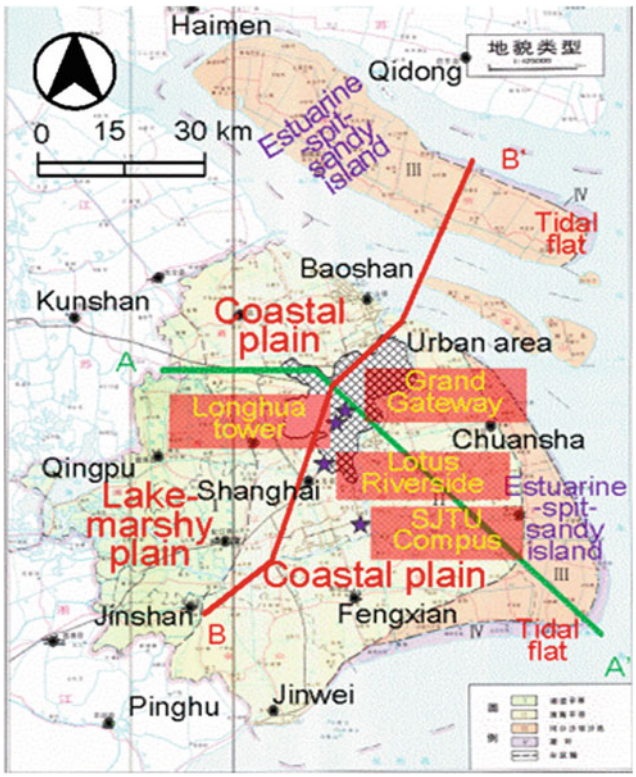

Fig. 1 Plan view of Shanghai area

bedrock to surface: lower Pleistocene series (Q1), middle Pleistocene series (Q2), upperPleistocene series (Q3) and Holocene series (Q4) (Zhang 2002). The Pleistocene series accounts for most portions of the quaternary sediment. It can be seen that these four series are almost horizontal distributed.

The ground within approximated 100 m depth is used to be divided into 11 layers by the engineering geologists. Each layer is further divided into several sub-layers. These 11 layers cover the Holocene series, upper Pleistocene series and partial middle Pleistocene series. Since most underground structures were constructed within the depth of 30 m, the mechanical properties of Shanghai clays has attracted the attentions of the geotechnical engineers.

3 Sea Level Changes through Geologic Time

During the most recent ice age (about 20 ka B.P.), the sea level was about 130 m lower than today, due to the large amount of sea water that had evaporated and been deposited as snow and ice in northern hemisphere glaciers.

The sea-level change curve representing the sum of eustatic sea-level change and local ground movement over the past 14 ka in Shanghai area is shown in Fig. 3 (Wei 1997). A rapid transgression, named as the Zhenjiangs Transgression in East China, was observed 12–7 ka B.P., which is equivalent to the worldwide Flandrian Transgression. The highest sea level 7 ka B.P. was about 5 m higher than present. After then, a slow regression started till now.

4 Sedimentary Process of Yangtze Delta

About 7.5 ka B.P., the huge amount of sediments brought by the Yangtze River deposited continuously. As the deposition rate became prominent, the Yangtze River delta came into formed gradually (Wang et al. 1981). As shown in Fig. 4, the sedimentary process of Yangtze delta can be divided into six successive stages (Li et al. 1980). The Yangtze River delta is divided into the delta plain and the coastal plain. Shanghai is located in the southern coastal plain, which deposited in a saline environment.

5 Depositional History of Shanghai Clays

From aforementioned eustatic change and sedimentation process of Yangtze delta, the depositional history of Shanghai clays can be obtained as following.

1. In the late of Pleistocene epoch (20–11 ka B.P.), the whole Shanghai area was over the sea level. Layer ⑥ and $⑤_{-4}$ were formed in lake or valley environment.
2. In the early phase of Holocene epoch (11–8 ka B.P.), the sea level rose up to +5 m. Layers $⑤_{-3}$–$⑤_{-1}$ were deposited in coastal or swamp environment.
3. In the middle phase of Holocene epoch (8–3 ka B.P.), the sea level turned to a slow decrease tendency, while still a little higher than today. Layer ④ and layer ③were deposited in a coastal-shallow sea environment.
4. In the late phase of Holocene epoch (3 ka B.P.～), the sea leave kept decreasing till today. Layer ② were deposited in a coastal-estuarine environment.

It can be seen that the layer ⑥ and $⑤_{-4}$ are diluvium clays, and layer $⑤_{-3}$～ layer ② are alluvium clays. Moreover, since layer ④ and layer ③ were deposited in marine environment, they may own strongest properties as marine clays.

6 Physical Properties of Shanghai Clay

The physical properties indexes of Shanghai clays obtained by laboratory tests are listed in Fig. 5. The geotechnical profile of Ariake clays and Bangkok clays obtained from literatures (Ohtsubo et al. 2000) are used for comparison.

The silt particle contents of Shanghai clays are more than 50 %, which are much more than those of Ariake and Bangkok clays. The sensitivities of Shanghai clays vary between 2 and 4, but those of Ariake clays and Bangkok clays are much larger.

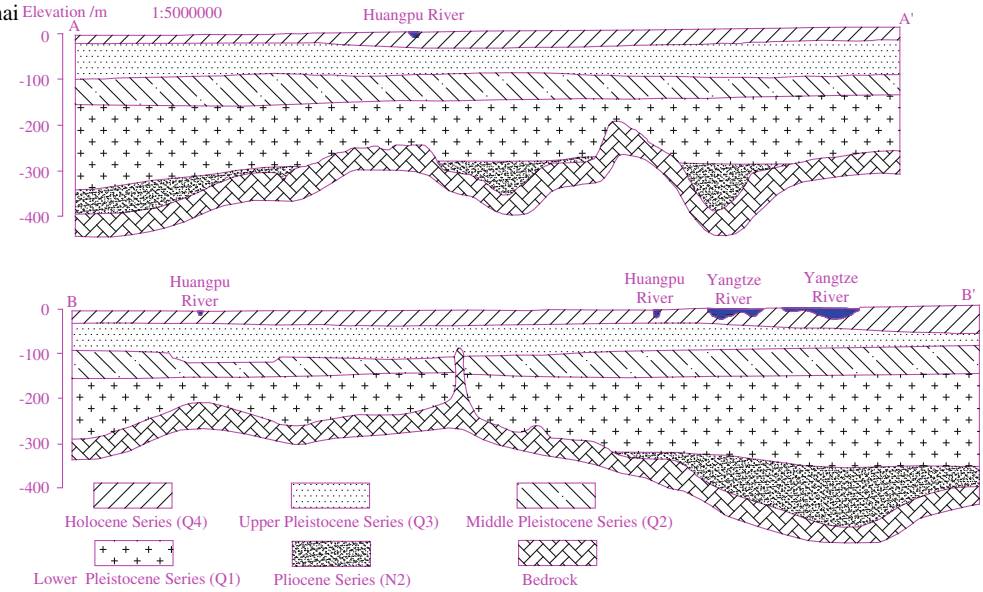

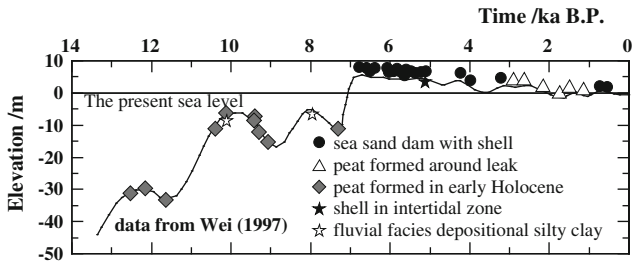

Fig. 3 Eustatic sea level change during Holocene in Shanghai area

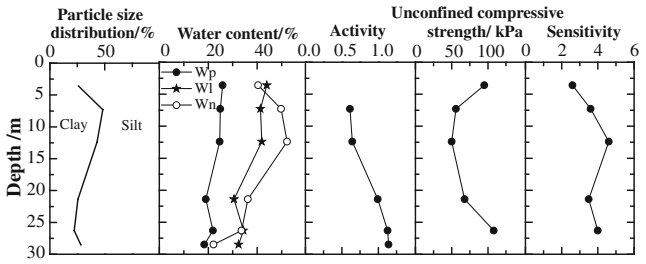

Fig. 5 Geotechnical properties of Shanghai clay profile

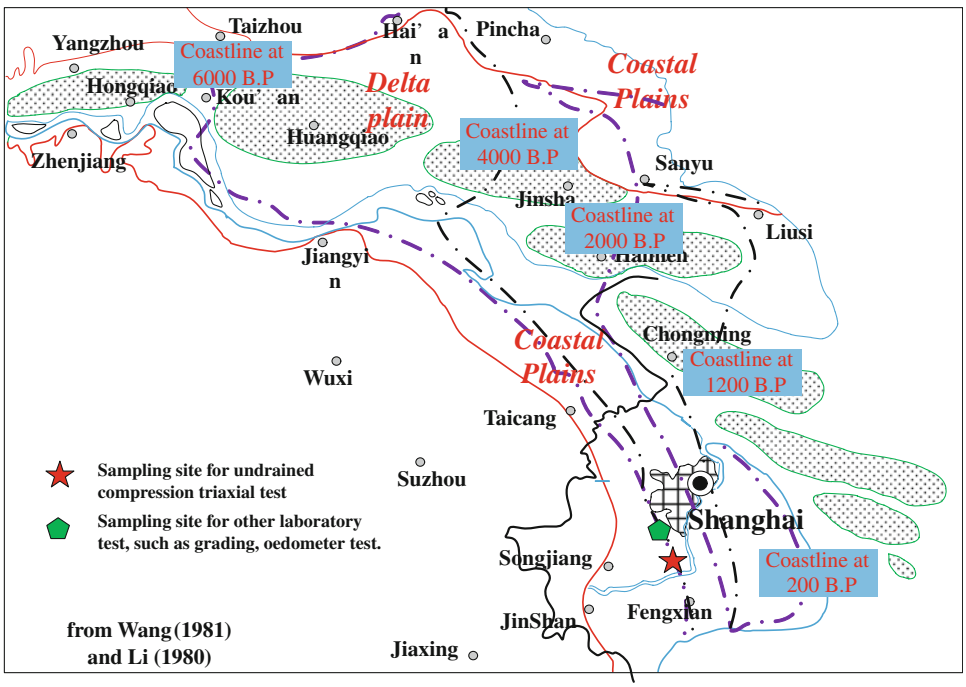

Fig. 4 Geographical division and sedimentary process of Yangtze delta

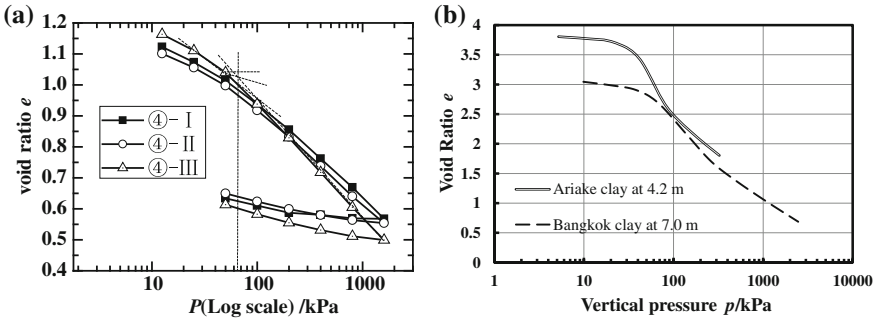

Fig. 6 Consolidation characteristic of Shanghai, Airake and Bangkok clays

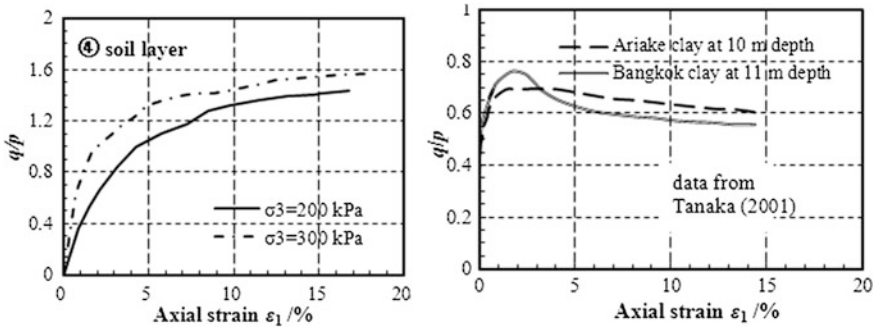

Fig. 7 Stress-strain relationship of Shanghai, Airake and Bangkok clays

7 Mechanical Properties of Shanghai Soil

Since layer ④ is typical Shanghai clay with the largest sensitivity, conventional oedometer tests and undrained triaxial compression tests were conducted on undisturbed layer ④ specimens. The specimens were obtained by a thin-wall tube sampler from two different sites shown in Fig. 4.

7.1 Oedometer Tests

In the conventional oedometer test for Shanghai clays, the load increment applied was twice as large as the previous load. Oedometer tests on Ariake and Bangkok clays were carried out with constant rate of strain (CRS). Typical $e - \log p$ curves of Shanghai, Ariake (Hanzawa et al. 1990) and Bangkok (Horpibulsuk et al. 2007) clays are shown in Fig. 6. Compression curves of Ariake and Bangkok clays showed very steep drop downs after a flat starting. While the curves of Shanghai clays show no obvious slope change. It indicates that the structure of Shanghai clays is relative weaker.

7.2 Triaxial Tests

Figure 7 shows typical stress–strain relations of Shanghai, Ariake and Bangkok clays (Tanaka et al. 2001). Since the confining stresses are different, the deviator stresses are normalized by the corresponding effective p to make the test results comparable. Since the strain-softening is typical behavior of structured clays, the triaxial tests also indicates that the structure of Shanghai clays is relative weaker than the other two clays.

8 Conclusions

In this paper the depositional history and environment of Shanghai clays were re-summarized, and the physical and mechanical properties were investigated by laboratory tests. The relation between the depositional history and the physical and mechanical properties was analyzed. Following conclusions can be obtained.

1. Comparing with the famous Asian marine clays, Ariake and Bangkok clays, the salinity of environment for Shanghai clay is relatively low.
2. Silt particle (75 to 5 μm) is the main component in Shanghai clays. While clay particle is predominant in Ariake and Bangkok clays.
3. From the oedometer tests and undrained triaxial tests, it can be seen that the structure of Shanghai clays is relative weaker than those of Ariake and Bangkok clays.

Acknowledgments The corresponding author would like to thanks Mr. Tadashi Hashimoto of Geo-Research Institute for his valuable discussion. The support of National Nature Science Foundation of China (Grant No.41002097 and 41172251) is also appreciated.

References

Hanzawa, H., Fuyaka, T., & Suzuki, K. (1990). Evaluation of engineering properties for an Ariake clay. *Soils and Foundations, 30*(4), 11–24.

Horpibulsuk, S., Shibuya, S., Fuenkajorn, K., & Katkan, W. (2007). Assessment of engineering properties of Bangkok clay. *Canadian Geotechnical Journal, 44*(2), 173–187.

Li, C., Wan, J., Xue, S., Guo, X., & Li, P. (1980). Holocene transgressive-regressive sequence in Yangtze delta area. *Chinese Journal of Geology, 4*, 322–330. (in Chinese).

Ohtsubo, M., Egashira, K., Koumoto, T., & Bergado, D. T. (2000). Mineralogy and chemistry, and their correlation with the geotechnical index properties of Bangkok clay: Comparison with Ariake clay. *Soils and Foundations, 40*(1), 11–21.

Tanaka, H., Locat, J., Shibuya, S., Soon, T. T., & Shiwakoti, D. R. (2001). Characterization of Singapore, Bangkok, and Ariake clays. *Canadian Geotechnical Journal, 38*(2), 378–400.

Wang, J., Guo, X., Xu, S., Li, P., & Li, C. (1981). Evolution of the Holocene Changjiang delta. *Acta Geological Sinica, 01*, 67–81. (in Chinese).

Wei, Z. (1997). Sea-level changes and environment evolution in Holocene of Shanghai area. *Shanghai Geology, 04*, 48–54. (in Chinese).

Zhang, A. (2002). Shanghai Geological Environmental Atlas: Editorial Board. Geological Publishing House: Beijing.

On the Using of Deformation Rates as Stability Control Parameters of PVD-Treated Soft Ground

Y. B. Gao

Abstract
The monitoring data of a real project in Shanghai show that using of displacement rates (vertical settlement rate at the center of embankment and the horizontal displacement rate at the toe of the embankment) as control parameters failed to give correct evaluation on the stability state of the PVD-treated soft ground. Embankments were stable at early construction stage when the observed deformation rates exceeded the control values, but suddenly collapsed even when observed deformation rates were lower than the control values. It is thought the complicated construction process used in field, degradation of the PVD drainage performance, and plastic hardening of soft soil caused by consolidation are maybe the reasons that caused this "abnormal phenomena". Because of the complexity of the displacement rates of PVD-treated soft ground, this traditional method should be used by caution. High quality ground stability analysis is essential for helping to make correct evaluation of the stability of PVD-treated soft ground.

Keywords
Soft soil • Deformation rate • Stability • PVD-treated soft ground

1 Introduction

Due to its low strength, soft ground is very easy to fail during construction of embankments on it, so stability monitoring of soft ground play a very important role in this kind engineering. Lots of experiences show that the deformation rate of soft ground will increase when it reaches failure, so in field monitoring, the vertical settlement rate $\Delta s_v/\Delta t$ at the center of embankment and the horizontal displacement rate $\Delta s_h/\Delta t$ at the toe of the embankment, are widely used as the control parameters of ground stability in this kind project. In China, the control values used are commonly 10–15 mm/d for $\Delta s_v/\Delta t$ and 5 mm/d for$\Delta s_h/\Delta t$ (Zou 2003; Yuan et.al. 2009). However, because the ground deformation rate can be influenced by many factors (Deng 2007; Zuo and Tu 2010), the efficiency of this method is argued by some authors (Ye et.al. 2010; Guo et.al. 2010). In this paper, based on several ground failure events occurred in a real project in Shanghai, the efficiency of this method for stability control of PVD-treated ground will be studied.

Y. B. Gao (✉)
Department of Geotechnical Engineering, Tongji University,
Shanghai 200092, China
e-mail: yanbin_gao@tongji.edu.cn

Key Laboratory of Geotechnical and Underground Engineering,
Ministry of Education, Tongji University,
Shanghai 200092, China

Y. Huang et al. (eds.), *New Frontiers in Engineering Geology and the Environment*,
DOI: 10.1007/978-3-642-31671-5_50,

2 Field Monitoring Data from a Real Project

2.1 Introduction of the Chenshan Botanic Garden Project

With a total area of 201 ha, Chenshan Botanic Garden locates in the southwest of Shanghai City. This project was completed by four construction stages. Several embankments with height of approximately 9 m were designed to be constructed. Soil layer distribution of the ground is shown in Fig. 1. The layer ③$_1$ and ③$_2$ are typical soft clay and their unconfined compression strength are only around 70 kPa. The total thickness of the soft soils is about 10 m. In order to accelerate the consolidation speed of the soft ground, Prefabricated Vertical Drains (PVD) were installed in the ground with a space of 1.5 m × 1.5 m and length of 12 m.

Field monitoring during embankment construction includes: lateral displacements s_v at the toe embankment, settlements s_h at the center of embankment, pore pressures and settlements in soil. The typical layout of monitoring instruments is presented in Fig. 2. The control value of the soft ground provided by designer is 10 mm/d for lateral displacement rates $\Delta s_v/t$ and 5 mm/d for settlement rates $\Delta s_h/t$ respectively.

2.2 Ground Collapse and Field Monitoring Data

The embankment in construction stage No. 1 was started to be constructed on Jun. 18, 2007 (see Fig. 3). When the embankment was being constructed from 7.5 to 8.0 m on May 6th, 2008, a total area of 1435 m^2 at the embankment surface collapsed suddenly. The collapse area was marked by bold dash line in Fig. 2. The point DZ8 (see Fig. 2) at the center of embankment settled about 1.1 m. The point BP11 (see Fig. 2) at the toe of the embankment uplifted 165 mm. A building adjacent to the embankment was made cracked by the movement of ground. These phenomena indicate that the soft ground was failure under embankment load.

Figure 3a, b show the $\Delta s_v/t$ at the center of embankment monitored by point DZ8, and the $\Delta s_h/\Delta t$ at the toe of embankment monitored by point BP11 in construction stage No. 1. Before the height of embankment reached 7.5 m, there are five times that $\Delta s_v/\Delta t$ exceeded the control value of 10 mm/d, and twice that $\Delta s_h/\Delta t$ exceeded the control value of 5 mm/d. However, in these conditions, the ground was stable and there was no sign of ground failure was observed in field. In contrast, in the several days before failure occurred on May

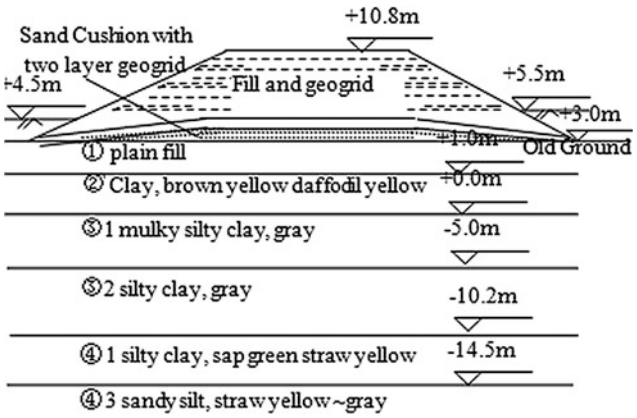

Fig. 1 Profile of soft ground and embankment

6th, the $\Delta s_v/\Delta t$ and $\Delta s_h/\Delta t$ was only 6–8 and 2 mm/d respectively, smaller than the control value of 10 and 5 mm/d. However, the PVD-treated ground failed abruptly when the construction continued on May 6th. Fig. 4

Because of this accident, in construction stage No. 4 of the project, embankment height was adjusted to 7.5 m. The ground was stable throughout the construction process. Figure 3 shows the typical monitoring data of $\Delta s_v/\Delta t$ and obtained in two monitor points. All measured $\Delta s_h/\Delta t$ is below the control value of 5 mm/d, but still there are six times the measured $\Delta s_v/\Delta t$ exceeded the control value of 10 mm/d.

Ground failure also occurred in construction stage No. 3 of the project when an embankment was constructed close to a river on March 31th, 2009. This collapse made three points at the toe of the embankment moved horizontally 843 , 729 and 269 mm respectively, and uplift 916, 715 and 530 mm respectively. In the several days before the ground failure, the monitoring data of $\Delta s_v/\Delta t$ and $\Delta s_h/\Delta t$ were only 6–8 and 2–4 mm/d respectively, which were apparently below the control values given by designer.

3 Factors Influencing on the Displacement Rates

In this part, factors influencing on the displacement rate of PVD-treated soft ground will be discussed. Three general factors are: (a) staged-construction characteristics; (b) ground consolidation characteristics; (c) shear stress level in soils. In real projects, the deformation rates of PVD-treated ground are in fact influenced by all these three kind factors, but the former two are very easy to be neglected. In the following, how these factors influence the displacement rates of PVD-treated soft ground will be discussed in detail. This will be helpful to explain the abnormal phenomena observed in field monitoring of Chenshan Botanic Garden project.

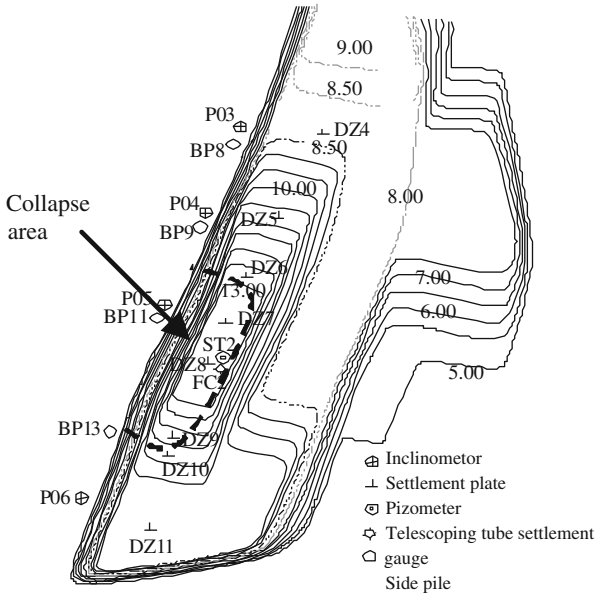

Fig. 2 Field monitoring arrangement

3.1 Staged-Construction Characteristics

Most embankments built on soft ground were staged-constructed. It is easy to understand that the displacement rates of ground are related to the loading speed used in staged construction. The displacement rates will be high if the load speed is quick, and it will be low if the load speed is slow.

The most used construction speed is 0.25 m –1.0 m each day, and various construction speeds are very often used in one project. Most designers like to use high construction speed at early stage because in this case embankment load is so small that the natural soft ground is safe enough when. When embankment is constructed higher and higher in late stage, lower construction speed is often used because the safety of ground decreases significantly. Another reason resulting in the adjustment of construction speed is the supply of fill material. When lack of fill materials in some conditions, construction speed has to be slowed down. Therefore, the displacement rates of ground high initially, and low lately.

3.2 Ground Consolidation Characteristics

During staged construction, soft ground can consolidate during resting period and the strength and stability of soft ground can increase with time. The permeability of natural soft ground is so small that the consolidation in a short period can be neglected. But with the installation of vertical drainage (such as PVD or sand column), permeability of ground will improve significantly. Therefore, displacement rates of PVD-treated ground will be much higher than that of natural ground, and the control values of the displacement rates for these two different grounds should be also different.

A factor influencing the consolidation speed of PVD-treated soft ground is the degradation of drainage performance with time. It will cause the ground deformation rates slow down gradually in several months after the PVD is installed. It may be one of the reason that the slower displacement rates is often observed in field in the lately stage of embankment construction.

Because of the high permeability of PVD-treated ground, consolidation will develop during construction and resting, and the void ratio of soft soil will decrease significantly. This will result in plastic hardening of soft soil. The plastic hardening of soil caused by consolidation will make the deformation rates decrease because of the increase of the modulus.

3.3 Shear Stress Level

According to the modern soil mechanics, the shear modulus of soil will decrease gradually when shear stress level (the ratio of shear stress τ to normal stress σ) increase up to its strength. Therefore, displacement rates of soft ground will increase with increase of stress level and reach a very high value when ground reaches failure. Therefore, displacement rates are used as the traditional control parameters to evaluate the stability of soft ground during embankment construction.

4 Conclusions and Advices

The monitoring data of Chenshan Botanic Garden project show that using of displacement rates $\Delta s_v/\Delta t$ and $\Delta s_h/\Delta t$ as control parameters failed to give correct evaluation on the stability of PVD-treated soft ground. The ground still keeps stable even when these two parameters exceed their control values, but it suddenly failed even when their values are blow the controlled values. For PVD-treated ground, the complicated construction process used in field, degradation of the drainage system with time, and plastic hardening caused by consolidated can influence the displacement rate of ground and they are maybe the reasons that caused this "abnormal phenomena".

In real projects, because the deformation rate of PVD-treated soft ground is so complicated, the method use displacement rates as control parameters will be very easy to give a wrong evaluation of the stability state of soft ground. Advices given here are: except by analyzing each monitor data carefully, such as pore-pressures and soil displacements, it is very necessary to carry out theoretical or numerical analysis that based on limit

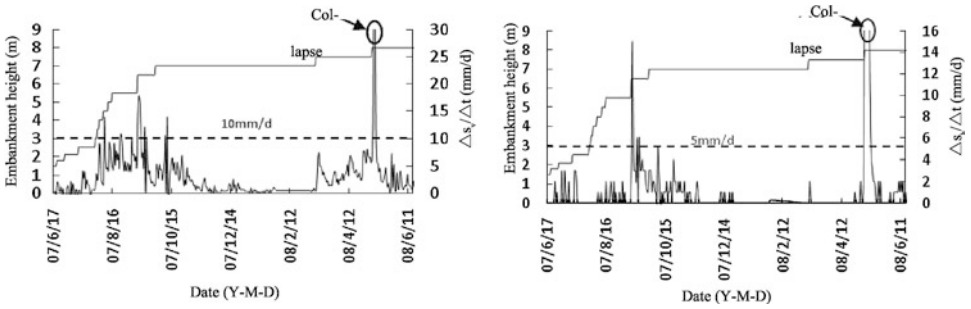

Fig. 3 Typical monitored deformation rates in stage No. 1. **a** Settlement rate measured at point, **b**Horizontal displacement rate measured at point

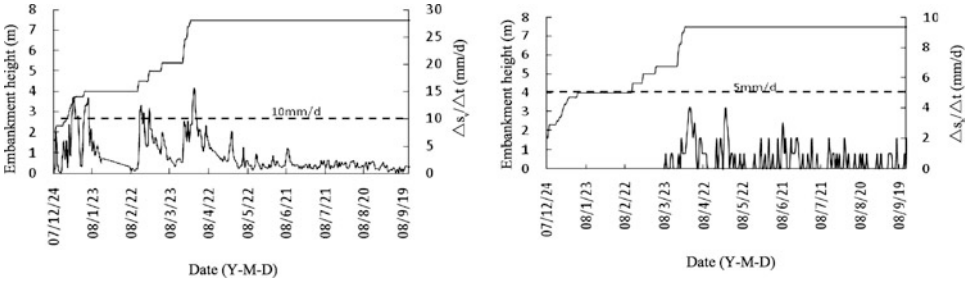

Fig. 4 Typical monitored deformation rates in stage No. 4.**a** Settlement rate measured at point 4-, **b** Horizontal displacement rate measured at point 4-

equilibrium method or stress path method to evaluate the stability of soft ground during construction. In order to improve the accuracy of the ground stability analysis, some important parameters, such as undrained strength of soft soil, consolidation degree of ground and pore-pressure in soil, are needed to be obtained by field monitoring data or high quality in situ tests.

References

Deng, S. Q. (2007). *Study relations between the earth filled speed of embankment and the soft soil ground distortion*. Nanjing: Hohai University.

Guo, Y. F., Liao, H., & Chen, J. (2010). Analysis on monitoring data and deformation characteristic of soft soil foundation dealt with plastic drain plate. *Subgrade Engineering, 148*(1), 9–11.

Ye, G. B., Guo, Y. F., & Ding, X. J. (2010). Discussion on monitoring system of stability of embankment on soft foudation. *Hydrogeology and Engineering Geology, 37*(1), 73–75.

Yuan, G. Q., Liu, H. J., & Yang, Y. Q. (2009). Dynamic safety monitoring of soft ground by subsidence and lateral displacement measurements. *Journal of Natural Disasters, 18*(3), 123–128.

Zou, J. (2003). *The roadbed reclamation trial of natural foundation for the second phase project of Cheng Gui Highway(Natural Science Edition)* . Sun Yat-sen University *42*(S3): 179–183.

Zuo, W., & Tu, W. J. (2010). Numerical analysis on the influence of filling speed on the soft soil embankment. *Journal of East China Jiaotong University, 27*(4), 18–21.

Application of Improved Vacuum Preloading Method in Tianjin Lingang Industrial Zone

C. Le, C. Xu, Y. W. Jin, and Y. Yang

Abstract

To make the soft clay consolidated and shorten the construction periods, vacuum preloading method has been widely used in coastal areas in China. However, the traditional vacuum preloading methods have some shortcomings in the treatment of coastal soft dredger fill. To promote the consolidation process of very soft soils, the traditional technique was improved by using new-type prefabricated vertical drains (PVDs) and directly connecting the vacuum tube to PVDs without sand drainage blanket. In this paper, the characteristics of the improved vacuum preloading technique were introduced, and the effectiveness of the new technique in improving the shallow soft soil foundation in Tianjin Lingang industrial zone were illustrated by test results. Results of the case study showed that the improved vacuum preloading method worked well and was more effective than the traditional one. The construction period was shortened and the bearing capacity of foundation soil was higher than that treated by the traditional vacuum preloading method in the same area.

Keywords

Coastal areas • Foundation treatment • Vacuum preloading • Less clogging prefabricated vertical drain (PVD) • Direct connection technique

1 Introduction

Characterized by high water content, poor permeability and low bearing capacity, the coastal foundation soil needs quite long periods to be consolidated. Vacuum preloading is one of a classical and popular method in practice (Indraratna et al. 2005). In China, vacuum preloading method is widely used in foundation treatment in coastal areas these years (Guan et al. 2011; Cao et al. 2011; Qi 2010), because it can shorten the construction periods, reduce the cost and greatly improve the engineering properties of soft soils.

In Tianjin Lingang industrial zone, the water content of the foundation soil was up to 80 % and the soil was mostly rheological, so that the traditional vacuum preloading was less effective than usual. This sort of soft soil was called "ultra-soft soil" (Cao et al. 2011). Traditional PVDs do not suit the characteristics of the soil there and the decrease of vacuum pressure in the sand drainage blanket makes the vacuum pressure in PVDs insufficient. As using PVDs as the tunnel to drain off pore water in the foundation soil and sand drainage blanket as medium to deliver it to vacuum tubes, PVDs and sand drainage blanket determine the drainage efficiency of vacuum preloading, the traditional

C. Le (✉) · C. Xu (✉) · Y. Yang (✉)
Department of Geotechnical Engineering, Tongji University, 1239 Siping Road, Shanghai 200092, P.R.China
e-mail: lechao2004@126.com

C. Xu
e-mail: axu@tongji.edu.cn

Y. Yang
e-mail: 2011yang@tongji.edu.cn

Y. W. Jin (✉)
Xinzhuang Town Dacheng Development Zone, Xintai Geotechnical Materials Company Ltd, Yixing 214267, P.R.China
e-mail: yxxintai@126.com

Y. Huang et al. (eds.), *New Frontiers in Engineering Geology and the Environment*,
DOI: 10.1007/978-3-642-31671-5_51,

Fig. 1 Less clogging prefabricated vertical drain

Fig. 2 Traditional vertical drain in China

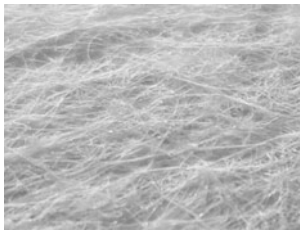

Fig. 3 Filter membrane of less clogging PVD

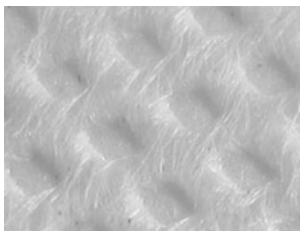

Fig. 4 Filter membrane of traditional PVD

method leads the undesirable result. The third problem was the cost of sand. For the policy of the environmental protection in coastal areas in China, the price of the sand rose sharply these years, which leads to the cost of sand drainage blanket greater than before.

In order to solve these problems, an improved vacuum preloading method patented by Xintai Geotechnical Materials Co., LTD in Yixing, Jiangsu, China was put into practice in Tianjin Lingang industrial zone. It consists of a special prefabricated drain, which is less clogging and breaking-resisted to ensure the vertical drains unclogged. A direct connection technique with four-way (or three-way) joints and hand-form connectors combining drains to vacuum tubes is designed to take the place of sand drainage blanket. Unlike the Beaudrain System, also called membraneless system (Chu et al. 2008), geomembrane is used as usual to seal the foundation soil so that the load of atmospheric pressure is fully used. Results of the case study showed that the improved vacuum preloading method worked well and was more effective than the traditionally used one. The construction period was reduced and the bearing capacity of foundation soil was higher than that treated by the traditional vacuum preloading method in the same area.

The improved vacuum preloading method was revised and used in other places in China. The application of Taihu Lake soil treatment (Jin et al. 2011), railway station soft foundation treatment (Shen et al. 2011) and Zhuhai West Station soft foundation treatment (Yang 2011) were also with good effect.

Two critical techniques of the improved vacuum preloading method: (1) less clogging PVDs and (2) direct connection technique were introduced, the construction application of the improved technique in Tianjin Lingang industrial zone was illustrated and the effect of this application was analyzed based on test results in this paper.

2 Critical Techniques

2.1 Less Clogging Prefabricated Vertical Drains

Less clogging PVD is a patented product. The new-type drains were originated from traditional PVDs which are widely used in vacuum preloading in China nowadays. Less clogging prefabricated vertical drains have similar appearance and size with the traditional PVDs as shown in Figs. 1 and 2, so that they can be set into the ground by same machines.

The less clogging PVDs consist of filter membrane and plastic core panel which were heat bonded together. This combination made about 50 independent channels to keep the ability of hydraulic conductivity. If some of the channels were clogged, others would still be clear and the PVD could work as usual.

The filter membrane was made of nonwoven fabrics. The fabrication technology is horizontal rolling and blended herding with short silk while the traditional technology is hot rolling with long silk. The filter membranes were shown in Figs. 3 and 4.

In Fig. 3, the whole membrane was permeable while the concave of the traditional membrane is impermeable in Fig. 4. Thus the permeating water amount per area of filter membrane of less clogging PVD is nearly two times as many as it of the traditional one.

To fit different soil and prevent clogging, filter membrane of the new PVD has different opening size. The equivalent opening size of the filter membrane is 75–150 μm. It can be

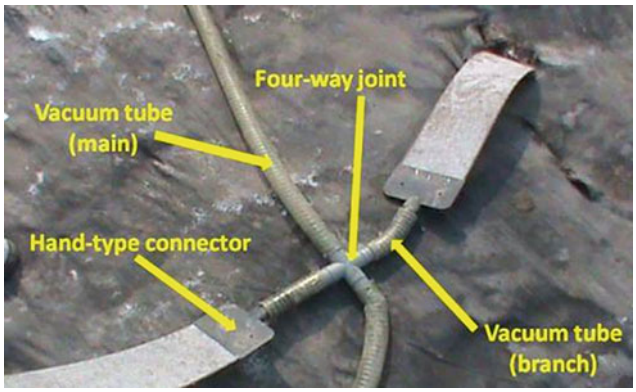

Fig. 5 Four-way joint, hand-type connector and vacuum tubes

reset according to the soil particle. It turned out that the measure was quite effective and the cases of silting were few in Tianjin Lingang industrial zone.

The core panel was made of polythene and polypropylene. It is 100 mm in width and 4 mm with thickness and has excellent anti-bending performance, which can be bend and folded without breaking at least for five times. It also has high lateral compressive strength so that it will not be squashed by the soil pressure. The anti-bending and anti-pressing performance ensured the drainage after they were set into the foundation soil and the proper functioning during the vacuum preloading periods.

The detail of less clogging PVD is listed in Tables 1 and 2.

2.2 Direct Connection Technique without Sand Drainage Blanket

Direct connection technique consists of four-way (or three-way) joints, vacuum tubes (main tubes and branch tubes), hand-shape connectors, geotextiles and geomembranes (four layers in all: woven geotextile, needle-punched geotextiles and two layers of geomembrane). The connectors and tubes were shown in Fig. 5.

Unlike the traditional vacuum preloading method which used sand drainage blanket as the medium to transmit vacuum pressure, direct connection technique can send the pressure from pump to PVDs through the tubes. It makes the vacuum degree in PVDs much higher than that of which used sand drainage blanket and provided higher vacuum pressure so that the drainage of pore water is more efficient.

Four layers of geotextiles and geomembranes were used in the new technique. Before PVDs were set into the foundation, one layer of woven geotextile was laid to prevent the influence of the soft soil and prepare for the construction. After the work of setting PVDs and connecting them with hand-type connectors, four-way (or three-way) joints and vacuum tubes, one layer of needle-punched geotextile was laid to separate them and the geomembranes above so that the geomembranes would not be punctured. At last, two layers of geomembranes were used to seal the area and ensured the vacuum degree under the membranes.

Fig. 6 Direct connection technique (set on natural soil surface)

Of course, if the natural foundation was enough for the construction, the first layer of woven geotextile could be left out to make the cost down. The PVDs, vacuum tubes, hand-type connectors and four-way (or three-way) joints could be set directly on the natural soil surface, as was shown in Fig. 6.

3 Application in Tianjin Lingang Industrial Zone

The construction site was located in Lingang industrial zone, Tianjin, China. The whole foundation treatment area was 49941 m^2, where the soil was mainly coastal soft dredger fill consisted of silt and soft clay. The water content of the soil was up to 80 % and it was mostly rheological. The physical and mechanical properties of each stratum were shown as follow: (1) Dredger Fill: The surface soil of the foundation was dredger fill with high compressibility and the average thickness was 11 m. The soil consisted of silt and soft clay, of which the water content was up to 80 % and it was mostly rheological; (2) Silt: It was marine deposit stratum with the average thick of 5 m. The silt was also rheological and with high compressibility. The water content of the soil was up to 60 % and the vane shear test strength was 13.8 kPa in average; (3) Silt Clay: It was also marine deposit stratum and the average thickness was 3.5 m. The clay was of high compressibility and flow status. The vane shear test strength was 24.5 kPa in average; and

Table 1 Detail of filter membrane

Material	Mass per unit area	Thickness	Tensile strength (dry)	Tensile strength (wet)	Equivalent opening size	Coefficient of permeability
Nonwoven fabrics	≥95 g/m^2	≥0.20 mm	≥20 N/cm	≥20 N/cm	75 ~ 150 μm	≥5 × 10^{-3} cm/s

Table 2 Detail of less clogging PVD

Material	Width	Thickness	Tensile strength	Tearing strength	Longitudinal flow capacity
polythene, polypropylene	100 ± 3 mm	≥4.0 mm	≥2.4KN /10 cm	≥50 N	>40 cm^3/s

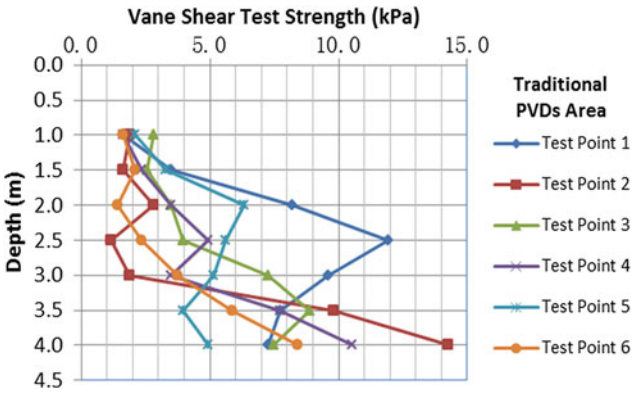

Fig. 7 Vane shear test strength of traditional PVDs area

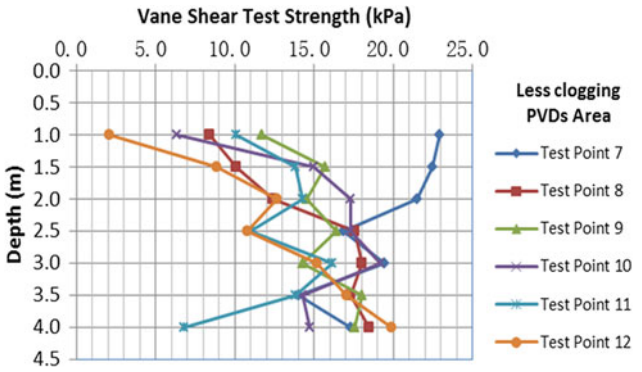

Fig. 8 Vane shear test strength of less clogging PVDs area

(4) Silty Clay: It was limnetic facies deposit stratum with the average thick of 11.5 m. The water content of it was 27 %. The clay was of medium compressibility and plastic status. The vane shear test strength was 42.8 kPa in average.

Since the special situation existed, the traditional vacuum preloading method used in this area got trouble: most of the PVDs were clogged by clay. And for the unsatisfactory effectiveness in early process, the driving machines could not work well on the soft ground so that many PVDs were broken off or set slant into the foundation. Finally, a lot of the constructions by traditional method could not meet the requirement of capacity or the construction periods. In order to solve these problems, the improved vacuum preloading method was put into practice in this area. After 2 months' shallow treatment and 2 months' deep treatment, the average water content of the foundation soil decreased from 80.0 to 33.4 %. At last, the performance was outstanding in contrast with those of the traditional method.

For the reason that the bearing capacity of natural soil was too low to support the construction machinery, the whole vacuum preloading construction was separated into two stages: the shallow vacuum preloading treatment and the deep vacuum preloading treatment. In the shallow treatment, a piece of woven geotextile was firstly laid on the soil surface so that the workers may stand on it and then begin to dig holes for the PVDs. In this stage, the panels were set into the foundation soil by man power and the depth of treatment was just 6 m. The purpose of the early stage was to improve the soil within 6 m so that the driving machines could work smoothly and stably in next process.

In the shallow treatment, the site was divided into two sections: Section I of 27706 m^2 and Section II of 22235 m^2. In Section II, there was a square area of 2500 m^2 where the traditional PVDs were used to compare with less clogging PVDs in the same condition.

The construction sequence of shallow treatment was carried out as follows: (1) Laying woven geotextile; (2) Setting less clogging PVDs on each 0.8 m by 0.8 m square grid to the depth of 6 m by man power; (3) Adding hand-type connectors to the top of each less clogging PVD; (4) Connecting the hand-type connectors and four-way (or three-way) joints with branch tubes, and then connecting these joints with main vacuum tubes; (5) Connecting main vacuum tubes to the collecting pipes which were connected with the vacuum pump; (6) Digging ditch around each section which were used to seal the area; (7) Laying needle-punched geotextile; (8) Laying two layers of geomembrane;

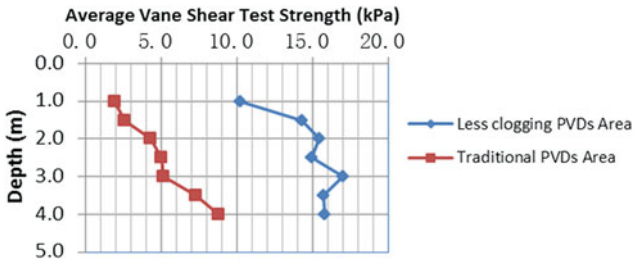

Fig. 9 The average vane shear test strength between different PVDs

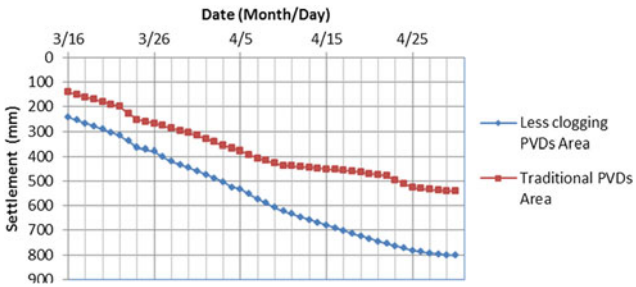

Fig. 10 The average settlement between different PVDs

(9) Depressing geomembrane in the ditch so as to seal the two sections; and (10) Starting the shallow vacuum preloading process.

After 2 months' shallow treatment, the water content in the vacuum preloading site which used less clogging PVDs (depth from 0 to 4 m) decreased to 40.4 % in average and the vane shear test was 14.8 kPa in average while the result of traditional PVDs was 5.0 kPa. The average settlement was 804.72 mm during the period while the result of the traditional panels was 543.5 mm. The vane shear test strength of traditional PVDs area and less clogging PVDs area was shown in Figs. 7 and 8.

The comparison results of vane shear test and settlement between using less clogging PVDs and traditional PVDs were shown in Figs. 9 and 10. Obviously, the effectiveness of less clogging PVDs was remarkable.

After the shallow treatment, the capacity of the foundation soil was enough for the work by the construction machinery which could set the PVDs deeper. That followed this stage is the deep treatment. In contrast with the shallow treatment, its aim was to make the capacity of the whole foundation soil greater than 60 kPa, the degree of consolidation greater than 90 % and the settlement less than 2.5 mm/d.

The area of deep treatment was only one section of 49941 m^2. The depth of the less clogging PVDs set into the foundation was 16.5 m and they were also set on each 0.8 m by 0.8 m square grid like those in the shallow treatment. Since the soil surface strength was enough for the

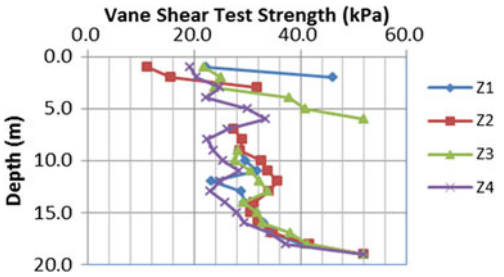

Fig. 11 Vane shear test strength after 2 months' deep treatment

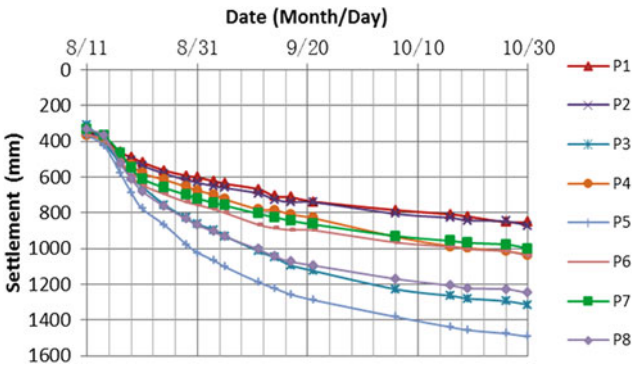

Fig. 12 Settlement during the deep treatment

work, woven geotextile were not used before the PVDs setting.

The construction sequence of deep vacuum preloading treatment was carried out as follow: (1) Setting less clogging PVDs on each 0.8 m by 0.8 m square grid to the depth of 16.5 m by driving machines; (2) Adding hand-type connectors to the top of each PVD; (3) Connecting the hand-type connectors and four-way (or three-way) joints with branch tubes, and then connecting these joints with main vacuum tubes; (4) Digging ditch around the construction area; (5) Laying needle-punched geotextile; (6) Laying two layers of geomembrane; (7) Depressing geomembrane in the ditch to the depth of 6 m and sealing the construction area; and (8) Starting the deep vacuum preloading process.

After 2 months' deep vacuum preloading treatment, the average water content in the site (depth from 0 to 16 m) decreased from 40.4 to 33.42 %, and the vane shear test strength in the site (depth from 0 to 16 m) was 26.2 kPa in average. 2 months later, the average settlement was 1107.59 mm of the deep treatment and the total settlement was 1912.31 mm of both shallow and deep treatment in the whole area. The results of vane shear test and settlement were shown in Figs. 11 and 12.

4 Concluding Remarks

Vacuum preloading was widely used in coastal areas in China these years. But each method has its own applicability. In very soft soils, the traditional PVDs were often clogged and the effectiveness of vacuum preloading could not meet the requirement of capacity. To promote the consolidation process, the vacuum preloading method was improved using new-type PVDs and direct connection of the vacuum tube to PVDs without sand drainage blanket (direct connection technique). The improved vacuum preloading method was put into practice in Tianjin Lingang industrial zone to solve the problem of coastal soft soils.

The result of the application in Tianjin Lingang industrial zone showed that the vane shear strength of the area after work was 20–30 kPa and the average settlement was nearly 2 m in all. The total construction period was just half a year and the requirement of the capacity of the foundation soil was met after work. Contrast to the traditional vacuum preloading, the improved method was effective and fit the special characteristics of the soil in this area.

For that the filter membrane of less clogging PVD can be reset according to the median particle diameter of the soil and the direct connection technique is more effective than sand drainage blanket, the improved vacuum preloading method can also be applied and fit in other coastal areas with very soft soils like Tianjin Lingang industrial zone.

References

Cao, Y. H., Li, W., Liu, T. Y. (2011). Surface-layer improvement technology for ultra soft soil by vacuum preloading. *Chinese Journal of Geotechnical Engineering*, *33*, Suppl.1.

Chu, J., Yan, S.W., Indraratna, B. (2008) Vacuum preloading techniques—recent developments and applications. geocongress 2008 (pp. 586–595). New Orleans.

Guan, Y. F., Tang, T. Z., Chen, H. J., Li, X. M. (2011). Field tests on shallow treatment of super-soft ground by vacuum preloading method. *Chinese Journal of Geotechnical Engineering* , *33*, Supp.1.

Indraratna, B., Sathananthan, I., Rujikiatkamjorn, C., Balasubramaniam, A. S. (2005). Analytical and numerical modeling of soft soil stabilized by prefabricated vertical drains incorporating vacuum preloading. *International Journal of Geomechanics*, 114–124.

Jin, Y. W., Zhang, Y., Wu, L. H., Qiao, B., Li, H., Bie, X. Q., Jia, S. J. (2011) Taihu lake, Tianjin, construction of silt clogging problems of consolidation. Journal of Lanzhou University (Natural Sciences) Vol. 47 Proceedings.

Qi, Y. Z. (2010). Case study on soft-clay foundation reinforcement by vacuum preloading. *Yangtze River, 41*(24)

Shen, Y. P., Yu, J., Liu, H., & Li, Z. (2011). Experimental study on air-boosted vacuum preloading of soft station foundation. *Journal of the China Railway Society, 33*(5)

Yang, Z. J., Yu, J., Liu, H., Jin, Y. W., & Jin, Y. J. (2011). Pressurized vacuum pre-compacting technology. *Railway Standard Design,* (8)

Observations on the New Trace of Quaternary Glacial Epoch in the Yangtze Three Gorges Area

Y. J. Li

Abstract
On the spot Investigation and Analysis for the Vestiges of Quaternary glacial epoch in the Tanjia Village, Badong County, Western Hubei. Inferences which has been formed early Pleistocene Epoch, and belong to the Long chuan glacial Epoch in Southern China.

Keywords
Quaternary Glacial Epoch • Early Pleistocene Epoch • Yesanguan

Recently, Quaternary glacial epoch remnant is discovered at the Tanjia Village of Yesanguan town in Badong County, which belongs to the west of Hubei province. The remnant is apart 102 km from the south of the Yangtze Rive, and the 318 National Highway and Shanghai–Chengdu Highway vertically pass through the U-shaped valley in Yesanguan. Here is a new development area of industry, and met a lot of issues in the engineering geologic exploration work.

Tanjia Village–Yesanguan–Huangjia Village is a valley with N20°E direction. The width of the valley bottom is about 500–1,000 m and the length of the valley is about 5,000 m. Also, the height above sea level of valley bottom is about 1,100–1,150 m. The elevation of the Lions Hill is 1341.6 m in the north and the elevation of the Sunjiatang is 1342.6 m in the south, which locate at the west-north bound of the valley. In parallel with, the mountain peaks at the east-south bound of the valley spread out, the elevation of the Tianjiping is 1455.4 meters in the north and the elevation of the Lingzihe is 1334.4 m in the south. The difference between the valley bottom and both sides of the peaks is about 200–300 m.

Our geological survey shows that the east side of the valley is the Daye formation limestone of Triassic period, the west side of the valley is the Maokou formation limestone of Permian. The two little faults distribute on the Yesanguan town, one trend is a direction of N20°E and the other trend is a direction of N340°W. The lengths of both faults are not more than 2,000 m.

The observation point of Quaternary glacial remnant is located at the north end of the U-shaped valley. Both the north and east sides of valley are extremely steep. The horizontal distance is less than 3,000 meters to Northward with the height difference of 500 m. The east side reaches to Sidu River, which has a horizontal distance of 8,000 m and a height difference of 800 m. Furthermore, observations of riegel topography on the east–west profile shows that the foundation bed is Silurian period shale, and the thickness of moraine is about 10 meters. Both east and west sides have in existence the incised wind gaps (Fig. 1). Field observations of the profile for mud gravel layer from bottom to top (Fig. 2), gives

(1) A brick-red sand and gravel interlayer, mélanges, few gravel and well rounded, gravel is quartz rock, about 2 meters thick;
(2) The yellow light red sand interlayer, 0.5 m thick;
(3) The brick-red clay interlayer, the gravel has a composition of quartz sandstone and is rounded with diameter up to 0.15 m, the interlayer of gravel and sand hybrid sedimentation, which is 0.5 m thick;

Y. J. Li (✉)
School of Civil Engineering, Wuhan University,
Wuhan 430072, China
e-mail: liyjwh@163.com

Y. Huang et al. (eds.), *New Frontiers in Engineering Geology and the Environment*,
DOI: 10.1007/978-3-642-31671-5_52,

Fig. 1 The glacial geomorphology of the Tanjia Village of Yesanguan town (on the south of Lions hill)

Fig. 2 The ice ridge terrain at the side of the profile. The soil-sand and soil-gravel layer is 120 °∠ 37°

Fig. 4 The top of profile has the erratic scratches and cut erosion phenomena

Fig. 3 The large quartz sandstone in the upper layer of profile, well rounded

(4) The red light yellow silt interlayer, the vertical stratification direction has small joint development, 0.3 m thick;
(5) The brick-red sand and gravel interlayer, 0.25 m thick, containing large quantities of black flint fragments with particle size of about 0.01 m, (up to 10 cm and well rounded). The angular and measurable occurrence of interlayer is 120 °∠37 °;
(6) The brick-red sand interlayer, 0.1–0.2 m thick;
(7) The clay gravel and sand and gravel interlayer, 2 m thick;
(8) The light yellow clay gravel interlayer is about 2 m thick. Most of the boulder is the nice rounded quartz sandstone and the large ones can be 60 cm × 30 cm × 20 cm and well rounded (Fig. 3). There are T-shaped scratches which are rounded due to the grinding of cutting erosion during the moving of the glaciers (Fig. 4).

In 1940, the famous Chinese geologist Li Siguang did a Geological Survey in the west of Hubei Province. He said, "This place has remnants of Quaternary glacial epoch all the place I seen and I reached. I am shocked by the large scale. There are enough evidences to prove the phenomena, and for which we couldn't image only by thought." The reference referred the place of Xianfeng, Enshi, Jianshi Badang (Lvcong Slope), Hefeng, Wufeng, Yidu, Yichang, etc. (Li 1940; Ma 1940). However, it is the first time to discover the Quaternary glacial epoch remnant at Yesanguan in Badong County.

The geomorphic terrain, bedrock strata, elevation, and moraine material characteristics of the remnants from Quaternary glacial in Yesanguan in the west of Hubei Province is highly similar to what was found at MaoTian in Jianshi county (Sun 1957). The moraine gravel is originated from the Devonian system or Carboniferous quartz sandstone rocks, while the contained fragments of flint is from the Permian System chert nodules or chert with limestone. The moraine locates at 1,000–1,200 m high, which belongs to the Three Gorges landforms Mountain in Zhoujianaoya period (development time before the N_2-Q_1). Therefore, to out knowledge, the moraine of Yesanguan should form at early Pleistocene period, which belongs to Longchuan glacial Epoch in Southern China.

References

Li, S. G. (1940). Brief accounts on quaternary glaciation in Western Hubei, Eastern Sichuan, Western Hunan and Northern Guangxi. *Geological Review, 5*(3), 171–184.

Ma, Z. T. (1940). Investigation of glaciation phenomena on the counties—Wufeng, Hefeng, Yichang and Yidu, Hubei province. *Geological Review, 5*(5), 423–429.

Sun, D. Q. (1957). *Summary for the relics of quaternary glaciation in China* (pp. 48–52). Beijing: Science Press.

Strengths of Unsaturated Silty Clay Used as Garden Hill Fill in Shanghai

Y. B. Gao, X. N. Ge, and J. Song

Abstract
The shear strength parameters of silty clay commonly used in garden landscape fill in Shanghai was investigated. Unsaturated soil samples were prepared with four different compaction degrees and three different water contents. Shear strength of these samples were obtained by direct shear tests, and the influences of compaction degree and water content on the strength parameters were studied. Water contents of a garden fill in Shanghai were investigated in site. Based on these works, advices on the strengths of the unsaturated fill considering the construction condition and climate effect were given.

Keywords
Garden hill • Silty clay • Shear strength • Unsaturated soil

1 Introduction

Due to the limitation of the natural topography at the plains, artificial hill filled by unsaturated soils are very popular, used in the garden of this kind area. The physical states (such as water content and compaction degree) will significantly influence the shear strength of unsaturated soils (Ling and Yin 2007); (Deng 2005). The strength theory of unsaturated soil is based on Mohr-Coulomb criterion and it is formulated as following (Fredlund and Rahardjo 1997); (Deng 2006):

$$\tau_f = C + (\sigma - u_a)\tan\varphi \quad (1)$$

where C is total cohesion, $\sigma - u_a$ is normal stress, φ' is effective friction angle. C is not constant and it will influenced by the density and saturation degree of unsaturated soil (Ye et al. 2006).

Silty clay is widely used in Shanghai as fill material of garden hills. The strengths of unsaturated Shanghai silty clay will be studied by laboratory testing, and the physical states of the fill in natural state will be investigated.

2 Fill Materials

Basic physical properties of silty clay commonly used in garden fill in Shanghai are shown in Table 1. The optimum water content of the Shanghai silty clay determined by compaction test is 17.9 % and its maximum dry density is 1.74 g/cm^3.

3 Test Programs

Artificial compacted samples were used for this study. They were prepared in three moisture states and four compaction degrees(K = 80, 85, 90, 95). The physical states of these

Y. B. Gao (✉) · X. N. Ge
Department of Geotechnical Engineering, Tongji University, Shanghai 200092, China
e-mail: yanbin_gao@tongji.edu.cn

Y. B. Gao
Key Laboratory of Geotechnical and Underground Engineering of Ministry of Education, Tongji University, Shanghai 200092, China

J. Song
Gansu Communication Plan Design Institute, Gansu 730030, China

Y. Huang et al. (eds.), *New Frontiers in Engineering Geology and the Environment*,
DOI: 10.1007/978-3-642-31671-5_53,

Table 1 Basic physical properties of Shanghai silty clay

Parameters	Values
Specific gravity G_s(g/cm^3)	2.73
Natural water content ω (%)	34.0
Natural unit weight γ (kN/m^3)	18.7
Liquid limit ω_L	37.3
Plastic limit ω_p	22.7
Plasticity index I_p	14.6
Optimum water content ω_{op} (%)	17.9
Maximum dry density ρ_{dmax} (g/cm^3)	1.74

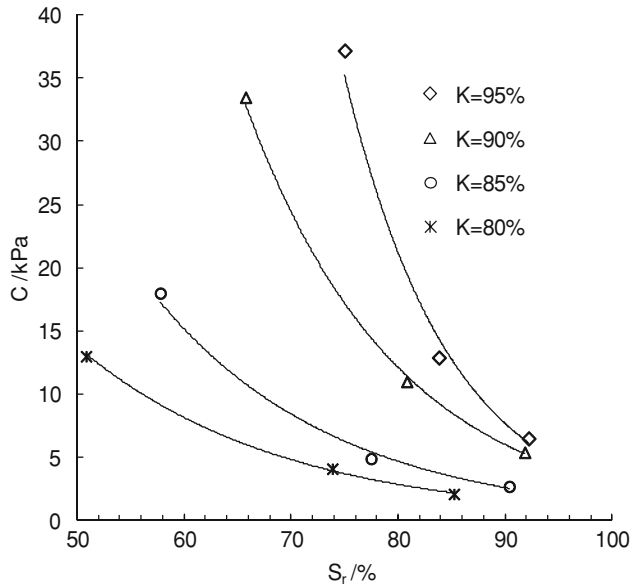

Fig. 1 Total cohesion C of unsaturated silty clay

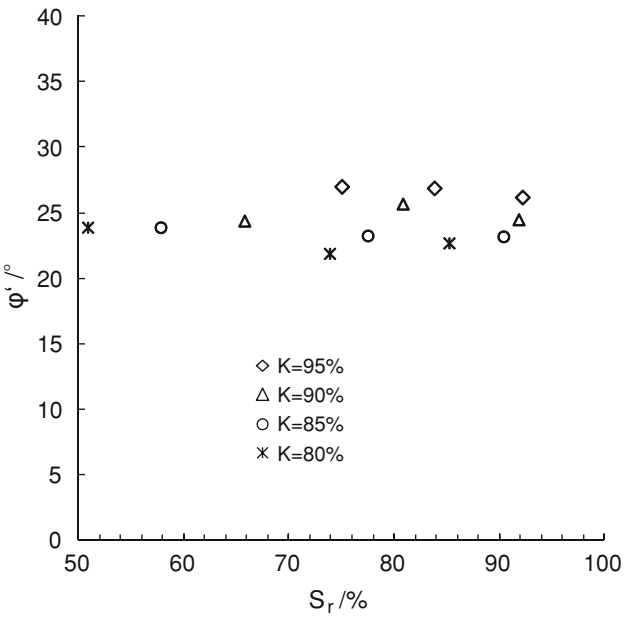

Fig. 2 Effective internal friction angle of unsaturated silty clay

samples were shown in Table 2. The strengths of these unsaturated soils were obtained by quick direct shear tests. The shear rate used in quick direct shear tests is 0.8 mm/min. Each test contains four samples, corresponding to vertical pressures p = 50, 100, 200 and 400 kPa. By these tests, the influence of moisture condition and compaction state on the strengths of silty clay can be obtained.

4 Test Results

4.1 Total Cohesion C

Figure 1 shows the influence of degree of compaction degree K and saturation degree S_r on total cohesion C of the unsaturated silty clay. It is obvious that saturation degree have a significant influence on the total cohesion C. The total cohesion C decreases with increasing of saturation degree. When the saturation degree is over 90 %, the total cohesion of unsaturated soils is only several kilopascals. The total cohesion C is also influenced by compaction degrees. It increases with increasing of compaction degrees. With increase of saturation degrees, influence of compaction degrees on total cohesion C will decrease.

4.2 Effective Internal Friction Angle φ'

Figure 2 gives the influence of saturation degree and compaction degree on the effective internal friction angle φ'. It was observed that the variation of effective internal friction angle φ' with the change of water content S_r is very small and it can be neglected. However, increasing of compaction degree K can increase the effective angle of internal friction. When compaction degree K changes from 80 to 95 %, internal friction angle φ' increases from 22 to 27° and the average effective internal friction angle is 24.5°.

Table 2 Physical state of artificial compacted samples

Compaction degree K (%)	Dry density ρ_d (g/cm^3)	Water content ω (%)	Saturation degree S_r (%)
80	1.39	17.9	50.8
		26	73.8
		30	85.2
85	1.48	17.9	57.8
		24.0	77.5
		28.0	90.4
90	1.57	17.9	65.7
		22.0	80.8
		25.0	91.8
95	1.65	17.9	75.0
		20.0	83.8
		22.0	92.2

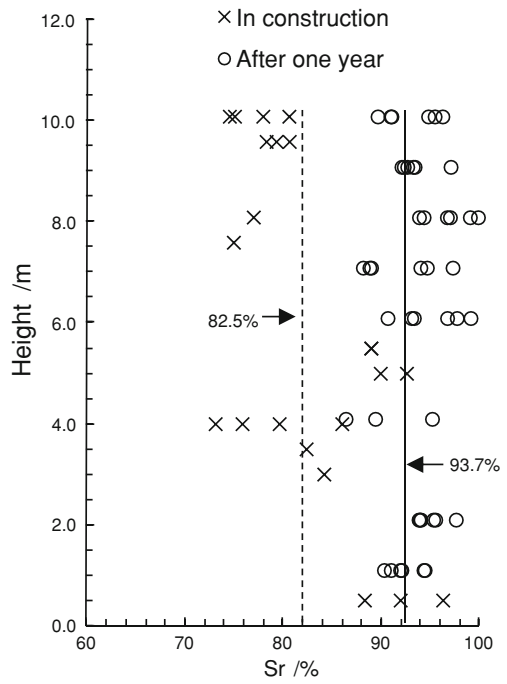

Fig. 3 Saturation degrees of a real garden hill

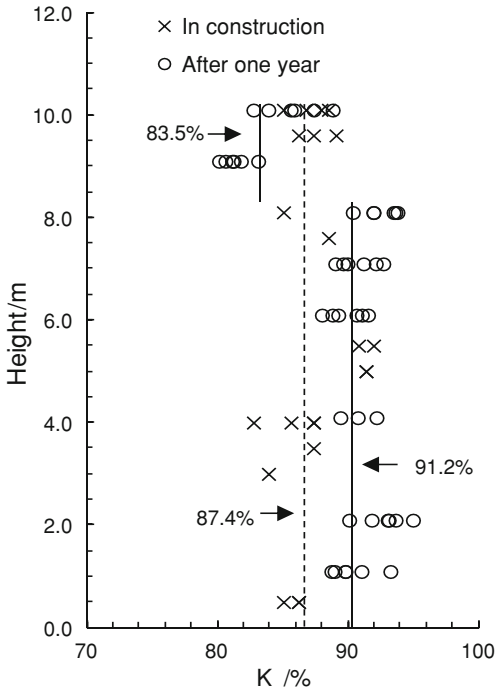

Fig. 4 Compaction degrees of a real garden hill

5 Physical States of Garden Hill Fill

In order to know the real state of moisture and density of garden hill fill in natural state, field sampling were conducted at different depths of 1 hill in Chenshan Garden in Shanghai after it was constructed one year. Then, the physical parameters such as water content and density were measured in laboratory. The saturation degree K and compaction degree S_r of the fill were shown in Figs. 3 and 4 respectively, and they were compared with the recorded data in construction. The saturation degrees S_r of the unsaturated soil in construction are higher and average saturation degree is 82.5 %. Shanghai belongs to north subtropical monsoon climate. Its mean annual precipitation is about 1103 mm. After being built a year, in the mountain, average saturation degree of mountain filling increases to 93.7 %. The compaction degrees K in construction were very low and the average value is 87.4 %. After 1 year, average compaction degree increase to 91.2 %. The

saturation degree of garden landscape in shanghai present here increased in the entire depth. It is possible because the high permeability caused by low compaction degree and high saturation degree.

6 Strengths Used for Stability Analysis

According to results of direct shear tests conducted under different compaction degrees and saturation degrees of silty clay commonly used in garden hill fill in Shanghai, and the field investigation of physical states of a real hill in Chenshan Garden in Shanghai, some proposals about determination of the unsaturated strength parameters of silty clay in stability analysis of garden hill are provided as following:

(1) The total cohesion C of Shanghai silty clay decreases significantly with the increase of saturation degree K. Because of the humid climate condition in Shanghai, the saturation degrees of hill fill are as high as 90 % and total cohesion C is very small in this condition.
(2) The effective internal friction angle φ' is between 22 and 27^{o} when the compaction degree K changes from 80 % to 95 %. Considering the compaction degrees of real fill are un-homogenous very much, it is advised that the average effective internal friction angle 24.5^{o} is used in design.

References

Deng, W. (2005). Experimental methods for shear strength parameters of embankment fill. *Technology of Highway and Transport*, (5): 7–11

Deng, W., et al. (2006). Stability technology of highway slope.Beijing: China Communation Press.

Fredlund, D.G., Rahardjo, H. (1997). Unsaturated soil mechanics. Chen, Z., Zhang, Z., Chen, Y., et al. Translation. Beijing: China Architecture and Building Press

Ling, H., & Yin, Z. (2007). Variation of unsaturated soil strength with water contents. *Chinese journal of Rock Mechanics and Engineering, 26*(07), 1500–1503

Ye, W., Chen, B., Bai, Z., Zhu, H., & Bai, Y. (2006). Tri-axial shear strength of shanghai unsaturated soft clay. *Chinese Journal of Geotechnical Engineering, 28*(3), 317–320

Index

Y. Huang et al. (eds.), *New Frontiers in Engineering Geology and the Environment*,
DOI: 10.1007/978-3-642-31671-5, © Springer-Verlag Berlin Heidelberg 2013

Author Index

Y. Huang et al. (eds.), *New Frontiers in Engineering Geology and the Environment*,
DOI: 10.1007/978-3-642-31671-5, © Springer-Verlag Berlin Heidelberg 2013